Strain-softening of concrete under multiaxial loading conditions

STRAIN-SOFTENING OF CONCRETE UNDER MULTIAXIAL LOADING CONDITIONS

JAN G.M. VAN MIER

Strain-softening of concrete under multiaxial loading conditions

Druk: Dissertatiedrukkerij Wibro, Helmond, Telefoon 04920-23981

STRAIN-SOFTENING OF CONCRETE UNDER MULTIAXIAL LOADING CONDITIONS

PROEFSCHRIFT

TER VERKRIJGING VAN DE GRAAD VAN DOCTOR IN DE TECHNISCHE WETENSCHAPPEN AAN DE TECHNISCHE HOGESCHOOL EINDHOVEN, OP GEZAG VAN DE RECTOR MAGNIFICUS, PROF. DR. S. T. M. ACKERMANS, VOOR EEN COMMISSIE AANGEWEZEN DOOR HET COLLEGE VAN DEKANEN IN HET OPENBAAR TE VERDEDIGEN OP DINSDAG 20 NOVEMBER 1984 TE 16.00 UUR

DOOR

JOHANNES GERARDUS MARIA VAN MIER

GEBOREN TE 'S-HERTOGENBOSCH

Dit proefschrift is goedgekeurd door de
promotoren: Prof.ir. B.W. van der Vlugt
en
Prof.dr.ing. H.W. Reinhardt

Acknowledgement

The author wishes to thank all who have contributed to the completion of this thesis.
The discussion with Prof. K.H. Gerstle of Colorado University during the entire research is greatfully acknowledged.
The help of Mr. Johan van den Oever in building the data acquisition system is very much appreciated.
Thanks are also due to Mrs. Muriel Norder for her prompt and careful typing of the manuscript.

Part of this research was funded by STW (Stichting Technische Wetenschappen) under grant nr. EBW 33.0462, and is gratefully acknowledged.

Aan mijn Ouders

Aan Ria

CONTENTS page

1. Introduction 1

2. Survey of literature 6
   2.1. The behaviour of concrete at the submacroscopic level 6
   2.2. Different stages in progressive fracture 13
   2.3. Softening behaviour under compressive or uniaxial tensile loading conditions 17
   - concrete in uniaxial compression 17
   - geomaterials in uni- and triaxial compressive loading 22
   - strain-softening of concrete in uniaxial tensile loading 24
   - strain-softening of concrete in triaxial compressive loading 29

3. Experimental technique 32
   3.1. Boundary conditions 32
   - load application systems 35
   - choice of load application system 39
   3.2. Triaxial experimental machine 40
   3.2.1. loading frame 40
   3.2.2. load and displacement measurement 47
   3.2.3. test-control 49
   3.2.4. data acquisition system 53
   3.2.5. calibration of brush deformations 56
   3.3. Manufacturing method for the specimens 57
   - specimens 57
   - materials used 59
   3.4. Summary of experiments 61

4. Uniaxial Experimental results 63
   4.1. Introduction to statistical analysis 63
   4.2. Influence of the manufacturing method of the specimens 65
   4.2.1. experimental design for uniaxial tests (series 2/3) 65
   4.2.2. statistical analysis of results 69
   - strength results 69
   - energy requirement 71
   4.2.3. uniaxial stress-strain behaviour 73
   - initial anisotropy 73
   - replication of uniaxial stress-strain curves 77

page

4.2.4. Fracturing in uniaxial compression 80
- observations from surface measurements 80
- post-peak surface strain measurement 84
- lateral surface strains 87

4.3. Deformation measurement - results of "10-series" 88
4.3.1. Experimental design for uniaxial tests (series 10) 89
- measuring devices 94
4.3.2. Statistical analysis of strength results 94
4.3.3. Deformation results 95
4.3.4. Some further comments on fracture in uniaxial compression 102

4.4. Size effect in uniaxial softening 109
- description of experiments 109
- experimental results 111

4.5. Concluding remarks 117

5. Multiaxial experimental results 118

5.1. Triaxial experimental design 118
- measuring devices 122

5.2. Experimental results 122
5.2.1. Response of constant displacement-ratio tests 123
5.2.2. Strength results 126
5.2.3. Multiaxial stress-strain behaviour 131
- influence of minor principal stress 131
- influence of intermediate principal stress 133
- tension-biaxial compression stress-ratio experiments 134
5.2.4. Failure-modes 136
- observations/triaxial compression 136
- further observations and classification of failure modes 142
- failure in the tension-biaxial compression region 145
- volume change 146
5.2.5. Initial anisotropy 150
5.2.6. Behaviour of concrete under multiaxial cyclic loading 152
- description of experiments 154
- deformation measurements in biaxial cyclic tests 156
- tangential stiffness in the major compressive direction 158
- mechanism of unloading and reloading 162
- dilatancy in cyclic experiments 166

page

5.3. Final remarks 166

6. Some aspects of constitutive modelling 171
6.1. Structural changes in concrete subjected to external mechanical loading 172
- isolated micro-cracking 174
- combined cracks 182
- macro-cracking 184
6.2. Characterisation of damage 186
- comments on previously developed models 187
- some results of crack detection experiments 192
6.3. Final remarks 199

7. Rotation of loading-axes with regard to the material-axes 205
7.1. Description of experiments 206
7.2. Results of rotation experiments 211
7.2.1. Response of a cylindrical mode rotation test 211
7.2.2. Comparison of 90^{o} planar and cylindrical rotation tests 216
7.2.3. Small angle rotations 220
7.3. Final remarks 225

8. Retrospective view and conclusions 227

Samenvatting 231
References 233

Appendices
A1. Uniaxial test results, series 2 and 3 245
A2. Uniaxial results, series 10 and 15 253
A3. Calculation of pre-loading for constant displacement-ratio tests 261
A4. Biaxial experimental results (series 5 - 6) 263
A5. Triaxial experimental results (series 8 - 9) 268
A6. Boundary shear due to bending of brush-rods 330
A7. Results of rotation tests (series 7) 335

In science there is progress in the sense that some *terra incognita* becomes passable and is consequently raided by some new development, but the distinctive feature of science is that in the process we make up new *terra incognita* ourselves. In that process, there is no progress, but this process might be called progress itself. Science is not the quest of reaching *Ultima Thule* , but the perpetual race of Achilles who pushes the turtle a little bit further in front of him so that he can race a little bit longer. It is an enjoyable race to run.

H.O.K. Kirchner

1. INTRODUCTION

Since the introduction of finite element methods for the analysis of reinforced concrete structures, much emphasis has been laid on the development of constitutive models for the constituent materials and their inter-relations. In the Dutch 'concrete mechanics' project /55,57,163/, a breakdown in 'basic building stones' was made as indicated in fig. 1.1.
Material models for plain concrete under multiaxial conditions and reinforcing steel, the bond zone and the crack zone (aggregate interlock and dowel action) should be incorporated in numerical models /18,19,56/, in order to compute realistic response of reinforced concrete structures.

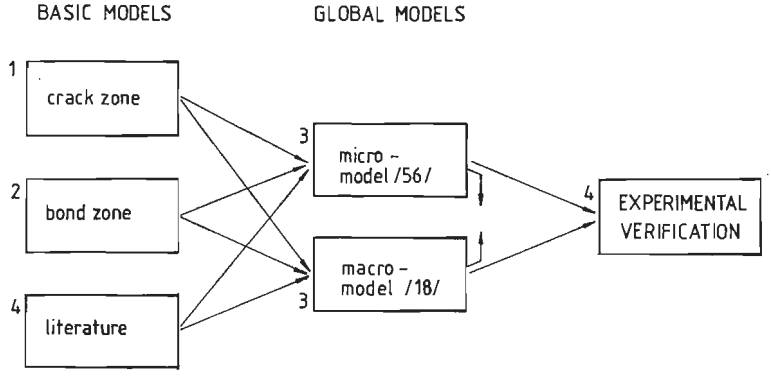

Fig. 1.1. Concrete mechanics project.

The concrete mechanics project is an on-going cooperative research program between the Dutch technical universities of Delft and Eindhoven, the Rijkswaterstaat, a division of the Netherlands Ministry of Transport and Public Works, and the Institute for Applied Scientific Research on Building Materials and Building Structures (TNO-IBBC). The first phase of the project, which ended in 1981, was concerned mainly with the development of material models for use in computer programs with the restriction of short term (static) loading.
The second phase which is in progress presently, puts more emphasis on off-shore applications (cyclic and sustained loading).

The problem of triaxial non-linear behaviour has so far been approached by means of a literature study. Current constitutive laws for plain concrete (hardening plasticity with various yield surfaces /19/, and the model developed by Link for biaxial loading in /56/) were adopted.

The description of non-linear triaxial behaviour is currently one of the main topics of research. The fact that, in 1983, two major symposiums (*) were organized on the topic illustrates its importance.
The increased demands with regard to general applicability of constitutive models is mainly due to the increasing complexity of modern concrete structures. New areas of application arise such as ocean structures, nuclear containments, tall buildings and large span bridges. Also the tidal surge barrier, which is presently under construction in the Eastern Scheldt, is a fine example of ever expanding boundaries of application of concrete as a structural material.
The above mentioned examples are concerned with structures that are situated in environments that impose complicated and uncommon loading histories to the material.

Not only are these huge unusual structures a reason for the growing general interest in non-linear triaxial behaviour of concrete, but also, safety considerations of beams and slabs subjected to combined shear-loading and bending moments, rely on assumptions related to concrete stress-strain behaviour. In analysing failure conditions (for example rotation capacity of plastic hinges in beams /36/), the descending branch of the stress-strain curve comes into play.
In the introductory report of the 1981 IABSE Conference in Delft, Eibl /44/proposes for future research: "A realistic investigation of the descending branch of the concrete constitutive law, including the rotational capacity of RC-slabs and RC-beams", and further, "Another interesting and still discussed technical problem is combined bending and shear in webs and flanges of T-beams. Although further tests are necessary especially for cases where failure is due to exceeding compressive strength, finite element methods based on realistic RC-behaviour could be very helpful".

In the same introductory report, Eibl /44/ states: "The fact that a priori known experimental results, especially load-deformation relations can be described after the experiment has taken place, should not be overestimated. Everybody doing such calculations knows how many parameter changes are possible and somtimes done to gain such data - fit".

(*) International Conference on "Constitutive laws for Engineering Materials", ed. C.S. Desai, and R.H. Gallagher, Tuscon (Az.), January 10-14, 1983.

William Prager Symposium on "Mechanics of Geomaterials: Rocks, Concretes, Soils", ed. Z.P. Bazant, Northwestern University, Evanston (Ill.), September 12-15, 1983.

Prediction competitions, such as the one organised by Collins of Toronto University /35/ are very appealing in this context. From the results of this competition it was concluded that very simple models can produce predictions just as good and just as bad as very complex models. Also it was concluded that the behaviour of concrete under non-proportional load paths is not very well understood.

In fact this is in agreement with considerations made by Blaauwendraad in his inauguration at Delft University. He stated that - for the time being - mechanics models are sufficiently developed, but further material properties should be obtained. And as Drucker states /43/: "Experiment is essential, it is vital and it is creative. Over the years, experiment alone provides the basis for the refinement and extension of existing theory and the development of new theory". However, Finite Element Methods provide a new and powerful tool which is helpful especially for research purposes (for example see /117/).

It is in the scope of this research to provide for additional multiaxial stress-strain data for concrete. Servo-controlled testing devices in combination with very stiff loading frames, provide new material data in addition to earlier predominantly load-controlled data. Earlier post-peak data was obtained mainly for uniaxial loading in tension /47,129/ and compression /126/, and more recently also very scarce for triaxial compression paths using conventional triaxial cylinder tests /1,79/. In this report, the results are shown of the very first experiments with cubical specimens, using a three-fold servo-control in a multiaxial apparatus. Major emphasis is laid on the study of non-proportional load-paths and the conditions for failure.

In evaluating stress-strain data for concrete, it must be realised that "the deformability and resistance to fracture under various conditions require for their real understanding and interpretation in terms of the internal structure of the material" /50/. An extensive study of the micro-structural changes in concrete subjected to external uniaxial compressive loading was carried out by Stroeven /152/. Macroscopic observations from the usual material tests, using cubes and cylinders, should be related to processes acting on a smaller size scale.

Most constitutive models 'simply' relate macroscopic stress and strain, and the material body is considered as a continuum. Simply adopting models, previously developed for materials with different internal structure, based on similarities at the macroscopic level is hazardous and, in principle, can lead to a wrong model.

Such a model may predict the response of common material tests successfully, but is likely to fail under different loading histories. An approach relating micro- and macro processes, in principle, can be based on energy-concepts. In this context however, it is important to decide which information or processes are important for describing macro-behaviour.
In view of the complicated internal structure of concrete such an approach is certainly not easy. A balance should exist between the effort expended and the accuracy obtained.
For example in determining stiffness degradation due to a process of distributed micro-cracking, it may be sufficient to analyse the effect of a single micro-crack and their mutual interactions, in order to obtain a 'smeared model' by means of a well chosen averaging process.
Possibly such an approach may lead to sufficiently accurate predictions, instead of taking into account aggregate positions and crack extension processes as detailed as possible (see for example /170/).
In principle a theory with 'internal memory' is required. As progressive cracking occurs under increasing external load, an approach using fracture mechanics would seem to be indicated. The application of fracture mechanics to concrete was first discussed by Glücklich /53/, and has been developed into a field of general interest.

In this thesis the above considerations are discussed in relation to the experimental results obtained. It is emphasized that, as far as theory development is concerned, only some first thoughts are presented. Main purpose of the study is to obtain further experimental stress-strain data for concrete under multiaxial load histories, including strain softening (i.e. the failure conditions), and to try to understand the governing phenomena. The experimental results are discussed critically in relation to the experimental technique that was adopted.

- short description of the contents of this thesis -

In chapter 2, a rather limited survey of the literature is given, regarding current knowledge on internal structural changes, typical 'failure-boundaries' and strain-softening. Since little information is available regarding strain-softening of concrete under multiaxial conditions, the discussion is limited to softening in uniaxial compression and tension.

In chapter 3 an extensive description of the adopted experimental technique is given. The construction of the triaxial cubical machine is explained. Furthermore test control, measuring devices and data aquisition system are described.

At the end of chapter 3, the manufacturing method of the specimens, and a complete review of the experimental program is shown.

Chapter 4 gives a review of the uniaxial compression results. Relatively many uniaxial tests were carried out in order to study the influence of the applied manufacturing method. Great emphasis is laid on the deformation measuring system too. Finally some results are shown regarding size effects in uniaxial softening.

In chapter 5, the main triaxial experimental results are shown. Major emphasis is laid on stress-strain behaviour under triaxial conditions including the softening branch, but also on observed rupture modes in relation to the stress-strain diagrams.

Chapter 6 discusses some very preliminary thoughts on constitutive modelling. The use of damage models, relating internal structural changes and macroscopic phenomena is discussed. Also some 'smearing methods' are examined. Important in the discussion is to decide if a continuum description of triaxial concrete behaviour is acceptable, or whether a discrete model is required.

In chapter 7, some additional experimental results following so-called 'rotation-paths' are shown. Also some very first small angle rotations using the pre-load/saw method are indicated. The results are discussed in relation to chapter 6.

2. SURVEY OF LITERATURE

In this chapter, a short review of literature is given. The survey is rather limited, while an extensive study was reported before /103/. In section 2.1 some attention is given to the behaviour of concrete at the submacroscopic level. Further in 2.2, typical boundaries in the fracture proces are discussed, both for uni- and triaxial loading. Finally in 2.3 stability models regarding strain-softening in compression are discussed. Also, some theories for tensile fracture are mentioned.

2.1. The behaviour of concrete at the submacoscopic level.

Concrete is often modelled as a two- or three phase material. We can distinguish between an aggregate phase and a cement-matrix phase which is built up from the smaller aggregate particles and the bonding constituent cement. Also a large amount of pores (air voids) is present.
The ratio between the subsequent constituents will influence the deformational properties of the concrete-mix and the final strength. Next to these internal-structure related variables, a large number of external factors will influence the observed behaviour too. For small-sized tests on cubical or cylindrical specimens, for example used for the determination of the strength and deformational properties of the material, these other factors are loading-rate, specimen-size, moisture-conditions, temperature, etc.
This study is confined to static (short-term) loading (loading rate $\dot{\varepsilon} \sim 10^{-5}$/sec or $\dot{\sigma} \sim 5.10^{-2}$ N/mm^2/sec), and moisture and temperature effects are excluded.

At this point a definition of the different size-levels should be given. In accordance with Mihashi and Wittman /105/ and later re-defined by Wittmann /169/the following three groups can be distinguished:

1. Macroscopic level,
   The characteristic length is in the order of 100 mm or more, properties to be studied are those for a continuum, that is average stress- and strain and non-linearity of mechanical properties. The corresponding engineering models should be presented preferably in such a form that they can be used immediately in numerical analysis.
2. Submacroscopic level or meso-level,
   The characteristic length is in the order 1 to 10 mm. Typical phenomena to be studied at this level are crack-formation and fracture mechanism. It is

obvious that the average stress and strain and the non-linearity of the mechanical properties at the macroscopic level will be largerly influenced by phenomena acting at this level.

3. Microlevel,
   Characteristic length in the order of 10^{-1} mm or less. Also here we may assume that the behaviour at the lower levels will be affected by mechanisms which are typical for this level. Physical and chemical processes will be active at this level. Models at this size level are called material science models.

It is an experimental fact that faults in concrete such as pores and micro-cracks are present before any loading is applied. (see for instance Stroeven /152,153/ and micro-crack studies performed at Cornell University /71,141,142,146,156/). A crack is defined as a discontinuity of which the boundaries were in an initial parallel position when crack formation occurred.

The micro-cracks mentioned before are at the submacroscopic level. With the fluorescenting technique, original developed by Forrester /49/, Stroeven /152/ showed that before any loading is applied to the specimen, already 50% of the total crack length at peak-stress-level (macro-level) was present. Only cracks with length exceeding 1 mm were taken into account. These micro-crack studies were carried out using uniaxial compressed prismatic specimens. After a specimen was loaded to a certain stress-level, the fluorescenting dye was applied at the specimen-surface and was allowed to dry, before the loading was released. After the specimen was completely dried, photographs were taken of the treated surface, in UV-light. One of Stroeven's photographs is shown in fig. 2.1.

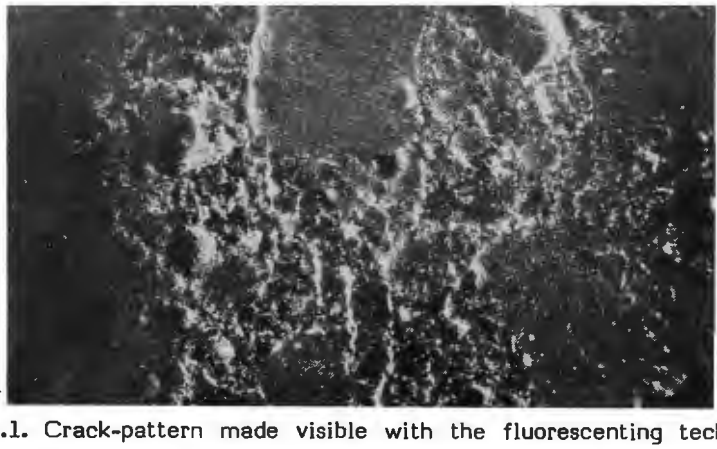

Fig. 2.1. Crack-pattern made visible with the fluorescenting technique (after /152/)

In a concrete system, the cracks, or better weaker planes will develop mainly under the larger aggregate particles. These 'weak planes' are the result of bleeding, shrinkage and temperature difference during the hardening process of the concrete. (fig. 2.2).

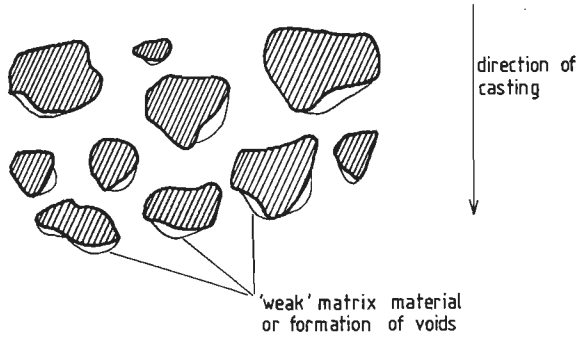

Fig. 2.2. Accumulation of weak planes under large aggregate-particles.

The effect of initial anisotropy on the uniaxial tensile strength was reported by several investigators /74,147,171/. A decreasing tensile strength was measured when loading was applied parallel to the direction of casting rather than perpendicular. Similar results were reported by Hughes & Ash /74/ for uniaxial compression on a low strength concrete.

- Crack-propagation and fracture of concrete -

Due to high tensile stress concentrations in the specimen, produced by interaction between larger aggregates and voids /77,128/, cracks may initiate and propagate in concrete under uniaxial compressive loading (fig. 2.3).

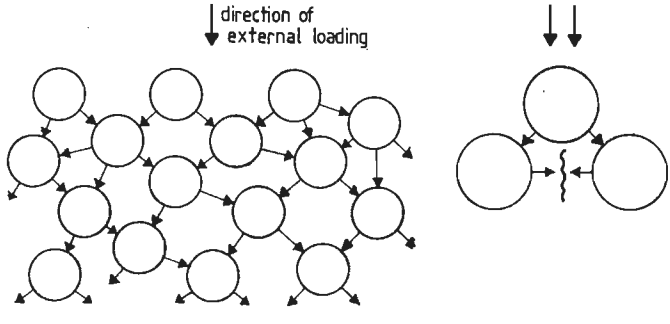

Fig. 2.3. Interaction between large aggregates, after /128/.

The micro-cracks are found to appear at the interface aggregate-cement matrix, and when loading is increased, tend to propagate along the aggregate surfaces. /143,71,152/. The findings that cracks initiate and propagate along the larger aggregate interfaces is consistent with research by Alexander, Wardlaw & Gilbert, /2/ on the nature of the aggregate-cement matrix bond. In normal strength concrete this bond between two phases is generally considered as the "weakest link" in the concrete structure.

In general three types of micro-cracks are distinguished: 'bond-cracks' at the cement-matrix aggregate interface, 'mortar-cracks' which run through the matrix material, and 'aggregate-cracks' /71,91,156/. As was reported by Stroeven /152/, mortar cracks also were observed to run along the interfaces of the larger sand-grains. Accordingly a better classification would be interfacial cracking (including all cracks at the aggregate-cement paste interface) and paste-cracking.
In a recent study on crack-formation and propagation in high-strength concrete, by Carrasquillo et. al. /26,27/, a classification in simple-cracks and combined cracks was proposed. The simple-cracks are isolated micro-cracks in either of the three above mentioned fashions, whereas combined cracks are formed from two or more simple-cracks.

The first link between micro-crack-propagation and stress-strain behaviour of concrete was made by Hsu et.al. /71/. Changes observed at the microscopic stress-strain behaviour of cylinders under uniaxial compressive loading, were accompanied by changes in crack-density and crack-mode. From cylinders, loaded to a certain strain-level, thin slices were cut (perpendicular to the direction of loading), and after dyeing, the micro-crack-length and modes according to the first classification were determined. In figure 2.4, three crack-maps and the governing stress-strain relation are shown.

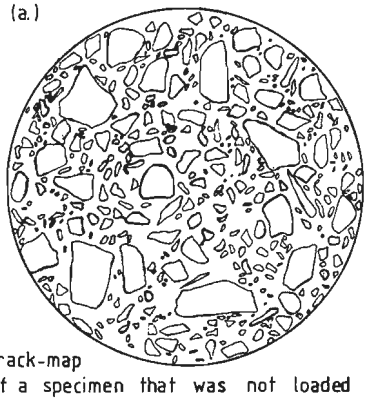

crack-map
of a specimen that was not loaded

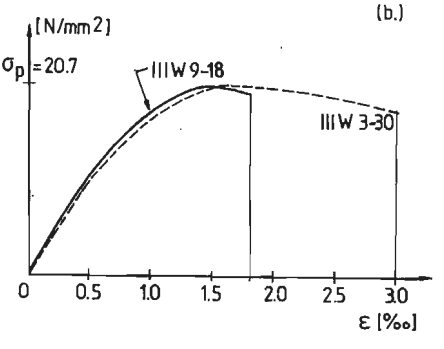

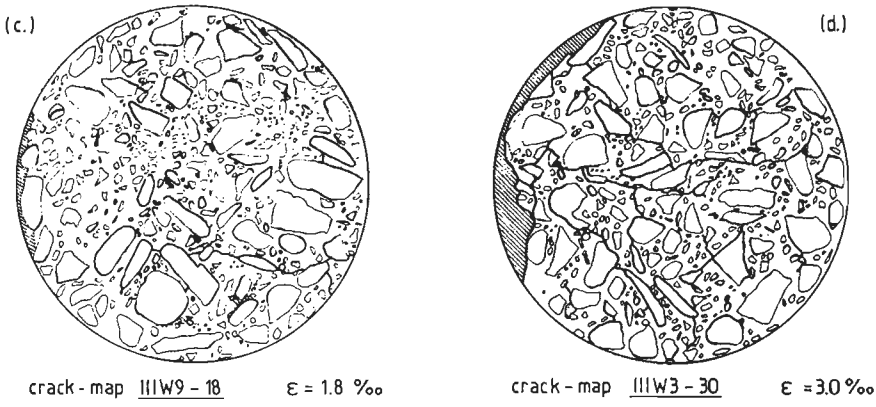

Fig. 2.4. Hsu et.al./71/, crack-maps at 0, 1.8 and $3^{o}/oo$.

At zero-strain level, only a number of bond-cracks are observed. With increasing strain, bond-cracks started to grow as soon as a stress-level of approximately 30% of ultimate was reached. The increase of bond-cracks (amount and length) was accompanied with a deviation of the macroscopic stress-strain curve from linearity. Further increasing of axial strain, showed a progressive accumulation of bond-cracks and at 70 - 90 % of ultimate load, mortar cracks started to propagate, and also crack-bridging was observed. Finally at a strain level of $3\,^{o}/oo$, a complete deterioration of the concrete structure occurred. In this stage the cracks only remained stable when an increase of strain was accompanied by a decreasing stress. The so-called softening branch was measured by Hsu et.al. /71/, while the loading-frame was stiffened by placing two springs parallel with the concrete specimen. In the descending branch of the stress-strain curve, the energy released by the macro-cracks could be taken by these springs. In section 2.3 some more attention is given on these aspects. The length of bond- and mortar cracks at several strain-stages is shown in table 2.5.

Strain ($^{o}/oo$)	0	- 1.2	- 1.8	- 2.4	- 3.0
Total aggregate perimeter (mm)	382.5	385.3	375.2	332.7	344.2
Total bond crack length (mm)	47.5	55.1	75.2	55.4	100.6
Percentage of perimeter cracked	11.9	14.3	20.0	16.6	29.2
Total mortar crack length (mm)	0.28	2.03	3.43	5.05	15.62

Table 2.5. Hsu et.al. /71/, bond-crack and mortar-crack length with increasing axial strain.

The load-level, where severe mortar-cracking starts, is often refered to as critical stress. At this level, a reversal in the volume strain vs. stress diagram is observed. Similar observations were made by Stroeven /153/. The minimum volume boundary is closely connected with a sharp increase of the load-induced portion of crack-surface per unit of volume. He concludes that phenomenological behaviour on the macro-level is directly related to the average structural changes. The observations of Stroeven /153/ are depicted in figure 2.6. The volumetic strain-stress curve is shown in the upper part, the increase of load-induced crack surface is shown in the lower part of the graph.

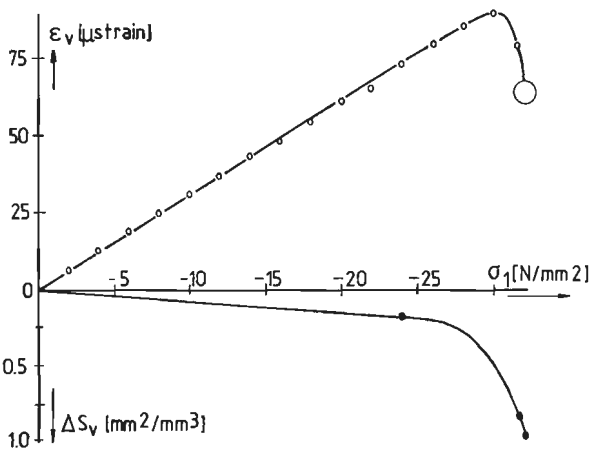

Fig. 2.6. Volumetric strain ($\varepsilon_v = (\varepsilon_1 + \varepsilon_2 + \varepsilon_3)/3$) and specific crack surface area versus applied axial stress after /153/.

Stroeven further states: "Rupture can now be interpreted in structural terms. A small but gradual, though discontinuous, rising of crack length and number is observed in the first stage of loading. During the second stage the dominating mechanism consists in joining of cracks".
The observations of Stroeven /152/, are consistent with the recent investigations by Carrasquillo et.al./26/. Indeed it seems that the joining of separate micro-cracks is a major step in the rupture propagation of concrete.
The minimum volume boundary was reported by numerous investigators, using different techniques. The above mentioned observations on changes at the micro-structural-level is one way. /71,152,91,156/. Other possibilities are direct surface-strain measurement /38,13/, or accoustic emission /139,132/.

The above mentioned results, reflect the behaviour of uniaxial compressed specimens. Crack-detection also was done on triaxial loaded cubes by

Krishnaswamy /91/. For a stress combination $\sigma_1 < \sigma_2 = -3.5\ N/mm^2 < \sigma_3 = -3.0\ N/mm^2$. The length of bond-and mortar cracks was determined at six different loading-levels. In figure 2.7 a comparison is made between the crack-history of a uniaxial compressed specimen, and a triaxial loaded specimen. At 80% of the maximum stress-level, identical crack-densities are measured (colored dye technique) for the uni- and triaxial loaded cubes. The higher strength in triaxial compression is the result of delayed micro-crack propagation. Also for the specimen loaded in triaxial compression, a fast increase of micro-crack density is observed at 80% of ultimate stress, indicating the existence of a minimum volume. No fiction reducing measures were taken in the crack-detection tests reported by Krishnaswamy. (see also chapter 3.1).

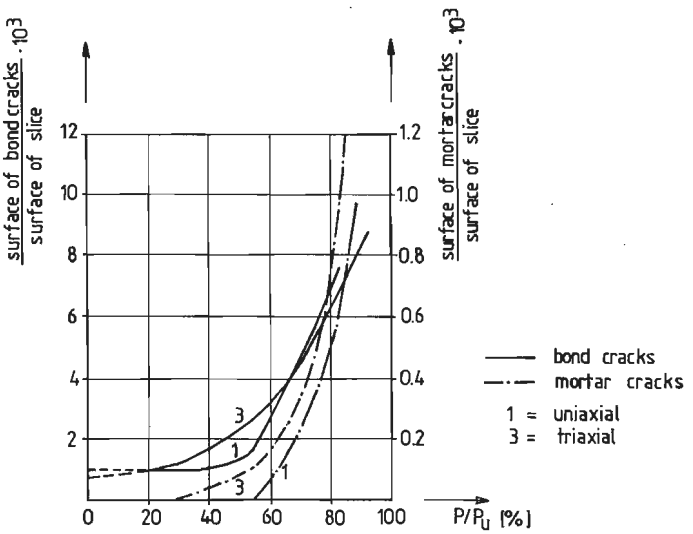

Fig. 2.7. Micro-crack development under uni- and triaxial compression, after /91/.

The above mentioned crack-detection techniques make use of X-rays /146,26/, fluorescenting dye /49,39,152,153/, or simple colored dye /71,91/, in order to visualise the micro crack structure. Recently, at much higher resolutions, crack detection was carried out on cement-paste and mortar specimens using a Scanning Electron Microscope by Darwin & Attiogbe /37/. Crack-densities obtained at a 1250 x magnification showed to be a factor ten larger than the conventional X-ray and dyeing techniques. In figure 2.8 the results of Darwin & Attiogbe obtained for cement-paste with varying w/c-ratio are shown. Also plotted are the results from Carrasquillo et.al./26/, obtained with the X-ray technique for high strength concrete.

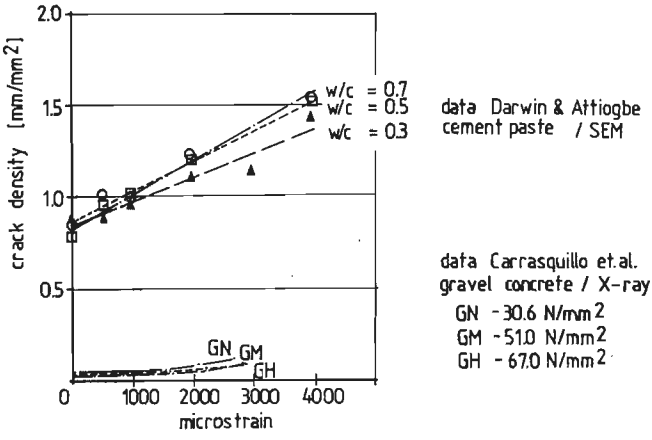

Fig. 2.8. Micro-crack density versus applied compressive strain for cement-paste after /37/ and for high strength concrete after /26/.

The crack-density in cement-paste varies inversely with the w/c-ratio for non-loaded specimens. A linear increase of crack-density with applied compressive strain was found. Furthermore based on these observations, the conclusion was drawn that the highly non-linear behaviour of concrete, mortar and cement-paste may be the result of the high crack-density in cement-paste.
The work of Darwin & Attiogbe shows a continuously increasing crack density with applied strain. No reference is made to existing critical boundary's for crack-initiation, propagation or crack-bridging.

2.2. Different stages in progressive fracture.

In the previous section the minimum volume ε_v (determined from the macroscopic strains ε_i, i = 1, 2, 3), was associated with the starting point of severe mortar-cracking (see fig. 2.6). The observations from the previous section, relating submacroscopic cracking with macro phenomena in uniaxial compression, may be extended to triaxial compressive loading situations.
At moderate stress-levels, when the fracture process is confined to isolate 'micro-cracking', an almost linear-elastic response is measured. According to Newman and Newman /112/, elastic response is observed up to stress-levels $\sigma_1 \approx 0.4 - 0.5\ \sigma_{1,peak}$ in uniaxial and triaxial compression. When this limit is exceeded, micro-cracks start propagating in a stable manner, and the limit is referred to as 'lower bound criterion for failure /112/. In a later investigation by Kotsovos and Newman /85/, this boundary is redefined as 'onset of stable crack

propagation' (OSFP).

For increasing principal stress σ_1, eventually the above mentioned minimum volume is obtained. Newman and Newman /112/ refer to this boundary as 'upper bound criterion for failure', and later Kotsovos and Newman as 'onset of unstable fracture propagation' (OUFP).

Upon further increasing stress, beyond OUFP, a maximum stress-level is reached (stress-failure in load controlled testing). Only when proper measures are taken, the fracture process also remains stable beyond peak-stress, and a descending branch is measured (see section 2.3).

In figure 2.9.a, the above mentioned stages in the progressive fracture process are shown in the meridian plane in principal stress space. The meridian plane contains all loading combinations that can be investigated with standard triaxial cylinder tests (i.e. the compressive meridian for stress combinations $\sigma_1 < \sigma_2 = \sigma_3$, and the tensile meridian $\sigma_1 = \sigma_2 < \sigma_3$, with σ_i negative compression, are both situated within this plane). In figure 2.9.b, the subsequent fracture surfaces are plotted in a similar cross-section in strain-space.

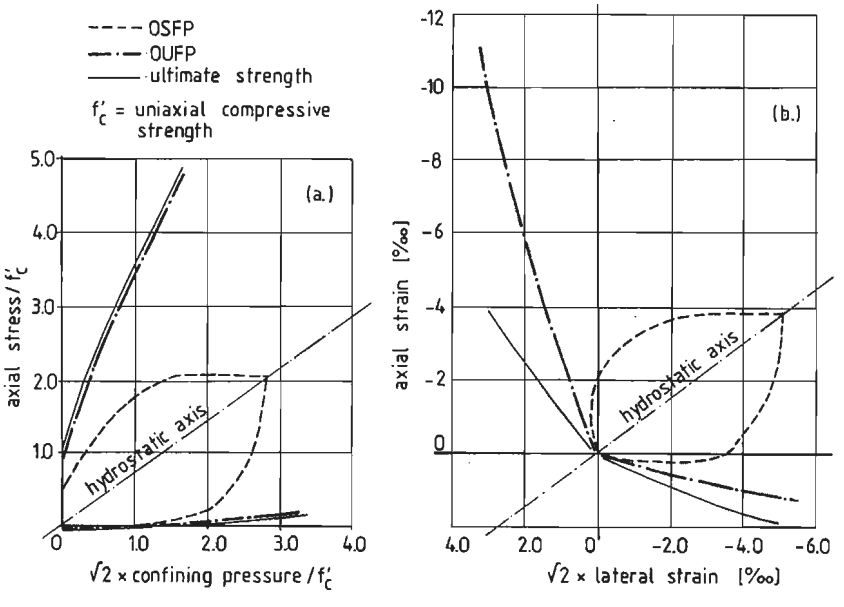

Fig. 2.9. OSFP, OUFP and ultimate strength envelopes for concrete subjected to axissymetric triaxial stress-states, after /85/.

The OSFP curve is closed, and appears symmetrically with respect to the hydrostatic axis, both in stress and strain space. According to Kotsovos and

Newman /85/, this symmetry implies that material is isotropic within the OSFP envelope, and responds similar to different deviatoric loading paths. The OUFP-envelope and ultimate strength envelope are both open ended and non-symmetric with regard to the hydrostatic axis. The material becomes anisotropic, due to oriented cracking dictated by the maximum principal compressive stress. The OSFP-envelope is associated with the fatigue strength of the concrete. Below this level, concrete does not suffer from any significant cracking. The OUFP-level is associated with the long-term strength of the material (see /85/, and also compare with /132/).

Boundaries in the fracture process of concrete subjected to multiaxial loading, were also proposed by several other investigators (Kupfer /92/, Launay and Gachon /93,94/), and are in principle similar.

In contrast to the above distinction, Spooner et.al. /148,149/ indicate that the fracture process of concrete is progressive. The definition of the above defined lower bound is dependent on the sensitivity of the measuring method, and rather subjective. Spooner at.al. /148,149/ argued that concrete behaves similar as an ideal material in which energy is dissipated by two processes. Due to the first mechanism (a), energy is dissipated during only the first loading over a given strain-range. A second mechanism (b) provides for energy dissipation both during increase and decrease of strain. The energy dissipated due to mechanism (a) can be taken as a measure of the damage sustained to the material. The second mechanism (b) provides a damping effect similar to that observed in real materials under repeated loading. By subjecting a material sample to a series of unloading-reloading cycles the subsequent dissipating mechanisms can be distinguished (see fig. 2.10).

Upon first loading, the total energy of the material given as the surface under the stress-strain curve includes damage energy W_γ, damping energy W'_δ (mechanism (b)), and elastic energy W_ε (which is recoverable). Upon unloading, no further damage is sustained, but energy is dissipated due to damping (mechanism, (b)), W''_δ . The total energy dissipated in the first load cycle ABC is equal to the surface of the stress-strain curve between the loading and unloading curve, and is given by

$$W_{diss} = W_\gamma + W'_\delta + W''_\delta \qquad .....(2.1).$$

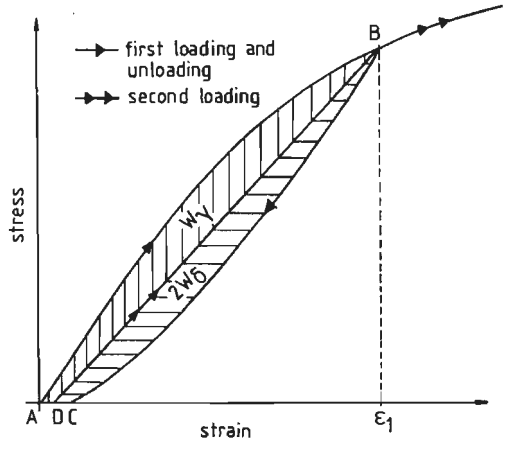

Fig. 2.10. Definition of damage energy, damping and recovery energy components, after /148/.

Note that the elastic energy W_ε is recovered. On reloading to the previous unloading point B, the additional work done is equal to $W'_\delta + W_\varepsilon$. No further damage energy dissipated while the previously attained maximum strain-level is not exceeded. The total energy dissipated in the second cycle is equal to $W'_\delta + W''_\delta$, where it is assumed that damping may be dependent on the direction of straining.
In /148/, no attempt was made to separate between the two damping energies, thus $W'_\delta + W''_\delta = 2W_\delta$. By adopting a cyclic loading history to a material sample, the above mentioned energy components can be determined.

Based upon a number of accoustic emission experiments, it was found that no further emission was observed before the previously attained strain was exceeded. (cyclic loading history, 'to the envelope', see fig. 3 and 4 in /148/, using concrete specimens).
It was concluded by Spooner /148/ that concrete behaves essentially similar to the model material displaying the above mentioned dissipating mechanisms. Adopting the described method, a break-down in energy components was derived from a series of cyclic experiments on concrete prisms /148/ and cement-paste specimens /149/. In fig. 2.11, the cummulative energy dissipated in damage for a concrete specimen is shown. It was concluded that damage starts at very low strain-levels and is progressive.

This type of 'damage function' (fig. 2.11) was proposed by Dougill /40/ and Dougill & Rida /41/ for use in a theory of progressively fracturing solids. In principle, this approach may also be adopted in triaxial loading situations. Attention to these aspects is given in chapter 5 and 6.

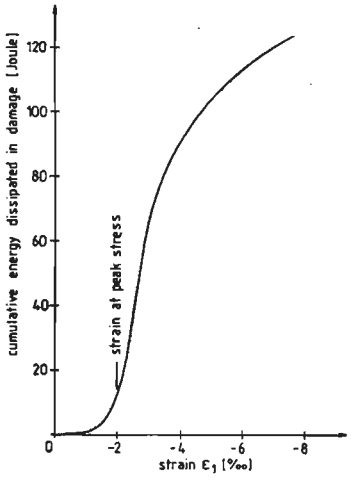

Fig. 2.11. Cumulative energy dissipated in damage in a concrete specimen, after /148/.

The damage dissipating function was derived from experiments displaying a stable softening branch. In such an approach, stress-failure is merely a casual quantity related to a certain damage level. Some aspects of strain softening are discussed in the next section.

2.3. Softening behaviour under compressive or uniaxial tensile loading conditions

- Concrete in uniaxial compression -

From uniaxial compression tests it is known that concrete displays a gradual decrease of load carrying capacity with increasing axial strain when a maximum load-level is exceeded. This so-called softening behaviour is observed when a proper strain-controlled test is carried out. In terms of damage (cracks), it is observed that large macro-cracks form after the peak-stress-level is exceeded. Normally it is assumed that these macro-cracks should run parallel with regard to the compressive loading direction. From previous investigations however, it was also observed that inclined cracks or multiple oriented cracks may develop

/39/. Also in biaxial tests, inclined crack-surfaces are observed, even when friction-poor boundary conditions are used /92/. The most common assumption on this matter however is that the inclined cracks solely are the result of constraint between loading application system and specimen. The constraint, although reduced considerable, also will be present in tests providing for 'friction-poor' boundary conditions (see also section 3.1).

The descending branch in the compressive stress-strain curve is observed only when proper measures are taken. The relatively large energy-release due to formation of macro-cracks, has to be supported by other elements in the complete structure, which are still in their pre-peak region. The complete structure mentioned before, includes the testing machine and the hydraulic system in cases of the normal small size tests on prisms or cylinders. In early investigations, the requirements for a stable test were obtained by placing springs parallel to the specimen /54/, or by performing an excentric loading test /126,70,132/. In the latter case, stress-redistributions were allowed to occur within the specimen. However, the coupling between stress- and strain is difficult, due to the non-linear behaviour of the material.

A test will remain stable when the energy released by the specimen can be supported by the machine: the energy increment of the total system always must be positive:

$$\Delta W_{tot} = \Delta W_{specimen} + \Delta W_{machine} > 0 \qquad .....(2.2.)$$

From the continuum mechanics point of view, the existence of the descending branch and thus negative elastic moduli is impossible.The material looses stability, and the tangential stiffness matrix becomes non-positive definite. As stated by Bazant /5/, it must be concluded that a structure (specimen) must loose stability as soon as the peak-stress-level is exceeded. However, as discussed before, it is possible to measure a stable descending branch when sufficient precautions are taken, and an energy redistribution is possible within the complete system.

In /5/, Bazant discusses the conditions for a stable strain-softening branch. The effects of size, heterogeneity and stored energy on the stability analysis are shown. The model used by Bazant is depicted in fig. 2.12. The strain softening is assumed to occur in a region with length $2l_1$. The strain-softening zone is assumed to undergo a uniform infinitesimal strain increment $\delta\varepsilon_1$, the remaining parts of the specimen will unload (strain increment $\delta\varepsilon_2$).

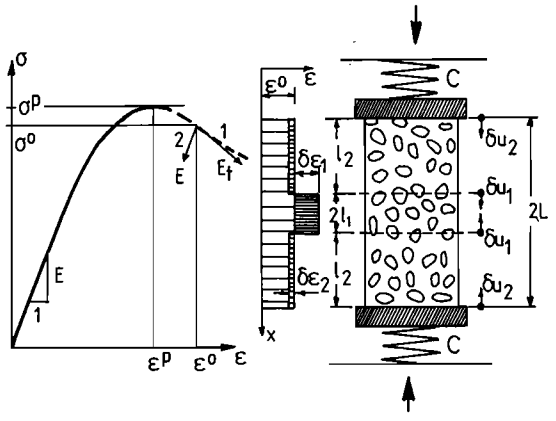

Fig. 2.12. Strain-softening localisation /5/.

The total work which has to be supplied to the system can then be calculated:

$$\Delta W = 2[A\, l_1(\sigma^o + \tfrac{1}{2} E_t\, \delta\varepsilon_1)\, \delta\varepsilon_1 + A l_2 (\sigma^o + \tfrac{1}{2} E\, \delta\varepsilon_2)\, \delta\varepsilon_2 + (P^o + \tfrac{1}{2} C\, \delta u_2)\, \delta u_2 \quad .....(2.3.)$$

where A = the cross-sectional area of the specimen and $P^o = A.\sigma^o$. The other parameters are shown in figure 2.12. As mentioned before, the system remains stable, if under any condition, energy has to be supplied to the specimen ($\Delta W > 0$).

The final form of the condition for instability is:

$$-E_t/E > -E_{t,crit}/E = 1/[L/l_1 - 1 + AE/(C\, l_1)] \quad .....(2.4.)$$

The assumption made in the analysis that the uniaxial stress-strain curve may be applied in the situation of figure 2.12 is discutable. The requirement that the strain-softening is localised in a small zone, leads to incompatibility of lateral strains between the localisation zone and the unloading zones. Due to this assumption, the influence of constraint on the strain-softening instability is neglected.

Some results concerning the influence of constraint between loading application system and specimen are recently published by Kotsovos /87/. In the context of the stability analysis, we will show some of his results here. A more comprehensive survey of the important aspects of boundary conditions in the testing of multiaxial stress-strain behaviour of concrete will be given in section 3.1.

Kotsovos /87/ investigates the influence of five types of "anti-friction" media on uniaxial post-peak stress-strain response of concrete:

- no "anti-friction" medium (dry steel platens),
- a layer of synthetic rubber (neoprene, 0.45 mm thick),
- a MGA-pad, consisting of a 0.008 mm thick hardened aluminium steel placed adjacent to the specimen. Molyslip grease (3 % MoS_2) and a Melinex polyester film were placed against the steel platens of the testing machine.
- brush bearing platens, and
- "active-restraint", by means of clamps which were placed at a distance of 3 mm from the loaded surfaces.

Results were obtained for two concrete mixes: mix 1, uniaxial compressive cyl. strength f'_c = 29 N/mm^2, and mix 2, f'_c = 50 N/mm^2. The tests were carried out using cubical specimen (d = 100 mm) and cylindrical specimen (ϕ 100 x 250 mm). The strains were measured by means of LVDTs, placed between the loading platen, and additionally by means of strain-gauges at the specimen surface. Fig. 2.13 shows the influence of the five loading application systems on the post-peak load-displacement curve, measured with the LVDTs, for the "higher-strength" concrete.
Based on these results, and on a number of tests on beams loaded in four-point bending /88,89/, in which lateral displacements were measured near the loading platen, the conclusion was drawn that concrete is a perfectly brittle material. According to Kotsovos, we can assume that the post-peak behaviour is solely the result of the constraining action of the loading application system. Furthermore based on the beam-tests, it was stated that the large deformations leading to a considerable amount of rotation capacity are rather the result of the constraint between loading-platens and beam surface instead of the normally existing softening branch. The constraint is considered to be responsible for a triaxial stress-state under the loading platen, thus providing the necessary conditions for an increase of axial deformation combined with a decrease of lateral deformation and an increasing load carrying capacity.

The questions which arise from the investigations by Kotsovos are important, although a less extreme point of view is preferred. The results shown in figure 2.13 all demonstrate brittle behaviour, resulting in an unstable (downwards directed) descending branch.
It is known that a soft load-application system will lead to a sign-reversal of the shear-stresses acting at the specimen - loading platen interface,and thus will

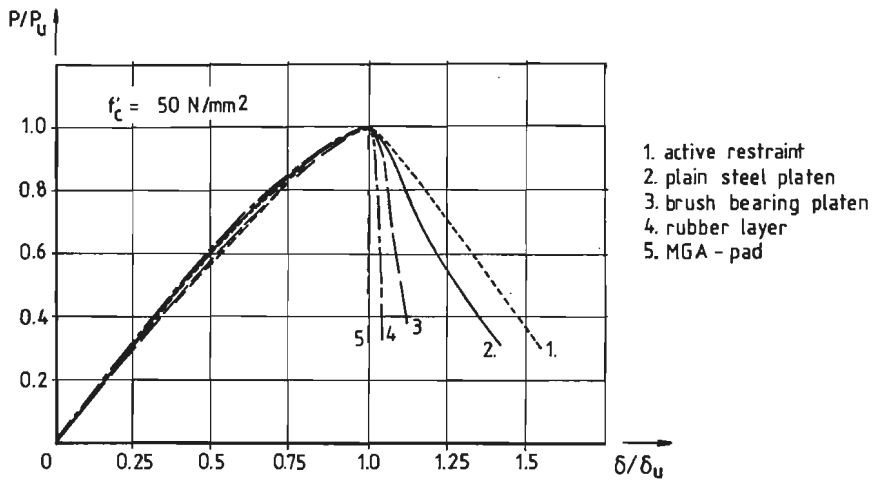

Fig. 2.13 Load-displacement curves for various loading application systems, after Kotsovos /87/.

provide additional micro-cracking in the pre-peak region due to tensile splitting. In this context it must be emphasized that the thickness of the soft-layer (rubber, MGA-pad) has a considerable influence on the behaviour /113/. (figure 2.14).

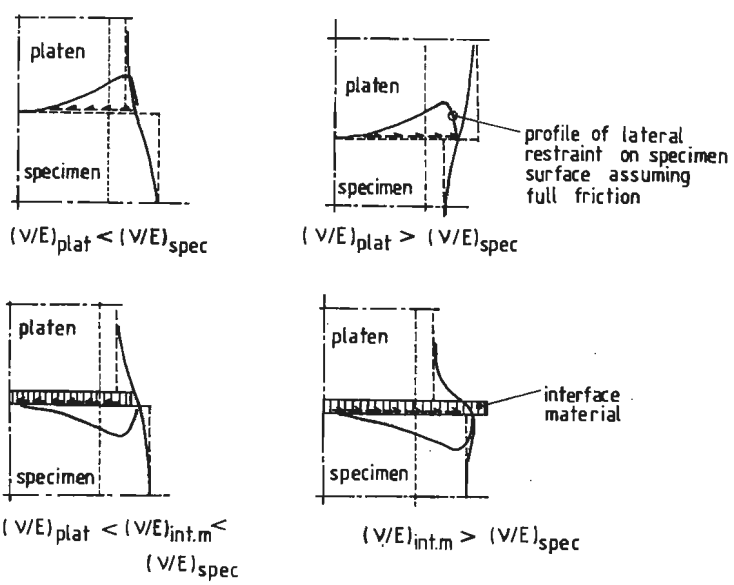

Fig. 2.14. Dependency of lateral deformation on loading application system, after Newman /113/.

In /5/ it was shown that ductility, expressed by the ratio $\varepsilon_f/\varepsilon_p$ (with ε_f = failure strain, and ε_p = strain at peak) is influenced by the size of the specimen with respect to the size of the aggregate (i.e. size of inhomogeneities) and by the spring constant C of the machine (see also equation (2.4.)).

Test-results obtained by Carrasquillo et.al. /26,27/, show a delayed crack-formation process for high-strength concrete, when compared to medium and low-strength concrete. At failure, a considerable amount of cracks (micro-cracks and combined cracks) run through the aggregate-particles. The delayed crack-propagation is also shown by the nearly straight pre-peak stress-strain response of the high strength concrete. Based on the paper by Bazant /5/, one might expect an increasingly instable behaviour of high strength concrete, due to the reduced effect of heterogeneities. (The high strength material is rather homogeneous due to similar strength properties of the aggregate phase and cement-matrix phase).

Similar observations hold for the post-peak behaviour of cement-paste (Spooner et.al./149/) and for the post-peak behaviour of light weight concrete (Wang et.al. /165/, Grimer & Hewitt /54/).
An additional important factor leading to a stable decending branch is the frictional behaviour of the material. Sliding in cracks over larger or smaller asperities will have a pronounced effect on the observed post-peak behaviour.

- Geomaterials in uni- and triaxial compressive loading -

Strain-softening is not a phenomenon which is characteristic for concrete only. Geo-materials such as rock also display strain-softening behaviour (see for example Ichikawa et.al./75/, and the work of Bieniawski and co-workers /16,17/).
In standard triaxial compression tests in a stiff machine, the development of a pronounced shear-band in the post-peak stress-strain curve is observed. For 'brittle' soft rocks such as coal, multiple stick-slips are found in the strain-softening branch /154/. In spite of the fact that in some cases also a multiple fracture mode is observed, the shear-band-mode is considered as typical for the behaviour of rock-masses under compressive loading.
The strain-softening is confined to the joint (shear band) and its immediate vicinity, the rock masses between the joints continue to behave in an elastic manner (Sture & Ko /154/). This means that strain-softening is not considered as a material property, but is rather the performance of a structure whose individual components such as joints and interfaces exhibit a loss of strength

with progressive displacement. The progressive failure of rock in a triaxial compressive test is shown in figure 2.15.

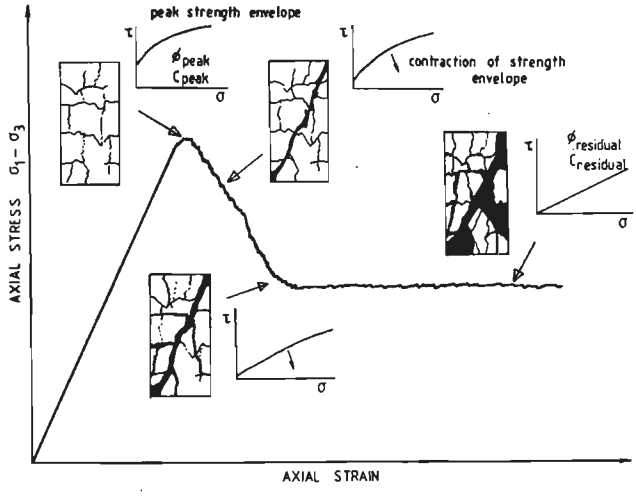

Fig. 2.15. Progressive failure of rock in a uniaxial or standard triaxial test, after Sture & Ko /154/.

Based on the above mentioned observations, a shear-strain softening model was developed by Sture & Ko (see fig. 2.16). The two intact pieces are assumed to be very stiff compared to the granular mass in the shear-zone. The stability of the structure is dependent on the geometry of the shear-zone as well as the material parameters (fig. 2.16). The variation in work ΔW, due to a machine displacement δu is given by

$$\Delta W = -\frac{1}{2} G_{ss} \cdot \frac{A\,t}{\sin\alpha} \cdot \delta\gamma_{ss}^{2} - \frac{\tau_o \cdot A\,t}{\sin\alpha} (\tan\delta\gamma_{ss} - \delta\gamma_{ss}) + \frac{1}{2} C \cdot t^{2} \sin\alpha \cdot \delta\gamma_{ss}^{2} \qquad \text{.....(2.5).}$$

Where $G_{ss} = \delta\tau / \delta\gamma_{ss}$ is the shear modulus in the shear-zone, and $\delta\gamma_{ss} = \tan^{-1}$ (u/t sin). A is the cross-sectional area of the specimen and t is the thickness of the shear-band. The angle α determines the orientation of the shear band normal to the loading direction.

Comparison of both the normal strain-softening model (eq.2.4) and the shear strain softening model with a number of standard triaxial compression tests (with critical stability in the post-peak region) under various confinements in a machine with adjustable stiffness, showed better agreement of the shear strain-softening model. The energy variations in the specimen and the machine support were found to be in the same magnitude for all cases investigated, which

indicates a balance between energy released and energy absorbed. The thickness t of the strain-softening zone was estimated by measuring the fine grains torn loose in the shear zone. In /143/, it is stated that the size of the fracture zone is initially of the order of microns, but the zone grows rapidly with the relative translation between the fracture surfaces as asperities are ground down and loose grains are torn apart. The shear modulus in the shear-zone was estimated to be on the order of 1 - 5% of the intact modulus. The inclination α of the shear band was, dependent of the material tested, between 65 and 75 degrees. A slight curvature of the shear-fracture plane was observed in some cases.

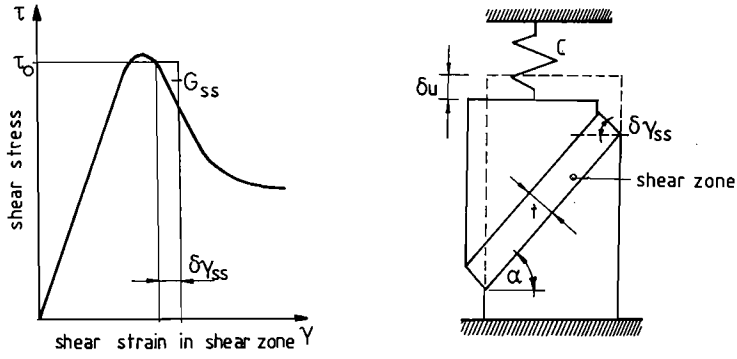

Fig. 2.16. Shear-strain softening model after /154/.

The normal and shear strain-softening models were developed in an attempt to take account of the localised failure modes of concrete and geo-materials in a numerical scheme. And as Bazant /5/ remarks: "strain-softening is impossible without heterogeneity of the material. This represents a certain inconsistency in the mathematical model, because by characterizing the strain-softening in terms of stress and strain, the state variables of a continuous medium, one implies the material to be a continuum, and this property is incompatible with the existence of strain-softening. One way to circumvent this inconsistency is to describe the strain-softening by means of a stress-displacement, rather than stress-strain relation, the displacement being a relative displacement over a certain characteristic length".

- Strain-softening of concrete in uniaxial tensile loading -

It is indicative of the state of the art that tensile cracking and shear transfer are discussed separately from the non-linear behaviour in compression, indicating a

basic lack of generally valid concepts for a full range of stress-states. Normally no relation is assumed to exist, or proven to exist between tensile failure of concrete and compressive failure, and the subjects are always treated separately. In studying the complete stress-strain behaviour of concrete under multiaxial loading conditions this lack of unification is annoying.

Some clarity in the progressive failure of concrete under uniaxial tensile loading has emerged from the work by Hillerborg, Modeer & Peterson /63/. Let us consider a prismatic specimen subjected to uniaxial tensile loading (fig. 2.17). Up to a certain stress-level, the stress-strain curve is nearly linear, and a similar behaviour is measured in the three regions A, B and C. At a certain instance, due to micro-crack propagation a deviation from linearity is observed /47,72,73/. When, with increasing strain, a peak stress-level is reached, a tensile macro-crack will start propagating at a very localised place.

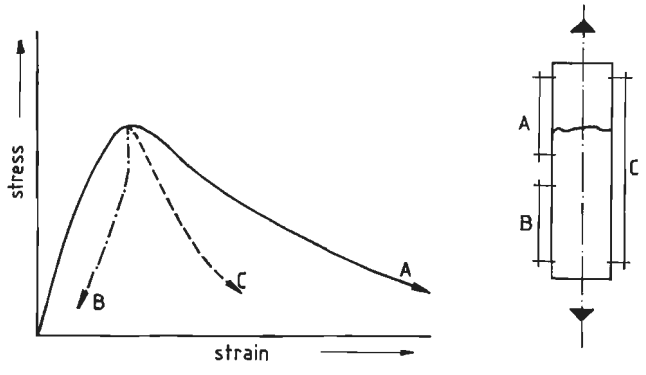

Fig. 2.17. Tensile "stress-strain" behaviour.

If the crack is covered by measuring length A, a clear strain-softening will be observed. However, in the area covered by gauge B, unloading is observed due to the decreasing load-carrying capacity in the tensile crack-zone. The overall deformation measurement will show a crude average of gauge A and B (fig. 2.17).

The step made by Hillerborg and co-workers, was to define a stress crack-width diagram rather than a stress-strain relationship. In fact the method is comparable with the plastic-zone model in fracture mechanics. The only difference is that the stress acting at the crack-tip, is now distributed according the 'strain-softening branch', where-as in the so-called Dugdale-model /20/ a constant stress distribution (yield stress, σ_y) is assumed. In front of the crack-tip a process-zone is formed, and the energy necessary for a crack with width w_o is exactly the

surface under the stress-crackwidth curve (fig. 2.18). In the so-called Fictitious Crack Model (FCM), developed by Hillerborg et.al. /63/, the falling branch was approximated by means of a linear relationship.

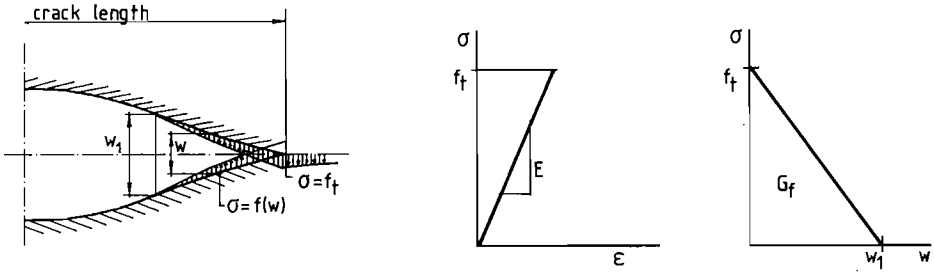

Fig. 2.18. Fictitious Crack Model, after Hillerborg et.al. /63/.

Recently some examples of application of the FCM were shown /64/. The most important fact underlying the proposed model, is that large deviations were observed when linear-elastic fracture mechanics were applied to normal scale concrete structures. As was mentioned in a recent paper by Bazant & Oh /7/, the large deviations are due to the heterogeneity of the concrete. Due to the large size of the aggregates, the fracture process zone is found to be relatively large when compared to the plastic zone in front of a crack-tip in the application of fracture mechanics in the field of metals. Peterson /122,123/ indicated that linear elastic fracture mechanics only could be used for concrete when the structure size $d/l_{ch} > 10$, where l_{ch} is the characteristic length of the material, and d is a characteristic dimension of the structure under consideration (for example the depth of a beam).
The characteristic length of a material can be calculated from the stress-crack width diagram, and is found to be equal to

$$l_{ch} = G_f.E / f_t^2 \qquad .....(2.6.),$$

where E is the elastic modulus, G_f the fracture energy and f_t the tensile strength. The large characteristic length for concrete, $l_{ch} \approx 400$ mm, shows that for the normal laboratory experiments, the influence of the process zone cannot be disregarded.

In the model proposed by Bazant & Oh /7/, the fracture energy G_f, consumed in the formation of all micro-cracks per unit area was assumed to act over an effective crack band width w_c :

$$G_f = f_t^2 / 2C_f . w_c \qquad .....(2.7.)$$

Where C_f is the slope of the descending branch in the uniaxial tensile stress-strain diagram. The strain ε_f/w_c is defined as the relative deformation over the process zone width. A simple relationship was derived in order to link the fracture energy with the total surface under the stress-strain curve, including the softening branch:

$$G_f = W.w_c \qquad .....(2.8),$$

where $W = \int \sigma.\delta\varepsilon$, the surface under the stress-strain curve. The crack-band theory was compared with a number of tests on notched specimen, and proved to be satisfactory when a width of the crack band equal to $w_c \sim 3d_a$ was used (d_a is the maximum aggregate size). Finite element calculations showed that the length l_f of the fracture process zone was generally between $2w_c$ and $6w_c$. The characteristic value was assumed to be $l_f \sim 4w_c \sim 12d_a$.
In /7/ it was mentioned, that the virtue of modelling fracture through stress-strain relationships - rather than through stress-crackwidth relation (FCM) -, the influence of triaxial effects due to compressive stresses acting parallel to the stress plane can easily be taken into account.

The behaviour under uniaxial tension also can be modelled in terms of continuous damage models (CDM).The principle of continuous damage mechanics by Janson & Hult /80/, has been worked by Løland /97/ for concrete under uniaxial tension. The models do not take into account the stress-concentrations ahead of crack-tips (such as is done in the Fictitious Crack Model), but merely assume that defects are initially present start propagating under various types of loading (mechanical loading, drying and swelling, temperature etc.). The mechanical intact area between the defects is able to carry load. Driving force for damage accumulation is considered to be the tensile strain.
When a concrete specimen is loaded under uniaxial tension, damage will propagate throughout the complete specimen when the strain-level does not exceed the strain-capacity ε_{cap}. When surpassing this strain-limit, damage will concentrate in a localised zone (see fig. 2.19). The longitudinal dimension is assumed to be in the order of the maximum aggregate-size, while most cracks will propagate through the cement-matrix phase and along the aggregate-cement matrix interface (at least for static loading).

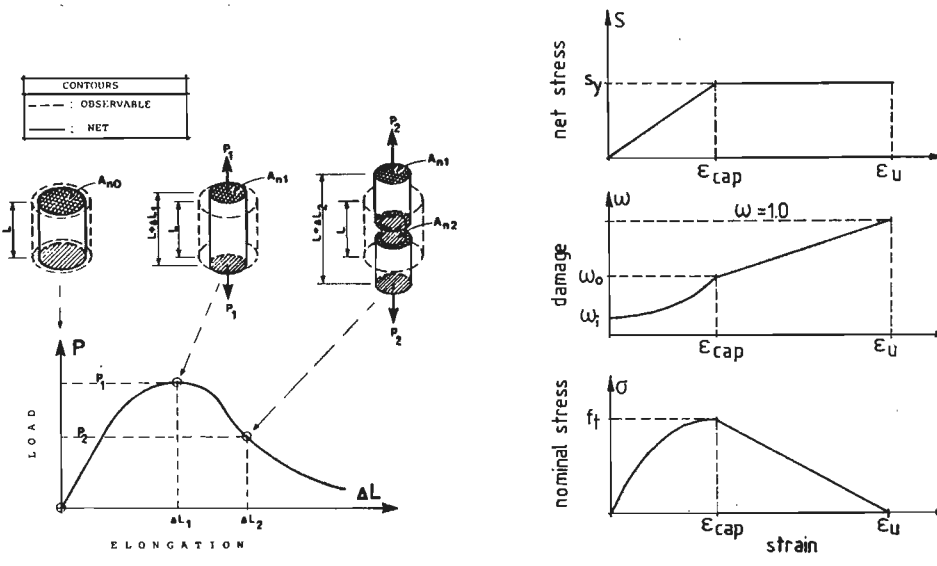

Fig. 2.19. Continuous Damage Model, after /97/.

Damage is defined as a scalar ω, representing the quotient between intact cross-sectional area (A_n) and the total macroscopic cross-sectional area (A).

$$\omega = A_d / A = (A-A_n) / A \qquad .....(2.8)$$

A net-stress s is defined, which is the average stress-value over the intact area, and is related to the applied strain ε by:

$$s = E.\varepsilon , \quad \text{for } 0 < \varepsilon < \varepsilon_{cap} \qquad .....(2.9),$$

and $$s = s_{yield} = E.\varepsilon_{cap}, \quad \text{for } \varepsilon_{cap} \leq \varepsilon \leq \varepsilon_{ult}$$

where E is the elastic modulus of the intact material, and ε_{ult} is defined as the maximum strain at the end of the softening branch. From this formula, it is obvious that the net-stress s will remain at a constant level after the strain-limit ε_{cap} is exceeded.

A stress-strain relationship can now be calculated when a relation is defined between damage and applied strain. In the pre-peak region, Lø land proposes an exponential relationship:

$$\omega(\varepsilon) = \omega_i + C_i . \varepsilon^{\beta} \quad , \text{for } 0 \leq \varepsilon \leq \varepsilon_{cap} \qquad \text{.....(2.10.a.)}$$

and in the post-peak region a linear relationship:

$$\omega(\varepsilon) = \omega_i + C_i . \varepsilon_{cap}^{\beta} + C_2 . (\varepsilon - \varepsilon_{cap}), \qquad \text{for } \varepsilon_{cap} < \varepsilon \leq \varepsilon_{ult} \text{ .....(2.10.b.)}$$

where C_1, C_2 and β are constants.

Finally the relation between nominal stress σ (averaged over the original cross-sectional area A) and the net-stress s is given by:

$$\sigma = s\,(1 - \omega) \qquad \text{.....(2.11.)}$$

The relation between net-stress, damage and nominal stress with strain ε is also shown in figure 2.19.
Complete fracture occurs when $\omega = 1$. In the paper by Løland, a good correlation is shown with the experiments by Evans & Marathe /47/. A similar model has been proposed by Mazars /100/, which was extended recently for compression and triaxial states of stress /101/. The criterion for damage accumulation is also considered to be the tensile strain. In the triaxial formulation damage is assumed to propagate when the second invariant of the strains exceeds a certain limit. Compressive strains are reduced to zero, before this condition is checked.

The continuous damage models, used for tensile loading, normally are considered to be applicable for compressive loading too. Similarities between the tensile and compressive stress-strain curves were observed by Hughes & Chapman /72,73/. Also the 'damage-function' (fig. 2.11) given by Spooner & Dougill /148/ for compressive loading shows similarities. In his thesis, Stroeven /152/ mentions an analogue model for concrete under compressive loading. The models may give an appropriate description of the stress-strain behaviour of concrete, the mechanism of damage-accumulation however is by far from understood. In notched beam tests, different post-peak behaviour for concrete, mortar and cement paste was reported by Moavenzadeh and Kuguel /108/. (compare with the uniaxial compression case, p. 22). The decreasing slope of the softening branch was attributed to side cracking in mortar and concrete specimens.

- Strain-softening of concrete in triaxial compressive loading -

Only scarce experimental results regarding strain-softening of concrete under multiaxial compressive loading have been published recently. Ahmad & Shah /1/

gave attention to the behaviour of steel tube confined concrete cylinders (fig. 2.20) in a very limited test-series.

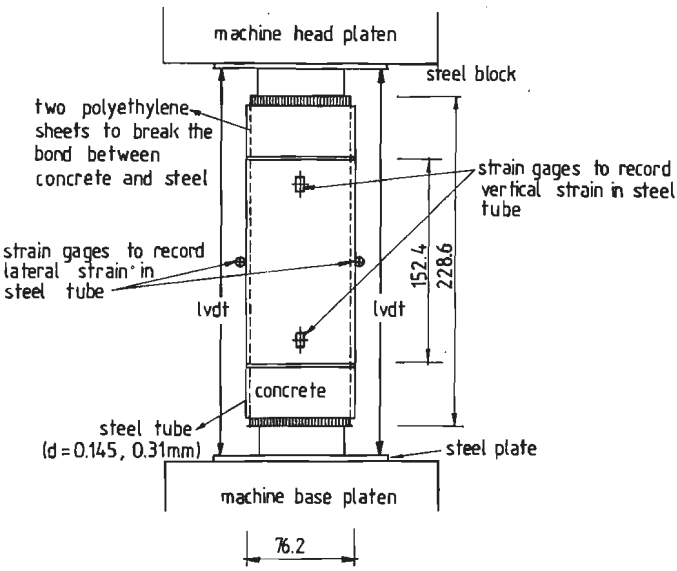

Fig. 2.20. Steel-tube confined cylinder test, after Ahmad & Shah /1/.

Special measures were taken, to assure that no vertical loading was carried by the steel cylinders. The lateral pressure, increased gradual with increasing vertical stress, until yielding of the steel occurred. The lateral pressure can be varried by using tubes of different thickness. In figure 2.21, the measured stress-strain response of a test with tube thickness of 0.145 mm, on a concrete cylinder with uniaxial compressive strength of 37.3 N/mm^2 is shown.

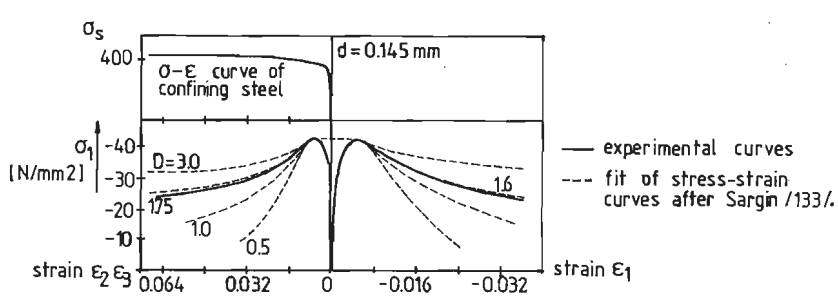

Fig. 2.21. Complete triaxial stress-strain curves for steel tube confined cylinder tests, after /1/.

The graph shows a slight increase of peak-stress-level, and a decreasing slope of the stress-strain curve descending branch in comparison with uniaxial data. The confining stress varied from -1.37 N/mm^2 at peak-stress-level to -1.50 N/mm^2 at the residual stress-level. The parameter D, shown in fig. 2.21 was used to fit a polynomal stress-strain relation, original developed by Sargin /133/ for uniaxial compressive stress-strain curves, to triaxial stress-strain curves ($\sigma_2 = \sigma_3$).

At the 1984 Toulouse Symposium results on a micro-concrete, using conventional triaxial cylinder tests were reported by Jamet et.al. /79/. The results of Jamet showed a decreasing slope of the stress-strain curve descending branch with increasing lateral confinement. Similar results are known for rock (see for example Ichikawa et.al. /75/).
In the next chapters, most of the topics mentioned in this chapter are discussed in relation with the current results.

3. EXPERIMENTAL TECHNIQUE

In this chapter, the experimental method and equipment that were adopted in the current investigation are described. In section 3.1 some aspects of load application systems (i.e. boundary conditions) are discussed. Further in section 3.2 the lay-out of the triaxial experimental machine, methods of load and deformation measurement, test-control and data aquisition system are given. Finally in section 3.3 the manufacturing method of the concrete specimens is indicated and an overview of the entire experimental program is given.

3.1. Boundary conditions

When a compression test on concrete is carried out, numerous problems regarding experimental procedures are encountered. The strength and deformational response will depend to a large extend on the lay-out of the experimental machine, and the loading application system (or boundary conditions) that is used.

Regarding the loading application system, two major principles can be distinguished. Either we can choose for a uniform stress-distribution along the specimen boundary, or we can choose for a uniform boundary displacement (see fig. 3.1).

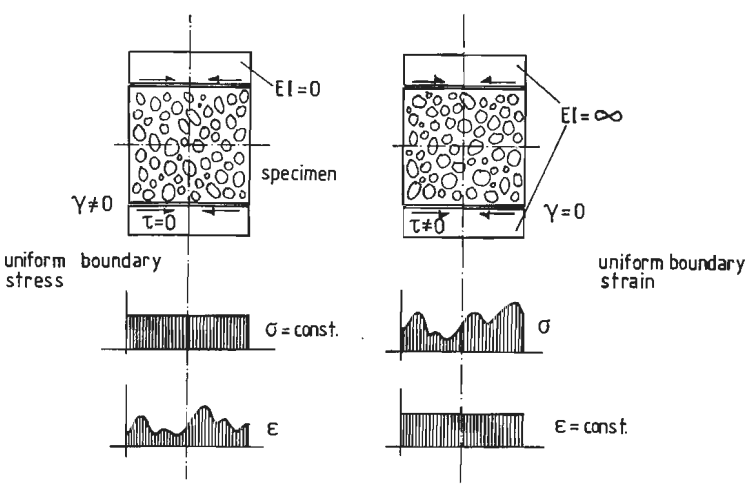

Fig. 3.1. Boundary conditions in the testing of material stress-strain response.

Under the condition of uniform boundary stress, the normal stress-distribution in the specimen will be very well defined. However, due to the heterogeneity of the

material under consideration, the displacements will be less smoothly distributed, and will take a form dependent on the grain distribution within the specimen. A uniform boundary stress can be obtained by means of a loading application system with zero-stiffness. The displacements must be determined by means of a proper averaging procedure. Implication of such a system is that no shear-forces will be acting at the specimen-loading system interface. When loading is applied through a zero stiffness medium, shear deformation of the specimen are allowed, which is important in the testing of anisotropic materials.

If on the contrary an infinitely stiff system (dry platen, fig. 3.4) is used, a uniform boundary displacement will be applied to the specimen. In this case a non-uniform stress-distribution will emerge and only an average strength can be determined (under the assumption that both loading platens are fixed). As a result of differences in lateral expansion of the stiff loading application system and the concrete specimen, constraining shear forces will develop at the specimen-loading application system interface. (see also fig. 2.14). Due to this constraint a triaxial stress-state will arise at the specimen-ends, and an over-estimation of the concrete strength will result. In general we can assume that a lower boundary for concrete strength is obtained when a zero-stiffness is applied, and an upper limit is formed when an infinite stiff system is used. No shear deformations of the specimen are allowed when both loading platen are fixed (indicated by $\gamma = 0$ in fig. 3.1).
The influence of constraint between loading platen and concrete specimen is since a long time understood. Only simple measures are necessary in uniaxial compressive tests. An increase of the specimen height h, leading to h/d-values of 2.5 to 3 (where d = the lateral dimension of a prismatic or cylindrical specimen), results in a bounding value for the uniaxial compressive strength. For higher values of h/d no further decrease of strength was observed. Decreasing the ratio h/d however would lead to a sharp increase of measured strength. This was shown by Schickert /139/, in a series of tests on prisms with varying height and constant cross-sectional area. The prisms were loaded between rigid loading platens. For specimens with h/d = 1, an increase of uniaxial compressive strength of about 20 to 25% was observed, when compared with the strength of prisms with h/d = 2.5.
In a linear elastic calculation the uniformity of the stresses in a middle section for prisms with h/d = 2 was shown by Schleeh /140/. The boundary conditions in the calculations were comparable with rigid loading platens.

As was mentioned before a triaxial stress-state will develop in the specimen-

ends as a result of the constraining action of the rigid-loading platens. This is shown in fig. 3.2.a for a cylinder under uniaxial compression.
In fig. 3.2.b a typical failure mode for this structure is shown. Due to the triaxial compressive stress-state in the specimen-ends (as was also shown to exist by the calculations of Schleeh), micro-cracks may initiate and propagate along the boundaries of these relatively stiff cones. When the load is increased, and micro-cracking becomes more pronounced (section 2.1), the structural response of the cylinder will change. Probably a splitting action is induced in the central part of the cylinder, resulting in a decreasing strength when compared to less slender specimens. It may therefore be assumed that the results obtained from such specimens (prisms and cylinders in uniaxial compression, or cylinders in a conventional triaxial test with a h/d-ratio ~ 2.5), loaded between rigid platens, do not represent the "true" material behaviour.

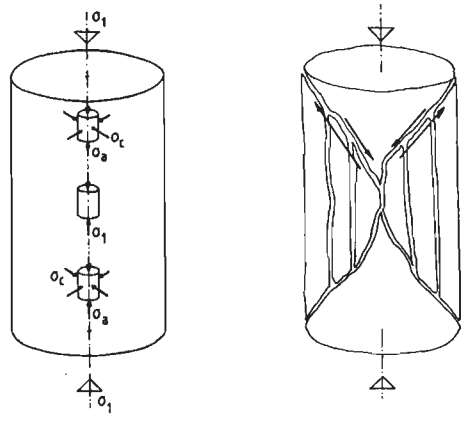

Fig. 3.2. Behaviour of a cylinder under uniaxial compressive loading between rigid steel platens.

Indicative in this context also may be the results obtained by Newman, K et.al. /115/. Strain measurements in the interior of cylinders, by means of cast-in gauges, showed a larger response to external load, when compared with strain-gauges mounted at the specimen-surface. Larger strains in the interior were recorded throughout the complete pre-peak stress-strain diagram. The effect was observed for dry specimens, as well as for completely saturated cylinders. Similar observations were also reported by Read /127/. The interior strains were about 14% higher than the surface strains.

Under multiaxial loading conditions another important aspect with regard to the loading application arises. When load is applied by means of rigid platens in a biaxial test, the loading in one direction will be partly carried by the two

adjacent loading platens in the second loading direction (fig. 3.3).
The result of this mutual interference is a further overestimation of the ultimate strength of concrete under multiaxial conditions. It will be obvious that when soft platens are used, the interference effect will be eliminated to a large extent. For a soft-system such as brush bearing platens (fig. 3.11), it was calculated that about 2% of the external load was carried by the adjacent loading platen in a biaxial test /111/.

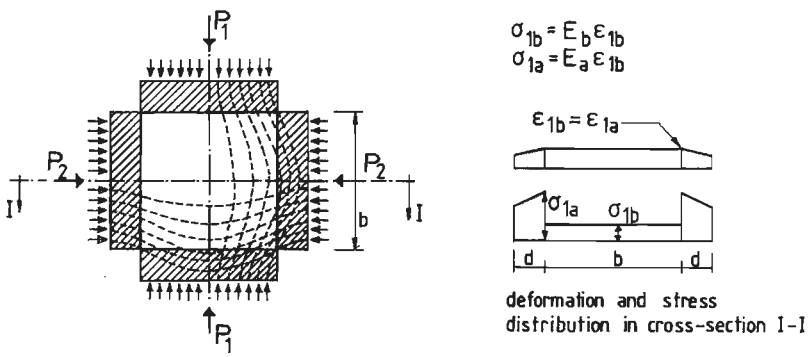

Fig. 3.3. Interference of loading-platens in a biaxial test using rigid steel platens , after Kupfer /92/.

- loading application systems -

Many loading application systems with more or less unconstrained boundary conditions are found in the literature. The main purpose of all these systems is to arrive at a uniform stress-state within the specimen, and thus reducing the constraint between loading application and specimen. The following systems are found in literature (see also fig. 3.4):

a) Loading through rigid steel platen, without friction reducing measures.
As we have mentioned in the previous section, the system is normally applied in tests concerning uniaxial strength properties of concrete. This system is also used in conventional triaxial tests on cylindrical specimens /112,113,85,86,66,67/. The lateral confinement in the cylindrical tests is by means of fluid pressure.
Rigid loading platens have also been applied in the early tests on cubical specimens /166/. Furthermore the method is used for comparison with friction-reducing load application systems /91,92,111/.

b) Rigid loading platens with friction reducing measures by means of intermediate layers.

Different types are found in literature, such as rubber (Kobayashi & Koyanagi, /84/, 3D), talc-powder with aluminium sheets (Launay & Gachon /93,94/, 3D), teflon (Mills & Zimmerman /106/, 3D), polyethylene sheets with molybdenum sulfide grease (Bertacchi & Bellotti /14/, 3D) and recently thin polished metal sheets (Erdei /45,46/). When intermediate layers are used, attention should be given to the thickness of the soft layers (grease, rubber). Increasing thickness will result in a sign-reversal of the constraint, thus leading to a splitting action at the specimen-ends. A comprehensive study of intermediate layers is given in /113/. A disadvantage of this system is that no tensile stresses can be applied to the specimen.

c) Loading through non-rigid platens.

Two different systems have been developed and used in recent years. Firstly we mention the well known brush-bearing platens, original developed by Hilsdorf /65/, and later applied by several investigators (Kupfer /92/, Nelissen /111/, and Liu et.al. /96/ in biaxial tests, and Linse /95/ in triaxial tests). The friction between the loading application system and specimen is reduced due to bending of the separate brush rods. The maximum allowable load transfer is confined to the buckling resistance of the brush-rods.

A second non-rigid loading platen has been developed by Schickert /137,138,139/, at the 'Bundesanstalt für Materialprüfung' in Berlin. A loading platen is formed by a number of pistons which are separated by thin rubber layers. The complete structure is placed on a rubber sheet, thus providing sufficient deformational freedom in axial and lateral directions. The system can be used at higher stress-levels when compared with brushes. Disadvantage of the system is however that no tensile loading can be applied to a test-sample.

d) Fluid cushions.

Loading is applied to the specimen directly by means of fluid pressure. The fluid is separated from the specimen by means of a flexible membrane. The method is used for producing lateral confinement in triaxial tests on cylindrical specimen. However at Colorado University, the system is used in a so-called 'true triaxial test' on cubical specimen. The cubical cell, original developed for the testing of geologic materials (Ko and Sture /83/, Sture and Desai /155/) also proved to be a powerfull tool in testing of concrete and mortar (Andenaes et.al. /3/, Gerstle et.al. /51,52/).

The above review is rather limited, but more comprehensive reviews are found

in literature /113/. A very clear qualitative classification of loading systems was given in a cooperative multiaxial testing program /51,52/. The loading systems were roughly classified to friction reducing ability and uniformity of the generated boundary stress distribution. This schematic classification is shown in figure 3.5. The dry platen system (DP) is situated at the right-top corner of the diagram. The system generates a uniform displacement distribution at the specimen boundary, and induces a considerable constraint.

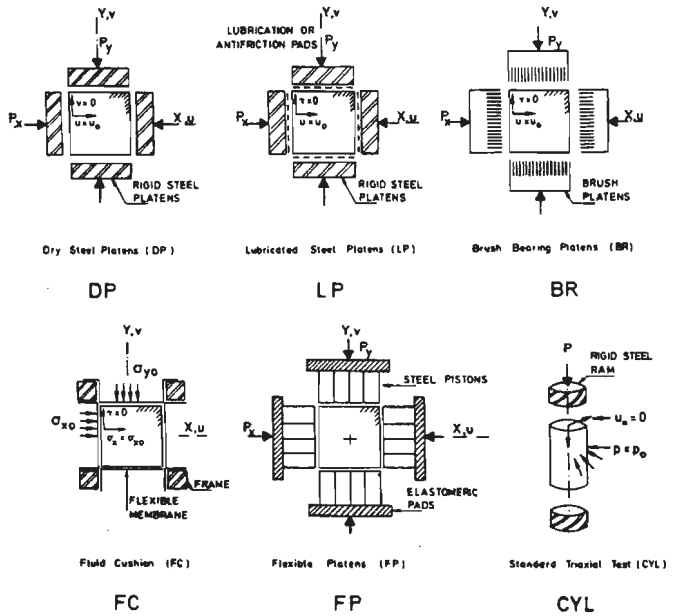

Fig. 3.4. Various loading application systems, after /51,52/.

The other extreme system, is the fluid cushion (FC) system, which imposes a uniform stress-field to the specimen, with zero lateral constraint. These extreme boundary conditions were also mentioned in the previous section. The other loading systems mentioned will lead to intermediate situations. The lubricated platens (LP) will provide only a reduction of the frictional behaviour at the specimen interface. The non-rigid loading system also produces a decreasing axial stiffness (brushes (BR), and flexible platens (FP)).

The cooperative international multiaxial testing program /51,52/ clarified in the problems encountered in triaxial testing of concrete. Differences between loading application systems, and deformation measurements were clearly shown. In fig. 3.6 the influence of the loading application systems mentioned in fig. 3.5 on the uniaxial and equal-biaxial strength is shown. The effect is obvious: friction reducing measures result in a decreasing uni- and biaxial strength.

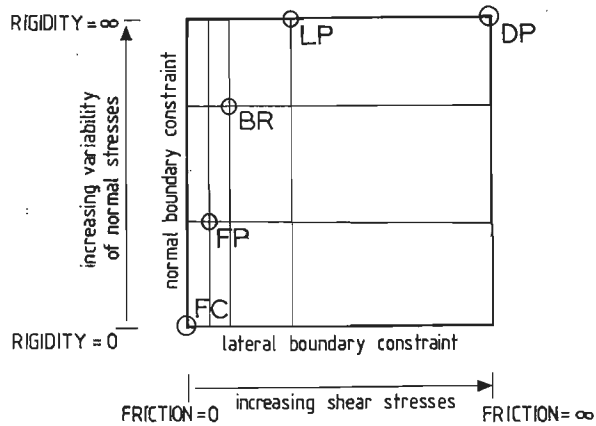

Fig. 3.5. Test specimen constraints, after /51,52/.

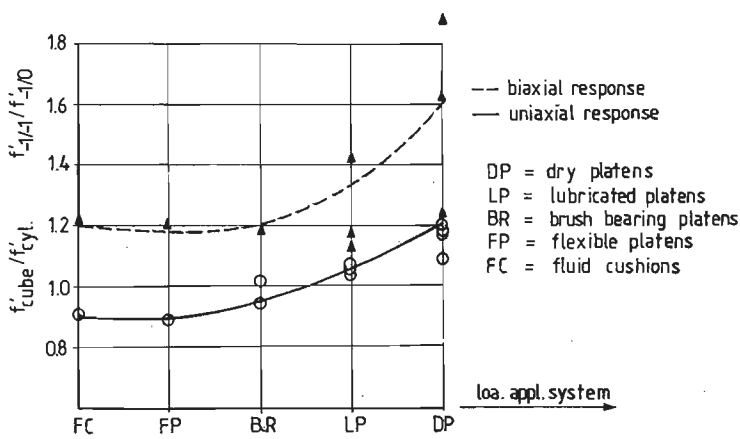

Fig. 3.6. Dependence of uniaxial and equal-biaxial strength on loading application system (after /51,52/).

Furthermore from the cooperative international multiaxial research program it was concluded that unconstrained boundary conditions are necessary in order to obtain strength and deformation results with limited scatter. Friction reducing measures are needed in order to acquire reliable strength results and also for measuring correct stress-strain relationships. As a third conclusion in /52/ it was stated that with the current testing procedures and the apparent brittle failure behaviour of concrete it is difficult to obtain strain data near or beyond the peak stress-level.

Only with the Munich triaxial apparatus, which was reported in detail by Linse

/95/, the onset of a strain-softening branch was measured for some of the loading paths investigated (see also Aschl, Linse and Stöckl /4/).

- Choice of the loading application system -

As it was mentioned in the introductory chapter, the major objective of the research is to learn more about the post-peak stress-strain response of concrete under multiaxial conditions. As we will see in the next section, a loading frame for cubic specimens coincides best with the available equipment in the laboratory.
The choice of a cubical machine was quite straightforward. We would not be confined to stress-states involving two equal principal stresses such as in standard triaxial tests on cylindrical specimens. However, it would be possible to investigate the influence of the intermediate principal stress on multiaxial strength and deformational behaviour. In general it is assumed that all possible combinations and parameters involving triaxial behaviour can be investigated by using a 'true triaxial test' on cubic specimens. As discussed by Bazant /8/, these tests do not take account of rotation of principal loading axes against the material axes. However, in the cubic test the directions of principal stresses and strains always coincide. While however no or very little experimental data is available regarding the softening behaviour of concrete under multiaxial loading conditions, it was considered useful to start with a cubical machine.

With the help of the classification for loading application systems, given in figure 3.5, brush bearing platens were chosen. From one side we had to fulfil the condition of unconstrained boundaries, on the other hand due to the need for a uniform displacement distribution, the loading application system should resemble a stiff platen system. In view of the classification of figure 3.5.a, brush bearing platen would be the best choice. Yet it must be realised that a stiff loading system will lead to an undetermined stress-distribution in the specimen: only an average strength can be determined. However, the requirements for measuring strain-softening resemble those of a stiff platen system.
It should have been possible to measure strain-softening by means of fluid-cushions, too. In this case, however, the displacement-state is undetermined and a reliable averaging procedure should be used in order to measure a mean-value for the displacement. Otherwise, probably, a considerable scatter in post-peak data would result.
Similar considerations were reported by Linse /95/. By means of a qualitative calculation, he showed that neither stiff loading platens, nor fluid cushions led to

correct results. The criterion in these calculations was that, in the specimen, a uniform stress- and strain state should occur near the boundary with the loading application system. The choice of brush bearing platens, also offers the possibility of tensile loading. In this case, the brushes are glued to the concrete surface. Care should be taken to see that none of the epoxy enters between the brush-rods, as this would prevent a proper action of the brushes /95,92,111/. Using another system, such as flexible platens, or lubricated platens would involve a separate system for tensile loading. This was not considered very appropriate, and also very time consuming while in such a case we had to learn to operate with two different systems (with probably different responses). As will be shown in chapter 4, the deformational response of the brushes is rather complicated already. For determining the dimensions of the brush-rods, the extensive publications of the Münich-group /92,95/ proved benificial.

3.2. Triaxial Experimental machine.

3.2.1. loading-frame

A three fold servo-control was available for use with the triaxial machine. Furthermore, three 2000 kN compression / 1400 kN tension hydraulic actuators were recently added to the laboratory equipment. The apparatus consists of three identical loading frames that are hung in a fourth overall frame by means of steel cables (see fig. 3.7.a and b). The three loading axes are not connected to each other and can act completely independent.
Movement of the axes with regard to one another is not restricted in the horizontal plane, in the vertical direction however, the frames are fixed. The translations and rotations of the three frames permitted, and the resulting specimen deformation are shown in fig. 3.8.

In fact a non-symmetric machine was constructed. A non-symmetric specimen deformation will occur in the vertical loading axis only. The situation is nearly the same as the Munich triaxial apparatus, the only difference being the degree of non-symmetry. The Munich apparatus consists of three fixed loading-frames, resulting in a three-fold non-symmetric deformation. A deviation between the measured specimen-load and true specimen-load will occur depending on the level of the specimen-deformations. From calculations by Linse /95/, it was shown that a negligible influence resulted from the non-symmetry. A similar analysis was recently published by Heyne /61/ that showed the influence of the lateral stiffness in the method of loading on the strength-results.

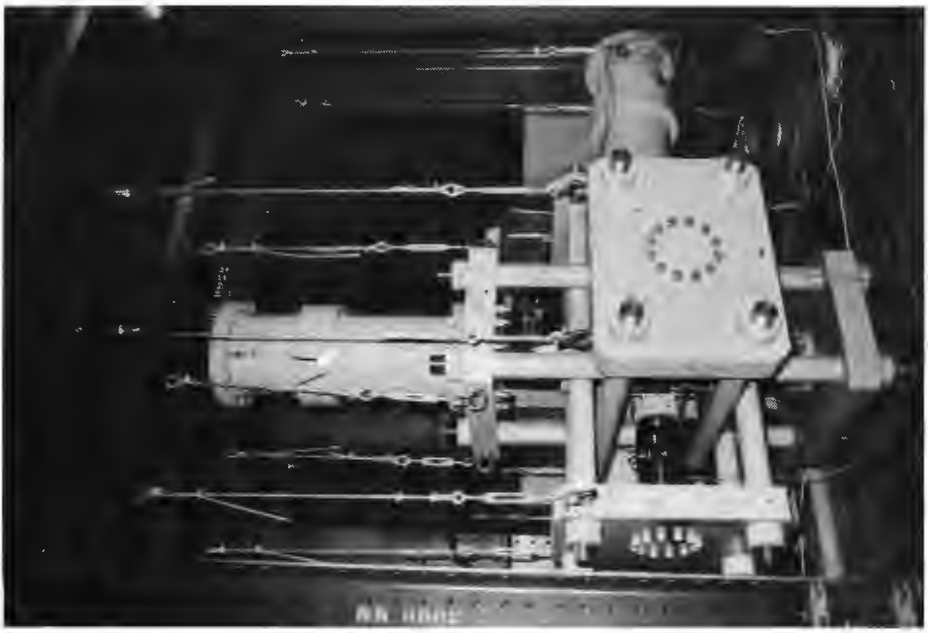

Fig. 3.7.a.

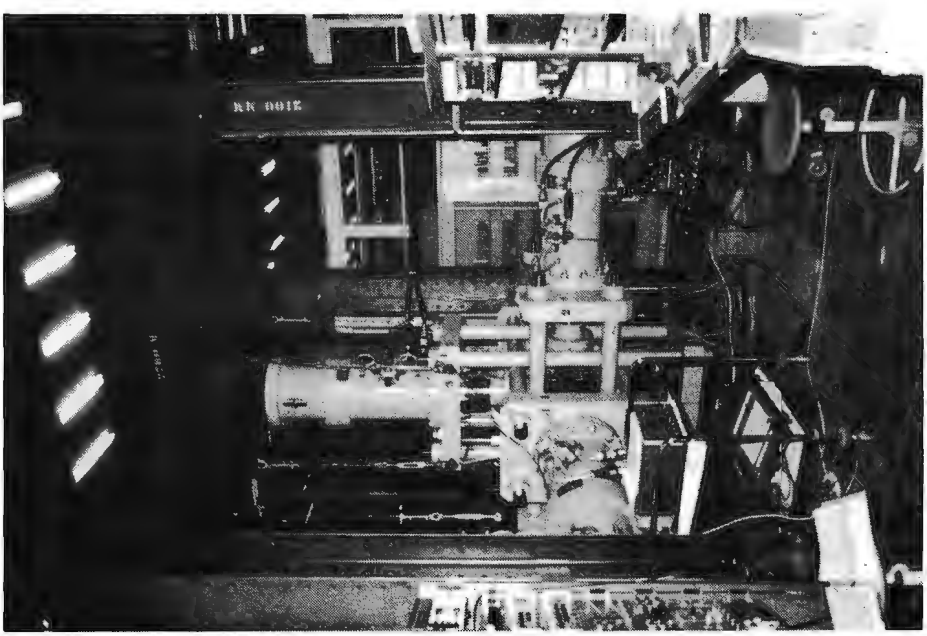

Fig. 3.7.b.

By means of an experimental study, Winkler /168/ showed that no appreciable effect on strength-results occurred when either a specimen was loaded through brush-bearing platens in a one-part triaxial machine (that is with fixed loading axes), or in a multipart machine. Indeed, at peak-stress-level, the influence of vertical boundary-shear force (which is the result of the frictional characteristic of the loading application system) on measured strength was negligible, as shown by a simple analysis in appendix A6. Yet in the descending branch of the stress-strain curves, the combination of increasing deformation and decreasing normal load was less favourable. Additional comments on this matter are made in section 5.2.4 and 7.2.3.

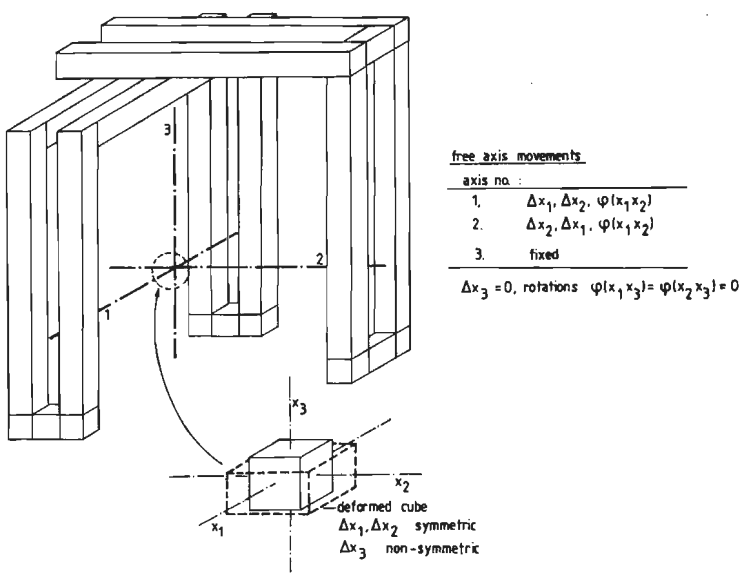

Fig. 3.8. Schematic view on triaxial apparatus (movement of loading axes and specimen-deformation).

The construction of a single loading axis is shown in figure 3.9. Each loading axes consists of four steel rods (1), fixed in a rectangular configuration (see fig. 3.7.a) between two rigid steel end platens (2). The position of the rods was chosen in order to allow for three identical loading axes.

At one side of this frame the hydraulic actuator (3) is connected, and the piston (no. 4, stroke max. $\pm$ 100 mm) can move freely through an opening in the upper end-platen.At the piston-side, a brush-bearing platen (7) is connected through a spherical seating (5). The radius of the spherical seating was chosen to ensure that the centre of rotation coincided with the specimen surface-centre (cube d = 100 mm, no. 8).

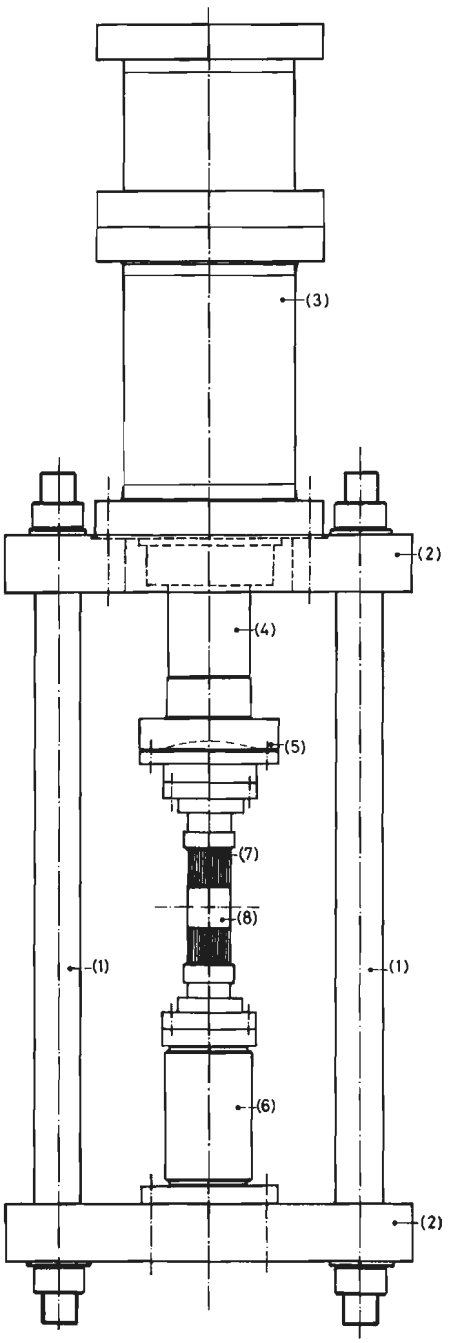

1. frame rods ϕ 110 mm
2. end-platens
3. hydraulic actuator
   (2000 kN compression/
   1400 kN tension)
4. piston
5. spherical seating
6. load-cell
7. brush-bearing platens
8. specimen, cube d = 100 mm.

Fig. 3.9. Construction of a single loading frame.

During a triaxial experiment, the spherical seating was fixed with three bolts in order to avoid rotation of the loading platens during the test. For triaxial tests involving cyclic loading to the envelope curve (see table 5.4 and fig. 5.3) it is considered favourable to have the spherical seating fixed. Especially in the descending branch of the stress-strain curve, rotation of the loading-platen during load-cycling could lead to a higher envelope stress-strain curve /148/. It must be mentioned that the axes were still allowed to rotate in the cables. The effect and the extent of this influence is not clear!

In the case of fixed loading platens, the specimen will experience a constant displacement but, due to inhomogeneities, the centre of loading of the specimen will not coincide with the centre of the loading axis. Yet a smooth prismatic rupture pattern is observed /114/.

In /114/ it was mentioned that testing between a fixed and a hinged loading platen is unsuitable. The test conditions are undetermined. It must be mentioned that, in the uniaxial experiments, the test conditions were for this "unfavourable" manner (series 2 and 3, see table 3.25). Yet, as will be shown in chapter 4, the displacement distribution was quite constant up to the peak-stress (series 3B2, see section 4.2, fig.4.12). In the triaxial experiments, the spherical seating was thus only used for a proper alignment of the specimen in the apparatus before test-initiation. In order to demonstrate the accuracy obtained, in fig. 3.10 the surface-strain measurements for a biaxial compressive stress-ratio experiment are shown (specimen 8A2-2, $\sigma_1/\sigma_2/\sigma_3$ = -1/-0.10/0, see table 5.4). The separate strain gauge readings are plotted against time. Strain gauges no. 10 and 11 are mounted in the σ_1-direction, and are compressive. Gauges no. 12 and 13 are mounted in the σ_2-direction and are tensile strains.

The difference between upper- and lower-surface strain measurement is negligible in the pre-peak region, both for $\varepsilon_{1,surf}$ and for $\varepsilon_{2,surf}$ (compare the response of gauge 10 with gauge 11, and no. 12 with no. 13). In the post-peak region splitting of the outer-concrete layers is observed, and for this particular experiment failure began at the lower surface (strain gauges no. 11 and 13).

Before such a (pre-peak) response could be obtained, a lot of practicing was necessary. In section 4.2, more attention is given to the post-peak surface strain-measurement.

Now return to figure 3.9. At the lower-end platen, the load-cell (6) is fixed. On top of this load-cell the second brush-bearing platen is connected. Due to the lay-out of the experimental machine, which was clarified in figure 3.8, two right angles are present in the "triaxial chamber" at the load-cell sides (between the horizontal and vertical loading axes).

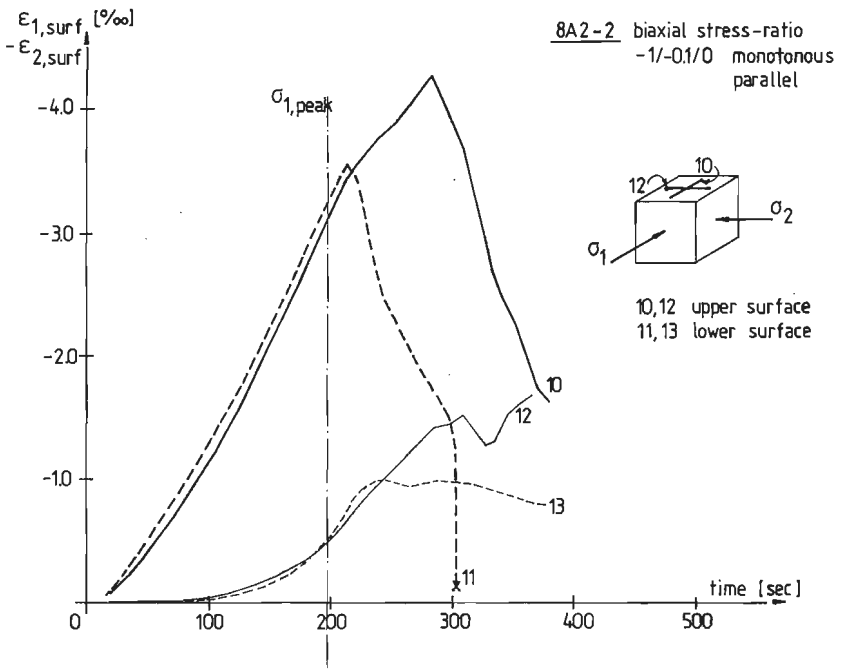

Fig. 3.10. Surface-strain measurement for specimen 8A2-2, biaxial compression, $\sigma_1/\sigma_2/\sigma_3$ = -1/-0.10/0, loading direction parallel (see table 5.4.).

This 'set-up' required an extremely accurate setting of the loading axes with respect to each other. By means of a water-level-instrument (WILD, accuracy 2mm/10000 m), the loading axes were hung orthogonally. A second check after six months showed that no additional lengthening of the cables had occurred.
As will be shown in chapter 4, the application of an epoxy-resin capping is more reliable for deformation measurement. Although sufficiently accurate specimens could be manufactured, the application of the capping was also considered favourable for the alignement of the specimen in the triaxial apparatus.

In figure 3.11 the brush construction is clarified. The brush-rods (5 x 5 mm^2) are separated by means of a grid consisting of 0.2 mm thick strips (phosfor bronze) at the clamped side of the rods. The rod-packet is clamped as a whole at a solid steel block. The effective length of the rods is 85 mm.

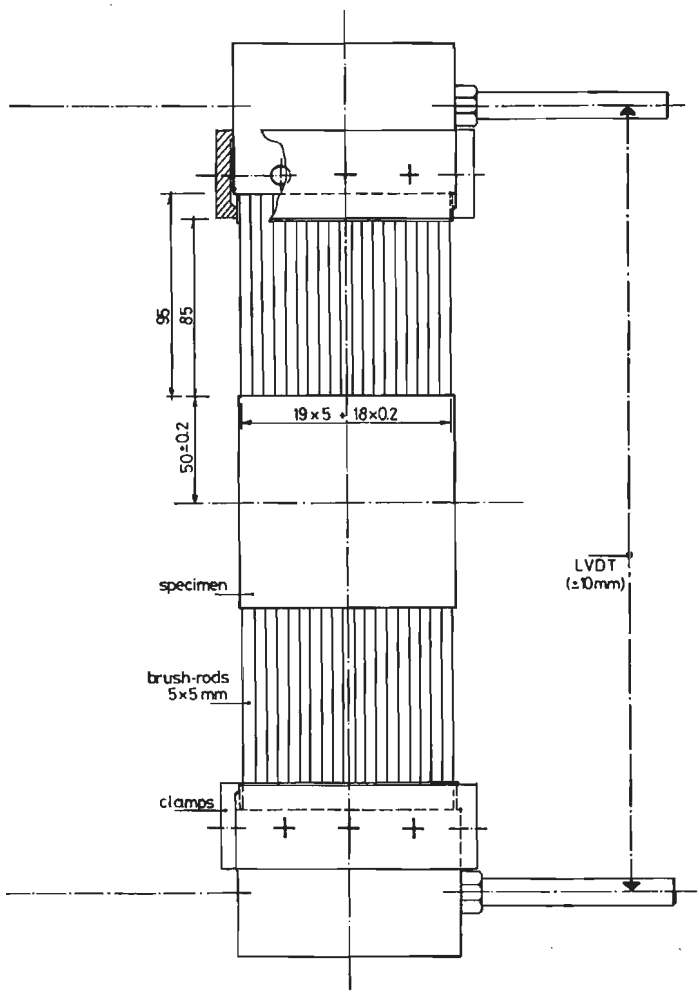

Fig. 3.11. Brush-construction and deformation measuring system (LVDT-measurement).

In the current set-up (multipart machine), the maximum allowable brush-deformation (and thus also specimen deformation) was determined and should not exceed 2.5 - 3.0 mm. For the calculation of the brush-rods the buckling of a complete loading-axis with respect to the specimen should be taken into account. The brush-surfaces had to be absolutely flat for accurate deformation measurement. At the start of a test, full contact between loading platen and specimen was desirable, yet unatainable. Especially in the case of deformation-ratio experiments, this requirement should be fulfilled (see chapter 5).

Before starting each test-series, the brushes were carefully ground. During grinding, 0.2 mm strips were inserted between the brush-rod-tips, and the complete rod-packet was rigidly clamped near the top in a special frame. A grinding sequence always started with the two inner contact surfaces (brush-rod packet - steel block interface).
After the inner contact surfaces were ground, the brush was put together under a small axial compressive load. Finally, the upper surface was ground carefully and the temporary clamps on the brush - rod - tips were removed. The accuracy (smoothness or flatness) of the method was approximately 10 - 20 μm. This accuracy diminished after a number of experiments was carried out, and as will be shown in section 4.3 the application of an epoxy-resin capping was an advantage.

In the case of a tensile experiment, two glue-connections had to be made. The rod -packet was glued to the solid steel block (adhesive: Degussa Agomet F 310, harder D), and a connection was made between the brush bearing platen and the specimen (epoxy-resin Edilon Dex'R). Before the specimen was glued between the brushes, a plastic filler was inserted between the brush-rods in order to prevent intrusion of epoxy between the rods. A similar technique was used earlier /92,95,111/.

3.2.2. load and displacement measurement

Forces were measured by means of calibrated load-cells (no. 6 in fig. 3.9). The load-cells consisted of a dumbbell-shaped steel measuring cylinder, upon which four strain gauges were mounted in a full Wheatstone bridge configuration. The measuring cylinder was covered by a second steel cylinder in order to protect the strain-gauges from damage and polution (the steel-cover was only fixed along one side to the measuring cylinder in order to avoid load-transfer through the cover).
The load-cells were checked carefully periodically during the investigation and no deviations were detected.

Deformations were measured using three different methods depending on the type of test. In a triaxial experiment no free surfaces are available for the measurement of deformation. Either some kind of cast-in measuring device has to be used (see for example /138/), or the specimen deformations have to be deduced from a 'system-displacement' (for example the deformation of the brushes, some methods are given in /95,52/).
A choice was made in favor of the second method. Displacements were measured

using the system depicted in figure 3.11. Between the rigid steel blocks, upon which the brush-rods were clamped, two or three LVDTs (depending on the type of test) were attached, measuring the relative displacement between two opposite loading platens. In a bi- or triaxial experiment and in the early uniaxial tests (series 2 and 3, see table 3.25), two LVDTs (type Hottinger W10-K, linearity deviation $\leq$ 0.2%) were placed in a diagonal position with regard to the specimen. In the later uniaxial experiments (series 8, 9, 10, 14 and 15, see table 3.25), the specimen deformation was determined with three parallel LVDTs, placed at 120^{0} intervals. The LVDTs were calibrated manually in a rig containing a microscrew (type Mitutoyo, range 25 mm, readings 0.002 mm). The LVDT-measurement (later referred to as loading platen measurement) was used for test-control as shown in the next section.
In uni- and triaxial tensile experiments, greater accuracy was required and two additional small-stroke LVDTs were mounted at the brush-rod tips (type Hottinger, W1 - TM, linearity deviation $\leq$ 0.2%, placed in a diagonal position (fig. 3.14)).

The uni- and biaxial experiments permitted additional surface strain measurement. All uni- and biaxial experiments provided for this extra measurement in the direction (s) parallel to the applied loading. Two 60 mm strain gauges (TML-PL-60-11, max. allowable strain 1.5 - 2%) were mounted on two opposite surfaces of a specimen using a polyester adhesive (type TML-PS). In some of the uniaxial experiments some additional strain gauges were used, both in the loading direction (σ_1, ε_1), and in the lateral directions (ε_2, ε_3). If any additional surface measurements were carried out, they are mentioned in the main text (chapter 4, uniaxial experimental results).

For measuring deformations in the unstressed directions in the case of a uniaxial or biaxial experiment (respectively Δl_2, Δl_3 and Δl_3), the measuring device shown in figure 3.12 was used. In the following it is referred to as "strain-reader".
In the middle (thin) part of the strain-reader two strain gauges were mounted. The bending of the thin part is a measure of the displacement between the regulation bolts. A linear relationship existed between the strain gauge response and the cube deformation (up to displacements of approximately 5 mm). The strain-readers were fixed to small circular aluminum plates (ϕ 8 mm) upon which a small steel ball was pressed. The circular plates were glued to the concrete surface. The regulation bolts were placed on the steel ball as shown in fig. 3.12. The strain-readers were always attached to the specimen under a small pre-stressing.

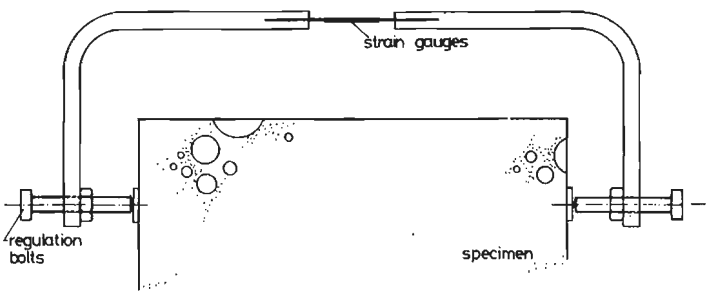

Fig. 3.12. Strain-reader, used for measurement of deformation in the 'unstressed' directions.

The strain-readers were able of an appropriate deformation measurement, also when severe cracking occurred in the concrete specimen (descending branch). In the uni- and biaxial experiments always four strain-readers were attached to the specimen. The arbitariness of the fracture process made a proper averaging method unavoidable.

The photographs shown in fig. 3.13 through 3.15 show fully instrumented specimens, respectively under uniaxial compression, uniaxial tension and biaxial compression. In case of a triaxial compression or tension-biaxial compression experiment (loading combinations investigated, see chapter 5), the displacements were measured by means of LVDTs only.

3.2.3. test-control

The regulation circuit for the triaxial experiments consists of a hydraulic and an electric part. The hydraulic part consisted of three servo-hydraulic actuators (actuators manufacturer, Hydraudine, servo-valve MOOG model 76-375, capacity 28.5 l/min) connected through accumulators (SCHENCK PN 250 T) with a high pressure oil pump (SCHENCK PP-20B, 280-285 bar).
The capacity of the oil pump was quite low (20 l/min), so the use of a stiff loading frame in combination with short oil-connections was necessary in order to measure a stable descending branch.
The electric part of the regulation circuit for a triaxial constant stress-ratio experiment ($-\sigma_1 > -\sigma_2 > -\sigma_3$, σ_i negative in compression), using a displacement control in the major loaded direction (i.e. the direction in which fracture occurs) is shown in figure 3.16.

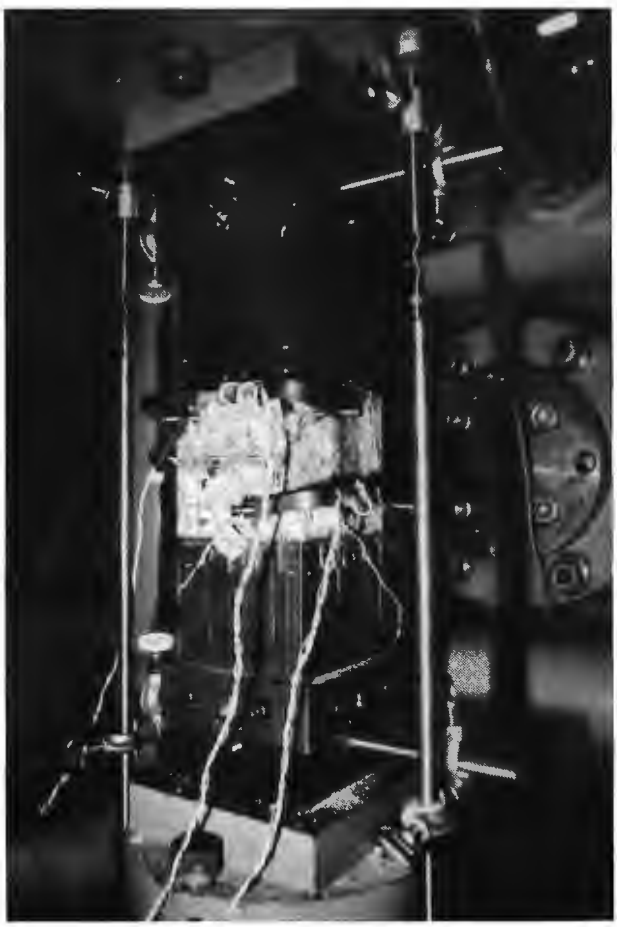

Fig. 3.13. Fully instrumented uniaxial compression tests, showing the loading-platen measurement (W10), surface measurement by means of strain gauges both in axial and lateral directions and the attachement of strain-readers.

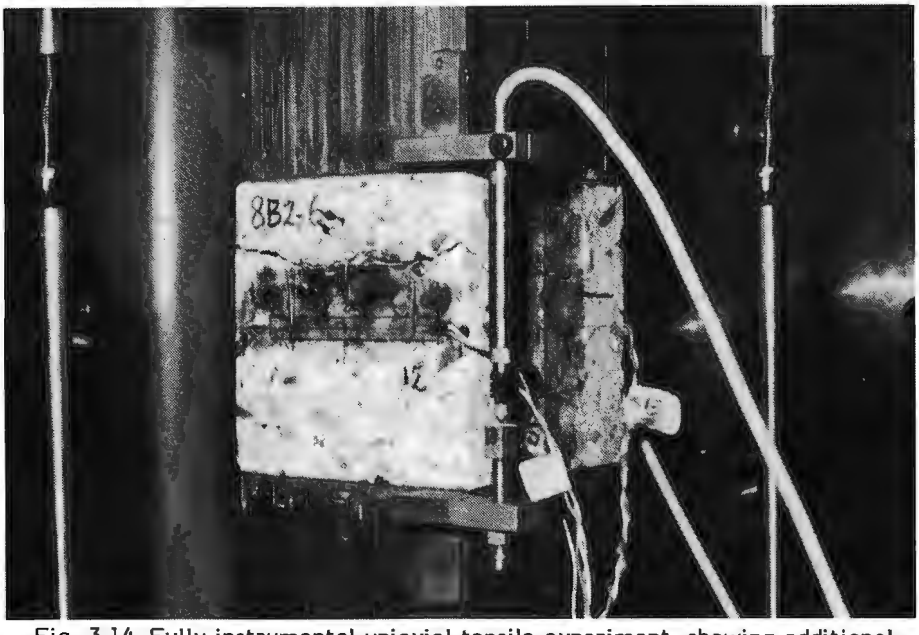

Fig. 3.14. Fully instrumental uniaxial tensile experiment, showing additional short stroke LVDTs (W1 - TM)

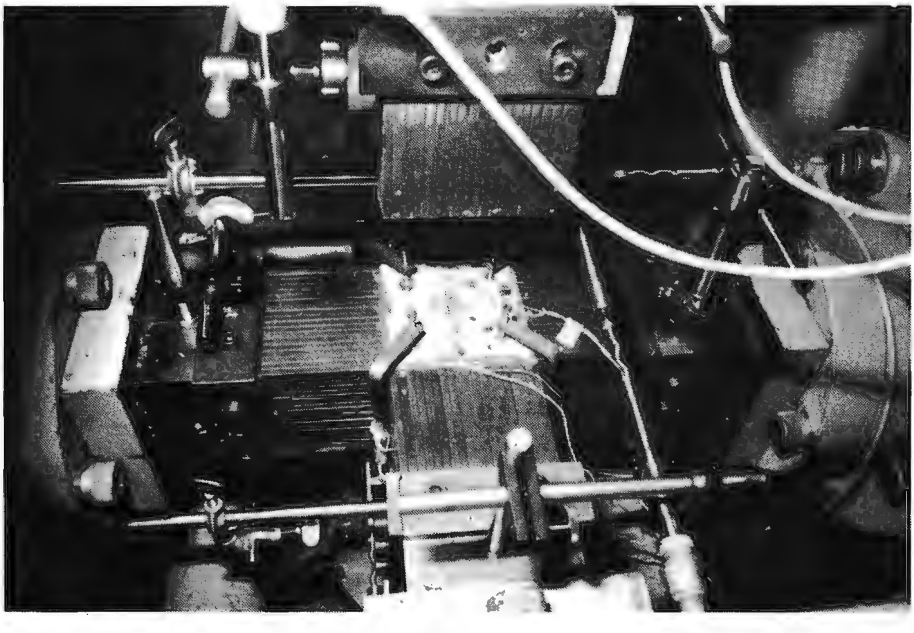

Fig. 3.15. Fully instrumented biaxial compressive experiment. The strain readers are attached in the corners between the brushes.

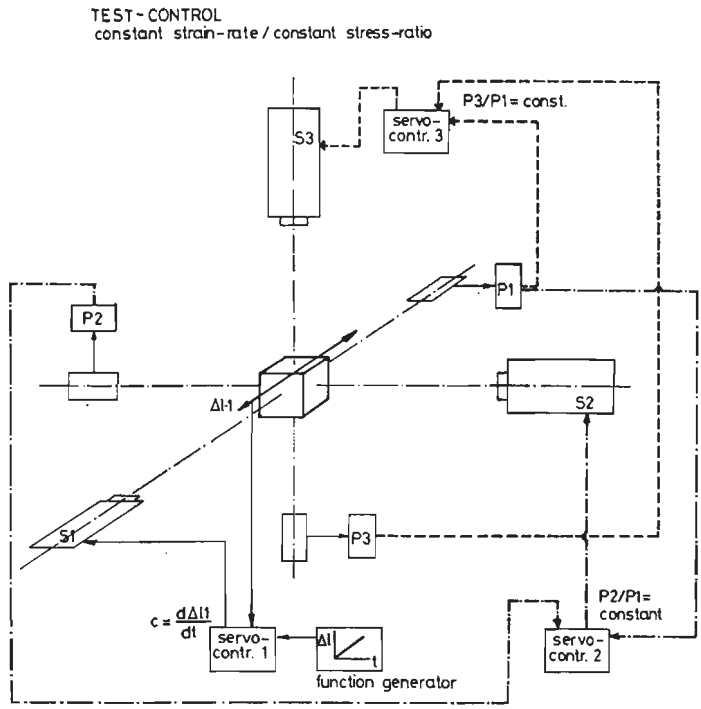

Fig. 3.16. Regulation circuit for constant stress-ratio experiments with a constant displacement rate in the major loaded direction.

The readings from the LVDTs (W10) near the specimen (fig. 3.11) in direction 1 were fed into servo-controller 1 (type SCHENCK-RV 35) via a 5 kHz carrier amplifier (SCHENCK-MV-15). Also connected to this servo-controller was a function generator (type EXACT, model 340 materials testing generator). The signals, both from the LVDTs and the function generator (i.e. the required loading-path and displacement rate) were compared and if necessary a signal was given to the servo-value S1 at the hydraulic actuator.

As a result of the specimen's displacement Δl_1 , a load P1 was measured (load-cell P1 via Hottinger KWS 3073, 5 kHz carrier amplifier).

The two other loading axes S2 and S3 were in force-control. In order to maintain a constant stress-ratio, the signal of P1 was fed into the servo-controllers no. 2 and 3 via the function-generator inputs. The ratios P2/P1 and P3/P1 could easily be set at the servo-controllers. In the case of a constant displacement-ratio experiment, the signal of the function generator was fed into the concerning servo-controllers. The required ratio between the displacements $\Delta l_i/\Delta l_j$ was set

at the servo-controllers.
The ratios between the several control components (load or displacement) of a triaxial experiment were quite accurate in this manner. Deviations could occur while an experiment always was started from a small initial stress-level. This requirement was a direct result of the fact that in all triaxial experiments a force-control was present in the minor loaded direction ($\sigma_3 = \beta \sigma_1$, β = 0, 0.05 and 0.10, see chapter 5). Of course, the ratio of the three stress-components always should correspond to the required ratio. For the stress-ratio tests this was easy to achieve, however, in the case of a constant displacement ratio experiment (for example $\Delta l_2 = \alpha \Delta l_1$ and $\sigma_3 = \beta \sigma_1$), the initial stress-ratio σ_2/σ_1 depended on the deformational behaviour of the concrete used (poisson ratio). For this class of experiments, the initial stress-ratio was estimated by means of a linear-elastic calculation (appendix A3).

Another complication should be mentioned here. The experimental design of the triaxial series (batch 8 and 9, see chapter 5) included a number of cyclic experiments (in terms of stress 'to the envelope', in the direction causing fracture (see section 5.2.6)).
After unloading, for example in a constant stress-ratio experiment ($\sigma_1/\sigma_2/\sigma_3 = 1/\alpha/\beta$), the zero-stress level was reached simultaneously in all three directions. Of course this is no objection if a loading direction is in 'displacement-control' (σ_1, ε_1). However, the two minor loaded directions (σ_2, σ_3) are in force-control, and therefore should never become zero. If a stress σ_2 of σ_3 would reach zero-level, the 'force-control' would become unstable and consequently the loading platen retracts from the specimen. This should be avoided under all circumstances, and therefore the initial stress-ratio (σ_2/σ_1 and σ_3/σ_1) was always taken 0.10 - 0.20 N/mm^2 too large with respect to the required values in the case of force control.

3.2.4. Data aquisition system

For scanning the measuring devices, processing and storing data during an experiment, a computer controlled data-logger (PEEKEL Autolog 900 S System) was available. Loading was applied to a specimen continuously, and no stops were made for measuring purposes.
A carrier amplifier (PP-100 S) and an input scanner were connected to the central data-logger (which contained a LSI-11, 16 bit computer). The system was provided with a high speed digital voltage meter with high resolution.

The central processor controled the scanning unit. Up to 100 channels can be connected to the system: all strain gauge input configurations are possible, including the use of LVDTs and strain gauge transducers for force and pressure. Also, DC-inputs could be connected.
All signals except the DC-inputs are amplified by the PP-100 S and transduced to a representative digital signal. DC-inputs were directly sent to the digital voltage meter. Further processing of the data is by means of suitable software. A simple console terminal (Texas Instruments 743 KSR) is used for input-commands and programming and it served as an output device too.
Only limited memory facilities were available. Therefore a single drive KERR minifile-6000 floppy disk unit was used as a data storage device. The floppy disk unit operated with 4 inch mini diskettes.

In the current research, the strain gauges (quarter bridge surface measurement and half bridge strain-readers) were connected directly to the input scanner. The load-cells and LVDTs were always connected via external amplifiers (SCHENCK-MV 15 in case of a 'control-component', and Hottinger KWS 3073 for the remaining devices). The output of the external amplifiers was fed into the input scanner (DC-inputs).
Two recorders (Philips x-y recorder PM 8041, and KIPP x-y, y' recorder BD 91) were available for visual control of load-displacement response during the experiment. A diagram of the complete system is shown in fig. 3.17.

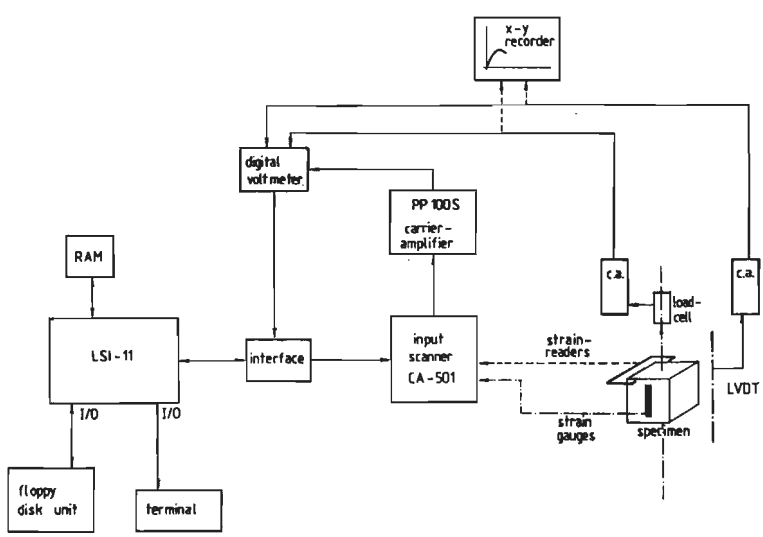

Fig. 3.17. Data aquisition system

Specifically developed software permitted continuous measuring during an experiment. A typical measuring sequence is shown in figure 3.18.

In each measuring step, all the connected devices, including the elapsed time (in sec.), were scanned, and the data were stored on a mini-diskette. A mini-diskette could store up to 300 measuring-steps. Four subsequent steps were stored directly and each fifth step was printed at the terminal too. A typical measuring step is also given in fig. 3.18. Each step starts with a scan of the connected load-cells (maximum 3), followed by a scan of all deformation measuring devices. Finally the load-cells were scanned a second time and the average values of the three loadings (P1, P2 and P3) were determined before the data were transported to the mini-file. A total scan took approximately 200 - 400 msec, depending on the number of devices that were connected. In the triaxial experiments a maximum load increase of 0.10 N/mm^2 was measured during a scan.

A relatively long time was necessary for data-storage. The minimum interval between two subsequent scans was approximately 5-6 sec, which increased to about 20 sec. when the data were printed.

The speed of the measuring system was generally sufficient for the triaxial experiments (see appendix A5, monotonous stress-strain curves (fig. A5.7-A5.13), each fifth measuring point is marked). Problems were encountered in the triaxial tension - biaxial compression experiments using a cyclic load-path. For future investigations allong these lines a further increase of speed will be required.

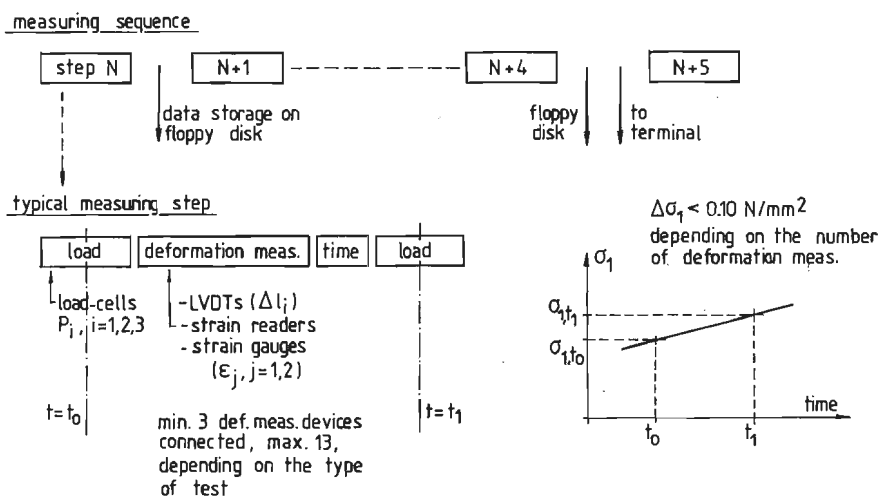

Fig. 3.18. Measuring sequence

Except for averaging the load-measurements, no data processing was carried out with the data-aquisition system. For further processing, such as correction for brush deformation, zero-correction, plotting, statistical analysis, etc., the data were transported to the university main computer system (Burroughs B 7700). Before this could be accomplished the data were copied on an 8 inch floppy disk using a Comm-Stor (RS-232) floppy disk unit.

3.2.5. calibration of brush deformation and zero-correction.

The brush construction is partly included in the LVDT measuring length, as was indicated in fig. 3.11. The total deformation, measured by means of the LVDTs should be corrected for brush deformations. A callibration test was carried out, using an aluminium cube (d = 100 mm), upon which six strain gauges (meas. length 10 mm) were mounted centrally in the axial loading direction. A linear relationship was measured between the applied axial stress σ_1, and the total brush deformation $\Delta l_{brush} = \Delta l_{LVDT} - \varepsilon_1 . d$. The results of the uniaxial calibration test and the linear regression analysis that was carried out are shown in fig. 3.19.

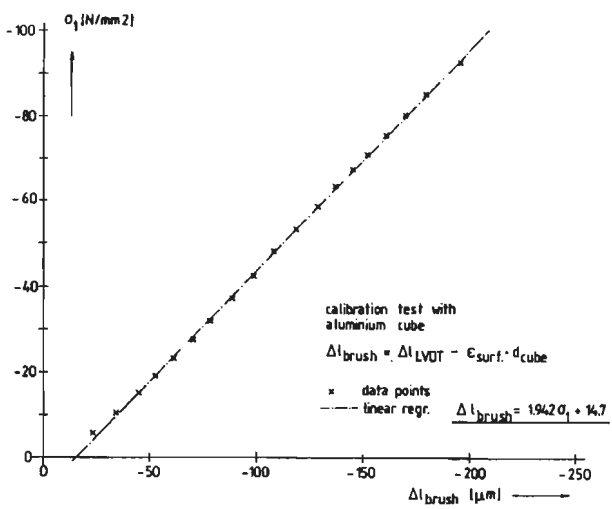

Fig. 3.19. Calibration of brush deformations.

When an experiment was carried out, always a small 'initial run' was observed in the load-deformation curve. An overestimation of initial deformation is the

result of non-smoothness of specimen and brush surface that are in contact.
A zero correction (translation along the ε-axis) was carried out to the stress-strain curve by calculating the maximum slope in the ascending branch. The zero strain was calculated from the maximum slope $E_{tan,0}$ and the stress-level at which it was measured (see fig. 3.20).

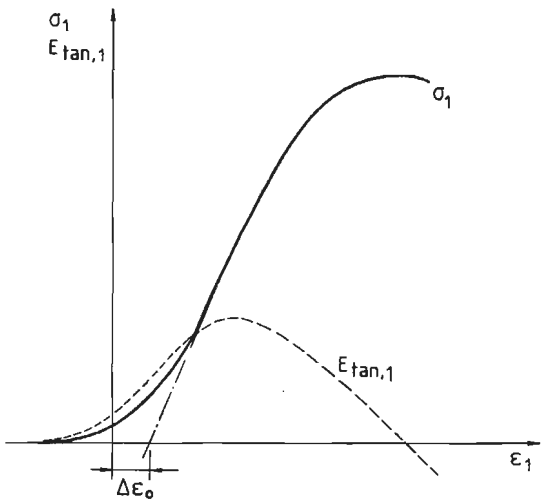

Fig. 3.20. Zero-correction for stress-strain curves.

The initial run could be prevented by adding a capping between the specimen and brush as indicated previously. This was considered especially useful in the triaxial experiments for those cases where a change in deformation direction was observed in the ascending branch of the stress-strain curve.

3.3. Manufacturing method for the specimens.

- specimens -

As it was mentioned in section 3.1, the triaxial testing machine was prepared for cubes with side d = 100 mm. As a result of the right angles between the horizontal frames and the vertical frame at the load-cell side (fig.3.8), very accurate manufacture of the cubes was demanded, therefore, great attention was paid to the planparallelity and rectangularity of the specimens.
Two major possibilities can be distinguished with regard to the manufacturing method. Either it was possible to cast the cubes in accurate stiff moulds of

the exact size, or larger blocks could be cast and the cubes sawn from them after the concrete hardened. As a consequence of the choice of brush bearing platens for load-application system, the use of moulded specimens was preferable. The high peak stresses induced at the specimen surface, due to the relatively small rod-size, would be smoothed out by the soft cement-matrix layer on the specimen surface. Furthermore, as the separate brush rods would intrude into this soft layer, an increasing safety against buckling of the rods would emerge /95/.
On the other hand, a highly heterogeneous specimen, suffering from all kinds of segregation effects would result /152,151/. A second disadvantage of this method is the fact that special measures had to be taken in order to obtain a smooth casting-surface (for example by casting a taller specimen and after hardening, sawing or grinding the casting-surface). The casting-surface is the upper surface when casted.

As a matter of fact, the second possibility was chosen. The specimens were cast in larger blocks - prisms -, with dimensions 700 x 135 x 135 mm^3 (see fig. 3.21).

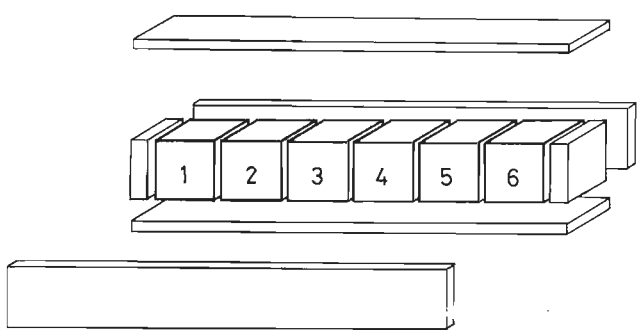

Fig. 3.21. Cubes (d = 100 mm), sawn from initial larger prisms.

The prisms were cast horizontally. Six cubes (d = 103 -104 mm) were sawn from the central part after 28 days hardening under water. The specimens were sawn by a local stone-mason, using a very stiff rotation diamond saw. After sawing the opposite sides of the cubes were ground flat and parallel to each other of the required size (d = 100 mm) using a diamond grinding disk.
The original prism-size assured that a layer with thickness d_a (= maximum aggregate size = 16 mm) was removed from each side of the cubes. This largely eliminated the segregation effect which arose during hardening of the concrete. Also by using sawn specimens, the six surfaces were treated similarly. Furthermore, when performing tensile tests where the cube had to be glued to

the loading-platen, the sawn surface provided the best boundary condition for obtaining a proper connection (v.Tongeren, see in /111/).
It will be obvious that neither moulded specimens, nor sawn cubes will give an ideal result. However, it was felt, that a homogeneous specimen was favourable in order to obtain proper results. As will be shown in chapter 4, a capping of epoxy-resin was inserted between cube and brush-bearing platen. The major reason for this measure was to obtain a reliable measurement of deformation. A second advantage, however, was that the specimen was loaded more uniformly (with regard to the peak-stresses).

In fig. 3.22, the different specimen-boundaries are shown for both the sawn and the moulded specimens.

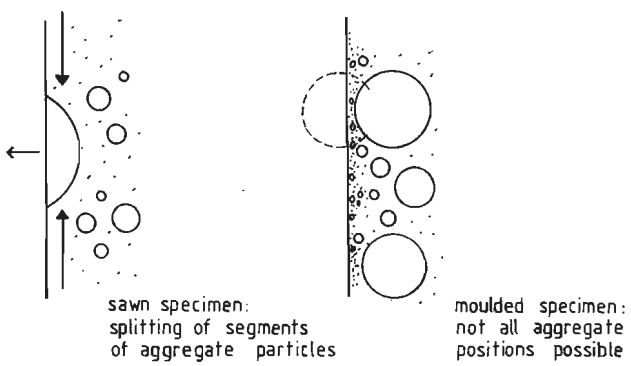

Fig. 3.22. Boundary conditions for moulded and sawn specimens.

Shrinkage and drying effects caused cracks in the specimen's surface if moulded /151/. Furthermore a basically different deformational behaviour may be expected from the different structural properties of the core concrete and the surface concrete of the moulded specimens. A difference in deformational behaviour was shown by Schickert /139/. However, in this context, the sawn specimens also are not ideal, while splitting of segments from aggregate particles could occur at the specimen-surface. (fig. 3.22) /151/.

- materials used -

For all tests, the same concrete mix was used. The maximum aggregate size chosen was d_a = 16 mm. The ratio between cube size and maximum aggregate size is equal to $d/d_a = 6 \sim 7$. This value was necessary in order to arrive at a proper strain measurement (Müller /109/). Also for this specimen configuration,

a continuum model using stress and strain as the state variables is still possible (at least in the pre-peak region).

The cement content used was 320 kg/m^3, the type of cement being an ordinary portland cement (type A). All cement needed was obtained from the same batch, and was stored under dry and air-tight conditions during the complete research. The w/c-ratio was chosen 0.50 in order to avoid segregation effects as much as possible. The grading-curve of the aggregate (sand and gravel larger than 0.25 mm originated from the river Meuse at Panheel, the sand smaller than 0.25 mm was obtained from the Kempen) was taken according to curve B16 of the Dutch codes VB 74, and is shown in table 3.23.

grain-size distribution (%)

Sieve mesh	16-8	8-4	4-2	2-1	1-0.5	0.5-0.25	0.25
%	24	20	14	10	12	12	8

Table 3.23. Grain size distribution of aggregates used.

The specimens were casted in batches containing two prisms (fig. 3.21), three control-cylinders ϕ 100 x 250 and 3 - 6 control-cubes (d = 150 mm). Always two batches (A and B) were casted at the same day.

During casting the specimens were vibrated (vibrating table, Ton industrie type 854613, 50 Hz, centrifugal force = 1 kN) for 180 seconds. Approximately 1 hour after casting, the specimens were vibrated a second time for 120 seconds. The casting-surfaces were finished, and the specimens were placed under a plastic cap to avoid drying out.

Two days after casting, the specimens were demoulded and placed in a fresh-water-bassin. At 28 days, the prisms were transported to a local stone-mason, and were sawn during the same day. After grinding the specimens in the laboratory, the specimens were sealed in plastic bags and placed in a room with a constant temperature of 20^0 C. During sawing and grinding, which in most cases took approximately 3 - 4 days, care was taken that the specimens were always in a wet-condition. The control cylinders and cubes were always kept in the same temperature and moisture conditions as the 100 mm-cubes. For clarity, the complete process from casting to storage is shown in figure 3.24. In case of surface-measurement the specimens were taken 2 days before testing from the plastic bags, and strain gauges or other measuring facilities were applied to the surfaces.

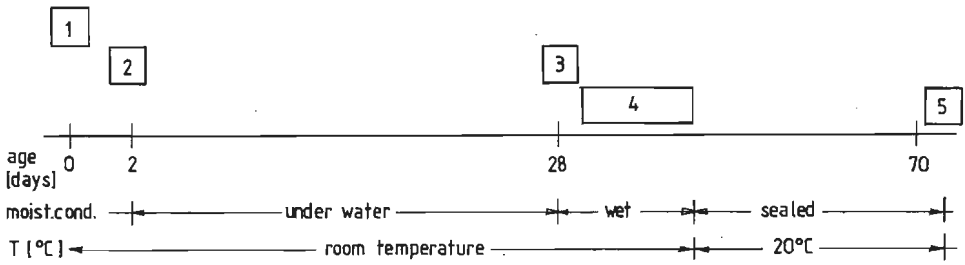

1. casting
2. de-moulding
3. sawing (stone-mason)
4. grinding (laboratory)
5. testing (age 70 days)

Fig. 3.24. Processing of the specimens before testing.

3.4. Summary of experiments.

In table 3.25, a summary of all the experiments that were carried out is shown. In the following chapters, a test-series is always identified with the batch number from which the specimens originate.
In the first column of table 3.25, the subsequent batch numbers are indicated. Further for each batch, the casting date, a short description of the purpose of a test series, the measurements that were carried out, and the results of the control-tests using cubes (d= 150 mm) and cylinders (ϕ 100 x 250 mm) loaded between rigid steel platens, are shown. The age at loading is the age of the control specimens when loaded. The age of the 100 mm cubes that were loaded in the triaxial apparatus may be slightly different. In the last column of table 3.25, the section in which the results of the concerning test-series are discussed is indicated.

The loading speed of the uni- and triaxial experiments, using 100 mm cubes, was slightly different in the subsequent test-series. A specimen was always loaded with a constant strain-rate in the major compressive direction (or tensile direction when fracture prevails in the tensile direction).
For series 2/3, the strain-rate was equal to $\dot{\varepsilon}_1 = 5.10^{-6}$/s, for series 5/6, 10 and 15, $\dot{\varepsilon}_1 = 10.10^{-6}$/s, and in the triaxial experiments (series 8/9 and 7), $\dot{\varepsilon}_1 = 20.10^{-6}$/s. These differences in loading speed are very small and will hardly affect the results /111,126/.

batch no.	casting-date(3)	short description	measurements (see section 3.2.2.)	f'_{k150} [1] (N/mm^2)	$f'_{c\,\phi\,100/250}$ [1] (N/mm^2)	age at loading (days)
2A	250182	- uniaxial compression	- force (P1)	-42.4 (1.58)	-39.0 (1.48)	72
2B		- manufacturing	- overall def. (Δl_1)	-46.8 (1.50)	-42.3 (0.71)	72
3A	170282	parameters	- lateral def. (Δl_2,Δl_3)	-46.3 (3.30)	-35.0 (3.82)	71
3B			- surface strains (ε_1, ε_2)	-49.9 (3.40)	-35.9 (4.81)	71
			- extended surface measurement (3B-series)			
			- crack-detection (2B2-prism)			
4A	100382	- first trials, bi-	- force (P1, P2, P3)	-39.9 (0.71)	-31.7 (1.10)	83
4B		and triaxial loading, tens./ compr., 3D compr.	- overall def. (Δl_1,Δl_2,Δl_3)	-48.3 (0.90)	-40.1 (1.69)	134
			- in some biaxial tests also surface measurement (ε_1, ε_2)			
5A	310382	- biaxial series	- force (P1, P2)	-51.8 (1.90)	-40.7 (3.30)	181
5B			- overall def. (Δl_1,Δl_2)	-48.0 (3.35)	-37.1 (3.62)	187
6A	210482		- surface strains (ε_1, ε_2)	-49.4 (1.58)	-38.9 (2.12)	181
			- lateral def. (Δl_3)			
6B	210482	- trials tension-compression (2D/3D)	- force (P1, P2, P3)		not determined (used for other purpose)	
		- saw-tests on 'cracked-concrete'	- overall def. (Δl_1,Δl_2,Δl_3)			
7A	120582	- rotation-experiments	- force (P1, P2, P3)	not determined	-43.2 (3.52)	468
7B		- triaxial compression	- overall def. (Δl_1,Δl_2,Δl_3)			
8A	140782	- triaxial series	- force (P1, P2, P3)	-48.9 (2.48)	-36.6 (2.36)	252
8B			- overall def. (Δl_1, Δl_2, Δl_3)	-50.0 (1.77)	-36.5 (2.99)	252
9A	040882		- uni- and biaxial also	-49.8 (1.10)	-39.9 (0.72)	251
9B			surface-strains (ε_1, ε_2) and lateral def. (strain-readers)	-50.0 (1.16)	-40.6 (0.83)	251
10A	241182	- callibration of def.	- force (P1)	-49.0 (2.34)	-35.8 (2.76)	76
10B		measuring system	- def. (Δl_1)	-51.9 (0.49)	-37.0 (1.12)	76
		- size effect	- extended surface meas.			
		- uniaxial compression	(ε_1, ε_2)			
			- lateral def. (Δl_2,Δl_3)			
14A [2]	030883	- check on age	- force (P1)		not determined	
		- uniaxial compression	- axial def. (Δl_1, Δl_2, Δl_3)			
			- surface strains (ε_1)			
15A [2]	240883	- size effect	- similar to series 10.	-46.1 (0.47)	-35.4 (3.30)	105
		- uniaxial compression				

Table 3.25. Summary of experiments

(1) loading speed $\dot{o}$ =0.25 N/mm^2/sec, mean value of three tests, (cube strength $f'_{k\,150}$ and cylinder strength $f'_{c\,\phi\,100/250}$) coëfficiënt of variation between brackets,
(2) sawn at the laboratory,
(3) date = day - month - year.

Specimen codification p Aq - r

p = batch number
q = prism number of concerned batch
r = specimen no. in prism q (see fig. 3.21).

4. UNIAXIAL EXPERIMENTAL RESULTS

During the complete investigation, several uniaxial compression tests were carried out serving different purposes. In this chapter the experimental designs and results of the subsequent test series are shown.
Before this is done, a short introduction to statistical analysis is given in section 4.1. The theory of linear models was adopted in the design and analysis of the experiments. Further in section 4.2. the results are shown of series 2/3, regarding the influence of several parameters related to the manufacturing method of the specimens (see section 3.3). In 4.3. the results of the 10-series are gathered (deformation measurement) and finally in section 4.4. some results of series 10/15 are shown, indicating the influence of specimenheight on the uniaxial stress-strain curve.

4.1. Introduction to statistical analysis.

For the design and analysis of the experiments, the theory of linear models was applied in the subsequent test-series. A summary of the method, which can be found in detail in Mendenhall /102/, is given below.
The experimental results are described by means of a linear model (linear in the parameters β_1), containing k variables.
The model is given by:

$$\underline{y} = \beta_0 + \beta_1 x_1 + \beta_2 x_2 + \ldots\ldots + \beta_k x_k + \underline{e} \qquad \ldots\ldots(4.1.),$$

where $\underline{y}$ is a vector of size n containing the experimental results. The variables x_i are dependent on the levels of the influence-factors and may either be quantitative, or by means of dummy-variables also be qualitative. The vector $\underline{e}$ contains all random errors, which are assumed to be mutually independent and have a normal distribution with expectation $E(\underline{e}) = 0$ and variance $\text{var}(\underline{e}) = \sigma_0^2$.
The expression (4.1.) may be written in a shortened form:

$$\underline{y} = X\beta + \underline{e} \qquad \ldots\ldots(4.2.),$$

where X is the design matrix, and which contains all information regarding the treatment-combinations. The purpose of the tests is to estimate the variables β_i by means of the method of least squares. The estimate $\underline{b}$ of β is determined through

$$\underline{b} = (X'X)^{-1} X\underline{y} \qquad \ldots\ldots(4.3.).$$

The vector $\underline{b}$ is of size $(k + 1)$ with expectation $E(\underline{b}) = \beta$.
In case of an orthogonal experimental design, $(X'X)$ reduces to a diagonal matrix.
The estimate of the random error can be determined from the sum of squares of deviations of the observations ($\underline{KS}r$) according to:

$$\sigma_0^2 = \underline{KS}_r / (n - k - 1) \qquad .....(4.4.),$$

in which the difference $n - (k + 1)$, between the number of observations and the number of parameters is the number of degrees of freedom.
The variances and covariances of the estimates $\underline{b}_i$ of β_i are fully determined by the matrix $(X'X)^{-1}.\sigma_0^2$. An estimate for the variance and covariance of $\underline{b}_i$ (and $\underline{b}_j$) is therefore given by:

$$\hat{\sigma}^2(\underline{b}_i) = \{(X'X)^{-1}\}_{ii} \quad \hat{\sigma}_0^2 \qquad .....(4.5.a.),$$

$$\text{and } \hat{\text{cov}}(\underline{b}_i, b_j) = \{(X'X)^{-1}\}_{ij} . \quad \hat{\sigma}_0^2 \qquad .....(4.5.b.).$$

Further, it can be proved that

$$(\underline{b}_i - \beta_i) / \hat{\sigma}(\underline{b}_i) \qquad .....(4.6.),$$

has a students-t distribution, with $n - (k + 1)$ degrees of freedom. Now it is possible to determine the $(1 - \alpha)$ confidence intervals for the β_i by means of

$$\beta_i \pm t_{\alpha/2} \cdot \hat{\sigma}(\underline{b}_i) \qquad .....(4.7.).$$

Also hypothesis concerning the parameters $\underline{b}_j$ or a linear combination of parameters of the form

$$\underline{l} = a_0\underline{b}_0 + a_1\underline{b}_1 + ... + a_k\underline{b}_k = a'\underline{b} \qquad .....(4.8.),$$

may be investigated.
For example, the hypothesis that $(k - g)$ variables are equal to zero,

$$H_0 : \beta_{g+1} = \beta_{g+2} = ... = \beta_k = 0 , \qquad (g < k) \qquad .....(4.9.),$$

may be checked using a F-distribution with $(k - g)$ and $n - (k + 1)$ degrees of freedom according to:

$$\underline{F} = \frac{(\underline{KS}_{r0} - \underline{KS}_r)/(k-g)}{\underline{KS}_r/(n-k-1)} \qquad .....(4.10.),$$

where $\underline{KS}_{ro}$ is the sum of squares of deviations of the observations for the reduced model with (k - g) values of β_i equal to zero, and $\underline{KS}_r$ is the sum of squares of the original model. When the value of $\underline{F}$ surpasses a critical value, the hypothesis H_o must be rejected; the parameters β_i (g+ $1 \leq i \leq$ k) have a significant influence.

We may also be interested in confidence limits for linear combinations l= a'b. These are fully determined by means of

$$\text{var } (\underline{l}) = a' (X'X)^{-1} a.\hat{\sigma}_0^2 \qquad .....(4.9.).$$

The procedure may now be summarized as follows. For a linear model containing all main-effects and two-factor interactions the $\underline{b}_i$ are determined with (eq.4.3), and the random error is estimated with (eq.4.4). Using the F-test, we can investigate if it is possible to reduce the model. Confidence limits for the $\underline{b}_i$ or linear combinations for the $\underline{b}_i$ are determined.
For the statistical analysis, the computer program 'Linear Regression', which is available at the University's main computer, was used.

4.2. Influence of manufacturing method of the specimens.

4.2.1. Experimental design for uniaxial tests (series 2 and 3)

Before the bi- and triaxial experiments were carried out, a relatively large number of uniaxial displacement controlled compression tests was performed. In order to measure the pure effects of triaxiality on the concrete stress-strain behaviour, it was considered favourable to use homogeneous specimens. If systematic differences are due to the applied manufacturing method (which was mentioned in section 3.3.) these factors should be known and if possible be eliminated. Three parameters were considered important in this context:

-1- the replicability between subsequent batches (i.e. the scatter in strength and deformational results of different batches),
-2- the influence of the direction of loading with regard to the direction of casting, indicating effects of initial anisotropy, and
-3- the position of a cube in the original prism before sawing (see fig. 3.21).

The experimental design provided for a total number of 48 uniaxial compression tests. The cubes originated from the eight prisms of batches 2A, 2B, 3A and 3B. The six cubes of each prism were treated as follows: specimens 1, 2 and 3 are loaded perpendicular with regard to the direction of casting, the three remaining

cubes (4, 5 and 6) are loaded parallel. Three different cube-positions are possible within a prism: the end position (no. 1 and 6), half-position (no. 2 and 5) and middle position (no. 3 and 4). A review of the experiments is given in table 4.1.

BATCH 2A 3A
2B 3B

total: 8 prisms, designated 2A1, 2A2, 2B1, 2B2, 3A1, 3A2, 3B1, 3B2

specimen no. in prism	loading-direction
1.	perpendicular
2.	"
3.	"
4.	parallel
5.	"
6.	"

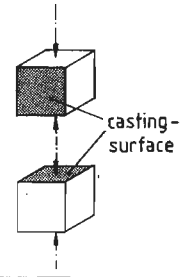

position of cubes

1,6	end position
2,5	half position
3,4	middle position

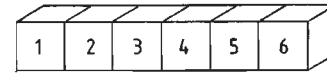

Table 4.1. Uniaxial experiments, series 2 and 3.

All uniaxial experiments of series 2 and 3 were carried out in the vertical loading axis of the triaxial apparatus (axis no. 3, see fig. 3.8). When loading was applied parallel to the direction of casting, the upper surface of the cube (when casted), was situated under the upper brush bearing platen (at the side of the spherical seating, see fig. 3.9). In case of perpendicular loading, the casting surface was one of the free surfaces of the specimens, as shown in figure 4.1. The loading speed (strain-rate) was held constant during the experiments: $\dot{\varepsilon}_1 = 5.10^{-6}$/sec.

In table 4.2. a review is given of the different measuring devices that were used in the subsequent uniaxial experiments. The measurement of Δl_i (i = 1, 2, 3) was similar for all experiments: overall displacement measurement Δl_1 by means of two LVDTs and lateral displacement measurement Δl_2, Δl_3 by means of strain-readers in a configuration as shown in fig. 4.2. The strain-readers were attached to the specimen at a distance of 20 mm from the brush-specimen interface.

prism no.		measuring devices
2A1 2A2 2B1	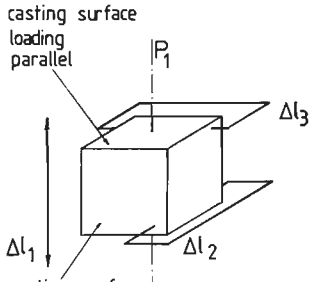	Δl 1 - LVDTs, 2W10, diagonal Δl 2 - strain readers, 2 in Δl 3 each direction, diagonal P1 - load cell
2B2	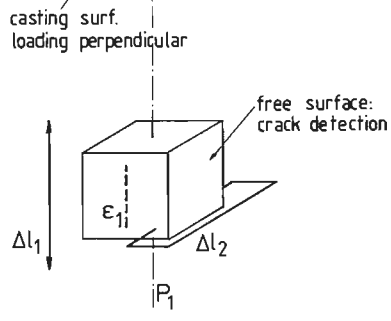	Δl 1 - LVDTs, 2W10, diagonal Δl 2 = Δl 3 - 4 strain readers in one direction ε 1 - 2 strain-gauges PL 60-11 In case of perpendicular loading, one gauge mounted at the casting surface, the other at the opposite surface. crack-detection on free surfaces, using fluorescenting technique /49,152/.
3A1 3A2 3B1	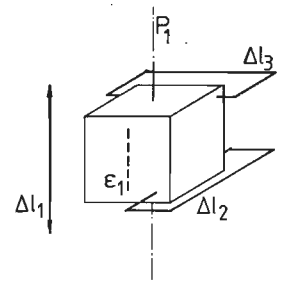	Δl 1 - LVDTs, 2W10, diagonal Δl 2 - 2 strain-readers, diagonal Δl 3 - 2 strain-readers, diagonal ε 1 - 2 strain gauges, PL 60-11 Specimens from prism 3B1 were subjected to 5-10 load cycles up to ε 1=0.001 strain before loading to failure.
3B2	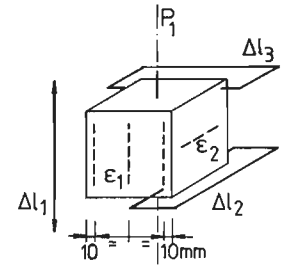	Δl 1 -LVDTs, 2W10, diagonal Δl 2 see 3A1-3B1 Δl 3 ε 1 - 6 strain gauges (PL 60-11), four at corner position (10 mm from the edge), two at central position. ε 2 - 2 strain gauges (PL 60-11) at half height.

Table 4.2. review of uniaxial experiments, measuring devices, series 2 and 3.

For the specimens originating from the prisms 2B2 through 3B2, additional surface strain-measurements were carried out (see also section 3.2.2). Two strain gauges (no. 10 and 11) were mounted in a central position at two opposite surfaces of the cube (see fig. 4.2). The measuring length of the gauges was 60 mm. For specimens 3B2-1 through 3B2-6 extended surface strain measurements were carried out. Six strain gauges (measuring length 60 mm) were mounted to the specimen at two opposite surfaces as shown in figure 4.2. The four corner gauges (no. 14, 15, 16 and 17) were placed at a distance of 10 mm from the specimen edge. Furthermore two lateral gauges (meas. length = 60 mm, no. 12 and 13) were mounted to the remaining free surfaces at half height.
Especially the results of these latter tests (3B2-1 through 3B2-6) provided much information on the complete deformational behaviour of the specimen. The fracture propagation through a uniaxial compressed cube (in the descending branch of the axial stress-strain curve) could be followed.

The six specimens originating from prism 2B2 were used for crack-detection purposes. The fluorescenting technique developed by Forester /49/ and applied by Stroeven /152/and Diaz & Hilsdorf /39/ was adopted. The specimens were subjected to a cyclic loading sequence. A specimen was loaded until a prescribed axial strain-value. When this strain-value was reached, the loading was stopped and the fluorescenting dye was applied to one of the free surfaces, and allowed to penetrate the specimen for about 60 seconds. There after the axial load was released (at the same loading speed ($\dot{\varepsilon}_1 = 5.10^{-6}$/sec) as for the ascending branch) until a stress-level $\sigma_1 = -5$ N/mm^2 was reached.
When the dye was completely dried, a colour slide was taken of the treated surface lighted by two ultra-violet lamps. For darkening purposes, a special tent was built around the 'triaxial chamber' for the photographic equipment and both lamps.

The crack-detection surface was chosen for investigating possible effects of initial anisotropy (see figure 4.3).
A crack-detection experiment took approximately 3 hours. A test consisted of 8 crack detection steps up to a strain-level $\varepsilon_1 = -0.0045$, which was in general beyond the inflection point in the axial stress-strain curve.
The 'crack-densities' and 'orientation distributions' obtained from these experiments are only indicative. As will be shown in the following sections, the behaviour of the specimen surface and the specimen core seems to be quite different. Some of the results obtained from the surface crack detection will be given in chapter 6.

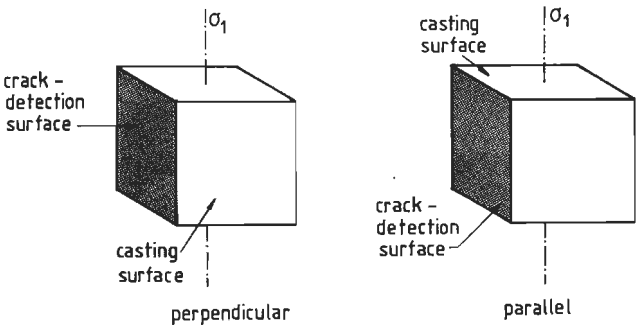

Fig. 4.3. Crack-detection for specimens 2B2-1 through 2B2-6.

For all uniaxial experiments of series 2 and 3 the conditions at peak (stress σ_{1p} and the corresponding strains ε_{ip}, i = 1, 2, 3 both for loading platen and surface-strain measurement) are given in appendix A1, table A.1.1 and A.1.2.

4.2.2. Statistical analysis of the results

- **strength results** -

A statistical analysis, using the theory of linear models (that was introduced in section 4.1) was carried out, adopting the peak stress level σ_{1p} as a response variable. The linear model is given by

$$\sigma_{1p} = E\underline{Y} = \sum_{i=0}^{17} \beta_i x_i \qquad .....(4.10)$$

The variables x_i represent the level of the influence factors: the loading direction with respect to the direction of casting (x_1), the cube position (x_2, x_3), the batch (x_4, x_5, x_6), and a number of two-factor interactions (x_7, x_8 ....., x_{17}).
The mean strength (100 mm cube) is given by the estimate b_o of β_o. All factors are qualitative.

The full details of the model and analysis are shown in appendix A1, table A.1.3., showing the values of the variables x_i, the estimates b_i of β_i (i = 0, 1, ..., 17), the coefficients of variation ($v\hat{a}r/\hat{o}_o^2$, equation 4.9) and the P-values.

The factors which were found to be significant at the 5% level are: the linear term for differences between positions (x_2), the three terms (x_4, x_5, x_6) for differences between batches and a two-factor interaction ($x_{13} = x_2\, x_5$). The reduced model, containing only significant factors is given by

$$\hat{\sigma}_{1p} = \hat{y} = -39.56 - 0.61\, x_2 - 1.25\, x_4 + 0.55\, x_5 + \\ - 0.67\, x_6 - 0.55\, x_2\, x_5 \qquad .....(4.11.)$$

The estimate for the random error is $\hat{\sigma}_o^2 = 1.51$ ($\nu = 29$). The average uniaxial compressive strength was $\bar{\sigma}_{1p,100} = b_o = -39.56$ N/mm^2, which was slightly higher than the uniaxial compressive cylinder strength $\bar{\sigma}_{1,cyl} = -38.1$ N/mm^2 (which was determined from the control cylinders of batches 2A - 3B, see table 3.25).

The experiments revealed a strength increase for specimens originating from the end positions (no. 1 and 6). The effect is depicted in figure 4.4, also showing the 95% confidence limits.

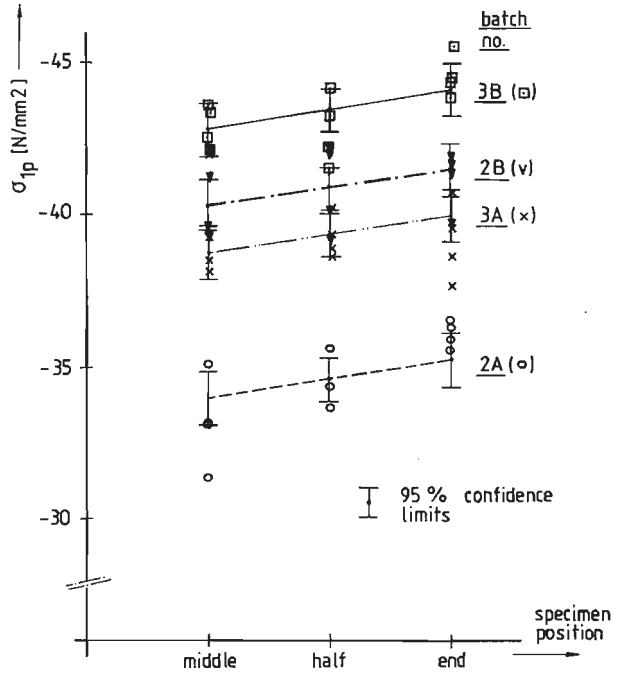

Fig. 4.4. Influence of specimen position before sawing on the uniaxial compressive strength.

The results indicate that a stiffening effect emerges from the end platens of the mould. When the prisms are casted, the concrete at the prism ends will be better compacted, due to the presence of the end plates in the mould.

The differences between batches were found to be significant at the 5% level. Yet the expression in eq. 4.11. is rather meaningless with respect to the terms x_4, x_5 and x_6. In fact the factor 'batches' is stochastic. The implication of this fact is that certain influence factors should not be tested against the random error σ_o^2, but rather against a combination of random errors, including the one for the stochastic factor batches.
An additional analysis, taking into account the factor batches as a stochastic factor showed no difference with the foregoing results.

The increase in strength from batch 2A - 3B is rather striking and must probably be attributed to differences in compaction of the specimens. For all further batches (no. 4 through 15), the compaction time was held constant (as was mentioned in section 3.3), resulting in a decreasing scatter.

The direction of loading with regard to the direction of casting did not have a significant effect on the ultimate strength level.

- energy requirement -

A second statistical analysis was carried out, now using the energy-requirement W_r as a response variable. The energy-requirement is defined as the amount of energy that is necessary to obtain a given strain-level ε_o:

$$W_{r,\varepsilon_o} = \int_0^{\varepsilon_o} \sigma_1(\varepsilon_1)\, \delta\varepsilon_1 \qquad \text{.....(4.12).}$$

Equation 4.12 represents the total surface under the axial stress (σ_1) - axial strain (ε_1) curve, and is different from the damage energy concept that was proposed by Spooner et.al. /148,149/ (see section 2.2).
The calculated values of W_r are given in appendix A1, table A.1.1. and A.1.2. for three levels of ε_o: $\varepsilon_o = \varepsilon_{1\ peak}$, $\varepsilon_o = 6\ ^o/oo$ and $\varepsilon_o = 7\ ^o/oo$ (compressive strain).

The linear model to be fitted was similar to the preceding model in which the strength results were adopted as a response variable. For the energy-requirement the model is given through

$$W_{r,0.006} = \int_0^{0.006} \sigma_1(\varepsilon_1)\,\delta\varepsilon_1 = E\underline{y} = \sum_{i=0}^{17} \beta_i x_i \qquad \text{.....(4.13).}$$

The full details of the model (eq.4.13) and the analysis are shown in appendix A1, table A.1.4. The reduced model, only containing the significant factors at the 5% level is given by:

$$\hat{W}_{r,0.006} = 159.45 + 6.48\,x_1 + 3.41\,x_2 + 1.87\,x_4 - 2.97\,x_5 + 4.39\,x_6 \qquad \text{.....(4.14).}$$

The estimate for the random error is $\hat{\sigma}_o^2 = 78.96$ ($\nu = 27$). It should be mentioned that the energy-requirement for the crack detection tests (specimen 2B2-1 through 2B2-6) was calculated using the envelope curve which connects all subsequent load-cycle peaks.

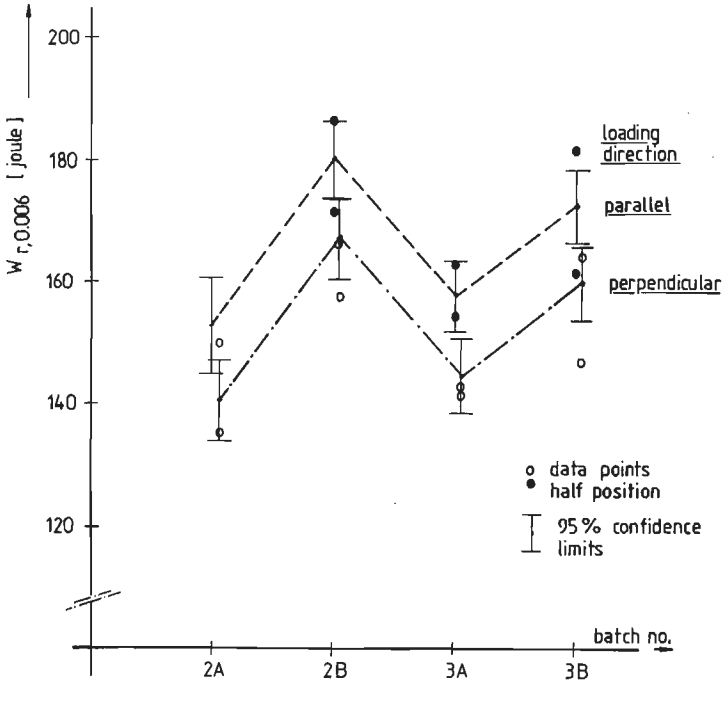

Fig. 4.5. Influence of position and loading direction for subsequent batches on the energy requirement at $\varepsilon_o = 0.006$.

The factors loading direction (x_4), position of specimen before sawing (linear term x_2) and differences between batches (x_4, x_5, x_6) could not be omitted from the model (eq.4.13). About 9% extra energy is required in order to reach a strain-level ε_o = 0.006, when loading is applied parallel rather than perpendicular with regard to the direction of casting.
Similar considerations should be made for the factor batches as were mentioned for the linear model describing the peak stress results (eq. 4.10).
The factor position also is found to have a significant effect when the energy-requirement is adopted as a response variable. The results of the second analysis are depicted in figure 4.5.

4.2.3. Uniaxial stress-strain behaviour

- **initial anisotropy** -

The influence of the direction of loading with regard to the direction of casting on the axial stress-strain curve is demonstrated in figure 4.6. The stress-strain curves for specimens 3B2-3 (loading perpendicular) and 3B2-4 (loading parallel) are representative for all uniaxial test results. In the ascending branch of the stress-strain curves, the initial slope is found to be smaller when loading is applied parallel.

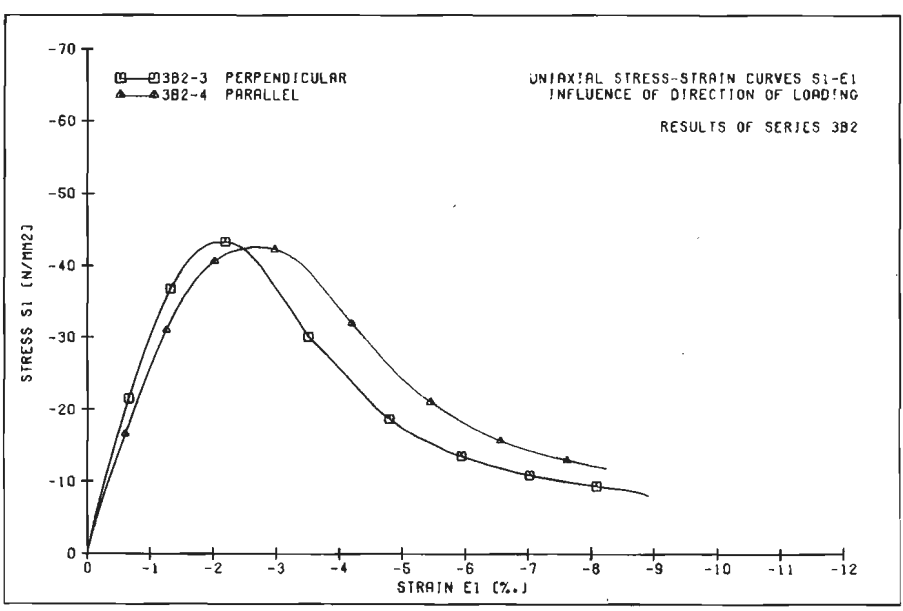

Fig. 4.6. Influence of initial anisotropy on the uniaxial stress-strain curve in compression.

Eventually the peak stress-level is reached, the strain at peak stress being higher in the case of parallel loading. In the descending branch of the stress-strain curves, similar behaviour is observed both for the parallel loaded specimen and for the perpendicular loaded cube.

The reason for the observed effects is obvious. Due to shrinkage, differential temperature and bleeding during the hardening process of the concrete, voids or weaker matrix material zones develop under the larger aggregate particles (this fact was mentioned in section 2.1). When loading is applied parallel, the initial 'micro-defects' are in a less favourable direction for their propagation. The micro-cracks have to round the aggregate particles, and the stress-strain curves indicate that a larger deformation is necessary in order to arrive at a 'damage-density' at which a maximum carrying capacity is reached. The effect is demonstrated in fig. 4.7.a.

When on the other hand loading is applied perpendicular with regard to the direction of casting, the initial 'micro-defects' are oriented in the same direction as the applied compressive load (fig. 4.7.b). The orientation is now very favourable for propagation, and will occur at relatively low displacement levels.

The formation and propagation of macro defects in the stress-strain curve descending branch seems not to be influenced by a simple change of the loading

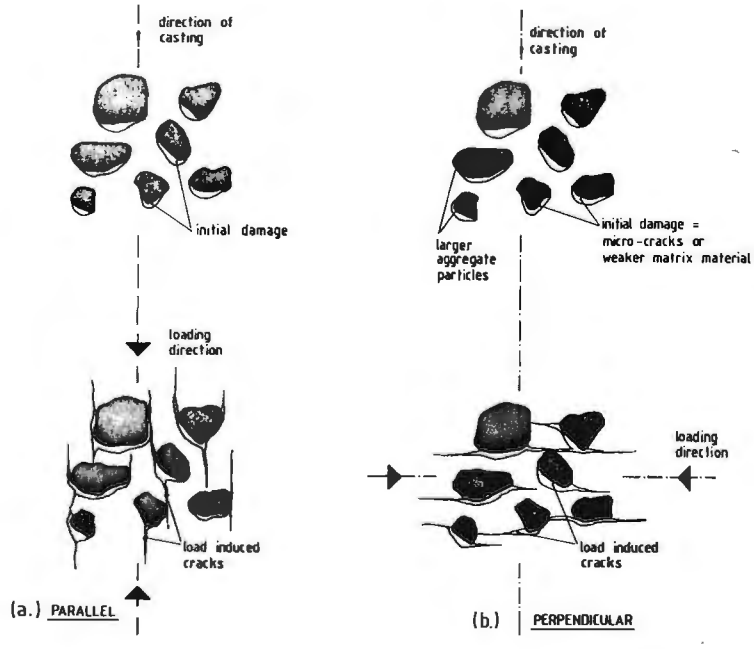

Fig. 4.7. Micro-crack propagation when loading is applied parallel (fig. a.) or perpendicular (fig. b.) with regard to the direction of casting.

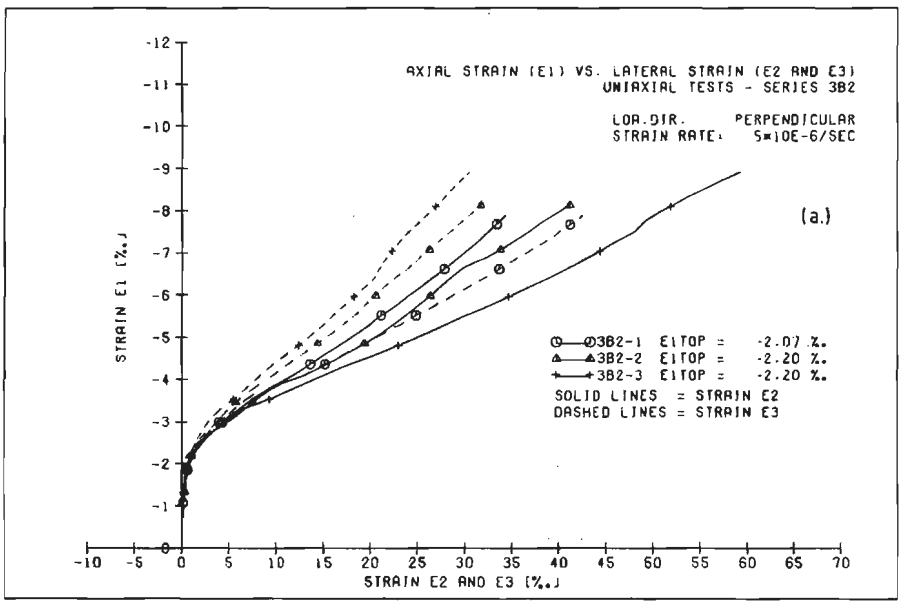

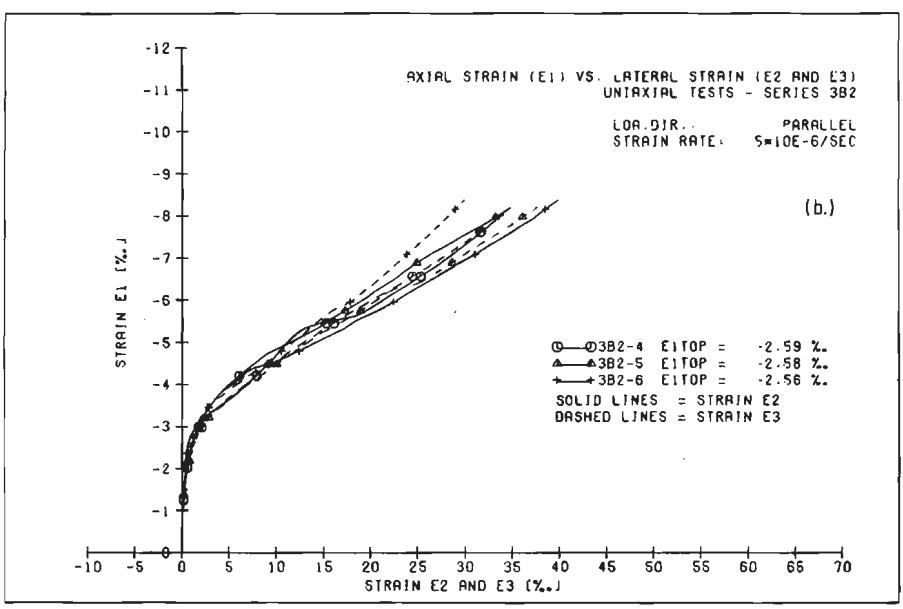

Fig.4.8. a. axial strain ε_1 vs. lateral strain ε_2 and ε_3 for specimens 3B2-1, 3B2-2 and 3B2-3, loading direction perpendicular.

b. idem, for specimens 3B2-4, 3B2-5 and 3B2-6, loading direction parallel.

direction. Only the 'damage-history' before joining of smaller cracks into (visible) macro-cracks occurs, seems to be important.

Differences in the pre-peak compressive stress-strain curve, due to initial anisotropy, were reported by Hughes and Ash /74/ too. In their paper, results were presented for a low strength concrete only (cube strength 28.5 N/mm^2, d_a= 19 mm). An increase of approximately 50% in peak stress was measured when loading was applied perpendicular to the direction of casting rather than parallel. Hughes and Ash mentioned that this increase is less for higher strength concretes, which is in agreement with the current results.

As a reason for the strength difference observed, it was mentioned /74/, that the porous zone beneath the coarse aggregate particles offers little resistance to deformation when loading was applied parallel. In this case shear failures may occur around the aggregate. When loading is applied perpendicular, lateral splitting of the mortar around the aggregate occurs /74/.

Mix parameters and compaction of the concrete when cast are responsible for the effect of initial anisotropy.

In view of the above discussion implications in the lateral (unstressed) directions should be expected too. In the case of parallel loading two equal lateral displacements should be measured ($\Delta l_2 = \Delta l_3$), while the conditions at the micro-structural level are similar for both lateral directions. When loading is applied perpendicular the micro-structure is different: the 'weak-planes' or 'micro-defects' are situated in planes which are oriented perpendicular to the direction of casting (fig. 4.7.b). While probably the majority of macro-defects will develop in the direction perpendicular to the direction of casting, the largest lateral displacements should be expected in the direction parallel to the casting direction.

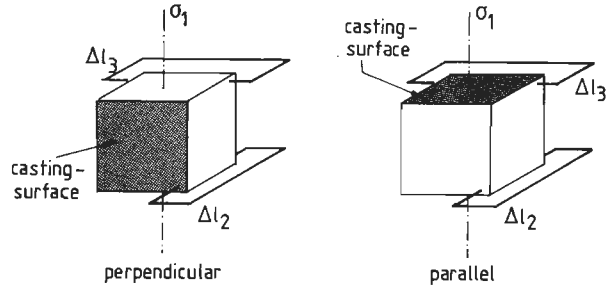

Fig. 4.9. Definition of ε_2 and ε_3 in case of perpendicular and parallel loading (uniaxial compression).

At the macro-level, indeed the indication was found that the lateral displacements are affected by the loading-direction too. In figure 4.8.a and b the lateral strains (ε_2, ε_3) are plotted against the axial strain (ε_1) for the six specimens originating from prism 3B2. In the upper figure (4.8.a) the lateral strain - axial strain plots are shown for the three perpendicular loaded specimens (3B2-1, 3B2-2 and 3B2-3). The lateral strain ε_2, depicted by the solid lines in fig. 4.8.a, is parallel to the direction of casting. The orientation of ε_2 and ε_3 with regard to the direction of casting is clarified in figure 4.9.
In the lower part of figure 4.8, the results of the three parallel loaded cubes are shown (3B2-4, 3B2-5 and 3B2-6). The broken lines in fig. 4.8.a and b represent the strain ε_3, which is perpendicular to the direction of casting, when loading is applied perpendicular or parallel.
The large scatter of lateral strain measurements for the perpendicular loaded specimens is striking. Figure 4.8.a indicates that the largest deformation occurs in the direction parallel to the direction of casting. Yet the effect is not systematic, and is probably disturbed by the splitting of the outer concrete layers which occurs in the stress-strain curve descending branch (and which seems to be a rather random process).

In case of parallel loading (fig. 4.8.b.) the lateral strain measurements are all situated in a narrow band, indicating a proper symmetric loading. From figures 4.8.a. and b. also the delayed fracturing of parallel loaded specimens may be observed. Large increments of ε_2 and ε_3 occur at higher levels of ε_1 when loading is applied parallel rather then perpendicular.
Similar effects are also observed in triaxial loading, as will be shown in section 5.2.5. In case of triaxial loading no boundary disturbances in the sense of splitting of outer concrete layers will occur and a systematic influence of loading direction on lateral strains was found.

These results indicate that only small changes at the micro-structural level (in this case a change of orientation of initial faults) has a pronounced influence on the macroscopic 'stress-strain' relationship. More attention is paid to the effects of initial anisotropy in sections 5.2.5 and 6.2.

- replication of uniaxial stress-strain curves -

In figures 4.10 and 4.11.a and b, a number of uniaxial stress-strain curves are gathered showing respectively the replication of stress-strain response (σ_1 - ε_1) for specimens originating from subsequent batches (2A - 3B) and for specimens originating from the same prism (3A1).

The results presented in figure 4.10 were all obtained from specimens originating from the prism ends (position no. 6). The loading direction was the same for all experiments: parallel to the direction of casting. The scatter in peak strength is rather large, the reasons for this fact being mentioned in the previous section.

In general a slight increase of strain ε_1 at peak stress level was measured when the peak stress increased. The shape of the axial stress-strain curve was however similar for all experiments.

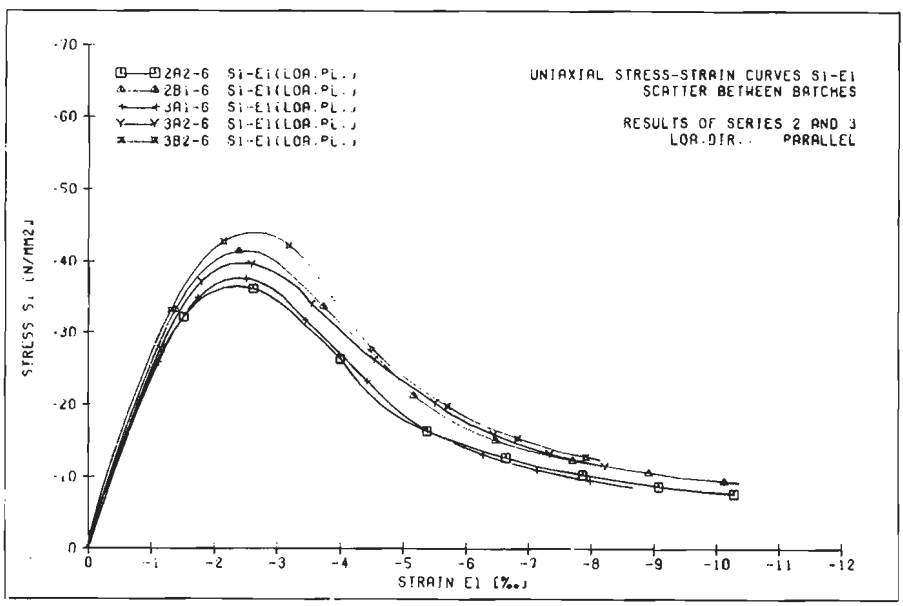

Fig. 4.10. Replication of stress-strain curves σ_1 - ε_1 for specimens originating from different batches (2A-3B), loading direction parallel.

The residual stress-level was the same for all tests presented in fig. 4.10 (about $\sigma_1 = -11$ N/mm^2 at $\varepsilon_1 = -8$ ‰).

The results shown in figures 4.11.a-b indicate that a good replication is obtained for specimens originating from the same prism. The solid lines in figures 4.11.a and b are results obtained from the overall LVDT-measurement (between the two opposite loading platens), the dashed lines are the stress-strain curves obtained from the surface strain measurement by means of the two central placed strain gauges (see fig. 4.2). Further attention to differences between loading platen and surface strain measurement is given in the next section. Replication of lateral deformation measurement was already shown in fig. 4.8.

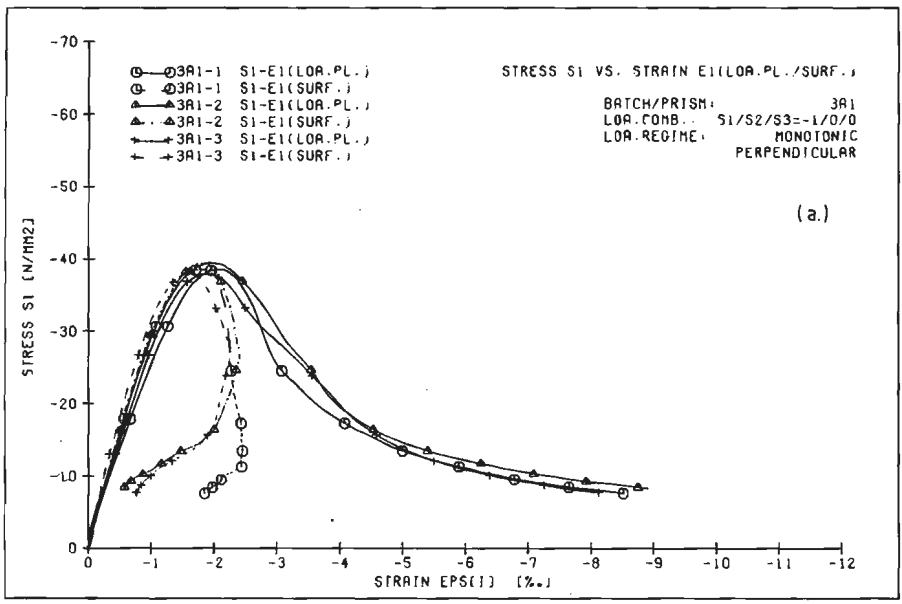

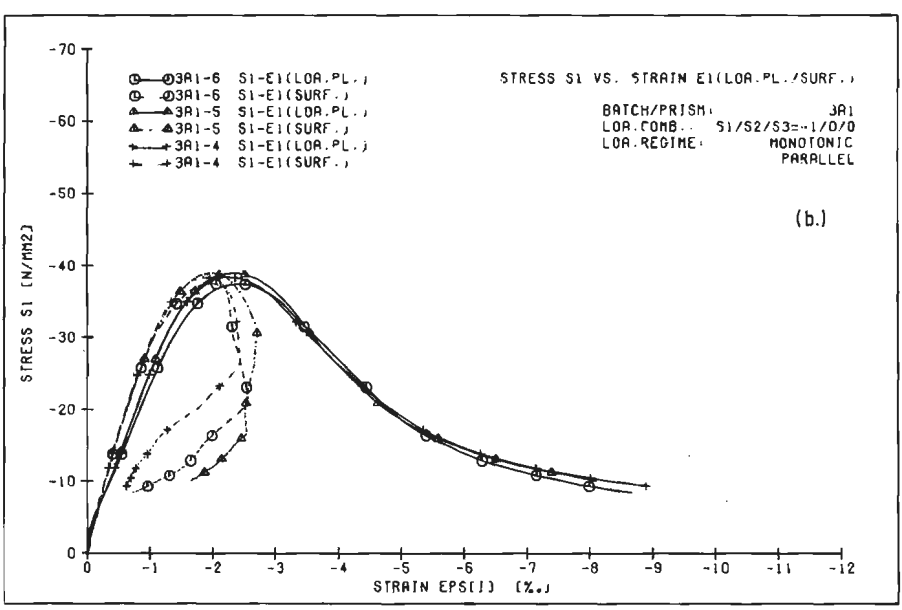

Fig.4.11. a. Uniaxial stress-strain curves (σ_1 - ε_1) for specimens 3A1-1, 3A1-2 and 3A1-3, loading direction perpendicular.

b. idem, for specimens 3A1-4, 3A1-5 and 3A1-6, loading direction parallel.

4.2.4. Fracturing in uniaxial compression

- observations from surface measurements -

The axial stress-strain curves, showing overall and surface strains (fig. 4.11.a and b), revealed a striking difference between the surface and core concrete response of a specimen. In the ascending part of the axial stress-strain curve, the surface strain $\varepsilon_{1,surf}$, was always behind the strain-value $\varepsilon_{1,loa.pl.}$ obtained from the overall displacement measurement between the two loading platens. The differences in pre-peak strain-measurement were systematic, as may be seen from the results in appendix A1 (table A1.1 and A1.2, peak strains, and fig. A.1.5 and A.1.6, stress-strain curves $\sigma_1 - \varepsilon_1$ for specimens originating from prisms 3A2 and 3B2).
The relative loading platen displacement Δl_1 was of course corrected for the total brush-deformations Δl_{brush}, which were determined from a calibration test on an aluminum cube (see section 3.2).

A difference up to 30% of $\varepsilon_{1,surf}$ with respect to $\varepsilon_{1,loa.pl.}$ was measured in the uniaxial compression tests. Similar results were reported by Schickert /139/, using the flexible platen system (fig. 3.4) and dry steel platens as load application system in an extensive experimental research on concrete and mortar prisms subjected to uniaxial compression.
The differences between $\varepsilon_{1,surf}$ and $\varepsilon_{1,loa.pl.}$ are mainly the result of the load-application system and disturbances at the specimen - load application interface. In section 4.3 more attention is given to the nature of these effects.

From the results presented in figures 4.11 and A1.5 - A.1.6, a pronounced difference in post-peak behaviour is observed when surface and loading platen strains are compared. The difference between $\varepsilon_{1,surf}$ and $\varepsilon_{1,loa.pl.}$ increases enormously beyond peak-stress level.
Just beyond peak, $\varepsilon_{1,surf}$ still increases, however at a considerable lower rate when compared with $\varepsilon_{1\ loa.pl.}$. Eventually, at the inflection point in the σ_1 $\varepsilon_{1,loa.pl.}$ curve, the surface strains $\varepsilon_{1,surf}$ start to decrease. It must be concluded that unloading takes place in the outer layers of the specimen, and the residual carrying capacity (of the now highly fractured specimen) seems to be the result of the 'more or less' intact specimen core.
At the same time that the uniaxial tests were carried out, similar results were reported by Kotsovos /87/. The results indicate that a structural response rather than a material response is being measured in the stress-strain curve descending branch.

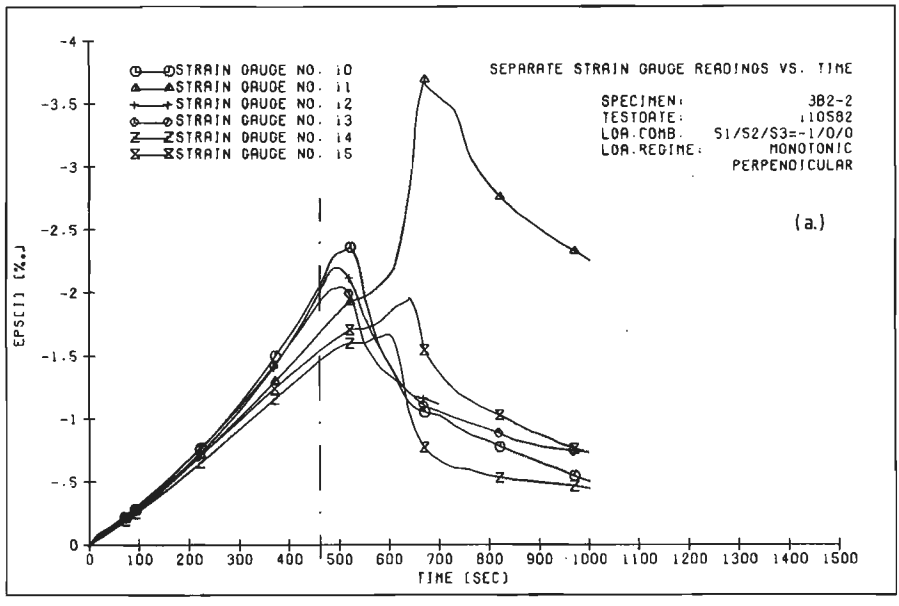

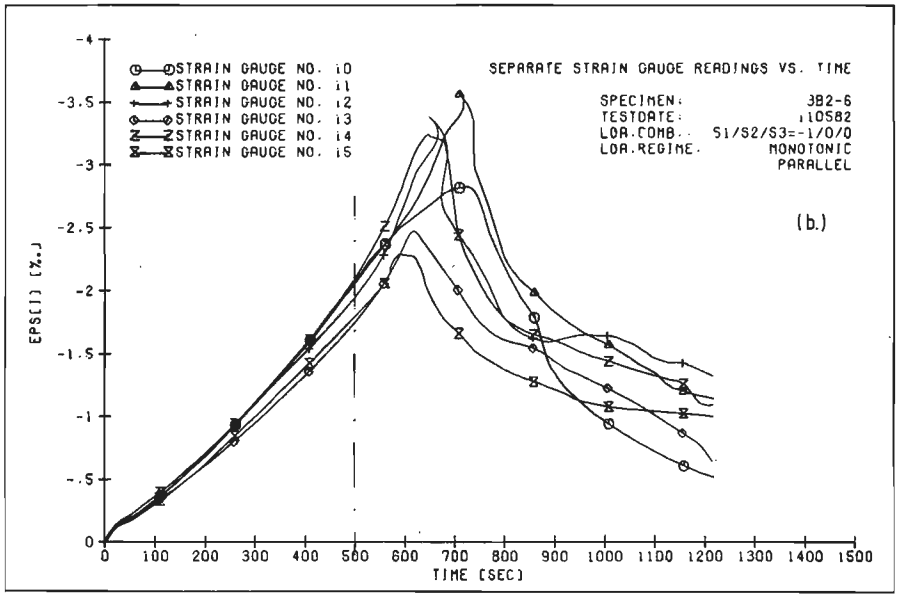

Fig.4.12. a. Separate strain gauge readings vs. time for specimen 3B2-2, loading direction perpendicular.

b. idem for specimen 3B2-6, loading direction parallel.

The six specimens originating from prism 3B2, were subjected to an extensive surface strain measurement. In axial direction six strain gauges were mounted at two opposite surfaces of the specimen (fig. 4.2). In Figure 4.12.a and b the separate strain gauge readings (of the six axial gauges) are plotted against the elapsed time for specimens 3B2-2 and 3B2-6.
The dashed dotted lines, which are plotted perpendicular to the time axis show where the peak-stress level σ_{1p} is reached (at t = 500 sec for 3B2-6 and t = 465 sec for 3B2-2).

In figure 4.13 the strain gauge locations (no. 10-15) both for specimen 3B2-2 (loading perpendicular) and specimen 3B2-6 (loading parallel) are shown in a cross section of the cube (perpendicular to the direction of σ_1). The shaded area in the cross-section of 3B2-2 indicates the upper surface of the specimen during casting. For specimen 3B2-6 this casting surface does not appear in the relevant cross-section.

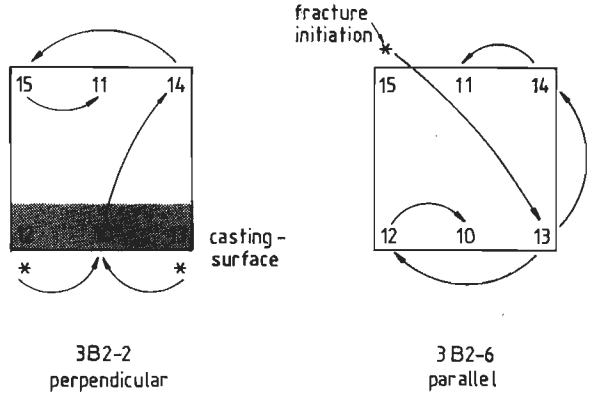

Fig.4.13. Strain gauge locations and 'fracture propagation' for specimen 3B2-2 (left figure) and 3B2-6 (right figure).

Up to peak stress level the strain gauge readings were situated in a relatively narrow band. The scatter in strain readings at peak stress was found to be larger when loading was applied perpendicular rather than parallel. The results in table 4.14 show the average surface strain at peak stress σ_{1p} determined from the six axial strain gauges, and the coefficient of variation as a percentage of the average value.

The increase of the coefficient of variation, in the case of perpendicular loading, must be attributed to the different less compacted structure of the casting surface probably. For specimens 3B2-1, 3B2-2 and 3B2-3, the largest strains (in the pre-peak region), always appeared at the side of the casting surface.

specimen no.	$\varepsilon_{1,surf.at}\ \sigma_{1p}$ (‰)	coeff. of variation (%)
3B2- 1	- 1.76	13.8
2	- 1.83	13.9
3	- 1.77	10.3
3B2- 4	- 1.88	7.7
5	- 1.98	9.8
6	- 1.96	7.8

Table 4.14. Surface strains at peak stress, average value and coefficient of variation for series 3B2.

The scatter of surface strain measurements is influenced by several factors. First of all the length of the measuring device (d_m = 60 mm) with respect to the maximum aggregate size (d_a = 16 mm) is important. According to /109/ a scatter of approximately 5% in strain readings should be expected when $d_m/d_a \sim 4$ (as in the current research).
Furthermore a more close evaluation of the experimental results showed a systematic difference between corner gauge measurement (no. 12-15) and central gauge measurement (no. 10-11). The average corner gauge value ($\Delta l_{corner} = (\varepsilon_{12} + \varepsilon_{13} + \varepsilon_{14} + \varepsilon_{15})/4) * d_{cube}$) was always behind the central gauge value ($\Delta l_{central} = ((\varepsilon_{10} + \varepsilon_{11}) / (2) * d_{cube}$).
At peak stress-level the average difference (for the six specimens) was $\Delta l_d = \Delta l_{central} - \Delta l_{corner} \approx 10\ \mu m$.

From figures 4.12.a and b it may be observed that this difference in central displacement and corner displacements appears from the initiation of a test to the peak stress-level. The results suggest that the specimen is loaded through a convex loading platen as shown in figure 4.15. Indeed due to bending of the brush-rods with increasing lateral deformations of the concrete specimen, a spherical loading platen surface will appear. The flexible platen system (fig. 3.4) that was used by Schickert /139/, responds in a similar manner.

By measuring the relative displacements of the separate pistons with respect to each other (a flexible platen is built from 25 pistons, A_p = 20 x 20 mm^2, specimen size A = 100 x 100 mm^2 with variable height), it was shown that differences up to 40 μm appear at 90% of σ_{lp}.
As was mentioned before (fig. 4.11), larger differences were measured when loading platen strains $\varepsilon_{1,\ loa.pl.}$ were compared with surface values $\varepsilon_{1,surf}$ (when brush bearing platens were applied).

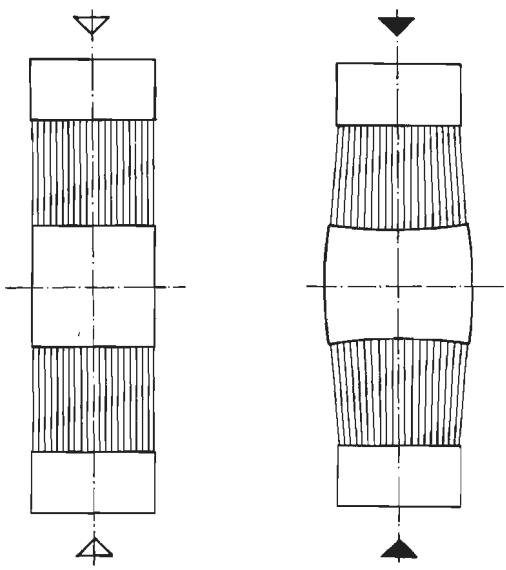

Fig.4.15. Deformation of the specimen - brush system in uniaxial compression.

The occurrence of a convex brush surface is no surprise, and has been indicated before /137,95/. The implication of this system deformation on the deformation response is shown here for the first time. It will be obvious that the curvature of the loading-platen will increase when lateral deformations increase (for example in the stress-strain curve descending branch). More attention is paid to this matter in the next section.

- post peak surface strain measurement -

Returning to figures 4.12 and 4.13. The differences between the separate strain gauge readings become even more pronounced when the peak stress-level is exceeded. Initially just beyond σ_{lp}, the surface strains continue to increase. Upon further axial straining (in terms of the loading platen value $\varepsilon_{1,loa.pl.}$), a sudden unloading is observed at the specimen surface.

In the case of specimen 3B2-2, this unloading is first observed for gauges no. 12 and 13 at t = 492 sec. (see fig. 4.12.a). Both gauges were mounted at the casting surface (fig. 4.13). For all three perpendicular loaded specimens (3B2, no. 1 through 3), unloading was first observed near the casting surface. It is therefore not too hazardous to assume that fracture starts at the casting surface in the case of perpendicular loading. Thus in spite of the removal of 16 mm thick outer layers of the original prism (fig. 3.19), still a rather heterogeneous structure remains. After a further increase of $\varepsilon_{1,loa.pl.}$ in the stress-strain curve descending branch (see fig. 4.11), the fracture (surface unloading) spreads throughout the entire cross-section of the specimen.
Surface unloading for specimen 3B2-2 is observed in the sequence 10, 14, 15 and 11, as depicted in figure 4.13. Similar results are presented for a parallel loaded specimen (3B2-6), but in this case, the fracture did not start at any particular place. All three parallel loaded specimens showed that the fracture started at a different place.

The delayed fracturing in case of parallel loading, which was mentioned in the previous section also becomes clear from the surface measurements. From fig. 4.12 it can be seen that for parallel loaded specimens, the surface strain measurement remained intact for a relatively long time after the peak stress level was exceeded (when compared with perpendicular loaded curves). The first surface unloading for specimen 3B2-6) was observed at t = 588 sec for gauge no. 15.

In general, visible cracks (that is visible with the unaided eye)appear in the specimen, just beyond peak stress-level. The results presented in figures 4.11 through 4.13 indicate that specimen degradation starts with surface spalling (fracture initiation by means of surface spalling was recently demonstrated by Ottosen /117/ too, in a finite element analysis of a uniaxial compressive cylinder test, adopting a continuum material model for strain softening!), which takes mainly place in the first part of the stress-strain curve descending branch (σ_1 - $\varepsilon_{1,loa.pl.}$) before the inflection point. Stress redistributions occur in the specimen when the peak stress level is exceeded, and it seems that the remaining carrying capacity is due to a more or less intact core.

It was mentioned before that macro cracks (visible with the unaided eye) appear and start propagating when the peak stress level is exceeded. It is assumed that a fully developed macro-crack pattern is developed when the residual stress-level in the σ_1 - $\varepsilon_{1,loa.pl.}$ curve is reached. Further decrease of load carrying

capacity at this stage, only will occur due to widening of the present macro cracks. From the stress-strain curves that were shown in figure 4.11 it can be seen that the decrease of σ_1, once this residual level has been reached, is a very slow process.

In general it was found that the macro-cracks with the largest width were situated near the specimen surfaces. In figure 4.16 the crack pattern of the upper loading surface of specimen 2B2-3 (uniaxial compression, loading direction perpenducular) after termination of the experiment is shown. This particular specimen was loaded up to $\varepsilon_{1,loa.pl.} = -8.6\ ^{o}/oo$. The residual deformation after unloading was equal to $\varepsilon_{1,loa.pl.,res.} = -5.8\ ^{o}/oo$. The lateral deformation after unloading, was determined from the four strain-readers (fig. 4.2) and was equal to $\varepsilon_2 = 38.6\ ^{o}/oo$.

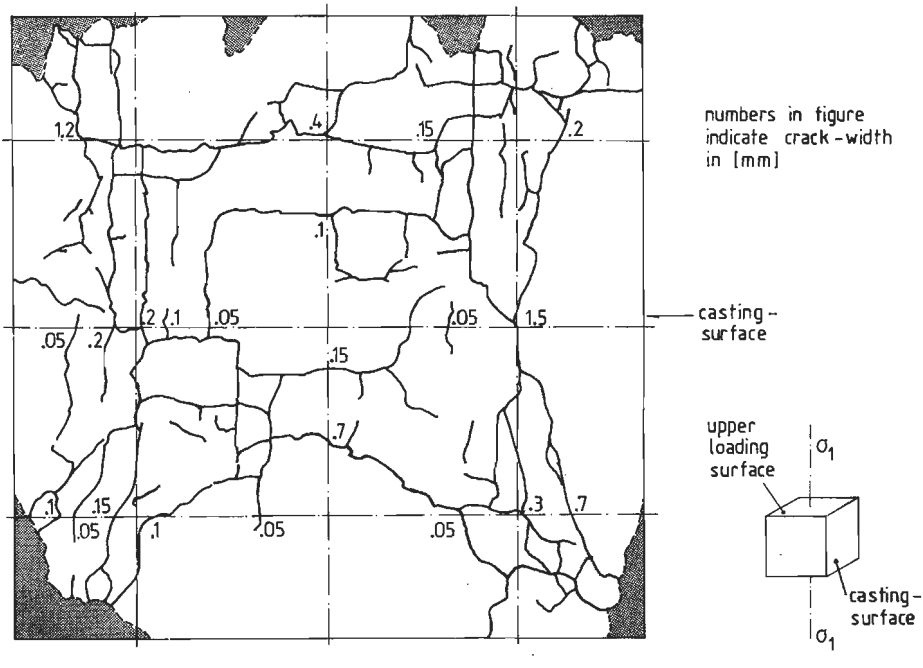

Fig.4.16. Crack pattern of the upper loading surface for specimen 2B2-3.

In figure 4.16 only those cracks which were visible with the unaided eye have been plotted. The shaded areas show where small pieces were torn loose. At three levels in horizontal direction and in vertical direction, the crack widths (magnified ten times) are indicated.

It can be seen that the wider cracks (in one case, near the casting surface even up to 1.5 mm) appear closest to the edges of the specimen. This may indicate that the innermost cracks are prevented from opening, probably as a result of constraint between brush bearing platen and the concrete specimen (see also appendix A6, fig. A6.2). From figure 4.16 also the more or less rectangular crack-pattern, which is imposed to the specimen by the brushes, is recognised. More attention is paid to uniaxial fracture in section 4.3 and 4.4.

- lateral surface strains -

In figure 4.17 the lateral strain determined from the two lateral strain gauges no. 12. and 13. ($\varepsilon_{2,surf} = (\varepsilon_{12} + \varepsilon_{13}) / 2$) is plotted against the average lateral strain value obtained from the four strain-readers ($\varepsilon_{2,str.reader}$) for specimens 3B2-1 through 3B2-3. All three specimens were loaded perpendicularly. The value of $\varepsilon_{2,surf}$ at σ_{1p} for the three experiments is indicated in figure 4.17.

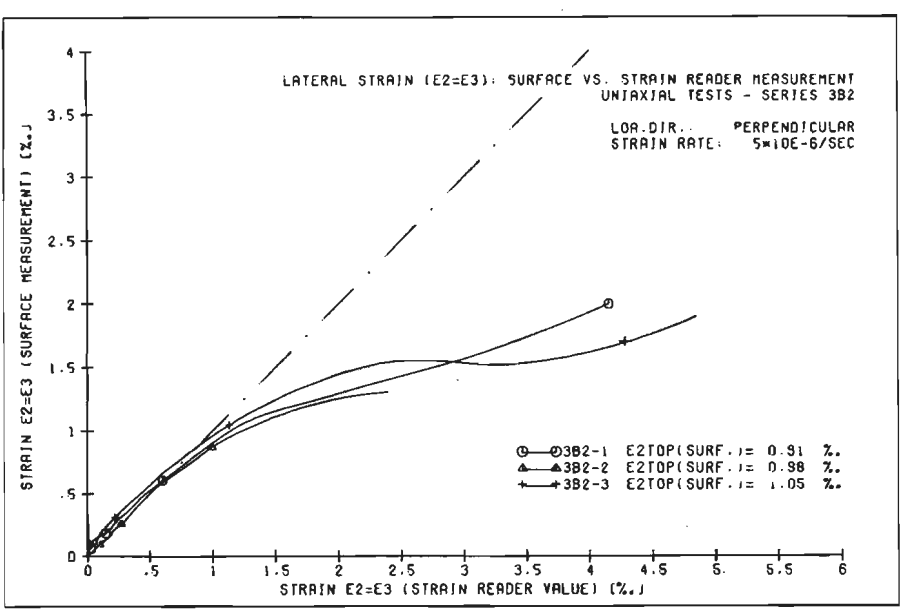

Fig.4.17. Lateral strains: $\varepsilon_{2,surf}$ vs. $\varepsilon_{2,str.reader}$ for specimens 3B2-1 through 3B2-3.

In the pre-peak region, it was found that $\varepsilon_{2,surf}$ was always larger than $\varepsilon_{2,str.reader}$. This may indicate a slight bulging of the specimen-surface (see

fig. 4.15): the strains determined from the strain-readers (at a distance of 20 mm from the specimen-brush interface) may be disturbed by the (reduced!) end constraint. From previous studies /137/, it is known that bulging of the specimen free surfaces is not entirely eliminated by using brush bearing platens. Nevertheless a considerable reduction is obtained when compared with load application through rigid steel platens.
For the flexible platen system /139/ the reduced bulging of the side surfaces was demonstrated by measuring the deformation of a specimen surface by means of a great number of proximity type transducers.

Beyond peak stress-level, the lateral surface strain $\varepsilon_{2,surf}$ stays behind the strain reader values. In fact the strain reader measurement corresponds to the loading platen measurement, and is not affected by cracking. The large differences between $\varepsilon_{2,surf}$ and $\varepsilon_{2,str.reader}$ is probably due to surface unloading (as suggested in the previous section). It must be mentioned that eventually the strain-gauges are damaged by surface cracking.

4.3. Deformation measurement - results of "10-series".

From the uniaxial preliminary tests (series 2/3, section 4.2) a rather large difference between surface and overall strains was measured (see figures 4.11 a - b). As can be seen from these figures, and the additional results in appendix A1 (peak results in tables A1.1 and A1.2, stress-strain curves in figures A1.4 and A1.5), differences up to 30% were measured at peak stress-level.
The surface strains always stayed behind the overall strains in the ascending part of the $\sigma_1 - \varepsilon_1$ curve. The discussion in this section is mainly restricted to the pre-peak region, that is with regard to differences between surface and overall strains. The "structural behaviour" in the post-peak region (see section 4.2.4) makes comparison of surface and overall strains impossible.
In the subsequent biaxial preliminary experiments (series 5/6, appendix A4), similar results were obtained however now in some cases up to 30 - 50% at peak stress level (see fig. A4.5).
The difference was considered important, and 16 additional uniaxial compression tests on prisms (height h = 200 mm, cross section A = 100 x 100 mm^2) and cubes (d = 100 mm) were carried out in order to unravel the complex deformational behaviour of the specimen brush system.

In the following, the experimental design (section 4.3.1), two statistical analyses using strength and deformational results as response values (section 4.3.2 and 4.3.3), and some further comments on the "structural behaviour" of a prism in the stress-strain curve descending branch (section 4.3.4) are given.

4.3.1. experimental design for uniaxial tests, series 10.

Several factors may influence the overall deformation measurement. In fact when discussing stress-strain results, the complete experimental environment should be taken into account. This was recently indicated by Clayton /31/.
Factors which are considered important in the current investigation are:

- 1 - the smoothness of the contact surfaces within the total LVDT-measuring length (see also figure 3.11),
- 2 - the intrusion of the brush-rods in the specimen and high local peak stresses at the brush-specimen contact surface will lead to different deformational behaviour up to a certain depth in the concrete specimen, and
- 3 - the bending of the brush rods during increasing lateral deformations will lead to a spherical loading platen.

In the specimen-brush system several contact surfaces are situated within the LVDT measuring length (see fig. 4.18). At each side of the specimen two contact surfaces are found. The most important contact surface is the interface between concrete specimen and brush bearing platen. The second contact surface is situated near the steel block (that is the steel-steel interface near the clamped side of the rods, see fig. 3.11).
In general it was no problem to manufacture a sufficiently accurate brush. After the grinding sequence, a non-smoothness smaller than 10 - 20 μm could be obtained. Yet, when several specimens were loaded, the brushes would wear out, due to mechanical damage of the upper surface, resulting in a decreasing accuracy.

The non-flatness of the contact surfaces may lead to a considerable run in the initial stage of the overall load-deformation curve. On one hand this will lead to an overestimation of the specimen deformation when measured between the loading platen, on the other hand, surface strains may be too small. The differences in response are depicted in fig. 4.18.

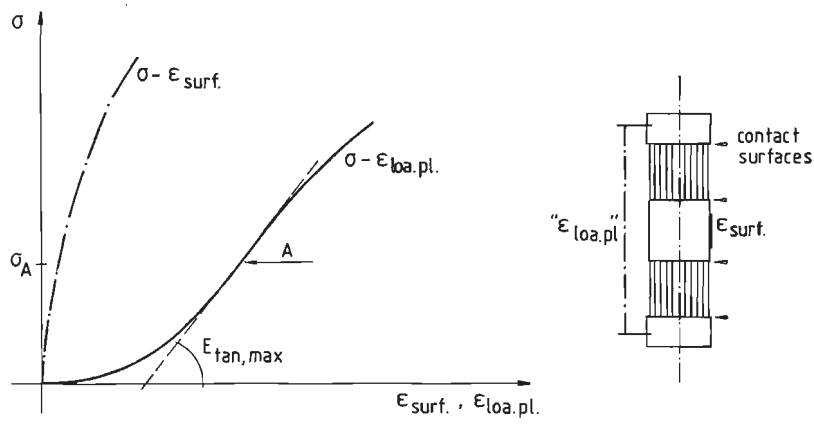

Fig.4.18. differences between surface strains and overall strains in the initial stage of the load-deformation curve in uniaxial compression.

In the uniaxial experiments of series 2 and 3, the inflection point in the σ_1 - $\varepsilon_{1,loa.pl.}$ curve denoted as A in figure 4.18, was reached at a rather high stress level: σ_1 = -15 N/mm^2. This may indicate a considerable non-smoothness of the contact surfaces (no capping was used in tests-series 2/3). It must be mentioned that the accuracy of the concrete specimen surfaces was in the same order as newly ground brushes (< 10 μm).

A closer look to the brushes after the experiments (series 5/6) were carried out, revealed that small dimples were pressed in the lower steel block of the brushes. The dimples were mainly situated near the edges of the steel block. Thus the largest contact area is situated in the brush-centre, and decreases near the edges, leading to stress concentration in the specimen centre. The plastic deformations that occurred are the result of too large lateral deformations that were allowed in the stress-strain curve descending branch.

Some insight in the response of a specimen loaded through "spherical" loading platen is obtained from an approximation for two spherical bodies in contact (p.409 e.v. in /159/). Damage starts from the specimen centre, and in fact a splitting action is induced. The difference between surface and overall strains is not surprising in such a "structure". These observations indicate that great care should be taken when using brush bearing platens. In the subsequent experiments (series 10, triaxial tests series 8/9, rotation tests series 7 and size-effect series 15), the brushes were carefully checked for mechanical damage on either of the

contact surfaces, and were ground carefully several times (adopting the grinding sequence that was mentioned in section 3.2.1).
Mechanical damage at the concrete brush interface could not be avoided completely (that is at the brush side, small dimples pressed in the steel surface), so a small "initial run" in the stress strain curve should always be expected.

Two other disturbances were mentioned in the beginning of this section. The intrusion of the brush-rods is not easily eliminated. The phenomenon will be different when an aluminum cube is loaded. This indicates that the initial calibration of the brush deformations (section 3.2) might be erroneous. The effect of the splitting forces of the separate brush rods is clearly demonstrated in fig. 4.16. The third factor, bending of brush rods, only becomes significant when large lateral deformations occur. In the pre-peak region of a uniaxial experiment the total lateral deformation of a cube is smaller than 100 μm. Very large lateral deformations occur in the stress-strain curve descending branch (up to a few mm). The deformation of the brush-surface due to bending of the brush rods was calculated by Linse /95/. It is not clear if very small differences in height will influence the stress-strain response dramatically. Yet it seems appropriate to check the original brush deformation calibration (see section 3.2.5), using concrete specimens.

Based upon the above discussion, the following factors were considered worthwhile for further study:

- 1 - The specimen height. If the height increases, the total effect of boundary disturbances reduces when compared with the total deformations. Experiments were carried out using 200 and 100 mm high specimens (with constant cross-section A = 100 x 100 mm^2). It is probably not too hazardous to assume that the central region of a 200 mm high prism, loaded between brush bearing platen is uniformly deformed.

- 2 - The use of a capping between specimen and brush bearing platen is considered favourable, especially, in bi- and triaxial displacement-ratio tests (see section 5.2.1), when a "run" in the initial part of the load-deformation curve is inadmissible. Yet, it should be assured that no capping penetrates between the brush-rods because this would inhibit their function.

A total of 16 specimens was loaded in uniaxial compression. Two further parameters were added: batches (10A and 10B) and positions (end and middle, see fig. 4.20), which are both due to the manufacturing method. Thus the complete experimental design consisted of four parameters, each on two levels, representing a full replicate of a 2^4 factorial (4 factors, each at 2 levels). A review of the 16 experiments is given in table 4.19.

			Capping (C)	
			yes	no
height (H)	position (P)	batch (B)		
100 mm	end	10A	10A1-1	10A2-1
		10B	10B1-1	10B2-1
	middle	10A	10A1-3	10A2-3
		10B	10B1-3	10B2-3
200 mm	end	10A	10A2-4	10A1-4
		10B	10B2-4	10B1-4
	middle	10A	10A2-2	10A1-2
		10B	10B2-2	10B1-2

Table 4.19. Experimental design for the 10-series.

The cubes and prisms were sawn from the original prisms that were used for all other batches (see figure 3.21). For the 10-series, the samples were sawn from the original prism as indicated in figure 4.20. Specimens no. 1 and 4 are end positions, no. 2 and 3 are middle positions.

As a result of this manufacturing method, all specimens were loaded perpendicularly with regard to the direction of casting. The strain rate for all experiments was fixed at $\dot{\varepsilon}_1 = 10.10^{-6}$/sec.

Once more it is emphasized that the brushes were carefully ground before the experiments were carried out!

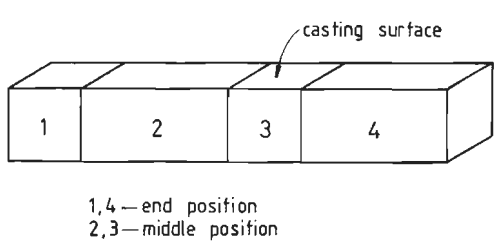

Fig.4.20. Sawing of cubes and prisms for the 10-series.

The capping material was the same epoxy resin which was used for the tensile experiments (epoxy resin Edilon Dex'R, elastic modulus approximately 8000 N/mm^2). The capping was applied under a small compressive load ($\sigma_1 \approx -1$ N/mm^2). In all cases the epoxy resin capping was applied in the evening, and testing was done the next morning (a number of preliminary tests showed that a hardening time of 6 - 8 hours is sufficient).

In order to avoid penetration of the epoxy resin between the brush rods, a silicon filler was applied between the rods. Furthermore in order to avoid the epoxy from sticking to the brush surface, this was slightly greased before it was applied.

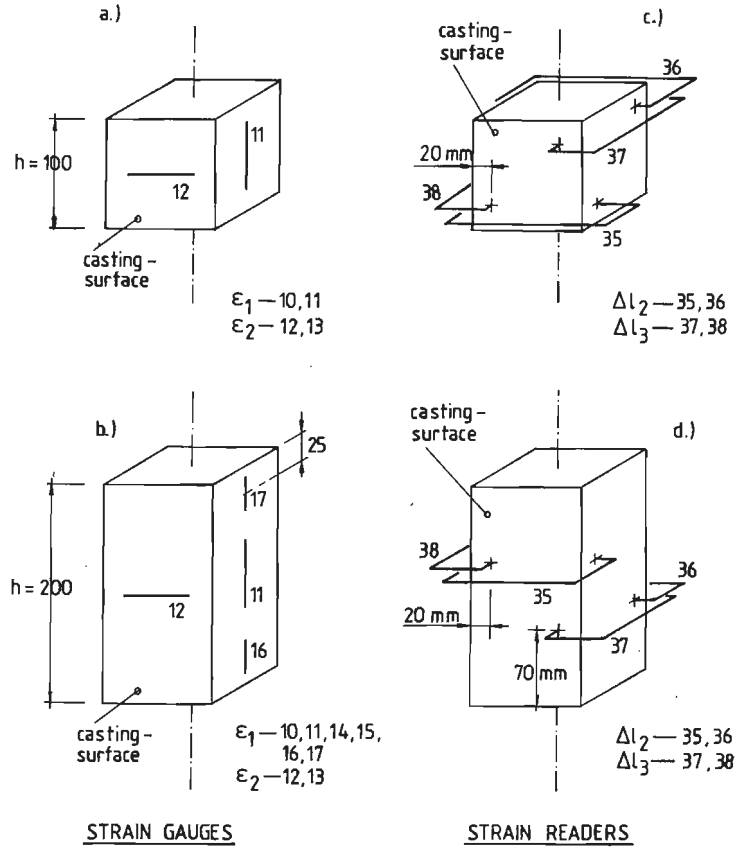

Fig.4.21.a-d Strain gauge and strain reader positions for cubes and prisms of batches 10A/10B.

- **measuring devices** -

Test control was by means of LVDTs (3 x 120 degrees) fixed between the loading platen. The positions of strain gauges and strain readers both for cube and prism tests of batch 10A/10B are shown in figure 4.21 a - d. In figure 4.21.a the strain gauge configuration is shown for a cube test. Two 60 mm gauges (no. 10, 11) were used for axial strain measurement (ε_1). The two gauges were mounted in a central position on two opposite free surfaces of the specimen. On the two remaining free surfaces, gauge no. 12 and 13 (meas. length 60 mm) were mounted for measurement of lateral strains ε_2. Gauge no. 12 was always mounted at the casting surface.
In case of a prism test (fig. 4.21.b.) also four 60 mm gauges were used for axial (ε_1, no. 10,11) and lateral (ε_2, no. 12,13) strain measurement. The four gauges were mounted to the free surfaces in a centre position (similar as for the cube), gauge no. 12 was always mounted to the casting surface. For the prism tests however also four additional 30 mm gauges (no. 14,15,16,17) were mounted in axial direction. Gauges no. 14,15 were mounted to the same surface as gauge no. 10, and 16 and 17 to the surface on which no. 11 is fixed. Gauges no. 14, 15, 16, 17 were mounted at a distance of 25 mm from the upper and lower specimen brush interface (that is distance from gauge centre to specimen edge).

Both for the cube and the prism test two strain readers were attached to the specimen for measuring Δl_2 (no. 35 and 36) and two for measuring Δl_3 (no. 37 and 38). The two strain readers for each lateral direction were placed in a diagonal position. For the cube tests, the distance between strain reader and (upper or lower) specimen-brush interface was equal to 20 mm. In case of a prism test, this distance was 70 mm (see fig. 4.21.c-d).

4.3.2. statistical analysis of strength results.

In appendix A2, table A2.1, the conditions at peak stress level σ_{1p} were gathered for the 16 experiments of batches 10A and 10B.
A statistical analysis, using the theory of linear models (section 4.1.) was carried out, adopting σ_{1p} as a response variable. The linear model is given by:

$$\sigma_{1p} = E\underline{y} = \sum_{i=0}^{10} \beta_i x_i \qquad .....(4.15)$$

The variables x_i represent the level of the influence factors: the specimen height (x_1 = (h - 150) / 50), the batch (x_2 = -1,1 for resp. 10A and 10B), the position (x_3

= -1,1 for resp. end and middle), the application of a capping (x_4 = -1,1 for resp. yes and no), and six two-factor interactions (x_5, x_6, ..., x_{10}). The mean strength of the experiments is given by the estimate b_o of β_o.

The full details of the model (eq.4.15) and the analysis that was carried out are given in appendix A2, table A2.2., showing the values of the variables x_i, the estimates b_i of β_i (i = 0, 1, ..., 10), the coëfficients of variation and the P-value. The factors that were found to be significant at the 5% level are underlined. The reduced model is given by,

$$\hat{o}_{1p} = -43.37 + 0.92\, x_2 \qquad .....(4.16.)$$

The model contains only the average strength and the only significant factor batches. The estimate for the random error is $\hat{o}_0^2 = 1.714$ ($\nu = 5$).

The results show that the application of an epoxy resin capping had no significant effect on the uniaxial strength of the specimen. Also no significant effect of height on strength was observed. This fact indicates that the brushes act well with regard to strength response. That is, assuming that a uniaxial strength does exist and it is unique!
This could be concluded from the uniaxial preliminary tests, series 2 and 3 (section 4.2.2) too, where the strength obtained from uniaxial tests on cubes (d = 100 mm) loaded between brush bearing platen was compared with the uniaxial cylinder strength (obtained from experiments on cylinders with ϕ/d = 1 / 2.5, loaded between rigid steel platens). The strength results of the 10-series confirm the observations by Schickert /139/, who adopted the flexible platen system as a friction reducing load application medium in a large number of uniaxial loaded prisms with variable height.

The position of a specimen in the original prism before sawing had no significant effect on the uniaxial strength. This observation is contradictory to the results of series 2/3 (section 4.2). These results indicate that the factor positions is rather uncertain. In the triaxial experiments (series 8/9, chapter 5) therefore the end positions were omitted from the experimental design.

4.3.3. deformation results

The main purpose of the uniaxial experiments of the 10-series was to determine the total disturbances in deformation measurement, which are an implication of

boundary conditions to which a specimen is subjected. It should be emphasized that the specimen response is a structural response, and it is rather hazardous to define a "true concrete strain". For the 16 experiments of series 10, the "brush-deformation" (or rather the sum of all disturbances within the LVDT measuring length) defined as

$$\Delta l_{brush}(\sigma) = \Delta l_{LVDT}(\sigma) - \Delta l_{surf.}(\sigma) \qquad .....(4.17.),$$

was determined at four levels of axial stress σ_1 = -10, -20, -30 and -40 N/mm^2. In equation 4.17, $\Delta_{LVDT}(\sigma)$ is the total (non-corrected) deformation measured by means of LVDTs between the brushes (fig. 3.11.) at a given level of axial stress, and $\Delta l_{surf}(\sigma)$ is defined as

$$\Delta_{surf}(\sigma) = h'.(\varepsilon_{10}(\sigma) + \varepsilon_{11}(\sigma))/2 \qquad .....(4.18.),$$

the 'equivalent specimen deformation', determined from the axial surface strain measurement by means of the two central placed (60 mm) straingauges no. 10 and 11, multiplied by a certain length h'. It is assumed that a more or less uniform deformation distribution is imposed to the length h' (h' < h, where h is the total specimen-height).

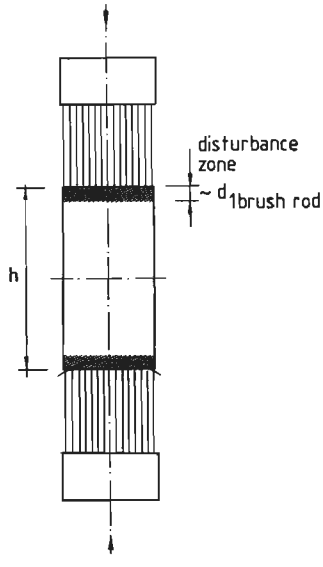

Fig.4.22. disturbance zones with different deformational response, near the specimen brush interface.

For simplicity it was assumed that h' = h, which implies that the local disturbances near the upper and lower specimen-brush interface are neglected. The depth of the disturbance zone near the specimen ends will be in the order of the lateral dimension of a single brush rod (that is before micro cracks start propagating, and the structural properties of the specimen have not yet significantly changed), see figure 4.22.
This means that for a prism (height h = 200 mm), the total disturbance zone will be approximately 5% of the total specimen height.

It is assumed that the local effects at the specimen ends do not influence the deformational response of the central region of the specimen for stress levels within the range under consideration ($10 < |\sigma_1| < 40$ N/mm^2). In figure 4.23 the $\sigma_1 - \Delta l_{brush}$ curves for some of the specimens of batch 10A (fig.a) and 10B (fig.b) are shown. The specimens that were loaded without capping show clearly the initial run due to the contact effects.

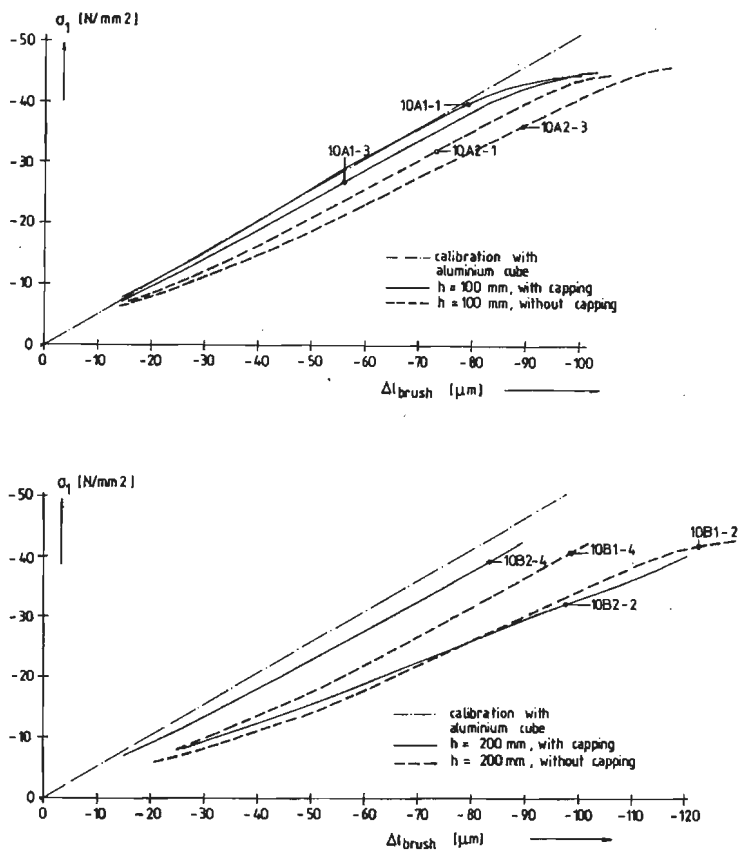

Fig.4.23. measured $\sigma_1 - \Delta l_{brush}$ relations for specimens of batch 10A / 10B.

The inflection point in the initial part of the axial stress-strain curve (point A in figure 4.18) was found at a slightly lower stress level, when compared with the experiments of series 2/3 (that is for those experiments of the 10-series, which had no capping, see table 4.19). In the experiments with capping, the initial "run" in the axial stress-strain curve disappeared completely. The effect is demonstrated in figure 4.25.a, in which for two experiments (10B2-3, h = 100 mm, no capping and 10B2-4, h = 200 mm, with capping), the tangential modulus $E_{tan} = \delta\sigma_1/\delta\varepsilon_1$ (loa.pl.) is plotted against the axial strain ε_1(loa.pl.). The difference in the initial part of the curve, due to contact effects is obvious.

For higher stress levels (near $\sigma_{1p} \approx -45$ N/mm^2), the rate of growth of Δl_{brush} increases (see fig. 4.23). The fast increasing difference between overall deformation and surface deformation in this stage of the experiment is probably due to the fact that a "spherical" loading platen develops as soon as the lateral deformations start to increase (at approximately 75% of σ_{1p}, the lateral strains start to increase significantly, see fig. A2.6 and A2.7).
As reported in section 4.2.4 (fig. 4.11), surface unloading is observed in the post-peak range of the overall stress-strain curve. This effect is probably influenced by the development of the spherical loading platen, while surface 'fracture' (see fig. 4.24) begins in the pre-peak region when separate micro-cracks join to form combined cracks (using the formulations by Carrasquillo et.al. /26/).

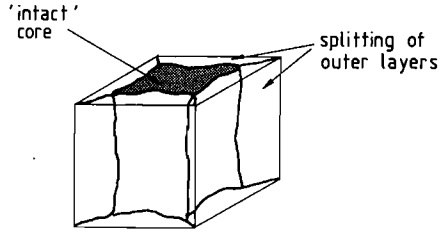

Fig.4.24. Intact specimen core, and surface splitting in uniaxial compression.

As was mentioned before, Δl_{brush} was determined for all 16 experiments of the 10-series, at four levels of axial stress σ_1. If the prescribed stress-level was missed, due to the measuring system used (see section 3.2.4, data aquisition system), then the value of Δl_{brush} was determined from a linear interpolation between the two nearest (that is in terms of stress!) upper and lower measuring steps.

Subsequently a statistical analysis was carried out, adopting Δl_{brush} at the four prescribed stress levels as a response variable. The linear model is given by

$$\Delta l_{brush} = E\underline{y} = \sum_{i=0}^{25} \beta_i x_i \qquad \text{....(4.19).}$$

The main effects in this model are, the specimen height (x_1), differences between batches (x_2), positions (x_3), capping (x_4) and the axial stress-level (x_5, x_6, x_7). Furthermore all two-factor interactions between the main effects were included (x_8.....x_{25}). In appendix A2, table A2.3., the full details of the model and the levels of the influence factors are given.

The total number of observations was 64. Thus the number of degrees of freedom that were available for estimating the random error is equal to $\nu = 64 - 25 - 1 = 38$. In table A2.3, the results of the analysis are shown also: the estimates b_i of β_i, the coefficients of variation and the P-values (significant P-values are underlined). The reduced model, that only contains the significant effects is expressed by

$$\hat{\Delta l}_{brush} = -60.38 - 3.08\, x_1 - 2.99\, x_2 - 4.45\, x_3 - 4.96\, x_4 - 11.25\, x_5 - 1.50\, x_1x_2 - 3.99\, x_1x_3 - 0.69\, x_3x_5 \qquad \text{.....(4.20),}$$

in which $x_1 = (h - 150) / 50$, $x_2 = -1,1$ for resp. batch 10A and 10B, $x_3 = -1,1$ for respectively end and middle position, $x_4 = -1,1$ for with and without capping respectively, and $x_5 = (-\sigma_1 - 25)/5$, where σ_1 is negative in compression (dimension [N/mm^2]). By means of eq. 4.20, the total disturbance effect Δl_{brush} is calculated in [μm]. The random error estimate is $\hat{\sigma}_0^2 = 28.277$ ($\nu = 38$). Eq. 4.20. may be written as

$$\Delta l_{brush} = a\, \sigma_1 + b \qquad \text{.....(4.21).}$$

For correction of 'overall deformations', only the slope a in eq. 4.21 is important. The constant factor may be eliminated while always a 'zero correction' is carried out (section 3.2). From eq. 4.20 it is observed that all main effects except the stress-level only add to the constant factor. Thus it seems that the factor capping, only influences the initial part of the stress-strain curve. This is important, and for all further experiments a capping was used. As was mentioned before the use of a capping is most favourable in the triaxial displacement ratio experiments (see section 5.2.1). A further advantage of the capping is that some small deviations from rectangularity of a specimen in a triaxial test can be taken more easily. The effect of application of capping in a uniaxial compression test is clearly shown in figures 4.25 a-b.

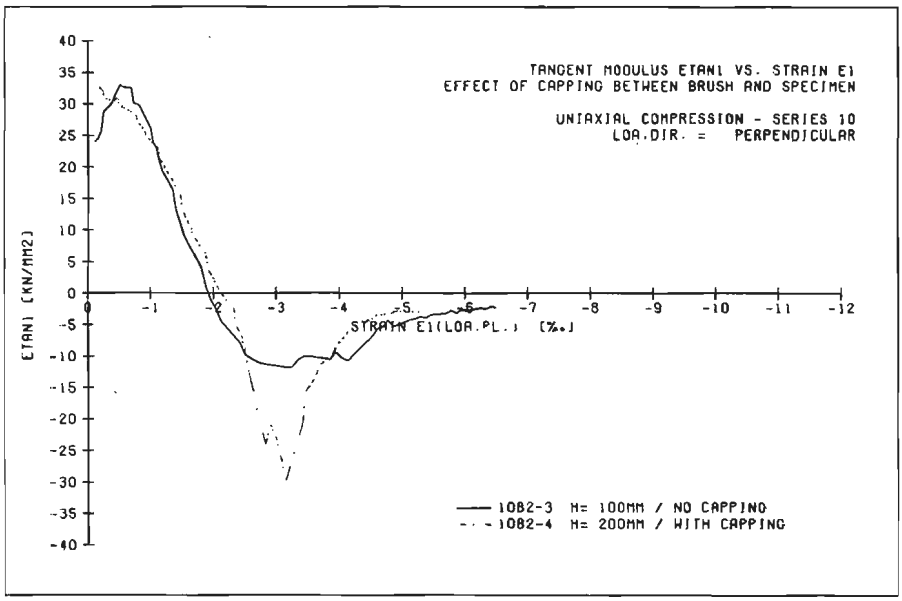

Fig.4.25.a. Tangential modulus $E_{tan,1}$, vs. axial strain $\varepsilon_{1,loa.pl.}$ for specimens 10B2-3 and 10B2-4, showing the influence of capping between specimen and loading platen.

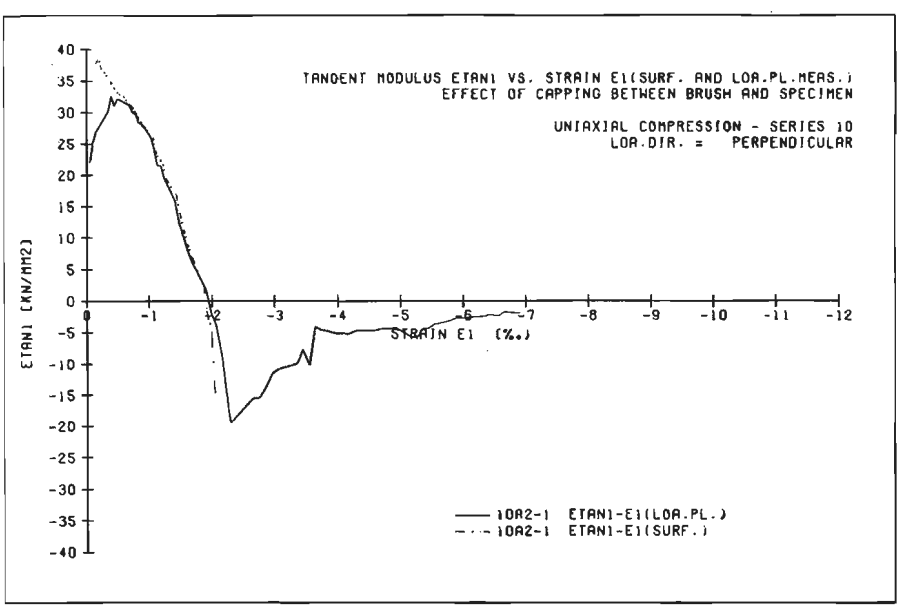

Fig.4.25.b. Tangential modulus $E_{tan,1}$, both determined from overall strains and surface strains for specimen 10A2-1 (height h = 100 mm, without capping).

The factors batches and specimenheight also add only to the constant factor b in eq. 4.21. Figure 4.26 demonstrates that only small differences in surface strain measurement exist between specimens with h = 100 mm and with h = 200 mm (resp. solid lines and dashed lines in fig. 4.26, all originating from batch 10B). Only in the post-peak branch large differences are found, as can be seen from the results in fig. 4.25.a, and the stress-strain curves in appendix A2, fig. A2.4 - A2.5. The prisms always show a very steep descending branch. In section 4.4 more attention is given to this matter.

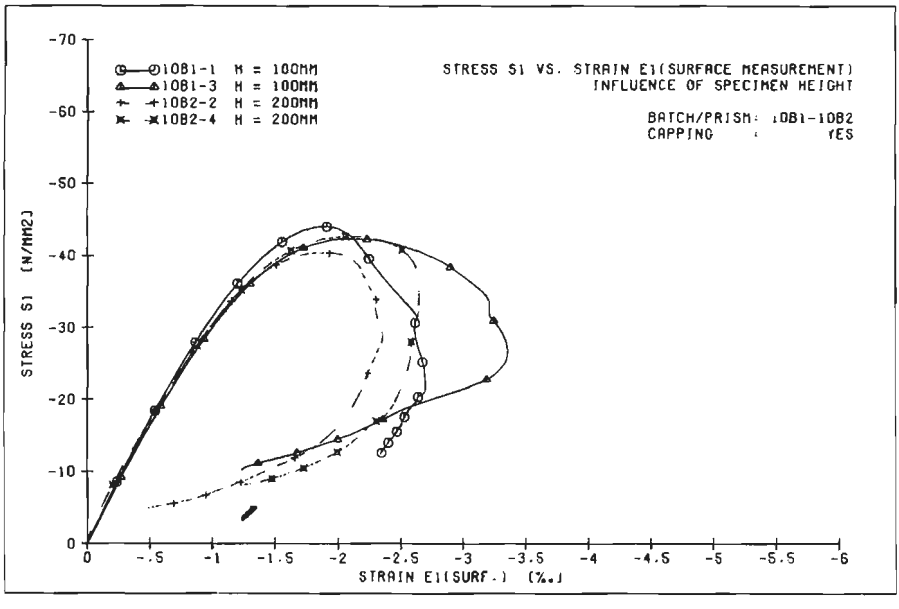

Fig.4.26. Stress vs. strain curves σ_1 - $\varepsilon_{1\ surf}$, for four specimens of batch 10B, loaded with capping.

Now return to equation 4.20. The slope of the Δl_{brush} - σ_1 relationship, calculated by means of this equation was used for the working of all experiments. Thus also the previous shown stress-strain curves (σ_1 - $\varepsilon_{1\ loa.pl.}$) in section 4.2, and the results of the 10-series that are shown in this section and appendix A2, have been worked using eq. 4.20.

It must be mentioned that the slope of the calibration curve (eq.4.20) is influenced by the factor position. This difference should however not be attributed to the brush deformation. In fact this approach is not entirely appropriate and therefore another approach should be followed. Either the slope determined from an end position specimen should be used (which is the smallest

value for a: a = 2.112 for end positions, and a = 2.388 for middle position specimens), or the original calibration with the aluminum cube should be used.

The differences are however not very large. For a uniaxial experiment with peak stress σ_{lp} = -45 N/mm^2, the absolute difference at peak is equal to (2.388 - 2.112). σ_{lp} = -12.4 μm. This value is small when compared with the total specimen deformation at peak (h = 100 mm $\rightarrow$ $\Delta l_{lp} \approx$ 200 μm). Using equation 4.20 implies that loading platen strains are translated to surface strains of a 200 mm prism or a 100 mm cube. The differences between specimens of different height are only reflected in the different constant factor of eq. 4.20, but they are not considered to be important. Also, these results may indicate that, for 100 mm cubes, the central section is uniformly strained.

As was mentioned before, all results in this thesis have been calculated from equation 4.20. One exception is made, the peak strains $\varepsilon_{lp,loa.pl.}$ in table A2.1 are based upon the original aluminum cube calibration. From table A2.1 it may be seen that accurate grinding of brush surfaces only produces differences between the surface and overall strains in the order of 10%.
Also for the triaxial tests (series 8/9) a number of uniaxial experiments was carried out, and adopting eq. 4.20, a perfect agreement between surface and overall strains was found (see figure A5.4. a - b). This may indicate that the brushes were in a good condition during the triaxial tests.

The brush deformation calibration, eq. 4.20 was also used for higher stress-levels (in triaxial experiments) and also for the post-peak measurements. In both cases however the brush deformation is only a fraction of the total strain, so no large errors are introduced.

4.3.4. Some further comments on fracture in uniaxial compression.

In section 4.2.4, the fracture of a cubical specimen loaded by means of brush bearing platens was described. By following the sequence of surface unloading, registrated by means of several strain gauges, it was indicated that in the descending branch of the axial stress-strain curve (σ_1 - $\varepsilon_{1,loa.pl.}$) structural response rather than material behaviour is measured (see fig. 4.12 and 4.13).
In this section the discussion is extended to the fracture of prisms (height h = 200 mm) in uniaxial compression. The prism experiments of series 10 also provided for an extensive surface measurement: as was indicated in figure 4.21.b., six

strain gauges were mounted in the axial (loading) direction, at two opposite side surfaces of a prism.

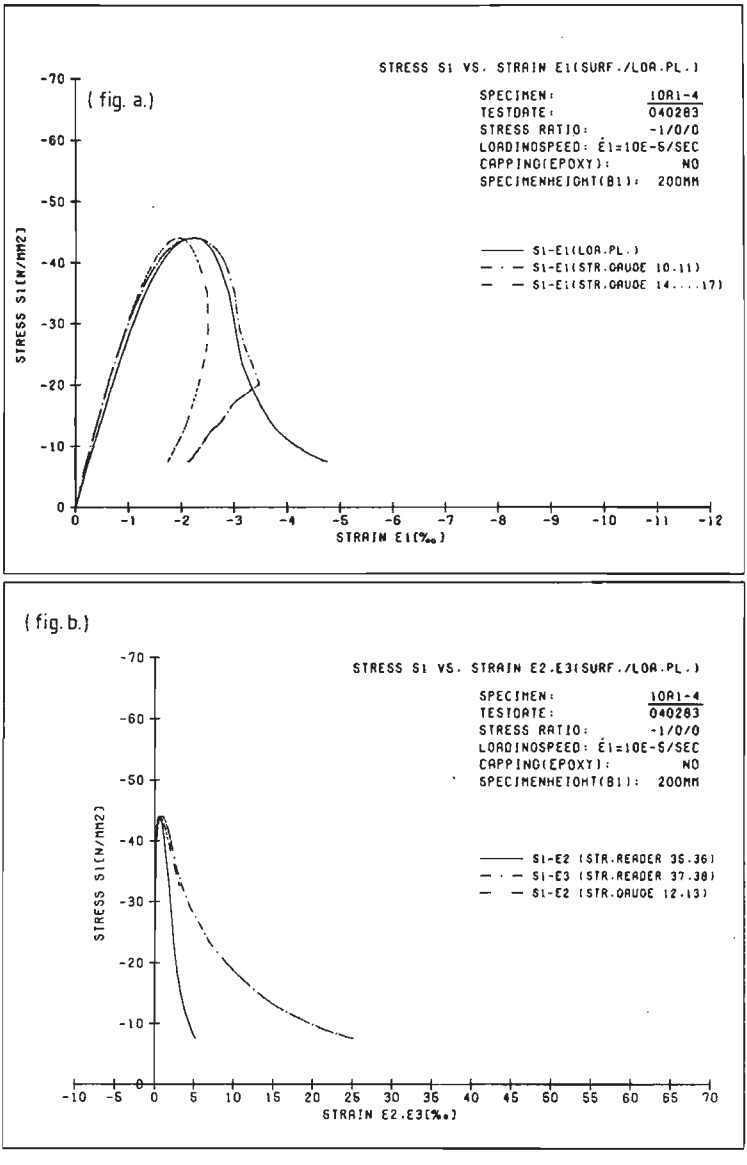

Fig.4.27. a. axial stress - axial strain curves for specimen 10A1-4 (h = 200 mm, loa.dir. perpendicular)

b. lateral strain - axial stress plots for 10A1-4.

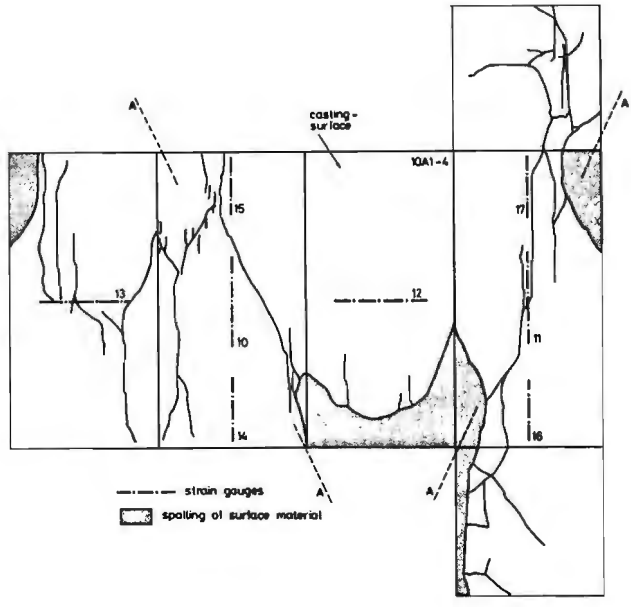

Fig.4.28. fracture pattern for specimen 10A1-4. Also the strain gauge positions are indicated.

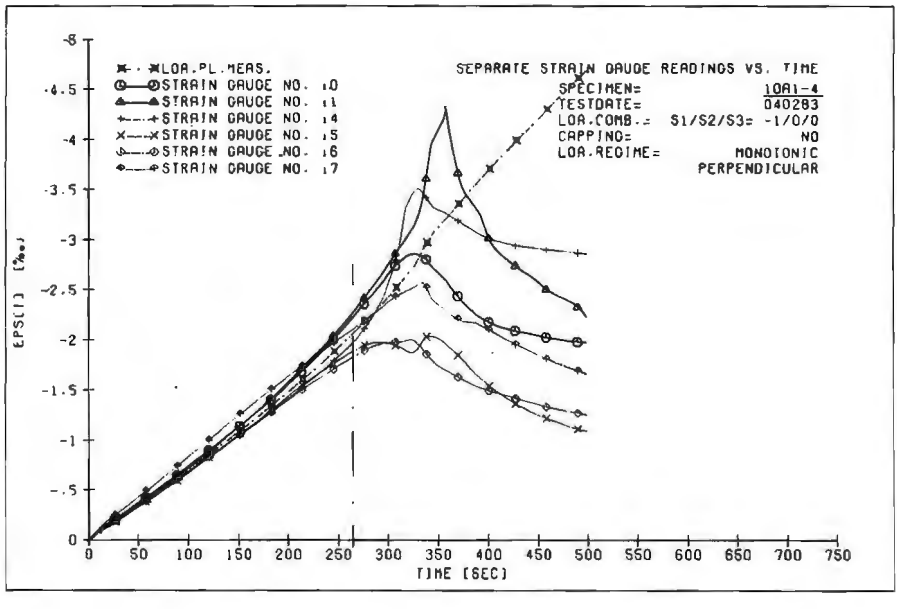

Fig.4.29. separate strain gauge readings vs. time for specimen 10A1-4 (h = 200 mm, uniaxial compression, loa. dir. perpendicular).

In figures 4.27 through 4.29 some results are shown for specimen 10A1-4. In figure 4.27. a-b, the axial stress - axial strain curves (σ_1 - ε_1(loa.pl.) and σ_1 - ε_1 (surf). in fig. a.) and the axial stress - axial strain curves (σ_1 - $\varepsilon_{2\ str.readers}$, σ_1 - $\varepsilon_{3,str.reader}$ and σ_1 - $\varepsilon_{2,surf}$ in fig. b.) are shown. With regard to the surface strains it should be mentioned that in figure 4.27.a. the axial surface strain at the specimen ends (average value of top and bottom gauges no. 14, 15, 16 and 17), and the average central surface strain (no. 10, 11) are shown. The dashed line in fig. 4.27.a, representing the average lateral strains measured by gauges no. 12 and 13 is plotted until mechanical damage was sustained to one of the gauges due to surface cracking.
In figure 4.28. the surface fracture pattern of specimen 10A1-4 is shown, indicating also the strain gauge positions on the specimen surface. The cracks shown in this figure were all visible with the unaided eye. The shaded areas show places where extensive surface spalling occurred.
Finally in figure 4.29, the separate strain gauge readings are plotted against time. The dash-dotted line in fig. 4.29, that is drawn perpendicular to the time axis indicates the peak-stress level σ_{1p} (t = 262 sec.).

First of all it must be mentioned that the σ_1 - $\varepsilon_{1,loa.pl.}$ curve displays a more steep descending branch when compared with cube experiments. This may also be observed from the axial stress-strain curves which are gathered in appendix A2, fig. A2.4 and A2.5 (results of batch 10A / 10B). The effect is explained in the following section (4.4).

The fracture pattern of specimen 10A1-4 displays a localised "shear-plane", that is the major fracture plane is inclined to the loading direction σ_1 (roughly along line A-A, as indicated in fig. 4.28). The shear fracture seems to be formed through an array of 'tensile cracks' that run parallel to the direction of loading. The inclination of the shear plane is approximately 25 - 30 degrees with regard to the direction of loading.
The shear plane fracture was observed for four of the eight prism tests of series 10A / 10B (specimens 10A1-4, 10A2-2, 10B1-2 and 10B2-2), and is also known from previous investigations (see for example /39/).
In the four experiments, the "shear-plane" was always oriented with regard to the casting surface as indicated in figure 4.30.

According to investigations carried out by Newman and Sigvaldason /114/, this "shear-plane" fracture mode should be attributed to a non-uniform stress-distribution within the specimen.

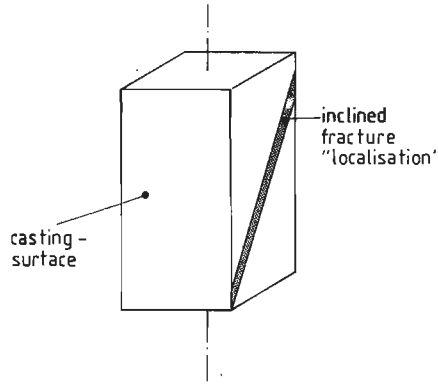

Fig.4.30. orientation of the shear-plane in a uniaxial compression test.

This non-uniform stress-distribution is the result of rotation of one of the loading platen, when an experiment is carried out with one end effectively fixed and the other end effectively pinned. The effect may even become more significant when a non-homogeneous specimen is used. In the current investigation, the prisms were loaded perpendicular, which implies that one side of the prism will be weaker. The specimen neutral axis does not coincide with the loading axis. The four remaining prisms failed with cracks running more or less parallel to the direction of loading (at the specimen surface). It must be mentioned that in three of four cases, shear-plane fracture occurred for specimens originating from the ("casting prisms") middle positions. So differences in positions, which were found to have no significant effect on strength, do show some influence on deformational response and fracture modes! This difference in fracture mode of a specimen does not seem to influence the macroscopic stress-strain curve $\sigma_1 - \varepsilon_1$ (loa.pl.) as may be seen from fig. A2.4.b and A2.5.b. This is an important observation: the macroscopic stress-strain curve does not appear to be influenced by the fracture mode. Probably the rotation of the upper loading platen is reflected by an unevenness in the descending branch and the effect is most pronounced when perpendicular loading is applied. It must be emphasized that the effect of rotating the loading platen decreases as the specimen length decreases. This implies that the effect will be less pronounced in cube tests, however the stress-distribution within the specimen will remain non-uniform.

From figure 4.27.a it is observed that the central surface strains ($\varepsilon_{1,surf}$, gauge no. 10, 11), follow the overall strain $\varepsilon_{1,loa.pl.}$ rather far into the descending branch. Surface unloading can be observed much later as compared with the other experiments (for example see the cube tests, fig. A2.4.a and A2.5.a). On the contrary, the average end surface strain (average value of gauges no. 14,

15, 16, 17) ceases to rise at an earlier stage. From fig. 4.28 it is observed that the major fracture plane runs "through" gauge no. 11, as a consequence it measured large strains (see fig. 4.29). The results indicate clearly the localised failure mode of the specimen, and also confirms the previous observation that structural response rather than material behaviour is measured in the stress-strain curve descending branch (section 4.2.4).

The 'structural response' in the stress-strain curve descending branch is also expressed by the lateral strain measurement. Those strain readers which do not measure 'over' the major fracture in the specimen, show far less strains when compared with the strain-readers that are placed over the "fracture localisation". (see fig. 4.27.b, strain-readers 35, 36, are situated at relatively intact blocks of the specimen, compare with the fracture pattern in fig. 4.28).
The same effect is more clearly shown in fig. 4.31 for specimen 10A2-2. The localised fracture mode was even more pronounced when compared with 10A1-4. In fig. 4.31 the lateral strains ε_2, ε_3 are plotted against the axial (loading platen) strain $\varepsilon_{1,loa.pl.}$. The strain-readers 37 and 38 are mounted "over" the fracture plane, and show large deformations in the post-peak region (the peak

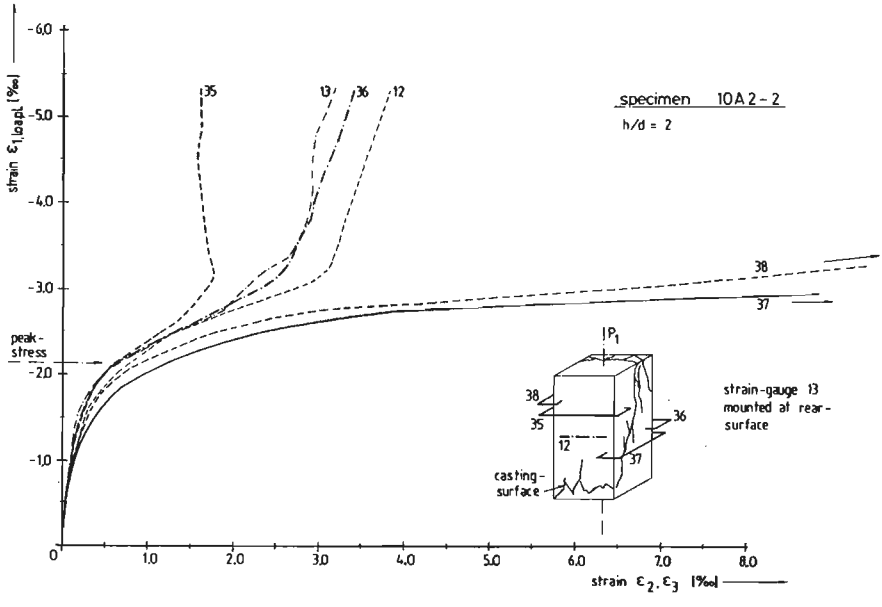

Fig.4.31. Lateral strains ε_2, ε_3 vs. axial strain $\varepsilon_{1,loa.pl.}$ for separate measuring devices of specimen 10A2-2.

stress level is indicated with an arrow). All other measurments cease to rise when the peak stress-level is exceeded. It is emphasized that the strain-reader measurement coincides with a 'loading-platen' measurement, and is independent from surface cracking, that is unless the fixing point is not disturbed by surface spalling. The strain gauges no. 12 and 13, showed no mechanical damage after termination of the experiment, so it may be assumed that the response of the 'intact blocks' is measured with the strain gauges.

The lateral strain - axial strain plots for the specimens that failed according the "shear-plane" mode (fig. 4.30), was found to be different when compared with the lateral strain - axial strain relations measured for the four other experiments (that displayed a parallel crack pattern). This may be observed from figures A2.6 and A2.7 in appendix A2. In these figures, the solid lines represent the average lateral strain measured by means of strain-readers no. 35 and 36, and the dashed lines show the average result of strain-readers no. 37 and 38 (these latter strain-readers were placed parallel to the direction of casting).

Based on similar lateral strain - axial strain plots obtained from uniaxial compression tests on cylindrical specimens, and from strain measurements on the compressive face of a beam loaded in four-point bending, Kotsovos /89/ concluded that the 'best' descending branch for concrete would be a complete and immediate loss of load carrying capacity when the peak stress-level was reached. From the prism tests, failing along a localised shear fracture, it was observed however that the lateral strain - axial strain relation is influenced by the position of the measuring devices. Behaviour as measured in case of a cubical specimen, for which fracture planes seems to be more gradual distributed through the specimen, is observed in the prism test when the concerning measuring device is placed over the "failure localisation". Of course, this will also apply to the beam tests. The above discussion may suggest that structural behaviour is being seen rather than material behaviour in the descending branch of the stress-strain curve. A descending branch is 'structure-dependent', but this is no reason to believe that similar phenomena will also occur in full scale structures.
As will be shown in chapter 5, the conditions for which a stable softening branch is measured, seem to be more important.

4.4. Size effect in uniaxial softening.

The uniaxial compressive experiments of series 10, that were reported in the previous section (4.3), revealed an increasingly steep gradient of the σ_1 - $\varepsilon_{1,loa.pl.}$ curve descending branch for the prism tests, when compared with the results obtained from cube tests (see fig. A2.4 and A2.5). The maximum tangential modulus $E_{tan,1} = \delta\sigma_1 / \delta\varepsilon_1$ in the stress-strain curve descending branch for prisms (h = 200 mm) was approximately twice the value obtained from cube tests. This may be observed from fig. 4.25.a, in which plots of $E_{tan,1}$ vs. $\varepsilon_{1,loa.pl.}$ are shown both for 100 mm and 200 mm high specimens (10B2-3 and 10B2-4). The stress-strain curve peak coincides with $E_{tan,1} = 0$, the tangential modulus becomes negative in the post-peak range.
Extrapolating these results suggests that a further decrease of the slope of the softening branch is being measured for small-sized specimens (with slenderness ratio h/d < 1), and an increasing slope for higher specimens (h/d > 2).
In addition to the 10-series experiments, a small number of uniaxial compression tests was carried out on 50 mm high samples (cross-section A = 100 x 100 mm^2, similar as for the 10-series experiments). Due to this extension, now results were obtained for three different specimenheights: h = 50, 100 and 200 mm. The title of this section refers to this variation in axial specimen dimension.

- description of experiments -

Starting point for these tests were six cubes (d = 100 mm) originating from batch 15A (specimens 15A1-1 through 15A1-6). The 50 mm prisms were obtained by sawing them from 100 mm cubes, positions no. 1, 3 and 5, as indicated in figure 4.32. The three remaining cubes (15A1-2, 4 and 6) were not altered, and also loaded in uniaxial compression. These three latter experiments could be compared with the 10-series results.

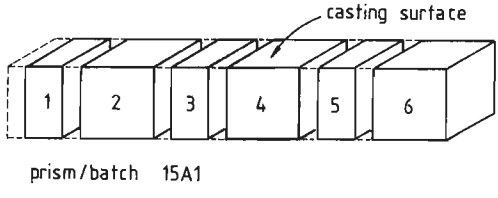

Fig.4.32. Sawing of prisms (h = 50 mm) and cubes from batch/prism 15A1.

In table 4.33, the relevant experiments for slenderness ratios h/d = 0.5, 1.0 and 2.0 (d = 100 mm) are gathered. From the 10-series, only those experiments loaded with capping are taken into consideration. The test-conditions for the 15-series experiments were similar as for the 10-series: capping between specimen and brushes, loading direction perpendicular, and strain rate $\dot{\varepsilon}_1 = 10.10^{-6}$/sec.

specimenheight	50 mm	100 mm	200 mm
batch 15A	15A1-1 15A1-3 15A1-5	15A1-2 15A1-4 15A1-6	
batch 10A/10B		10A1-1 10A1-3 10B1-1 10B1-3	10A1-2 10A2-4 10B2-2 10B2-4

Table 4.33. Uniaxial size effect, review of experiments.

Surface and overall strain measurements were carried out as shown in figure 4.34. a-b. In figure a. the strain gauge configuration for a 50 mm prism is shown. In the axial (loading) direction, two 30 mm strain gauges were mounted to the two side surfaces of the specimen (no. 10 and 11, the measuring length was reduced as a consequence of the smaller specimenheight).

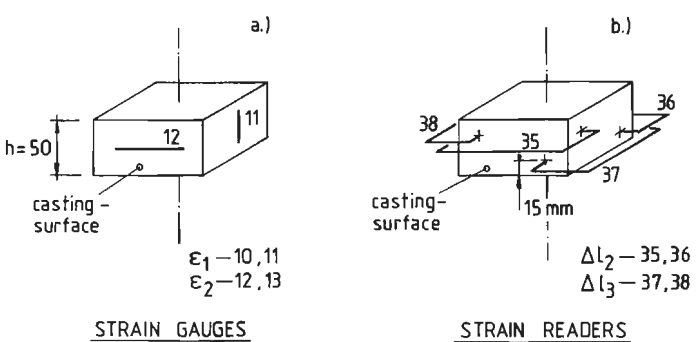

fig.4.34. a. strain gauge configuration for 50 mm prisms, batch 15A.
b. idem, strain-reader positions.

In the lateral direction (ε_2), two strain gauges (no. 12 and 13, measuring length = 60 mm) were mounted in a central position to the bottom and upper (= casting) surfaces of the specimens.
The positions of the four strain-readers were similar to the previous 10-series experiments, with the exception that the distance between specimen-brush interface and the strain-readers was reduced to 15 mm (see figure 4.34.b)
The 100 mm experiments (15A1-2, 4 and 6) used identical instrumentation as the 10-series cube tests (see fig. 4.21.a. and b.).

- experimental results -

In the following discussion, the combined results of the 10 and 15 series experiments (table 4.33) are examined. It must be mentioned that specimen 15A1-4 was loaded excentrically due to malfunction of the spherical seating, and is therefore omitted. The average uniaxial compressive peak-stress, obtained from 100 mm cubes loaded by means of brush bearing platens, was some what smaller for the 15-series ($\bar{\sigma}_{1p}$ = - 40.1 N/mm^2), when compared with the 10-series ($\bar{\sigma}_{1p}$ = -43.9 N/mm^2, obtained by averaging the peak stress-levels of the four 100 mm specimens, indicated in table 4.33).
In figure 4.35, the stress and strain conditions at peak for specimens with different height are indicated. In the upper part of this figure, the dimensionless value $\sigma_{1p}/\bar{\sigma}_{1p}(100)$ is plotted for the three different specimenheights. $\sigma_{1p}(100)$ is the average uniaxial compressive strength obtained from 100 mm cube tests and is indicated in the upper right corner of fig. 4.35, both for batch 10A/10B and for batch 15A. In section 4.3.2, it was shown that no significant difference in strength response is measured for the 100 and 200 mm high specimens of the 10-series. Figure 4.35 shows that no increase of uniaxial compressive strength was recorded for the small-sized 50 mm samples either, compared with the strength response of the 100 mm cubes. This observation coincides with results reported by Schickert /139/. In fact it was to be expected; the response of the flexible platen system used in his investigation almost corresponds to that for brushes. For both systems a spherical loading platen surface develops during an experiment, when lateral deformations of the specimen start to increase.
In /139/ it was also shown, that a hugh increase of uniaxial compressive strength emerges when tests are carried out, adopting rigid steel platens for load application. For the concretes tested by Schickert (B25/15 and B35/16, max. aggregate size d_a = 16 mm), an increase of approximately 90% was measured, when the uniaxial strength of 50 mm samples were compared with the results of

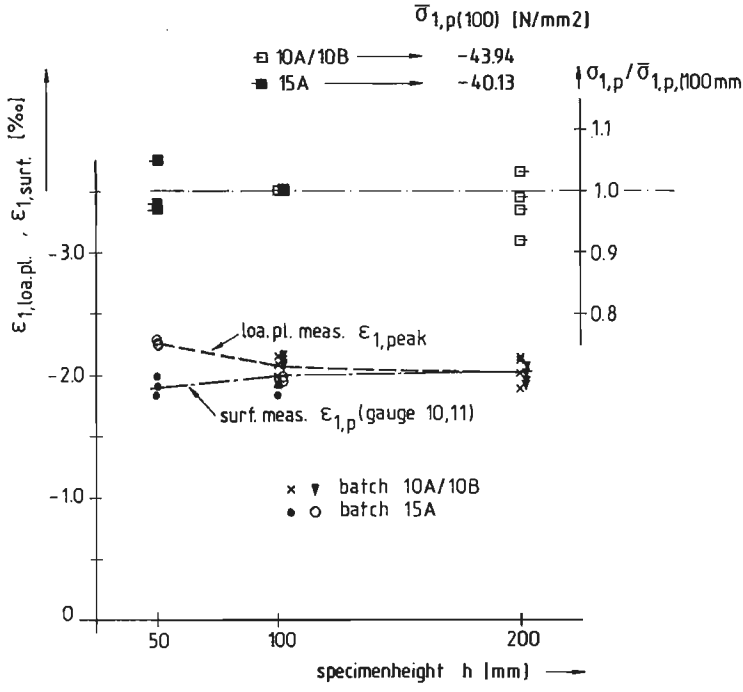

Fig.4.35.Conditions at peak stress level for specimens with different height.

100 mm specimens (both with cross-sectional area A = 100 x 100 mm^2, which is similar to the current research). The constraint between rigid loading platen and concrete specimen was responsible for the greatly increased uniaxial compressive strength of small specimens.

In the lower part if fig. 4.35, the strains at peak stress level, both measured between the loading platen ($\varepsilon_{1,loa.pl.}$) and at the specimen surface ($\varepsilon_{1,surf}$, gauge no. 10,11) are plotted for the three different specimenheights. The discrepancy between loading platen deformation and surface deformation increases for decreasing specimenheight, indicating that disturbances at the specimen-brush interface become more important. The specimen deformations are for these small sized specimens relatively small when compared with the total deformation within the LVDT measuring length.

In appendix A2, figures A2.8.a and A2.8.b, the complete stress-strain curves (σ_1 -$\varepsilon_{1,loa.pl.}$ as solid lines and σ_1 - $\varepsilon_{1,surf}$ as dashed lines in fig. A2.8.a) and the axial strain - lateral strain plots ($\varepsilon_{1,loa.pl.}$ - ε_2 (35,36) as solid lines and

$\varepsilon_{1,loa.pl.} - \varepsilon_3$ (37, 38) as dashed lines in fig. A2.8.b) are shown for the three 50 mm tests of batch 15A.

Similar observations as were mentioned before in section 4.2 and 4.3., also apply for the 50 mm samples. Surface unloading is observed in the post-peak region. Furthermore a slight difference in lateral-strains ε_2 and ε_3 is measured in the post-peak range, indicating the influence of initial anisotropy on the deformational response of the specimens. The 50 mm samples were loaded perpendicular with regard to the direction of casting. Thus ε_3 is parallel and ε_2 perpendicular to the direction of casting as indicated in fig. 4.34.

From figure A2.8.a a gradual descending branch of the $\sigma_1 - \varepsilon_{1,loa.pl.}$ curve is observed. In figure 4.36 the axial stress-strain curves $\sigma_1 - \varepsilon_{1,loa.pl.}$ obtained from experiments on specimens with different height are compared. (resp. 15A1-5 (h = 50 mm), 10B1-3 (h = 100 mm) and 10B2-2 (h = 200 mm)). The axial stress σ_1 is made dimensionless with regard to the peak-stress σ_{1p} for each experiment.

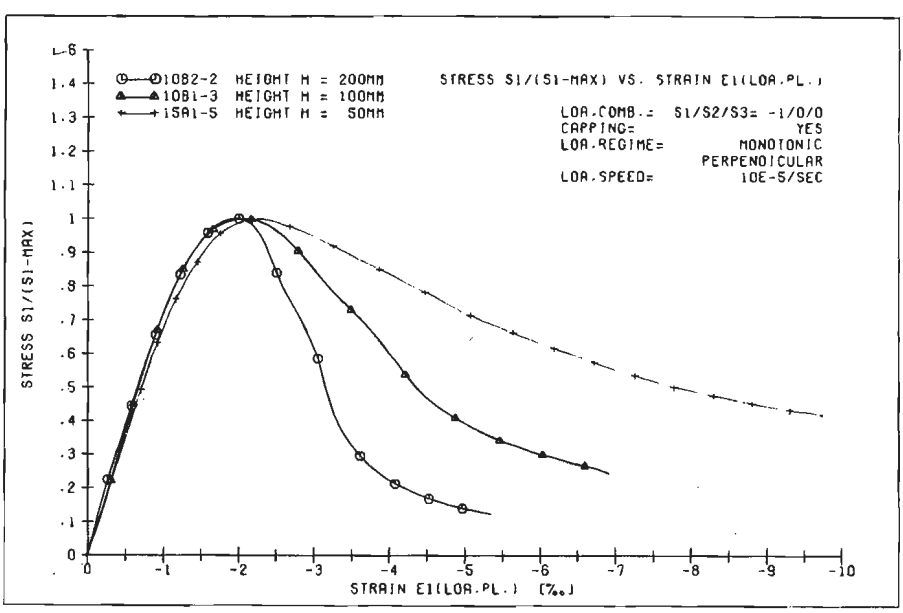

Fig.4.36. Influence of specimenheight on the uniaxial stress-strain curve.

The difference is obvious: decreasing the specimenheight results in a decreasing slope in the stress-strain curve descending branch. Similar results are found

when prisms are loaded in uniaxial compression, reinforced with rectangular stirrups, and the distance between the stirrups is varied /131/. In the pre-peak region the curves are almost identical, independent of the specimensize.
The phenomenon becomes clearer when the post-peak displacement $\Delta l_{1,tot}$ - $\Delta l_{1,\sigma_{1p}}$ is plotted against the dimensionless stress σ_1/σ_{1p}. In figure 4.37, plots of σ_1/σ_{1p} vs. $(\Delta l_{1,tot} - \Delta l_{1,\sigma_{1p}})$ are shown for three specimens of different height (their $\sigma_1 - \varepsilon_{1,loa.pl.}$ curves are shown in fig. 4.36). The differences in post-peak response for specimens with different axial dimensions almost disappears completely, and in fact the localised failure in uniaxial compression is demonstrated.

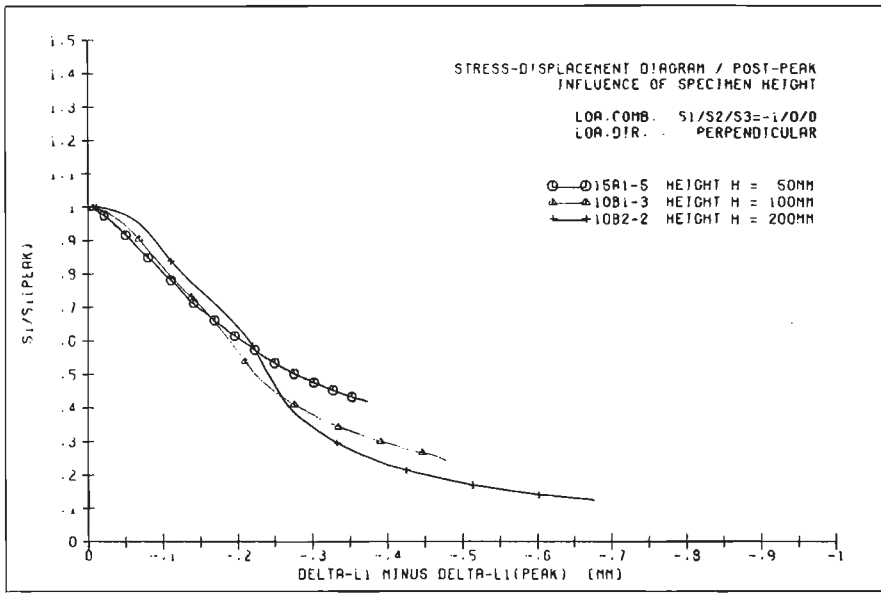

Fig.4.37. Post-peak stress-displacement diagrams for specimens 10B2-2 (h = 200 mm), 10B1-3 (h = 100 mm) and 15A1-5 (h = 50 mm).

The differences in the stress-strain curve descending branch are due to the fact that a localised deformation is smeared over different specimenheights (the measuring length is equal to the specimensize!). As was mentioned in section 2.3 (figure 2.17), similar phenomena are observed in uniaxial tensile fracture.

The localised fracture mode in uniaxial compression was found to be very clear from the final structure of a prism (h = 200 mm), see section 4.3, figure 4.28 - 4.31. A fractured prism (h = 200 mm) broke into relatively large pieces

and this affected surface measurement in axial direction as well as lateral strains measured with strain-readers and strain gauges (figure 4.31).
In the case of a 50 mm prism or a 100 mm cube the broken pieces were generally much smaller. In fact the specimen size did not allow for the development of a large continuous fracture plane as was observed for some of the 200 mm specimens. In figure 4.38, some of the cone-shaped restpieces of broken specimen 15A1-3 (h = 50 mm) are shown.

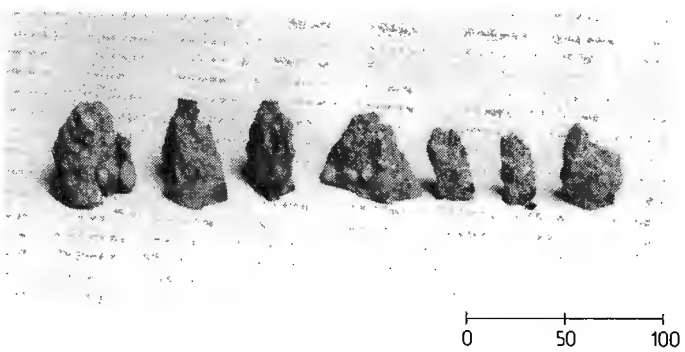

Fig. 4.38. Cone-shaped rest-pieces of broken specimen 15A1-3.

The height of these cones was restricted to the size of the specimen. From a failed 50 mm prism it could be observed that is was built from cone-shaped rest pieces in mutual alternating positions as indicated in fig. 4.39. Cone-shaped 'rupture-elements' (see definition in section 5.2.4, page 139) on top of larger aggregate particles have been reported before /152,161/.

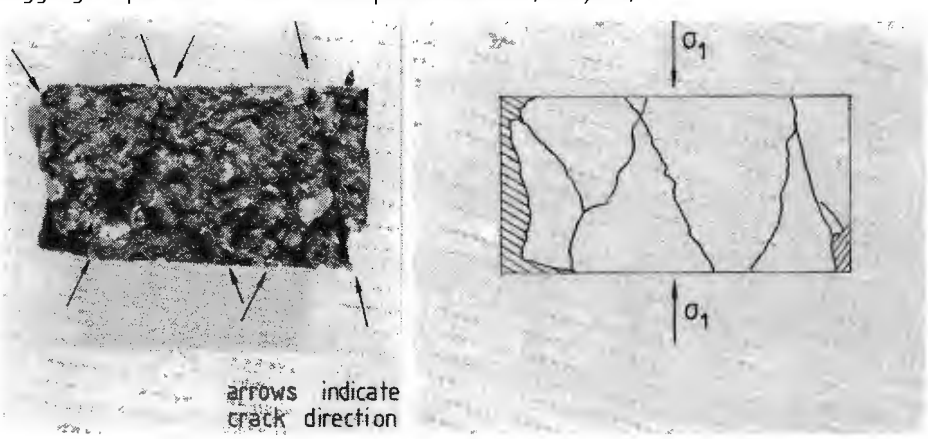

Fig.4.39. Alternating positions of cone-shaped rest-pieces for small sized specimens.

In spite of the different manifestations at failure, the amount of energy required for fracturing a specimen seems to be independent from the specimenheight. In this context the failure energy requirement is defined as the surface under the post-peak stress-displacement diagram (figure 4.37). It is noted that for values of $(\Delta l_{1,tot} - \Delta l_{1,0_{lp}}) > 0.25$ mm, the stress-displacement diagram of the small sized (50 mm) specimens remains above the curves for the higher specimens. This phenomenon may probably be explained from increasing influence of boundary shear in the post-peak region (appendix A6), which is probably more important for small sized specimens.

As was mentioned before, the failure mode of prisms (h = 200 mm) has a considerable influence on the lateral strain - axial strain relations in the post-peak region (fig. 4.31). In figure 4.40, a comparison is made between axial strain - lateral strain plots for specimens with different height.

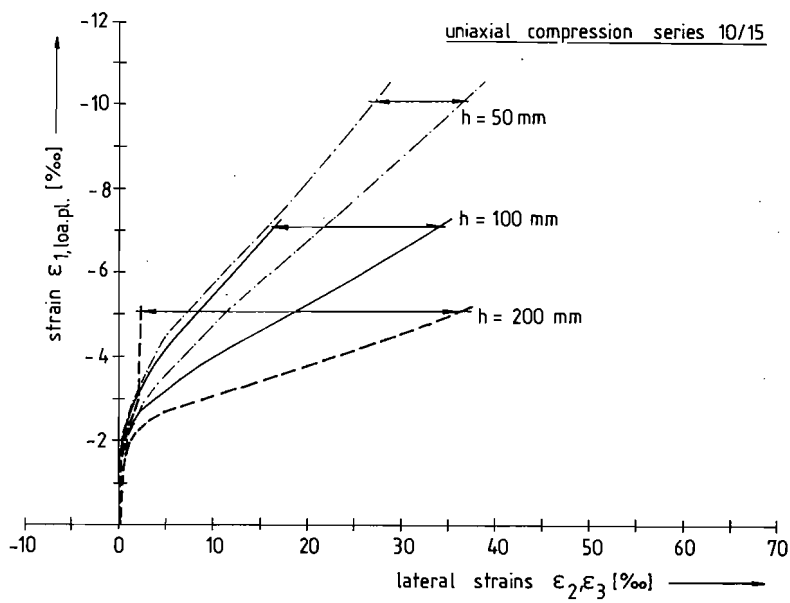

Fig.4.40. Axial strain - lateral strain plots for specimens with different height.

For each specimen size, the range of the lateral strain readings (ε_2 and ε_3) is indicated in figure 4.40. The width of the zone in which lateral strains are recorded decreases for decreasing specimenheight. In fact the desintegration of prisms in rather larger rest pieces is responsible for the very long range that is measured for the 200 mm specimens. A measuring device may accidently be situated on a larger rest piece, thus registrating unloading. For the smaller sized

specimens (h = 50, 100 mm) this is simply impossible as a result of the large number and smaller size of the rupture elements. Therefore large differences in lateral strain readings can not occur.

This observations might be extrapolated for even higher prisms, or also to different structures. For example the beam-tests reported by Kotsovos /89/ are interesting. Based on lateral strain - axial strain plots, originating from uniaxial compressive cylinder tests, and from the compressive zone of a beam test, it was concluded by Kotsovos that rotation capacity in such a structure is the result of a triaxial state of stress in the compression zone, rather than the result of 'strain-softening'. In view of the size-effect his conclusion may be essentially wrong. The chance that in case of a beam test precisely over the 'deformation localisation' is measured is relatively small. On the other hand, the cylinder compression tests, loaded between rigid steel platens, results in a large number of small sized rupture elements, thus leading to a completely different axial strain - lateral strain relation.

4.5. Concluding remarks

In this chapter, the results of numerous uniaxial compression tests were described and interpreted in terms of structural changes. A uniaxial experiment was essentially considered as triaxial.
Major conclusions are that a thorough knowledge of manufacturing parameters can be used as a 'scatter reduction measure' in triaxial testing. In general, triaxial results suffer from large scatter (see for example /51,52/). In the current set-up, specimens were sawn from initially larger prisms, and it was found that specimen position (P) and the direction of loading with regard to the direction of casting (D) had a significant influence on strength (P) and deformational response (P and D) of the specimens.
Further, emphasize is laid on the deformational behaviour of the specimens. It was found that, especially in the stress-strain curve descending branch the specimen should be considered as a structure. Fracture initiation is observed at the outer layers. It seems more appropriate to describe the specimen response as 'structural' rather than as 'material property'. Deformation measurement is complicated when brush bearing platens are used. The results obtained are well within 'engineering accuracy'.
From the experiments on specimens with varying height it was found that a constant fracture energy prevails. Description of the descending branch in terms of a load-displacement curve, rather than stress-strain curve seems preferable.

5. MULTIAXIAL EXPERIMENTAL RESULTS

As was mentioned in the review of experiments in table 3.25, three series of multiaxial tests were carried out. The first series covered a number of biaxial tests, of which only the strength results are mentioned in this chapter. Some additional results of the biaxial series (5A - 6B) are shown in appendix A4.
More detailed information regarding stress-strain behaviour and failure modes is given for the two other series. In this chapter a review is given of the triaxial series (batch 8A - 9B). The rotation test-results (batch 7A/7B) are shown in chapter 7.

5.1. Triaxial experimental design.

The experimental design of the triaxial series was constructed using the theory of linear models (section 4.1). A half replicate of a 4.2^4 factorial in four blocks was carried out (4 factors at 2 levels each, and 1 factor at 4 levels). The experimental design was taken from Cochran & Cox /34/, and is shown in table 5.4. Variables in the test-series were:

a) The loading path in the $\sigma_1 - \sigma_2$ plane.
Loading was applied folowing a constant stress-ratio path or a constant deformation-ratio path, each on four levels as is shown in figure 5.1.

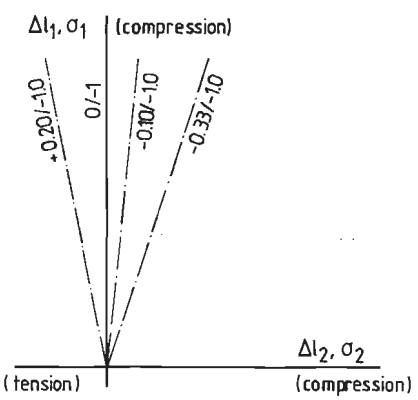

Fig. 5.1. Radial stress- and deformation paths.

The four stress-paths due to the constant displacement-ratio paths, and the four radial stress-paths were chosen in the tension-compression and triaxial-compression regions.

b) The confining-stress σ_3 in the third principal direction.
The level of σ_3 was always chosen proportional to the major compressive stress σ_1 : $\sigma_3 = 0.05\ \sigma_1$ and $\sigma_3 = 0.10\ \sigma_1$. The confinement σ_3 was always compressive. The brush-bearing platens set a limitation to the maximum allowable deformation level (maximum = $\pm$ 3 mm, tensile or compressive deformation). Because the peak-strain-level will increase with increasing confinement in the third direction /4,138/, it was of no use to choose a confinement at a higher level. The limitation set by the maximum allowable brush-deformation was already noticeable for the confinement $0.10\ \sigma_1$. As will be shown in the next sections, it was not possible to follow the complete descending branch to the residual stress-level for some of the cases investigated.

c) The orientation of the initial damage field with regard to the applied triaxial stress-state.
Either a cube was loaded parallel with regard to the direction of casting or loading was applied perpendicular. In case of parallel loading, the casting surface was oriented perpendicular to the major compressive direction σ_1, as depicted in figure 5.2a. When loading was applied perpendicular, the initial damage in the form of weak planes under the larger aggregate particles (fig. 2.2), was aligned in a very favourable direction for crack-propagation. In case of a triaxial compression test ($\sigma_1 < \sigma_2 < \sigma_3 < 0$), the casting surface was oriented perpendicular to the minor principal

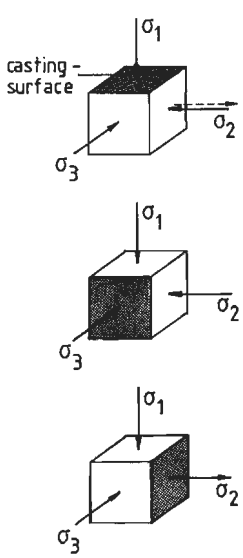

a) parallel loading
- triaxial compression
  $\sigma_1 < \sigma_2 < \sigma_3 < 0$
- tension-biaxial compression
  $\sigma_1 < \sigma_3 < 0 < \sigma_2$

b) perpendicular loading
- triaxial compression
- tension-biaxial compression

Fig. 5.2. Orientation of the initial damage field with regard to the applied external loading.

compressive stress σ_3.

For the tension-biaxial compression tests, the situation was slightly different. When loading was applied perpendicular, the casting surface was oriented perpendicular with regard to the tensile direction (fig. 5.2.b).

d) Monotonic loading or cyclic loading to the envelope curve.

Two basic loading paths were adopted in the investigation. Either a specimen was loaded monotonically to failure, or loading was applied with cycles to the envelope curve. In the triaxial cyclic compression tests and the cyclic tension-biaxial compression displacement-ratio tests, the load-displacement curve in the major compressive direction was used for defining the unloading conditions. The other two loading directions were related to the major compressive direction by means of the test-control which was described in section 3.2.3.

In the pre-peak region, deformation steps Δl_1 = 0.15 mm (LVDT reading) were allowed before the loading was reversed. In the post-peak region the descending branch was the criterion, and as soon as a load-decrease ΔP_1 with increasing deformation Δl_1 was observed, the loading direction was reversed. The stress-difference for deciding for unloading was 0.1 - 0.2 N/mm^2.

The loading and unloading cycles were applied manually by means of an immediate change of polarity of the function generator signal. The pre- and post-peak criteria for load-reversal are depicted in figure 5.3.

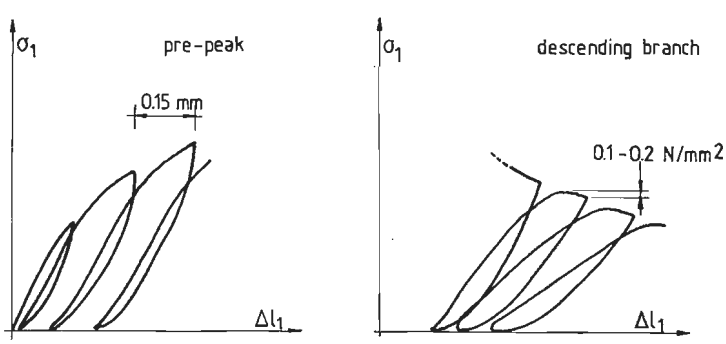

Fig. 5.3. Criteria for load-reversal for cyclic tests.

In the tension-biaxial compression stress-ratio tests, the tensile stress-strain curve was guiding. No load-cycles were carried out in the pre-peak region for these tests.

Implication of the experimental design (fractional factorial 4.2^4) was that one of the two-factor interactions coincided with the block-effect. In the current set-up the block-effect determined the differences between the four batches 8A -9B. The combined effect of monotonic/cyclic and displacement/stress ratio was confounded with the block-effect and therefore not estimateable.

			σ_3/σ_1 = - 0.05/-1.0		σ_3/σ_1 = -0.10/- 1.0	
			perp.	para.	perp.	para.
σ_2/σ_1 =	+ 0.2/-1.0	M		8A1-4	9A1-5	
		C	8B1-5			9B1-4
	0.0/-1.0	M	9A1-3			8A2-2
		C		9B1-3	8B1-4	
	- 0.1/-1.0	M		9A2-4	8A2-5	
		C	9B1-2			8B1-2
	- 0.33/-1.0	M	8A1-3			9A2-5
		C		8B2-4	9B1-5	
$\Delta l_2/\Delta l_1$ =	+ 0.2/-1.0	M	9B2-5			8B2-2
		C		9A1-4	8A2-3	
	0.0/-1.0	M		8B2-5	9B2-4	
		C	8A2-4			9A2-3
	- 0.1/-1.0	M	8B1-3			9B2-3
		C		8A1-2	9A2-2	
	-0.33/-1.0	M		9B2-2	8B2-3	
		C	9A1-2			8A1-5

M = monotonic loading

C = cyclic loading to the envelope

para. = parallel loading

perp. = perpendicular loading

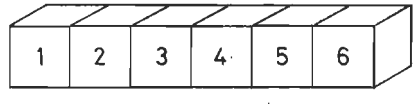

9 A 2 - 4

batch

prism no. 2

position

position 1, 6 end

2, 5 half

3, 4 middle

Table 5.4. Triaxial Experimental Design.

As can be seen from table 5.4, the use of the specimens at the prism end (no. 1 and 6) was omitted in the triaxial experimental design. From the uniaxial experiments, reported in section 4.2, the influence of original position of the cube on strength and energy-response was reported. An increase of strength was observed towards the prism-ends. The effect was also observed in the biaxial series (appendix A4), and there was an indication that it was even more pronounced in biaxial loading.
Therefore it was considered expedient to rule out the effects of position in the triaxial tests by simply omitting the specimens originating from the prism-ends.
The uniaxial experiments also showed similarities in deformational behaviour if all specimens originated from the same prism (see fig. 4.11, series 3A-3B).
Although the strength-response would be slightly overestimated compared with the inner-positions, it was considered usefull to check the uniaxial response under tensile and compressive loading by means of the two end-cubes from each prism.
Thus the total number of experiments was extended to 48 tests, including 8 uniaxial compressive and 8 uniaxial tensile tests. The uniaxial tests were always loaded parallel. The strain rate for all tests was fixed at $\dot{\varepsilon}_1 = 20.10^{-6}$/sec.

- **measuring devices** -

The instrumentation of the triaxial experiments was indicated before in section 3.2.2.
In the four biaxial experiments (see table 5.4, stress-ratio $\sigma_2/\sigma_1 = 0/-1$, $\sigma_3 = \beta\sigma_1$), additional surface measurements were carried out. In each stressed direction, two 60 mm straingauges were mounted at the upper and lower free surfaces (see fig. 3.10).
In all uniaxial control tests (tension and compression, 100 mm cubes), two 60 mm straingauges were mounted in axial direction. In the uniaxial compression tests, lateral strains were measured by means of four strain-readers, in a configuration similar as for previous uniaxial tests (compare with fig. 4.21.c). In the uniaxial tension tests, lateral strains were measured with two 60 mm straingauges.

5.2. Experimental results

An overwhelming amount of data came available from the multiaxial experiments. The data-aquisition system, described in section 3.2, was of great help in the working of the results. The advantage of the system was that in a rather

simple manner, a large number of results could be displayed graphically. In this section some of the strength and deformational results are given, the full triaxial results are gathered in appendix A5.

5.2.1. Response of constant displacement-ratio tests.

The experimental designs both for the bi- and triaxial series provided for a number of displacement-ratio tests. The response of such experiments is rather complicated (at least in stress-space), when compared with the constant stress-ratio tests. Before the 'failure-envelopes' are shown, the behaviour of a concrete specimen loaded by means of a constant displacement-ratio is described.

The constant displacement-ratio tests were carried out in order to provide data for non-proportional stress-paths. From investigators involved in constitutive modelling, the objection is often raised, that with the early constant-stress-ratio paths /95,96,4/ and hydrostatic-deviatoric loading paths /51,52,138/, results are obtained which do not coincide with the actual response of structural components. With regard to stress- or strain induced anisotropy this objection is quite justified.
Also with the constant displacement-ratio experiments it would be possible to match stiffness and compliance descriptions, probably leading to new insights of the structural response of the material.
The experimental designs provided for displacement-ratio tests in the biaxial compression as well as in the tension-compression region. Actually a biaxial displacement state was defined, also for the triaxial tests, while the confinement always was taken proportional to the major compressive stress ($\sigma_3 = \beta \sigma_1$, $\beta = 0$, 0.05 and 0.10). Furthermore the experimental designs included a number of tests under plane-strain conditions ($\varepsilon_2 = 0$). It should be mentioned that recently monotonic and cyclic biaxial tests, with a constant displacement-confinement were carried out by Buyukozturk & Zisman /23/. The sequence of loading in their tests was as follows: a horizontal load was applied to the specimen (square plate, loaded by brushes) to a predescribed deformation level. Secondly, the vertical load was increased until failure occurred, while the horizontal displacement was maintained at a constant level. The loading in vertical direction was by means of a stress-control, so no information regarding post-peak behaviour was obtained.
The behaviour of a constant displacement-ratio test is clarified by means of figure 5.5. In the figure the stress-path corresponding to a biaxial displacement-ratio is shown (specimen 5B2-3, $\Delta l_1/\Delta l_2 = -1/-0.33$, $\sigma_3 = 0$, loading direction = perpendicular). The initial slope of the stress-path is defined by the initial

poisson-ratio of the material, and in case of a non-zero confinement (σ_3), also by the third loading component (see appendix A3). With increasing applied deformation, an increased curvature of the stress-path is observed due to the growth of the poisson-ratio under external loading (see also chapter 4, uniaxial experiments). It must be emphasized that the increase of loading in the intermediate direction (σ_2), due to a poisson-ratio coupling with direction 1, may be less than calculated by means of linear theory, using the initial poisson-ratio obtained from uniaxial tests. A predominant cracking in the unconfined direction, will lead to different values of ν in a biaxial experiment. As was shown by Walsh /164/, the ever increasing poisson-ratio under external loading, is the result of crack-initiation and propagation. In our tests indeed a steeper ascend of the stress-path was observed, when compared with values obtained from calculations with linear elastic theory, using the poisson-ratio from uniaxial experiments. Also in the test reported by Buyukozturk & Zisman /23/, a decreasing poisson-ratio was observed under asymmetric constant confining displacement. (0.08 instead of the poisson-ratio $\nu = 0.15 - 0.20$ under uniaxial compression).

At a certain deformation level, $\Delta l_{1,ult}$ the major compressive stress σ_1 will reach a maximum. Large macro-defects start to develop in an orientation depending on the governing loading combination. In the case of the biaxial compression test of figure 5.5, large deformations occur in the unconfined direction (ε_3), as is shown in fig. 5.6.
The major principal stress-strain curve σ_1-ε_1 will enter the descending branch. While σ_1 decreases, the level of σ_2 remains almost constant, but increases again after the residual stress-level is reached in direction 1. For this specimen, a rather unstable descending branch was measured. This was in general a problem in biaxial tests (see also appendix A4). Eventually a second peak-stress level is observed, however now in the original intermediate direction. In fact the loading is rotated against the specimen's damage-axes. The peak-level of σ_2 is considerable lower than the first peak-stress in direction 1, and the effect must be attributed to the presence of large macro-defects in the specimen. From this behaviour it is concluded that damage due to a certain deformation in direction 1 leading to a descending branch in the σ_1-ε_1 curve, does not substantially influence the intermediate direction (intermediate in terms of deformation). In fact failure occurs in first instance in the plane normal to the intermediate direction, which is confined by means of a compressive displacement Δl_2. In section 5.4.2. more attention will be given to the observed failure-modes.
In the tension-compression displacement-ratio tests, similar behaviour is observed. However in these cases, a first peak-stress is reached in the tensile

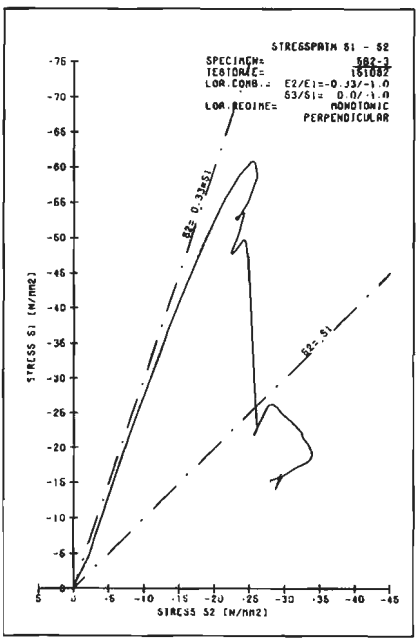

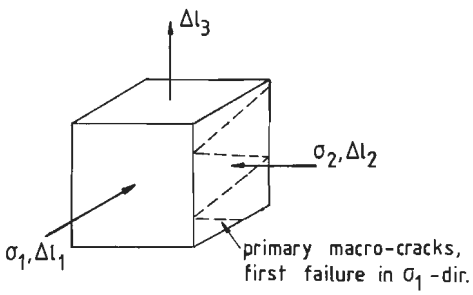

Fig. 5.5. Stress-path in the σ_1-σ_2 plane for a constant deformation-ratio test (biaxial compression)

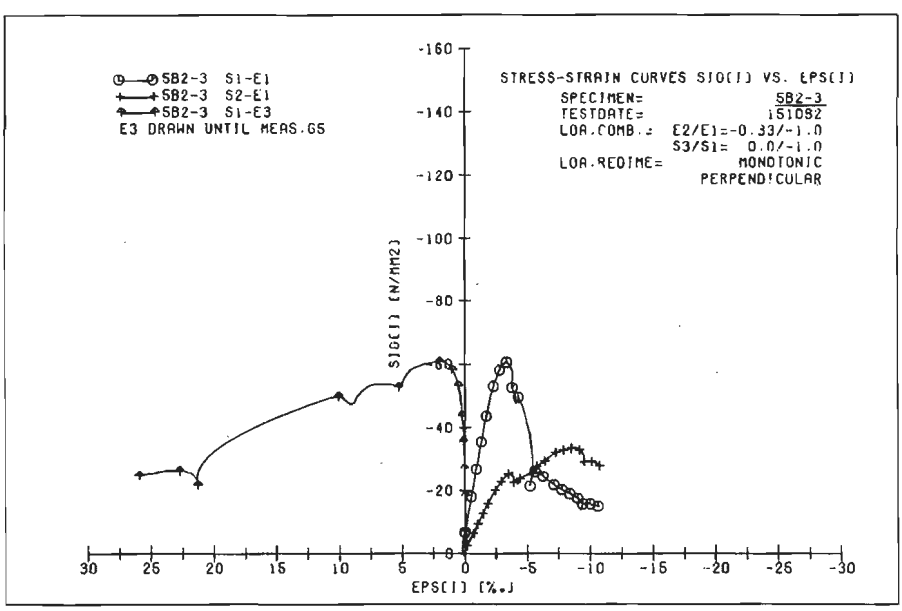

Fig. 5.6. Stress-strain curves for specimen 5B2-3, biaxial deformation-ratio.

direction, and when the ratio between the tensile and compressive displacement is chosen properly, a second peak will be observed (dependent on the type of test) in the bi- or triaxial compression region. The behaviour can be explained from the fact that before the tensile crack will open, it is closed again due to the increasing 'poisson-action' of both compressive stresses. In the next section, more attention is given to this matter.

Of course also triaxial displacement-ratio tests may be carried out. In fact in the trial-experiments preceding the triaxial series (8A-9B) a test was performed with deformation-ratio $\Delta l_1/\Delta l_2/\Delta l_3$ = -1/-0.33/0. While the three deformations involved were all compressive, no (stress) failure was observed. In fact, under these conditions no such failure ever can be found. The stress-path may eventually reach the failure envelope, but will then probably proceed into the high triaxial compression region (fig. 5.7).

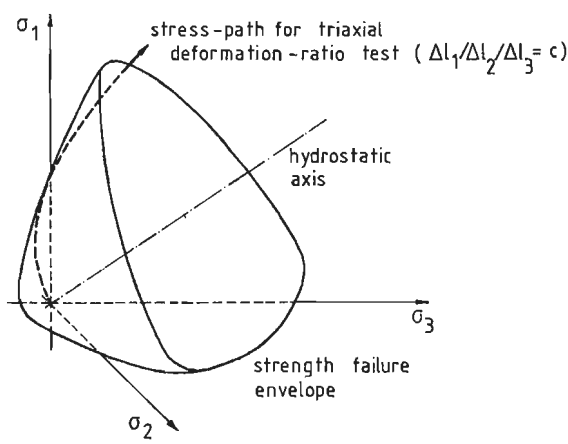

Fig. 5.7. Response of a triaxial deformation-ratio experiment.

5.2.2. Strength results

In figure 5.8 the strength results for both the bi- and triaxial experiments are shown in the plane $\sigma_3 = 0$. For the triaxial tests in fact the projection of the planes $\sigma_3 = \beta \sigma_1$, with β= 0.05 and 0.10, on the plane $\sigma_3 = 0$ is shown.
Each data-point in fig. 5.8 is the result of a single experiment. As was mentioned in section 5.1, the use of the end-position specimens was omitted for the triaxial series. From the biaxial tests, which are in more detail reported in appendix A4,

a clear effect of position on strength was measured. For comparitive reasons therefore, the end-positions are omitted also for the biaxial tests in fig. 5.8.
In table A5.1, for all triaxial experiments the conditions at peak (stresses σ_{ip} and strains ε_{ip}, i = 1, 2, 3) are gathered. The peak results of the 100 mm uniaxial control tests have also been included. The uniaxial compressive strength for batch 8A/8B was equal to $\sigma'_{lp,100}$ = - 45.3 N/mm^2 (n = 4), the uniaxial tensile strength was $\sigma_{lp,100}$ = 2.8 N/mm^2 (n = 3), where n is the number of successful tests from which these averages are obtained. For batch 9A/9B, these values were respectively $\sigma'_{lp,100}$ = - 47.9 N/mm^2 (n = 4) and $\sigma_{lp,100}$ = 3.1 N/mm^2 (n = 4). The stress-strain curves of the eight (100 mm) uniaxial compression tests are shown in fig. A5.3. In fig. A5.4. a-b the surface strains are compared with LVDT measurement for the same uniaxial tests. These results may indicate that the response of the brushes was satisfactory (compare with section 4.3).
Furthermore in table A5.1, the peak results of three preliminary triaxial tests are shown (indicated with (1) in fig. 5.8).

The biaxial results are consistent with previous investigations (Kupfer /92/, Liu et.al. /96/ and the cooperative international research by Gerstle et.al. /51,52/). A comparison with previous research is shown in fig. A4.3.
The triaxial tests show a similar shape of the failure envelope as was found for the biaxial tests. A slight difference was observed between the batches 8A-9B, the effect being magnified in the triaxial compressive stress-space (respectively the open and closed marks in fig. 5.8). A fast increase of strength is observed in the triaxial compression region, with increasing confinement in the intermediate and minor principal direction.

The response of a stress-ratio test is obvious, and the peak-level is reached simultaneously for all three loading-directions. As was shown in the previous section, the response of a deformation-ratio tests, is highly non-linear in stress-space, and depends largely on the deformational characteristics of the material. As in general an increased scatter is observed in deformation measurements, an increased scatter also seems to occur for the strength response of deformation-ratio tests.
The peak-strengths of the deformation tests are situated on the same failure locus as the constant-stress-ratio experiments. This is obvious when the results obtained from the plane-strain tests are compared with the stress-ratio paths σ_1/σ_2 = -1/-0.33 for different confinement levels σ_3.

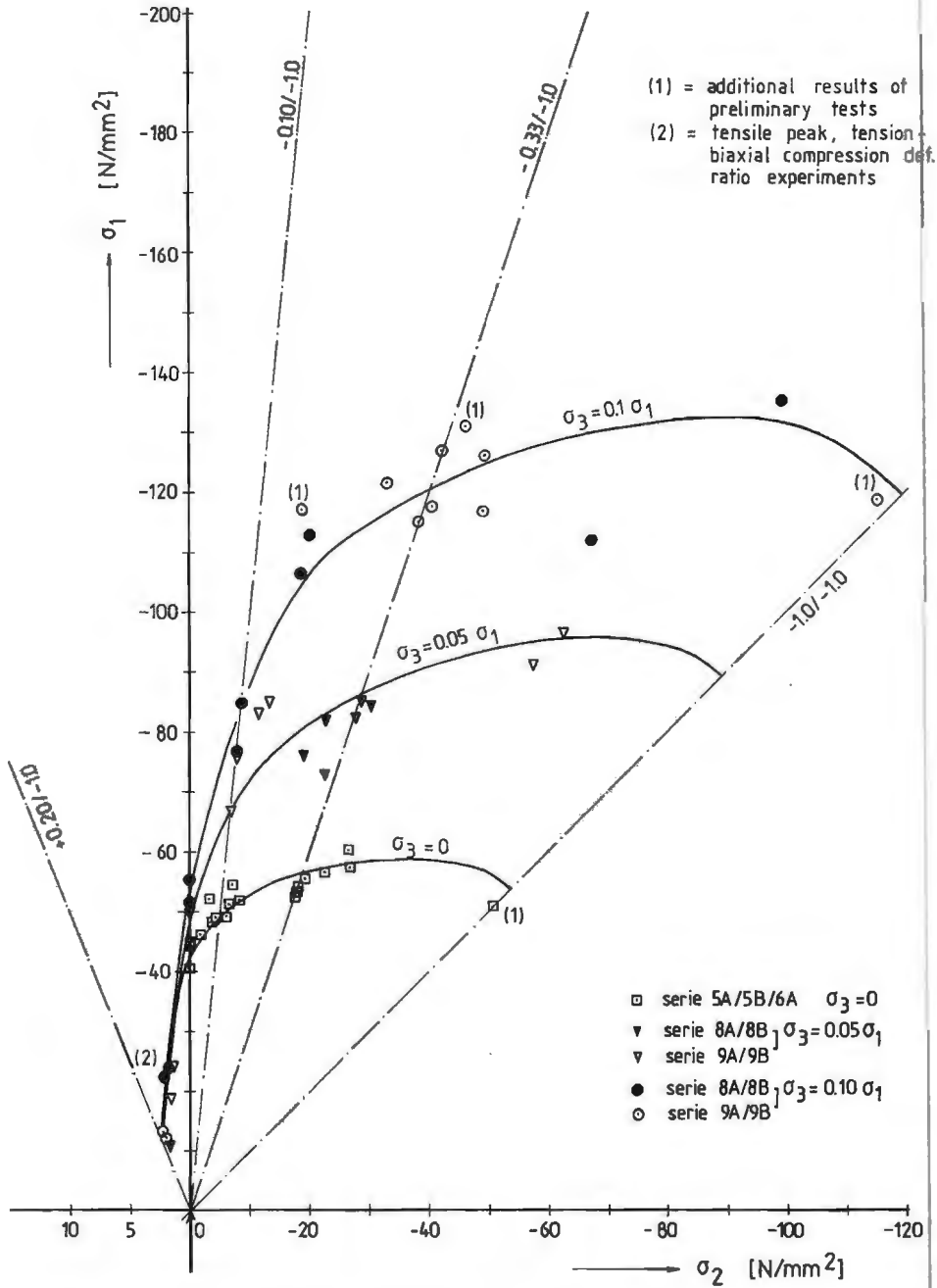

Fig. 5.8. Strength-envelopes for the bi- and triaxial experiments.
(The tensile axis σ_2 is drawn at a larger scale!).

The tensile peaks of the tension/compression deformation ratio tests are also indicated in fig. 5.8 (compare with values in table A5.1).

A similar statistical analysis as was done for the biaxial tests, was carried out for the triaxial tests, although in this case the results were not successful. The random-error was large, which is mainly due to the large number of effects which had to be estimated with a small number of experiments. The number of degrees of freedom available for estimating the random error only was 3.
From the analysis the main-effects due to the intermediate and minor principal stress, and the effects due to a displacement or stress-ratio test were found to be significant at the 5% level. These effects are also very apparent from figure 5.8.
No refinements were made, trying to fit different, possibly more accurate models. It is felt that the description of the failure-locus is not sufficient, and a full constitutive law should in fact include the failure-surface. Also the treatment of the deformation-ratio tests, which was included by means of a linear term in the model, was not satisfying. The tests show clearly the interaction between stress- and deformation.

Very illustrative in this relation is the response of the deformation tension-compression experiments. The stress-paths for the four tension-compression displacement-ratio tests are shown in figure 5.9.
The tests show a first peak-level in the tensile direction, and due to the poisson-effects of the compressive directions, the tensile stress-state is transformed in a compressive-stress, leading to a second, but now triaxial compressive failure.

Also shown in this figure are the results of eight constant stress-ratio tests along the axes $\sigma_2 = 0$ and $\sigma_2 = 0.10.\sigma_1$, for confinement σ_3 at both levels (0.05 and 0.10). Comparison of the stress-path σ_1-σ_2 in the biaxial compression region with the constant stress-ratio tests, indicates that the failure locus is followed by the displacement-ratio tests. If the same effect occurs in the tensile region is not sure, while no constant stress-ratio tests have been carried out for combinations between σ_2/σ_1 = + 0.2/-1.0 and 0/-1.0. The failure locus in the tension-compression region might be followed if the tensile crack is prevented from opening by an increasing poisson-effect due to the compressive directions. The subject may be interesting for future research. If indeed the failure locus is followed for these tests, only a few tests are needed to study the transition stage from tensile to compressive failure. The stress-paths of all constant displacement-ratio experiments are given in appendix A5 (fig. A5.28 - A5.33).

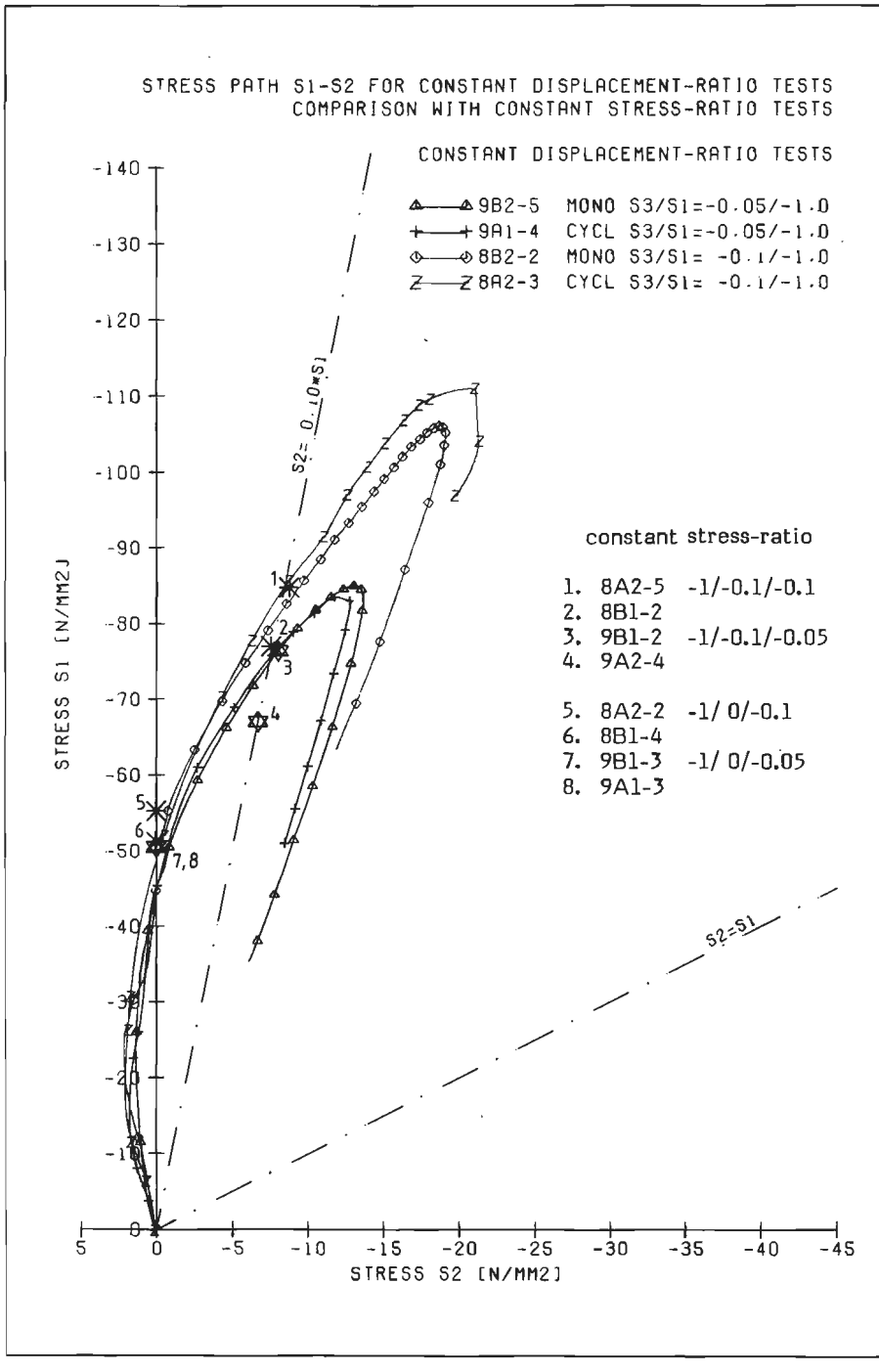

Fig. 5.9. Stress-path σ_1-σ_2, for tension-compression constant displacement-ratio tests.

5.2.3. Multiaxial stress-strain behaviour

This is in fact the main-purpose of this investigation. With the aid of the three-fold servo-control, it was possible to measure the complete stress-strain response under multiaxial conditions. For comparative reasons, the stress-strain curves of the cyclic tests are shown as envelope-curves. From the statistical analysis, of both the bi- and triaxial series no effect of cyclic or monotonic loading on the envelope curve was observed. Similar indications are available from litterature, for uniaxial compression (Spooner et.al./148/, Karsan & Jirsa /81/), as well as for uniaxial tensile loading (Reinhardt & Cornelissen /129/). The stress-strain curves for concrete seems to be unique, and all stress- and strain conditions within the envelope-curve may exist. More attention to the cyclic stress-strain behaviour is given in section 5.2.6.

An example of the biaxial stress-strain behaviour was already shown in fig. 5.6. The stress-strain results of the biaxial series are not completely reported, while there are some doubts about their validity. The observed unstable descending branch, and the poor correlation between surface and overall deformation measurement, indicated that a splitting type of failure occurred (see appendix A4). Indeed a considerable non-flatness of the brushes was observed after the tests were carried out. This was due to the large lateral deformations that were allowed (in the unconfined direction, $\sigma_3 = 0$).

In this section the influence of the intermediate and minor compressive-stress on the observed stress-strain behaviour is shown. Only a selection of measured stress-strain curves is given in the main text, the full details of the measured stress-strain curves are given in appendix A5, fig. A5.7 through A5.27. Furthermore very first results of tension-biaxial compression results are shown.

- Influence of the minor principal stress -

In figure 5.10, three stress-strain curves for experiments under plane strain conditions ($\varepsilon_2 = 0$) are shown. In the upper part of the figure, strains ε_1 and ε_3 are plotted versus the major compressive stress σ_1. In the lower graph, the increase of σ_2 is shown. All three tests were loaded perpendicular. The effect of confinement $\sigma_3 = \beta \sigma_1$ is evident. The increase of strength was already reported in the previous section. From the stress-strain curves, an increasing strain at peak stress ($\sigma_1 - \varepsilon_1$) is observed. The softening branch shows a similar shape for the three confinement-levels, only an increase of the residual stress-level is

observed with increasing confinement. The rate of increase of lateral deformation (ε_3) is decreased by the presence of confinement (σ_3).

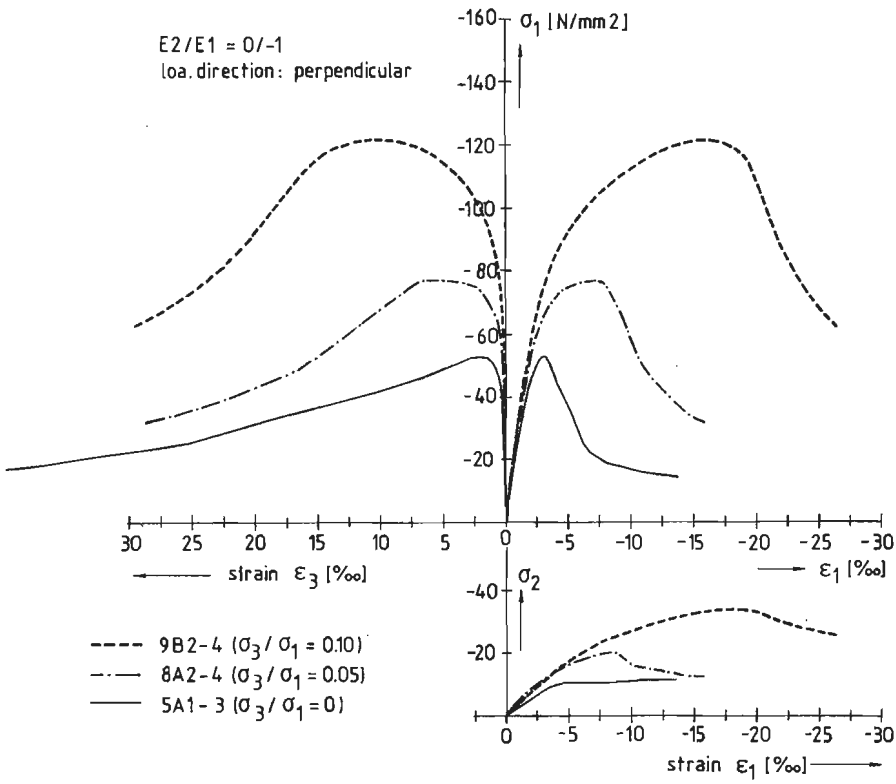

Fig. 5.10. Stress-strain curves for plane strain-tests, with increasing confinement $\sigma_3 = \beta\sigma_1$ (β= 0, 0.05 and 0.10).

The increase of σ_2 is due to the poisson-effect. Calculation of the initial poissons-ratio from the plane-strain tests indicates a value of 0.10-0.15, which is smaller than values measured in uniaxial compression. Probably the orientation of micro-crack development is important in this context.

Until the peak-stress-level, an ever increasing value of σ_2 is measured. In the descending branch, the stress σ_2 decreases, indicating unloading in this direction. Failure mainly is confined to the directions 1 and 3, and the intermediate direction seems undesturbed. Some more attention to these features is given in section 5.2.4. (failure-modes).

- Influence of the intermediate principal stress -

In figure 5.11. the stress-strain curves for three levels of σ_2 are plotted: the results of the tests 9B1-3 (σ_2/σ_1 = 0/-1), 9A2-4 (-0.1/-1.0) and 8B2-4 (-0.33/-1.0), loaded by a constant stress-ratio with confinement $\sigma_3 = 0.05\ \sigma_1$.

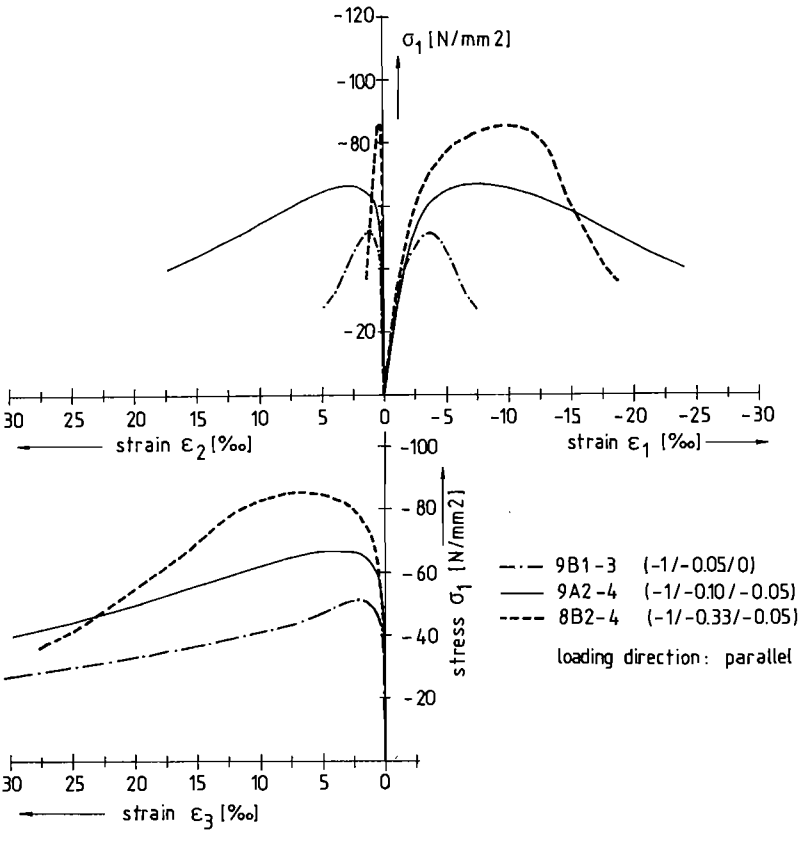

Fig. 5.11. Stress-strain curves for experiments with different intermediate stress-level. Constant stress-ratio tests with $\sigma_3 = 0.05\ \sigma_1$, loading direction: parallel.

All tests were loaded parallel with regard to the direction of casting. In the upper part of fig. 5.11, the strains ε_1 and ε_2 are plotted against the major compressive stress σ_1, in the lower part the $\sigma_1 - \varepsilon_3$ curves are shown.
The difference in post-peak behaviour is striking. Where the experiments -1/0 and -1/0.33 show a steep descending branch, the third experiment -1/-0.10 shows a completely different behaviour. In this case a smooth, gradual decreasing

descending branch is measured. This type of failure was observed for all tests leading to two large (not necessarily equal) tensile deformations i.e. the experiments with failure points near the compressive meridian of the strength envelope.

Comparison of the constant-stress-ratio tests -1/-0.33/β, with the plane-strain tests reveals the similarities at the peak-level. The conditions at peak are almost identical (ε_2 0, also for the constant stress-ratio tests), although the path to reach the conditions are quite different. The tests indicate that there is no difference between stress and strain-ratio tests at (stress) failure.

This observation is not consistent with data reported by Buyukozturk & Zisman /23/. An increase of strength under displacement confined biaxial tests was reported, in comparison with the previous experiments by Kupfer /92/. It must be emphasized that the results of Buyukozturk et.al. /23,24/, were obtained with a different experimental machine, and as shown in the international cooperative research by Gerstle et.al. /51,52/, one should be careful with comparing results obtained with different experimental techniques. The differences measured by Buyukozturk are within the range reported by Gerstle et.al.

- tension-biaxial compression stress-ratio experiments -

As can be seen from the experimental design, table 5.4, only a very limited number of tension-biaxial compression (t/c/c) stress-ratio experiments was carried out (stress-ratio $\sigma_1/\sigma_2/\sigma_3$ = -1/0.2/β, β= -0.05 and -0.10). One of the t/c/c tests failed along one of the epoxy layers between specimen and brush bearing platen (8A1-4, $\sigma_1/\sigma_2/\sigma_3$ = -1/+0.2/-0.05, C, para), the three remaining experiments, all showed a stable descending branch in the tensile direction. The distance of the tensile crack was in all cases larger than 10 mm from the specimen-brush interface.

In figure 5.12. a-b, two examples of σ_2 - ε_2 curves are shown. In figure a, the result is shown for a monotonic test (9A1-5) with stress-ratio -1/+0.2/-0.10. The specimen was loaded perpendicular, which implies for a t/c/c experiment that the tensile loading direction is applied unfavourable with regard to the initial damage (see fig. 5.2.b).

Figure b shows the result of the companion test 9B1-4 (stress-ratio -1/+0.2/-0.1), loa.dir. parallel. The second specimen was loaded following the cyclic path. The implications in σ_1 and σ_3 direction are not shown. In both directions an elastic un- and reloading was observed. The conditions at peak in both lateral compressive directions are indicated in table A5.1.

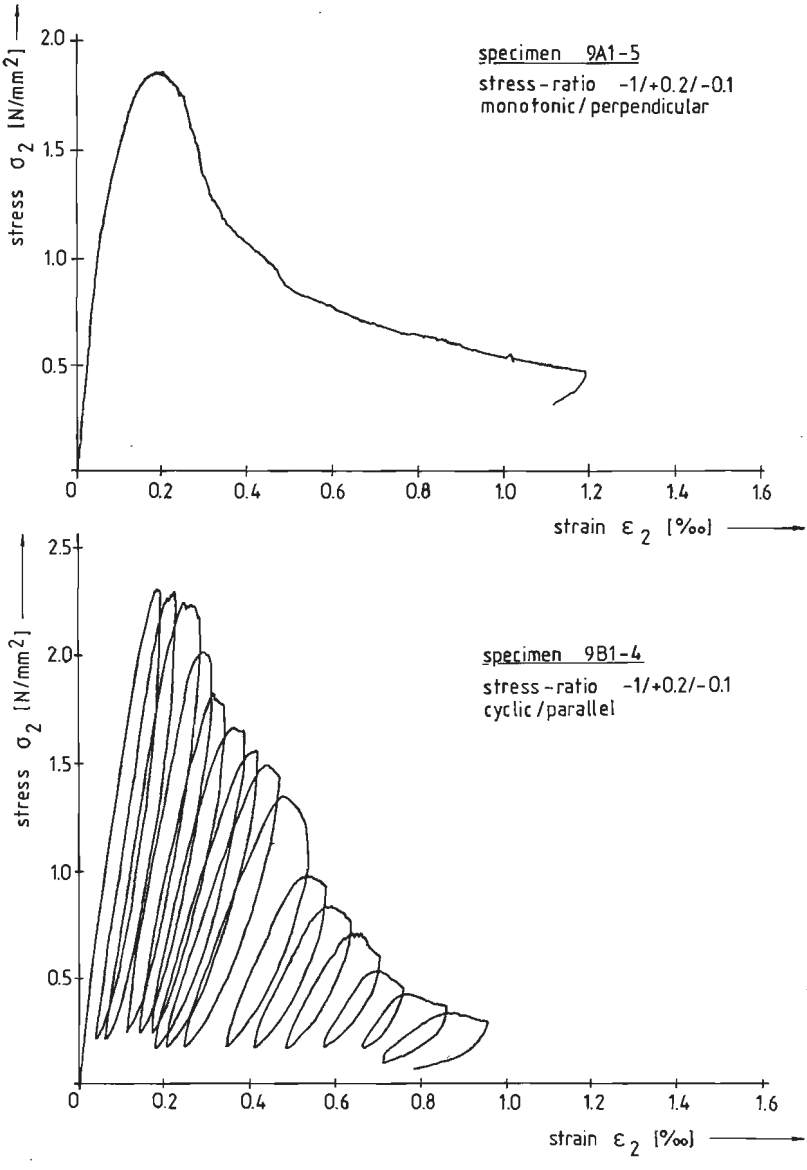

Fig.5.12. a-b. σ_2-ε_2 curves for tension-biaxial compression tests, stress-ratio -1/+0.2/-0.1. Specimen 9A1-5, perpendicular (fig. a) and 9B1-4, parallel (fig. b).

From the plots in fig. 5.12, the difference in peak strength is obvious (see also table A5.1). The difference is probably the result of different orientation of the initial damage with regard to the tensile loading direction. Similar results (a decrease of tensile strength when initial crack planes are oriented perpendicular to the tensile stress), were reported before for uniaxial tension /147,171/. Yet it is emphasized that only one pair of t/c/c stress-ratio tests was available. This is

very limited, especially if the increasing scatter in the t/c/c region is taken into consideration (compare with results reported by Kupfer /92/).
For specimen 9A1-5, the energy-requirement, i.e. the surface under the σ_2 - ε_2 curve (related to the total specimen volume) was determined, and approximately equal to $W_2 \approx 1$ Nm. This result is about the same values as obtained for the uniaxial tensile experiments (respectively 9B1-6, W ≈ 0.9 Nm, and 9B2-6, W ≈ 1.2 Nm, see fig. A5.5. a-b). The presence of the compressive stress-components does not seem very much of influence for these stress-combinations. Note the large difference in energy-requirement when compared with compressive stress combinations (see table A1.1 and A1.2, uniaxial compression, and fig. 5.23, bi- and triaxial compression).

5.2.4. Failure modes

- observations/triaxial compression -

From the uniaxial compression tests on prisms (section 4.3 and 4.4) with variable height, it was concluded that failure occurs in a very localised zone. The structure that is formed, is however not very apparent from the final remains of an uniaxial compressed specimen. The outer layers which seems to behave quite different do not add in a positive sense to the explanation of the phenomenon. Modelling of the descending branch by means of a stress-displacement diagram however seems to be more appropriate than the conventional stress-strain diagram. In fact similarities are suggested to exist between the tensile and compressive failure of concrete.
The localised failure mode of the material under compressive loading becomes more clear when the final structure of a specimen loaded under multiaxial conditions is studied. When a cube was removed from the experimental machine after an experiment had been carried out, the cube was completely covered by the epoxy-resin layers. An orthogonal crack pattern was imposed to the cube surface, mainly due to local splitting of the separate brush-rods. With the aid of a diamond grinding disk, the outer layers of the cube were removed to a depth of approximately 2 mm. Although the grinding of the highly fractured structure was carried out very carefully, it could not be avoided that some of the material was torn loose during the process.
In figure 5.13. a and b the surfaces of the specimen 8B2-4 ($\sigma_1/\sigma_2/\sigma_3$ = -1/-0.33/-0.05, C, parallel) and 9A2-4 ($\sigma_1/\sigma_2/\sigma_3$ = -1/-0.10/-0.05, M, parallel) are shown after the epoxy layer and some of the outer concrete were removed. The stress-strain curves of both specimens were already shown in figure 5.11.

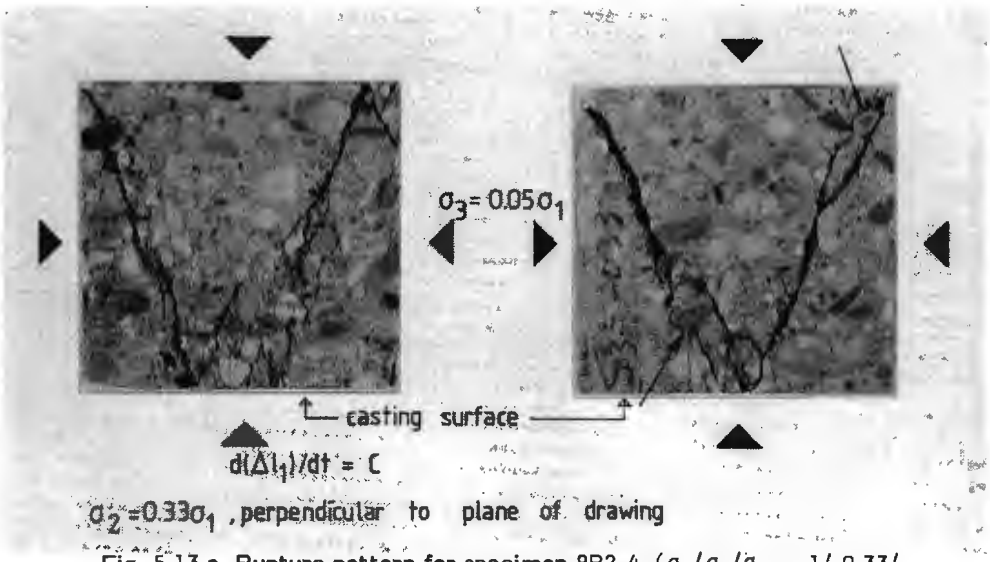

Fig. 5.13.a. Rupture pattern for specimen 8B2-4, ($\sigma_1/\sigma_2/\sigma_3$ = -1/-0.33/-0.05, C, parallel)

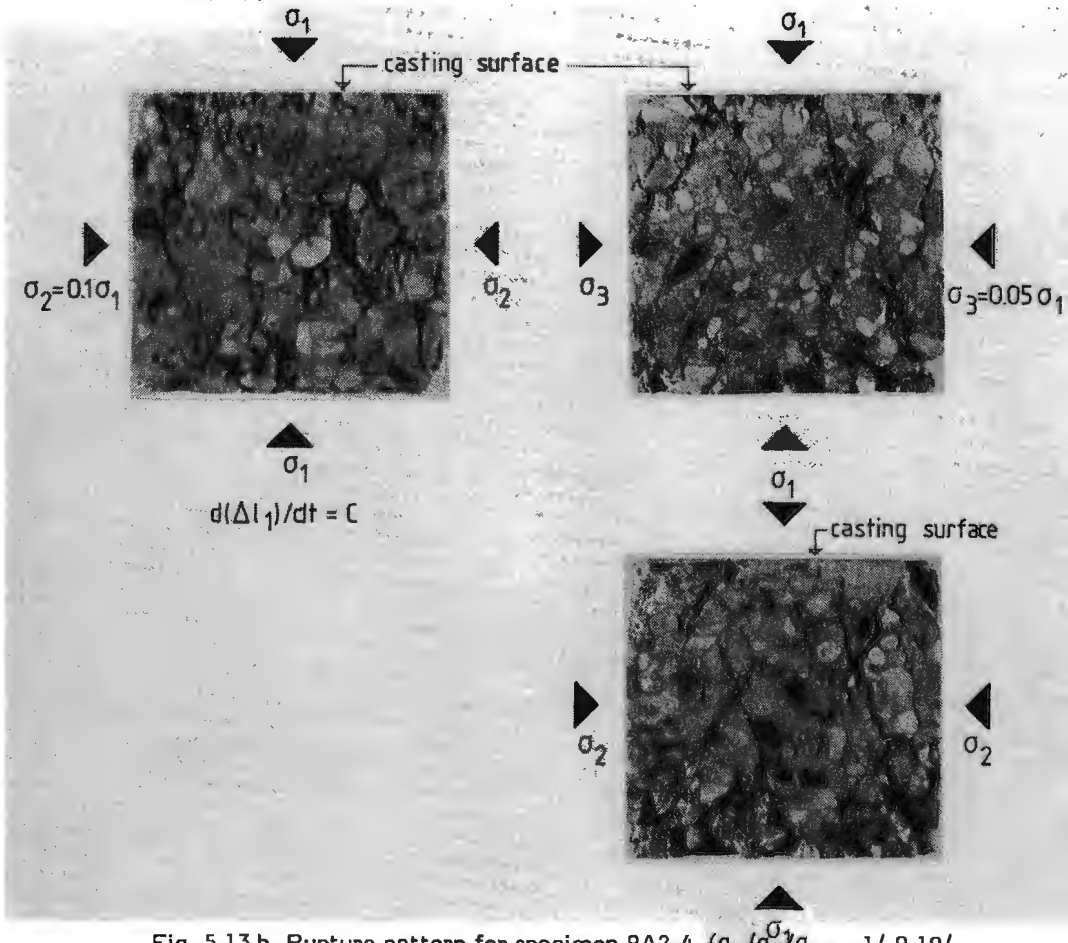

Fig. 5.13.b. Rupture pattern for specimen 9A2-4, ($\sigma_1/\sigma_2/\sigma_3$ = -1/-0.10/-0.05, M, parallel)

The distinct post-peak stress-strain behaviour for different levels of intermediate compressive stress is also expressed by the "final-structure" of a failed specimen. Where 8B2-4 displays a very localised shear-band, the other specimen 9A2-4 (shown in fig. 5.13.b) fails in a rather crumbly manner. A closer view of figure 5.13.b reveals that the crumbly structure is the result of mutual crossing shear-bands. All experiments, carried out under similar loading conditions displayed this type of failure. A cube (d = 100 mm) loaded in uniaxial compression also fails along these lines.
In this context it is perhaps preferable to use the term rupture, defined as the failure by which a structure disintegrates into two or more pieces (Bieniawski et.al. /16,17/). The ruptured specimens, shown in figure 5.13 and A5.6, form (in case of the localised shear-band mode) rigid jointed block systems. The joint (= shear-band) between the blocks seems rather weak, however in order to separate the blocks along the shear-planes, a considerable splitting force is required (the blocks cannot be separated by hand). From the photographs of the ruptured specimens, one could get the impression that the shear-planes have a rather large width. Yet it must be emphasized once more, that material (partly debonded aggregate particles or heavily cracked mortar pieces) is torn loose during the grinding process used for removal of the epoxy-resin layers.

The cubes loaded at the higher confinement level (σ_3 = 0.10 σ_1), also showed the shear-band rupture mode. In some of the experiments, for example 8A1-5 (stress-strain curves, fig. A5.27), it was not possible to measure the complete descending branch, due to the limitation set by the maximum allowable deformation of the brushes. In these cases, the onset of a shear-localisation is observed (see fig. A5.6.b), and the impression is that it is formed from initial parallel 'tensile-cracks'.In a more advanced stage of rupture, the effect is also visible for specimen 9B1-2 (fig. A5.6.c).

When the blocks are separated, loose material (small-sized granular material) is found in the joint. In fig. 5.14. a joint surface is shown after splitting of specimen 8B2-5 (stress-strain curves, see fig. A5.10.b). The major stress-strain curve (σ_1 - ε_1) was near the residual stress-level, and the shear-localisation may expected to be fully developed. It was found that very small sized grains, but also some larger elements are 'released' from the joint. Probably the larger rupture-elements are torn loose during the splitting action, and the small-sized fraction may have formed due to frictional sliding in the shear-band.
The total weight of the released particles was 4.9 grams. By sieving the material, the fraction smaller than 250 μm was determined: about 20% of the

total mass (0.9 gr.) was found to be smaller than 250 μm. This value is less than rigorous, also it was found that a considerable amount of dust remained at the joint-surfaces. The joint-surface showed rather large global curvatures. The fracture plane showed a schist-like structure. Also it was found that a large number of aggregate particles in the joint was fractured. It is however questionable if the aggregates are fractured during the formation of the shear-band in the stress-strain curve descending branch, or are merely the result of the splitting of the joint. A view of the surface rupture modes, reveals in fact very few fractured aggregates. (fig. 5.13.a and b). For specimen 8B2-4, but also for 9B1-2 (fig. A5.6.c), larger aggregate particles have a widening effect on the shear bands, and remain uncracked (The spots are indicated with an arrow). On the other hand highly fractured aggregate particles are also observed (see specimen 8B2-4), but this is probably the result of the splitting action of the separate brush-rods.

Fig. 5.14. Joint-surface for specimen 8B2-5.

From previous investigations by Stroeven /152/, and also by Vile /161/, it is known that 'cone-like' matrix-material deposits form on top of large aggregate particles as depicted in figure 5.15. The 'cone-like' rupture elements are formed when a shear-band develops through an array of initial parallel tensile micro-cracks. This tensile crack-array was visualised by Stroeven using the fluorescenting technique, and was shown in fig. 2.1.

A close observation of the surfaces of the ruptured specimens, reveals quite a number of these 'rupture-elements'. (see for example 9A2-4 and 9B1-2, resp. fig. 5.13.b and A5.6.c). It may be argued that these rupture-elements are important in the formation of macroscopic shear-bands.

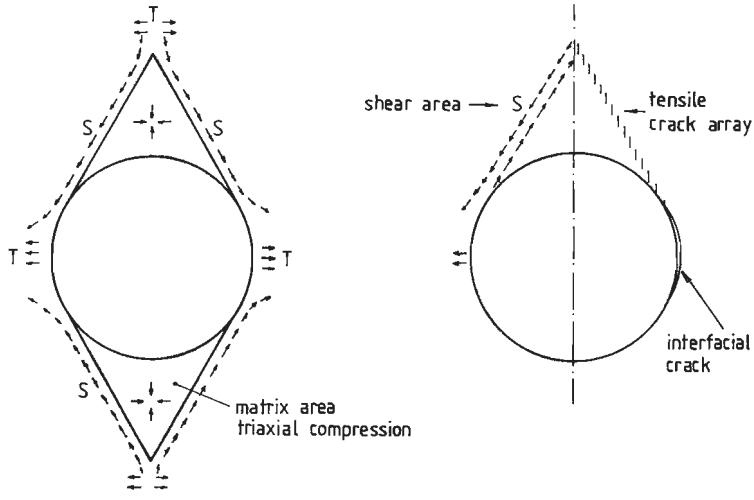

Fig. 5.15. Relevant stress-components for the formation of 'cone-like' matrix material deposits on top of large sized aggregate particles, after /152/.

The shear-band type of rupture is normally considered typical for geological materials such as rocks and soils (Bieniawski et.al. /16,17/, Sture & Ko /154/). The descending branch which is observed in uni- and triaxial compressive tests, must be merely attributed to the behaviour of a structure, which includes the loading machine. In view of the observed rupture modes in the present investigation, a similar conclusion must be drawn for concrete. The softening branch is the result of a stable 'strain-localisation' and future research should be concerned with the conditions at onset of the 'strain-localisation', but also with the boundary conditions (loading application system and loading frame), which assure a stable behaviour.

It was discussed by Bieniawski and co-workers that a stable descending branch is measured if the specimen/machine stiffness during unloading is larger than the slope of the descending branch of the stress-strain curve. Some stability models, taking into account the influence of the loading device, were already mentioned in section 2.3. Probably more complex boundary conditions are guarding the phenomenon.

In section 2.3, also the experiments carried out by Kotsovos /87/ were mentioned. The shear-stresses induced at the specimen-loading application system

interface were shown to have considerable influence on the slope of the descending branch of the uniaxial compressive stress-strain curve. In figure 5.16, the ruptured specimens from the investigation by Kotsovos are shown. From left to right, the failed cylinders using active restraint, plain steel platens, brush bearing platens, MGA-pad and rubber as a load application system are shown. The results were obtained for concrete with a uniaxial strength f'_c = 51 N/mm^2, which is very close to the uniaxial strength in the present investigation ($f'_{k=100}$ = 46.6 N/mm^2, for batch 8A-9B).

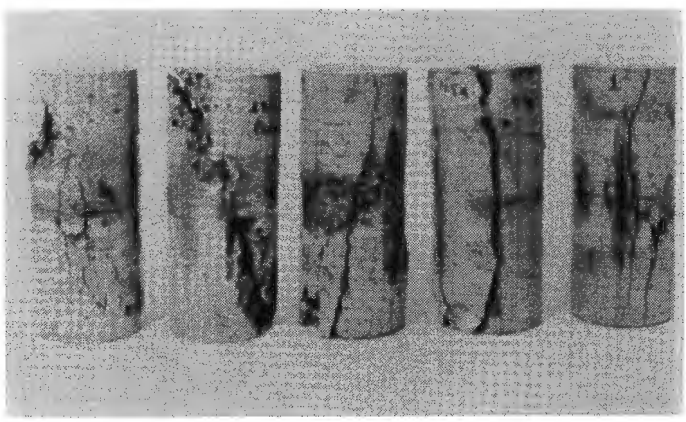

Fig. 5.16. Rupture modes of concrete cylinders, using different loading application systems, after /87/.

The rupture modes shown in fig. 5.16 resemble those reported for prisms (h = 200 mm) in section 4.3. The localised failure mode for concrete under uniaxial compression is evident.

From the figure it becomes clear that the orientation of the strain-localisation with respect to the major compressive direction occurs, when the frictional characteristics at the specimen boundary are changed. The strain-localisation is almost parallel with the loading direction when MGA-pads or rubber-layers are used. The stress-strain curves for these systems show a very steep descending branch as was shown in figure 2.13. In view of the normal strain-softening model (Bazant /5/), the thickness of the lumped softening zone approaches zero and also the critical tangent modulus will approach to zero, indicating a complete loss of load carrying capacity at peak-stress-level (equation 2.3).

It is obvious from the above discussion, that a refinement of the stability models that where mentioned in section 2.3 is necessary. Boundary shear is an important factor for obtaining a stable descending branch.

When brushes are used, the shear forces acting at the specimen surface may be

estimated by means of a simple calculation. In appendix A6 such an analysis is shown for uniaxial and triaxial loaded specimens. The boundary shear is nearly zero, and may be neglected in the pre-peak region. Beyond peak a sharp increase of boundary shear results from fast increasing deformations. The subject is considered very important, and future investigations are necessary.

- further observations and classification of failure modes -

The shear-bands in the multiaxial compression tests develop in planes formed by a large positive (tensile) deformation and a large compressive deformation. Therefore the normal on a shear-plane is always oriented perpendicular with regard to the intermediate compressive stress.
For a number of ruptured specimens, the average value of φ, i.e. the orientation of the shear-planes with respect to the major compressive direction is determined and shown in table 5.17. (Note: the average inclination of all shear-bands in a specimen is indicated).

specimen no.	loading-combination	φ (deg)
8B2-4	S -1/-0.33/-0.05, C, para	21
9A2-5	S -1/-0.33/-0.10, M, para	21.5
9B1-5	S -1/-0.33/-0.10, C, perp	25
9B1-2	S -1/-0.10/-0.05, C, perp	20
9A2-4	S -1/-0.10/-0.05, M, para	24.5
8B2-5	D -1/-0, S -1/-0.05, M, para	21.5
9B2-2	D -1/-0.33,S-1/-0.05, M, para	20
9B2-3	D -1/-0.10,S-1/-0.10, M, para	25

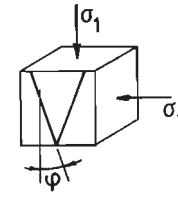

$\sigma_1 < \sigma_2 < \sigma_3$
triaxial compression

Table 5.17. Average value of φ, denoting the orientation of the shear-band with respect of the major compressive direction.

The shear-bands are not smooth, but show rather large local and global curvatures. The value of φ is always taken as the average inclination of the shear-band. For biaxial tests similar values were found, and are in agreement with the experiments by Kupfer /92/. He reported values of approximately 30 degrees for uniaxial compressive loading, and 18 - 27 degree for biaxial compression.

The concrete in between of the shear-bands is almost uncracked when the shear-localisation is observed in only one direction (specimen 8B2-4, fig. 5.12.a).

Deformation is confined to the joint and its immediate vicinity. Sliding in the shear-planes only is allowed when accompanying crushing occurs at the crossing of the shear-bands (fig. 5.18). The local crushing is also demonstrated in the photographs of the ruptured specimens: a highly fractured or granular mass is formed on top of the blocks (shear-cones = macroscopic rupture-elements, compare with fig. 5.15.).

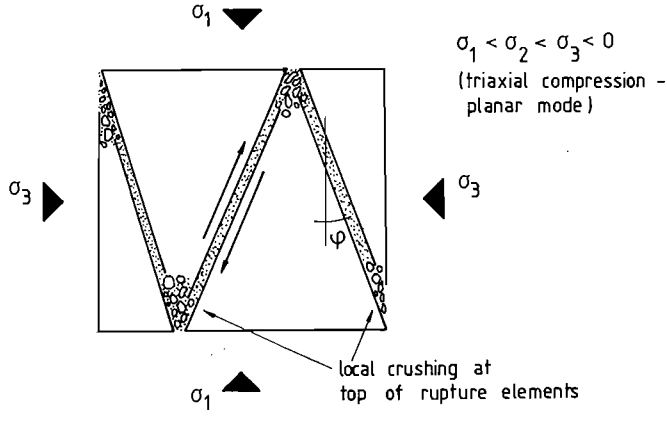

Fig. 5.18. Mechanism of shear-plane rupture.

In rock-mechanics frequently the assumption is made that unloading occurs in the 'uncracked blocks' between the joint /16,17,154/. The assumption is confirmed by a close examination of the behaviour of plane-strain tests.
The intermediate compressive stress σ_2 in these experiments is solely the result of a poisson-coupling with the two other compressed directions ($\sigma_2 = \nu(\sigma_1 + \sigma_3)$). The observed stress-strain behaviour was already shown in figure 5.10. As discussed before, the shear planes develop in the descending branch of the major compressive stress-strain curve ($\sigma_1 - \varepsilon_1$), the fact being consistent with observations from rock-mechanics (see fig. 2.15). The plane-strain test demonstrates a clear unloading in the intermediate stress-direction when a loss of load-carrying capacity is measured in the major compressive direction σ_1 (fig. 5.10).

In figure 5.19. the different observed rupture modes for different levels of intermediate stress are shown. The 'classification' is valid for all three levels of minor compressive stress that were investigated ($\sigma_3 = \beta\ \sigma_1$, β = 0, 0.05 and 0.10).

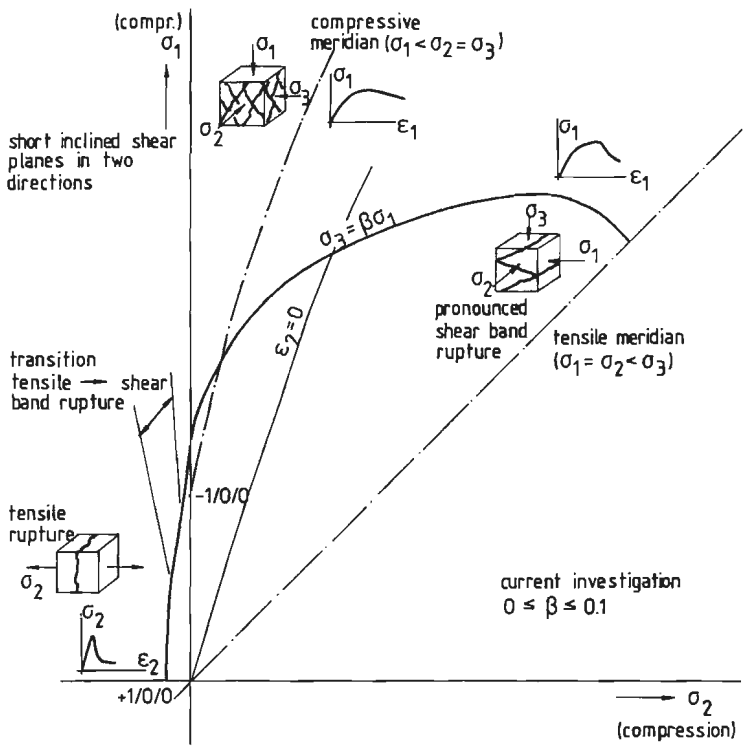

Fig. 5.19. Classification of rupture modes.

The two different types of rupture in the triaxial compression region were already demonstrated by fig. 5.13. The classification was already mentioned in a previous publication /104/.

A steep descending branch was observed for those experiments allowing for only one tensile deformation:

$$\Delta l_1 \leq \Delta l_2 \leq 0 < \Delta l_3 \qquad \text{.....(5.1.)}$$

The ruptured specimens showed very pronounced inclined shear-bands with the normal oriented perpendicular to the intermediate compressive direction.
A second typical rupture mode in the triaxial compressive region was observed when an experiment allowed for two large possitive (tensile) deformations:

$$\Delta l_1 < 0 < \Delta l_2 \leq \Delta l_3 \qquad \text{.....(5.2).}$$

The rupture mode, shown in figure 5.13.b. is representative for this type. The first type is referred to as planar mode, the second type allowing for two tensile deformations is defined as cylindrical mode.
The transition stage between the two distinct rupture modes is defined by a plane-strain test ($\varepsilon_2 = 0$). Of course not a sudden switch between rupture-modes will occur, the ratio between compressive and tensile deformations in the plane where a shear-band develops is considered important.
Palaniswamy and Shah /119/ reported different rupture modes at high confinement levels in standard triaxial compression tests using cylindrical specimens ($\sigma_1 < \sigma_2 = \sigma_3$). Under low confining pressure a significant internal microcracking and decrease of pulse velocity was observed, under high confining pressure very little micro-cracking and drop of pulse velocity occurred at failure. Yet the implications in the descending branch could not be measured with their stress controlled equipment. More recently, Jamet et.al. /79/, demonstrated an increasing ductility with increasing confinement in a series of triaxial compression tests ($\sigma_1 < \sigma_2 = \sigma_3$) on micro-concrete cylinders. These observations are in agreement with experiments on rock /16,17,75/.

A decreasing softening slope with increasing confinement was also observed in the current investigation for loading combinations along the compressive meridian (i.e. cylindrical rupture mode, compare for example stress-ratio tests -1/-0.1/-0.1 with results reported in chapter 7, fig. 7.13, and with uniaxial compression tests).
The planar mode experiments did not show a decreasing softening slope with increasing minor compressive stress (that is, for the confinement levels investigated, see fig. 5.10).

- failure in tension-biaxial compression -

The experiments, loaded along a t/c/c stress-ratio path displayed a single tensile crack, perpendicular to the tensile stress direction at failure. The tensile fracture energy in these experiments was approximately equal to the energy requirement in uniaxial tension (see section 5.2.3).
Probably for low values of σ_3 (as in the current investigation), comparison of the t/c/c tests with biaxial tension-compression experiments is allowed. Isenberg /78/observed a transition from cleavage (tensile) failure to compressive failure (which he referred to as crushing) near a stress-ratio $\sigma_1/\sigma_2 = 17$ (with σ_1 compressive and σ_2 tensile) in a number of torsion-compression tests on concrete

cylinders. In this context the agreement between the t/c/c experiments and the uniaxial tensile tests is no surprise.

In the t/c/c displacement ratio tests, it is quite likely that the failure-locus is followed. The appearance of a single tensile crack has apparently no effect on a second triaxial compressive failure (see section 5.2.2). In fact these displacement-ratio paths provide for a gradual 90^{o} rotation of principal stresses. Some abrupt rotation test results will be presented in chapter 7.
One last comment should be made regarding failure in t/c/c stress-ratio experiments. A similar analysis as was shown in appendix A6 for triaxial compression is required for estimating the boundary shear, and its effect on crack-opening.
Such an analysis was not carried out, but the effect should certainly be checked for future investigations.

- volume change -

In figure 5.20 the volumetric strain $\varepsilon_v = \varepsilon_1 + \varepsilon_2 + \varepsilon_3$ is plotted against the major compressive strain ε_1 for six constant stress-ratio experiments. In fig. 5.20.a three experiments with $\sigma_3 = 0.05\ \sigma_1$ are shown, in figure b the samples loaded at the higher confinement level $\sigma_3 = 0.10\ \sigma_1$. When a specimen was loaded according the cyclic path (to the envelope), only the envelope curve is drawn. The six samples were all loaded parallel with regard to the direction of casting.
At initiation the experiments show compaction. The complete relationship between volumetric strain and major principal strain is non-linear, and no such boundary as onset of micro-crack propagation /112,85/ is detected. The graphs suggest a continuous damage process under triaxial compressive loading, as was concluded by Spooner et.al. /148/ for uniaxial compression.
With increasing compressive strain ε_1, a decreasing rate of compaction was measured, and a minimum volume was observed in most triaxial compressive experiments just before the peak stress-level ($\sigma_{1,max}$ marked with an asterisk in figure 5.20) is reached. Beyond peak a sharp increase of volume was measured, the rate of volume-increase being higher for the lower confined specimens (with a limit for uniaxial and biaxial compression). The different rupture modes for various levels of intermediate compressive stress σ_2, as were reported in the previous section are expressed by different volumetric strain-axial strain (ε_1) curves too.
For the planar rupture modes (which appears most frequently), the minimum

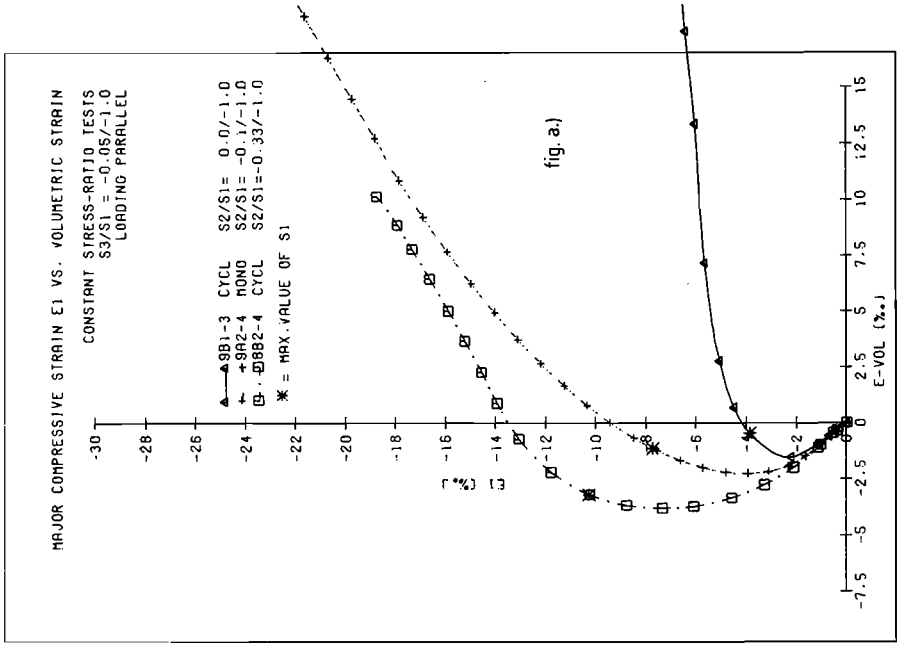

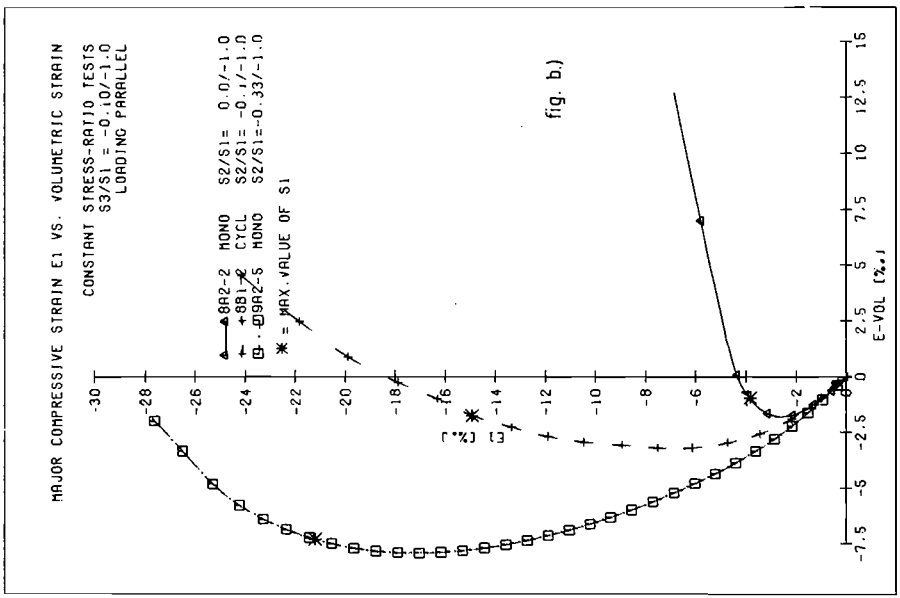

Fig. 5.20 a. Volumetric strain vs. axial strain ε_1, constant stress-ratio experiments, $\sigma_3 = 0.05\ \sigma_1$, loading parallel.

b. Idem, $\sigma_3 = 0.10\ \sigma_1$.

volume was reached at values of η_ε = (ε_1 at $\varepsilon_{v,min}$) / (ε_1 at $\sigma_{1,peak}$) varying between 0.7 and 0.8. In the cylindrical case (crushing-mode) this value was about 0.5 - 0.6. The average value of $\bar{\eta}_\varepsilon$ for the eight accompanying uniaxial compressive tests was $\eta_{\varepsilon\ ,uniaxial}$ = 0.70 (coef. of variation = 5.7 %). In general a faster increase of volumetric strain beyond peak is observed for those tests failing in a planar mode.

As was shown in the previous section, specimens loaded in triaxial compression (in terms of stress) may either fail along a pronounced shear-plane or by forming a multitude of short inclined shear-planes in several directions. The occurence of the large volume-increase that is observed beyond peak stress-level (σ_1) is no surprise in view of these rupture modes (fig. 5.13. a - b). Sliding over asperities in the shear-planes results in a dilatant uplift.
Void formation becomes significant when the macroscopic shear-planes are formed.

In the pre-peak region when only micro-defects are present, the effect of void-formation however also appeared. The curvature in the pre-peak region of the ε_v - ε_1 graphs (fig. 5.20 and A5.34 - A5.36), leading to a minimum volume, suggests void-formation.

In figure 5.14. the rather rough surface of a shear-plane was shown. It was also mentioned that loose material was found in the joint. The question is where this small-sized granular material remains during sliding (under the assumption that the grains are formed during the rupture process, and are not the result of the splitting action induced to the specimen at termination of the experiment in order to separate the blocks). Either the grains are distributed more or less uniformly over the contact surfaces or they are gathered in larger air-voids (pores). Also possible is that the grains accumulate at specific sites before or beyond macroscopic asperities (such as global curvatures in the matrix material or larger aggregates). Some possibilities are depicted in figure 5.21.

The answer to this problem is crucial in arriving at a proper model for the sliding mechanism. The volumetric strain - axial strain (ε_1) curves shown in fig. 5.20 and A5.34 - A5.36, indicate that the granular material in the shear-joint has some influence. For the triaxial loaded specimens, that display a clear shear-plane rupture (planar-mode), an upward directed curvature is observed near the end of the ε_v - ε_1 curve. This phenomenon is for example very clear for specimen 8B2-4 (fig. 5.20.a) and 8B2-3 (fig. A5.35.b). The upward directed curvature is

probably the result of a second compaction phase when the shear-planes are completely formed (that is at the residual stress-level in the $\sigma_1 - \varepsilon_1$ curve).

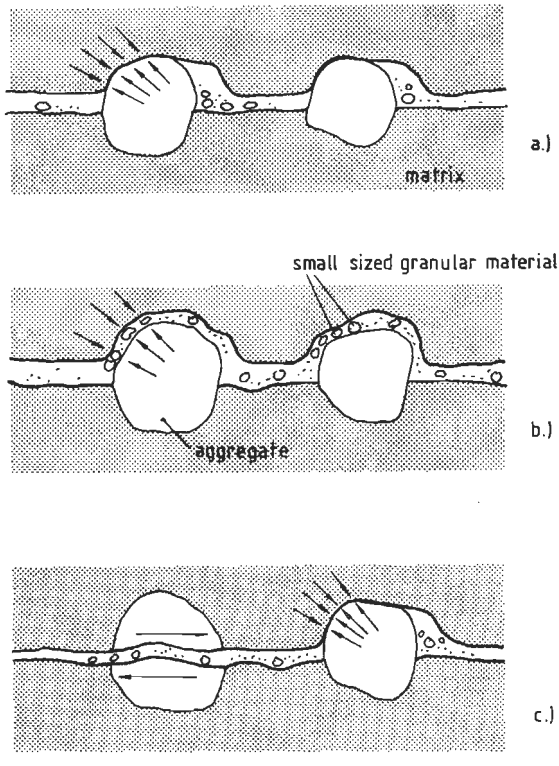

Fig. 5.21. Sliding over asperities in macroscopic shear-planes.

The granular material in the shear localisation is probably responsible, while it may compact under shear-loading. (compare with the behaviour of granular materials such as soils).

In several constitutive models, for example /28/ the term 'shear-compaction dilatancy' is used. This terminology refers to volumetric compaction under (deviatoric) shear loading, and may be measured when specific hydrostatic-deviatoric loading-paths are used. Recently the effect has been demonstrated in the pre-peak region /135/. The physical meaning is however not very clear, and the effect should not be confused with the above mentioned compactions (or rather decrease of volumetric strain) once the shear-plane is formed.

The localised rupture modes, forming inclined shear-planes, and the sliding which occurs in these highly deformable zones might suggest that recently developed 'aggregate interlocking' theories /162/ apply for this class of problems. It should be emphasized that these models only work when the shear-plane is completely developed, and assume that no granular material is present in the joint. While in our tests fractured aggregates and loose material were observed (for a medium strength concrete mix) it is necessary to do some further testing on low strength concrete, before such an attempt is undertaken. It is likely that the granular material is in conflict with assumptions made in these theories.

5.2.5. Initial anisotropy.

Closely related to the effects of stress and strain induced anisotropy is the influence of damage sustained during casting and hardening of the specimens. In section 4.2, the effect was shown to have significant influence on the energy-requirement of specimens loaded in uniaxial compression. An increase of energy-requirement of approximately 10% was measured when a specimen was loaded parallel rather than perpendicular with regard to the direction of casting (see fig. 4.6). Similar effects, however now more pronounced, are measured when triaxia

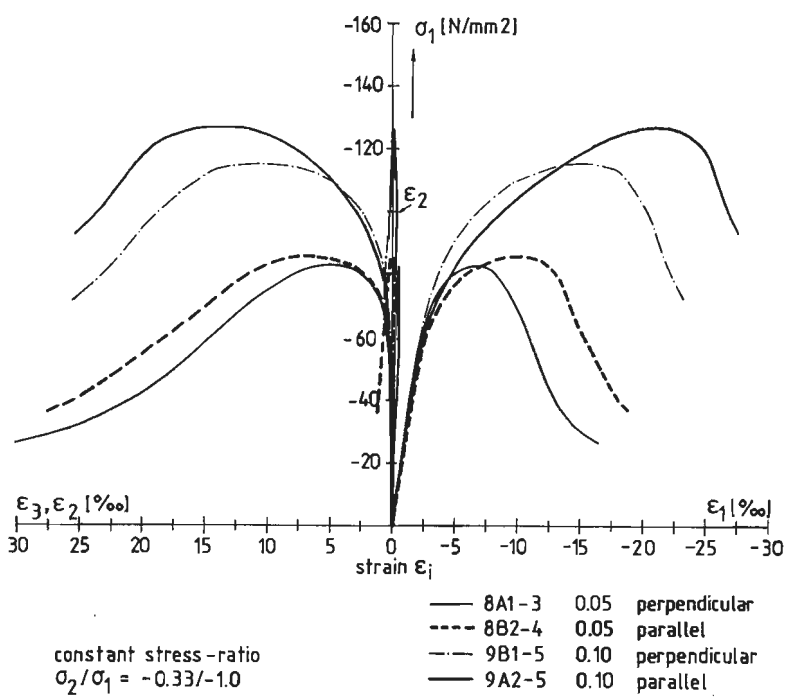

Fig. 5.22. Influence of initial anisotropy on triaxial stress-strain behaviour.

compressive loading is applied. In figure 5.22 the stress-strain curves for specimens 8A1-3 and 8B2-4, loaded according a constant stress-ratio $\sigma_1/\sigma_2/\sigma_3$ = -1/-0.33/-0.05 and the specimens 9B1-5 and 9A2-5, both loaded according the proportional stress-path -1/-0.33/-0.10 are shown. From each pair of specimens, one cube was loaded parallel, the other was loaded perpendicular with regard to the direction of casting (see also section 5.1).

Identical conclusions as for the uniaxial loaded samples can be drawn. The pre-peak stress-strain response is considerably affected by the orientation of the initial damage field with regard to the governing stress-state. The same effect is observed for all pairs of specimens, including those loaded by a constant displacement-ratio. Only the tension-compression deformation-ratio experiments showed a different response. The effects of initial anisotropy were less pronounced due to the slight differences in orientation (see section 5.1).

The statistical analysis of the strength results of the triaxial series showed no significant effect due to the orientation of the loading with regard to the initial damage field. There is an indication however that for higher confinement levels a slight increase of strength occurs, when loading is applied parallel rather than perpendicular. Yet more experiments at higher confinement levels are necessary to quantify the effect.

The effects of initial anisotropy are clearly demonstrated by the energy-curves shown in figure 5.23. For the proportional stress-path tests at the higher-confinement level, the energy-requirement was determined and plotted against the major compressive strain ε_1. The energy-curves are shown for three levels of intermediate stress: σ_2/σ_1 = 0, 0.1 and 0.33. Both curves for parallel and perpendicular loading are shown.

Comparison of the perpendicular loaded specimens response with the parallel loaded cubes reveals a delayed increase of energy for the parallel loaded specimens. The ultimate level of energy-requirement of the parallel loaded samples is for all cases higher and the difference increases with increasing level of intermediate stress. (Note: this is not very clear from the meassured relationships, but these can probably be extrapolated as indicated in fig. 5.23).

The experiments that fail in the cylindrical mode show a delayed energy-requirement when compared with samples failing in the planar mode (compare the experiments σ_2/σ_1 = -0.1/-1.0 and those with σ_2/σ_1 = -0.33/-1.0). The effect only displays the difference in descending branch response (section 5.2.4).

By changing the direction of the initial damage field with respect to the applied triaxial loading, an increasing ductility is observed for parallel loading. The

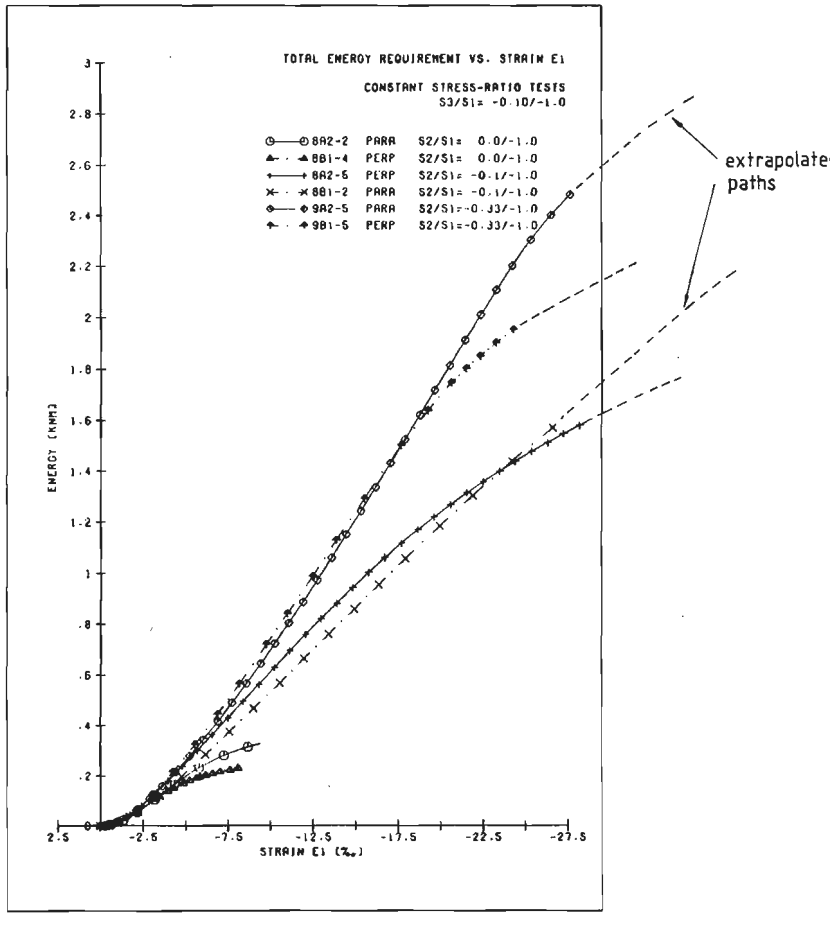

Fig. 5.23. Total energy requirement vs. major compressive strain ε_1, for constant stress-ratio tests, $\sigma_3 = 0.10\ \sigma_1$.

increased ductility is responsible for a significant increase of strain at peak-stress-level.

The effect is considered to be dependent on compaction and hardening conditions of the concrete when casted. The uncertainity of these conditions will bring about difficulties in quantifying the effect. Further research, using concrete mixtures with different strength and deformational behaviour is necessary.

5.2.6. Behaviour of concrete under multiaxial cyclic loading.

A constitutive model describes in fact the changes at the micro-structural level (or macro-level in the post-peak region) of a material subjected to external

loading conditions.
The rupture modes shown in section 5.2.4 shed some light on the governing phenomena. Yet the history of damage accumulation for example under monotonic increasing load, is highly complex and a proper evaluation of the phenomena leading to rupture is probably only possible when a criterion for crack-propagation, interaction and joining is established.
The quantitative analysis of the damage sustained to a concrete specimen, subjected to multiaxial loading, is a complicated matter. In uniaxial compression experiments, damage accumulation is described by a sequence of non-recoverable deformation /81,99/, or by separating the dissipated energy in various components by means of a well chosen loading history /148/. Yet the analysis performed are confined to the axial loading direction only, and generally no attention is given to implications for lateral displacements. The damage-function is a complicated three dimensional structure, and can (likely) not be modelled by a simple one-dimensional function.

The cyclic tests with load-cycles to the envelope, which were previously used in uniaxial compression tests /81,99,148,145/, biaxial compression tests /12,23,24/and in uniaxial tension /129/ may be helpfull in determining the complex damage-surface.
Theories based on the 'damage-function' of the material have recently been suggested /41/, however experimental background still is lacking or as recently formulated by Dougill /42/: "As yet the quantitative analysis of energy dissipation has not been extended to other stress-states (except for uniaxial compression) it would be informative to do so and in particular to observe how the quantities W_γ (damage energy dissipation) and W_δ (damping energy dissipation) are influenced by the mean normal stress. It might be supposed that, at a given strain, W_γ would be decreased and W_δ increased by an increase in the volumetric component of applied loading" (see also section 2.2).

The experimental design (table 5.4) included a limited number of multiaxial cyclic experiments. Load cycles with variable amplitude (in terms of stress: "to the envelope", in the direction decisive for fracture), were applied using the same static loadingspeed as for the monotonic tests ($\dot{\varepsilon}_1 = 20.10^{-6}$/sec).
A proper constitutive model should include the unloading and reloading characteristics of the material. The experimental results reported in this section may be helpfull in studying these aspects. To my knowledge no other cyclic triaxial experimental results, including post-peak behaviour have been published before.

It is emphasized that the results reported herein should be considered as a first attempt to unravel the complicated deformational behaviour of concrete under multiaxial load-histories. Many improvements are still needed.
While the number of experiments is very limited (16 cyclic experiments), only some general observed trends are discussed.

- description of experiments -

The conditions for loading and unloading were already mentioned in section 5.1. The stress-strain curve in the major compressive direction was guiding, except in the tensile-biaxial compressive stress-ratio experiments, for which the tensile stress-strain curve was decisive for rupture. The discussion following below is mostly concerned with those experiments that fail in the triaxial compression region.
The stress- and displacement-ratio experiments respond slightly different to load-cycling. In the case of a proportional stress-path experiment, the sample is loaded in the major compressive direction (or tensile direction in case of a tension-biaxial compression test) by means of a constant displacement rate $d(\Delta l_1)/dt$ = constant. The increment of Δl_1 leads to a non-proportional increase of σ_1: $\Delta\sigma_1 < 0$ (compression). Due to the proportional coupling of σ_2 and σ_3 with σ_1, this results in: $\Delta\sigma_2 = \alpha\ \Delta\sigma_1 < 0$ and $\Delta\sigma_3 = \beta\ \Delta\sigma_1 < 0$.
Unloading occurs simply by an instantaneous change of the polarity of the displacement increment and results in a simultaneous (stress-) unloading in the three principal directions. Reloading is initiated as soon as the zero-stress-level is reached. This zero-stress-level is reached at the same moment in the three principal directions.
Damage (formation of micro-cracks and frictional energy dissipation in the pre-peak region, and shear-band formation and frictional sliding in the post-peak region) results in non-recoverable deformations Δl_i (i = 1, 2, 3). The behaviour of a cyclic stress-ratio test is depicted in figure 5.24.a.
The response of a cyclic displacement-ratio experiment is somewhat different (fig. 5.24.b). Loading is done by maintaining a constant ratio between two displacements ($\Delta l_2 = \alpha\, \Delta l_1$) and a constant stress-ratio between the major and minor compressive direction ($\sigma_3 = \beta\, \sigma_1$). The displacement rate is constant:
$d(\Delta l_1) / dt = C$, implying $d(\Delta l_2) / dt = \alpha.C$. Unloading is done by an immediate reversal of the displacement increment (simultaneously in direction 1 and 2).
This measure results in nonrecoverable deformations in the three principal directions at zero stress-level (σ_1 and σ_3), and additionally a non-recoverable stress in the direction loaded by a displacement coupling.

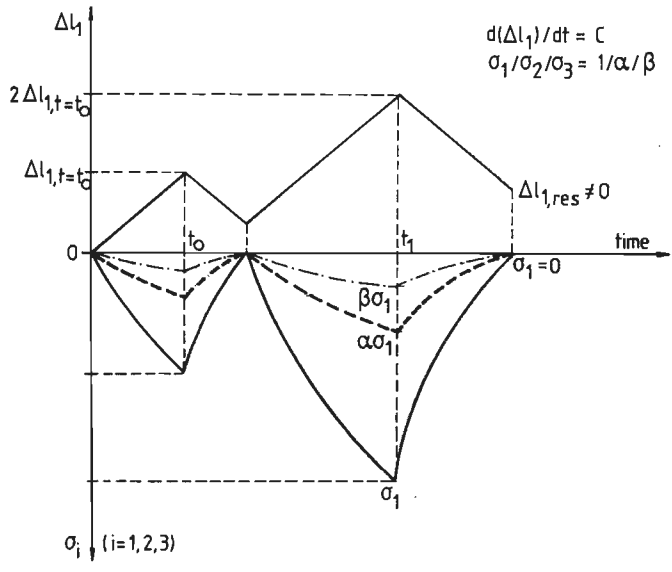

Fig. 5.24.a. Response of a cyclic triaxial stress-ratio experiment.

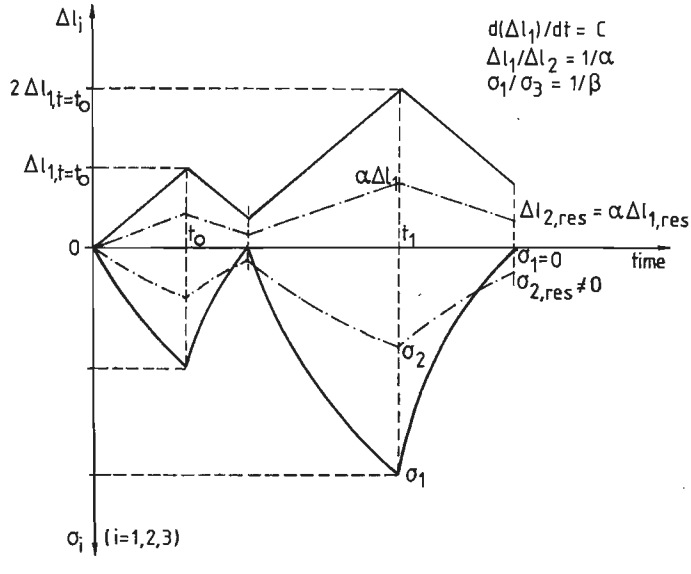

Fig. 5.24.b. Response of a cyclic triaxial displacement-ratio experiment.

Thus load-cycling in the intermediate stressed direction, loaded through a deformation coupling with the major compressive direction (σ_1, Δl_1), results in a variable stress-amplitude (σ_2) between two compressive envelope curves.

The stress-strain curves for the cyclic experiments are gathered in appendix A5 (figure A5.14 - A5.27). In case of a stress-ratio experiment, the strains ε_i (i = 1, 2, 3) are plotted against the major compressive stress in three separate figures (a, b and c).
Also shown are the strain paths ε_1 - ε_2 and ε_1 - ε_3 for each test (figure d). In case of a displacement-ratio experiment similar graphs are shown: σ_1 -ε_1, σ_2 - ε_1 and σ_1 - ε_3, completed with the strain paths (ε_1 - ε_2, ε_1 -ε_3).
The two cyclic biaxial (stress-ratio) experiments 9B1-3 and 8B1-4, allowed for comparison of surface deformation measurement and overall (LVDT) measurement. Surface strains were measured with two 60 mm strain gauges mounted at the upper and lower surfaces of the specimen (see fig. 3.10). In fig. A5.14.c and A5.17.c, both ε_1 (surf) and ε_2 (surf) are the average value of the two strain gauges mounted in the concerning loading direction.

No appreciable effect on stress-strain behaviour was found when either loading was applied monotonic or cyclic to the envelope curve (i.e. when the monotonic curve and envelope curve are compared). The observation is consistent with previous uniaxial investigations by Spooner et.al. /148/ (uniaxial compression) and Reinhardt and Cornelissen /129/ (for uniaxial tension). Yet it should be emphasized that the total number of triaxial cyclic experiments is very limited. More experiments are necessary in order to arrive at statistically secured conclusions.

- deformation measurements for biaxial cyclic tests -

From the biaxial cyclic experiments (9B1-3 and 8B1-4) a different response of surface and overall deformation measurement was observed. The surface measurements are confined to the pre-peak region only while rupture of the specimen (post-peak branch) was accompanied with splitting of the outer concrete layers (see also chapter 4).
In figure 5.25 a comparison is made between the pre-peak load-cycles obtained from surface-strain measurement and overall (LVDT) measurement for specimen 9B1-3 ($\sigma_1/\sigma_2/\sigma_3$ = -1/-0.05/0, C, parallel). In the right part of the figure, ε_1 is plotted, in the left part ε_2. It should be mentioned that the ε_2-surface measurement remained intact until the 8th reloading curve (ε_2 is indicated in the left part, only the first two cycles are not indicated while they coincide with the third cycle). This is no surprise, while shear-bands are formed in the σ_1 -σ_3 plane, while the intermediate stressed direction remains almost undesturbed (see section 5.2.4).

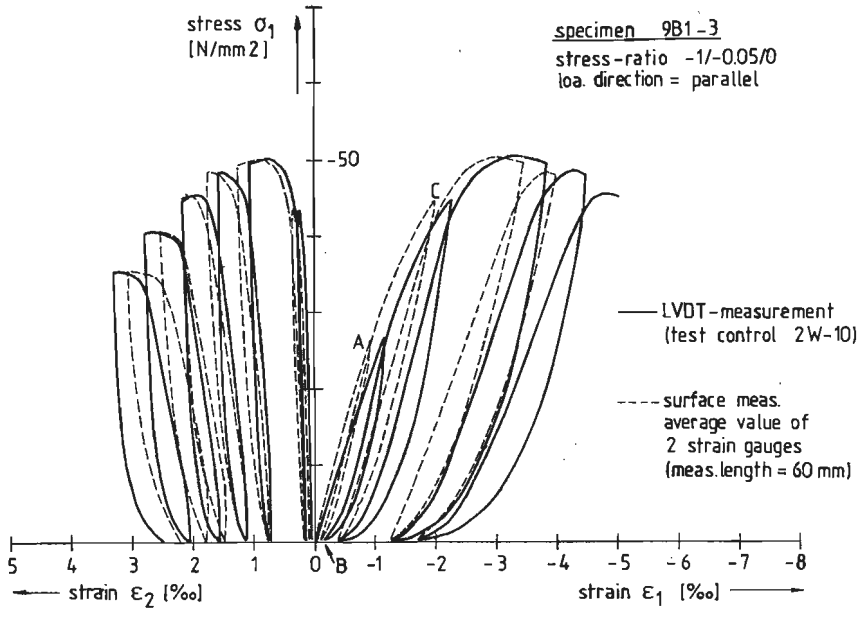

Fig. 5.25. Differences in deformational response (surface and overall strain measurement) for specimen 9B1-3.

In the major compressive direction (σ_1 - ε_1), a distinct behaviour of surface and loading platen measurement is observed for near-zero stress-levels in the unloading and reloading curves, appart from the deviations in absolute strain value (ε_1 (surf) - ε_1 (loa.pl.), as was reported in chapter 4).

The first loading branch (O-A), has undergone a zero-correction following the method described in section 3.2. At point A, the displacement-increment is reversed, and both curves (surface and loading-platen measurement) show a fast stress-unloading. With decreasing ε_1, the stress-unloading decreases, and both curves approach the 'strain-axis' very gradual. It is noted that the approach of the loading-platen curve is more gradual. Upon reloading (B-C), the loading platen curve initially follows the unloading curve (A-B), but soon the stress-rate will increase, resulting in a steep ascending reloading curve.

On the other hand the surface measurement shows a fast increasing stress, directly after the reloading point B.

Comparison of the σ_1 - ε_2 curves reveals that the effects are less pronounced in the intermediate stressed direction.

The results (σ_1 - ε_1 curves) suggest that still some kind of contact-effect disturbes the deformation measurement by means of LVDTs between the loading platens. Yet in the triaxial experiments this is the only (more or less) reliable

deformation measuring method. Neither the surface measurement nor the loading platen measurement will lead to correct strain values for these small-sized specimens (see also chapter 4). The truth will be somewhere in between.
From uni- and biaxial cyclic experiments, the differences of measuring method on observed stress-strain behaviour can also be detected from previous investigations (Karsan & Jirsa, uniaxial compression, surface measurement, /81/, and Spooner & Dougill, 1D-compression, loading platen measurement /148/).

- tangential stiffness in the major compressive direction -

In figure 5.26, the tangential stiffness $E_{tan,\,1} = \delta\sigma_1/\delta\varepsilon_1$ is shown for the first four loading-curves of specimen 9B1-3, both obtained from surface measurement and loading platen measurement. The tangential modulus is plotted against the major compressive strain ε_1.
The initial stiffness (1st loading curve) is slightly higher for the values obtained by surface measurement. The second loading curve shows an increasing stiffness, which is at about the same level for both surface and loading-platen measurement.

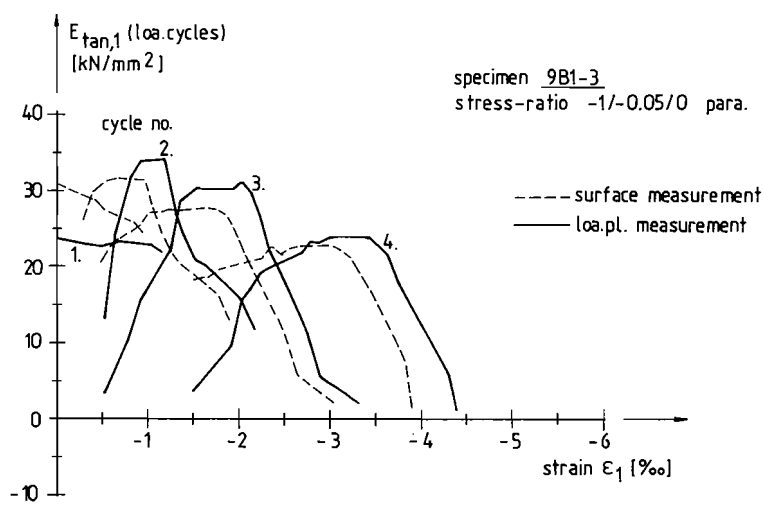

Fig. 5.26. Tangential modulus for loading curves (no. 1-4), specimen 9B1-3 ($\sigma_1/\sigma_2/\sigma_3$ = -1/-0.05/0, C, parallel).

The increasing stiffness after the first loading cycle must be attributed to an initial compaction or consolidation within the specimen. Similar effects have been observed by others in uni- and biaxial cyclic compression tests on mortar and concrete too /99,23/.

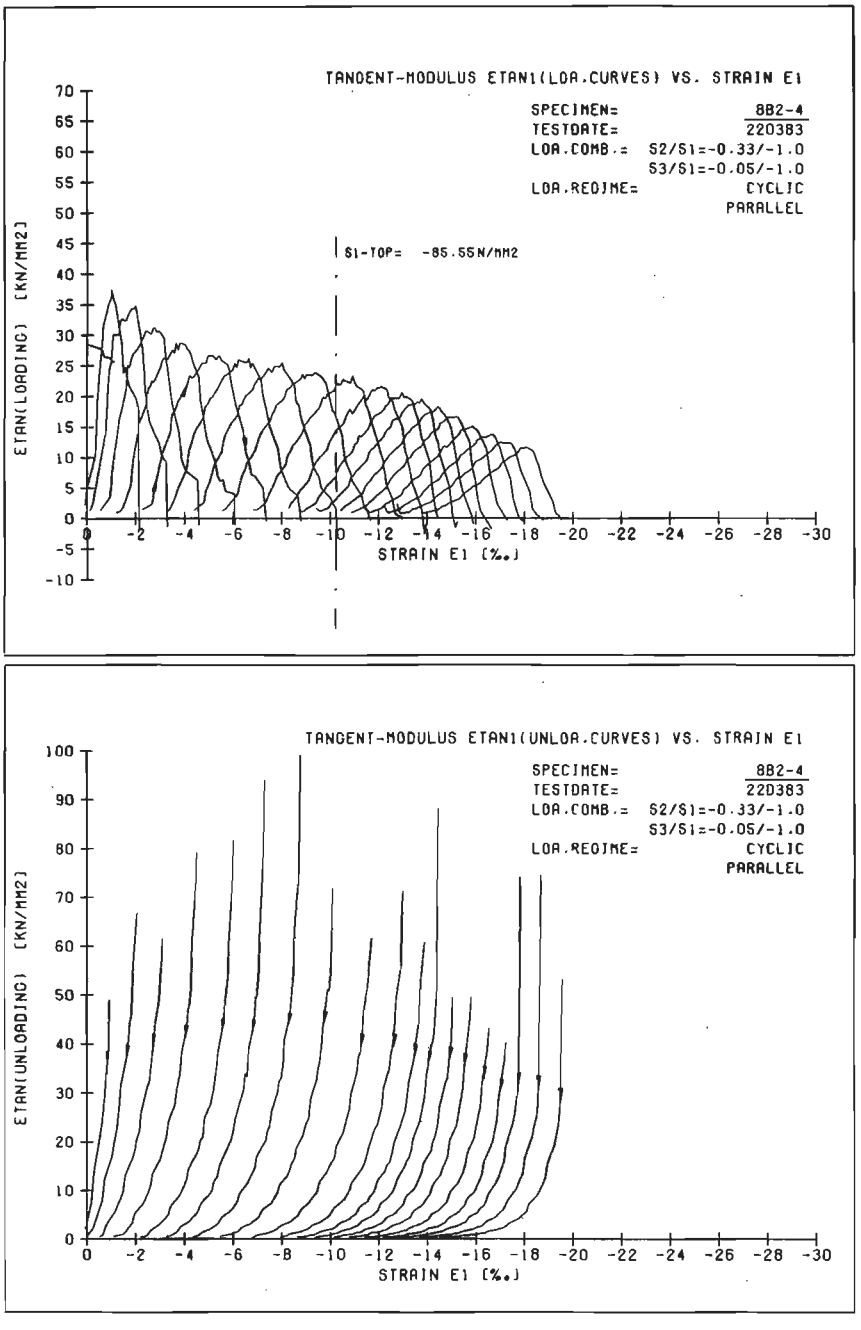

Fig. 5.27.a-b Unloading (fig. a) and reloading (fig. b) stiffness for subsequent cycles, specimen 8B2-4 ($\sigma_1/\sigma_2/\sigma_3$ = -1/-0.33/-0.05).

The following loading curves show a decreasing maximum tangential modulus. From fig. 5.26 it is obvious that the maximum stiffness is approximately equal

for surface and overall deformation measurement. The 'strain-history' before reaching the maximum value of $E_{tan,1}$ is however very different and the strain-value for which $E_{tan,1,max}$ is reached is higher in case of loading platen measurement.

The loading and unloading stiffness of the 'specimen-machine' system is determined for all cyclic experiments that fail in the triaxial compressive region. In figure 5.27 a typical example is shown (specimen 8B2-4, $\sigma_1/\sigma_2/\sigma_3$ = -1/-0.33/-0.05, C, parallel).
In the upper graph, a plot of the loading modulus against the major compressive principal strain ε_1 is shown. An increase of approximately 30% of $E_{tan,1}$ with respect to the first loading stiffness is measured in the second cycle. In the subsequent cycles a further decrease of stiffness (that is maximum stiffness for each load cycle) is observed. A fast decrease is observed after the second cycle, and again when the stress-strain curve (σ_1 - ε_1) describes a descending branch.

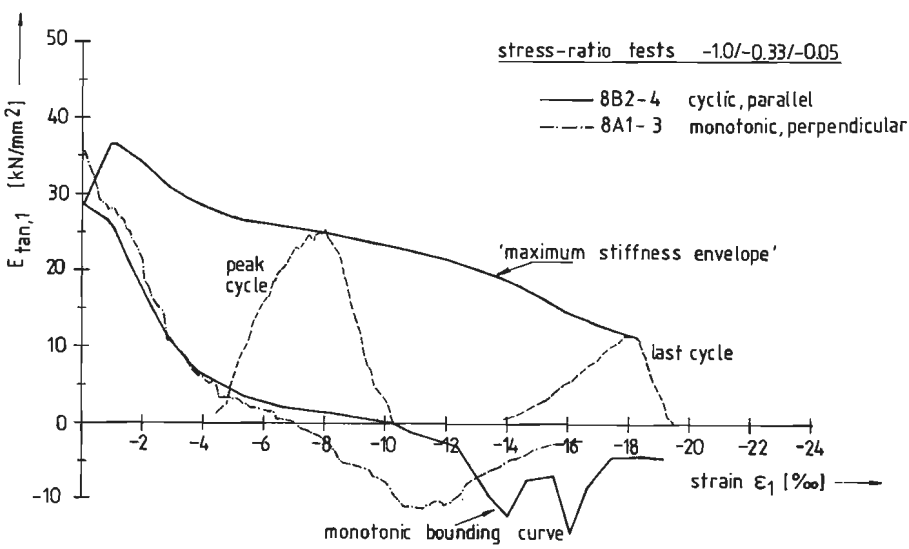

Fig. 5.28. Bounding curves for tangential stiffness (specimens 8B2-4 and 8A1-3, $\sigma_1/\sigma_2/\sigma_3$ = -1/-0.33/-0.05).

The stiffness reduction is considerable less than was expected from a monotonically loaded specimen. The effect is demonstrated in fig. 5.28, where the maximum stiffness of each load cycle is gathered in an upper envelope stiffness curve, and also the monotonic bounding curve is shown. The monotonic curve is calculated from the envelope stress-strain curve σ_1 - ε_1.

The tangential modulus becomes eventually negative (in the descending branch of the stress-strain curve) when the monotonic curve is considered. Yet the cyclic 'maximum-stiffness' bounding curve indicates that the stiffness decrease is considerably less and in fact never becomes negative. In the peak cycle, i.e. the loading cycle preceding to the peak stress σ_1, a stiffness decrease of 30% is observed with respect to the maximum stiffness measured in cycle 2. At test-termination, the maximum tangential stiffness is approximately 50% of the stiffness measured in the peak-cycle. At termination, the residual stress-level is just being reached, and if the similarities with uniaxial compression tests exists, a further, but now more slow decrease of stiffness may be expected.

The family of 'loading-stiffness' curves, shown in fig. 5.27, shows an increase of strain-range before the maximum stiffness is reached. The difference becomes very clear from comparison of the pre-peak and post-peak cycles. The long run before maximum $E_{tan,1(loa.)}$ in the post-peak range suggest that 'contact-effects' within the specimen become more important. In view of the reported failure (rupture) modes in section 5.2.4. this is no surprise.

The upper and lower tangential stiffness bounds are shown in appendix A5, fig. A5.35- A5.40 for all triaxial cyclic compressive experiments. Additionally in fig. A5.41 the stiffness results obtained from five uniaxial compressive experiments (2B2-2 through 2B2-6) are given. These latter tests were used in a micro-crack study by means of the fluorescenting technique, and were in fact subjected to cyclic loading sequence to the envelope stress-strain curve (σ_1 - ε_1 curves, see fig. A1.7).
Unloading in the uniaxial experiments was done to a lower stress-level σ_1 = -5N/mm^2, and not to zero-stress as was done in the triaxial experiments. This means that the increasing contact effect at low stress-levels in the subsequent reloading curves is almost entirely eliminated. While in general the maximum stiffness was reached at higher stress-levels, as shown in figure 5.29 for specimen 8A2-4 (plane strain, σ_3 = 0.05 σ_1), comparison of the uni-and triaxial results is allowed.

Spooner et.al. /148/ demonstrated that the initial modulus of elasticity is a sensitive measure for damage accumulation in concrete under uniaxial compression. Similar results were recently also reported for mortar by Maher & Darwin /99/. Yet the term 'damage' remains vague, and mostly all kinds of effects are included (cracking, frictional effects, voids (pores), etc.). In the uniaxial experiments by Spooner and Maher, the initial tangential or secans modulus at a

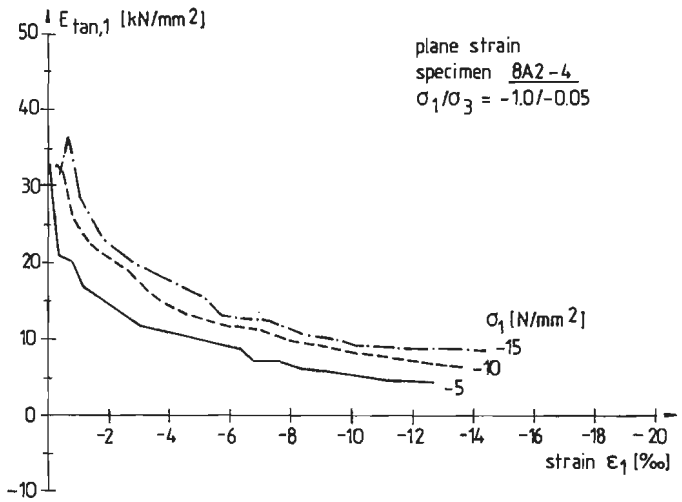

Fig. 5.29. Tangential stiffness decrease for constant levels of major compressive stress for specimen 8A2-4 (loading curves).

constant (low) stress level (about 5 N/mm^2) was determined for the subsequent reloading cycles and plotted against the compressive axial strain. However it is not sufficient to define damage at one stress-level, and a more complete description of the acting mechanism is necessary. The upper tangential stiffness envelope suggests that the 'true-stiffness' of the material (whatever that is) is considerably higher.

- mechanism of unloading and reloading -

It was mentioned before that the decreasing stiffness of the subsequent loading cycles, and the increasing run in the reloading curves (at higher deformation levels) before arriving at the maximum attainable tangential stiffness (fig. 5..27) in the concerning load-cycle, is the result of increased "contact-effects" within the specimen. In fig. 5.30 an attempt is made to clarify the governing phenomena.

In case of a planar rupture mode (pronounced shear-band), the influence of the intermediate compressive direction on sliding mechanisms is negligible. Large deformations occur in the plane formed by the major and minor compressive

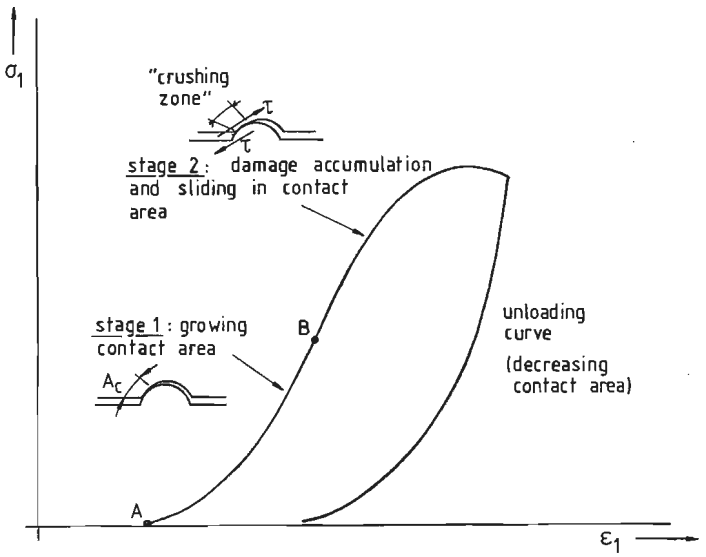

Fig. 5.30. Mechanism of reloading and unloading.

stress. In the post-peak region the behaviour of the localised deformation zones is important (see section 5.2.4). Upon loading, starting from point A (macroscopic stress-free state), the total contact area capable for the transfer of compressive forces, will grow under increasing compressive displacement. The maximum possible contact-area at a certain level of "shear-band development" will be dependent on the amount of tensile deformation in the minor compressive direction (i.e. the shear-band width).

The areas that are in first contact will suffer from large stress-concentrations, which can eventually lead to further damage. Due to increasing deformation a further extension of the contact area will result.

Also important is the frictional effect acting at the contact surface. Once the frictional restraint in the contact areas is surpassed, a further sliding in the "shear-band" will occur, resulting in an increasing tensile deformation perpendicular to the compressive direction. Progressive damage (micro-cracking and local crushing near the contact areas) and frictional effects become significant when the inflection point in the reloading curve is reached (point B)

Spooner et.al. showed that in uniaxial compression further damage occurs to a specimen when the maximum obtained strain-level ε_1 in the previous unloading cycle is exceeded upon reloading. The conclusion was drawn based on accoustic emission measurements /148/.

On the other hand, the uniaxial cyclic experiments on mortar by Maher & Darwin /99/, with load-cycles between fixed stress-levels also showed further damage

accumulation depending on the total number of cycles. Unfortunately these experiments and others /12,23,24,145/ do not show the implications of load cycling on lateral displacements.

In the triaxial cyclic experiments it was observed that the deformation in the minor compressive direction (ε_3) in a reloading cycle exceeded the previous obtained maximum unloading strain ($\varepsilon_{3,\ unl.}$ at the envelope stress-strain curve $\sigma_1 - \varepsilon_3$) of the preceeding load cycle, before the 'common point' /145/ was exceeded in the major compressive direction $\sigma_1 - \varepsilon_1$. The effect can be observed from the strain-path curves $\varepsilon_1 - \varepsilon_3$ in fig. A5.14 through A5.27 (figures d), but also from comparison of the level of σ_1 at the common-points both for the $\sigma_1 - \varepsilon_1$ and $\sigma_1 - \varepsilon_3$ curves. If a simultaneous increase of ε_1 and ε_3 would occur, then the reloading curve ($\varepsilon_1 - \varepsilon_3$) should cross the previous unloading branch exactly at the envelope curve $\varepsilon_1 - \varepsilon_3$. Sliding in the shear-bands, causing increasing deformation ε_3 occurs before $\varepsilon_{1,max,unl}$ is exceeded, the limit that is considered as descisive for further damage accumulation in uniaxial experiments /148/. The effect is observed in all triaxial cyclic experiments and becomes more pronounced at higher confinement levels.

A proper hypothesis may be that before the inflection point in the reloading curve ($\sigma_1 - \varepsilon_1$) is reached, the effects of increasing contact area are dominant, beyond the inflection point further damage accumulation occurs primarily by sliding (causing increasing lateral deformations ε_3) and eventually also by further micro-crack propagation and local crushing (causing a decreasing stiffness $E_{tan,1}$ of the material). The contact area capable for compressive load-transfer in the shear-bands increases until the inflection point of the reloading curve is reached, providing for an increasing stiffness in the major compressive direction. Beyond the inflection point the total contact area will decrease due to sliding, thus allowing for further weakening of the material near the contact surfaces. The stiffness of the material decreases again. Finally under increasing axial deformation a new "failure-point" at the envelope stress-strain curve ($\sigma_1 - \varepsilon_1$) is reached.

Upon unloading a sudden stress-drop is observed in the major compressive direction ($\sigma_1 - \varepsilon_1$ curve, see fig. 5.30). The rate of stress-decrease slows down, probably when the total compressive contact area in the shear band decreases and thus also the elastic energy-recovery. The stiffness $E_{tan,1}$ measured just after unloading exceeds the initial 'elastic' tangential modulus considerably (see fig. 5.27).

A large part of the total applied strain ε_1 is non-recoverable due to frictional effects in the shear bands. The non-recoverable strain increases when the total applied strain increases. In the minor compressive direction (ε_3) which is considerably influenced by the shear band, an almost total non-recoverable strain is observed (see fig. A5.14 through A5.27, σ_1 - ε_3 curves).
Only when the residual stress-level (σ_1) is reached, the hysteresis loops in the σ_1 -ε_3 curves becomes flatter and the unloading strain decreases. This may also be due to irregularities in the load-application. As was mentioned in chapter 3, the setting of the pre-loadings at test-initiation can give rise to deviations of about 5% with respect to the required value. A small remaining stress σ_3 at unloading may have this 'push-back' effect of the relatively intact blocks between the shear bands (fig. 5.18), in the shear-bands. The effects will be more pronounced when the shear-band is in a more developed stage (see also chapter 7).

The above discussion is limited for the case of a fully developed shear-band. The continuous decrease of tangential stiffness and other related aspects suggests that similar phenomena are acting at a smaller (size) level in the pre-peak region.
Sliding in micro-fissures and/or the behaviour of 'tensile crack arrays' /152/ may be responsible for the macroscopic cyclic pre-peak stress-strain behaviour (see fig. 5.31).

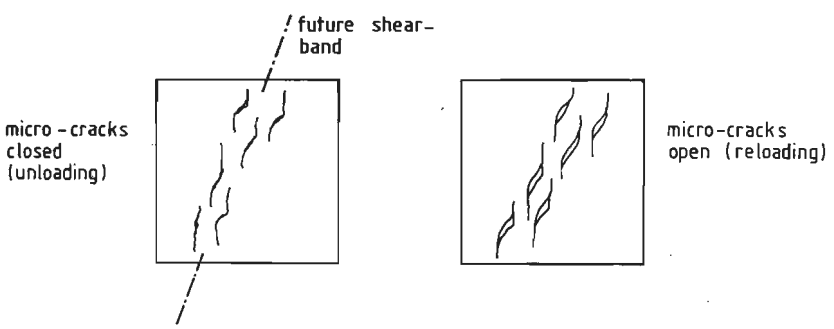

Fig. 5.31. Sliding in 'tensile crack arrays'.

A similar mechanism was proposed by Reinhardt and Cornelissen /129/ for uniaxial tensile cyclic loading. These aspects should be given more attention in future investigations.

- dilatancy in cyclic experiments -

In section 5.2.4 plots of volumetric strain ε_v against major compressive strain ε_1 were shown for all monotonic and cyclic experiments. As no appreciable difference between monotonic curves and cyclic envelope curves was detected this comparison was considered admissible. In the concerning figures 5.20 and A5.34 -A5.36, only the envelope curve was shown in the case of a cyclic experiment. In fig. 5.32 the complete ε_v - ε_1 curves are shown for two cyclic constant stress-ratio experiments. Fig. 5.32.a shows the volumetric strain curve for specimen 8B2-4 ($\sigma_1/\sigma_2/\sigma_3$ = -1/-0.33/-0.05, C, parallel), figure 5.32.b shows the ε_v - ε_1 curve for specimen 9B1-5 ($\sigma_1/\sigma_2/\sigma_3$ = -1/-0.33/-0.10, C, perpendicular).
Both specimens were loaded until the residual stress-level in the σ_1 - ε_1 curve was reached (see fig. A5.16 and A5.19). Samples loaded following these stress-paths have a nearly zero intermediate strain as can be seen from the stress-strain curves in the appendix, so an estimate for the volumetric strain is given by $\varepsilon_v = \varepsilon_1 + \varepsilon_3$.
The loading-unloading loops in fig. 5.32 have an average inclination of 45 degrees with the ε_1-axis, indicating a total non-recoverable deformation in the minor compressive direction ($\varepsilon_{envelope,3} = \varepsilon_{unloading,3}$).
The implication is that a rather large part of the volumetric strain in non-recoverable and upon unloading an increase of volume is observed for the load cycles just preceding the peak-cycle and all load-cycles beyond peak-stress (σ_1).
The graphs demonstrate differently that the behaviour of the localised shear bands in the plane formed through the major and minor compressive directions is guarding the complete degradation process of the material. On the other hand, the curves suggest that a continuous description of the behaviour possible.

5.3. Final remarks.

The triaxial experiments, that were described in detail in the previous sections (5.1 and 5.2), all showed localised rupture. In the tension-biaxial compression region, a single tensile crack appeared, similar as in uniaxial tension. In the triaxial compressive region, two different rupture modes were observed. The planar mode, characterised by one large tensile deformation, showed localised shear planes in the plane formed by the major and minor compressive stress components. This type of rupture is observed for rock subjected to triaxial compressive states of stress as well (see for example /16,17/), and the similarities in behaviour for the different materials is evident.

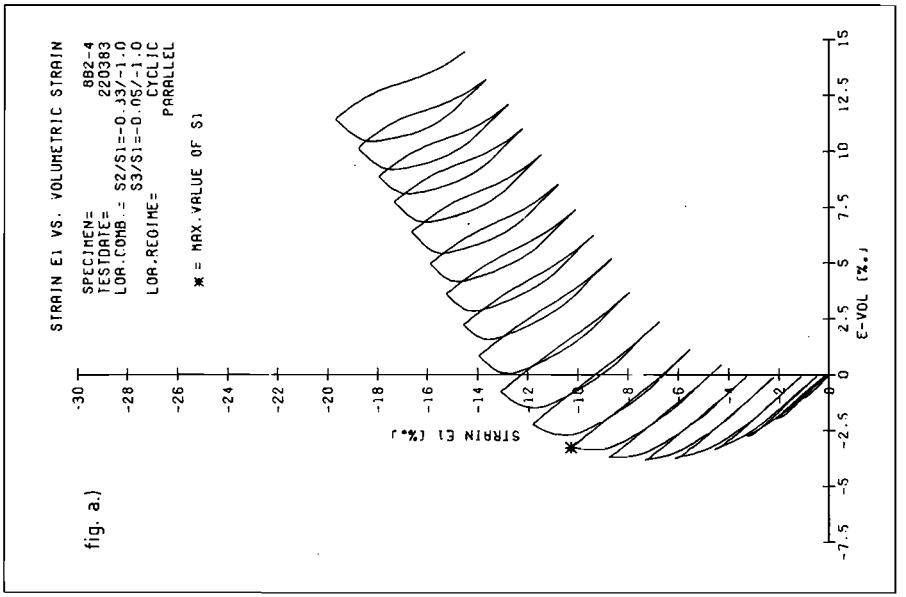

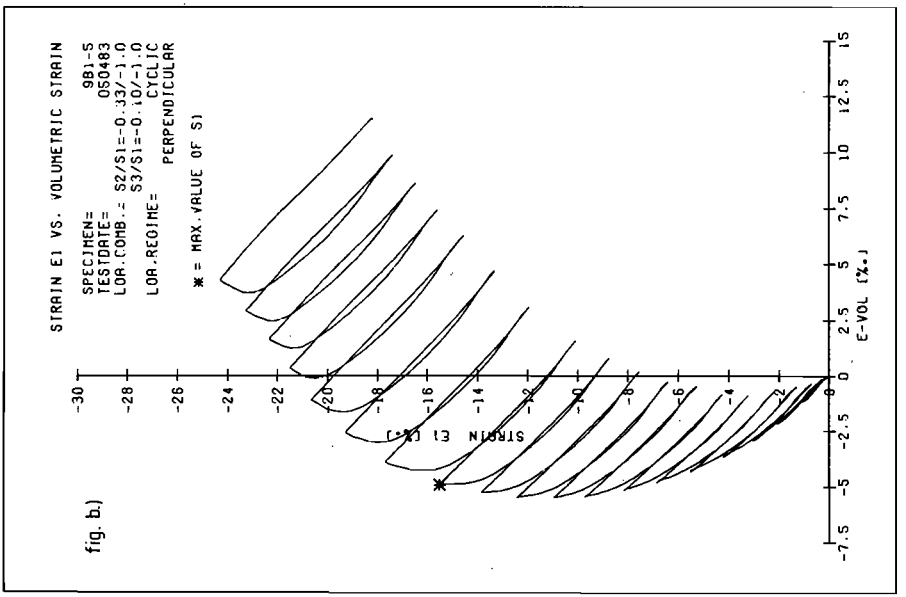

Fig. 5.32. a. Volumetric strain ε_v vs. major compressive strain ε_1 for specimen 8B2-4 ($\sigma_1/\sigma_2/\sigma_3$ = -1/-0.33/-0.05).

b. idem for specimen 9B1-5 ($\sigma_1/\sigma_2/\sigma_3$ = -1/-0.33/-0.10).

For the stress-states near the compressive meridian, a multitude of short inclined fracture planes was observed. Two large tensile deformations allow for development of fracture planes both in the $\sigma_1 - \sigma_2$ and $\sigma_1 - \sigma_3$ planes. This type of rupture was referred to as cylindrical mode.
This last mentioned rupture mode seems not very 'localised' (see fig. 5.13). The cylindrical mode also is observed in uniaxial compression, and the results presented in section 4.4 indicate that failure is localised. A constant fracture energy requirement was measured for prisms with varying height, loaded in uniaxial compression.

Differences in rupture for varying states of stress can be shown in terms of 'energy-requirement'. For all triaxial experiments, the energy-requirement was calculated separately for the three principal directions. The amount of energy at 'peak' W_i (i = 1, 2, 3) was calculated from the governing $P_i - \Delta l_i$ diagrams. A concrete volume equal to the specimen-volume was considered. In fig. 5.33. a-b, the energy at peak is shown for all experiments at the lower confinement level ($\sigma_3 = 0.05\ \sigma_1$, see table 5.4).
The separate energy-components W_i (i = 1, 2, 3) are plotted for the different ratios $\alpha = \sigma_2/\sigma_1$ that were investigated. Both the results of stress and deformation experiments are indicated.
In fig. 5.33.a, the peak energy-requirement W1 in the major compressive direction is shown, in fig. 5.33.b, the values of W2 and W3 in the intermediate and minor stressed directions are shown.

An increasing energy-requirement W1 was measured when the σ_2/σ_1-ratio changes from tension-compression to biaxial compression (respectively $\alpha < 0$ and $\alpha = 1$). Very clear from this figure is the influence of initial anisotropy, leading to higher values of W1 when loading is applied parallel rather than perpendicular. Note that W1 always is positive.

The energy-component W3 in the minor compressive direction is always negative, and decreases for increasing α. The negative values for W3 are simply the result of tensile deformations in the minor compressive direction in a triaxial compression experiment.

In the intermediate direction, W2 is almost equal to W3 when $0 < \alpha < 0.10$. When α increases, W2 changes eventually of polarity and becomes positive. W2 = 0 when a plane strain is carried out. In section 5.2.4 the plane strain tests were considered as a transition from cylindrical to planar rupture.

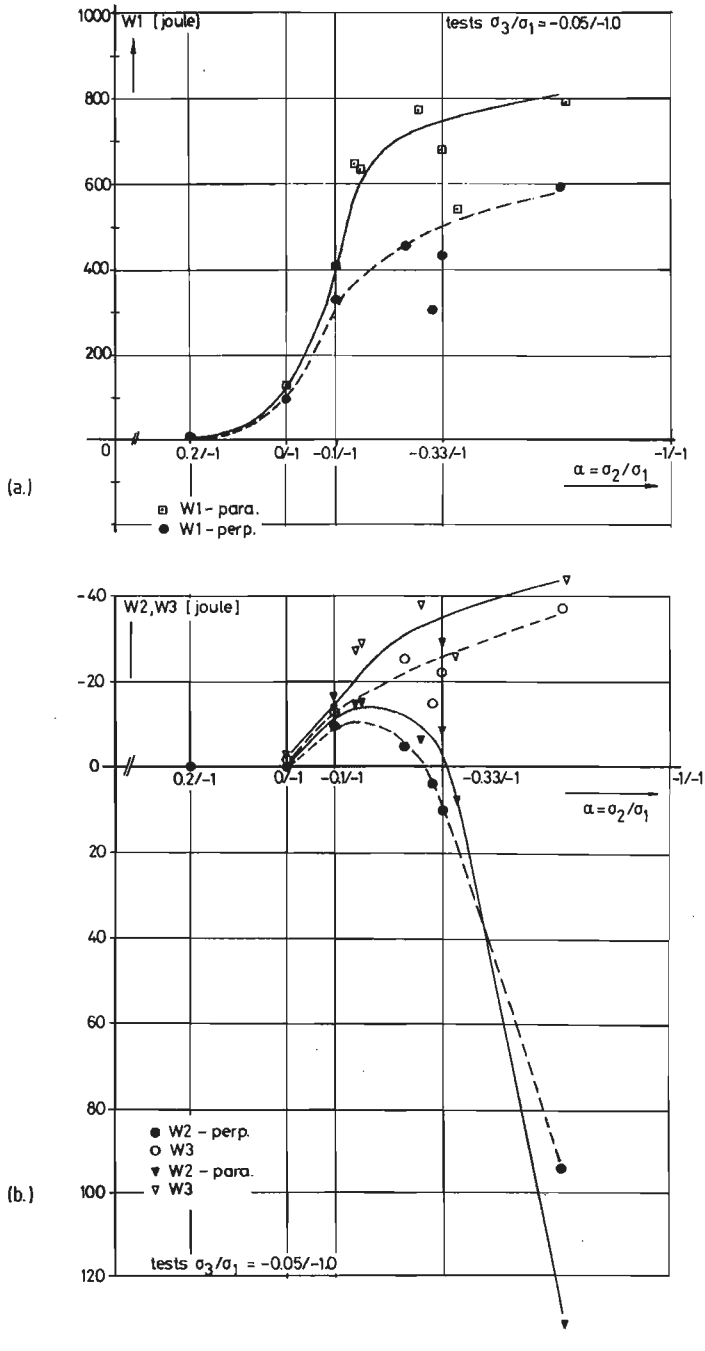

Fig.5.33. a. Energy-requirement at peak (W1) in the major compressive direction for various values $\alpha = \sigma_2/\sigma_1$ at the lower confinement level $\sigma_3 = 0.05\ \sigma_1$.

b. idem, W2 and W3, respectively in the intermediate and minor stressed directions.

Now define negative energies as passive components, and positive energies as active. When two active components are present, failure is along the planar mode. In the case of two passive components, the cylindrical mode will be observed. In principle this reasoning can be extrapolated for different loading combinations.
Palaniswamy and Shah /119/ reported a change of failure modes in triaxial compression tests ($\sigma_1 < \sigma_2 = \sigma_3$) when the lateral confinement increases.
Probably the W2 - α diagram can be extrapolated. In a triaxial compression test W2 = W3. Thus eventually (when the same values are also valid at high confinement levels) if $\sigma_2 = \sigma_3 > 0.33\ \sigma_1$ a different rupture mode can be expected.

The diagrams should be extended for the missing values $\alpha = \sigma_2/\sigma_1$. In the tension-compression regions also a transition stage is expected (compare with the results by Isenberg /78/for tension-compression tests). Furthermore, stress-combinations along the tensile meridian should be investigated ($\sigma_1 = \sigma_2 < \sigma_3$). As can be seen from fig. 5.8, two preliminary equi-biaxial experiments at different confinement level were carried out. Both specimens showed a rather instable post-peak behaviour. The specimen loaded in biaxial compression $\sigma_1/\sigma_2 = 1$, $\sigma_3 = 0$, showed an explosive failure after a short excursion in the descending branch. Also the gradient of the softening branch increased when compared with other triaxial compression tests, failing according the planar mode.

Loading combinations along the tensile meridian can be investigated with triaxial cylinder tests. Yet available experimental results are mainly in the crushing regime, i.e. along the compressive meridian (see Lowe /98/). Yet in view of the highly instable behaviour at failure combinations along the tensile meridian are possibly more important and critical.

6. SOME ASPECTS OF CONSTITUTIVE MODELLING

The type of experiments that were described in detail in chapter 4 and 5, are normally used for purposes of constitutive modelling. During the last decade many models ranging from rather simple plasticity (see for example in /30/) to complicated continuous damage models /48,90/ have been introduced, mainly for application in non-linear finite element programs. It is without doubt that the introduction of numerical methods in engineering has had an enormous impact on the development of these material models.
The numerical programs are able of a three dimensional analysis of complicated structures, taking into account non-linear material laws. Yet the increased activity in the field of constitutive modelling has hardly added to a more basic understanding of material behaviour. Problems such as 'shear' failure are still open questions. Also conditions at rupture, and crack initiation processes are hardly understood.

Many models have been proposed based on resemblance at the macroscopic level with other materials. For example, plasticity models have been proposed for concrete, while under increasing confinement concrete displays an increasing ductility, and in the pre-peak region the unloading slope is roughly equal to the initial slope of the stress-strain diagram (see fig. A5.37 through A5.40). For low confinement levels this is certainly not true, and the analogy stops. Furthermore, it is not possible to model strain-softening.
At this point Freudenthal /50/ may be quoted: "Most of our knowledge concerning the mechanical behaviour of engineering materials is derived from phenomenological (large scale) observations, and frequently, an empirical interpretation of a large volume of partially coordinated observed facts. The shortcomings of this approach become more and more evident as the materials increase in complexity, as the conditions of service under which the materials will perform become more diversified, and, finally, as the number of "laws" that must be deviced to express the interrelation between the relevant variables necessary increases. In general such "laws" are valid only within the range of the observations that serve as a basis for their derivation". Freudenthal continues "Hence, the volume of experimental work required to provide the empirical "laws" needed to solve the increasingly complex problems of engineering design is becoming especially unwieldy".

As was mentioned in section 2.1, the average stress and strain and the non-linearity observed at the macroscopic level will be largely influenced by

processes acting at a lower size level. The large scale behaviour becomes predictable, at least qualitatively from knowledge of the internal structure of the material.
The highly heterogeneous structure of concrete makes an analysis along these lines certainly difficult, and considerable simplifications will be necessary.
In the following sections some attention will be given to the requirements for a smeared micro mechanics approach. It must be emphasized that only some first thoughts are discussed, and still a lot of work has to be done. When this investigation was initiated, it was assumed that a continuum description would be possible.
Now in view of the localised rupture modes presented in section 4.4 and 5.2.4, it is also important to decide if a continuum theory is appropriate for modelling the discrete behaviour beyond peak. This fact will also be included in the discussion.

No attempt is made to give a complete review of previously developed constitutive models for concrete. Throughout the entire investigation developments in this field were followed with great interest. Several comprehensive surveys are available in literature (for example Chen and Saleeb /29/).

6.1. Structural changes in concrete subjected to external mechanical loading.

At the sub-macroscopic level (see section 2.1), concrete displays a complex heterogeneous structure consisting of several types of inclusions embedded in a more or less homogeneous cement-matrix. Two types of inclusions are distinguished: first the larger aggregate particles (for example those particles larger than 1 mm), and secondly larger air voids or pores (for which of course the same size limit should apply as for the aggregate particles). The definition of a size limit is rather arbitrary, while in general a continuous particle size distribution is used. It may also depend on the phenomena that are described. For example, in the aggregate interlock theory by Walraven /162/, a size limit was defined at 0.25 mm.

Hsu et.al./71/, Stroeven /152/ and others demonstrated that micro-cracks are present in the concrete structure before any external load is applied. The micro-cracks are the result of shrinkage, differential temperatures and segregation during the hardening process of the concrete. In fig. 4.6 and 4.7 it was demonstrated that the direction of loading with regard to the direction of casting has a considerable influence on the uniaxial compressive stress-strain curve. The effect was also systematically detected in the multiaxial experiments

(see fig. 5.22). It seems that the micro-cracks, but probably also weaker matrix material zones develop preferential under the larger aggregate particles. The concrete structure displays clearly initial anisotropy and differences in micro-structure were recognized from the crack detection experiments of series 2B2 (see also section 4.2). Some of the results of these tests will be shown in the next section.

Now consider a specimen in uniaxial compression. The specimen is a material body from a spatial limited shape and is fully defined by geometrical and material properties.
When it is assumed that no structural changes occur at small stress-levels, the specimen will have an initial stiffness ($E_{tan,1,0}$), which is fully determined by the mechanical properties of the constituents. In figure 6.1 the material body consisting of a matrix material with randomly dispersed inclusions Ω_i is shown schematicly.
If the mechanical properties of the inclusions are known (in terms of the shear modulus μ_i and bulk modulus K_i), and the volume fractions of the constituents are known too, the mechanical properties of the composite material may be estimated. Several theoretical approximations are available and a number of these models were gathered by Mura (/110/, page 364).

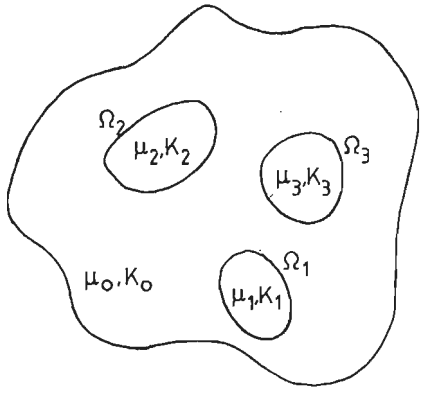

Fig. 6.1. Composite material containing inhomogeneities Ω_1, Ω_2... (μ = shear modulus, K = bulk-modulus).

For concrete with a defined aggregate phase, the measured elastic modulus was compared with theoretical values obtained with the Hashin and Shtrikman model (see /110/, p. 375). The comparison was carried out by Stroeven /152/, and the experimental data coincided reasonably well with the theoretical results.

Yet for a 'normal' concrete, it is rather difficult to obtain the elastic properties (μ, K) of the aggregate phase. Several multiphase models were presented also by Hansen /60/.
When the external applied loading increases, the micro-cracks in the concrete structure will start propagating. Interaction between large aggregate particles (see fig. 2.3), results in high tensile stress concentrations at the aggregate-cement matrix interface. The occurrence of these tensile stresses was shown by Buyukozturk et.al. /25/, by means of a finite element analysis of a biaxial loaded plate containing large rigid disks. From the analysis, and also from a model test it was shown that crack propagation initiates from the aggregate cement matrix interface. Bond-cracking was observed earlier by Hsu et.al. /71/, among others.
In the past many studies have been undertaken in order to investigate the nature of the cement aggregate bond, which was considered responsible for concrete failure (see for example papers by Alexander et.al. /2/, and Taylor & Broms /158/).

An analytical solution for the problem of a partially debonded rigid disk embedded in an infinite matrix with different properties was given by Perlman & Sih /121/. An example was worked for the case of uniaxial tension at infinity. Adopting the general solution by Perlman & Sih, Stroeven /152/ carried out an analysis for uniaxial compression. Calculations were performed for symmetric and non-symmetric loading application with regard to the crack position. It was concluded that in case of non-symmetric loading, the crack is forced to grow along the particle - matrix interface until symmetry is re-established. A symmetrically situated small crack did not influence the stress situation around the inclusion when compared to a completely bonded disk. (that is apart from the area close to the crack-tip). No attention was given to crack-closure, although this is likely to occur for certain crack positions (with regard to the direction of loading).

- isolated micro-cracking -

It will be obvious that due to aggregate interaction, and the presence of micro-cracks at the aggregate matrix interface the rate of crack extension will be influenced.
In the initial stage (up to stress levels $\sigma < 0.3 \cdot \sigma_p$), the size d_c of the isolated micro-cracks is small when compared with the specimen dimension d_s:

$$d_c/d_s \ll 1 \qquad \text{.....(6.1)}$$

The crack is considered as a lineal feature in a plane. In this stage of loading only a very small increase of d_c will occur, and the energy released due to the formation of new crack area is small when compared with the total energy requirement of the specimen. The energy release will influence the macroscopic stiffness of the material. In the initial stage of the macroscopic stress-strain curve a slight curvature is measured, however it may be neglected, and the material is assumed to behave linear elastic.
In the (small sized) micro-crack stage the material can undoubtetly be considered as a continuum.
It should be mentioned that in acoustic emission measurements by Spooner and Dougill /148/ a significant acoustic emission was detected in the initial part of the stress-strain curve. It was concluded that significant damage occurs at test initiation. However it is not clear what will be the nature of the damage. The initial emission may be the result of the consolidation of the material during first loading, leading to a significant higher stiffness (see plots of $E_{tan,1}$ against axial strain ε_1 of triaxial cyclic experiments in section 5.2.6, fig. 5.28). Probably the initial acoustic emission can not be associated with crack-extension.

When the applied external load increases, further crack extension will occur. The process of crack propagation is still a stable process at these moderate loading levels. Several types of crack arrest mechanisms appear as a result of the heterogeneity of the concrete. For example a crack approaching a tough aggregate particle will be arrested while the amount of energy required for fracturing the aggregate or for crack extension by rounding the interface of the inclusion will in general be larger. Several crack arrest mechanisms were indicated by Shah and McGarry /144/, and lately by Zielinski /171 /.
Not necessarily those micro-cracks for which extension was observed in the initial loading stage will propagate under further increasing external load. In fact the conditions at the micro-crack tips of those cracks which showed initial growth are relieved by means of a crack arrest mechanism, and by increasing the overall stress, other potential (formerly relatively stronger) fracture zones may start propagating.

It was indicated by Glücklich /53/, that the energy-requirement curve for a crack in concrete, either in a uniaxial tensile or compressive stress field is a curve with an increasing slope (see fig. 6.2 for tensile loading).
Glücklich discussed the application of linear elastic fracture mechanics to concrete. For a perfectly brittle material the energy requirement is given by

$$W = 2\,a\gamma \qquad \text{.....(6.2),}$$

in which a is the semi-major axis of an elliptical crack loaded in uniaxial tension (fig. 6.2, opening mode), and γ is the surface energy of the material (which is assumed to be homogeneous).

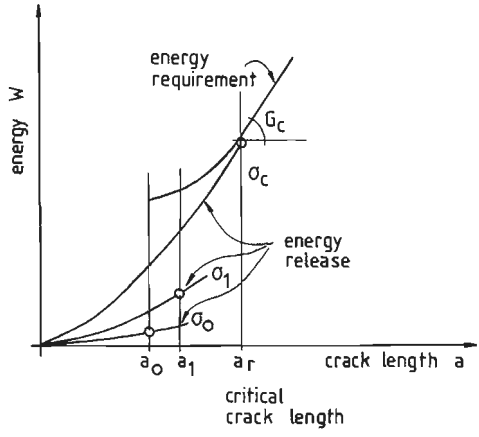

Fig.6.2. Forced growth of a crack in tension, after Glücklich /53/.

The Griffith criterion for fracture states /20/: crack growth can occur if the energy required to form an additional crack of size da can just be delivered by the system.
For a plate of unit thickness, containing an elliptical crack with length 2a, the condition for crack growth becomes

$$d(U - F + W) / da = 0 \qquad .....(6.3.a),$$

or

$$d(F - U) / da = dW/da \qquad .....(6.3.b),$$

where U is the elastic strain energy contained in the plate, F is the work done by the external force and W is the energy for crack formation. In eq. 6.3.b, d (F -U) /da = G, the "energy release rate" or "crack extension force", which is equal to

$$G = \pi a \sigma^2 / E \qquad .....(6.4),$$

where E is the Young's modulus of the surrounding material.
By solving eq. 6.3.b, it follows after substitution of eq. 6.2, that the critical stress for crack propagation is equal to

$$\sigma_c = \sqrt{2E\gamma / \pi a} \qquad .....(6.5),$$

which is the original Griffith criterion. In case of crack-tip blunting, i.e. when energy is consumed due to plastic deformations at the crack tip, the surface energy γ should be replaced by $\Gamma = \gamma + \gamma_p$, where γ_p represents the amount of energy consumed in plastic processes.

The stresses at the crack tip in plane stress conditions (see fig. 6.3) may be written in the generalised form

$$\sigma_{ij} = K_I / \sqrt{2\pi r}.\ f_{ij}(\vartheta) \text{ with } K_I = \sigma \sqrt{\pi a} \qquad .....(6.6),$$

where K_I is known as the stress intensity factor for mode I cracks (tensile opening). The whole stress field at the crack tip is known when the stress intensity factor K_I is known.

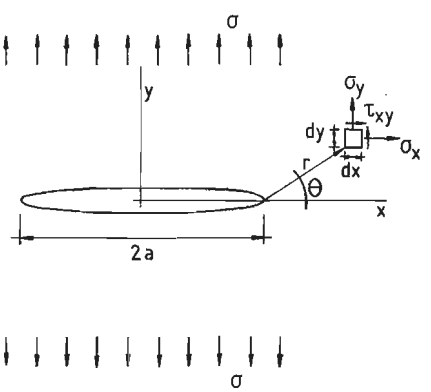

Fig.6.3. Crack in an infinite plate.

For the explicit form of the functions $f_{ij}(\vartheta)$ is referred to Broek /20/. Crack extension will occur when stresses and strains at the crack tip reach a critical value. Thus fracture occurs when K_I reaches a critical value K_{Ic}:

$$K_{Ic} = \sigma_c \sqrt{\pi a} \qquad .....(6.7).$$

This criterion is equivalent to the energy criterium, since it follows from eqs. (6.4) and (6.7) that

$$K^2_{Ic} / E = G_{Ic} \qquad .....(6.8).$$

For a heterogeneous material such as concrete, the surface energy is not a constant value, but it takes a different value for each of the constituent materials. It was indicated by Glücklich /53/, that with increasing size of the crack, the size of the highly stressed zone in front of the crack tip would increase too. This is evident from eq. (6.6).
The cracking process for a material such as concrete is not only limited to the crack tip, but it includes the entire highly stressed zone too, which implies that the amount of energy required for further crack extension, increases with increasing crack size (process zone concept, see also section 2.3). Also the crack arrest mechanisms that were indicated before, are responsible for the increasing energy requirement of concrete.

Now return to figure 6.2. An initial crack of length a_o will initiate under stress σ_o, but will be arrested at a_1 as a result of the increasing energy demand. When the slope of the energy requirement curve dW_r/da ceases to increase, no further increase of stress is needed, and the crack will grow spontaneously.

An inclined elliptical crack in a compressive stress field will have tensile stresses near the crack tip, provided that the crack has a certain width. This becomes clear from a simple linear elastic analysis of the stresses $\sigma_{\eta(\xi = \xi_o)}$, acting at the boundary of an elliptical hole in an (isotropic homogeneous) plate, loaded at infinity (η, ξ elliptical coordinates, solution taken from Timoshenko and Goodier /159/, p. 192).
In figure 6.4 the stresses at the edge of the hole (that is $\sigma_{\eta(\xi = \xi_o)}$, $\sigma_\xi = 0$ along the edge) are plotted for an elliptical void with aspect ratio n = a/b = 100 loaded in plane stress ($\sigma_2 = \alpha \sigma_1$). The loading direction σ_1 is 30 degrees inclined to the major ellips axis as indicated in the inset of figure 6.4.
The dimensionless value $\sigma_{\eta(\xi = \xi_o)} / \sigma_1$ is plotted against the coordinate η ($0 < \eta < 180$ deg., symmetric with regard to the major ellips axis) for three values of α (respectively $\alpha = 0$ (uniaxial compression), $\alpha = 0.5$ and $\alpha = 10$).
In case of $\alpha = 10$, the dimensionless stress is with respect to σ_2, which is the major loading component for values $\alpha > 1$.

As expected, high tensile (negative values of $\sigma_{\eta(\xi = \xi_o)} / \sigma_1$) and compressive stresses are found near the 'crack tips'. In the case of uniaxial compression, the largest tensile stress-concentrations are observed near $\eta = 0$ deg. For each loading combination $\sigma_2 = \alpha \sigma_1$, with $\alpha < 1$, the tensile stress concentration was found at the same side of the crack-tip. For increasing values of α, $\alpha > 1$, the maximum tensile stress switches to the other side of the crack-tip.

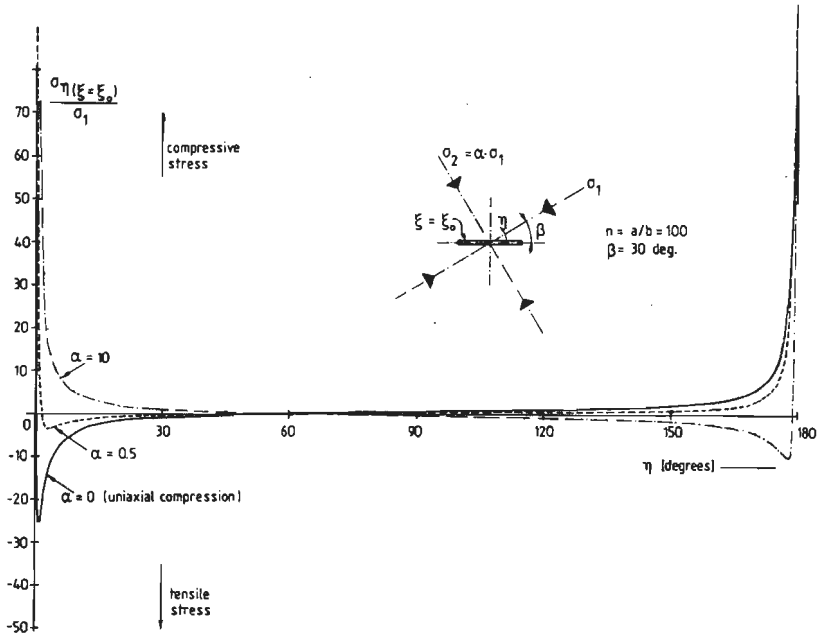

Fig.6.4. Dimensionless stress $\sigma_{\eta(\xi=\xi_o)} / \sigma_1$, along the edge of an elliptical hole in a homogeneous isotropic material, loaded at infinity in plane stress.

It is noted that with increasing values of σ_2, the tensile stress peak at the crack-tip is blunted. A higher external load is needed for crack extension. The tensile peak stress in the case of uniaxial compression ($\alpha=0$), reaches its maximum when

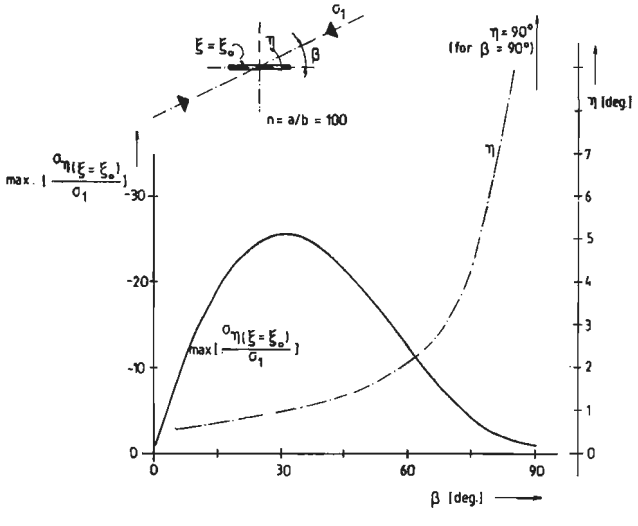

Fig.6.5. Maximum tensile stress at the edge of an elliptical hole, loaded by a remote compressive stress for several orientations.

the major ellipse axis has an orientation of approximately $\beta = 30$ deg. to the direction of the compressive loading. This is indicated in figure 6.5, in which the maximum value $(\sigma_{\eta(\xi=\xi_o)}/\sigma_1$ is plotted for each value of $\beta (0 \leq \beta \leq 90$ deg.). The value of η(the coordinate along the edge of the elliptical hole) is indicated by means of the dash-dotted line in fig. 6.5, for which the maximum tensile stress is obtained for a given orientation β. When β approaches $\beta = 90$ deg., the maximum tensile stress is located at the centre of the major ellipse axis, provided that the crack is not closed.
Similar values for critical crack orientation in a compressive stress field were reported by Glücklich /53/.

A strain energy density criterion was proposed by Sih /82/. The criterion states that crack growth takes place in the direction of the minimum strain energy density. The strain energy dW per unit volume dV is calculated from the three stress intensity factors for the three basic crack modes (K_I, K_{II} and K_{III}, respectively opening, sliding and tearing mode). The strain energy density can be expressed as

$$dW / dV = S / r \qquad .....(6.9),$$

where S is the strain energy density factor determined by the stress intensity factors and some geometrical and material constants (e.g. see Kassir & Sih /82/). The coordinate r determines the distance from the volume element dV to the crack-tip. The factor S is only determined for values of $r \neq 0$.
Fracture takes place in the direction of minimum S, and the angle ϑ for which this occurs may be calculated

$$dS / d\vartheta = 0 \quad \text{and} \quad d^2S / d\vartheta^2 > 0 \qquad .....(6.10).$$

The strain energy density method may be used for analysing mixed mode problems (i.e. combinations of crack modes).

In /82/, an example is given for the application of the S-criterion for crack initiation under compression. In figure 6.6 values of the critical compressive stress σ'_c for three different crack shapes are indicated qualitatively. The magnitude σ'_c for crack initiation is at a minimum when β, the angle of load application is approximately 40 deg., and is nearly independent of the crack shape. For small and large angles of β, the magnitude of σ'_c increases fast.

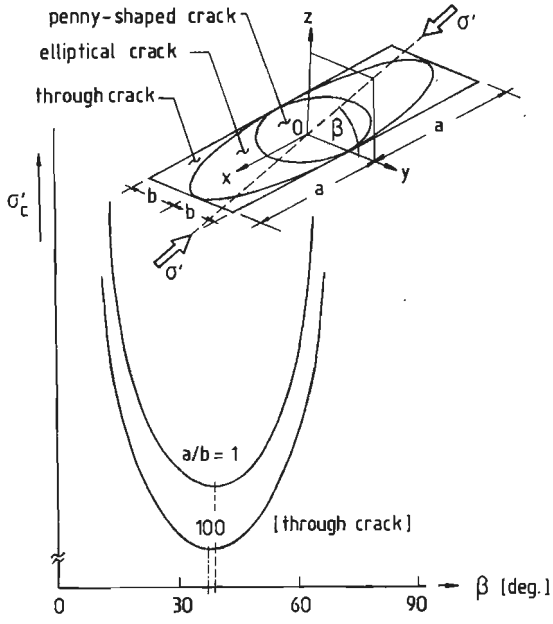

Fig.6.6. Critical compressive stress for fracture initiation versus β, after Kassir & Sih /82/.

The critical orientation of a crack in a compressive stress field is thus approximately similar when either the stress criterion or the strain energy density criterion is applied.

Propagation of an inclined crack in a compressive stress field, occurs by crack branching in a direction parallel to the compressive stress as indicated in figure 6.7 (see for example Ingraffea /76/, Glücklich /53/, Paul /120/).

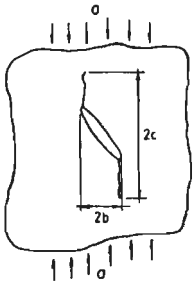

Fig.6.7. Crack-branching, initiating from an inclined crack in uniaxial compression.

For the crack in fig. 6.7, the energy release rate was calculated by Glücklich /53/.

The strain energy release is expressed by

$$\Delta W'_e = \pi b\, a\, \sigma^2 / 2E \qquad .....(6.11).$$

This value is equal to the amount of energy contained within an ellipse whose major axis is parallel to the compressive direction (length 2a) and the other axis is 2b. (see fig. 6.7).
The strain energy release rate is given by

$$d(\Delta W'_e) / da = \pi b\, \sigma^2 / 2E \qquad .....(6.12),$$

which is the driving force for crack extension in compression. It is noted that the driving force is independent of the crack length a, and thus it is quite probable that the crack is immobilized after branching.

Thus as a result of the crack arresting mechanisms, and the branching, slow crack extension will occur at moderate stress levels (let's say $\sigma_c < 0.5\ \sigma_{peak}$). In compression many isolated micro-fracture planes will develop throughout the entire specimen volume, whereas in tension only one discrete crack will appear. The increased curvature in the pre-peak stress-strain curve in compression is, as Glücklich /53/ concludes, the result of many discrete growths. The stiffness-ratio between aggregate and matrix material will undoubtedly influence the extent of crack-arrest, and probably also the curvature of the stress-strain curve (see /170/).

The isolated fracture sites in the specimens can be considered as a spreaded energy dissipating mechanism, which is responsible for the deviation of the concrete stress-strain curve from linearity. In the initial loading stage, the fracture sites may be considered uniformly distributed (that is when the effects of initial anisotropy are neglected), and the material is modelled as a continuum.

- combined cracks -

When size and number of isolated cracks increase, the probability of crack-joining, resulting in a sudden growth of crack length, will increase. If these crack-joining events appear more frequently, a larger deviation from the ideal material response is observed. Probably the energy dissipation at higher overall stress levels, should not only be attributed to the formation of new crack surface, while this will be rather limited when two isolated cracks join to form a combined crack (definition after Carasquillo et.al. /26/).

Also the greeat increase in size of the stress-relieved zones, leading to partial unloading is considered important. The crack joining mechanism is depicted in figure 6.8. The case of tensile loading is shown, but similar effects may also appear in a specimen subjected to compressive loading.

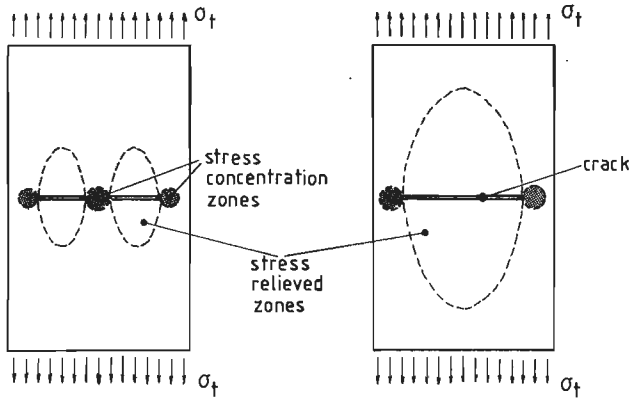

Fig.6.8. Increase of stress relieved zones due to joining of separate micro-cracks.

Due to increasing overall stress, the number of crack-joining events will increase, and the average size of the micro-cracks will also grow. The dimensions of the cracks will however still remain smaller when compared to the specimen size:

$$d_c < d_s \qquad .....(6.13).$$

As a result of the increased size of stress-relieved area, due to crack-joining (fig. 6.8), not all potential 'dissipation sites' will remain equally important. Small micro-cracks situated within the sphere of influence of combined cracks will be prevented from further extension.
Additional growth will only occur at those areas where high stress-concentrations are present due to the interaction between combined cracks, as indicated in figure 6.9.

Due to the branching effect, the majority of the combined cracks will be oriented parallel to the direction of loading (assume uniaxial compression).
It will be obvious that a continuum description will become more and more discutable at this stage of material degradation. At these stress levels ($\sigma \sim 0.7$

- 0.8 σ_{1peak}), the minimum volume is obtained (that is in uniaxial compression), which boundary is normally associated with the long term strength of concrete (see also section 2.2).
If the overall stress is kept constant at this high level, failure will be unavoidable. Crack propagation is now unstable, and a complete and sudden loss of load carrying capacity will occur when no measures are taken to absorb the excess of energy release.

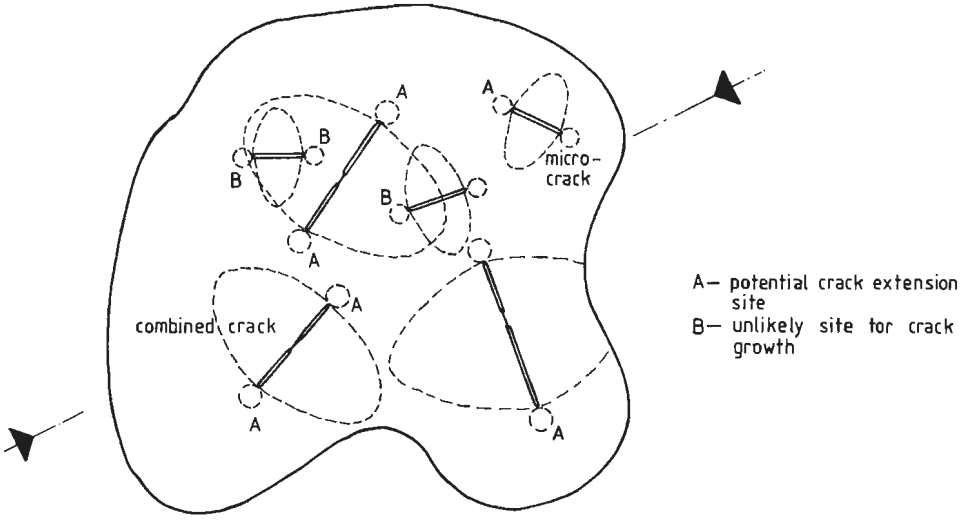

Fig.6.9. Development of preferential crack-propagation sites, due to increased size of stress-relieved zones.

- macro cracking -

Upon further increasing overall stress, the combined cracks will join to form continuous macro-cracks. Again a sudden crack length jump occurs, accompanied by a further extension of the stress relieved zones. When the specimen is under 'stress-control', a sudden loss of load carrying capacity is observed. The energy-requirement curve has reached its maximum slope, see fig. 6.10.
Only if certain boundary conditions are fulfilled, the structure, which contains now large macro-cracks, will remain stable. In the experiments that were described in chapter 4 and 5, stable crack growth was obtained by adopting an appropriate deformation control in combination with a stiff loading frame.

The second joining mechanism, leading to the formation of large macro-cracks, gives rise to a further increase of energy release, resulting in a gradual loss of load carrying capacity. The enormous amount of energy released in the stress-strain curve descending branch must be taken by other elements in the complete loading system.

The concrete specimen is gradually transformed into a structure consisting of several relatively intact blocks separated by increasingly weakening joints.

In this stage of specimen degradation (i.e. in the stress-strain curve descending branch), the size of the fracture zones is of the same order of magnitude as the specimen dimensions:

$$d_c \approx d_s \qquad \text{.....(6.14).}$$

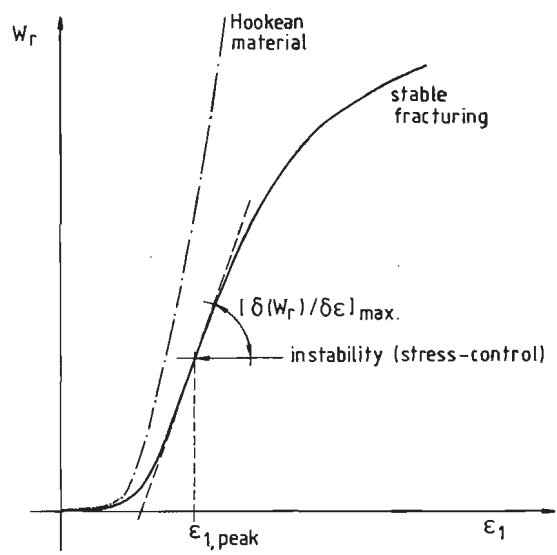

Fig.6.10. Energy-requirement curve for stable crack growth in compression.

From the triaxial results, the impression was obtained that the macro-cracks develop through an array of parallel micro-cracks (see section 5.4.2). The 'shear-failure' thus observed seems only of secondary importance /152,54/.

If the macro-cracks are fully developed, which may probably be assumed as soon as the residual stress level in the axial stress-strain curve is reached (that is the $\sigma_1 - \varepsilon_1$ curve, the direction decisive for fracture in case of a multiaxial experiment), the stiffness of the specimen is fully determined by the frictional characteristics of the "weak joint" between the more or less intact blocks (see sections 5.2.4 and 5.2.6).

The degradation process of the specimen is characterised by the occurence of crack length jumps, influencing the stiffness of the total structure. As a result of the sudden increase of the crack length and related with this the growth of stress relieved zones, the fracture planes are very localised. It might be argued that the size of the fracture zones relative to the specimen size determines if a continuum description is possible or not.

6.2. Characterisation of damage

It was indicated before (section 5.2.6 and 6.1), that a constitutive model should describe the internal structural changes of the material under consideration. It would be preferable to calculate the damage propagation from the applied displacement field (which is in general three dimensional) to which a specimen is subjected.
It is noted that a material is subjected to displacements, rather than stresses, which are the computed (engineering) response of displacements. In fact this statement indicates that a 'strength criterion' for material failure is rejected. The tension-compression displacement ratio experiments (fig. 5.9) may indicate the importance of tensile displacement in fracture (see also /98/). An energy approach, combining both stress and strain, and which can provide in principle for a link with smaller size levels seems to be preferable.

Before any loading is applied to the specimen, the behaviour is linear elastic, and stresses may be calculated using the generalised Hooke's law.

$$\sigma = S . \varepsilon \qquad \text{.....(6.15).}$$

The fourth-order tensor S of the elastic moduli can in principle be determined from the elastic properties of the constituent materials and their volume fractions (aggregate and matrix phase).

As indicated in the previous section, structural changes occur when a displacement field is applied, and energy is released due to progressive micro-cracking. The energy release is normally associated with newly formed crack area, and the stiffness tensor is affected by the increasing crack density

$$\varepsilon . (S^{*} - S) . \varepsilon = 2 \Delta W \qquad \text{.....(6.16),}$$

where S^{*} is the stiffness tensor of the material containing a certain amount of micro-cracks, and ΔW is the total amount of released energy.

The most general description is obtained when ΔW is calculated from an applied displacement field, taking into account the present cracks and their propagation. Equation 6.16 indicates in fact the total deviation of the actual material from idealised material behaviour. The surface between the linear elastic stress-strain curve and the actual concrete stress-strain curve is the total energy release and demonstrates nicely the increasing size of the damage sites with regard to the specimen dimensions.

While the damage evolution can not be deduced from an applied loading history, simply as a result of a lacking (micro-)propagation law, a phenomenological description of damage must be used. In the last years numerous efforts have been undertaken to investigate a possible application of fracture mechanics to concrete (see also the discussion in section 2.3 and 6.1). For macro-crack propagation in small sized structures, the linear elastic formulation cannot be used /63/, and a non-linear variant was developed /63,7/, which seems to give proper results for the structural size effect /11/.
Yet it is by no means clear, if the non-linear formulation (taking into account the energy absorbed in a large process zone, containing micro-cracks, in front of the macro-crack tip, see section 2.3) may also be applied for micro-cracks.
Until a 'micro-crack propagation' criterion is developed, taking into account the behaviour of isolated micro-cracks and the interactions and joining effects of separate micro-cracks, a phenomenological description of damage seems to be the only appropriate manner.

- comments on previously developed models -

Recently several continuum damage models have been proposed for modelling the non-linear macroscopic concrete stress-strain behaviour in relation with underlying micro-crack processes. /97,100,101,48,90,157,40,41/.
The aspect of both degradation of strength and stiffness was adopted by Dougill /40/and Dougill and Rida /41/ in a theory of progressively fracturing solids. The model material displayed the property of strain-softening. Underlying the progressively fracturing theory is an energy dissipation function J, which takes essentially the shape of the energy-requirement curve for stable crack propagation in concrete as shown in figure 6.10.
It was suggested by Dougill and Rida /41/ that the dissipation function J should be determined from the results of physical experiments, rather than by deducing J from theoretical considerations. In this context they referred to the results

obtained by Spooner et.al. /148,149/, that were indicated in section 2.2. Figure 5.23 shows the energy requirement curves for triaxial loading, however these curves are not corrected for damping and recovery as was suggested by Spooner et.al. The triaxial cyclic experiments can be used for a break-down in energy-components (section 5.2.6).

The progressively fracturing theory provides for elastic unloading and reloading as indicated in figure 6.11.

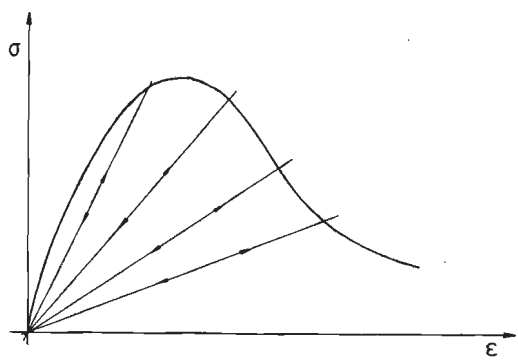

Fig.6.11. Progressively fracturing solid.

Although this behaviour does not coincide with observed unloading - reloading characteristics of concrete (see section 5.2.6), the model provides for valuable insights in the material behaviour. A plastic fracturing variant was proposed by Bazant & Kim /6/ in order to accomodate this shortcoming. Using a linear relationship for $J(\varepsilon)$, the stress-path response was calculated for biaxial strain ratio experiments as shown in fig.6.12. The predicted stress-path coincides qualitatively remarkably well with measured response, presented in figure A5.28 through A5.33, 5.5 and 5.9 in this thesis. (Although these represent, a triaxial test, the deformation ratio was biaxial.)

Deviations are observed in the compression - compression region. Whereas the experiments show a second peak stress in the second strained direction (i.e. ε_2, $\varepsilon_1 / \varepsilon_2$ = constant, see figure 5.5), this is not predicted by the model, probably as a direct implication of the choice of a linear form of the energy dissipation function $J(\varepsilon)$.

The energy dissipation function may be considered as a 'damage evolution law' of the material. The shape of this function (fig.6.10) is essentially similar to the damage laws that were proposed for use in the continuous damage models for tension (e.g. Lland /97/, Mazars /100,101/, see section 2.3, fig. 2.19).

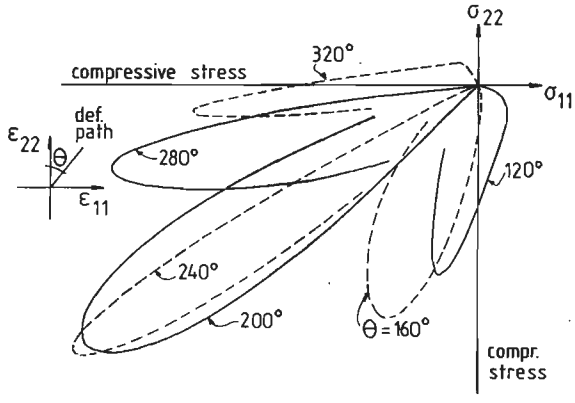

Fig.6.12. Stress-paths for radial deformation paths, after Dougill and Rida /41/.

The 'damage evolution law' reduces in fact to a scalar, representing the surface under the stress-strain curve in the direction decisive for fracture. Thus,

$$\omega(\varepsilon_o) = \int_0^{\varepsilon_o} \sigma_1(\varepsilon_1)\, d\varepsilon \qquad .....(6.17),$$

in which $\omega(\varepsilon_o)$ represents the amount of damage sustained to the material at a given strain level ε_o.
Recently also a general applicable model on thermodynamics basis was formulated, adopting damage as an internal state variable affecting the free energy of the material (Fonseka and Krajcinovic /48,90/).

Similar results as those obtained with the theory of progressively fracturing solids may be obtained by adopting the self consistent method for estimating the effective elastic properties of a cracked solid (e.g. Budiansky & O'Connell /22/, O'Connell & Budiansky /116/, Cleary /32,33/ and others). The self consistent approximation was exploited earlier in analogous analysis of the elastic properties of composite materials /21,62/. The model predicts the elastic properties of a material consisting of a homogeneous isotropic matrix in which flat elliptical cracks are dispersed. The amount of cracks is defined by a crack-density parameter, which depends on the average size and number of micro-cracks. In case of elliptical cracks /22/, the crack density ω is given by:

$$\omega = 2N / \pi \cdot \left\langle A^2 / P \right\rangle \qquad .....(6.18),$$

in which A is the area of a crack ($A = \pi ab$), P is its perimeter ($P = 4a.\ E(k)$, where E (k) is the complete elliptical integral of the second kind with $k = (1 - b^2/a^2)^{\frac{1}{2}}$), and N is the total number of cracks per unit volume. Angle brackets denote an average.

Also crack shape and orientation distribution of the micro-defects will influence the result. The effective moduli are calculated by estimating the total amount of potential energy ΔW, dissipated as a result of a certain crack density. The key step in the analysis is to compute the energy loss due to a single elliptical crack in a matrix which has the properties of the cracked solid.

It is assumed that the micro-cracks are smoothly distributed over the total material volume, and do not mutual interact (thus no clustering and crack joining effects are allowed for).
The self consistent models require a crack orientation distribution as an input parameter, and in general it is assumed that this distribution is random /22,33/. A solution for non-random crack distributions (in fact orthotropic variants) were recently reported by Hoenig /68,69/. Results were obtained for two general cases: all cracks parallel to a plane (referred to as planar transverse isotropy), and secondly the case with all cracks parallel to an axis (cylindrical transverse isotropy). In fact these two types of anisotropy are observed in the triaxial cube tests (that is stress or strain induced anisotropy, see section 5.2.4).

In fig. 6.13 the results of an analysis, using the self consistent approximation as it was formulated by Budiansky & O'Connell /22,116/, as a starting point, are shown. In the upper part of this figure, the measured secans modulus $E_{sec,1}/E_o$ in the axial loading direction is plotted against the axial strain ε_1. The secans stiffness is dimensionless with regard to the initial stiffness E_o.
Although the self consistent method applies for situations involving tensile load, it may also be used in cases under compressive load (provided that tensile stresses may appear locally, see section 6.1).
The equations for a material body in which saturated circular cracks (with radius a) are randomly dispersed are used (eq. 53 - 57 and fig. 8 in /22/). The crack volume is assumed to be filled with a fluid of bulk modulus $\tilde{K}$. The cracks must have a non-zero volume, and for circular cracks this is equal to $4/3.\pi a^2 c$ (c is the minor axis of the ellipsoid). For circular cracks, the saturation parameter which defines the stiffness of the fluid phase, is expressed through,

$$\zeta = (a/c) . \tilde{K}/K \qquad .....(6.19).$$

An empty (dry) crack is defined by $\zeta = 0$, a crack filled with a 'hard' fluid is given through $\zeta = \infty$. For air-filled cracks in rock, Budiansky & O'Connell mention values of $\tilde{K} / K \approx 10^{-6}$. For cracks filled with cool water, a value of $\tilde{K} / K \approx 0.03$ is indicated. For cracks with aspect ratio $a/c \approx 10^{3}$, these values result in values of the saturation parameter $\zeta \approx 10^{-3}$ in case of air-filled cracks, and $\zeta \approx 30$ for cracks filled with cool water.

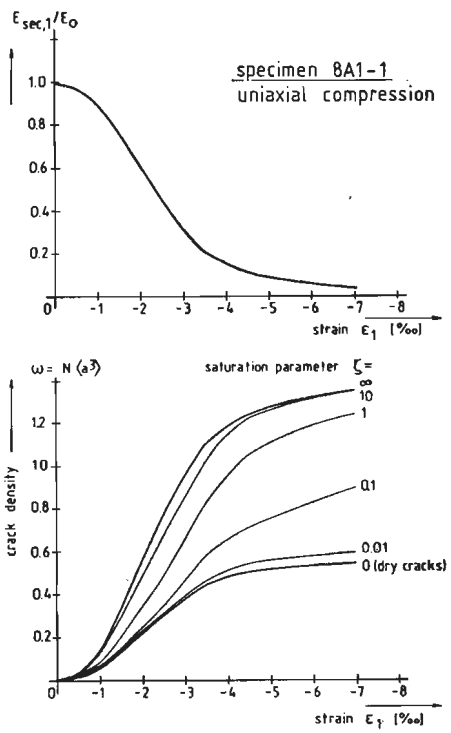

Fig. 6.13. Estimate of the crack density ω for specimen 8A1-1, using the self consistent approximation, after /22,116/.

In the lower part of fig. 6.13, the estimated crack density $\omega = N \langle a^3 \rangle$ (for circular cracks) is indicated for different values of ζ. Qualitatively the $\omega(\varepsilon)$ curve (crack density curve) takes the same shape as the energy requirement curve (compare with fig. 6.10). In case of cracks filled with 'hard fluid', the crack density necessary for a certain stiffness decrease, grows enormously when compared with dry-crack estimates ($\zeta = 0$). The equations for dry-cracks and cracks filled with hard fluid reduce to a linear relation between E^*/E and ω. (see fig. 8 in /22/). As there is no large difference between the estimates for $\zeta = 0.01$

and $\zeta = 0$, the air-filled cracks can be estimated with the equations for dry cracks. Similar the cracks filled with cool water are approximated quite well for $\zeta = \infty$.

It is not certain which density should apply for the experiments that were described in chapter 4 and 5. The specimens were sealed until the experiment was carried out (see section 3.3), and the rest-pieces of a cube after test termination were always moist.

In the self consistent approach, as it was formulated by Budiansky and O'Connell /22,116/, the energy dissipated due to the presence of a certain amount of micro-cracks was computed using linear elastic fracture mechanics concepts. The crack density parameter $\omega(\varepsilon) = N(\varepsilon). \langle a^3 \rangle (\varepsilon)$ takes the same shape as the energy requirement curve in uniaxial compression (compare fig. 6.13 and 6.10 for the case of stable crack growth).

The paradox is evident: the model is fed with parameters that are in fact derived from the stress-strain relations that must be computed. In this case it might be argued that a simple direct fit of stress-strain curves would suffice, for example by extending available uniaxial expressions as were proposed by Popovics /125/and Sargin /133/, into a three dimensional formulation. In fact such an extension was carried out by Ahmad & Shah /1/ (see also section 2.3, fig. 2.21) for triaxial loading combinations along the compressive meridian.
Yet the description of internal micro structural changes in terms of number and size of micro-cracks and their orientation distribution may have some advantages. Especially in the case of loading axes rotation with regard to the principal damage axes of the material seems to be important. By including an orientation distribution, path dependent behaviour may in principle be accounted for. The recent micro-plane models, developed for uniaxial tension by Bazant & Oh /10/and extended for combined tensile and shear loading by Bazant and Gambarova /9/ are a promising extension in this direction. These models can in principle also describe compressive loading conditions.

- some results of crack detection experiments -

From the crack detection experiments of series 2B2, that were only shortly mentioned in section 4.2.1, some insight in the progressive cracking of a specimen loaded in uniaxial compression may be obtained. Using the fluorescenting technique /49,152/ the progressive cracking on a surface of the specimen could be followed. The specimens were subjected to a cyclic loading sequence as

was indicated in section 4.2.1. For two of the experiments, the stress-strain curves σ_1 - ε_1 and σ_1 - ε_2 (with $\varepsilon_2 = \varepsilon_3$, the four strain readers were all attached in one direction, see table 4.2) are shown in appendix A1, fig. A1.7. a -d (specimen 2B2-2, loa. dir. perpendicular and 2B2-4, loa. dir. parallel).

Two examples of crack maps, both for specimens 2B2-2 (at ε_1 = -4.53 $^{o}/_{oo}$) and for 2B2-4 (at ε_1 = -5.62 $^{o}/_{oo}$) are shown in figure 6.14.a and b. The crack maps were carefully copied from a two fold magnified slide image, and only the cracks with length exceeding 2 mm are indicated. The shaded areas in the crack maps indicate positions of pores. For both specimens the casting surface and the loading direction are indicated in fig. 6.14.

In figures 6.15 and 6.16 a-b, the results of a stereological analysis of the crack maps are shown, both for specimen 2B2-2 and 2B2-4. The stereological method proposed by Saltikov is based on the coverage of a sample plane by a line grid. The method was described in detail by Stroeven /152,153/, who was the first to apply it for examination of micro-crack patterns in concrete.

The number of intersections N of a test line with micro-cracks must simply be counted. Two and three dimensional characteristics of the micro-crack structure can be derived from the value $N_L = N / L$, where L is the length of the test-line. For example the total crack length per unit of sampled area is given by

$$L_a = \pi / 2 \, . \, N_L \qquad .....(6.20),$$

where N_L is determined by means of a system of random secants. For a detailed description of the method is referred to publications by Stroeven /152,153/.

In the current investigation, only attention is given to the number of intersections per unit of test-line $N_L(\vartheta)$, where ϑ is the angle between the test-line and the loading axis (indicated in fig. 6.16). In figure 6.15 the results of countings along 11 parallel test lines at mutual distance of 10 mm are shown. The countings are made both in the direction parallel to the direction of loading (ϑ = 0, referred to as $N_{L,//}$) and in the direction perpendicular to the loading direction ($\vartheta = 90^{o}$, referred to as $N_{L,\perp}$).

Results for specimens 2B2-2 and 2B2-4 are indicated in fig. 6.15. A continuous increase of both $N_{L,\perp}$ and $N_{L,//}$ was observed with increasing axial strain ε_1. For both specimens a significant difference between $N_{L,//}$ and $N_{L,\perp}$ was observed. In the case of the perpendicular loaded specimen (2B2-2, dash-dotted lines) $N_{L,//}$ hardly increased up to the peak level (at ε_1 = -2.26 $^{o}/_{oo}$), beyond peak only a slight increase was observed.

The results indicate that continuous parallel cracks develop faster when loading is applied perpendicular to the direction of casting (rather than parallel).

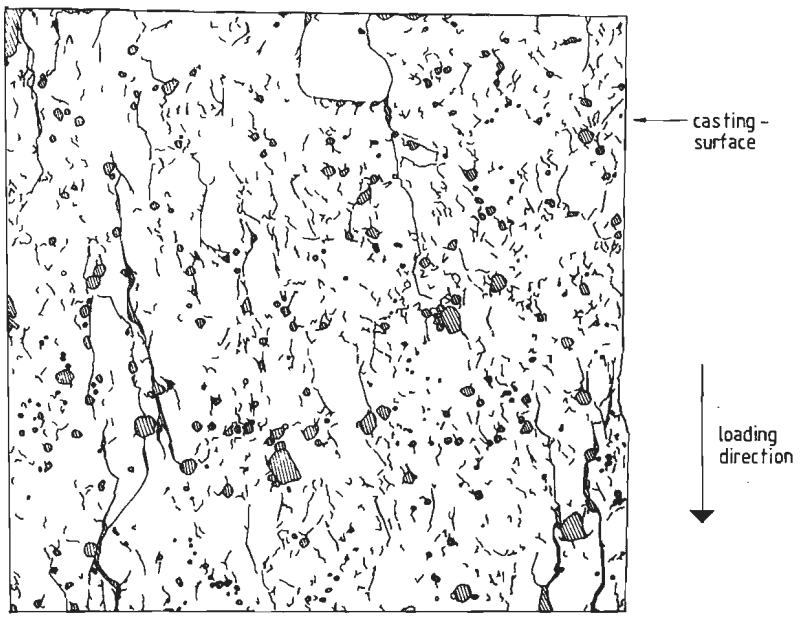

Fig. 6.14.a. Crack map for specimen 2B2-2, loa.dir. = perpendicular, loading level ε_1 = -4.53 °/oo.

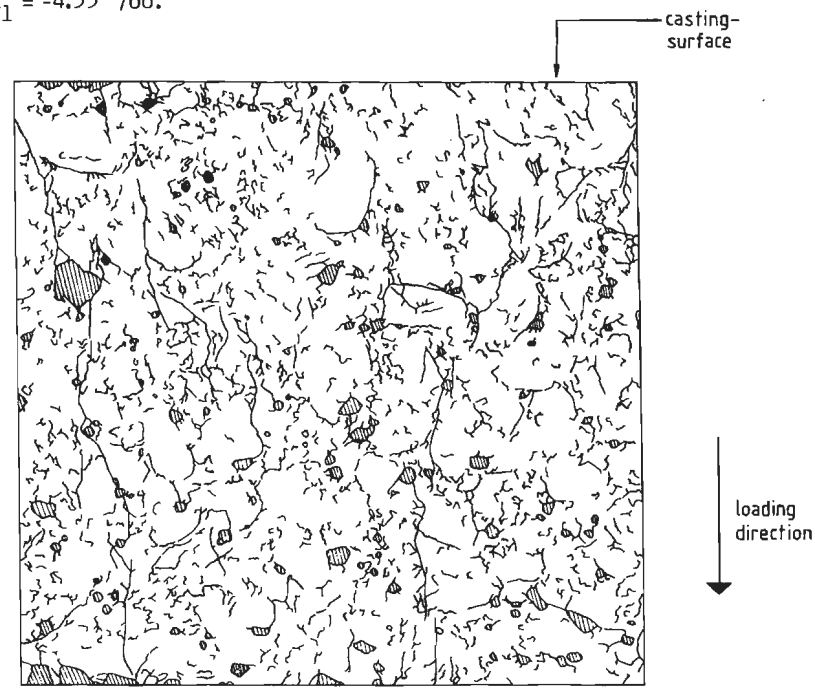

Fig. 6.14.b. Crack map for specimen 2B2-4, loa. dir. = parallel, loading level ε_1 = -5.62 °/oo.

The differences due to initial anisotropy were indicated before at the macro level and are thus also recognised from the micro structure. A visual check on the two crack maps that are shown in fig. 6.14 also indicate the difference.
It must be mentioned that the residual stress-level at the last crack detection measurement is approximately the same for both specimens (σ_1 = -19.6 N/mm^2 at ε_1 = -4.53 $^o/_{oo}$ for 2B2-2, and σ_1 = -19.5 N/mm^2 at ε_1 = -5.62 $^o/_{oo}$ for specimen 2B2-4, see also fig. A1.7).

In fig. 6.16, a-b the roses of number of intersections are shown at two levels of axial strain ε_1 for both specimens 2B2-2 and 2B2-4. The roses of number of intersections are constructed from measurements of $N_L(\vartheta)$ at various angles ϑ. The roses of number of intersections reflect the actual crack orientation distribution in the sampled plane (see /153/). The shape of the roses is dependent on the size of the cracks that are taken into consideration.
Only a quarter of the complete roses is shown in fig. 6.16. Symmetry may be assumed along the loading axis ($N_{L,//}$) and the normal to the loading axis ($N_{L,\perp}$) with both lines intersecting at the centre of the sampled area. The values of $N_L(\vartheta)$ that are indicated in fig. 6.14 represent the averages of four corresponding orientations (thus at $\vartheta = \pi/8$, the average is shown for countings at $\vartheta = \pi/8$, $7\pi/8$, $9\pi/8$ and $15\pi/8$).

In order to reach a certain decrease of load carrying capacity in the stress-strain curve descending branch, a higher strain level ε_1 is required when loading is applied parallel to the direction of casting. The strain levels ε_1 at which the roses are measured in fig. 6.16 correspond to stress-levels in the descending branch equal to $\sigma_1 \approx$ -19.6 N/mm^2 (2B2-2, ε_1 = -4.53 $^o/_{oo}$ and 2B2-4, ε_1 = -5.62 $^o/_{oo}$) and $\sigma_1 \approx$ 38.5 N/mm^2 (resp. 2B2-2, ε_1 = -2.91 $^o/_{oo}$ and 2B2-4, ε_1 = -3.41 $^o/_{oo}$).
In general it was observed that larger crack densities are needed in the case of parallel loading. Furthermore at the low strain level in fig. 6.16, specimen 2B2-2 showed an elliptical crack orientation distribution, whereas the distribution for the parallel loaded specimen was almost circular. At higher strain levels, the ellipse increased in size for the perpendicular loaded specimen. The major ellipse axis remained along the $N_{L,\perp}$-axis. For specimen 2B2-4 (parallel loading), also an elliptical orientation distribution was measured at the higher strain level.

The amount of cracks also increased in the direction parallel to the (compressive) loading direction. This was probably due to the fact that the crack did not follow a straight path, but rather had to round the larger aggregate particles.

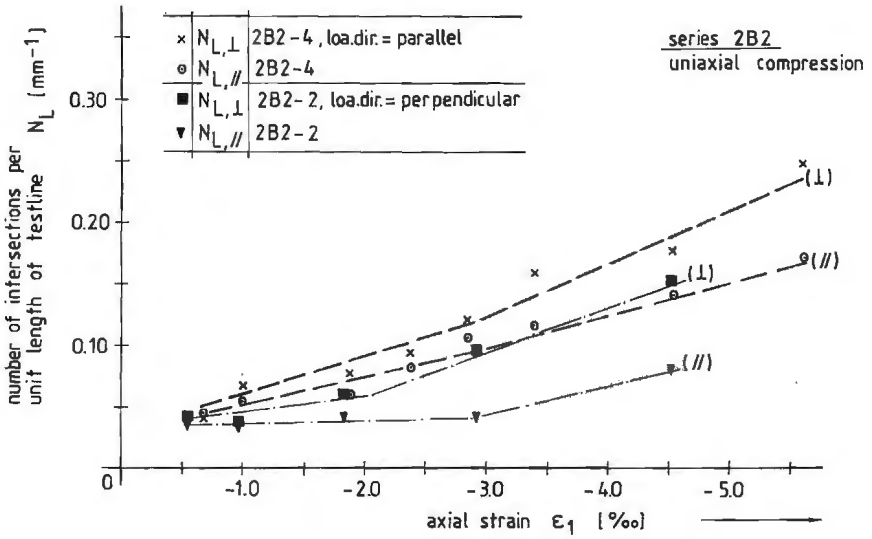

Fig.6.15. Number of intersections per unit of test line ($N_L(\vartheta)$, for $\vartheta = 0^o$ and 90^o) versus axial strain ε_1, for specimens 2B2-2 and 2B2-4.

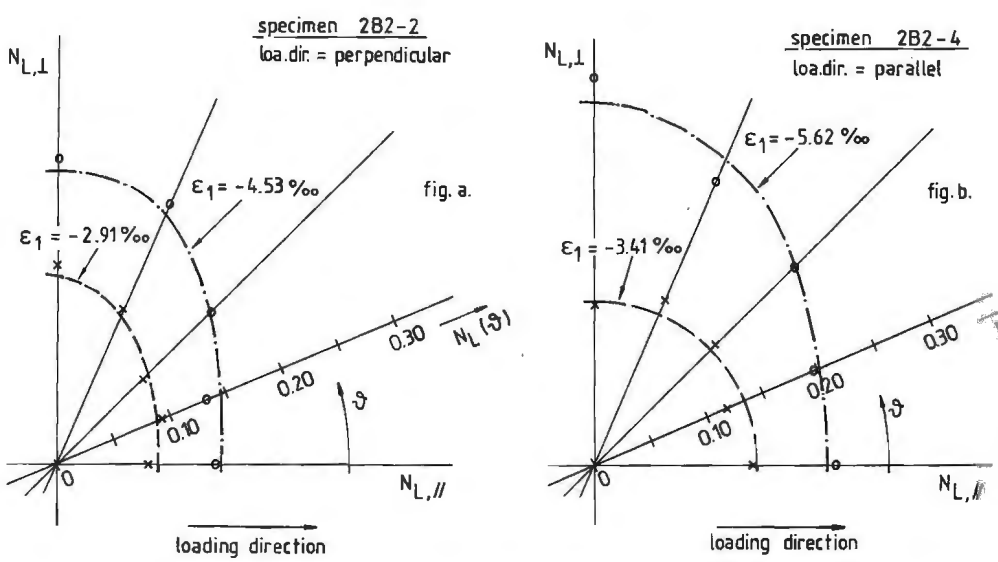

Fig.6.16. a. Roses of number of intersections per unit test-line for specimen 2B2-2 (perpendicular).

b. idem for 2B2-4 (parallel).

Probably the shape of the ellipse is dependent on the size of the aggregates.
The reasons for the distinct behaviour due to initial anisotropy were indicated before (see section 4.2). In case of parallel loading, the initial elliptical orientation distribution ($N_{L,//} / N_{L,\perp} > 1$) must be 'rotated' over an angle of 90 degree in order to obtain the rupture orientation distribution ($N_{L,//} / N_{L,\perp} < 1$).
The results may be extrapolated to a three dimensional orientation distribution, and for a parallel loaded specimen (uniaxial compression) an oblate spheroid will emerge with the smaller axis parallel to the direction of loading (see fig. 6.17, $N_{L,x} = N_{L,y}$, loa. dir. along the z-axis).

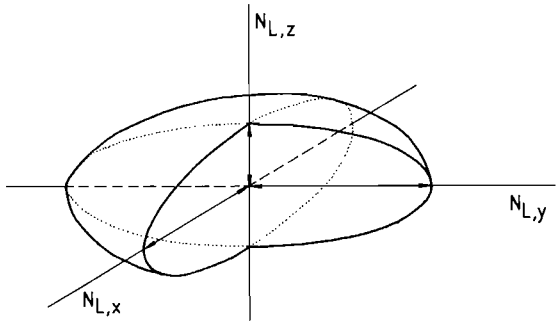

Fig.6.17. Hypothetical three dimensional crack-orientation distribution.

In case of perpendicular loading, the majority of the cracks will be situated in planes parallel to the casting surface. The orientation distribution in the x-y plane will deviate from a circular distribution and $N_{L,x} \neq N_{L,y}$. It is suggested that a relation exists between the crack orientation distribution and the deformation field to which a specimen is subjected.

A non-random crack orientation distribution can in principle be applied in a self-consistent scheme for estimating the effective elastic properties of a cracked solid /22,33/. Also the micro-plane model for tension and shear /9,10/, requires an orientation distribution of the weak planes as an input parameter.
However, when for example an ellipsoidal orientation distribution is adopted in a self-consistent scheme, then the basic assumption of isotropy is violated when loading axes are rotated against the major ellipsoid axes (for rotation angles $\varphi \neq n.\pi/2$).
The degree of anisotropy, which can be expressed in terms of the ratios $N_{L,x}/N_{L,y}$ and $N_{L,x} / N_{L,z}$, at which violation becomes serious is of course important in this context. Probably when the orientation distribution is nearly spherical,

only a small deviation from reality will occur. This will however only be true for very small loading levels. In the pre-peak region, path dependency was observed from tests under hydrostatic-deviatoric loading paths (i.e. experiments carried out at Colorado University /135,136,150/). The hydrostatic-deviatoric loading regimes that were investigated are essentially similar to a number of 90 deg. rotations of principal stresses. In chapter 7 some results of triaxial 90 degree rotation experiments in the post-peak region are shown.

Other problems arise when such a smeared approach is chosen, which does not take into account the interaction effects between cracks. The size of the cracks with regard to the specimen size seems to be important. In fig. 6.18 the dimensionless value d_c/d_s is plotted against the applied major compressive strain.

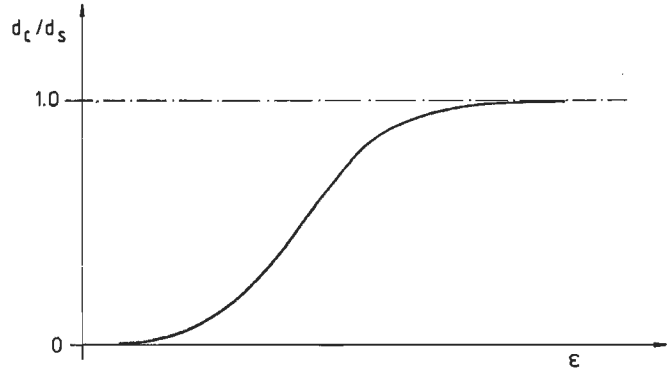

Fig. 6.18. Increase of crack size d_c with regard to the specimen size d_s versus axial strain ε_1.

At rupture, i.e. when the residual stress-level is reached in the major compressive direction, the size of the cracks is approximately equal to the characteristic specimen dimensions, thus $d_c / d_s = 1$.
The increase of d_c / d_s will be roughly according fig. 6.18, which represents graphically the degradation process that was described in section 6.1.
At test initiation the value d_c / d_s represents an average of many small cracks. Upon increasing axial strain ε_1, the value d_c / d_s will increase, but the number of active cracks will probably decrease. This process continues until a few macroscopic cracks are formed, which determine the complete specimen response.
When the crack density is given through $\omega(\varepsilon) = N(\varepsilon)$, $\langle a^3 \rangle$ (ε), then N will decrease with increasing ε, and $\langle a^3 \rangle$ will increase.

It seems that we should not try to find high crack densities using very high resolution methods (see fig. 2.8, results by Darwin and Attiogbe /37/ using SEM), but rather should try to determine the 'critical' circumstances under which a macroscopic crack will develop through an array of micro-cracks (Bienianski et.al./16,17/ for rock, see section 5.2.4).
An important fact is that the observed stiffness degradation of the specimen is far less when compared with results obtained from monotonic experiments. If stiffness and crack density are related, as was assumed in the example of the self-consistent model, then a far less crack density is predicted from the 'true stiffness' measured in cyclic experiments (see section 5.2.6, results of cyclic triaxial tests, fig. 5.28 and A5.37 through A5.41).
Another factor, which was not discussed before, is important in this context. Shear in cracks is a potential source of energy absorption, and was completely neglected in the previous discussion for the sake of "simplicity". Sliding over rough-crack surfaces also leads to dilantancy (see fig. 5.20), which cannot be modelled using a self-consistent scheme. The maximum value for the effective Poisson's ratio is only 0.5 in the self-consistent model. In uniaxial compression tests values up to 5 are measured !

6.3. Final remarks

In the previous sections, the damage propagation in a concrete specimen, subjected to a certain deformation field (with at least one compressive direction), and some comments on continuous damage models were discussed.
Theoretically the behaviour of a specimen can be modelled starting from a 'background' material with a certain stiffness (or compliance), which can be determined from the volume fractions and initial stiffness of the constituent phases.
Subsequently when a certain deformation field is applied, the energy released due to the appearance and propagation of single micro-defects should be calculated. It would be preferable to calculate the damage propagation from the applied external deformation field (and history), rather than assuming an energy dissipating function, which is in general deduced from the stress-strain curves that should be modelled. In such an approach, strength is a casual quantity, dependent on the amount and width of cracks in the concrete-structure.
For use in finite element packages (for example /19/) a continuum description seems to be preferable, although for tensile crack modelling also discrete formulations have been developed (Grootenboer /56/, Saouma and Ingraffea /134/).

Thus in order to obtain a certain curvature in the stress-strain curve, a dissipating mechanism is needed, and when also path dependency should be described, the orientation distribution of the energy dissipation sites with regard to the current deformation field should be known.
It is not certain if a fracture mechanics approach (either the linear-elastic (see section 6.1) or a non-linear elastic formulation /63,7/) can be applied at the submacroscopic level.
When a tensile crack is considered (for example in a plate (with finite dimensions) under uniaxial uniform deformation) the surface under the stress-strain curve descending branch is associated with the fracture energy release rate /63/. This amount of energy contains several components including friction and side cracking. As recently indicated experimentally by Reinhardt /130/, the tensile crack developes from one side of the specimen gradual to the other side, indicating that in the tensile stress-strain curve descending branch a gradual decreasing effective area able for load-transfer. This is essentially the assumption of the continuous damage models in tension (see section 2.3, fig. 2.19).

Similar observations apply for triaxial compression. The macro-cracks or rather shear bands, develop gradual in the stress-strain curve descending branch (compare the photographs in fig. A5-6.a-d, and the corresponding stress-strain curves $\sigma_1 - \varepsilon_1$).

Some critical reflections on fracture mechanics were reason for Zielinski /171/, to use a surface energy concept, associated with total fractured area for each constituent phase, rather than a fracture mechanics formulation as an energy absorption mechanism in a model for the impact tensile strength of concrete.
Yet if the non-linear fracture mechanics formulation (process zone model) indicates only the degree of crack arrest and frictional capacity of the macro-crack, then also the same mechanism might apply at the submacroscopic level or at the micro level. As was indicated by Grudemo /58/, crack arrest mechanisms also appear in cement paste at the micro-level !

A 'damage model' adopting the internal damage propagation as a starting point, may be described phenomenological in terms of:

- the number and total area of cracks at a certain given deformation level, and due to a certain loading history,
- the size of the cracks with respect to the specimensize (that is the size of the largest cracks at a certain deformation level),
- the crack width,

- the orientation distribution of the cracks, and,
- the frictional characteristics of a crack.

In the previous section (6.2) some results of surface crack detection were shown. It is emphasized that these results are only indicative. The surface behaviour is different from the core concrete behaviour (see section 4.2 fig. 4.11).
Furthermore another complication arrises. As was observed from the uniaxial prism tests (h = 200 mm, section 4.3), and the triaxial compression tests, failure in compression is a very localised phenomenon. Deformation concentrates in a narrow zone, and the adjacent blocks remain apparently intact. Also the side surfaces of the crack-detection tests on cubes showed only a few macroscopic cracks (that are visible with the unaided eye). In fig. 6.19, the macro-cracks that were observed at the crack-detection surface of specimen 2B2-2 are shown (fig.c). The axial deformation at test termination was equal to ε_1 = -6.19 °/oo. The macro-cracks for this particular specimen, indicate that also inclined cracks develop in the uniaxial cube tests.

In figure 6.19.a-b, the micro-crack patterns at strain levels ε_1 = -2.91 °/oo and ε_1 = -4.53 °/oo are indicated. Only those micro-cracks that are situated near or at the sites where macro-cracks eventually develop are shown.
If only the indicated micro-cracks are active, an enormous reduction of crack density occurs (compare fig. 6.14.a and 6.19.b). It is emphasized that these results are only indicative. Macro-cracks develop inside the specimen as well (for example by splitting of surface layers), and subsequently become visible at the specimen surfaces. For this particular specimen there was no indication that the crack detection surface was split from the rest of the cube (observations from upper and lower loading surfaces !). From this particular test (2B2-2, load.dir. perpendicular), macro-cracks predominantly developed in planes parallel to the casting surface.

In view of these results, and also from the experimental results reported in section 4.4 (uniaxial size effect) and 5.2.4 (triaxial compression rupture), a continuum model seems rather doubtfull, and a discrete formulation at failure seems preferable (similar as for tensile fracture). A smeared crack approach is only possible when the actual crack density is exaggerated.

In this context, the recently developed composite damage model should be mentioned (Willam /167/, Bičanic et.al. /15/). The composite damage model is an attempt to take into account the localised fracture mode in tensile cracking and

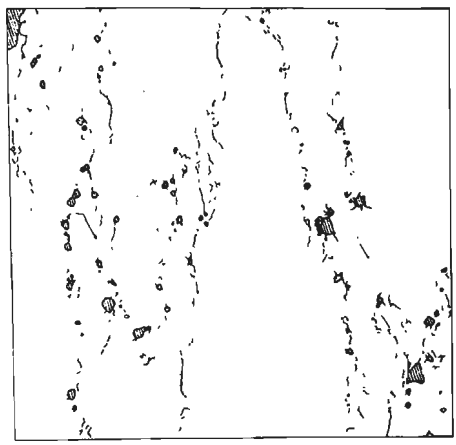

loading direction

fig. a. $\varepsilon_1 = -2.91$ ‰

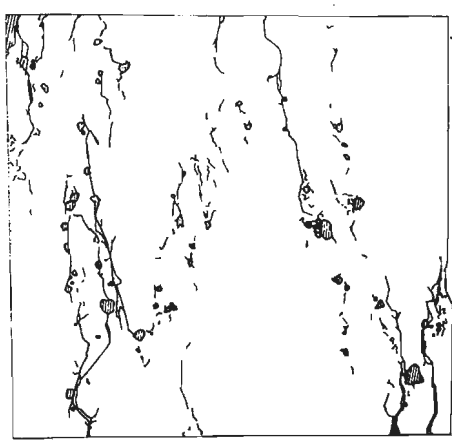

casting-surface

fig. b. $\varepsilon_1 = -4.53$ ‰

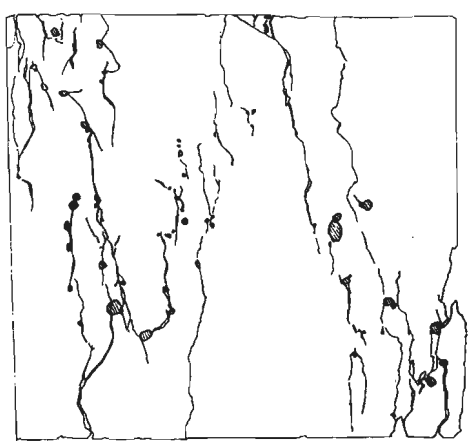

fig. c. $\varepsilon_1 = -6.19$ ‰

Fig. 6.19.a-c. Crack maps for specimen 2B2-2, at three subsequent loading levels: ε_1 = -2.91 °/oo (fig.a), ε_1 = -4.53 °/oo (fig.b) and ε_1 = -6.19 °/oo (macro-crack pattern, fig. c).

frictional slip (that also occurs in triaxial compression), in a smeared model. The softening modulus of an equivalent continuum element is derived from a series model, consisting of an 'intact elastic' zone and a localised damage zone (see fig. 6.20). The series model was used before by Bazant /5/ and Sture & Ko /154/ for the description of localised fracture in uni- and triaxial compression (see section 2.3).

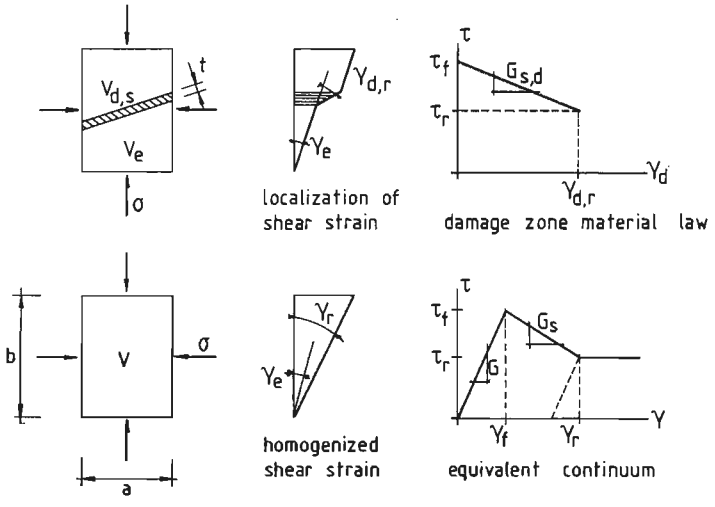

Fig. 6.20. Composite damage model in shear, after /167/.

If the size t of the localised damage zone approaches to zero, the model reflects the usual smeared softening approach. The fracture energy for the equivalent continuum model is invariant if the softening modulus is adjusted with the size of the elementary volume. This is in agreement with experimental results presented in section 4.4. of this thesis.

If on the other hand the size and law for the localised damage zone are kept constant, the crack band model /7/ is recovered. As mentioned in /15/, the composite damage model provides the link between the usual softening approach for continuous distribution of micro-defects (see also section 6.2), and the crack band approach for localised fracture (/7/ for tensile cracking).

Finite element analysis with the composite damage model were carried out for the case of uniaxial tension and triaxial compression on cylindrical specimens (NX mortar specimen, ϕ 54 x 108 mm). Since only post-peak behaviour was important, the material behaviour was described with a simple bilinear elastic - softening model, with the triaxial strength being defined by the extended Mohr - Coulomb criterion with tension cut-off.

The computations revealed that mesh insensitive results (radial and axial variations in mesh-size) in tension are obtained when the fracture energy content of the various size elements was kept constant. Considerable deviations were observed when a constant softening slope was adopted in uniaxial tension. The conclusion is in agreement with the localised fracture models for tension /63,7/.
In the case of triaxial compression (identification of material properties from experimental results on NX specimen with confining pressure σ_c = 0.69 N/mm^2), mesh insensitive results were obtained when the fracture energy density of the various size elements was kept constant, i.e. when the shear softening modulus is considered as a material property. Willam /167/ states: "Clearly, this result indicates that distributed fracture prevails in the case of shear failure and infers that the fracture mechanics postulate of an invariant fracture energy release rate (or rather fracture energy requirement, sic) is highly questionable".
The results of Willam /167/ and also Bičanic et.al. /15/ are in contradiction with computations by Pietruszczak and Mróz /124/, who concluded that the relation of shear band size t with respect to the element size should be taken into account in order to obtain results that are insensitive for the chosen element discretisation.
Also in view of the experimental results in section 4.4, the conclusion by Willam /167/ seems contradictory. It was indicated by Willam that the differences with computations by Pietruszczak and Mróz are due to the specimen configuration (cylinder and square panel under plane strain conditions respectively).

It should be mentioned that for increasing lateral confinement, the slope of the softening branch decreases, as was noted in /15/. It is considered worthwhile to investigate the nature of the above mentioned inconsistencies, and also to study cases where asymmetric confinement occurs (see chapter 5).

It seems that a check on stability of strain-softening is inevitable, and is dependent on the size of the strain softening volume. Also when a continuum model is proposed (see section 6.2), the conditions under which a strain-softening element remains stable should be checked.
In terms of real structures this implies that the excess energy due to progressive fracturing in the strain softening region, should be taken by other (neighbouring) elements that are still in their pre-peak regime.

7. ROTATION OF LOADING AXES WITH REGARD TO MATERIAL AXES

Concrete is an anisotropic material. Upon loading an oriented progressive cracking process is observed (see section 6.2). The orientation distribution of the cracks is dependent on the loading history (ratio of principal stresses and maximum loading level) to which a specimen is subjected. For the concrete used in the current investigation, also effects due to initial anisotropy were observed (see sections 4.2 and 5.2.5). The objection against conventional proportional stress-paths (see for example /4/, and also some of the experiments in chapter 5), and the hydrostatic-deviatoric loading histories (that were for example adopted in the international cooperative research program /51,52/) is that they do not yield information on path dependent behaviour.
Information on progressive degradation is obtained from cyclic loading regimes (in terms of stress'to the envelope curve', see section 5.2.6). For such loading regimes in uniaxial compression, a break down in several energy components was proposed by Spooner et.al. /148/ (see section 2.2).
Recently two extensive experimental studies were carried out (Scavuzzo, Stankowsky, Gerstle and Ko /136/, and Traina /160/), using multiaxial non-proportional loading paths. In both investigations a cubical machine was used, and the non-proportional load paths were in fact a series of 90 degrees rotations. The experiments that were carried out at Colorado University (Stankowsky & Gerstle /150/, Scavuzzo et.al. /135/), which adopt the octahedral formulation as a starting point, revealed that principal stresses play a larger role in defining material behaviour than originally had been suggested in the octahedral formulation. This remark is in agreement with the results obtained in the current investigation. The implication is that the assumption of coaxiallity of incremental stress and strain vectors in the octahedral formulation is rejected. This was shown in /150/.

As was discussed by Bazant /8/, the "true triaxial test" in a cubical machine does not allow for continuous loading axes rotation at angles $0 < \varphi < 90^{o}$. An abrupt rotation may however be obtained when specimens are sawn at a certain orientation from initial larger pre-loaded specimens.
As an alternative, Bazant /8/ proposed cylindrical specimens subjected to axial load, lateral external and internal pressure (i.e. solid or hollow cylinders may be used) and torsion. In such an experiment the principal stress direction may be rotated continuously or abruptly during the loading process. Yet when solid cylinders are used, the shear stress distributions varies with the distance to the specimen axis, and the influence on the fracturing process will be rather uncertain. In fig. 7.1 the two rotation possibilities are indicated.

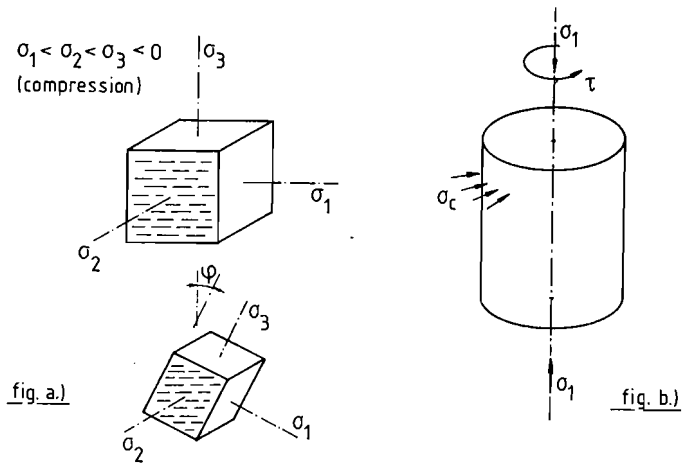

Fig. 7.1. Rotation of loading axes with regard to material axes. Abrupt rotation in cubical tests (fig. a) and triaxial torsional test (fig. b).

In the following sections the results of a small number of preliminary rotation tests are described. Due to the layout of the experimental apparatus, rotation for angles $0 < \varphi < 90^o$ only can be done using the pre-loading/sawing method (fig. 7.1.a). Major emphasize in the following sections is laid on 90 deg. rotation tests. Only two 30 deg. rotation tests were carried out, and some complications that arise in these experiments are discussed.

7.1. Description of experiments.

Specimens originating from batch 7A/7B were used for the preliminary rotation tests. While two basic different failure modes were observed in the triaxial compression region (see section 5.2.4), two different loading regimes were chosen for the 90^o rotation tests.
The two basic loading paths are:

-1- planar mode rotation test (fig. 7.2.a).
first loading: $\sigma_1/\sigma_2 = -1/-0.5$, $\dot{\varepsilon}_1 = 10.10^{-6}$/sec.
σ_3 = constant = -1 N/mm^2

The first loading was carried out until a certain point ($\sigma_{1,unl}$, $\varepsilon_{1,unl}$) in the major stress-strain curve descending branch (σ_1 - ε_1) was reached. At this point severe damage was sustained to the specimen, and the specimen was

unloaded until a stress-level $\sigma_1 = -1$ N/mm^2 (fig. 7.3).
Subsequently a 90 deg. rotation was carried out by simply changing the major and minor compressive directions, thus,

second loading: $\sigma_3/\sigma_2 = -1/-0.5$, $\dot{\varepsilon}_3 = 10.10^{-6}$/sec.
σ_1 = constant = -1 N/mm^2

The second loading was carried out until a tensile strain level was reached $\varepsilon_1 \sim 20$ $^{o}/_{oo}$ in the minor compressive direction. Occasionally a unloading-reloading cycle was carried out, either in the first loading or the second loading sequence.

-2- cylindrical mode rotation test (fig. 7.2.b).

first loading: $\dot{\varepsilon}_1 = 10.10^{-6}$/sec.
$\sigma_2 = \sigma_3$ = constant = -1 N/mm^2

Again first loading was carried out into the $\sigma_1 - \varepsilon_1$ curve descending branch, and the specimen was unloaded to a stress-level $\sigma_1 = -1$ N/mm^2. Subsequently a 90 deg. rotation was carried out by simply changing the major and minor compressive directions, thus,

second loading: $\dot{\varepsilon}_3 = 10.10^{-6}$/sec,
$\sigma_1 = \sigma_2$ = constant = -1 N/mm^2.

An experiment was terminated when a tensile strain level equal to 15 $^{o}/_{oo}$ was reached in both minor compressive loading directions. Also for the cylindrical rotation tests, several unloading-reloading cycles were carried out at arbitrary points in the loading history.

The direction of casting was defined with respect to the major and minor compressive direction. Either loading was applied parallel or perpendicular, similar as was indicated in fig. 5.2 for the triaxial compression tests. The reason for the small compressive load in the minor loaded direction was to provide for a plane specimen surface.
In table 7.4, a review is given of all preliminary rotation experiments and the accompanying control tests that were carried out. Indicated are the specimen number, testdate, loading history and the figure where the concerning result is shown.

Four specimens originating from prism 7A1 were loaded in the planar mode (7A1-2 and 7A1-6), and in the cylindrical mode (7A1-3 and 7A1-4). Rotation in these

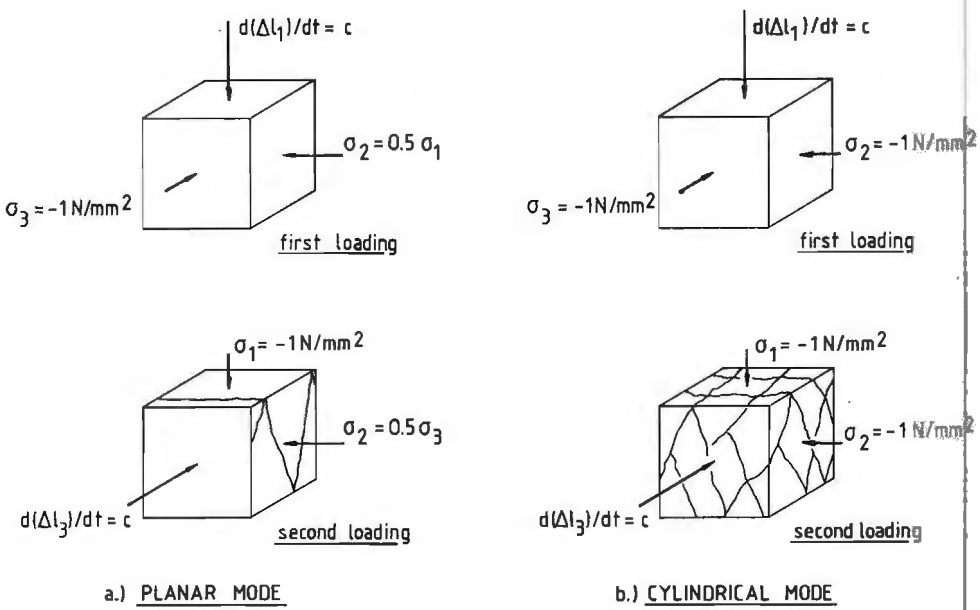

Fig. 7.2. Planar mode rotation test (fig. a) and cylindrical mode rotation test (fig. b).

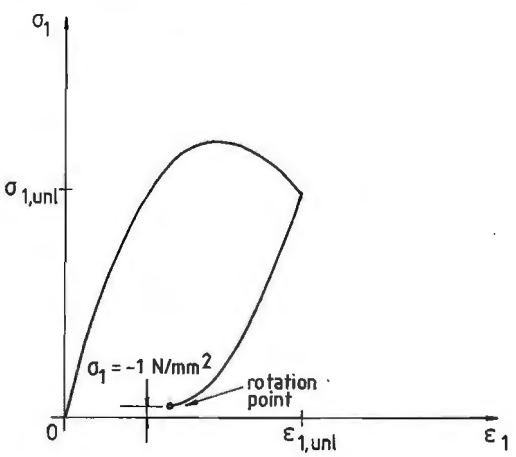

Fig. 7.3. Definition of rotation point.

experiments was carried out at an arbitrary point in the σ_1 - ε_1 curve descending branch. The indicated loading direction is the orientation of the casting direction with regard to the σ_1-direction. Thus, for example, specimen 7A1-2, loa.dir. perpendicular, indicates loading σ_1 perpendicular to casting direction, and after rotation, σ_3 parallel to the direction of casting.

specimen no.	test-date (1)	loading-path (see fig. 7.2)	figure number
7A1-2	020883	planar mode rotation test, perpendicular (2)	A7.2
7A1-3	290783	cylindrical mode rotation test, perpendicular.	7.6
7A1-4	280783	cylindrical mode rotation test, parallel.	A7.4
7A1-6	040883	planar mode rotation test, parallel	A7.3
7A2-3	230883	$\sigma_1/\sigma_2/\sigma_3$ = -1/0/0, $\dot{\varepsilon}_1 = 10.10^{-6}$/s, monotonic, parallel	-
7A2-4	230883	$\dot{\varepsilon}_1 = 20.10^{-6}$/s, $\sigma_2 = \sigma_3$ = constant = -1 N/mm^2, cyclic, parallel.	A7.8
7A-K1(3)	100883	cylindrical mode rotation test, loa.dir. = 30 degrees.	A7.5
7A-K2(3)	110883	$\dot{\varepsilon}_1 = 10.10^{-6}$/s, $\sigma_2 = \sigma_3$ = constant = -1N/mm^2, monotonic, parallel.	7.13 7.14
7A-K3	120883	$\sigma_1/\sigma_2/\sigma_3$ = -1/0/0, $\dot{\varepsilon}_1 = 10.10^{-6}$/s, monotonic, parallel.	-
7B-K1	150883	$\sigma_1/\sigma_2/\sigma_3$ = -1/0/0, $\dot{\varepsilon}_1 = 10.10^{-6}$/s, monotonic, parallel.	-
7B-K2	150883	$\sigma_1/\sigma_2/\sigma_3$ = -1/0/0, $\dot{\varepsilon}_1 = 10.10^{-6}$/s, monotonic, parallel.	-
7B-K22(3)	170883	cylindrical mode rotation test, $\varphi = 0^o$	A7.6
7B-K3	160883	$\sigma_1/\sigma_2/\sigma_3$ = -1/0/0, $\dot{\varepsilon}_1 = 10.10^{-6}$/s, monotonic, parallel.	-
7B-K32(3)	180883	cylindrical mode rotation test, $\varphi = 30^o$.	A7.7

(1) testdate = day - month - year

(2) orientation of σ_1 with regard to casting direction.

(3) 100 mm cube sawn from 150 mm control cubes.

Table 7.4. Review of preliminary rotation experiments, casting series 7.

Two specimens from prism 7A2 were used for control purposes (respectively uniaxial compression and triaxial compression $\sigma_1 < \sigma_2 = \sigma_3$ = -1 N/mm^2 with cycles to the envelope curve (see also triaxial series, section 5.2.6)).

All further experiments were carried out using specimens that were sawn from initial larger cubes (d = 150 mm). These specimens are encoded 7A-K1 through 7B-K3.

Specimen 7A-K1 also was loaded following the cylindrical rotation path. The 100 mm cube was sawn from the 150 mm cube under an inclination $\varphi = 30^{o}$ with the direction of initial damage (fig. 7.5).

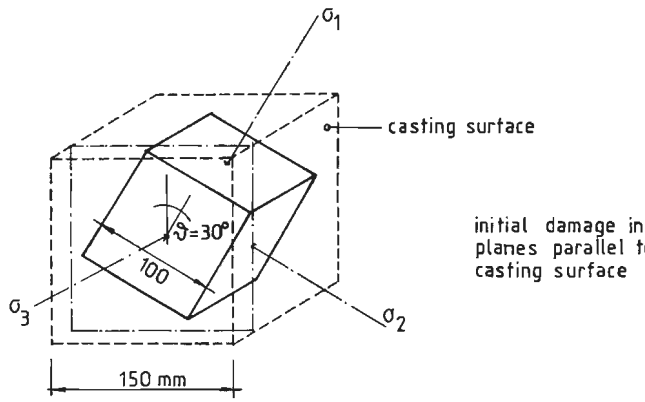

Fig. 7.5. Orientation of specimen 7A-K1, with regard to the direction of casting, and loading directions.

Specimen 7A-K2 was another control test, sawn under an inclination $\varphi = 0^{o}$ from the 150 mm cube and loaded monotonically to failure (loa.comb. $\sigma_1 < \sigma_2 = \sigma_3 = -1$ N/mm^2, $d(\Delta l_1) / dt$ = constant).

The four remaining specimens (7A-K3, 7B-K1 through 7B-K3) were pre-loaded in uniaxial compression using 150 mm brushes. Two of these larger brushes were available, the construction principle being similar as for the 100 mm brushes. (A 150 mm brush consists of 28 x 28 rods, $A_{lrod} = 5 \times 5$ mm^2, distance between rods $d_{rod} = 0.3$ mm and effective length $l_{rod} = 100$ mm, construction principle compare with fig. 3.11).

The 150 mm cubes were provided with four 60 mm strain gauges, mounted in the axial (loading) direction (one strain gauge in a middle position to each side surface), in order to check the uniformity of the deformations. The 150 mm cubes were always loaded parallel.

From the pre-cracked 150 mm samples, small (100 mm) cubes were sawn, and loaded according the cylindrical rotation path. Results are given for two of such rotation tests, indicated with the number of the original 150 mm cube, extended

with the additional number 2 (thus 7B-K22 and 7B-K32).
Specimen 7B-K22 was rotated over an angle $\varphi = 0^o$ (thus in fact no rotation), and 7B-K32 was rotated over $\varphi = 30^o$ and loaded similar as specimen 7A-K1 (see also fig. 7.5).

The deformation measurement was carried out, using the loading platen system (fig. 3.11), and was similar as for the triaxial series. No surface or strain-reader measurements, other than indicated above were carried out for the 150 mm cubes.

In appendix A7, the results of the rotation experiments are gathered. In table A7.1, the conditions at peak (σ_{ip} and ε_{ip}, i = 1, 2, 3) are given both before and after rotation. Each rotation experiment is shown in four figures, and one of the tests is explained in detail in the next section (specimen 7A1-3).

The uniaxial compressive strength of batch 7 was determined from the six control cylinders only and is indicated in table 3.25 ($f'_c = 43.2$ N/mm^2).
The six 150 mm control cubes were used for small angle rotations as mentioned before. The strength values of four of the pre-loadings are given also in table A7.1. The average uniaxial compressive strength obtained from 150 mm cubes loaded between brushes was equal to $\sigma'_{150mm} = -44.2$ N/mm^2, which is only slightly higher than the cylinder result.

7.2. Results of rotation experiments.

In this section the results of the rotation tests are shortly discussed. The results have a rather preliminary character, and no hard conclusions can be drawn at this moment. Yet the results provide a valuable extension to the previous reported triaxial experiments (see chapter 5), and can be used for purposes of constitutive modelling. In section 7.2.1, the response of a cylindrical mode rotation test is described. Further in section 7.2.2, the different response of planar and cylindrical mode experiments is indicated, and finally in 7.2.3 some comments are given regarding small angle ($0 < \varphi < 90^o$) rotations.

7.2.1. Response of a cylindrical mode rotation test.

In figure 7.6 a-d, the results of experiment 7A1-3 are shown. The specimen was loaded according the cylindrical mode rotation path (see fig 7.2 b), and the orientation of σ_1 was chosen perpendicular with regard to the direction of casting (σ_3 was oriented parallel).

In figure 7.6 a the $\sigma_1 - \varepsilon_1$ curve is shown. First loading leads to a maximum stress-level σ_{1p}, where after a smooth descending branch is measured. This was expected in view of the results of the triaxial experiments, series 8/9 (chapter 5). In the $\sigma_1 - \varepsilon_1$ curve descending branch, an additional unloading - reloading cycle was carried out, and after a short range in the descending branch, the specimen was unloaded in σ_1-direction to $\sigma_1 = -1$ N/mm^2 (indicated with rp = rotation point in fig. 7.6).

During the first loading in the σ_1-direction, the lateral stresses remain at a constant (low) level ($\sigma_2 = \sigma_3 = -1$ N/mm^2). The lateral strains are almost equal up to the rotation point (see fig. 7.6 d, strainpaths $\varepsilon_1 - \varepsilon_2$ and $\varepsilon_1 - \varepsilon_3$). In figure 7.6 b, ε_2 is plotted aganist the axial stress σ_1. Note that for this particular experiment, ε_2 is not completely irrecoverable as was observed in the triaxial cyclic experiments of series 8/9 in the minor compressive direction (see appendix A5, fig. A5.14 - A5.27).

Obviously the concrete specimen is partly restored to its original dimensions due to the "push back effect" of the constant lateral stress $\sigma_2 = -1$ N/mm^2. Larger macro defects, that develop in the $\sigma_1 - \varepsilon_1$ curve descending branch are oriented parallel to the σ_1-direction, and are partially closed due to the presence of the constant lateral confinement. In the triaxial cyclic experiments (series 8/9), this could not occur while σ_3, the minor compressive stress, always was unloaded proportional to the major compressive stress σ_1 (note: although the actual loading history may differ, the loading conditions of the macro-cracks may be compared!).

Now return to figure 7.6. In figure c, the lateral strain ε_3 is plotted against the stress σ_3, and before rotation, the $\sigma_3 - \varepsilon_3$ curve appears as a straight line parallel to the ε_3-axis. The maximum tensile strain in ε_3-direction is measured when the most remote point in the $\sigma_1 - \varepsilon_1$ curve descending branch is reached (that is of course before the rotation point).

When the rotation point is reached, the loading is stopped for some time (appr. 5 -10 min). During this interval, adjustments are made to the circuit of regulation in order to provide for loading in the σ_3-direction, using a displacement control $d(\Delta l_3) / dt$ = constant, while $\sigma_2 = \sigma_1$ are kept at a constant level (- 1 N/mm^2). When the loading direction was changed only small distortions in deformation measurement were observed. These deviations appear as small dimples in the stress-strain curves near the rotation point and can be neglected.

When loading proceeds in the σ_3-direction, again a peak stress-level is reached (σ_{3p}), whereafter a smooth descending branch is measured (see fig. 7.6 c, after the rotation point is exceeded). The $\sigma_3 - \varepsilon_3$ curve shows a considerable run

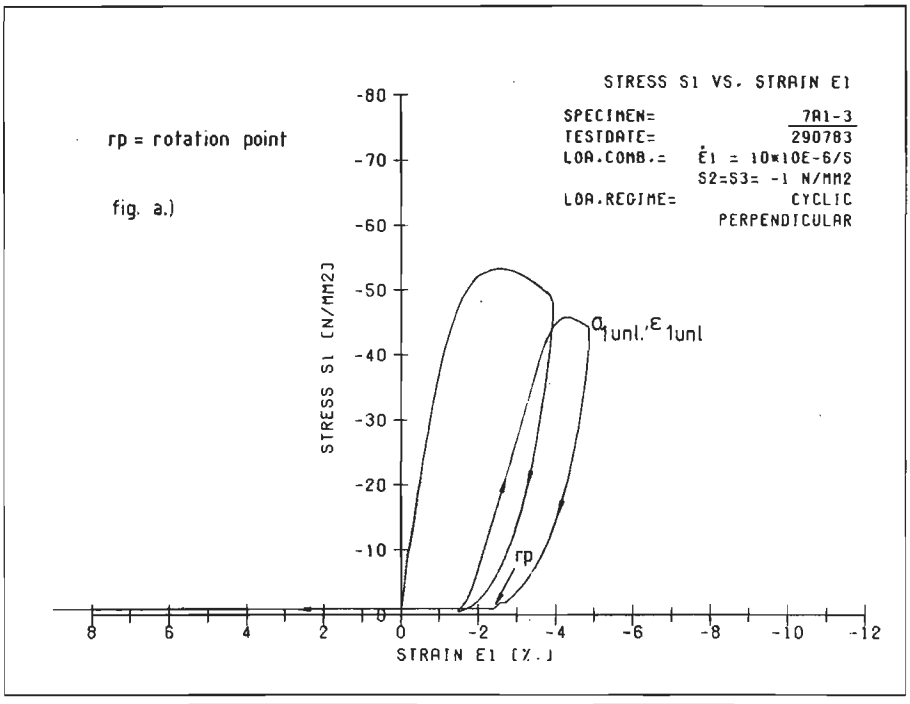

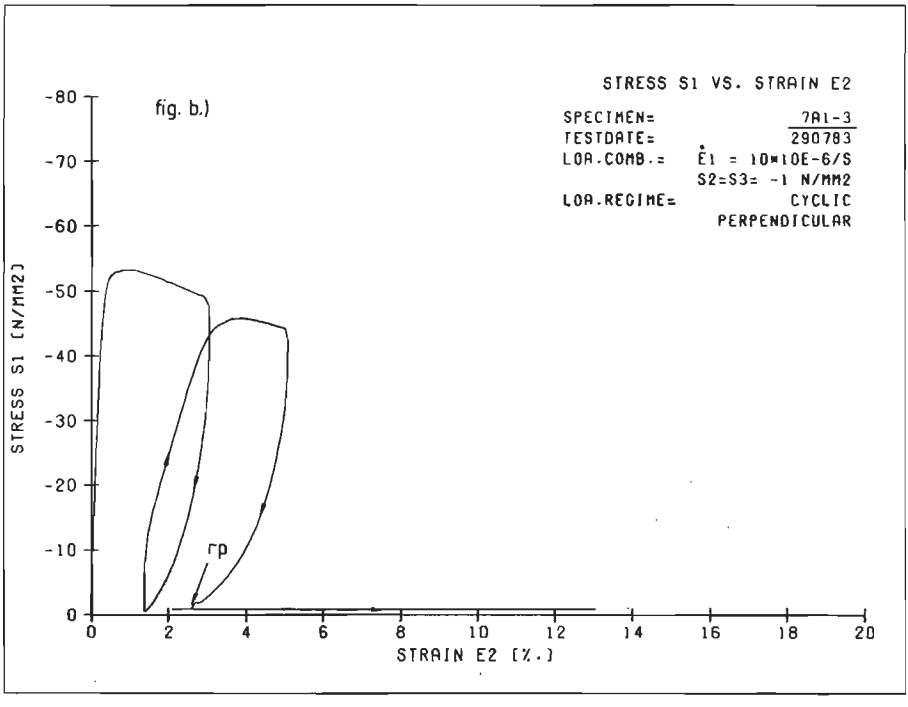

Fig.7.6 a. results of cylindrical rotation test 7A1-3, loa.dir. perpendicular, $\sigma_1 - \varepsilon_1$ curve.
b. idem, $\sigma_1 - \varepsilon_2$ curve.

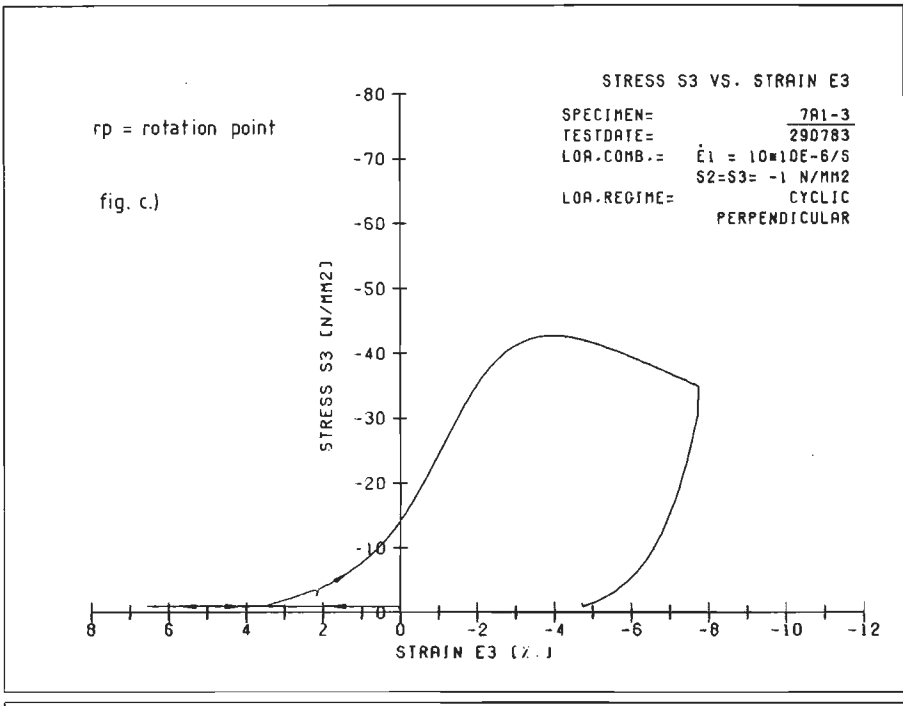

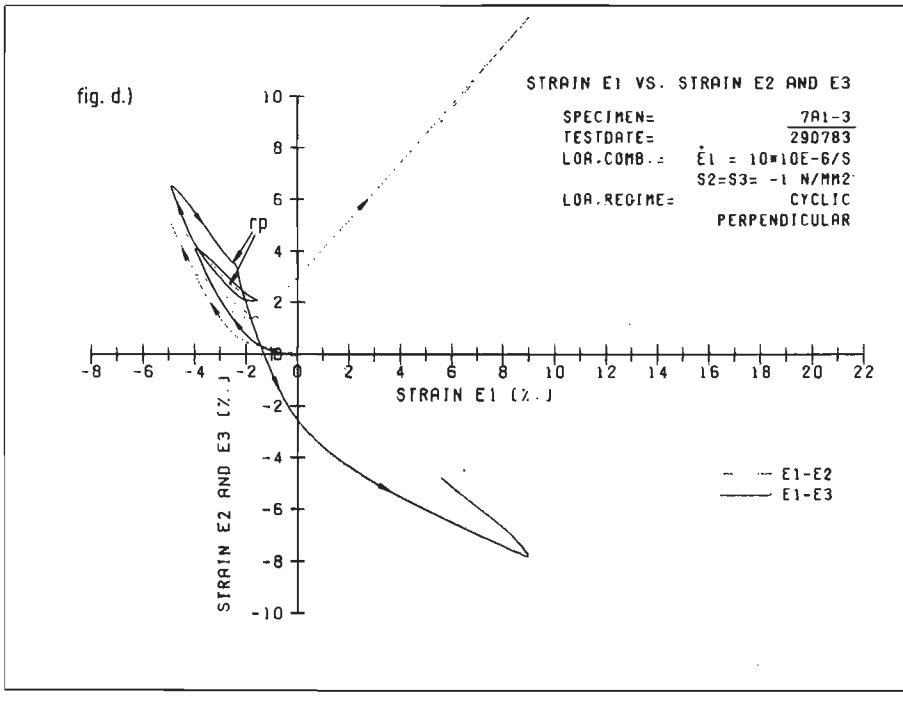

Fig.7.6 c. results of cylindrical rotation test 7A1-3, loa.dir. perpendicular, $\sigma_3 - \varepsilon_3$ curve.

d. idem, strainpaths $\varepsilon_1 - \varepsilon_2$ and $\varepsilon_1 - \varepsilon_3$.

before the peak level is reached. This is due to the fact that macro-cracks which are the result of the first loading sequence, and which are partly oriented in planes perpendicular to the σ_3-direction, must be closed again.
Probably the run in the σ_3 - ε_3 curve, before the inflection point is reached, can be used as a measure for the damage sustained to the specimen in the first loading sequence.
In both lateral directions, tensile strains are measured when loading proceeds in σ_3-direction. In the ε_1-direction the strain increment is instantaneously positive. In the ε_2-direction however, initially a small decrease is observed (viz. the small horizontal branch in the σ_1 - ε_2 curve in fig. 7.6.b, at the left side of the rotation point; see also strain path ε_1 - ε_2 in fig. 7.6.d), whereafter also a positive increment of ε_2 is measured.
The mechanism is evident from fig. 7.7. Poissons action v_{31}, due to the second loading in σ_3 direction ($\sigma_3 < \sigma_1 = \sigma_2$, compression), is not hindered by cracking due to the first loading, and will therefore increase immediately.

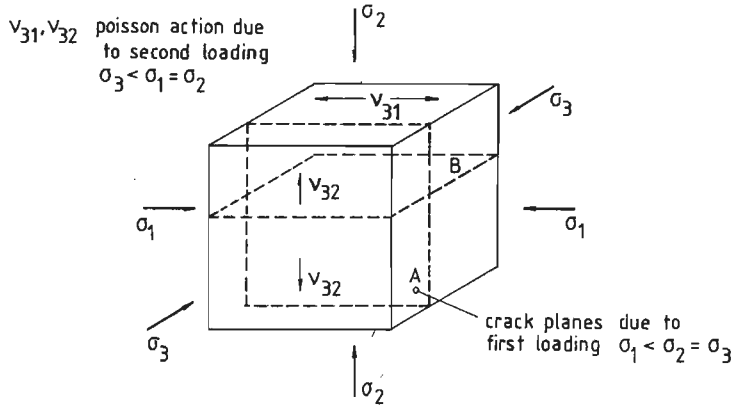

Fig. 7.7. Mechanism of Poissons action due to second loading in a cylindrical rotation test.

The rate of increase will grow with increasing contact area in crack planes A perpendicular to stress σ_3. On the other hand, Poisson action v_{32} is affected due to the presence of crack plane B, and macroscopic strain increase will only be observed when crack-planes B are closed.

From fig. 7.6.d it may be observed that the second stress-peak (i.e. $\sigma_{3,p}$) stays behind of the previous atained level in the σ_1-direction descending branch (that is the stress-level $\sigma_{1,unl}$, just before unloading to the rotation point). Thus it

seems that the carrying capacity after rotation is affected by cracking due to the first loading. This is no surprise when the orientations of the crackplanes B is considered (see fig. 7.7).

7.2.2. Comparison of 90^{o} planar and cylindrical rotation tests.

The major difference between the two types of rotation experiments is most clearly shown from a comparison between the major stress-strain curves before (σ_1 - ε_1 curve) and after rotation (σ_3 - ε_3 curve). In fig. 7.8.a-b, such a

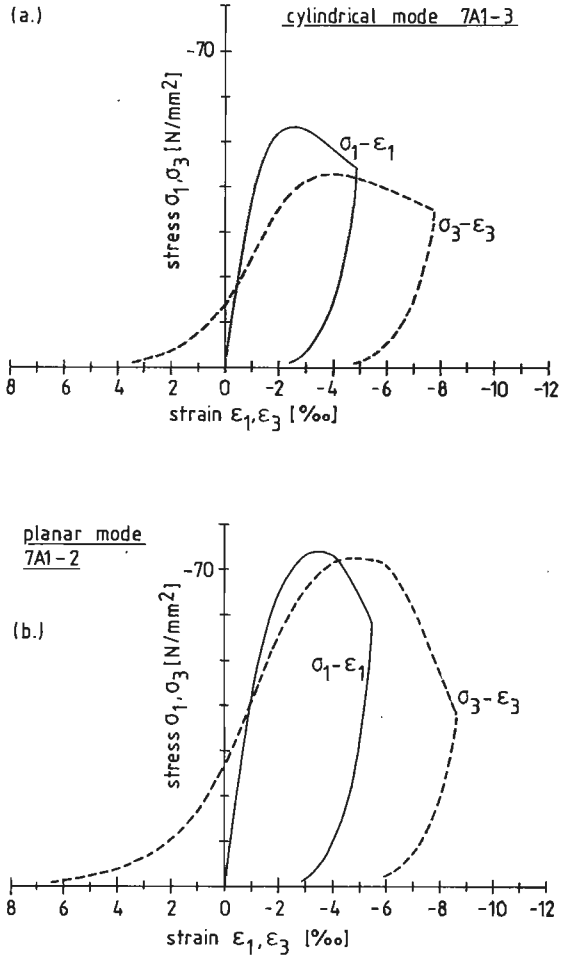

Fig.7.8. Response of 90^{o} cylindrical (fig. a, 7A1-3) and planar (fig. b, 7A1-2) rotation tests.

comparison is given for both planar and cylindrical experiments. In figure 7.8.a the σ_1 - ε_1 curve before rotation and the σ_3 - ε_3 curve after rotation are given in the same plot for specimen 7A1-3 (cylindrical mode). In figure 7.8.b a similar plot is given for a planar test (7A1-2, see also fig. A7.3).
Upon first loading, both specimens (7A1-3 and 7A1-2) were loaded perpendicular with regard to the direction of casting.

The most important difference between planar and cylindrical rotation tests is the peak stress level that may be reached after rotation (σ_{3p}). The cylindrical experiment (fig. 7.8.a) - as was also described in the previous section - shows a decreasing carrying capacity σ_{3p} upon rotation. The unloading stress $\sigma_{1,unl}$ in the first loading sequence (σ_1 - ε_1 curve descending branch) before the rotation point is not exceeded, and it seems as though the σ_3 - ε_3 curve joints the σ_1 - ε_1 curve descending branch. For all cylindrical rotation tests this type of behaviour was observed, as may be seen from the concerning graphs in the appendix (viz. fig. A7.4 through A7.7).
The planar rotation test (fig. 7.8.b) shows a distinct behaviour after rotation when compared with the cylindrical test. In σ_3-direction the same maximum stress level is reached as was measured in the first loading sequence.

The difference in strength response can be explained from the different rupture modes for the two types of rotation tests (see also section 5.2.4). In the planar experiments, cracks develop predominantly in planes perpendicular to the minor compressive direction as a result of the first loading sequence ($d(\Delta l_1) / dt = C$, $\sigma_2 = 0.5\,\sigma_1$, $\sigma_3 = -1$ N/mm^2).
When the major loading axis is rotated to the σ_3-direction, the previously developed cracks are in a very unfavourable direction for propagation. When it is assumed that linear elastic fracture mechanics concepts are valid, this fact may be obvious from figures 6.5 and 6.6 with $\beta = 90^0$. In principle the situation is similar for the case of a parallel loaded specimen with regard to initial damage. The only difference is the amount and width of cracking.

The phenomena also becomes clear when the concept of an ellipsoidal crack orientation distribution is adopted as a thought model. Upon first loading a prolate ellipsoid will develop with $N_{L3} > N_{L2} \approx N_{L1}$ (see also section 6.2). When the major compressive stress is rotated, the largest amount of cracks should be expected along N_{L1}. Thus eventually the case $N'_{L1} > N'_{L3} > N_{L2}$ will emerge. In the intermediate direction (σ_2) no large changes will occur. In the experiments a more or less elastic un- and reloading was observed. The amount

of cracks in σ_2 direction will thus not exceed the initial amount of cracks. It might be assumed that a considerable amount of energy is required to "rotate" the crack orientation ellipsoide, in order to obtain the required amount of cracks necessary for failure. The phenomenon is demonstrated in fig. 7.9.a.

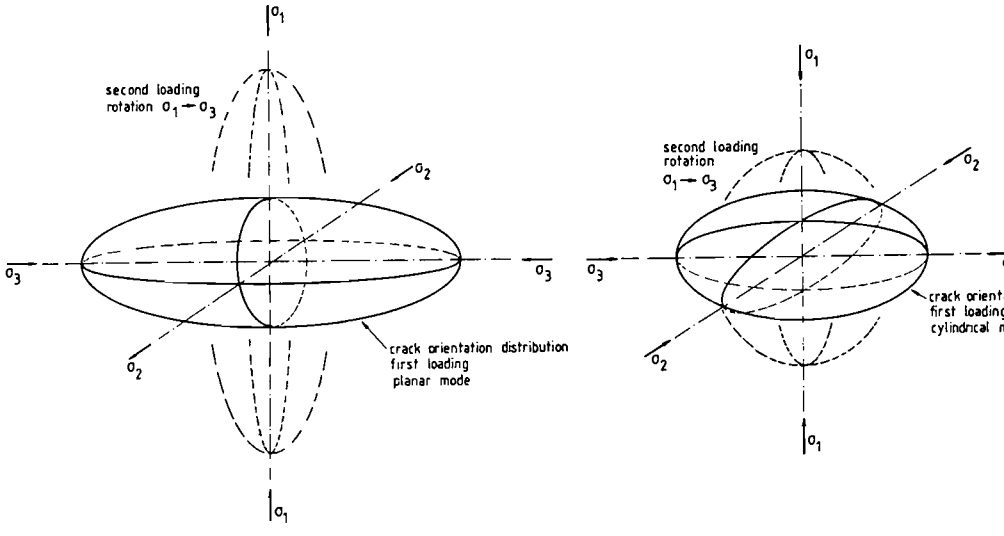

Fig.7.9 a. Hypothetical crack orientation distribution before and after rotation for a planar experiment.
b. idem for a cylindrical test

A similar line of reasoning may be followed for a cylindrical rotation experiment. Before rotation, the cracks may be assumed to be distributed according an oblate spheroidal distribution (fig. 7.9.b). Upon rotation, the required crack density for failure is present in σ_2-direction, and further extension is only necessary in the σ_1-direction.
In principle, also the orientation distribution of the initial damage may be taken into consideration. As was demonstrated in section 6.2 the orientation distribution is quite different in case of perpendicular or parallel loading with regard to the direction of casting.
The thought-model can in principle also be extended for small angle rotations ($0 < \varphi < 90^0$), as will be shown in the next section.

Remains a last result of the planar rotation tests to be shown. In figure 7.10 a-b, the tangential stiffness modulus of the subsequent loading curves is plotted against the major compressive strain both before and after rotation for specimen 7A1-6 (see also fig. A7.3).

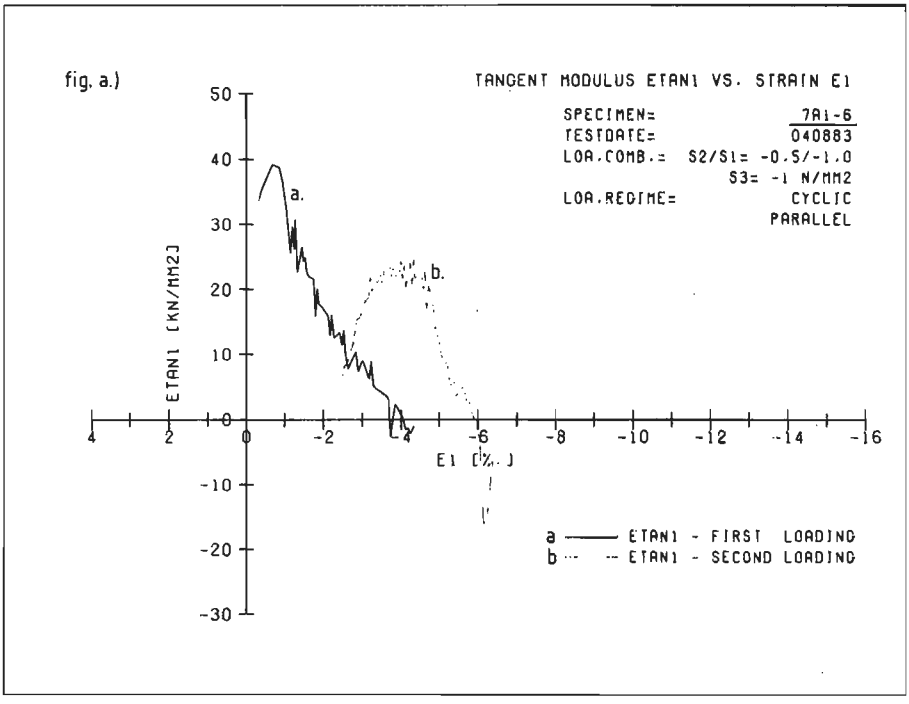

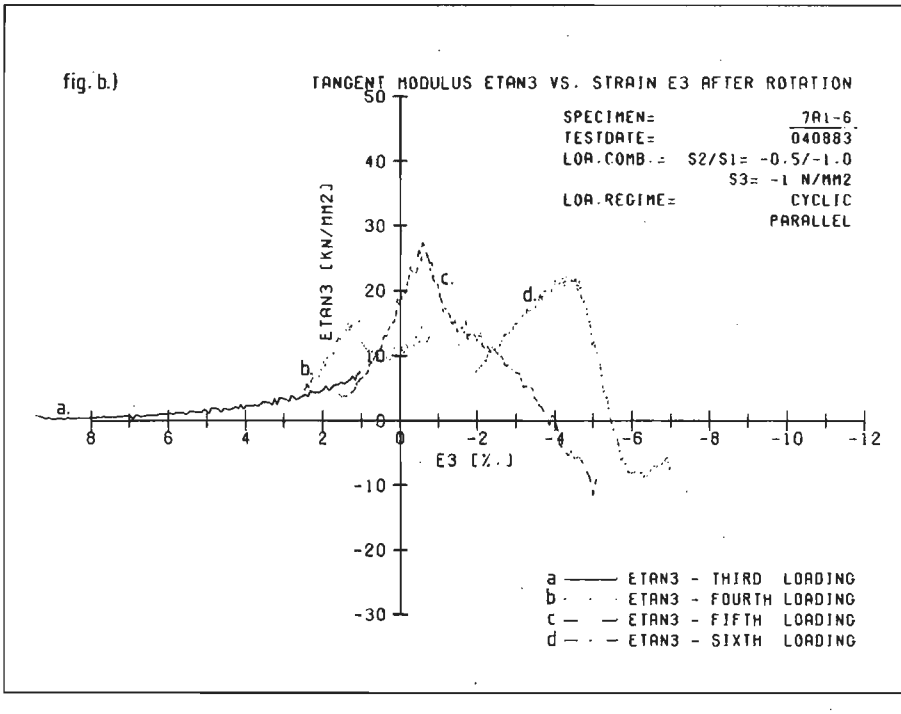

Fig.7.10 a. Tangential modulus $E_{tan,1}$ for loading curves before rotation, specimen 7A1-6, planar mode.

b. Idem, $E_{tan,3}$, after rotation.

In figure 7.10.a the tangential stiffness $E_{tan,1}$ is plotted against ε_1 for the two pre-rotation cycles (only loading curves). This result is in agreement with the observations from the cyclic triaxial tests in section 5.2.6. The 'true stiffness' decrease of the specimen is far less when compared with the stiffness determined from a monotonic test.
After rotation a similar response is measured as indicated in fig. 7.10.b for the four post-rotation cycles (loading curves, $E_{tan,3}$ - ε_3). Very apparent in this context is the maximum stiffness measured in cycle C after rotation. The strain ε_3 is compressive, thus it may be assumed that the cracks due to the first loading sequence are closed again. It seems that the 'true stiffness' $E_{tan,3}$ of the specimen is hardly influenced by the damage sustained due to the first loading sequence. In view of this result it is also no surprise that almost the same carrying capacity is measured after rotation.

7.2.3. Small angle rotations.

As was mentioned in the introduction to this chapter, small angle rotations ($0 < \varphi < 90^0$) are possible in the cubical machine following the pre-crack/saw method (see fig. 7.1.a). As may be seen from table 7.4, four specimens originating from initial larger cubes (d = 150 mm) were loaded in triaxial compression ($d(\Delta l_1) / dt = C$, $\sigma_2 = \sigma_3 = -1$ N/mm^2, respectively specimen 7A-K1, 7A-K2, 7B-K22 and 7B-K32).
Two of these 150 mm cubes were pre-loaded in uniaxial compression (i.e. cylindrical rupture mode) between large brushes (see section 7.1). Specimen 7B-K2 was loaded to 0.92 σ_{1p} in the descending branch and 7B-K3 was loaded to 0.62 σ_{1p}. Both specimens contained visible macro-cracks. From the pre-loaded specimens, 100 mm cubes were sawn carefully at orientations $\varphi = 30^0$ (7B-K32), see also fig. 7.5) and $\varphi = 0^0$ (7B-K22).
The sawing of the cracked specimens was a rather hazardous task. From some preliminary saw tests on cracked concrete, it was found that no additional damage was sustained to the specimen when it is only moderately loaded in the descending branch. The diamond saw was allowed to 'grind' smoothly through the material. The specimen was taped at both sides of the saw-cut during sawing.

The other two specimens (7A-K1 and 7A-K2) were not pre-cracked, but directly sawn to smaller cubes (respectively at orientations $\varphi = 30^0$ (7A-K1) and $\varphi = 0^0$ (7A-K2), with regard to the direction of initial damage planes).

Before the results of these experiments are shown, the crack orientation distribution concept is discussed in relation to small angle rotations.

Consider a two-dimensional crack orientation ellipse with semi-axes a and b, a b, as indicated in fig. 7.11.

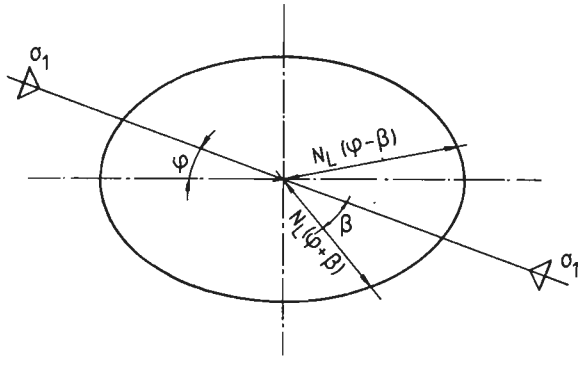

Fig. 7.11. Elliptical crack orientation distribution (2D-case).

A two dimensional case is shown for the sake of simplicity. A compressive stress σ_1 is applied to the material under an angle φ ($0 < \varphi < 90^o$) with the major ellipse axis. If $\varphi = 0$, and the ellipse reflects the initial damage orientation distribution, then the case of parallel loading is obtained. The case $\varphi = 90^o$ represents perpendicular loading with regard to the direction of casting (see also section 6.2).

In section 6.1, it was demonstrated that an inclined elliptical crack in a uniaxial compressive stress field, is in the most favourable direction for propagation when the angle of inclination is approximately 30^o (see fig. 6.5). Using figure 7.11 as a starting point, the number of cracks that are in a critical position for propagation (angle β) can be calculated for different values of φ, following

$$N_L = N_L(\varphi - \beta) + N_L(\varphi + \beta) \qquad .....(7.1),$$

where $N_L(\varphi - \beta)$ and $N_L(\varphi + \beta)$ represent the length of radii at $\vartheta = \varphi - \beta$ and $\vartheta = \varphi + \beta$, and are indicated in fig. 7.11.
The length of a radius at a certain angle ϑ is given by

$$N_L(\vartheta) = a/\sqrt{\cos^2\vartheta + (a^2/b^2).\sin^2\vartheta} \qquad .....(7.2).$$

In figure 7.12, results for the dimensionless value N_L/a are plotted for various φ and different aspect ratios a/b of the ellipse. The critical orientation of a single

defect is taken $\beta = 30^{o}$. When a/b = 1, the crack orientation distribution is random (isotropic case), and no critical orientation for φ is found.

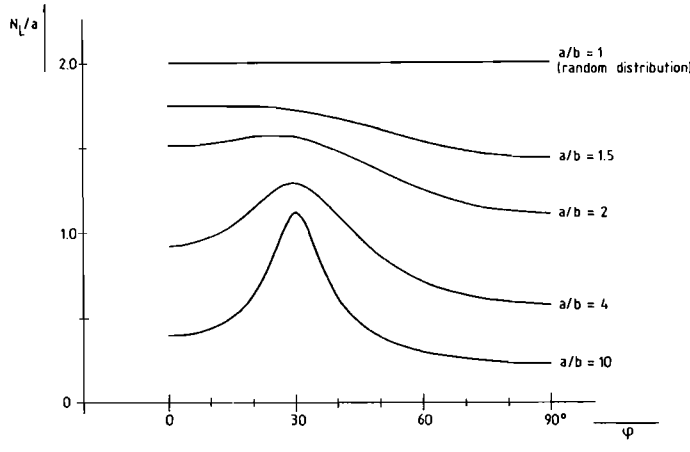

Fig.7.12 Number of critical oriented cracks N_L/a in a material body with an elliptical crack orientation distribution.

For small values of a/b (<2), a gradual decrease of critically oriented cracks is observed for increasing values of φ. The largest number of critical oriented cracks is calculated when $\varphi = 0^{o}$ (i.e. parallel loading in the case of initial anisotropy). Large values of N_L/a lead probably to an increasing curvature in the overall stress-strain curve ascending branch.
For more slender elliptical distributions, the critical orientation for σ_1 is equal to the critical orientation of a single micro-defect ($\beta = 30^{o}$). For other values of φ a fast decreasing number of critically oriented cracks is calculated.

The above reflections, only consider the tensile crack opening mode. For shear, in principle the same line of reasoning may be followed. In fact the shear loading is considered to be very important in triaxial compression.
In view of the discussion in chapter 6, the total number and orientation of isolated micro-cracks will mainly influence the stiffness of the specimen in the first part of the ascending stress-strain curve. At high stress-levels, the interaction between isolated micro-cracks will become important.
The size of the defects increases, and eventually will be close to the specimen size (i.e. finite dimensions of the material body).
It is suggested however that the crack orientation distribution concept also can be used in the case of localised fracture. A coupling between crack-size and

orientation must be derived.
It is emphasized that, in the case of initial anisotropy, the strength and deformational properties of the porous zones beneath the coarse aggregate particles should be taken into account too /74/.

In section 6.1, it was indicated that at failure, macro-cracks develop in a skew direction through an array of parallel micro-cracks (these macro-cracks are also referred to as shear-bands, see section 5.2.4). On basis of the observations from the triaxial compression tests (series 8/9), it is argued that when a large number of critically oriented cracks is present in the specimen, the conditions for development of a shear-band are fulfilled much earlier. It is hypothesized that in such a case a decreasing carrying capacity is measured.

Now consider some first test results. When the initial crack structure is rotated over an angle $\varphi = 30^{o}$ (specimen 7A-K1, see fig. A7.5 a-d), and the axial stress-strain curve $\sigma_1 - \varepsilon_1$ ($\sigma_2 = \sigma_3 = \text{const.} = -1\ N/mm^2$) is compared with the result of a monotonically parallel loaded specimen (7A-K2, see fig. 7.13 - 7.14), hardly no difference is observed.
The orientation distribution of the initially present micro-cracks will hardly deviate from a circular distribution (i.e. aspect ratio a/b is close to 1, when a 2-dimensional case is considered). In view of figure 7.12, indeed no large differences in response are expected for values a/b = 1 à 1.5.

In figure 7.13 and 7.14, the results of the two pre-cracked rotation tests (7B-K22 and 7B-K32) are compared with two parallel loaded cubes, following conventional loading paths (respectively 7A-K2, monotonic/parallel and 7A2-4, cyclic/parallel). In fig. 7.13 the axial stress-strain curves are shown for these four specimens, and in fig. 7.14 the strain-paths are shown (resp. $\varepsilon_1 - \varepsilon_2$ and $\varepsilon_1 - \varepsilon_3$).

Specimen 7B-K22 was in fact not rotated, and the load induced cracks due to the uniaxial pre-loading were kept parallel with the σ_1-direction. The 150 mm cube was pre-loaded to a stress-level $\sigma_1 = 0.92\ \sigma_{1p}$ in the descending branch.
The reloading shown in fig. 7.13, in triaxial compression shows a decreasing stiffness and a decreasing carrying capacity. The peak stress level for specimen 7B-K22 is approximately 90 % of the average peak stress of the specimens loaded according conventional paths (that is $\sigma_{1p} = -43.6\ N/mm^2$ for 7B-K22, and $\sigma_{1p} = -49.3\ N/mm^2$ for 7A2-4 and 7A-K2). Furthermore the descending branch of specimen 7B-K22 seems to join the descending branch of the conventional loaded samples (7A-K2 and 7A2-4).

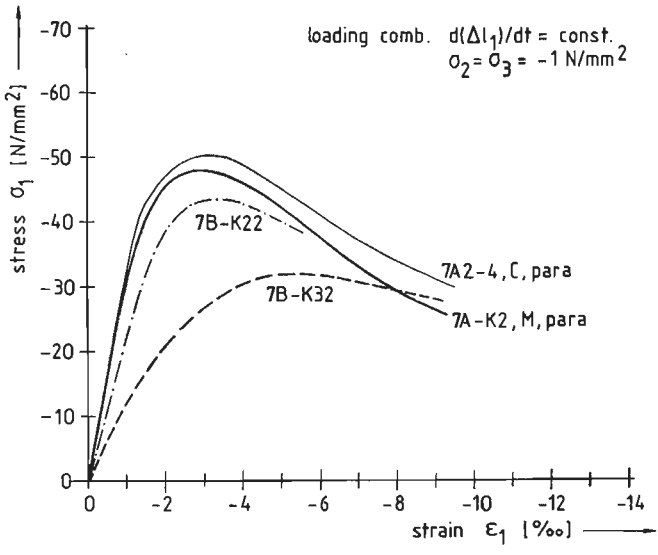

Fig.7.13 Axial stress-strain curves σ_1 - ε_1 for specimens 7B-K22 and 7B-K32 (both precracked) and 7A-K2 and 7A2-4.

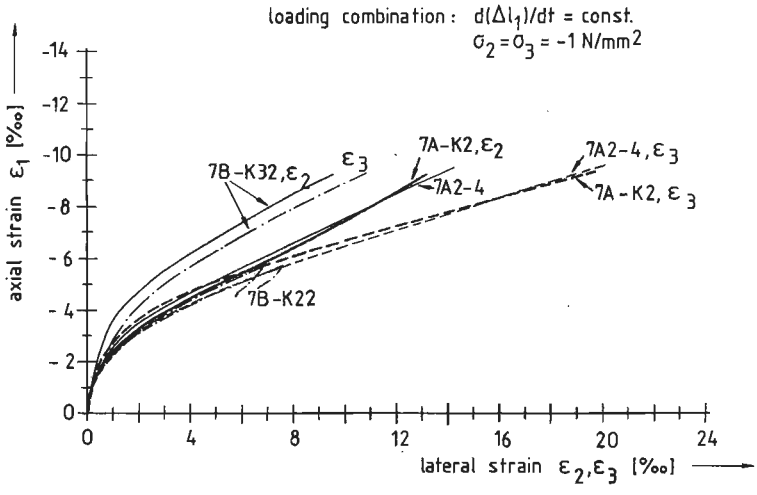

Fig.7.14 Lateral strains (ε_2 , ε_3) plotted against axial strain ε_1 for specimens 7B-K22, 7B-K32, 7A-K2 and 7A2-4.

The other pre-cracked specimen 7B-K32 was rotated before the second loading was applied ($\varphi = 30^{\circ}$, see also fig. 7.5). The uniaxial pre-loading was now up to 0.62 σ_{1p} in the descending branch.

The second loading shows an enormous decrease of initial stiffness (σ_1 - ε_1 curve) and a large decrease of load carrying capacity. Also for specimen 7B-K32 the descending branch seems to join the descending branch of the conventional tests.
Remarkable is that the peak stress-level, obtained in the second (now triaxial) loading is approximately 64% of the average peak stress of the conventional loaded samples (respectively σ_{1p} = - 31.9 N/mm^2 for 7B-K32, and σ_{1p} = - 49.3 N/mm^2 for the conventional loaded samples 7A-K2 and 7A2-4).

The results indicate that the previously obtained stress-level in the uniaxial pre-loading (that is the unloading stress in the descending branch) is again obtained in the triaxial re-loading, as a percentage of the strength obtained in conventional tests (monotonic loading or cyclic loading to the envelope curve).
The decreasing stiffness is in agreement with the results from the orientation distribution concept in fig. 7.12. The expected tendency for decreasing stiffness with increasing amount of critically oriented cracks is found in the tests (fig. 7.13). Yet, also the width of the present cracks will influence the stiffness of the material !

The results in fig. 7.13 and 7.14 indicate the replication of the triaxial experiments. Specimens 7A-K2 and 7A2-4 showed a remarkable little difference. Also when these results are compared with the σ_1 - ε_1 curves of 7A1-4 (fig. A7.4) and 7A-K1 (fig. A7.5) it is observed that the replication is satisfactory.
The strainpaths ε_1 - ε_2 and ε_1 - ε_3 can hardly be distinguished for tests 7A2-4 and 7A-K2. Although both specimens were loaded parallel, different lateral strains are measured. This may be due to the orientation of the cube in the experimental machine, and the influence of boundary shear (see section 5.2.4 and appendix A6). Yet it is also possible that by coincidence failure prevailed in the ε_3-direction which showed the largest deformations !

7.3. Final remarks.

It is emphasized that only some very first results are shown, and no hard conclusions can be drawn yet. The greatest care should be exersized in implementing these results in constitutive models. Many questions remain. First of all, in view of the uniaxial test results (failure starts at the outer layers, chapter 4), it is questionable to what extend the core of a uniaxial preloaded 150 mm cube is damaged. The rotated specimens are sawn from the central part.
In this context it would be preferable to use triaxially pre-loaded specimens, in

order to have a better control on fracture in pre-loading. Also by adopting uniaxial pre-loaded specimens we are confined to the cylindrical rupture mode. To my opinion more insight in the problem may be obtained using the planar fracture mode, which may be obtained from a triaxial pre-loading using 150 mm cubes.

A second problem involved in the rotation experiments is indicated in fig. 7.15. The application of non-rotatable 'rigid' loading platens is undesirable in the testing of anisotropic materials /59,118/.

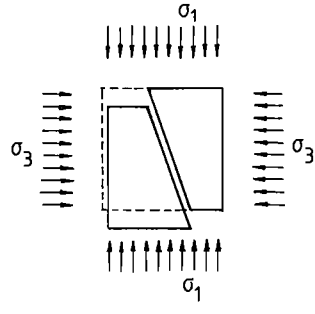

Fig.7.15 Shear failure in a jointed block system.

The brush bearing platens that are used in the current investigation impose plane boundary conditions to the specimen. An inclined anisotropic specimen is enforced to fail along an 'orthogonal' crack-pattern. Shear deformations are not allowed for. The type of deformations indicated in fig. 7.15 may be investigated by adopting fluid cushions as a load application system /83/.
Yet it remains questionable which boundary conditions apply for real structures. Therefore it seems appropriate to carry on along both lines (brushes and fluid cushions, or also other load application systems) in order to investigate the sensitivity of an inclined cracked concrete structure.
The tests presented herein may be used as a starting point.

8. RETROSPECTIVE VIEW AND CONCLUSIONS

The principal objective of this investigation was to extend the current knowledge about the strain-softening of concrete subjected to multiaxial loading histories. The introduction of numerical models for the analysis of reinforced concrete structures, has had a great impact on the development of constitutive equations; particularly, when the models take into account realistic material behaviour (triaxial non-linearity, cracking, etc.).
Few experiments have been done to confirm these models and no experimental data for strain-softening of concrete when subjected to multiaxial loading was available at the start of this investigation.

A triaxial apparatus for testing cubical specimens was developed and its construction was completed in 1981; thereafter, an extensive testing program was carried out. The triaxial apparatus was provided with a triple servo-control which made it possible to measure stable strain-softening under triaxial loading conditions. Loads were applied to the specimen by using brush-bearing platens which deforms the cube uniformly with reduced friction.
Emphasis was placed on measuring the deformation and the results obtained are presented in chapters 4, 5 and 7; they indicate the effectiveness of the triaxial apparatus.
Stress-strain results were obtained for only a medium strength concrete (uniaxial compressive strength obtained with 100 mm cubes loaded between brushes $f'_{k,100} \approx 45$ N/mm^2).

In a series of preliminary uniaxial compression tests, several factors were investigated relating to the method of making specimens. Initial anisotropy was observed in these tests. A significant increase of ductility in the axial stress-strain curve was found when the uniaxial loading was applied parallel to the direction of casting rather than perpendicular. Also the amount of lateral deformation varied. The uniaxial compression strength was not influenced by initial anisotropy.
Strength and deformation of the specimens depended upon where the cube had been sawn from the prism. Results were consistent for all the experiments.

In the uniaxial experiments, deformation was measured at the specimen's surface, as well as between the loading platens. When the overall strain-softening was measured, surface unloading was observed. Stress was widely redistributed throughout the specimen. The behaviour observed in the descending

branch of the stress-strain curve should be considered as a structural characteristic rather than a material property.

A number of uniaxial compression tests were performed on prisms of different slenderness-ratio ($0.5 \leq h/d \leq 2$, d= 100 mm) and they revealed that the amount of energy required for fracturing the specimen was independent of its size. A stress-displacement diagram seems preferable to a stress-strain diagram for describing the post-peak behaviour. The failure mechanism in uniaxial compression was obviously similar to tensile failure.

Stable strain-softening was measured under bi- and triaxial loading conditions too. Experiments were carried out mainly in the triaxial compression region, but only a limited number in the tension-biaxial compression region.
The triaxial experiments were replicated satisfactorily (see chapter 7 and fig. A5.42 to A5.46). Different load-paths were investigated and a detailed description of all the results was given in chapters 5 and 7. Here, only the general trends that were observed during triaxial fracture will be mentioned.

In the triaxial compression region, two different types of fracure could be distinguished: for stress-combinations near the compressive meridian ($\sigma_1 < \sigma_2 \approx \sigma_3$), fracture occurred, with a multitude of inclined planes. This type of fracture is referred to as cylindrical.
This type of failure shows a gradually descending branch of the stress-strain curve. Two large tensile deformations, not necessarily equal, result in a two-directional fracture.
The other type of fracture is planar and will be observed when failure occurs mainly in one direction. The inclined local shear-bands that are developed, pass through the plane of the major and minor compressions. The stress-strain curves in the major compressive direction show a steeply descending branch. In fig. 8.1, the types of fracture observed are shown, both for the uniaxial size tests and the triaxial compression experiments.

In the planar type of fracture (triaxial compression), the specimen disintregrates into a few relatively intact blocks that are separated by local shear-zones. This type of fracture is observed in triaxial compression tests on rock too, /16,17/. It can be concluded that both concrete and rock behave similarly when subjected to triaxial loading.
The local shear-band gives the impression that it develops after the material has been weakened by parallel micro-cracks.

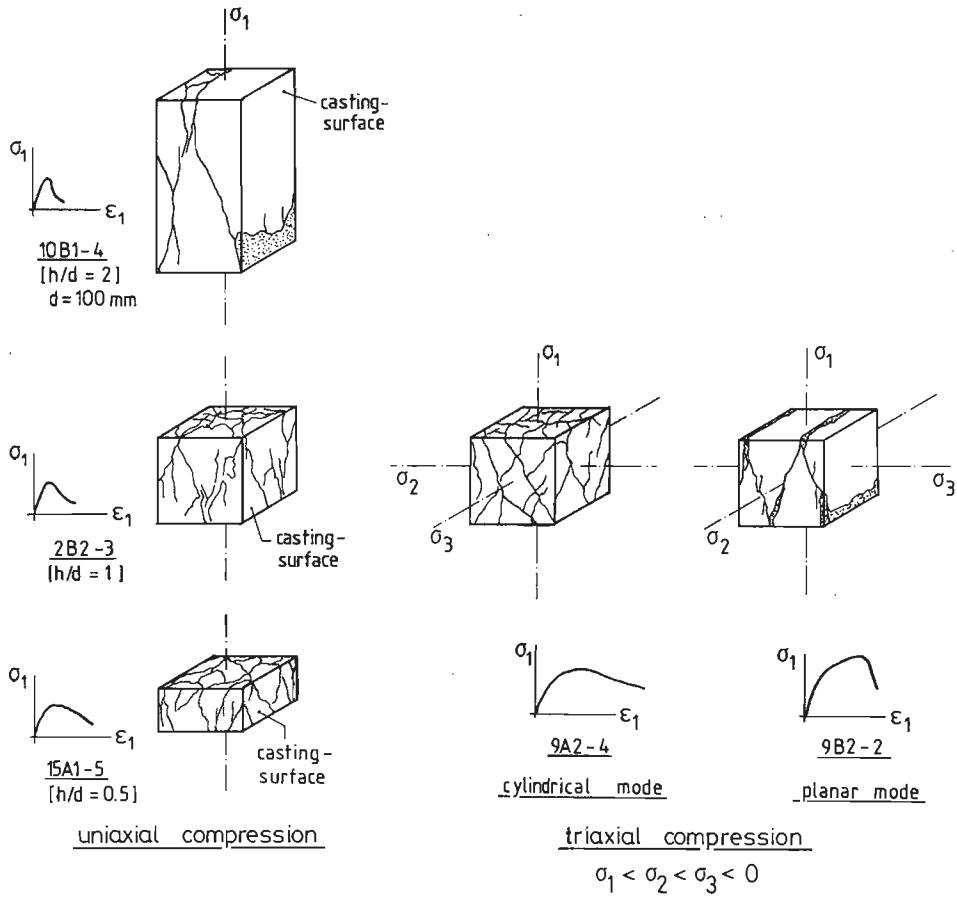

Fig. 8.1. Review of observed fracture modes in uni- and triaxial compression.

The cylindrical type of fracture can be measured in the standard triaxial cylinder tests, too. Recently, some results were reported for confined cylinder tests on micro-concrete, /79/ in which the cylinders were found to fail along a single inclined shear-band. The cubes in this investigation failed by forming many small 'rupture-elements', for which a size-effect, similar to the one reported for uniaxial compression (fig. 8.1), is responsible probably.

The slope of the descending branch of the stress-strain curve in a planar experiment was not influenced by the level of the minor compressive stress (i.e., for the confinements investigated, $\sigma_3 = \beta\sigma_1, \beta = 0$, 0.05 and 0.10). The descending branch of the stress-strain curve in the cylindrical experiments was greatly influenced by the level of lateral stresses.

Effects of initial anisotropy were observed in the triaxial experiments, similar to those reported for uniaxial compression.

In chapter 6, some theoretical models were discussed in relation to the experimental results that were obtained. A damage model, which takes into account internal structural changes such as the amount and orientation of defects was proposed. The size of the defects (cracks) with respect to the specimen's size is considered to be responsible for the decreased carrying capacity of the specimen in the descending branch. The conditions for stability in the descending branch require further investigation.

It should be emphasized that the model has not been developed yet for use in computer codes. In fact, only some first thoughts have been presented and much work is still needed.

The triaxial apparatus produces new accurate results; however, only a limited triaxial program has been carried out. It is hoped that the apparatus will continue to be used in the near future !

SAMENVATTING

In een uitgebreid experimenteel onderzoek is aandacht besteed aan 'strain-softening' van beton onder meerassige spanningstoestanden.
Het toenemende complexe karakter van bouwconstructies is de oorzaak van de toenemende vraag naar gedetailleerde en fundamentele kennis van het materiaal beton. Ongetwijfeld heeft de introductie van niet-lineaire berekeningsmethoden op basis van de eindige elementen methode een grote invloed op de ontwikkeling van constitutieve vergelijkingen. Het voorspellen van bezwijkcondities van driedimensionale gewapend beton constructies wordt mogelijk indien meer kennis beschikbaar komt omtrent het bezwijkmechanisme van beton onder meerassige spanningstoestanden.

Een drieassige kubusmachine werd ontworpen en gebouwd. Het meten van een stabiele dalende tak in het spannings-vervormingsdiagram (dat wil zeggen gecontroleerd bezwijken) werd bereikt met behulp van een drievoudige servo-control in combinatie met stijve belastingframes. Toepassing van de welbekende borstelpakketten leidde tot een praktisch wrijvingsloze invoer van belasting (uniform verplaatsingsveld).

In een uitgebreid vooronderzoek met behulp van eenassig gedrukte kubussen werd de invloed van een aantal met de vervaardigingsmethode van de proefstukken samenhangende parameters onderzocht (reproduceerbaarheid, stortrichting en posities). Eveneens werd nauwkeurig de invloed van het belastingssysteem onderzocht.
Uit een aantal eenassige drukproeven op prisma's met variabele hoogte kon worden geconcludeerd dat een constante hoeveelheid breukenergie nodig is bij het bezwijken, onafhankelijk van de proefstukhoogte.

Drieassige proefresultaten zijn nu verkregen voor één betonkwaliteit. Een grote verscheidenheid van belastingpaden werd onderzocht in het drieassige drukgebied en het trek-druk-druk gebied.
In het drieassige drukgebied bezwijkt een proefstuk onder de vorming van een aantal min of meer ongescheurde reststukken gescheiden door schuifvlakken. De indruk is, dat deze schuifvlakken zich ontwikkelen door een 'array' van oorspronkelijk evenwijdige trekscheurtjes. De afmetingen van de reststukken bleek afhankelijk te zijn van de opgelegde spanningstoestand (en zoals bleek uit de eenassige proeven op prisma's ook van de proefstukafmetingen). De invloed van de stortrichting werd eveneens gemeten onder drieassige spanningstoestanden.

Met behulp van verschillende belastingpaden kan kennis worden verkregen omtrent voortschrijdende beschadiging in het proefstuk. Dergelijke proeven zijn van belang voor het ontwikkelen van een op 'damage' gebaseerd constitutief model. In het laatste deel van dit proefschrift worden enkele facetten van dergelijke modellen besproken. Belangrijk bij de ontwikkeling van een beschadigingsmodel zijn onder andere de oriëntatieverdeling en de afmetingen van (micro)scheuren. De afmeting van de scheuren ten opzichte van de proefstukafmetingen wordt verantwoordelijk geacht voor de afnemende draagcapaciteit van het proefstuk in de dalende tak. De condities waarbij de dalende tak stabiel blijft, zijn hierbij van belang en vragen nader onderzoek.

REFERENCES

1. Ahmad, S.H. - Shah, S.P., "Complete triaxial stress-strain curves for concrete". Journal of the Structural Division, proceedings of ASCE, vol. 108, no. ST.4 , April 1982, pp. 728-742.

2. Alexander, K.M. -Wardlaw, J. - Gilbert, D.J., "Aggregate-cement bond, cement paste strength and the strength of concrete", Proceedings of the international Conference on the structure of concrete, London, September 1965, Cement & Concrete Association, 1968, session 3, pp. 59-81.

3. Andenaes, E. - Gerstle, K. - Ko, H.Y., "Response of Mortar and Concrete to biaxial Compression", Journal of the Engineering Mechanics Division, proc. of ASCE, vol. 103, no. EM.4., August 1977, pp. 515-526.

4. Aschl, H. - Linse, D. - Stöckl, S., "Versuche zum verhalten von Beton under mehrachsiger beanspruchung", Report, Technische Universität München, May 1976.

5. Bazant, Z.P., "Instability, Ductility, and size effect in Strain-Softening Concrete", Journal of the Engineering Mechanics Division, Proc. ASCE, vol. 102, no. EM 2, April 1976, pp. 331-344.

6. Bazant, Z.P. - Kim, S.S., "Plastic fracturing Theory for Concrete", Journal of the Engineering Mechanics Division, proc. of the ASCE, vol. 105, no. EM3, June 1979, pp. 407-428.

7. Bazant, Z.P., Oh, B.H., "Crack band theory for fracture of concrete", RILEM, Materials and Structures, vol. 16, no. 93, 1983, pp. 155-177.

8. Bazant, Z.P., "Comment on orthotropic models for concrete and geomaterials", Journal of Engineering Mechanics, proc. ASCE, vol. 109, June 1983, no. 3, pp. 849-865.

9. Bazant, Z.P. - Gambarova, P.G., "Crack shear in concrete crack band microplane model", Report no. 83-9/679c, Center for Concrete and Geomaterials, The Technological Institute, Northwestern University, May 1983, pp. 34.

10. Bazant, Z.P. - Oh, B.H., "Model of weak planes for progressive fracture of concrete and rock", Report nr. 83-2/448m, Center for Concrete and Geomaterials, The Technological Institute, Northwestern University, February 1983, pp. 34.

11. Bazant, Z.P., "Size effect in blunt fracture: Concrete, Rock, Metal", Journal of Engineering Mechanics, proc. ASCE, vol. 110, no. 4, April 1984, pp. 518-535.

12. Beams, G.W. - Gerstle, K.H. - Ko, H.J., "Response of concrete to cyclic biaxial compressive loads", Preprint 82-015, ASCE National Convention, Las Vegas, Nevada, April 1982.

13. Beres, L., "Investigation on structural loosening of compressed concrete", RILEM-bulletin, no. 36, 1967, pp. 185-190.

14. Bertacchi, P. - Bellotti, R., "Experimental Research on deformation and failure of concrete under triaxial loads", RILEM-Symposium on "the deformation and the rupture of solids subjected to multiaxial stresses", Cannes 1972, part I, "Concrete", pp. 37-52, paper I/3.

15. Bićanić, N. - Sture, S. - Hurlbut, B. - Day, S., "On the prediction of the peak and post-peak behavior of concrete structures", paper presented at the Int. Conf. on Computer Aided Analysis and Design of Concrete Structures, Split, Yugoslavia, Sept. 17-21, 1984.

16. Bieniawski, Z.I., "Mechanism of brittle fracture of rock", part I, II and III, Int. J. Rock Mech. Min. Sci., vol. 4, pp. 395-430, 1967.

17. Bieniawski, Z.I., Denkhaus, H.G., Vogler, U.W., "Failure of fractured rock", Int. J. Rock Mech. Min. Sci, vol. 6, (1969), pp. 323-341.

18. Blaauwendraad, J. - Leijten, S.F.C.H. - Van Mier, J.G.M., "Comparison of plastic prediction with STANIL/1 Analysis", IABSE Colloquium on "Plasticity in Reinforced Concrete", Copenhagen 1979, pp. 247-254.

19. De Borst, R. - Kusters, G.M.A. - Nauta, P. - De Witte, F.C., "DIANA: a three-dimensional, nonlinear finite element package on a micro-computer", in "Engineering Software for Micro-computers" (eds. B.A. Schrefler, R.W. Lewis and S.A. Odonizzi), Pineridge Press, Swansea, U.K., 1984, p. 435.

20. Broek, D., "Elementary Engineering Fracture Mechanics", Martinus Nijhoff Publishers, 1982, 3rd revised edition.

21. Budianski, B., "On the Elastic Moduli of some Heterogeneous Materials", Journal of Mechanics and Physics of Solids, vol. 13, 1965, pp. 223-227.

22. Budianski, B. - O'Connell, R.J., "Elastic Moduli of a cracked solid", International Journal of Solids & Structures, vol. 12, 1976, pp. 81-97.

23. Buyukozturk, O. - Zisman, J.G., "Behavior of concrete in biaxial cyclic compression", research paper, Massachusetts Institute of Technology, 1982.

24. Buyukozturk, O. - Tseng, T.M., "Behavior of concrete in biaxial cyclic compression", research paper, Massachusetts Institute of Technology, 1983, p. 39.

25. Buyokozturk, O. - Nilson, A.H. - Slate, F.O., "Deformation and fracture of particulate composite", Journal of the Engineering Mechanics Division, Proc. ASCE, no. EM.3, June 1972, pp. 581-593.

26. Carrasquillo, R.L. - Slate, F.O. - Nilson, A.H., "Micro-cracking and behavior of high strength concrete subject to short term loading", ACI-Journal, title no. 78-15, pp. 179-186, May-June 1981.

27. Carrasquillo, R.L. - Nilson, A.H. - Slate, F.O., "Properties of high strength Concrete Subject to short term loads", ACI-Journal, May-June 1981, pp. 171-178, .

28. Chen, E.S., - Buyukozturk, O., "Damage models for concrete in multiaxial cyclic stress", research paper, Massachusets Institute of Technology, 1983.

29. Chen, W.F. - Saleeb, A.T., "Constitutive equations for engineering materials", vol. 1, Elasticity and modelling, Wiley & Sons, 1982.

30. Chen, A.C.T. - Chen, W.F., "Constitutive Relations for Concrete", Journal of the Engineering Mechanics Division of the ASCE, EM4, vol. 101, Aug, 1975, pp. 465-481.

31. Clayton, N., "Concrete in Context", RILEM-CEB Symposium "Concrete under multiaxial conditions", INSA Toulouse, 1984, session 2, testing methods, volume 1, pp. 31-40.

32. Cleary, M.P. - Chen, I.W. - Lee, S.M., "Self consistent techniques for heterogeneous media", Journal of the eng. mech. div, proc. ASCE, vol. 106, no. EM.5, October 1980, pp. 861-887.

33. Cleary, M.P., "Elastic and Dynamic Response Regimes of Fluid Impregnated Solids with Diverse Microstructures", Int. Journal of Solids Struct., vol. 14, 1978, pp. 795-819.

34. Cochran, W.G. - Cox, G.M., "Experimental Designs", John Wiley & Sons, inc. New York, 2nd edition, 1957,

35. Collins, M.P. - Vecchio, F. - Mehlhorn, G., "An international competition to predict the response of reinforced concrete panels", in "Festschrift prof. D. Bruno Thürlimann zum 60 Geburtstag", ETH Zürich, 1983, pp. 471-491.

36. CUR-VB rapport 108, "plastische scharnieren", Zoetermeer, september 1982 ('plastic hinges', in Dutch).

37. Darwin, D. - Attiogbe, E.K., "Load Induced Cracks in Cement Paste", paper presented at the Fourth Engineering Mechanics Division Speciality Conference, ASCE, Purdue University, West Lafayette, Indiana, May 23-25, 1983, vol. II, pp. 1051-1054.

38. Desayi, P. - Viswanatha, C.S., "True ultimate strength of plain concrete", RILEM-bulletin, no. 36, September 1967, pp. 163-173.

39. Diaz, S. - Hilsdorf, H.K., "Fracture mechanisms of concrete under compressive loads", Cement and Concrete Research, vol. 3, pp. 363-388, 1973.

40. Dougill, J.W., "On stable progressively Fracturing Solids", Zeitschrift für Angewandte Mathematik und Physik, vol. 27, Fasc. 4, 1976, pp. 423-437.

41. Dougill, J.W. - Rida, M.A.M., "Further Consideration of Progressively Fracturing Solids", Journal of the Engineering Mechanics Division, Proceedings of the ASCE, vol. 106, no. EM5, October 1980, paper 15764, pp. 1021-1038.

42. Dougill, J.W., "Constitutive Relations for Concrete and Rock: applications and extensions of elasticity and plasticity theory", Preprints, William Prager Symposium on "Mechanics of Geomaterials: Rocks, Concretes, Soils", Ed. by Z.P. Bazant, Northwestern University, Evanston (Ill.), 1983, pp. 17-54.

43. Drucker, D.C., "Thoughts on the Present and Future Interrelation of Theoretical and Experimental Mechanics", Experimental Mechanics, March 1968, pp. 97-106.

44. Eibl, J., "Application and Experimental Verification of Advanced Mechanics in Reinforced Concrete", IABSE-Colloquium, "Advanced Mechanics of Reinforced Concrete", Delft, Introductory Report, 1981, pp. 135-156.

45. Erdei, C.K., "A new load-transmitting medium to measure strength of brittle materials", Journal of Testing And Evaluation, JTEVA, vol. 7, no. 6, November 1979, pp. 317-325.

46. Erdei, C.K., "Finite element analysis and tests with a new load-transmitting medium to measure compressive strength of brittle materials", RILEM, Materials & Structures, vol. 13, no. 74, 1980, pp. 83 - 90.

47. Evans, R.H. - Marathe, H.S., "Microcracking and stress-strain curves for concrete in tension", RILEM, Materiaux et Constructions, no. 1, Janvier/-Fevrier 1968, pp. 61-64.

48. Fonseka, G.K. - Krajcinovic, D., "The continuous Damage Theory of Brittle Materials", part 2: Uniaxial and Plane Response Modes, Journal of Applied Mechanics, Transactions of the ASME, vol. 48, Dec. 1981, pp. 816-824.

49. Forrester, J.A., Discussion: Propagation of cracks and their detection under short- and long-term loading, Proc. Int. Conf. on "The Structure of Concrete", ed. Brooks, A.E., Newman, K., C & C. Ass. 1968.

50. Freudenthal, A.M., "The inelastic Behavior of Engineering Materials and Structures", John Wiley & Sons, 1950.

51. Gerstle, K.H. et.al., "Strength of concrete under multiaxial stress states", Douglas Mc.Henry International Symposium on Concrete and Concrete Structures, Publication Sp55-5, pp. 103-131, 1978. American Concrete Institute, Detroit.

52. Gerstle, K.H. et.al., "Behavior of Concrete under Multiaxial Stress States". Journal of the Engineering Mechanics Division, Proceedings of the ASCE, vol. 106, no. EM6, December 1980, pp. 1383-1403.

53. Glücklich, J., "Fracture of plain concrete", Journal of the Engineering Mechanics Division, Proceedings of the ASCE, December 1963, pp. 127-138.

54. Grimer, F.J. - Hewitt, R.E., "The form of the stress-strain curve of concrete interpreted with a diphase concept of material behaviour", Proceedings of the Southampton Civil Eng. Mat. Conf. on "Structure, Solid Mechanics and Engineering Design", 1969, Te'eni, M. editor, Wiley Interscience 1971, pp. 681-691.

55. Groot, A.K. de - Kusters, G.M.A. - Monnier, Th., "Concrete Mechanics, part B - Numerical modelling of bond-slip behaviour", HERON, vol. 26, no. 1b, 1981.

56. Grootenboer, H.J., "Finite element analysis of two-dimensional reinforced concrete structures, taking account of non-linear physical behaviour and the development of discrete cracks", dissertation, Delft University of Technology, 1979.

57. Grootenboer, H.J. - Leijten, S.F.C.H. - Blaauwendraad, J., "Concrete Mechanics, part. C - Numerical models for reinforced concrete structures in plane stress", HERON, vol. 26, no. 1C, 1981.

58. Grudemo, A., "Microcracks, Fracture mechanism, and strength of the cement paste matrix", Cement and Concrete Research, vol. 9, 1979, pp. 19-34.

59. Halpin, J.C. - Pagano, N.J., "Observations on Linear Anisotropic Viscoelasticity", Journal of Composite Materials, vol. 2, no. 1., January 1968, pp. 68-80.

60. Hansen, T.C., "Theories of multi-phase materials applied to concrete, cement mortar and cement paste", Proceedings of an international conference on "The structure of Concrete", London, September 1965, Session A: "Concrete as a composite material", pp. 16-23.

61. Heyne, K.H., "Uber den Einfluss der Endflächenreibung bei versuchen im echten Triaxialgerät", Zeitschrift für angewandte Geologie, Bd. 28, (1982), Heft 9, pp. 446-453.

62. Hill, R., "A self-consistent Mechanics of Composite Materials", Journal of Mechanics and Physics of Solids, vol. 13, 1965, pp. 213-222.

63. Hillerborg, A. - Modéer, M. - Peterson, P.E., "Analysis of crack formation and crack growth in concrete by means of fracture mechanics and finite elements", Cement and Concrete Research, vol. 6, 1976, pp. 773-782.

64. Hillerborg, A., "Examples of practical results achieved by means of the fictitious crack model", Preprints William Prager Symposium on Mechanics of Geomaterials: Rocks Concretes, Soils, ed. by Z.P. Bazant, Northwestern University, September 11-15, 1983, pp. 611-614.

65. Hilsdorf, H. "Die bestimmung der Zweiachsiger Festigkeit des Betons", Deutscher Ausschuss für Stahlbeton, Heft 173, Berlin 1965.

66. Hobbs, D.W., "Strength of concrete under combined stress", Cement & Concrete Research, vol. 1, pp. 41-56, 1971.

67. Hobbs, D.W., "The strength and deformation properties of plain concrete under combined stresses", RILEM-Symposium on "the deformation and the rupture of solids subjected to multiaxial stresses", Cannes 1972, Part I, "Concrete", pp. 97-111, paper I/7.

68. Hoenig, A., "Elastic moduli of a non-randomly cracked body", International Journal of Solids and Structures, vol. 15, 1979, pp. 137-154.

69. Hoenig, A., "The behavior of a flat elliptical crack in an anisotropic elastic body", International Journal of Solids and Structures, vol. 14, pp. 925-934, 1978.

70. Hognestad, E. - Hanson, N.W. - Mc.Henry, D., "Concrete stress distribution in Ultimate Strength design", Journal of the American Concrete Institute, Proceedings , vol. 52, title 52-28, December 1955, pp. 455-479.

71. Hsu, T.T.C. et.al., "Microcracking of plain concrete and the shape of the stress-strain curve", ACI-Journal, February 1963, title 60-14, pp. 209-224.

72. Hughes, B.P. - Chapman, G.P., "The complete stress-strain curve for concrete in direct tension", RILEM-bulletin, no. 30, 1966, pp. 95-97.

73. Hughes, B.P. - Chapman, G.P., "The deformation of concrete and micro-concrete in compression and tension with particular reference to aggregate size", Magazine of Concrete Research, vol. 18, no. 54, March 1966, pp. 19-24.

74. Hughes, B.P. - Ash, J.E., "Anisotropy and failure criteria for concrete", RILEM, Materials and Structures, vol. 3, no. 18, 1970, pp, 371-374.

75. Ichikawa, Y.et.al., "Brittle-ductile fracture of a tuffaceous rock and plasticity theory", in "Constitutive laws for Engineering Materials", ed. Desai, C.S., Gallagher, G.H., Tuscon (Az), 10 - 14 January 1983, pp. 349-355.

76. Ingraffea, A.R., "Fracture propagation in Rock", Preprints, William Prager Symposium on "Mechanics of Geomaterials: Rocks, Concretes, Soils", Ed. by Z.P. Bazant, Northwestern University, Evanston (Ill.), 1983, pp. 227-279.

77. Iqbal, M.A. - Krokosky, E.M., "Interaction stresses in composite systems", Journal of the eng.mech. division, proc. ASCE, vol. 96, no. EM 6, December 1970, pp. 825-845.

78. Isenberg, J., "Properties of concrete change when micro-cracking occurs", in "Causes, Mechanism and Control of cracking in concrete, ACI-Special Publication, SP. 20, 1968, pp. 29-41.

79. Jamet, P. - Millard, A. - Nahas, G., "Triaxial behaviour of a micro-concrete complete stress-strain curves for confining pressures ranging from 0 to 100 MPa", RILEM-CEB Symposium on "Concrete under multiaxial conditions", INSA Toulouse, 1984, session 4, experimental results, vol. 1, pp. 133-140.

80. Janson, J. - Hult, J., "Fracture mechanics and damage mechanics a combined approach", Journal de Mécanique Appliquée, vol. 1, no. 1, 1977, pp. 69-84.

81. Karsan, I.D. - Jirsa, J.O., "Behavior of Concrete under Compressive Loadings", Journal of the Structural Division, proc. of ASCE, vol. 95, no. ST12, December 1969, paper 6935, pp. 2543-2563.

82. Kassir, M.K. - Sih, G.C., "Mechanics of fracture 2: Three dimensional crack problems", Noordhoff International Publishing, Leyden, 1975.

83. Ko, H.Y. - Sture, S., "Three-dimensional Mechanical Characterization of Anisotropic Composites", Journal of Composite Materials, vol. 8, April 1974, pp. 178-190.

84. Kobayashi, S. - Koyanagi, W., "Fracture criteria of cement paste, mortar and concrete subjected to multiaxial compressive stresses", RILEM-Symposium, Cannes 1972, "the deformation and the rupture of solids subjected to multiaxial stresses, Part I, "Concrete", pp. 131-148, paper I/9.

85. Kotsovos, M.D. -Newman, J.B., "Behavior of concrete under multiaxial stress", ACI-Journal, September 1977, pp. 443-446.

86. Kotsovos, M.D., "Effect of stress path on the behavior of concrete under triaxial stress states", ACI-Journal, February 1979, pp. 213-223.

87. Kotsovos, M.D., "Effect of testing techniques on the post-ultimate behaviour of concrete in compression", Materials & Structures, RILEM, vol. 16, no. 91, January/February 1983, pp 3-12.

88. Kotsovos, M.D., "A fundamental explanation of the behaviour of reinforced concrete beams in flexure based on the properties of concrete under multiaxial stress", Materials & Structures, RILEM, vol. 15, no. 90, November-December 1982, pp. 529-537.

89. Kotsovos, M.D., "Deformation and failure of concrete in a structure", RILEM-CEB Symposium on "Concrete under multiaxial conditions", INSA Toulouse, 1984, session 4, experimental results, volume 1, pp. 104-113.

90. Krajcinovic, P. - Fonseka, G.K., "The Continuous Damage Theory of Brittle Materials", part I: General theory, Journal of Applied Mechanics, Transactions of the ASME, vol. 48, Dec. 1981, pp. 809-815.

91. Krishnaswamy, K.T., "Strength and microcracking of plain concrete under triaxial compression", ACI-Journal, October 1968, pp. 856-862.

92. Kupfer, H., "Das Verhalten des Betons unter mehrachsiger Kurzzeitbelastung unter besonderer Berücksichtigung der zweiachsiger Beanspruchung", Deutscher Ausschuss für Stahlbeton, Heft 229, Teil I, Berlin 1973.

93. Launay, P. - Gachon, H. - Poitevin, P., "Déformation et Résistance ultime du béton sous étreinte triaxiale", Annales de l'institut technique du Bâtiment et des Travaux Publics, Mai 1970, no. 269, pp. 23-48.

94. Launay, P. - Gachon, H., "Strain and ultimate strength of concrete under triaxial stress", Proceedings of the First International Conference on Structural Mechanics in Reactor Technology, Berlin, September 1971, paper H 1/3, pp. 23-34.

95. Linse, D., "Lösung Versuchstechnischer Fragen bei der Ermittlung des Festigkeits und Verformungs verhaltens von Beton unter Dreiachsiger Belastung", Deutscher Ausschuss für Stahlbeton, Heft 292, Berlin 1978.

96. Liu, T.C.Y. - Nilson, A.H. - Slate, F.O., "Stress-strain response and fracture of concrete in uniaxial and biaxial compression", ACI-Journal, May 1972, title no. 69-31, pp. 291-295.

97. Løland, K.E., "Continuous Damage Model for load-response estimation of concrete", Cement and Concrete Research, vol. 10, pp. 395-402, 1980.

98. Lowe, P.G., "Deformation and fracture of plain concrete", Magazine of concrete research, vol. 30, no. 105, December 1978, pp. 200-204.

99. Maher, A. - Darwin, D., "Mortar Constituent of Concrete in Compression", ACI-Journal, title no. 79-11, March-April 1982, pp. 100-109.

100. Mazars, J., "Mechanical damage and fracture of concrete structures", Advances in Fracture Research, 5th Int. Conf. Fracture, Cannes 1981, vol. 4, pp. 1499-1506.

101. Mazars, J., "Description du comportement multiaxial du beton par un modele de materiau elastique endomageable", RILEM-CEB Symposium on "Concrete under multiaxial conditions", INSA Toulouse, 1984, session 6, parameters for constitutive modeling, vol. 1, pp. 190-200.

102. Mendenhall, W., "Introduction to linear models and the Design and Analysis of Experiments", Wadsworth, 1968.

103. Mier, J.G.M. van, "Multiaxial behaviour of concrete - test methods and results", Survey of litterature, Report Eindhoven University of Technology, pp. 129, June 1981 (in Dutch).

104. Mier, J.G.M. van, "Complete stress-strain behaviour and damaging status of concrete under multiaxial conditions", RILEM-CEB Symposium on "Concrete under multiaxial conditions", INSA Toulouse, 1984, session 3, experimental results, volume 1, pp. 75-85.

105. Mihashi, H. - Wittmann, F.H., "Stochastic approach to study the influence of rate of loading on strength of concrete", Heron, Volume 25, 1980, nr. 3.

106. Mills, L.L. - Zimmermann, R.M., "Compressive strength of plain concrete under multiaxial loading conditions", ACI-Journal, October 1970, pp. 802-807.

107. Mindess, S. - Diamond, S., "A preliminary SEM Study of crack propagation in mortar", Cement & Concrete research, vol. 10, 1980, pp. 509-519.

108. Moavenzadeh, F. - Kuguel, R., "Fracture of Concrete", Journal of Materials, vol. 4, no. 3, 1969, pp. 497-519.

109. Müller, R.K., "Der Einfluss der Messlänge auf die Ergebnisse bei Dehnmessungen an Beton", Beton nr. 5, 1964, pp. 204-208.

110. Mura, T., "Micromechanics of Defects in Solids", Martinus Nijhoff publishers, 1981.

111. Nelissen, L.J.M., "Biaxial testing of normal concrete", Heron, vol. 18, 1972, no. 1.

112. Newman, J.B. - Newman, K., "The cracking and failure of concrete under combined stresses and its implications for structural design", RILEM-Symposium on "the deformation and the rupture of solids subjected to multiaxial stresses", part I, "Concrete", Cannes 1972, paper I/10, pp. 149-168.

113. Newman, J.B., "Concrete under complex stress", Developments in Concrete Technology - 1, ed. by F.D. Lydon, Applied Science Publishers ltd., London 1979, pp. 151-220.

114. Newman, K. - Sigvaldason, O.T., "Testing machine and specimen characteristics and their effect on the mode of deformation, failure and strength of materials", Proc. Inst. Mech. Engrs, 1965-1966, vol. 180, part 3A, pp. 399-410.

115. Newman, K. - Lachance, L. - Loveday, W.W., "Strain measurements on saturated concrete specimens", Magazine of Concrete Research, vol. 15, no. 45, November 1963, pp. 143-150.

116. O'Connell, R.J. - Budiansky, B., "Seismic velocities in dry and saturated cracked solids", Journal of Geophysical Research, vol. 79, no. 35, December 1974, pp. 5412-5426.

117. Ottosen, N.S., "Evaluation of concrete cylinder tests using finite elements", Journal of engineering mechanics, vol. 110, no. 3, March 1984, pp. 465-481.

118. Pagano, N.J. - Halpin, J.C., "Influence of End Constraint in the testing of Anisotropic Bodies", Journal of Composite Materials, vol. 2, no. 1, January 1968, pp. 18-31.

119. Palaniswamy, R. - Shah, S.P., "Fracture and stress-strain relationship of concrete under triaxial compression", Journal of the Structural Division of the ASCE, ST5, 1974, pp. 901-916.

120. Paul, B., "Macroscopic criteria for plastic flow and brittle fracture", in Liebowitz, H. (ed.), Fracture an advanced treatise 2, Academic Press, New York, 1968, pp. 313-491.

121. Perlman, A.B. - Sih, G.C., "Elastostatic problems of Curvilinear cracks in bonded dissimilar materials", Int. Journal of Engineering Science, vol. 5, 1967, pp. 845-867.

122. Peterson, P.E., "Fracture energy of concrete: method of determination", Cement and Concrete Research, vol. 10, 1980, pp. 78-89.

123. Peterson, P.E., "Fracture energy of concrete: practical performance and experimental results", Cement and Concrete Research, vol. 10, 1980, pp. 91-100.

124. Pietruszczak, St. - Mróz, Z., "Finite element analysis of deformation of strain-softening materials", Int. Jou. Num. Meth. Engng. vol. 17, 1981, pp. 327-334.

125. Popovics, S., "A numerical approach to the complete stress-strain curve of concrete", Cement & Concrete Research, vol. 3, 1973, pp. 583-599.

126. Rasch, C., "Spannungs-Dehnungs Linien des Betons und Spannungsverteilung in der Biegedruckzone bei konstanter Dehngeschwindigkeit", Deutscher Ausschuss für Stahlbeton, Heft 154, Berlin 1962.

127. Read, J.B., discussion on an article by Newman, K. et.al. on "Strain measurements on saturated concrete specimens", Magazine of Concrete Research, vol. 16, no. 49, December 1964, pp. 243-244.

128. Reinhardt, H.W., "Ansprüche des Konstrukteurs an den Beton, hinsichtlich Festigkeit und Verformung", Beton 5/1977, pp. 195-199.

129. Reinhardt, H.W. - Cornelissen, H.A.W., "Post-peak cyclic behaviour of concrete in uniaxial tensile and alternating tensile and compressive loading", Cement & Concrete Research, vol. 14, (1984), no. 2, pp. 263 - 270.

130. Reinhardt, H.W., "Fracture mechanics of an elastic softening material like concrete", HERON, Vol. 29, no. 2, 1984.

131. Roy, H.E.H. - Sozen, M.A., "Ductility of Concrete", ACI-Special Publication SP 12, "Flexural Mechanics of Reinforced Concrete", Miami 1964, pp. 213-235.

132. Rüsch, H., "Researches toward a General Flexural Theory for Structural Concrete", Journal of the American Concrete Institute, proceedings 57-1, pp. 1-28, July 1960.

133. Sargin, M., "Stress-strain Relationships for concrete and the Analysis of Structural Concrete Sections", Solid Mechanics Division, University of Waterloo, Waterloo, Ontario, Canada, studies-series no. 4, 1971.

134. Saouma, V.E. - Ingraffea, A.R., "Fracture Mechanics Analysis of discrete cracking", IABSE Colloquium on "Advanced Mechanics of Reinforced Concrete", Delft, 1981, pp. 413-436.

135. Scavuzzo, R. - Cornelius, H.V. - Gerstle, K.H. - Ko, H.Y. - Stankowski, T., "Simple formulation of concrete response to multiaxial load cycles", Int. Conf. on "Constitutive laws for Engineering Materials", ed. Desai, C.S., Gallagher, G.H., Tuscon (Az.), 10-14 Jan. 1983, pp. 421-426.

136. Scavuzzo, R. - Stankowski, T. - Gerstle, K.H. - Ko, H.Y., "Stress-strain curves for concrete under multiaxial load histories", Research report, Dept. of Civil, Env. and Arch. Eng., University of Colorado, Boulder, August 1983.

137. Schickert, G., "On the influence of different load application techniques on the lateral strain and fracture of concrete specimens", Cement & Concrete Research, vol. 3, pp. 487-494, 1973.

138. Schickert, G. - Winkler, H., "Versuchsergebnisse zur Festigkeit und Verformung von Beton bei mehraxialer Druckbeanspruchung", Deutscher Ausschuss für Stahlbeton, Heft 277, Berlin 1977.

139. Schickert, G., "Schwellenwerte beim Betondruckversuch", Dissertation T.U. Berlin, November 1979, Deutscher Ausschuss für Stahlbeton, Heft 312, Berlin 1980.

140. Schleeh, W., "Die Spannungszustände in den Versuchs-körpern zur Ermittlung der Betondruck-festigkeit", Beton und Stahlbetonbau, 8/1975, pp. 194-201.

141. Shah, S.P. - Chandra, S., "Critical stress, volume change, and microcracking of concrete", Journal of the American Concrete Institute, September 1968, title 65-57, pp. 770-781.

142. Shah, S.P. - Slate, F.O., "Internal microcracking, mortar-aggregate bond and the stress-strain curve of concrete", Proceedings of the International Conference on "the structure of concrete", London 1965, Cement & Concrete Association, 1968, pp. 82-92.

143. Shah, S.P. - Chandra, S., "Fracture of concrete subjected to Cyclic and Sustained Loading", ACI-Journal, October 1970, pp. 816-825.

144. Shah, S.P. - Mc. Garry, F.J., "Griffith fracture criterion and concrete", Journal of the engineering mechanics division, Proc. ASCE, vol. EM.6, Dec. 1971, pp. 1663-1676.

145. Sinha, B.P. - Gerstle, K.H. - Tulin, C.G., "Stress-strain Relations for concrete under cyclic loading", ACI-Journal, vol. 61, February 1964, no. 2, pp. 195-210.

146. Slate, F.O. - Olsefski, S., "X-rays for study of Internal Structure and microcracking of concrete", Journal of the ACI, title no. 60-31, May 1963, pp. 575-588.

147. Soshiroda, T., "Anisotropy of concrete", International Conference on Mechanics Behaviour of Materials, Japan, Kyoto, 1971.

148. Spooner, D.C. - Dougill, J.W.,"A quantitative assessment of damage sustained in concrete during compressive loading", Magazine of Concrete Research, vol. 27, no. 92, September 1975, pp. 151-160.

149. Spooner, D.C. - Pomeroy, C.D. - Dougill, J.W., "Damage and energy dissipation in cement pastes in compression", Magazine of Concrete Research, vol. 28, no. 94, March 1976, pp. 21-29.

150. Stankowski, T., - Gerstle, K.H., "Simple Formulation of Concrete Behaviour under Multiaxial Load Histories", paper submitted for publication in Journal ACI, Sept. 1983.

151. Stöckl, S., "Das Unterschiedliche Verformungsverhalten der Rand- und Kernzonen von Beton", Deutscher Ausschuss für Stahlbeton, Heft 185, Berlin 1966.

152. Stroeven, P., "Some aspects of the micromechanics of Concrete", Dissertation, Delft, 1973.

153. Stroeven, P., "Geometric probability approach to the examination of microcracking in plain concrete", Journal of Materials Science, 14 (1979), pp. 1141-1151.

154. Sture, S. - Ko, H.Y., "Strain-softening of brittle geologic materials", Int. Journ. Num. Anal. Methods in Geo. Mech. vol. 2, 1978, pp. 237-253.

155. Sture, S. - Desai, C.S., "Fluid Cushion Truly Triaxial or Multiaxial Testing Device", Geotechnical Testing Journal, GTJODJ, vol. 2, March 1979, pp. 20-33.

156. Sturman, G.M. - Shah, S.P. - Winter, G., "Effects of flexural strain gradients on micro-cracking and stress-strain behaviour of concrete". Journal of the ACI, July 1965, title no. 62-50, pp. 805-822.

157. Suaris, W. - Shah, S.P., "Rate sensitive damage theory for brittle solids", Journal of Engineering Mechanics, ASCE, vol. 110, no. 6, June 1984, pp. 985-997.

158. Taylor, M.A. - Broms, B.B., "Shear Bond Strength Between Coarse Aggregate and Cement Paste or Mortar", ACI-Journal, August 1964, pp. 939-957.

159. Timoshenko, S.P. - Goodier, J.N., "Theory of elasticity", 3rd edition Mc Graw - Hill, 1970.

160. Traina, L.A., "Experimental stress-strain behavior of a low strength concrete under multiaxial states of stress", Report AFWL-TR-82-92, Air Force Weapons Laboratory, January 1983.

161. Vile, G.W.D., "The strength of concrete under short-term static biaxial stress", Proceedings of the International Conference on the structure of concrete, London, 1965, Cement and Concrete Association, London, 1968, pp. 275-288.

162. Walraven, J.C., "Aggregate Interlock: A theoretical and experimental analysis", dissertation, Delft University of Technology, 1980.

163. Walraven, J.C. - Reinhardt, H.W., "Concrete Mechanics, part A - Theory and experiments on the mechanical behaviour of cracks in plain and reinforced concrete subjected to shear loading", HERON, vol. 26, no. 1A. 1981.

164. Walsh, J.B., "The effect of cracks in Rocks on Poisson's Ratio", Journal of Geophysical Research, vol. 70, October 15, 1965, no. 20, pp. 5249-5257.

165. Wang, P.T. - Shah, S.P. - Naaman, A.E., "Stress-strain curves of normal and lightweight concrete in compression", ACI-Journal, November 1978, pp. 603-611.

166. Weigler, H. - Becker. G., "Untersuchungen über das Bruch- und Verformungsverhalten von Beton bei zweiachsiger Beanspruchung", Deutscher Ausschuss für Stahlbeton. Heft 157, Berlin, 1963.

167. Willam, K.J., "Experimental and Computational Aspects of Concrete Fracture", Invited paper, presented at Int. Conf. on Computer Aided Analysis and Design of Concrete Structures, Split, Yugoslavia, Sept. 17-21, 1984.

168. Winkler, H., "Fundamental investigations on the influence of test-equipment on multiaxial test results of concrete", RILEM-CEB Symposium on "Concrete under multiaxial conditions", INSA Toulouse, 1984, session 2, testing methods, volume 1, pp. 9-19.

169. Wittmann, F.H., "Creep and Shrinkage Mechanisms", chapter 6 in "Creep and Shrinkage in Concrete Structures", ed. by Z.P. Bazant and F.H. Wittmann, Wiley, 1982.

170. Zaitsev, J.B. - Wittmann, F.H., "Simulation of crack propagation and failure of concrete", RILEM, Matériaux et Constructions, vol. 14, no. 83, Sept.-Oct. 1981, pp. 357-365.

171. Zielinski, A.J., "Fracture of concrete and mortar under uniaxial impact tensile loading", dissertation, Delft University of Technology, 1982.

APPENDICES page

A1.	Uniaxial test results, series 2 and 3	245
A2.	Uniaxial results, series 10 and 15	253
A3.	Calculation of pre-loading for constant displacement-ratio tests	261
A4.	Biaxial experimental results (series 5 - 6)	263
A5.	Triaxial experimental results (series 8 - 9)	268
A6.	Boundary shear due to bending of brush-rods	330
A7.	Results of rotation tests (series 7)	335

specimen no.		testdate	loading-direction	σ_{1p} (N/mm^2)	ε_{1p} ($^o/oo$)	$\varepsilon_{1p}^{(surf)}$ ($^o/oo$)	ε_{2p} ($^o/oo$)	ε_{3p} ($^o/oo$)	W (Joule)[4] peak	0.006	0.007	
2A 1 -	1	060482	perp.	-35.55	-2.41	-	1.02	1.13	60.0	148.4	161.4	
	2	070482	"	-33.63	-2.05	-	0.63	0.64	45.5	135.3	146.7	
	3	050482	"	-31.16	-1.91	-	0.95	0.84	39.0	118.0	128.1	
	4	050482	para.	-33.14	-1.97	-	0.99	0.98	47.1	144.3	157.9	
	5	050482	"	-34.37	-	-	-	-	-	-	-	1)
	6	070482	"	-35.86	-2.26	-	0.51	0.84	55.3	154.8	168.7	
2A 2 -	1	070482	perp.	-36.58	-2.25	-	1.18	0.86	57.2	151.9	165.0	
	2	060482	"	-35.60	-2.34	-	1.31	1.16	57.8	150.0	163.6	
	3	070482	"	-35.08	-2.10	-	0.77	0.84	49.2	143.3	155.9	
	4	060482	para.	-33.07	-2.03	-	0.93	0.68	45.8	151.9	165.0	
	5	070482	"	-	-	-	-	-	-	-	-	2)
	6	060482	"	-36.36	-2.40	-	1.00	0.92	61.9	157.1	170.9	
2B 1 -	1	060482	perp.	-41.72	-2.50	-	1.08	1.10	72.6	176.1	191.0	
	2	060482	"	-39.15	-2.27	-	0.57	0.63	60.6	157.5	170.1	
	3	060482	"	-39.59	-2.40	-	1.17	1.02	65.4	157.7	170.1	
	4	060482	para.	-39.35	-2.53	-	0.85	1.00	69.7	175.0	191.3	
	5	070481	"	-40.21	-2.43	-	1.24	1.31	66.8	171.8	186.1	
	6	070482	"	-41.34	-2.43	-	1.01	0.78	69.1	181.8	197.7	
2B 2 -	1	130482	perp.	-39.64	-	-	-	-	-	-	-	3)
	2	140482	"	-42.04	-2.26	-2.31	1.11	1.11	67.7	166.9	-	
	3	140482	"	-41.29	-2.09	-1.90	0.69	0.69	58.9	166.8	178.7	
	4	150482	para.	-42.27	-2.73	-2.20	1.05	1.05	80.3	184.9	-	
	5	150482	"	-42.12	-2.69	-2.15	1.18	1.18	79.2	186.8	-	
	6	130482	"	-41.83	-2.69	-2.34	1.25	1.25	79.1	185.8	201.1	

1) fault in measuring system
2) malfunction of spherical seating
3) excentric loaded
4) energy requirement at peak-stress-level, 0.006 strain and 0.007 strain

Table A1.1. Experimental results, series 2A/2B

Appendix A1

specimen no.		testdate	loading direction	σ_{1p} (N/mm^2)	ε_{1p} (‰)	$\varepsilon_{1p}^{(surf)}$ [3] (‰)	ε_{2p} (‰)	ε_{3p} (‰)	$\varepsilon_{2p}^{(surf)}$ (‰)	W (Joule)[4] peak	0.006	0.007
3A 1 -	1	280482	perp.	-38.71	-2.10	-1.83	0.88	1.06	- 1)	51.9	131.2	141.5
	2	280482	"	-39.42	-1.92	-1.78	0.62	1.03	-	48.4	142.8	154.1
	3	280482	"	-38.09	-1.90	-1.61	0.85	1.06	-	45.5	136.7	146.8
	4	290482	para.	-38.49	-2.20	-1.84	1.07	0.89	-	53.9	154.5	167.9
	5	290482	"	-38.95	-2.34	-1.98	0.93	1.14	-	59.6	154.4	167.6
	6	290482	"	-37.63	-2.35	-1.92	0.86	1.03	-	57.4	151.8	164.4
3A 2 -	1	290482	perp.	-40.75	-2.17	-1.76	0.85	0.84	-	55.5	153.8	166.2
	2	290482	"	-38.66	-2.10	-1.31	0.89	1.10	-	50.5	141.7	153.3
	3	290482	"	-42.07	-2.29	-1.92	0.99	1.22	-	61.9	157.7	170.0
	4	290482	para.	-39.33	-2.42	-1.67	1.41	0.87	-	61.8	159.3	173.7
	5	290482	"	-40.22	-2.53	-2.08	1.10	1.30	-	66.9	163.0	177.5
	6	290482	"	-39.67	-2.44	-1.78	1.18	0.95	-	63.1	166.6	182.4
3B 1 -	1	060582	perp.	-44.49	-2.07	-1.73	0.95	1.59	-	65.2	158.8	169.2
	2	070582	"	-42.20	-1.78	-1.44	1.05	0.91	-	49.6	146.8	156.9
	3	070582	"	-43.60	-1.73	-1.71	0.87	0.67	-	48.4	155.0	2)
	4	070582	para.	-42.16	-2.03	-1.75	0.77	0.99	-	57.9	165.3	178.2
	5	100581	"	-41.51	-2.13	-1.47	0.95	1.17	-	59.1	161.2	174.0
	6	100582	"	-44.37	-2.12	-1.96	1.12	0.97	-	65.5	166.5	2)
3B 2 -	1	110582	perp.	-45.53	-2.07	-1.70	0.97	0.75	0.80	61.4	173.2	186.4
	2	110582	"	-44.21	-2.20	-1.93	1.16	0.87	0.87	62.8	164.1	176.6
	3	110582	"	-43.31	-2.20	-1.86	1.32	1.01	1.04	63.5	164.0	175.8
	4	120582	para.	-42.55	-2.59	-1.90	1.17	1.29	1.60	72.5	179.3	195.4
	5	120582	"	-43.29	-2.58	-2.06	1.08	1.29	0.86	73.5	181.9	197.8
	6	120582	"	-43.88	-2.56	-2.09	0.75	0.92	1.07	74.0	181.8	198.2

1) $\varepsilon_{2,surf}$ not measured in series 3A1, 3A2 and 3B1
2) test terminated before strain-level was reached
3) $\varepsilon_{1\ surf}$ is average value of two central placed strain gauges (see fig. 4.2.)
4) energy requirement at peak, 0.006 strain and 0.007 strain.

Table A1.2 Experimental results, series 3A/3B

Appendix A1

factor and levels	value of x_i	estimated value b_i (N/mm^2)	st.dev. ($v\hat{a}r/\hat{\sigma}_0^2$)	P-value ($\alpha = 0.05$)
mean	$x_0 = 1$	$b_0 = -39.56$	0.0215	0.000
loa.dir.D (perp.,para.)	$x_1 = -1,1$	$b_1 = 0.11$	0.0215	0.541
position P E,H,M	$x_2 = 1,0,-1$	$b_2 = -0.61$	0.0312	0.009
position P2	$x_3 = 3x_2^2 - 2$	$b_3 = -0.08$	0.0111	0.532
batch B 2A,2B,3A,3B	$x_4 = -3,-1,1,3$	$b_4 = -1.25$	0.0044	0.000
batch B2	$x_5 = (x_4^2 - 5)/4$	$b_5 = 0.55$	0.0215	0.005
batch B3	$x_6 = (5x_4^3 - 41x_4)/12$	$b_6 = -0.67$	0.0042	0.000
DP	$x_7 = x_1 x_2$	$b_7 = -0.05$	0.0313	0.800
DP2	$x_8 = x_1 x_3$	$b_8 = 0.07$	0.0111	0.588
DB	$x_9 = x_1 x_4$	$b_9 = 0.10$	0.0044	0.240
DB2	$x_{10} = x_1 x_5$	$b_{10} = 0.12$	0.0215	0.498
DB3	$x_{11} = x_1 x_6$	$b_{11} = -0.07$	0.0042	0.413
PB	$x_{12} = x_2 x_4$	$b_{12} = 0.12$	0.0062	0.230
PB2	$x_{13} = x_2 x_5$	$b_{13} = -0.55$	0.0312	0.016
PB3	$x_{14} = x_2 x_6$	$b_{14} = -0.03$	0.0062	0.773
P2B	$x_{15} = x_3 x_4$	$b_{15} = -0.05$	0.0023	0.444
P2B2	$x_{16} = x_3 x_5$	$b_{16} = -0.08$	0.0111	0.555
P2B3	$x_{17} = x_3 x_6$	$b_{17} = -0.01$	0.0021	0.812

estimate for random error $\hat{\sigma}_0^2 = 1.51$ ($\nu = 29$)

Table A1.3. Strength-results of series 2 and 3.

Appendix A1

factor and levels	value of x_i	estimated value b_i (Joule)	st.dev. ($v\hat{a}r/\hat{o}_0^2$)	P-value (α=0.05)
mean	x_0=1	b_0 = 159.45	0.0253	0.000
loa.dir.D (perp.,para.)	x_1=-1,1	b_1 = 6.48	0.0248	0.000
position P E,H,M	x_2=1,0,-1	b_2 = 3.41	0.0328	0.044
position P2	$x_3=3x_2^2-2$	b_3 = 0.46	0.0140	0.662
batch B 2A,2B,3A,3B	x_4=-3,-1,1,3	b_4 = 1.87	0.0055	0.008
batch B2	$x_5=(x_4^2-5)/4$	b_5 = -2.97	0.0248	0.043
batch B3	$x_6=(5x_4^3-41x_4)/12$	b_6 = 4.39	0.0045	0.000
DP	$x_7=x_1x_2$	b_7 = -0.82	0.0328	0.612
DP2	$x_8=x_1x_3$	b_8 = -0.70	0.0142	0.513
DB	$x_9=x_1x_4$	b_9 = 0.12	0.0054	0.854
DB2	$x_{10}=x_1x_5$	b_{10} = -0.74	0.0253	0.606
DB3	$x_{11}=x_1x_6$	b_{11} = 0.07	0.0046	0.913
PB	$x_{12}=x_2x_4$	b_{12} = -1.13	0.0063	0.122
PB2	$x_{13}=x_2x_5$	b_{13} = 1.65	0.0328	0.313
PB3	$x_{14}=x_2x_6$	b_{14} = 0.41	0.0068	0.582
P2B	$x_{15}=x_3x_4$	b_{15} = 0.38	0.0033	0.460
P2B2	$x_{16}=x_3x_5$	b_{16} = -0.44	0.0142	0.680
P2B3	$x_{17}=x_3x_6$	b_{17} = 0.32	0.0023	0.457

estimate for random error $\hat{o}_0^2$ = 78.96 (ν=27)

Table A1.4. Energy results (at 0.006 strain) of series 2 and 3

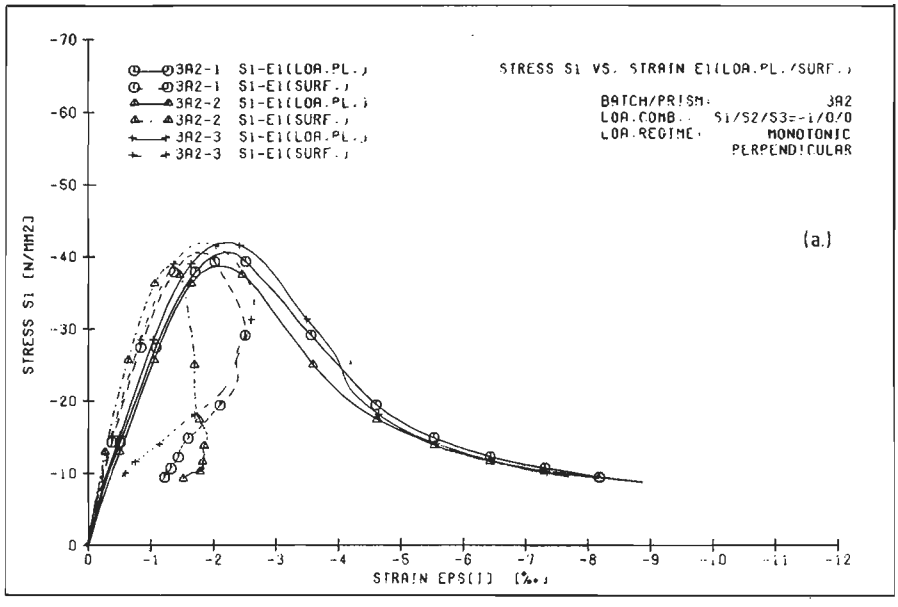

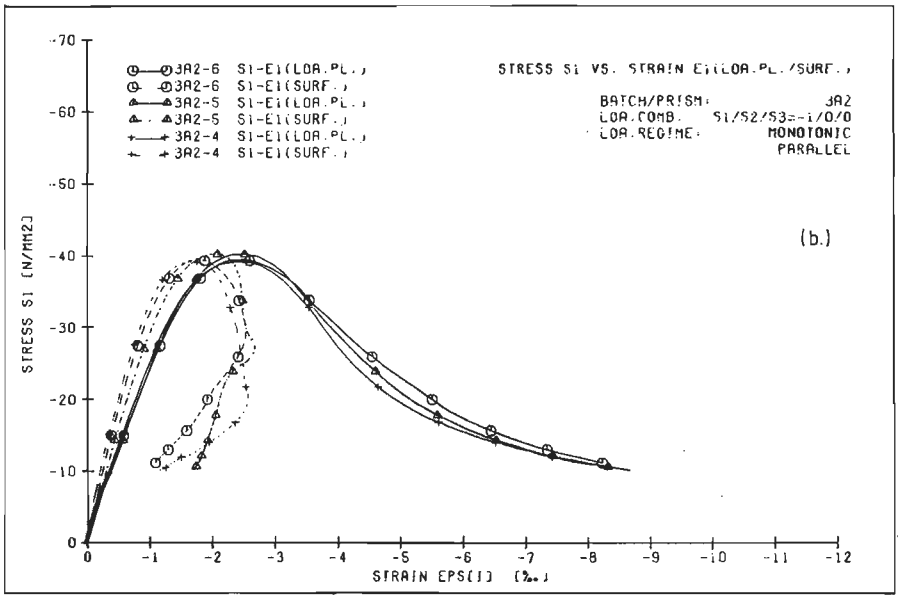

Fig.A1.5. a. Uniaxial stress-strain curves, specimens 3A2-1, 3A2-2 and 3A2-3, loading direction perpendicular.

b. idem, for specimens 3A2-4, 3A2-5 and 3A2-6, loading direction parallel.

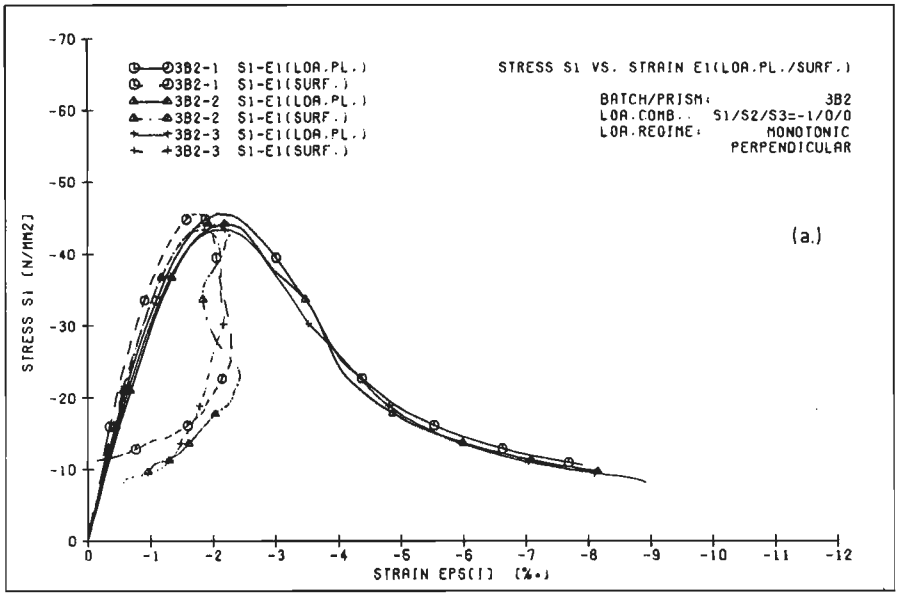

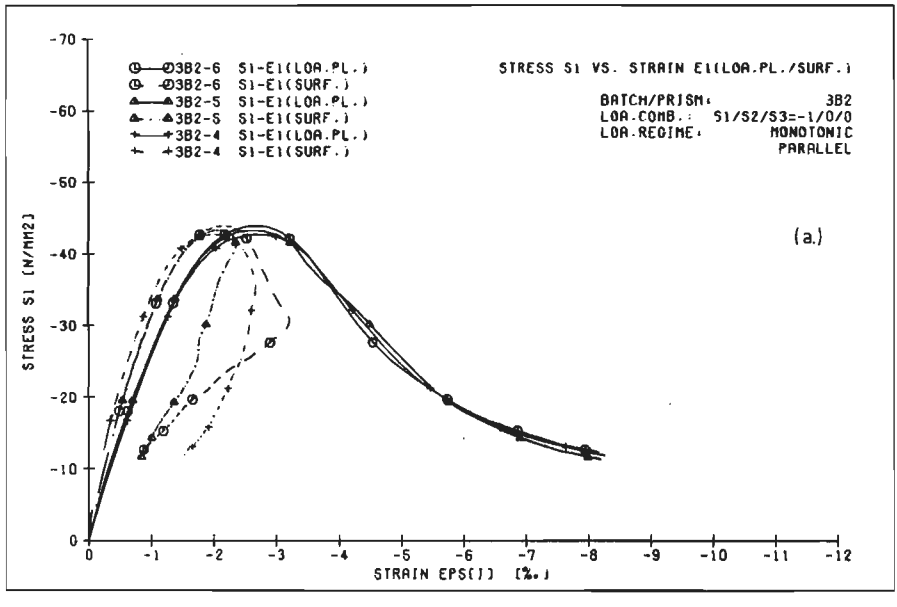

Fig.A1.6. a. Uniaxial stress-strain curves, specimens 3B2-1, 3B2-2 and 3B2-3, loading direction perpendicular.

b. idem for specimens 3B2-4, 3B2-5 and 3B2-6, loading direction parallel.

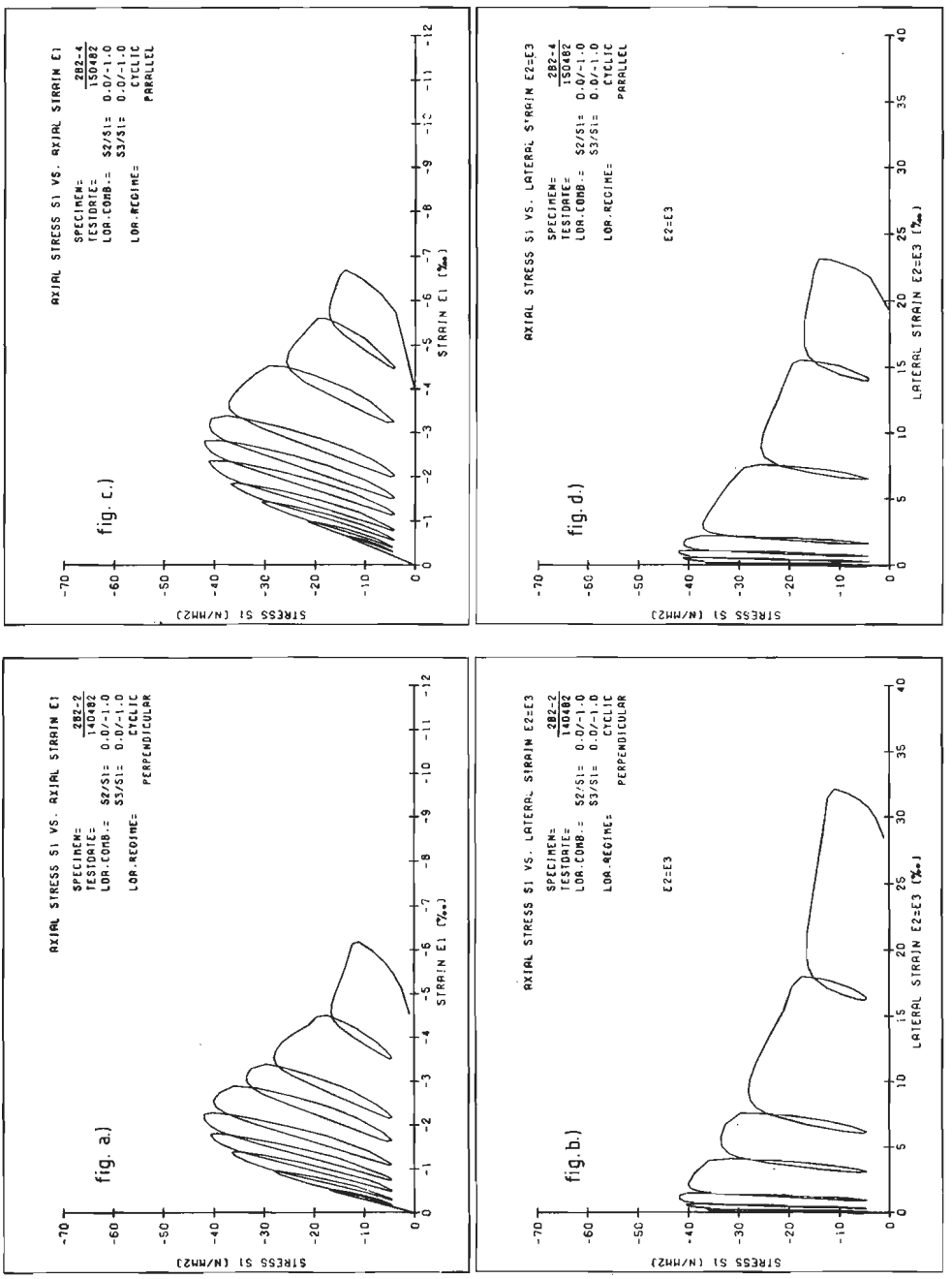

Fig.A1.7. a-b Uniaxial stress-strain curves for specimen 2B2-2, loa.dir. = perpendicular. ($\sigma_1 - \varepsilon_1$ curve, fig. a and $\sigma_1 - \varepsilon_2$ ($\varepsilon_2 = \varepsilon_3$) curve, fig. b).

c-d idem for specimen 2B2-4, loa. dir. = parallel. ($\sigma_1 - \varepsilon_1$ curve, fig. c and $\sigma_1 - \varepsilon_2$ ($\varepsilon_2 = \varepsilon_3$) curve, fig. d).

Appendix A2

Specimen no.		testdate	σ_{1p} (N/mm^2)	ε_{1p} (o/oo)	$\varepsilon_{1p,surf}$ (o/oo)	ε_{2p} (o/oo)	ε_{3p} (o/oo)	$\varepsilon_{2p,surf}$ (o/oo)
10A1 -	1	070283	- 44.31	- 2.14[3]	- 2.00[1]	0.65	0.86	1.08[2]
	2	090283	- 42.19	- 2.12	- 1.86	0.80	0.75	0.90
	3	110283	- 44.68	- 2.24	- 2.07	0.71	0.62	0.80
	4	040283	- 44.38	- 2.14	- 2.10	0.65	0.96	0.68
10A2 -	1	040283	- 44.44	- 2.06	- 1.86	0.95	0.86	1.20
	2	080283	- 45.11	- 2.06	- 2.00	0.64	1.09	0.75
	3	090283	- 45.68	- 2.23	- 1.96	0.85	0.81	0.74
	4	090283	- 43.57	- 2.07	- 2.12	0.73	0.92	0.87
10B1 -	1	090283	- 44.22	- 1.98	- 1.91	0.72	0.91	0.85
	2	070283	- 42.46	- 2.03	- 1.78	0.68	0.73	0.85
	3	080283	- 42.55	- 2.23	- 2.16	0.78	0.96	0.99
	4	080283	- 42.14	- 2.16	- 2.07	0.73	0.95	0.96
10B2 -	1	080283	- 43.29	- 2.19	- 1.83	0.70	0.70	0.93
	2	100283	- 40.51	- 2.07	- 1.87	0.73	0.77	0.77
	3	070283	- 42.41	- 2.09	- 1.84	0.83	0.92	0.95
	4	100283	- 42.77	- 2.09	- 2.06	0.86	1.19	1.16

Table A2.1. Results of 10-series.

1) average value of two central placed strain gauges no. 10,11 (see fig. 4.21)
2) average value of two lateral gauges no. 12, 13 (see fig. 4.21)
3) loading platen value, determined using brush-calibration test with aluminum cube

Appendix A2

factor and levels	value of x_i	estimated value b_i (N/mm^2)	st.dev. ($v\hat{a}r/\hat{\sigma}_0^2$)	P-value (α= 0.05)
mean	$x_0 = 1$	$b_0 = -43.37$	0.06	0.00
height H = 100, 200 mm	$x_1 = (h-150)/50$	$b_1 = 0.49$	0.06	0.195
batch 10A, 10B	$x_2 = -1,1$	$b_2 = 0.92$	0.06	0.038
position E, M	$x_3 = -1,1$	$b_3 = 0.17$	0.06	0.616
capping yes, no	$x_4 = -1,1$	$b_4 = 0.09$	0.06	0.789
HB	$x_5 = x_1x_2$	$b_5 = -0.01$	0.06	0.986
HP	$x_6 = x_1x_3$	$b_6 = 0.14$	0.06	0.681
HC	$x_7 = x_1x_4$	$b_7 = 0.01$	0.06	0.965
BP	$x_8 = x_2x_3$	$b_8 = 0.30$	0.06	0.407
BC	$x_9 = x_3x_4$	$b_9 = -0.03$	0.06	0.922
PC	$x_{10} = x_3x_4$	$b_{10} = -0.08$	0.06	0.822

estimate for random error $\hat{\sigma}_0^2 = 1.714$ ($\nu = 5$)

Table A2.2. Strength-results of 10-series.

Appendix A2

factor and levels	value of x_i	estimated value b_i (μm)	st.dev. ($v\hat{a}r/\hat{\sigma}_0^2$)	P-value ($\alpha = 0.05$)
mean	$x_0 = 1$	$b_0 = -60.38$	0.0156	0.000
height H 100, 200 mm	$x_1 = (h-150)/50$	$b_1 = -3.08$	0.0156	0.000
batch B 10A, 10B	$x_2 = -1,1$	$b_2 = -2.99$	0.0156	0.000
position E, M	$x_3 = -1,1$	$b_3 = -4.45$	0.0156	0.000
capping, yes, no	$x_4 = -1,1$	$b_4 = -4.96$	0.0156	0.000
stress-level S	$x_5 = (-\sigma-25)/5$	$b_5 = -11.25$	0.0031	0.000
stress-level S1	$x_6 = (x_5^2-5)/4$	$b_6 = 0.71$	0.0156	0.293
stress-level S2	$x_7 = (5x_5^3 - 41x_5)/12$	$b_7 = -0.10$	0.0031	0.729
HB	$x_8 = x_1x_2$	$b_8 = -1.50$	0.0156	0.030
HP	$x_9 = x_1x_3$	$b_9 = -3.99$	0.0156	0.000
HC	$x_{10} = x_1x_4$	$b_{10} = 0.04$	0.0156	0.952
HS	$x_{11} = x_1x_5$	$b_{11} = -0.17$	0.0031	0.578
HS1	$x_{12} = x_1x_6$	$b_{12} = 0.49$	0.0156	0.465
HS2	$x_{13} = x_1x_7$	$b_{13} = 0.07$	0.0031	0.809
BP	$x_{14} = x_2x_3$	$b_{14} = 0.61$	0.0156	0.363
BC	$x_{15} = x_2x_4$	$b_{15} = 0.95$	0.0156	0.161
BS	$x_{16} = x_2x_5$	$b_{16} = -0.46$	0.0031	0.130
BS1	$x_{17} = x_2x_6$	$b_{17} = -0.19$	0.0156	0.779
BS2	$x_{18} = x_2x_7$	$b_{18} = -0.04$	0.0031	0.905
PC	$x_{19} = x_3x_4$	$b_{19} = -0.30$	0.0156	0.654
PS	$x_{20} = x_3x_5$	$b_{20} = -0.69$	0.0031	0.025
PS1	$x_{21} = x_3x_6$	$b_{21} = 0.13$	0.0156	0.845
PS2	$x_{22} = x_3x_7$	$b_{22} = 0.01$	0.0031	0.968
CS	$x_{23} = x_4x_5$	$b_{23} = -0.49$	0.0031	0.108
CS1	$x_{24} = x_4x_6$	$b_{24} = 0.31$	0.0156	0.641
CS2	$x_{25} = x_4x_7$	$b_{25} = -0.09$	0.0031	0.765

estimate for random error $\hat{\sigma}_0^2 = 28.277$ ($\nu = 38$)

Table A2.3. Deformation-results of 10-series.

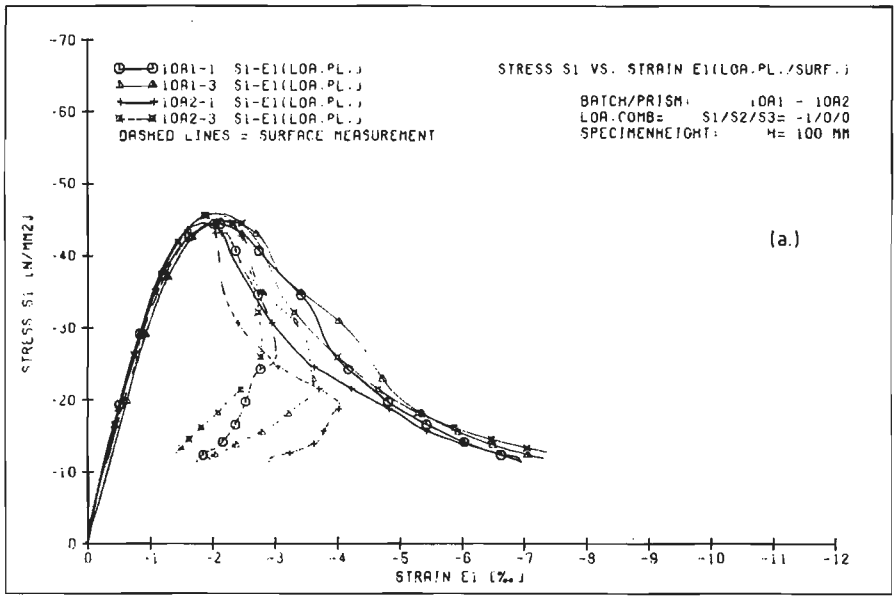

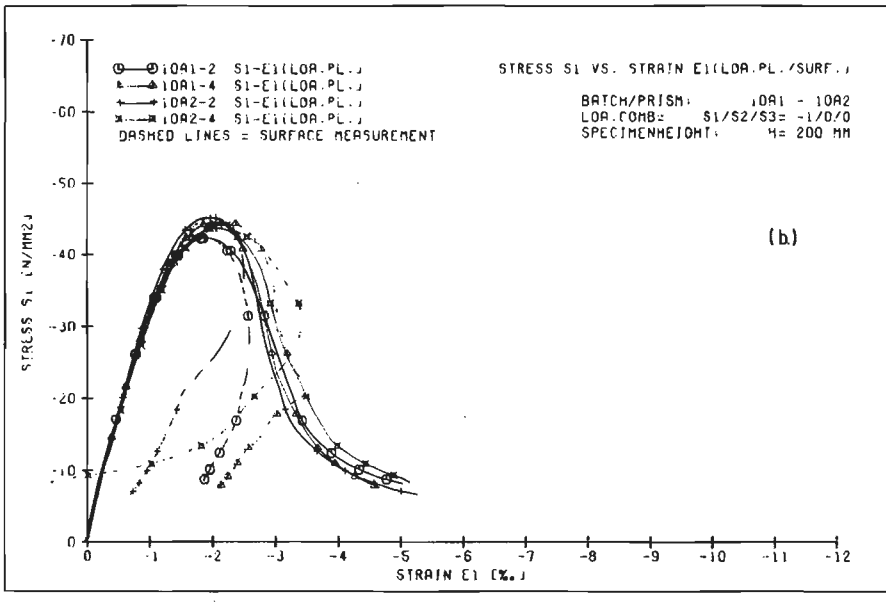

Fig.A2.4. a. Uniaxial stress-strain curves σ_1 - ε_1, batch 10A, specimenheight h = 100 mm.

b. idem, specimenheight h = 200 mm.

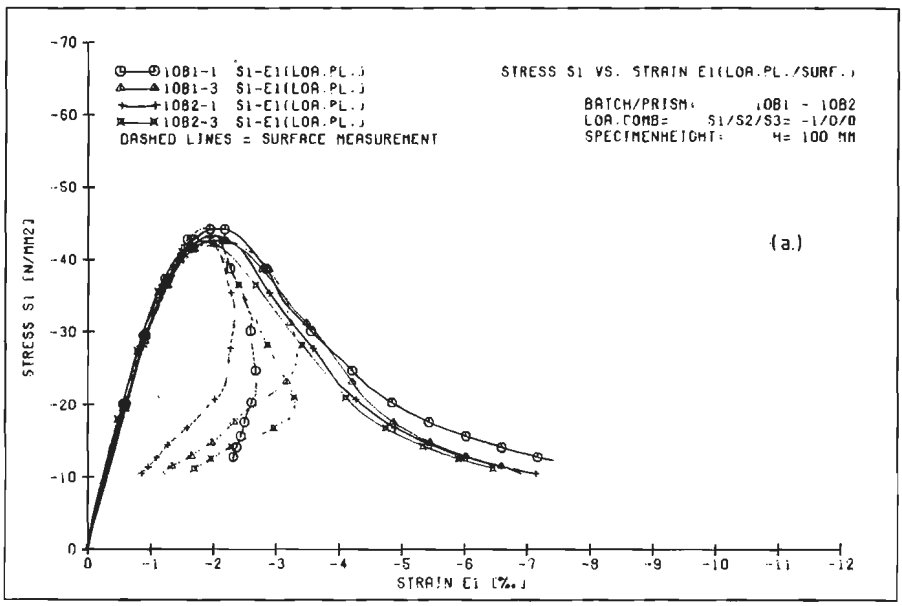

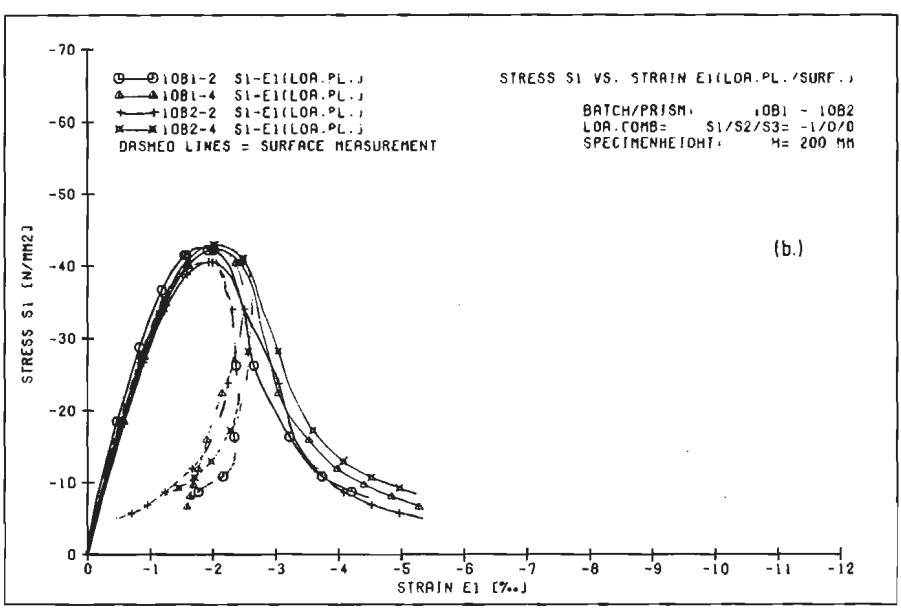

Fig.A2.5. a. Uniaxial stress-strain curves σ_1 - ε_1, batch 10B, specimenheight h = 100 mm.

b. idem, specimenheight h = 200 mm.

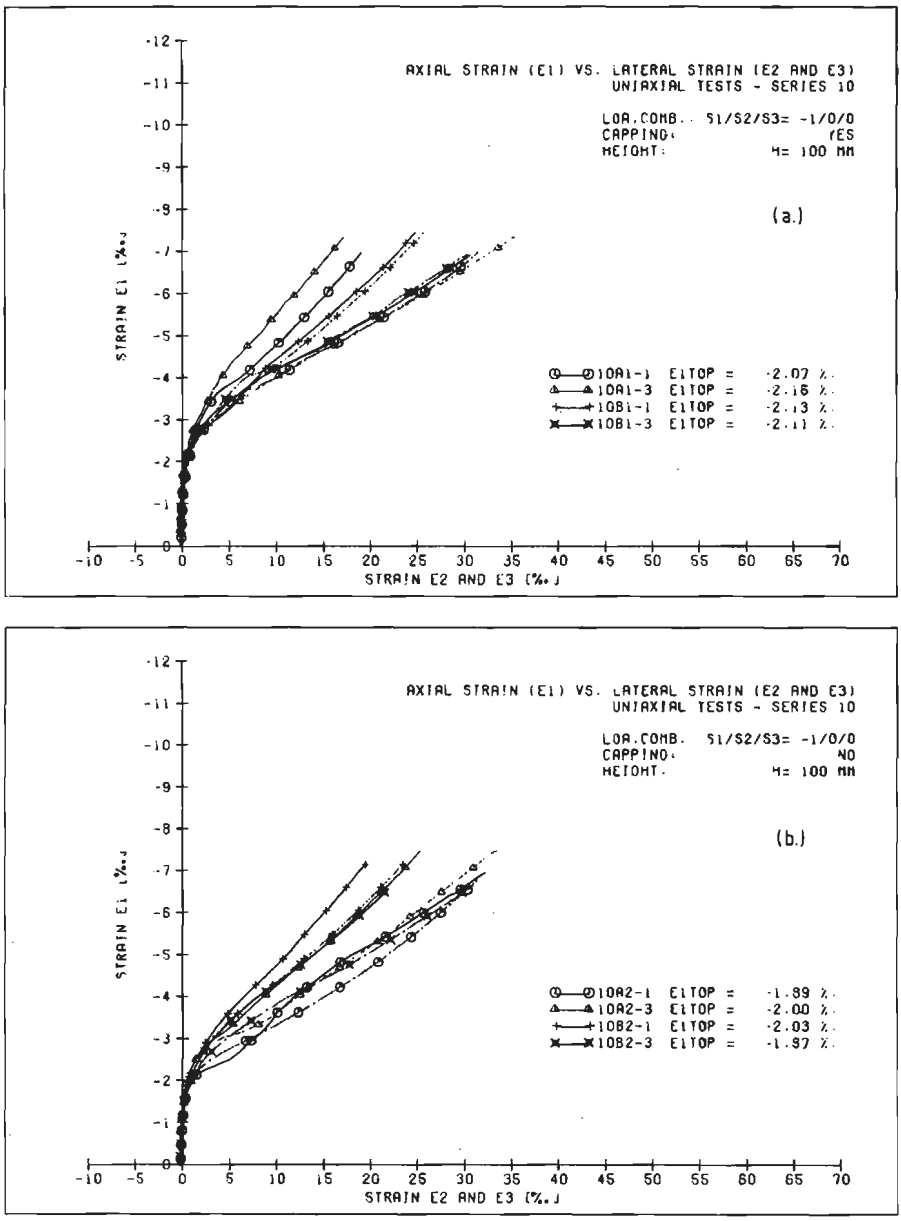

Fig.A2.6. a. Axial strain (ε_1, loa.pl.value) vs. lateral strain (ε_2, ε_3, strain readers), uniaxial tests series 10, capping = yes, specimenheight h = 100 mm.

b. idem, capping = no, specimenheight h = 100 mm.

*) The solid lines in fig. A2.6 and A2.7 represent ε_2, the dashed dotted lines, the lateral strain ε_3 (see also fig. 4.21 in the main text).

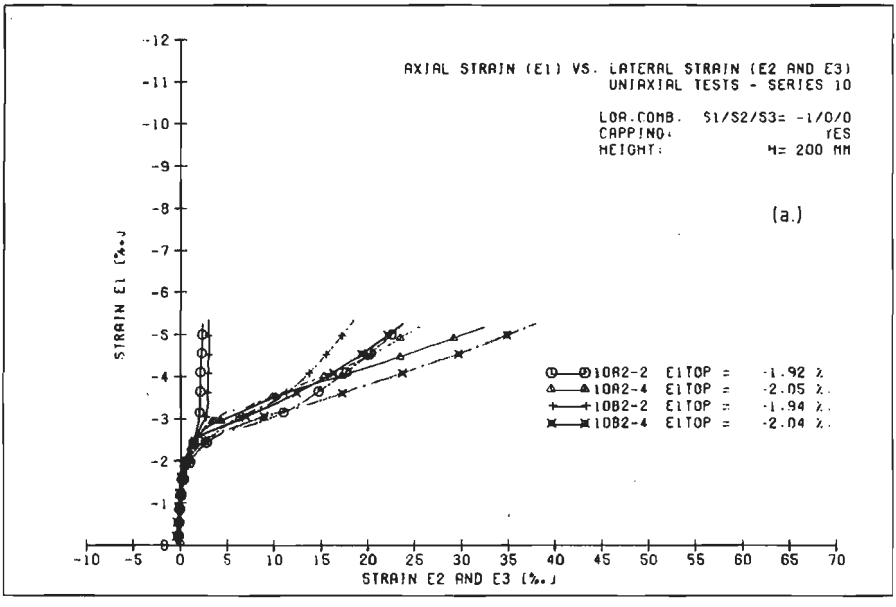

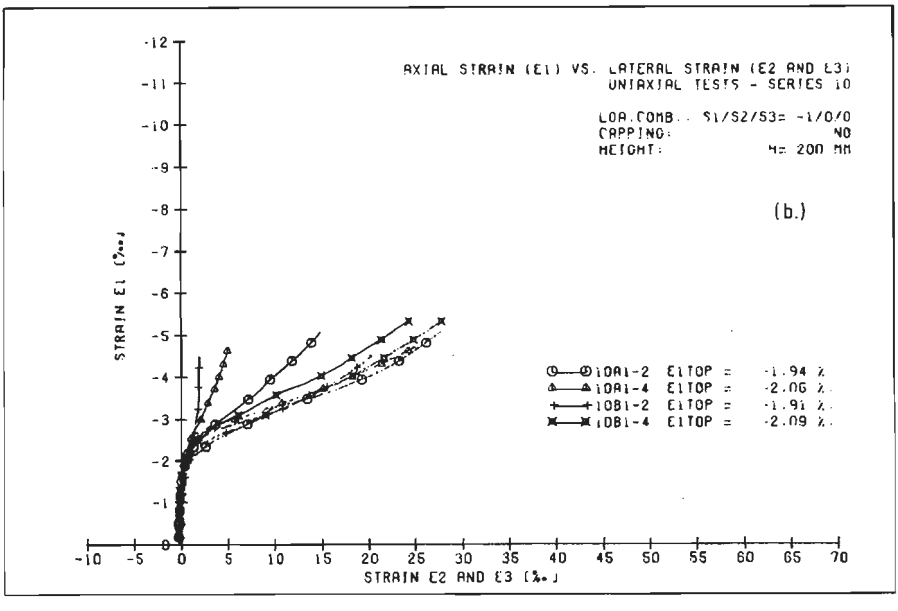

Fig.A2.7. a. Axial strain (ε_1, loa.pl. value) vs. lateral strain (ε_2, ε_3, strain readers), uniaxial tests, series 10, capping = yes, specimenheight h = 200 mm.

b. idem, capping = no, specimenheight h = 200 mm.

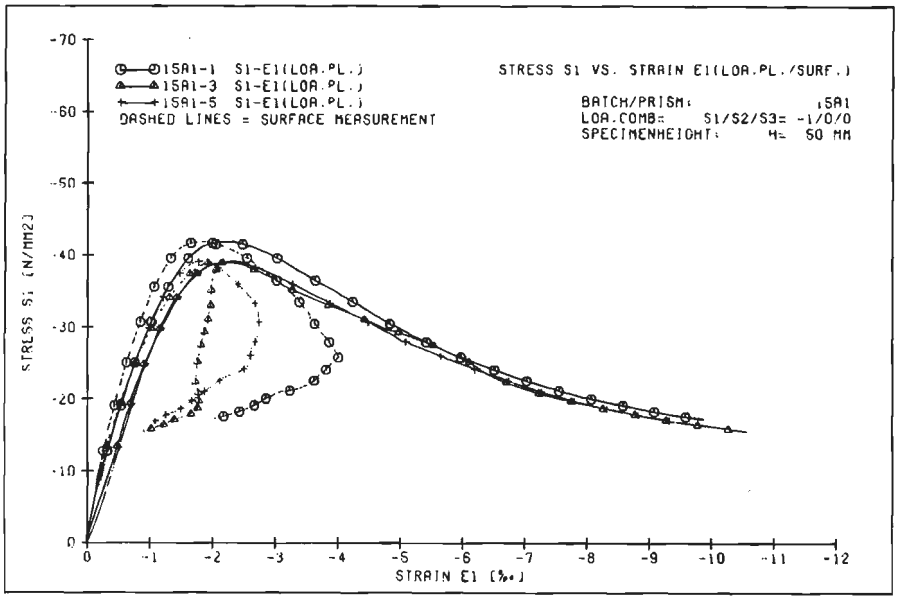

Fig.A2.8. a. Uniaxial stress-strain curves σ_1 - ε_1, batch 15A, specimenheight h = 50 mm.

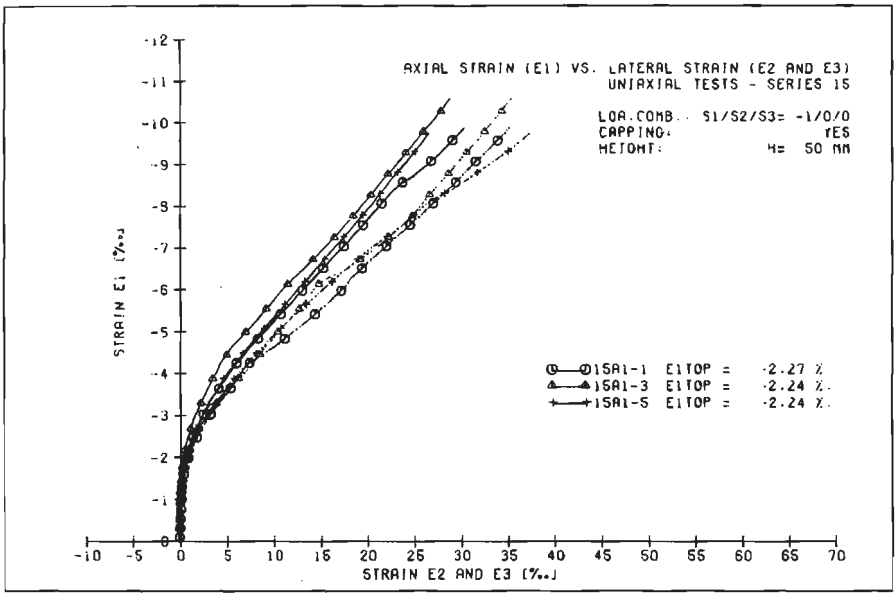

Fig.A2.8. b. Axial strain (ε_1, loa.pl.value) vs. lateral strain (ε_2, ε_3, strain-readers), uniaxial tests series 15, capping = yes, specimenheight h = 50 mm.

APPENDIX A3

Calculation of initial loading-ratio for constant displacement-ratio experiments

Let $\beta = \sigma_3/\sigma_1$ and $\alpha = \varepsilon_2/\varepsilon_1$. We assume $\sigma_1 < \sigma_2 < \sigma_3$, where σ is negative in compression.

From linear-elastic theory we know:

$$\varepsilon_1 = \frac{1}{E}(\sigma_1 - \nu\sigma_2 - \nu\beta\sigma_1)$$

$$\varepsilon_2 = \alpha\varepsilon_1 = \frac{1}{E}(-\nu\sigma_1 + \sigma_2 - \nu\beta\sigma_1) \qquad \text{.....(A3.1)}$$

$$\varepsilon_3 = \frac{1}{E}(-\nu\sigma_1 - \nu\sigma_2 + \beta\sigma_1)$$

Under the assumption that linear elastic theory holds for very low stress-levels (up to -5 N/mm^2), we can calculate the level of σ_2, given an initial-loading in σ_1-direction and the required deformation ratio α:

$$\sigma_2 = \frac{\alpha(1 - \nu\beta) + \nu(1+\beta)}{(1+\nu\alpha)}\ \sigma_1 \qquad \text{.....(A3.2)}$$

From the uniaxial cube tests (100 mm cubes, compressed between brushes) the initial Poisson-ratio was found to be in the order of 0.15 - 0.20. For the biaxial and triaxial experiments (respectively casting series 5, 6 and 8, 9) the following value for σ_2/σ_1 were used (table A3.1).

values for σ_2/σ_1		ν = 0.15	ν = 0.20
β = 0.0	α = - 0.2	-0.052	0.000
	0.0	0.150	0.200
	0.33	0.460	0.500
β = 0.05	α = - 0.2	-0.042	0.012
	0.0	0.158	0.210
	0.1	0.254	0.305
	0.33	0.467	0.510
β = 0.10	α = - 0.2	-0.033	0.025
	0.0	0.165	0.220
	0.1	0.263	0.316
	0.33	0.476	0.522

Table A3.1. Boundary-values for σ_2/σ_1 in displacement ratio tests.

In the multiaxial test, the initial loading level was taken as small as possible, with the ratio between the above mentioned boundaries.

APPENDIX A4

Biaxial experimental results, series 5/6

In this appendix, shortly some results of the biaxial experiments (series 5/6) are shown. The experimental design is shown in table A4.1. Variables were, the loading combination, stress or deformation-ratio, monotonic or cyclic loading to 'the envelope' (see fig. 5.3), position of the specimen before sawing and batches (5A, 5B and 6A). In total, 36 biaxial experiments were carried out.
In table A4.2 and figure A4.3 the strength results are shown. In figures A4.4.a-b and A4.5, some deformational results are indicated.

		loading regime	
		monotonic	cyclic to the envelope
stress-ratio σ_1/σ_2=	-1/+0.2	5A2-4 5B2-6 6A2-5	5A2-6 5B2-5 6A2-4
	-1/0	5A2-5 5B2-4 6A2-6	5A1-4 5B1-6 6A1-5
	-1/-0.33	5A1-6 5B1-5 6A1-4	5A1-5 5B1-4 6A1-6
deformation ratio $\Delta l_1/\Delta l_2$=	-1/+0.2	5A1-1 5B1-2 6A1-3	5A1-2 5B1-3 6A1-1
	-1/0	5A1-3 5B1-1 6A1-2	5A2-1 5B2-2 6A2-3
	-1/-0.33	5A2-2 5B2-3 6A2-1	5A2-3 5B2-1 6A2-2

table A4.1. Biaxial experimental design.

Statistical analysis of biaxial strength results, series 5/6.

Linear model : $y = \sqrt{\sigma_1^2 + \sigma_2^2} = \sum_{i=0}^{7} \beta_i x_i + \underline{e}$ ....(A4.1)

Only taken into consideration are the main effects (see table below). The response values of all biaxial compression tests were taken into account (thus stress-ratio and displacement-ratio experiments -1/0 and -1/-0.33).

factors and levels	value of x_i	estimated value b_i (N/mm^2)	st.dev. (var/σ_0^2)	P-value (α=0.05)
mean	x_0= 1	b_0= 55.58	0.04	0.00
loa.comb.C -1/0 and -1/-0.33	x_1= -1,1	b_1= 5.90	0.04	0.00
stress- or def.-ratio path S	x_2= -1,1	b_2= 3.92	0.04	0.00
monotonic or cyclic loading	x_3= 1,-1	b_3= -0.19	0.04	0.80
position P E,H,M	x_4= -1,0,1	b_4= -2.39	0.06	0.017
position P2	x_5= $3x_4^2$-2	b_5= 1.03	0.02	0.076
batch B 5A,5B,6A	x_6= -1,0,1	b_6= -1.33	0.07	0.171
batch B2	x_7= $3x_6^2$-2	b_7= -0.21	0.02	0.088

estimate for the random error: $\hat{\sigma}_0^2$= 12.42 (v= 15).

Table A4.2 statistical analysis of strength results, series 5/6.

Reduced model: $y = 55.58 + 5.90x_1 + 3.92x_2 - 2.39x_4$ ....(A4.2)

The significant factors (α= 0.05) are factors affecting the stress-path (respectively C and S) and positions (linear term P). The factor monotonic/cyclic loading was not significant at the 5% level. This is in contradiction with biaxial results obtained by Beams et.al. /12/, however in agreement with previous uniaxial experiments /81, 148/. Maybe the comparison with earlier experiments under monotonic loading as was done by Beams et.al. is not allowed (for example differences in batches).

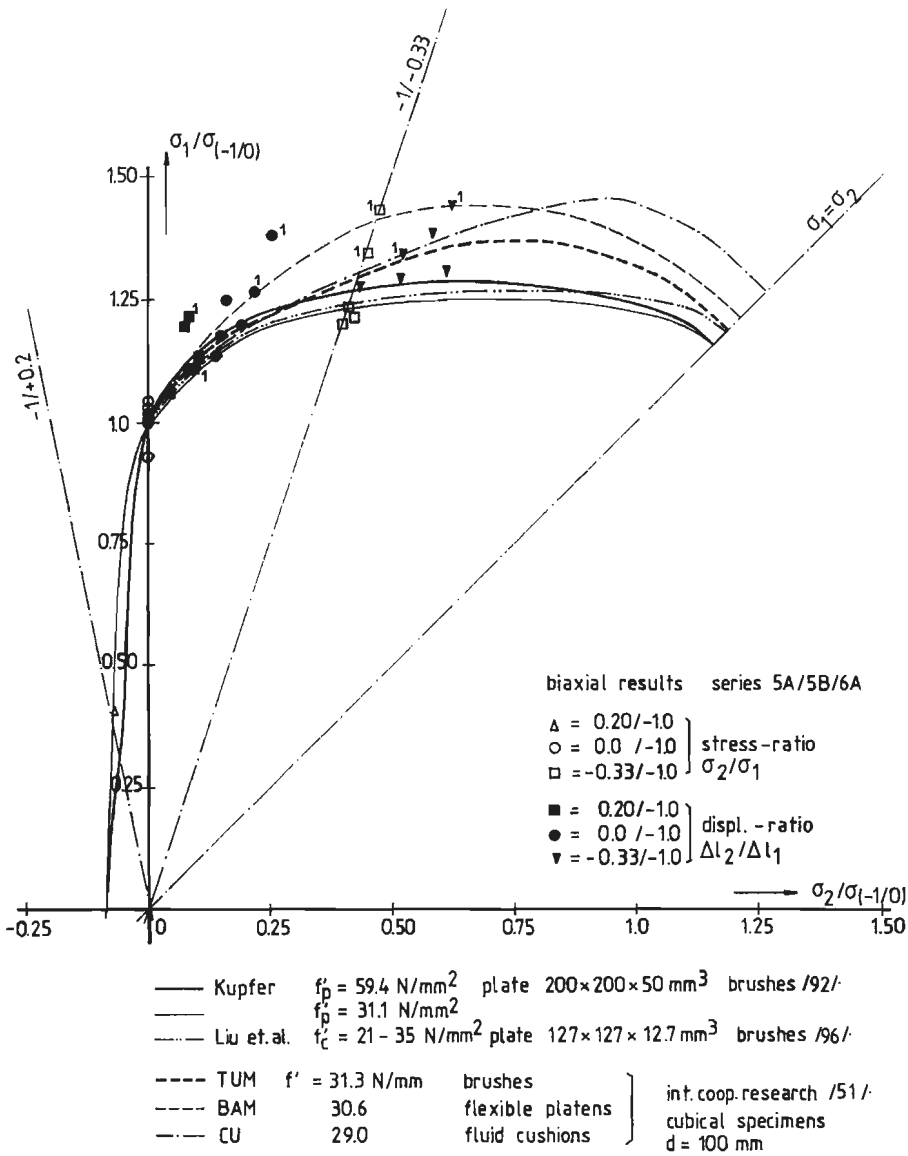

Fig. A4.3. Comparison of biaxial strength results with previous investigations.

Uniaxial compressive strength (obtained from six 100 mm cubes, loaded between brushes, see table A4.1), $\sigma_{-1/0} = -44.1$ N/mm^2. The end positions are indicated with (1) in figure A4.3.

Deformation results of biaxial experiments.

In figures A4.4.a-b and A4.5, limited deformational results of the biaxial experiments are shown. In figure A4.4.a-b, two examples of measured stress-strain curves are shown (respectively plane strain test 5B1-1, and constant stress-ratio test 6A1-4, -1/-0.33/0). In the main text, chapter 5, two additional results were shown (respectively 5B2-3, fig. 5.5 and 5.6, $\Delta l_1/\Delta l_2$= -1/-0.33, σ_3= 0, and 5A1-3, plane strain test in fig. 5.10). In fig. A4.4.a, the σ_1-ε_1, σ_1-ε_3, σ_2-ε_1 and σ_1-$\varepsilon_{1,surf}$ curves are shown, in fig. A4.4.b, the σ_1-ε_i curves (i= 1,2,3).
Obvious will be the unstable behaviour in the σ_1-ε_1 curve descending branch. In the case of the stress-ratio tests with ratio -1/-0.33/0, no stable descending branch could be measured.
From fig. A4.4.a-b, the poor correlation between surface and overall strains will be obvious. In fig. A4.5, the discrepancies between surface and overall strains are shown more clearly for the four above mentioned experiments.
Although a capping between specimen and brush was used, a large difference between surface and overall strains was measured. The reason for this behaviour, only was found after the tests were carried out. Small dimples were pressed near the edges of the lower steel block of the brushes (fig. 3.11), apparently the result of too large lateral strains in the unconfined direction (see for example fig. A4.4.a). The result of the small plastic deformations in the brush steel block is, that at test initiation, the largest contact area will be situated in the central part. In fact the specimen is loaded by means of 'spherical loading platen'. As a result large differences between surface and loading platen strains appear, and addition of a capping will hardly affect the deformational results. However, the strength results seem not to be influenced by this phenomenon (fig. A4.3).

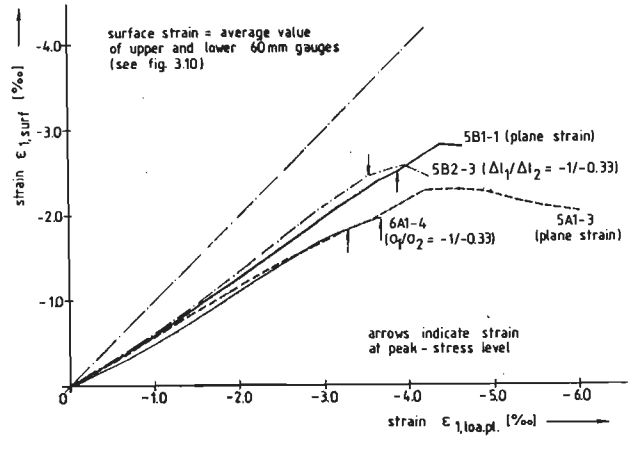

Fig. A4.5. Plots of $\varepsilon_{1,loa.pl.}$ against $\varepsilon_{1,surf}$ for four biaxial experiments.

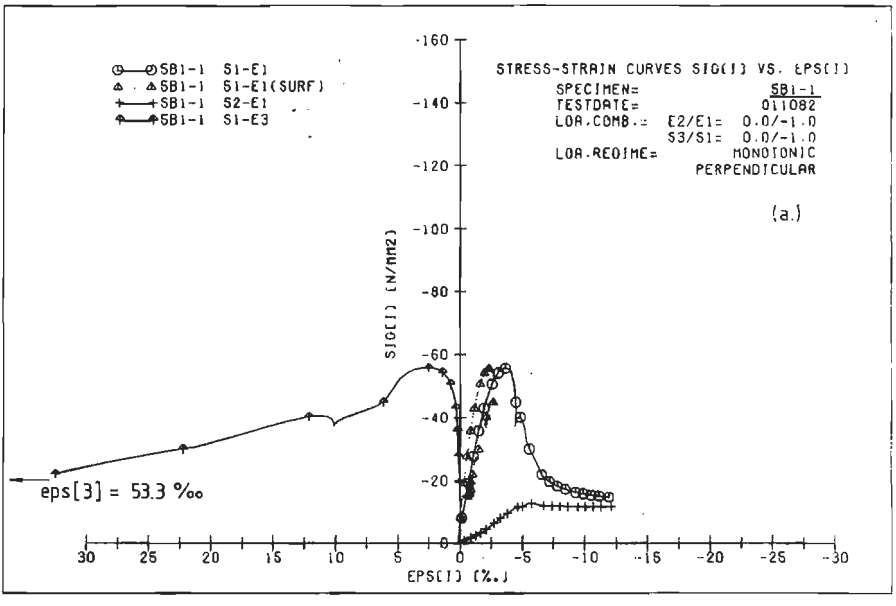

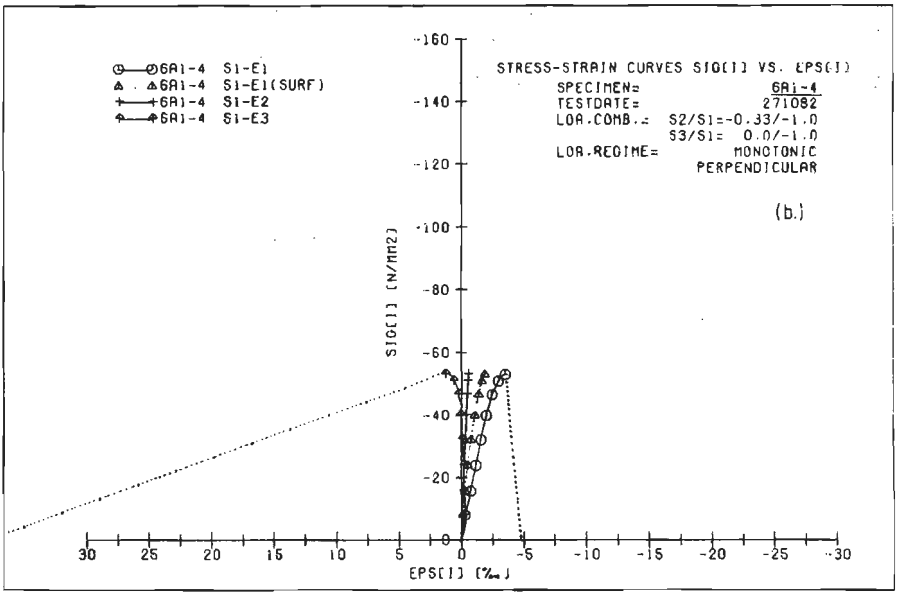

fig. A4.4 a. Biaxial monotonic deformation-ratio test, specimen 5B1-1, loa.dir. perpendicular (E2/E1= 0/-1, σ_3= 0).

b. Biaxial monotonic stress-ratio test, specimen 6A1-4, loa.dir. perpendicular ($\sigma_1/\sigma_2/\sigma_3$= -1/-0.33/0).

APPENDIX A5

Triaxial experimental results (series 8 and 9)

Summary of results

		page
A5.1.	Peak stress and strain results for triaxial experiments	269
A5.2.	Orientation of specimens in the triaxial apparatus	271
A5.3. - A5.5.	Results of uniaxial control tests, series 8/9	272
A5.6.	Photographs of failed specimens	276
A5.7. - A5.9.	Stress-strain curves of monotonic stress-ratio experiments	279
A5.10.- A5.13.	Stress-strain curves of monotonic displacement-ratio experiments	282
A5.14.- A5.19.	Stress-strain curves of cyclic stress-ratio experiments	286
A5.20.- A5.27.	Stress-strain curves of cyclic displacement-ratio experiments	298
A5.28.- A5.33.	Stress-paths of displacement-ratio experiments	314
A5.34.- A5.36.	Volumetric strain - axial strain curves	320
A5.37.- A5.41.	Tangential stiffness plots	323
A5.42.- A5.46	Strain-paths	325

A review of the triaxial experiments is given in table 5.4, page 121.

Table A5.1. Details of triaxial experiments, serie 8/9.

specimen-no.		testdate 2)	ratio r_2/r_1 1)	σ_3/σ_1	M/C 6)	loading-direction 5)	σ_{1p}	σ_{2p} (N/mm^2)	σ_{3p}	ε_{1p}	ε_{2p} (o/oo)	ε_{3p}	age (days)
8A 1 -	1	230383			M	para.	-44.84			- 1.91	0.89	0.70	252
	2	150383	D 0.10	0.05	C	"	-84.26	-30.69	-5.03	- 8.59	-0.32	5.59	244
	3	180383	S 0.33	0.05	M	perp.	-82.91	-27.95	-4.61	- 6.94	-0.58	5.19	247
	4	220483	S-0.20	0.05	M	para.	4)						282
	5	160383	D 0.33	0.10	C	"	-135.12	-99.20	-13.88	-19.98	-5.33	18.63	245
	6	120483			M	"	2.55						272
8A 2 -	1	240383			M	"	-47.55			- 2.27	0.91	0.81	253
	2	210383	S 0.0	0.10	M	"	-55.26	0	-5.66	- 3.84	2.39	0.44	250
	3	040583	D-0.20	0.10	C	perp.	-112.97	-20.33	-11.66	-19.13	4.81	11.37	294
	4	170383	D 0.0	0.05	C	"	-76.27	-18.96	-4.15	- 7.30	0.44	5.67	246
	5	180383	S 0.10	0.10	M	"	-84.76	-8.79	-9.00	- 9.45	3.69	3.61	247
	6	130483			M	para.	3)						273
8B 1 -	1	240383			M	"	-45.30			- 2.30	0.79	0.89	253
	2	210383	S 0.10	0.10	C	"	-76.82	-7.57	-7.96	-14.82	7.05	5.94	250
	3	140383	D 0.10	0.05	M	perp	-73.02	-22.35	-4.11	- 6.07	-0.26	3.87	243
	4	220383	S 0.0	0.10	C	"	-51.20	0	-5.28	- 2.73	1.45	0.15	251
	5	030583	S-0.20	0.05	C	"	-11.49	1.79	-0.96	- 0.43	0.071	-0.03	293
	6	140483			M	para.	2.87						274
8B 2 -	1	250383			M	"	-43.64			- 2.22	0.88	1.22	254
	2	040583	D-0.20	0.10	M	"	-106.32	-18.81	-10.92	-18.64	4.69	10.46	294
	3	150383	D 0.33	0.10	M	perp.	-111.25	-67.13	-11.44	-12.83	-3.53	8.90	244
	4	220383	S 0.33	0.05	C	para.	-85.59	-28.67	-4.62	-10.27	0.14	6.89	251
	5	170383	D 0.0	0.05	M	"	-82.16	-22.70	-4.51	-12.06	0.53	9.23	246
	6	150483			M	"	3.03						275
9A 1 -	1	250383			M	"	-46.95			- 2.43	1.06	1.13	233
	2	280383	D 0.33	0.05	C	perp.	-91.48	-57.79	-5.11	- 8.42	-2.18	7.95	236
	3	080483	S 0.0	0.05	M	"	-50.56	0	-3.56	- 2.91	1.92	0.64	247
	4	060583	D-0.20	0.05	C	para.	-83.51	-11.86	-4.74	-10.30	2.74	6.35	275
	5	020583	S-0.20	0.10	M	perp.	-12.15	1.86	-1.56	- 0.71	0.18	-0.12	271
	6	180483			M	para.	3.95						257

Appendix A5

specimen-no.		testdate 2)	ratio r_2/r_1	σ_3/σ_1	M/C 6)	loading-direction 5)	σ_{1p}	σ_{2p} (N/mm^2)	σ_{3p}	ε_{1p}	ε_{2p} (o/oo)	ε_{3p}	age (days)
9A 2 -	1	280383			M	para.	- 45.92			-2.27	1.05	0.77	236
	2	290383	D 0.10	0.10	C	perp.	-125.91	-49.91	-12.66	-15.45	-0.66	10.28	237
	3	300383	D 0.0	0.10	C	para.	-117.59	-40.81	-12.13	-21.13	0.95	13.64	238
	4	070483	S 0.10	0.05	M	"	- 67.06	- 6.70	- 3.91	- 7.74	2.68	3.84	246
	5	310383	S 0.33	0.10	M	"	-127.00	-42.02	-13.30	-21.21	-0.02	13.88	239
	6	190483			M	"	3.00						258
9B 1 -	1	110483			M	"	-48.29			-2.40	1.16	1.17	250
	2	310383	S 0.10	0.05	C	perp.	-76.35	-8.05	-4.61	-5.96	1.30	2.96	239
	3	080483	S 0.0	0.05	C	para.	-50.51	0	-3.29	-3.34	1.48	0.75	247
	4	030583	S-0.20	0.10	C	"	-13.05	2.32	-1.71	-0.48	0.17	-0.12	272
	5	050483	S 0.33	0.10	C	perp.	-115.02	-38.41	-11.68	-15.42	-0.11	10.65	244
	6	190483			M	para.	2.79			0.088			258
9B 2 -	1	130483			M	"	-50.43			-2.48	1.03	0.85	252
	2	070483	D 0.33	0.05	M	"	-96.92	-62.33	-5.17	-10.71	-2.84	9.55	246
	3	290383	D 0.10	0.10	M	"	-116.85	-49.06	-11.77	-20.59	-1.17	12.70	237
	4	060483	D 0.0	0.10	M	perp.	-121.12	-33.13	-12.15	-16.03	0.77	10.38	245
	5	060583	D-020	0.05	M	"	-85.13	-13.13	- 4.64	-9.90	2.76	7.09	275
	6	200483			M	para.	2.49			0.073			259

for each prism: no. 1. uniaxial compression, no. 6. uniaxial tension / control tests

1) D = displacement-ratio test
   S = stress-ratio test
2) test-date: day, month, year
3) excentric loaded, due to malfunction of spherical seating
4) failure of epoxy layer
5) see section 5.1.
6) M = monotonic loading
   C = cyclic loading

- tension - compression displacement ratio tests / tensile peak stress-level.

8A 2 -	3	040583	D-0.20	0.10	C	perp.	-24.13	1.84	-2.80	-0.73	0.14	0.04	294
8B 2 -	2	040583	D-0.20	0.10	M	para.	-22.98	2.08	-2.60	-0.58	0.14	0.02	294
9A 1 -	4	060583	D-0.20	0.05	C	para.	-18.43	1.59	-1.51	-0.75	0.18	0.05	275
9B 2 -	5	060583	D-0.20	0.05	M	perp.	-24.21	1.28	-1.61	-0.97	0.33	0.05	275
6B 2 -	5	220683	D-0.20	0.10	M	perp.	-117.99	-10.10	-11.77	-14.46	3.93	7.65	427
4B 2 -	4	240283	S 0.33	0.10	M	perp.	-131.09	-45.53	-13.70				351
4B 2 -	5	250283	D 1.0	0.10	M	perp.	-118.49	-114.44	-12.69	-11.32	-11.34	12.46	352

		Loading-axis 1.	2.	3.
8A1 -	2	D = -1.0	S = -0.05	D = -0.10
	3	S = -1.0	S = -0.05	S = -0.33
	4			
	5	D = -1.0	S = -0.10	D = -0.33
8A2 -	2	S = -1.0	S = -0.10	
	3	D = -1.0	D = +0.20	S = -0.10
	4	D = -1.0	S = -0.05	D = 0.0
	5	S = -1.0	S = -0.10	S = -0.10
8B1 -	2	S = -1.0	S = -0.10	S = -0.10
	3	S = -0.05	D = -1.0	D = -0.10
	4	S = -1.0	S = -0.10	
	5	S = -1.0	S = +0.20	S = -0.05
8B2 -	2	D = -1.0	D = +0.20	S = -0.10
	3	S = -0.10	D = -0.33	D = -1.0
	4	S = -1.0	S = -0.05	S = -0.33
	5	D = -1.0	S = -0.05	D = 0.0
9A1 -	2	D = -1.0	S = -0.05	D = -0.33
	3	S = -1.0	S = -0.05	
	4	D = -1.0	D = +0.20	S = -0.05
	5	S = -1.0	S = +0.20	S = -0.10
9A2 -	2	D = -1.0	S = -0.10	D = -0.10
	3	D = -1.0	S = -0.10	D = 0.0
	4	S = -1.0	S = -0.05	S = -0.10
	5	S = -1.0	S = -0.10	S = -0.33
9B1 -	2	S = -1.0	S = -0.05	S = -0.10
	3	S = -1.0	S = -0.05	
	4	S = -1.0	S = +0.20	S = -0.10
	5	S = -1.0	S = -0.10	S = -0.33
9B2 -	2	D = -1.0	S = -0.05	D = -0.33
	3	D = -1.0	S = -0.10	D = -0.10
	4	D = -1.0	S = -0.10	D = 0.0
	5	D = -1.0	D = +0.20	S = -0.05

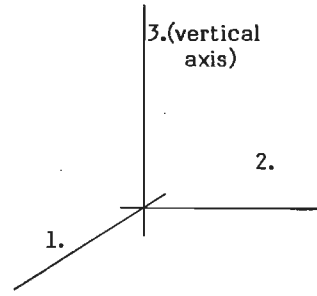

D = deformation-control
S = stress-control

Table A5.2.
Orientation of the specimen with respect to the loading axes in the triaxial apparatus for the multiaxial experiments / series 8A - 9B.

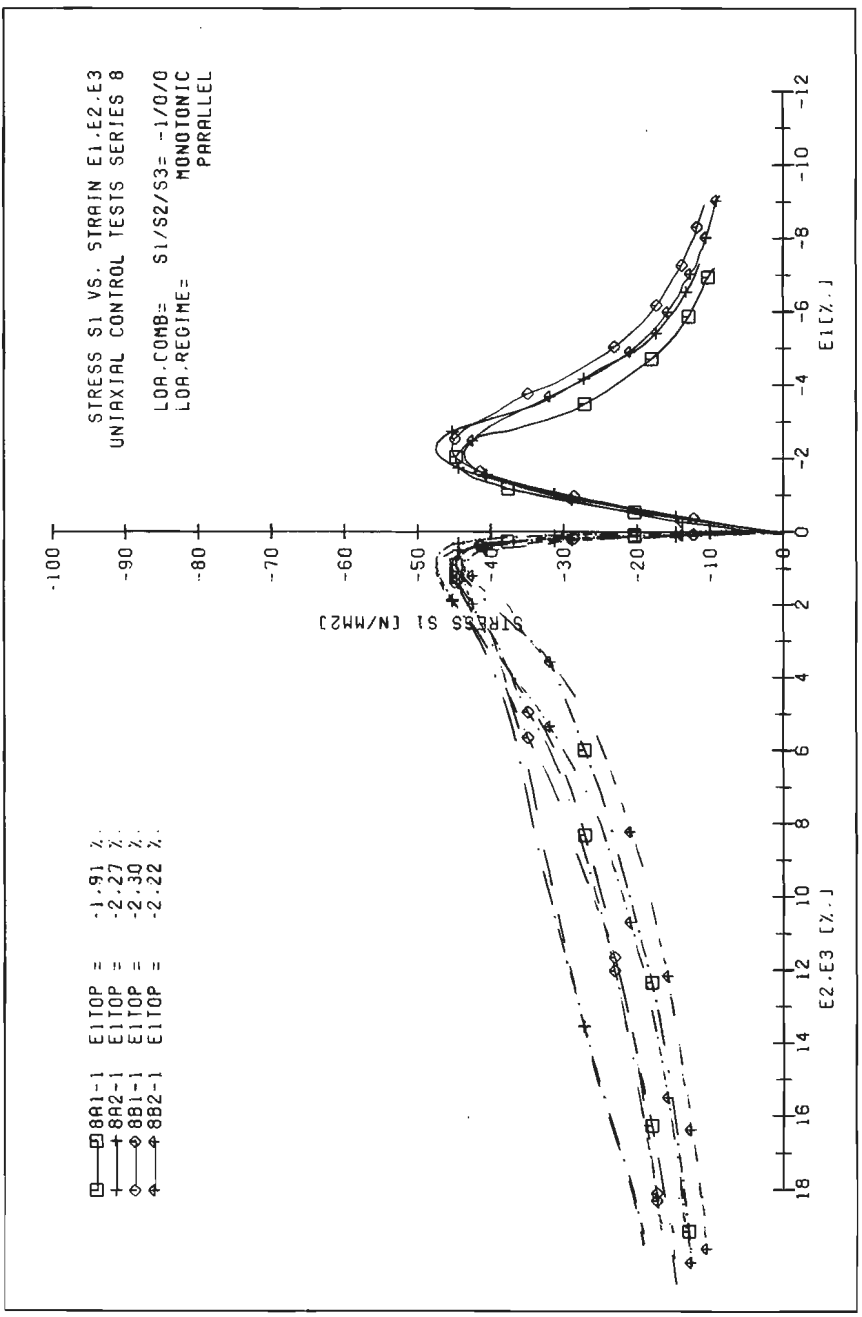

Fig.A5.3.a. Uniaxial control tests series 8, 100 mm cubes, stress-strain curves $\sigma_1 - \varepsilon_1$, $\sigma_1 - \varepsilon_2$ and $\sigma_1 - \varepsilon_3$ (specimen 8A1-1, 8A2-1, 8B1-1 and 8B2-1). Lateral strains ε_2 and ε_3 are not plotted until test-termination.

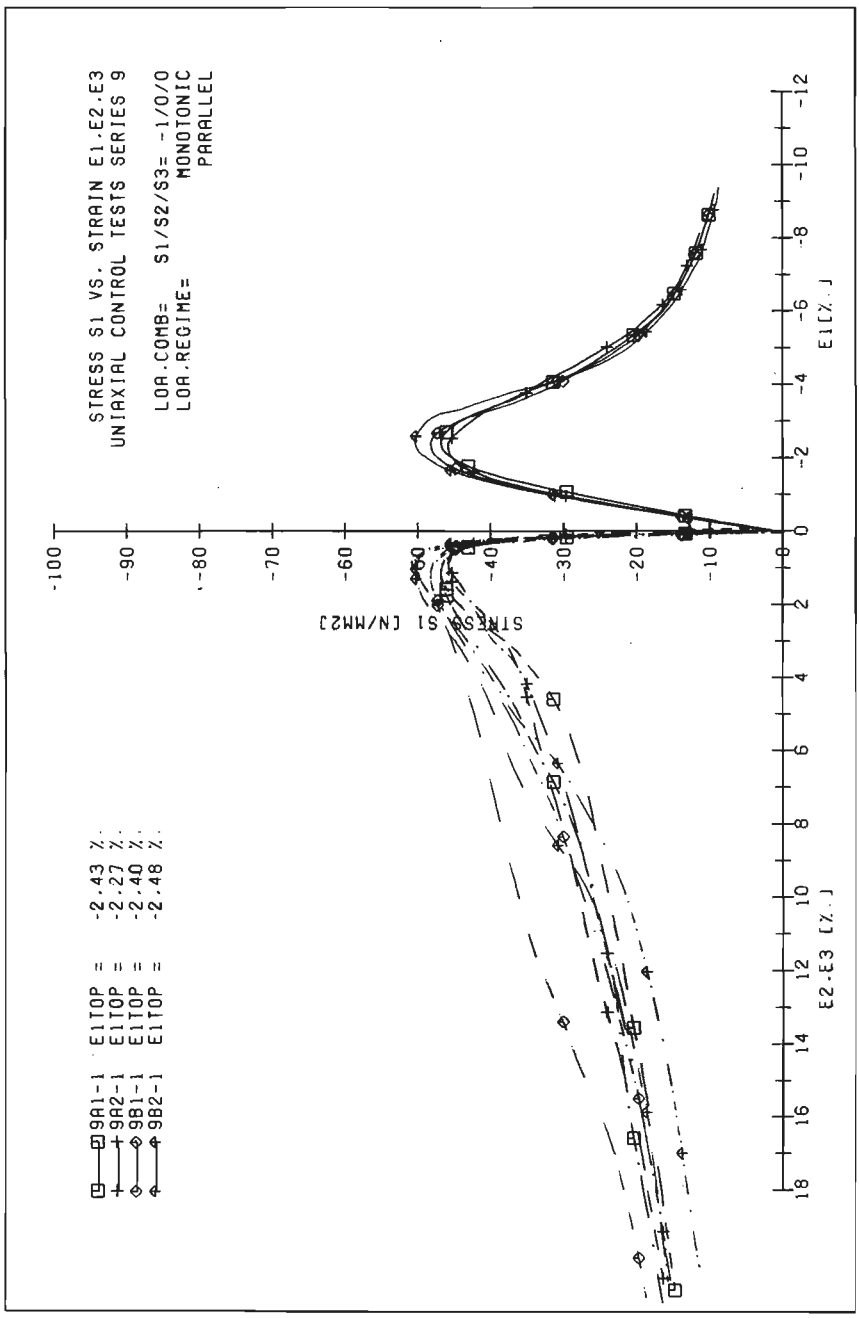

Fig.A5.3.b. Uniaxial control tests series 9, 100 mm cubes, stress-strain curves $\sigma_1 - \varepsilon_1$, $\sigma_1 - \varepsilon_2$ and $\sigma_1 - \varepsilon_3$ (specimen 9A1-1, 9A1-2, 9B1-1 and 9B2-1).

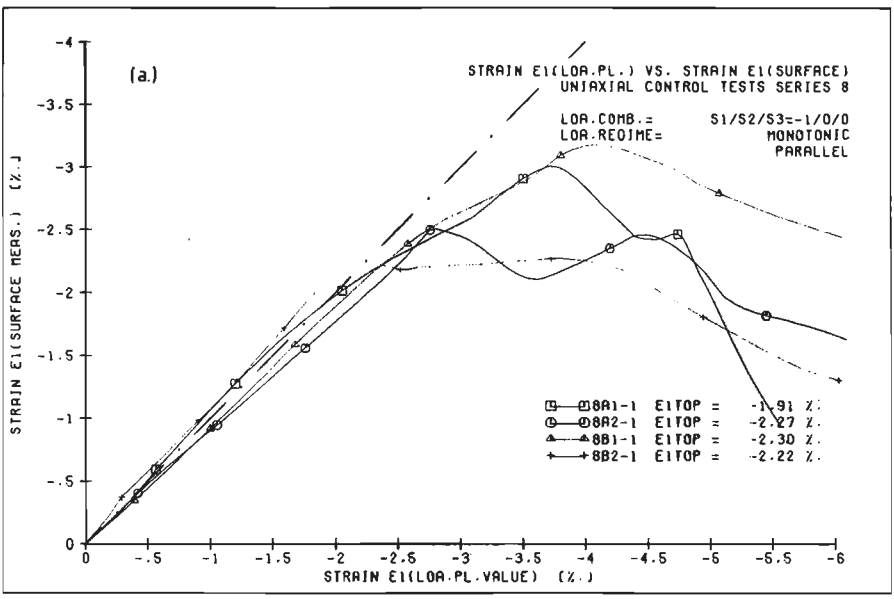

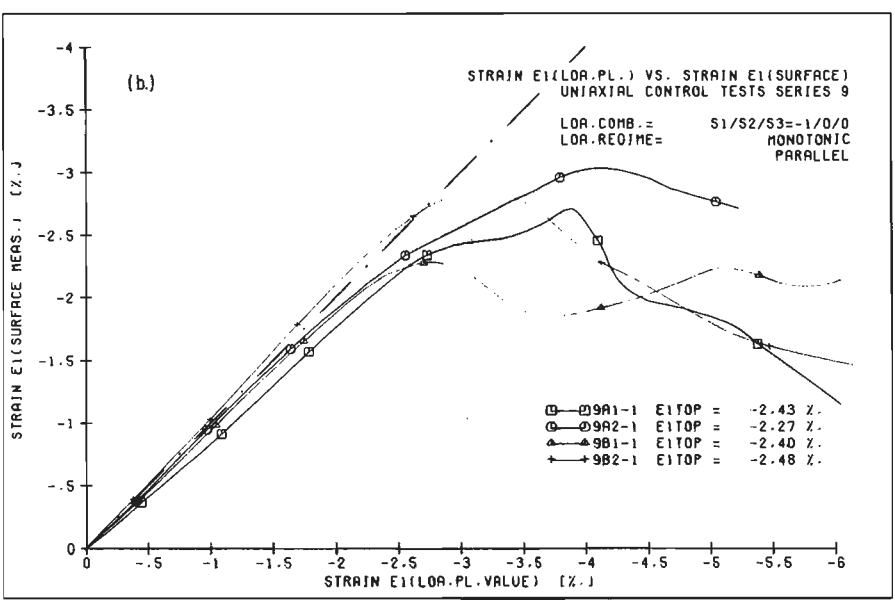

Fig.A5.4 a. Uniaxial control tests, series 8, strain ε_1 (loa.pl.) vs. strain ε_1 (surf), check on brushes.

b. idem, uniaxial control tests series 9.

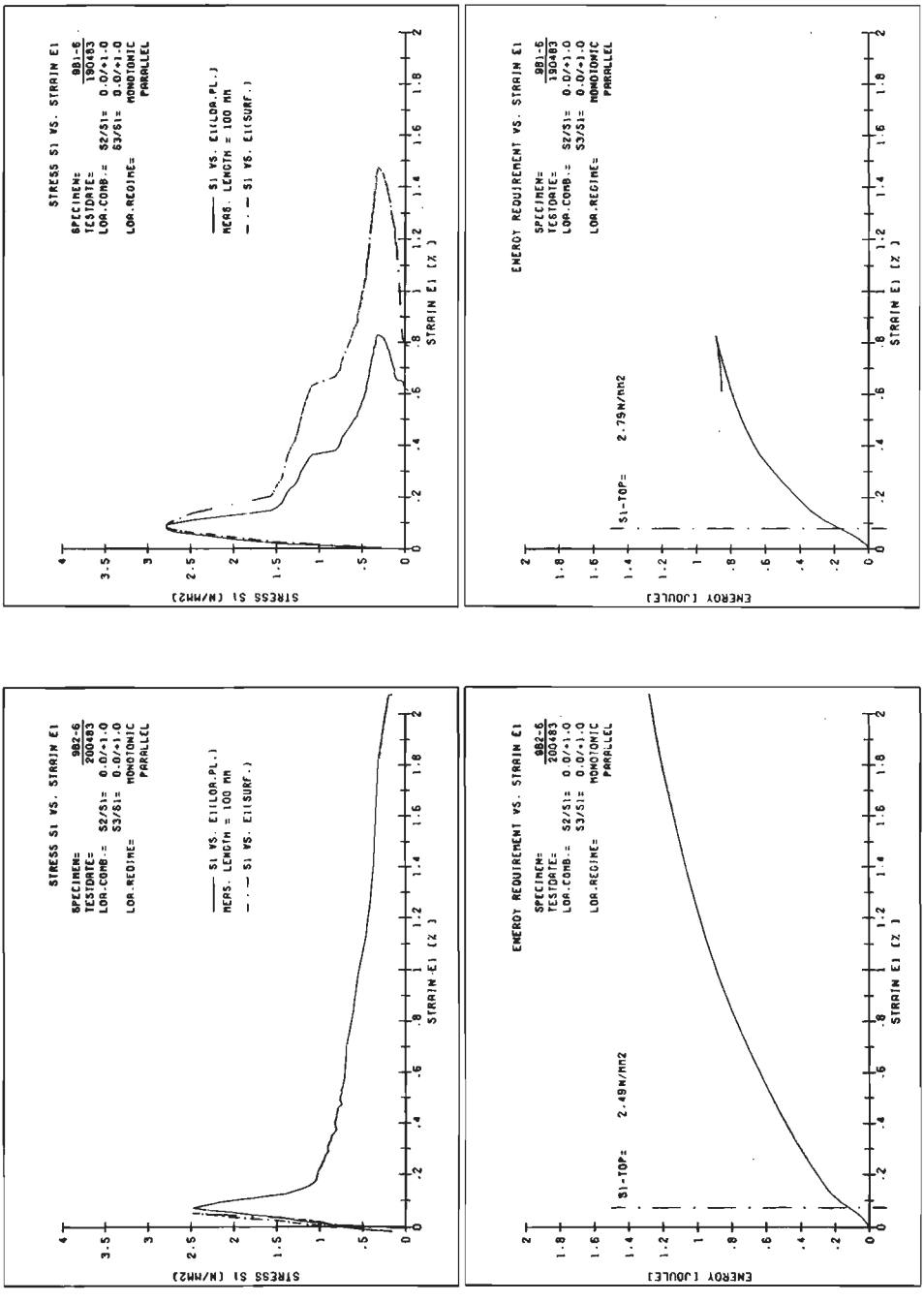

Fig.A5.5.a-b Control tests, series 9, uniaxial tension. Specimens 9B1-6 and 9B2-6 (loa.dir. parallel). Stress-strain-curves σ_1 - ε_1 and energy-requirement curves.

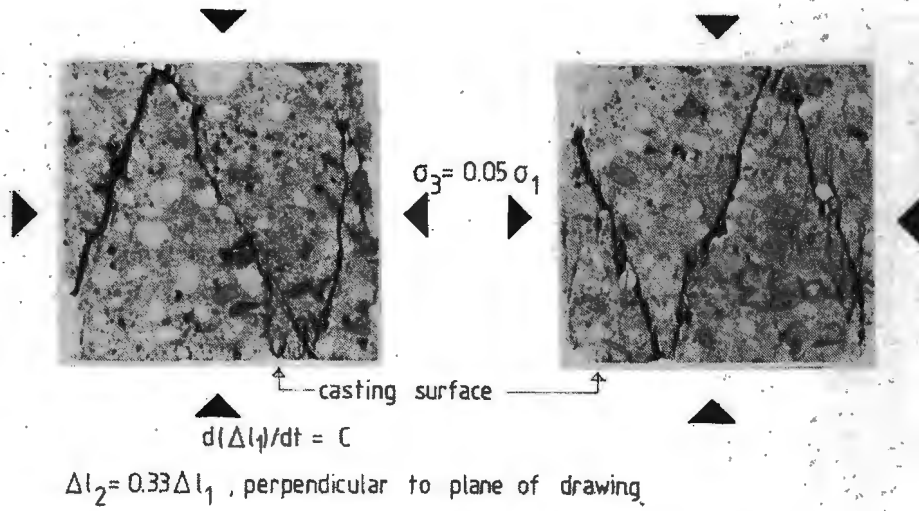

Fig.A5.6. a. Rupture pattern for specimen 9B2-2 (E2/E1 = -0.33/-1.0, σ_3/σ_1 = -0.05/-1.0, M, para).

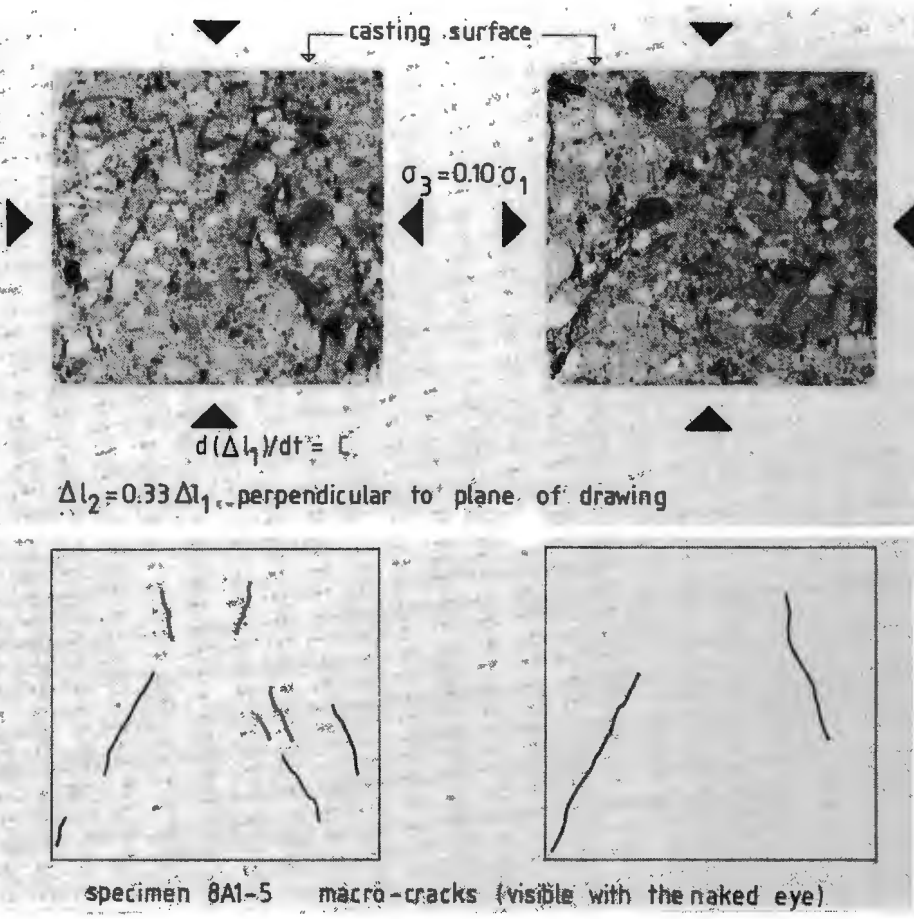

Fig.A5.6. b. Rupture pattern for specimen 8A1-5 (E2/E1 = -0.33/-1.0, σ_3/σ_1 = 0.10/-1, C, para).

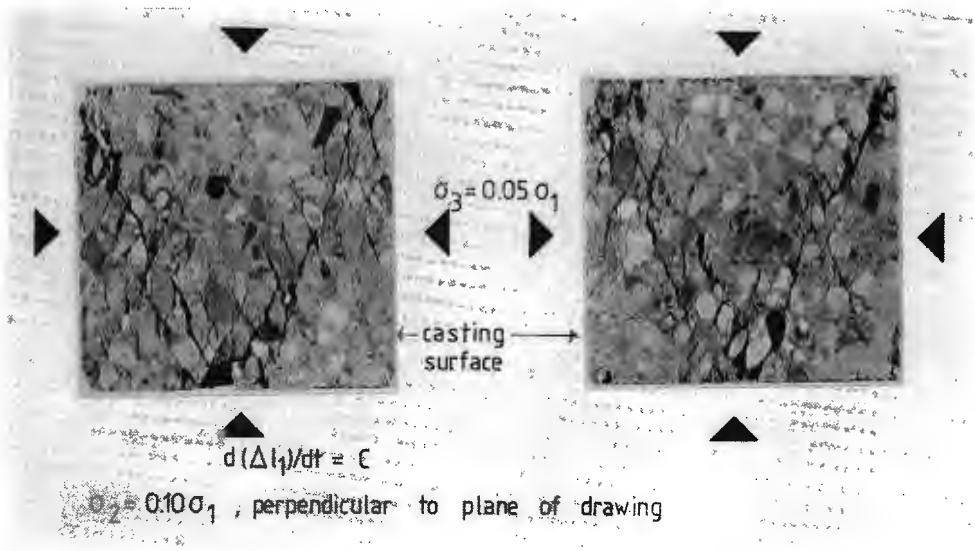

Fig.A5.6. c. Rupture pattern for specimen 9B1-2 ($\sigma_1/\sigma_2/\sigma_3$ = -1.0/-0.10/-0.05, C, perp.)

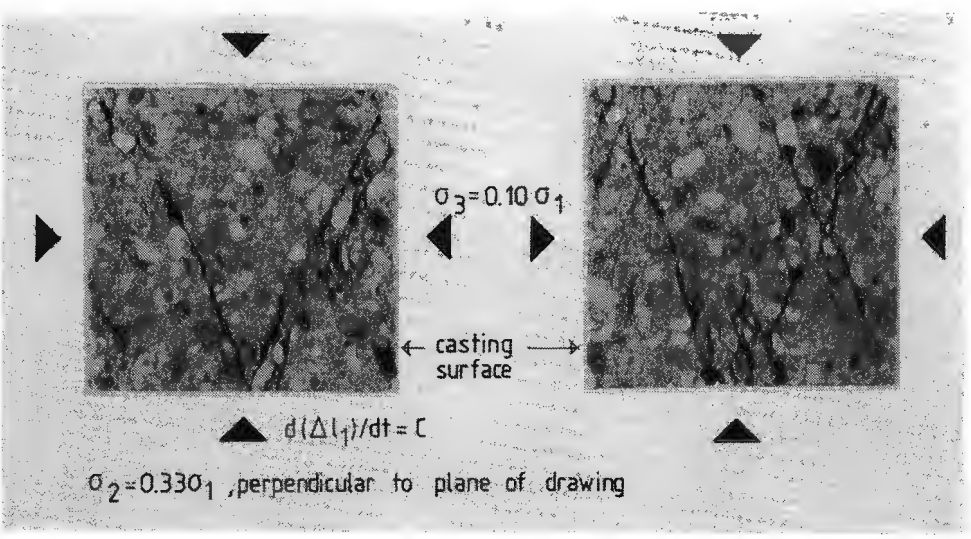

Fig.A5.6. d. Rupture pattern for specimen 9B1-5 ($\sigma_1/\sigma_2/\sigma_3$ = -1.0/-0.33/-0.10, C, perp.)

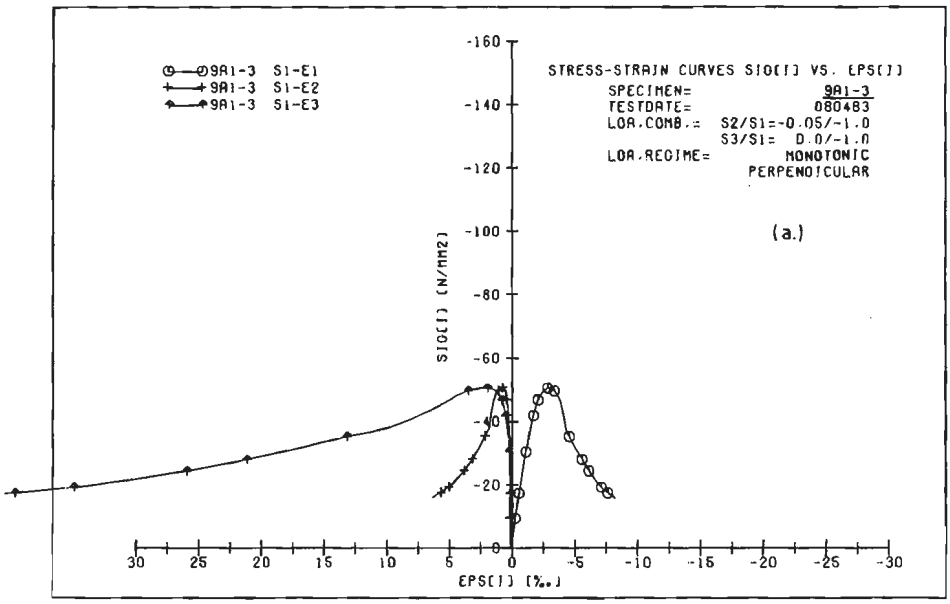

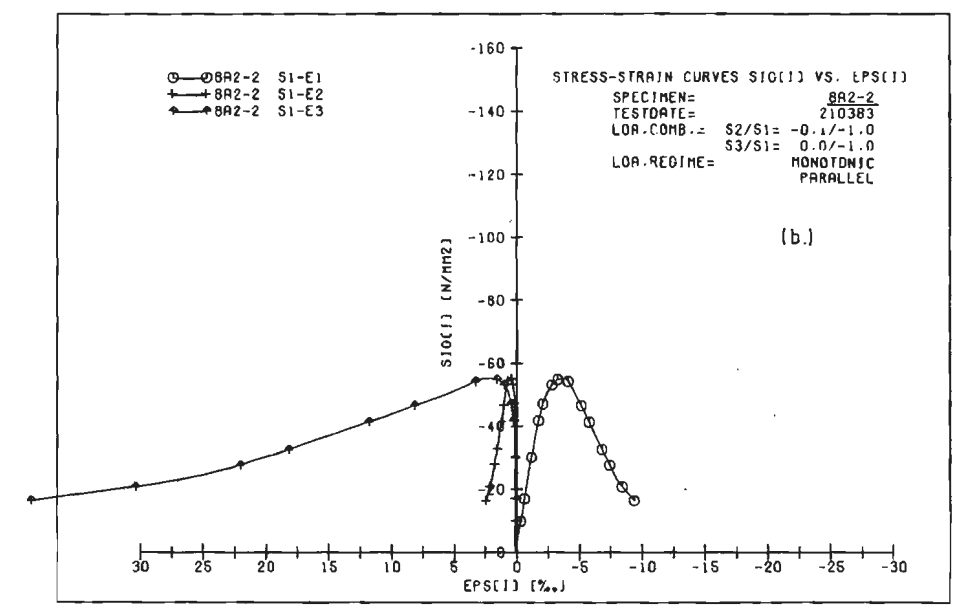

Fig. A5.7. a-b biaxial monotonic stress-ratio tests, specimens 9A1-3 and 8A2-2 (σ_1/σ_2 = -1/-0.05 and -1/-0.10, σ_3 = 0)

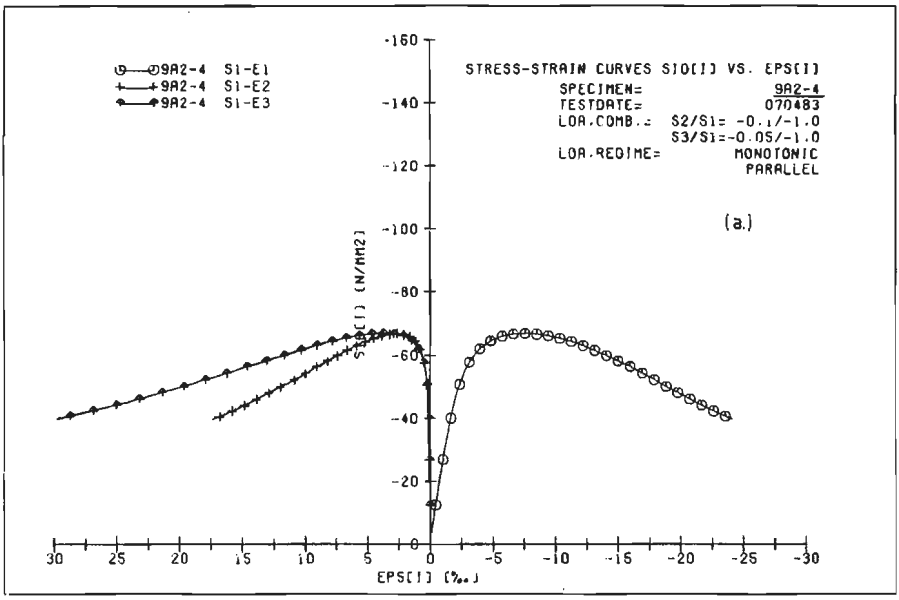

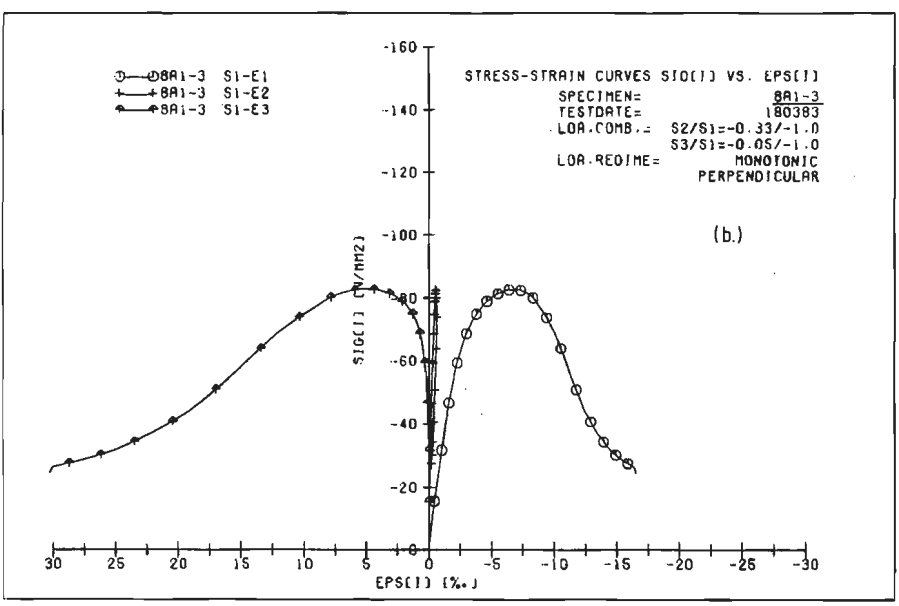

Fig. A5.8. a-b triaxial monotonic stress-ratio tests, specimens 9A2-4 and 8A1-3 (σ_1/σ_2 = -1.0/-0.1 and -1.0/-0.33, $\sigma_3 = 0.05\sigma_1$)

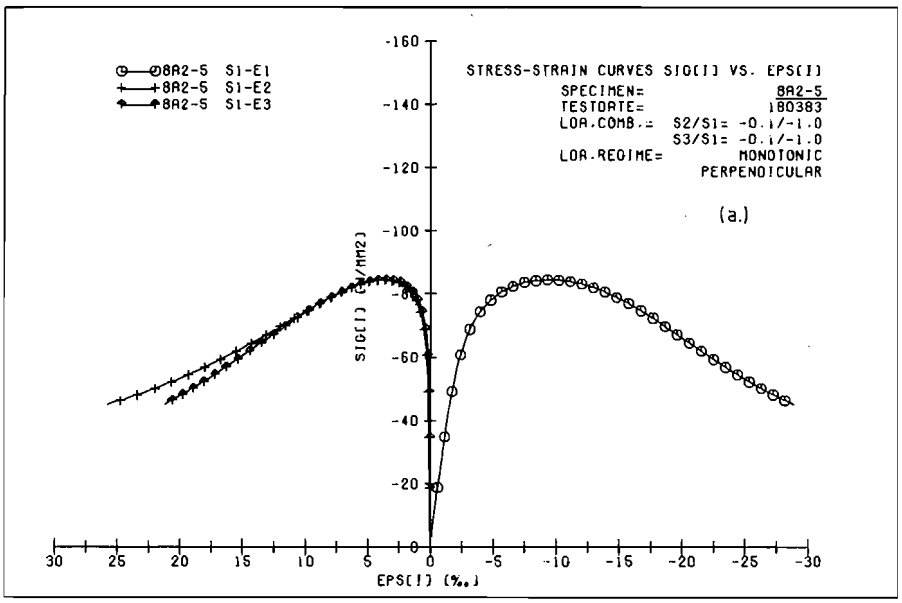

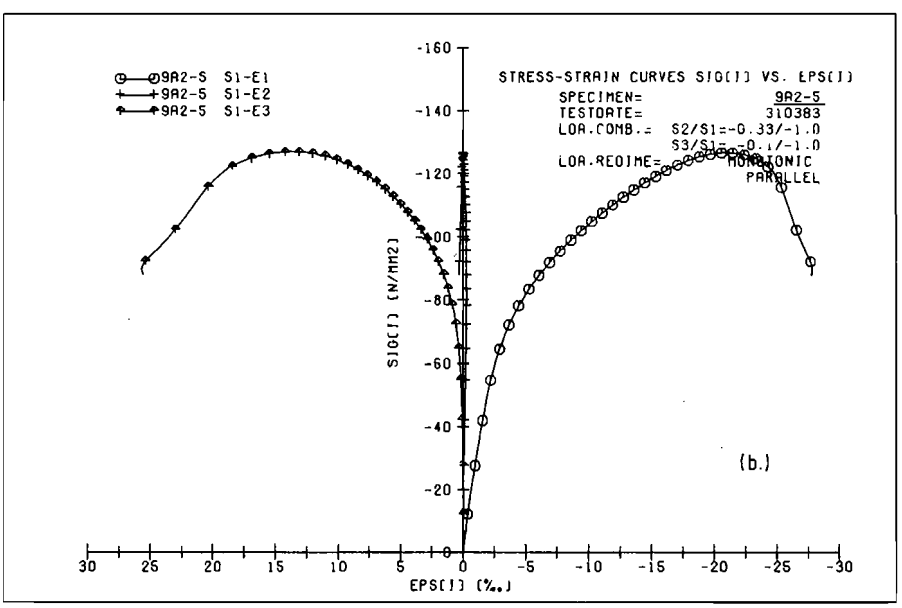

Fig. A5.9. a-b triaxial monotonic stress-ratio tests, specimens 8A2-5 and 9A2-5 (σ_1/σ_2 = -1.0/-0.1 and -1.0/-0.33, $\sigma_3 = 0.10\sigma_1$)

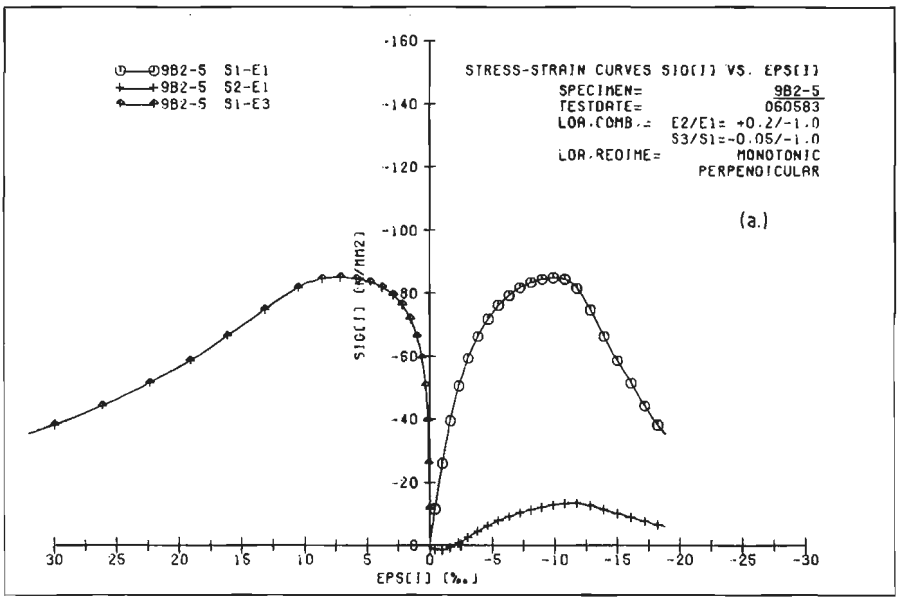

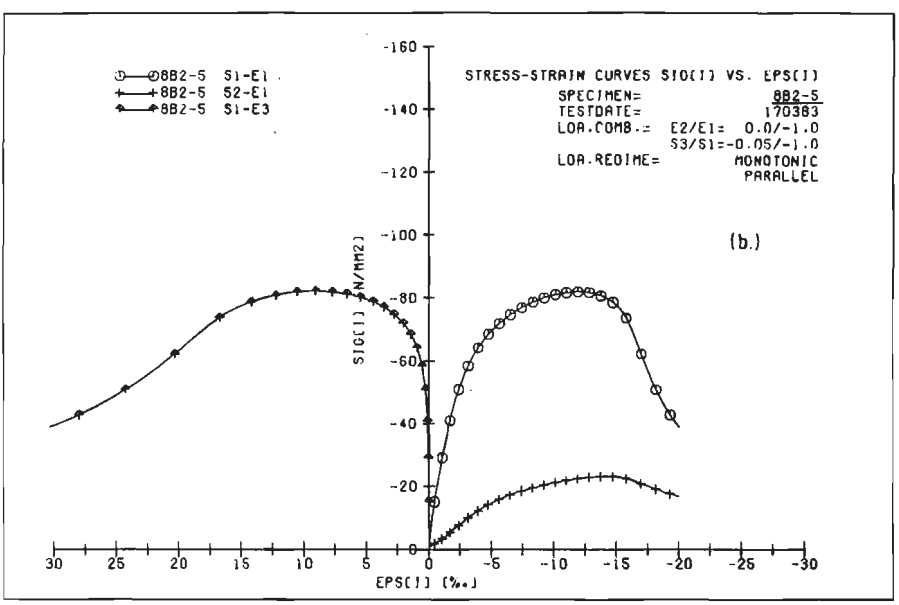

Fig. A5.10, a-b triaxial displacement-ratio tests, monotonic loading, specimens 9B2-5 and 8B2-5 (E2/E1 = 0.2/-1.0 and 0/-1.0, σ_3 = 0.05 σ_1)

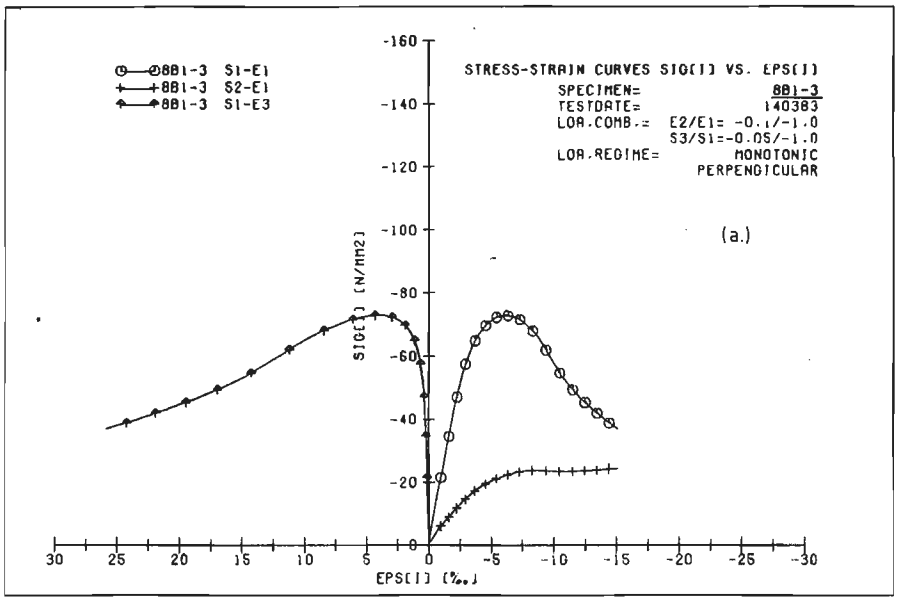

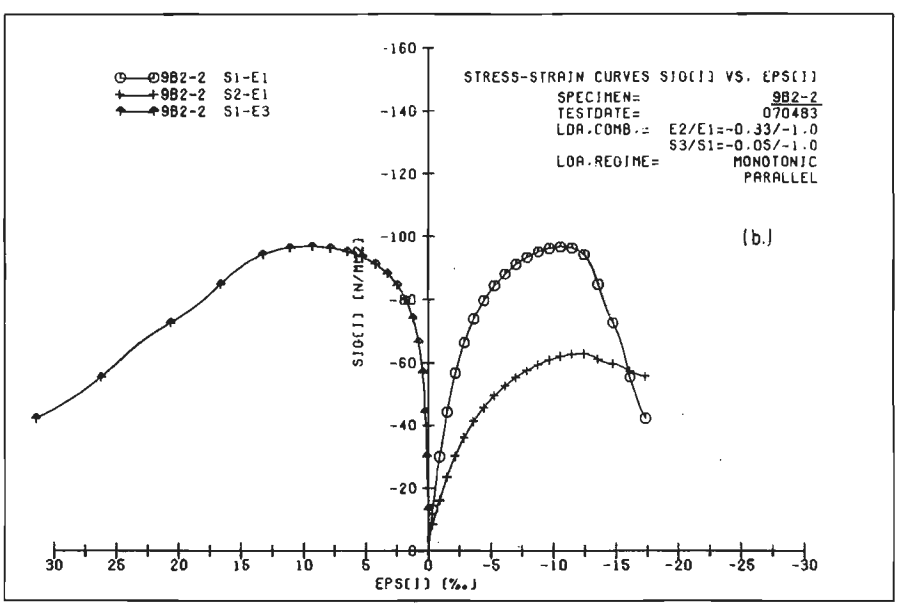

Fig. A5.11, a-b triaxial displacement-ratio tests, monotonic loading, specimens 8B1-3 and 9B2-2 (E2/E1 = -0.1/-1.0 and -0.33/-1.0, $\sigma_3 = 0.05\,\sigma_1$)

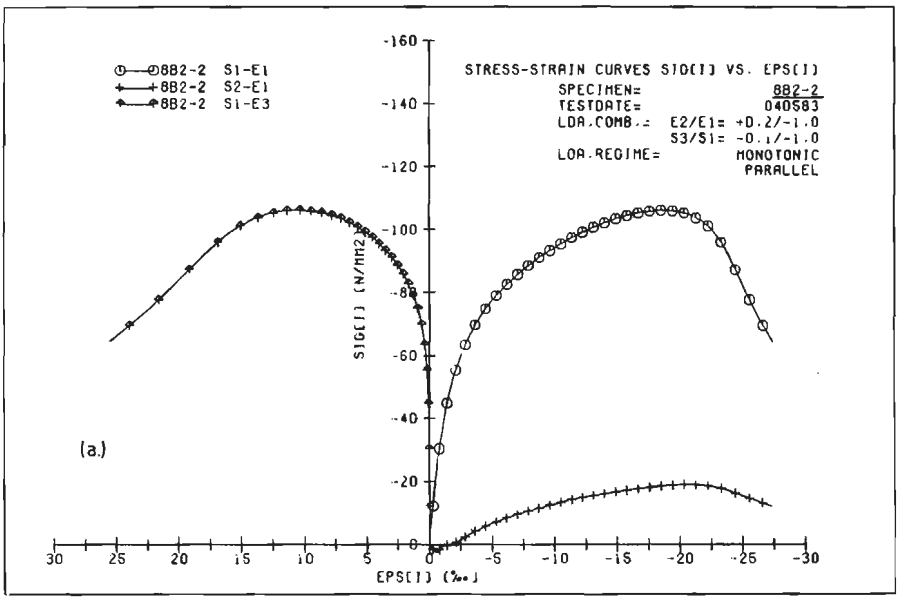

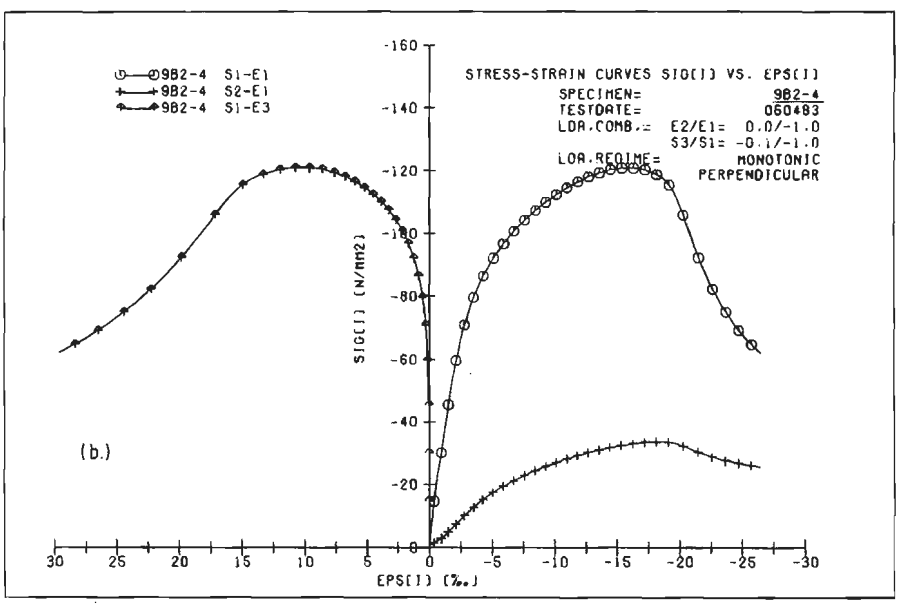

Fig. A5.12, a-b triaxial displacement-ratio tests, monotonic loading, specimens 8B2-2 and 9B2-4 (E2/E1 = 0.2/-1.0 and 0/-1.0, σ_3 = 0.10 σ_1)

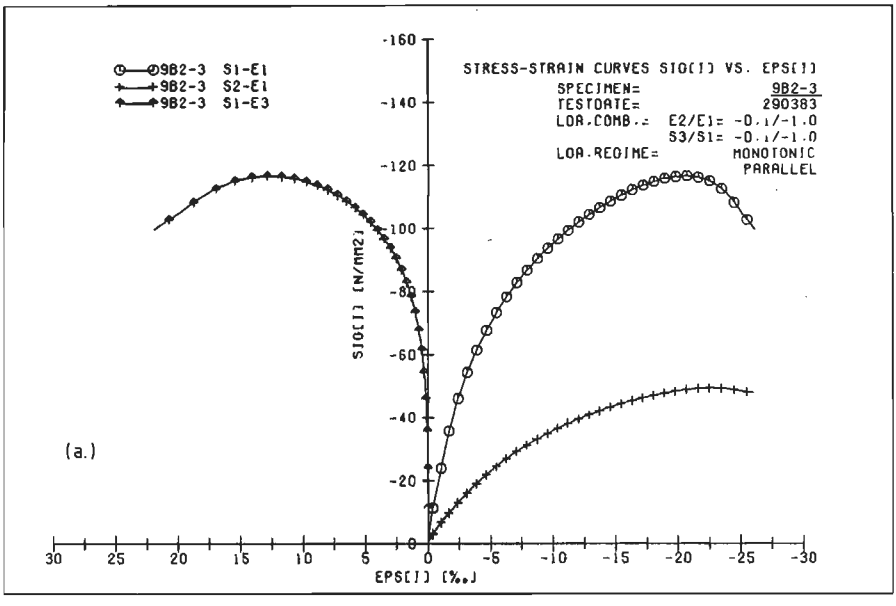

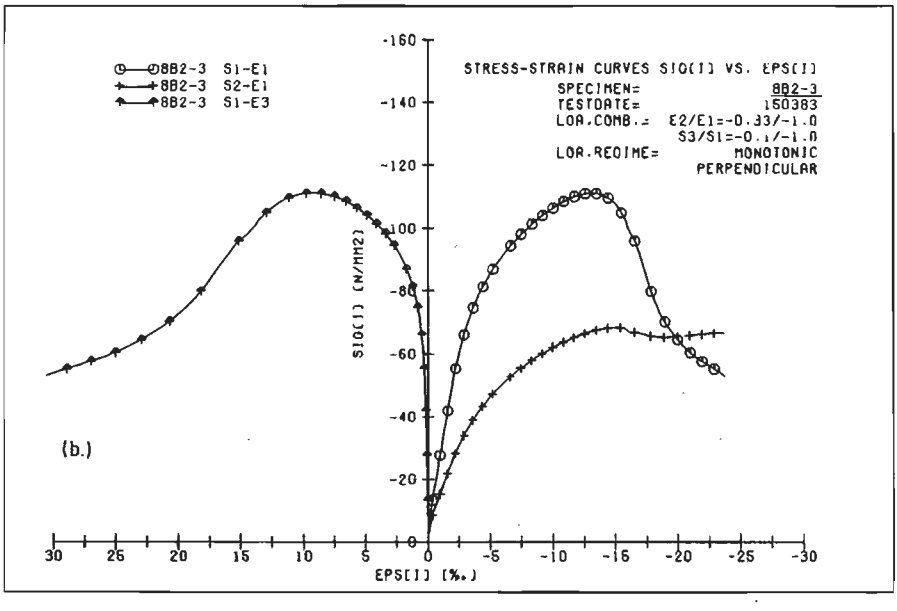

Fig. A5.13, a-b triaxial displacement-ratio tests, monotonic loading, specimens 9B2-3 and 8B2-3 (E2/E1 = -0.1/-1.0 and -0.33/-1.0, $\sigma_3 = 0.10\ \sigma_1$)

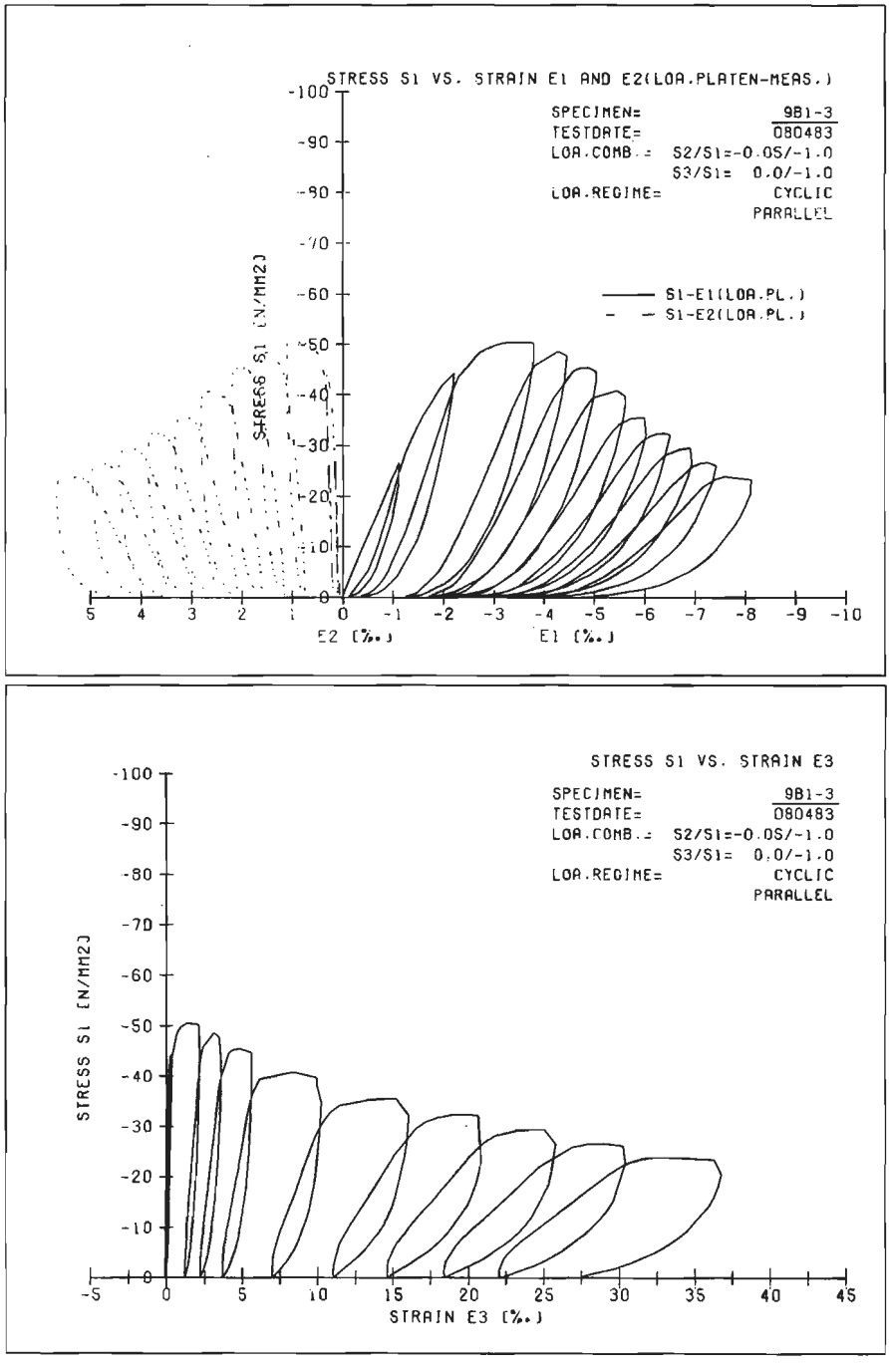

Fig. A5.14, a-b, biaxial stress-ratio test, cyclic loading, $\sigma_1 - \varepsilon_1$, $\sigma_1 - \varepsilon_2$ and $\sigma_1 - \varepsilon_3$ curves for specimen 9B1-3 ($\sigma_1/\sigma_2/\sigma_3$ = -1/-0.05/0)

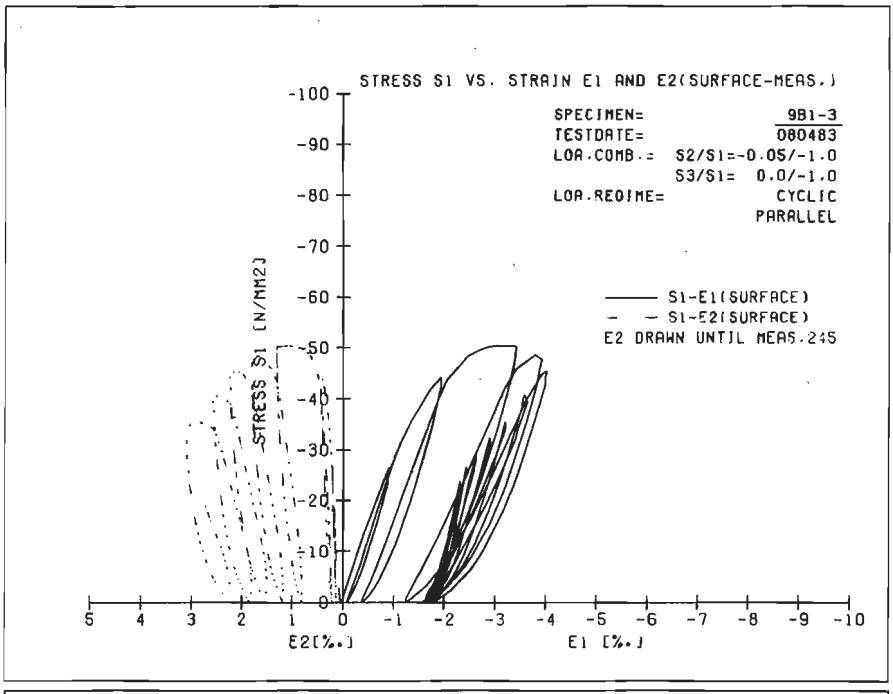

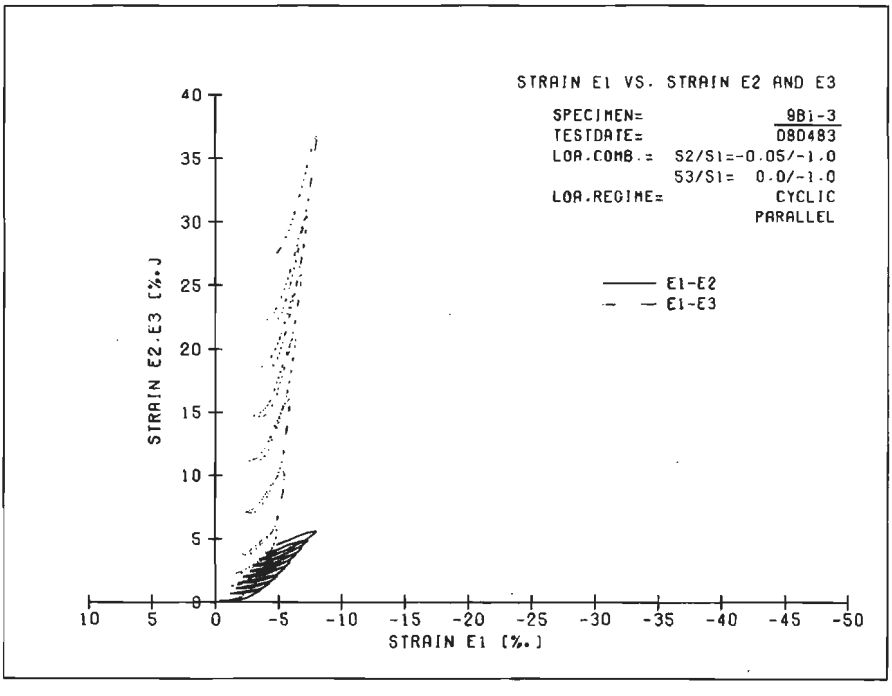

Fig. A5.14, c-d, specimen 9B1-3 ($\sigma_1/\sigma_2/\sigma_3$ = -1/-0.05/0), stress-strain curves σ_1 - ε_1(surf) and σ_1 - ε_2 (surf), and strain-paths ε_1 -ε_2, ε_1 - ε_3.

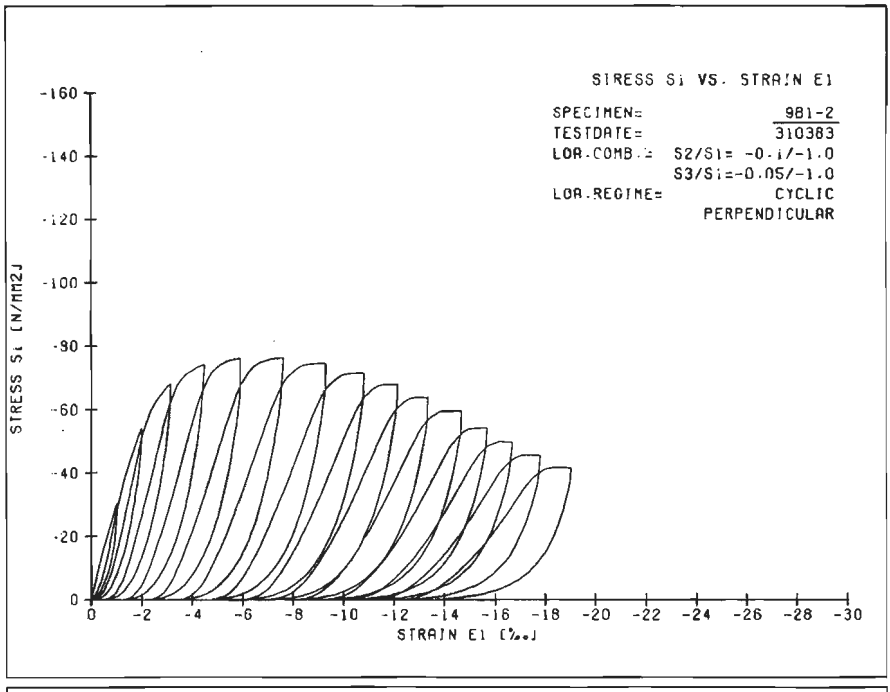

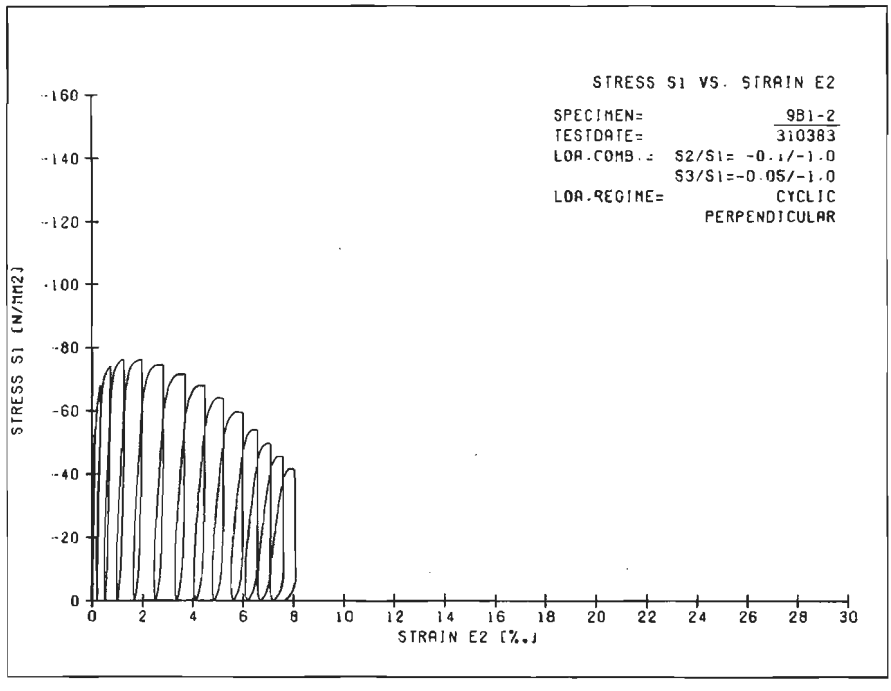

Fig. A5.15, a-b, triaxial stress-ratio test, cyclic loading, $\sigma_1 - \varepsilon_1$ and $\sigma_1 - \varepsilon_2$ curves for specimen 9B1-2 ($\sigma_1/\sigma_2/\sigma_3 = -1/-0.10/-0.05$).

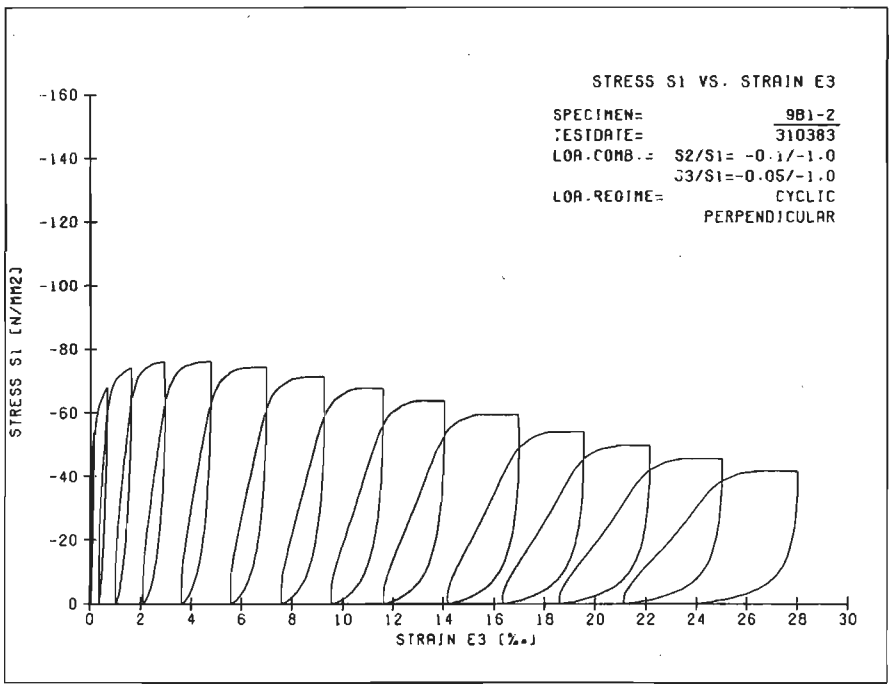

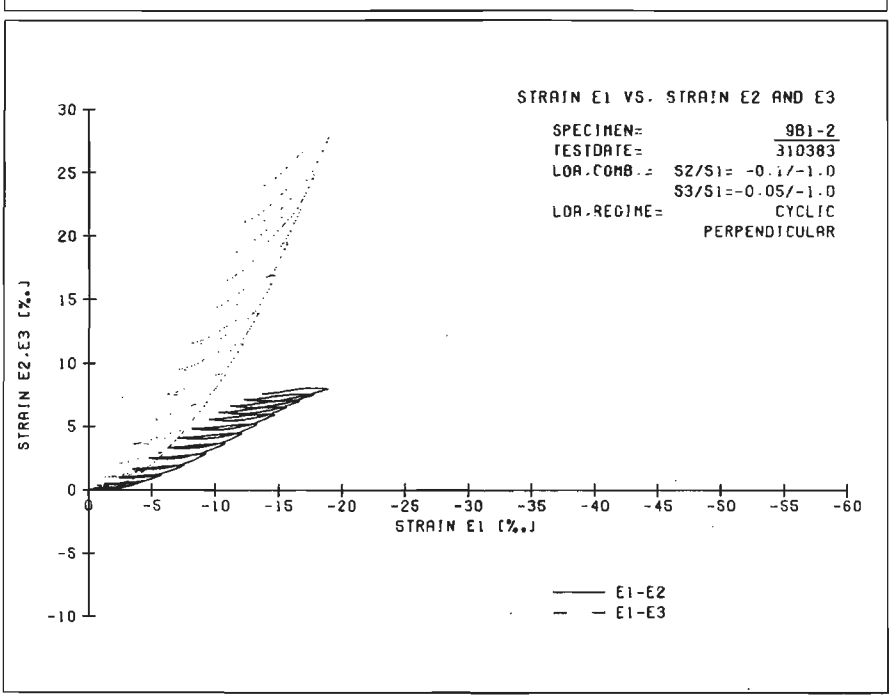

Fig. A5.15, c-d, specimen 9B1-2 ($\sigma_1/\sigma_2/\sigma_3$ = -1/-0.10/-0.05), $\sigma_1 - \varepsilon_3$ and strain-path curves, $\varepsilon_1 - \varepsilon_2$ and $\varepsilon_1 - \varepsilon_3$.

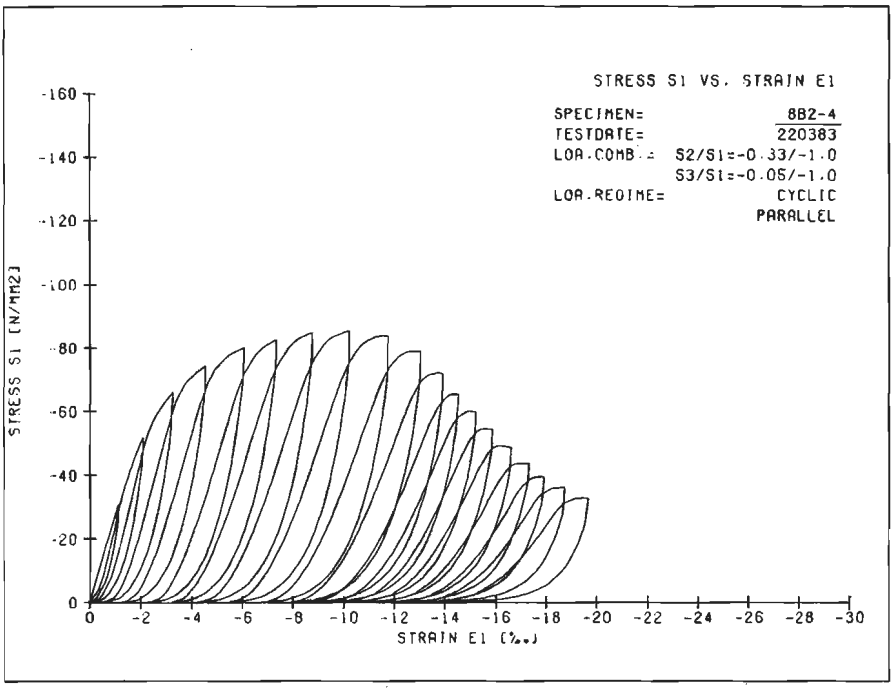

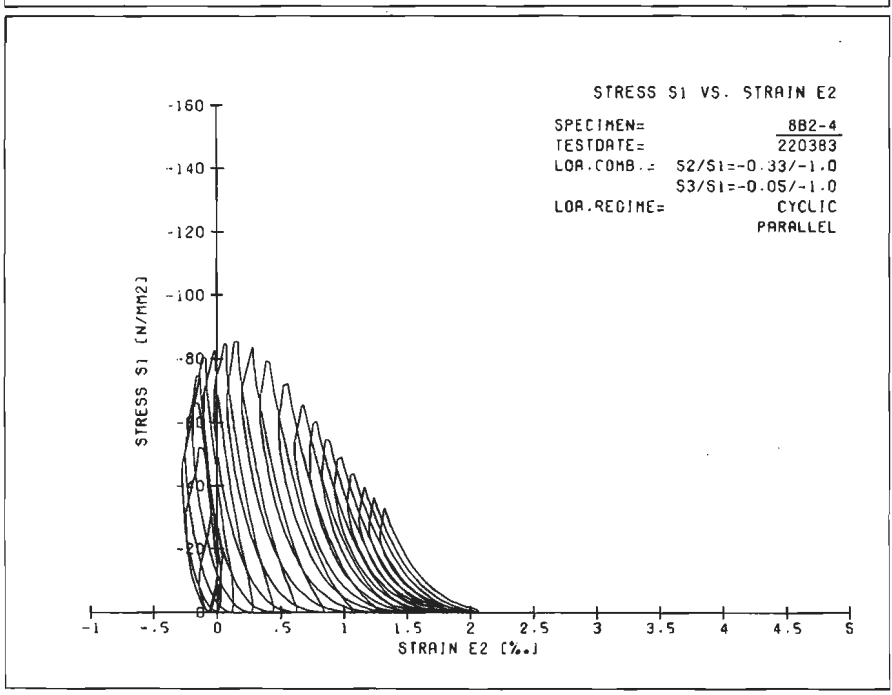

Fig. A5.16, a-b, triaxial stress-ratio test, cyclic loading, $\sigma_1 - \varepsilon_1$ and $\sigma_1 - \varepsilon_2$ curves for specimen 8B2-4 ($\sigma_1/\sigma_2/\sigma_3 = -1/-0.33/-0.05$).

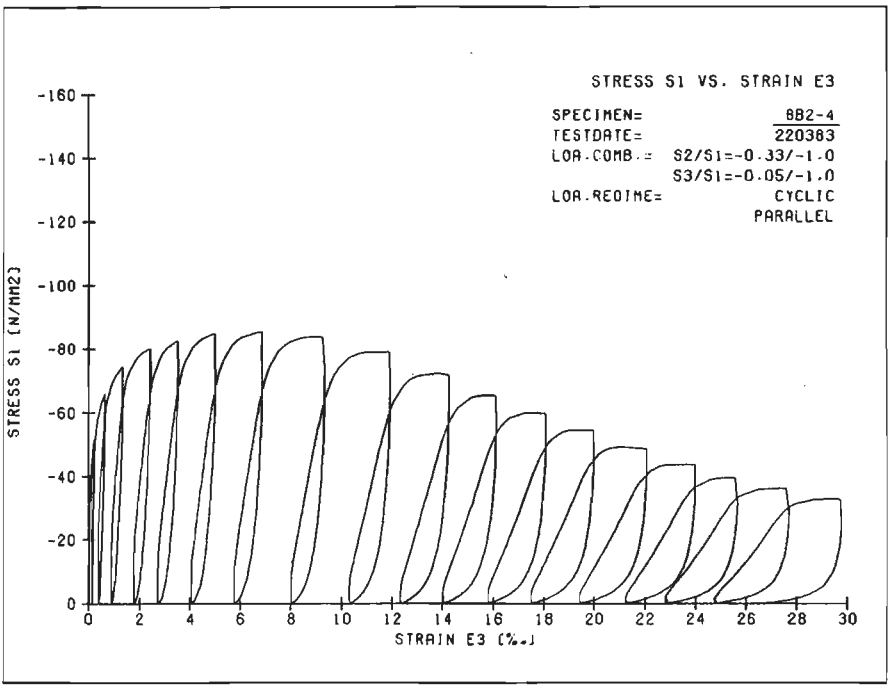

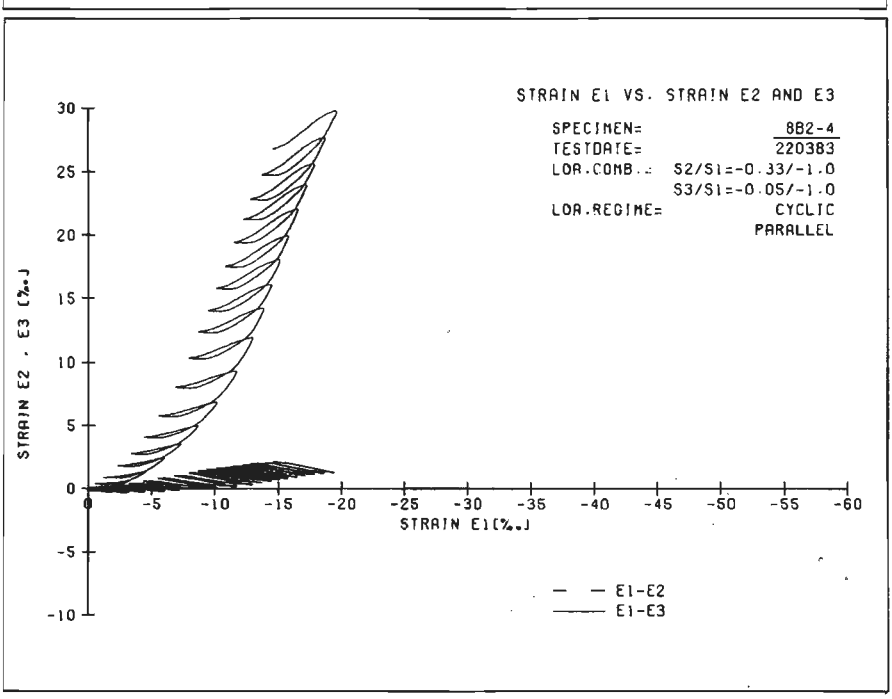

Fig. A5.16, c-d, specimen 8B2-4 ($\sigma_1/\sigma_2/\sigma_3$ = -1/-0.33/-0.05), $\sigma_1 - \varepsilon_3$ and strain-path curves, $\varepsilon_1 - \varepsilon_2$ and $\varepsilon_1 - \varepsilon_3$.

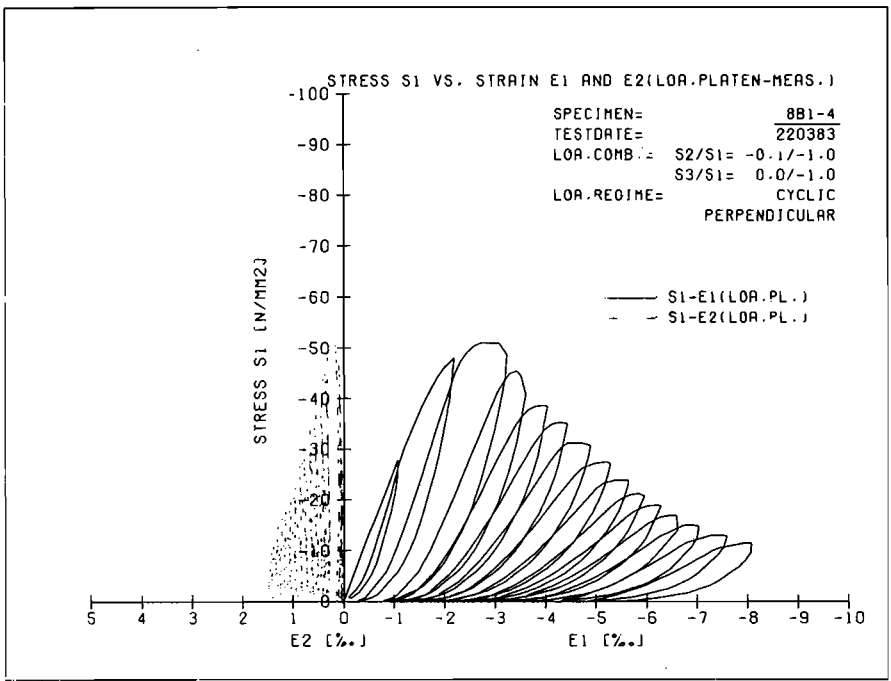

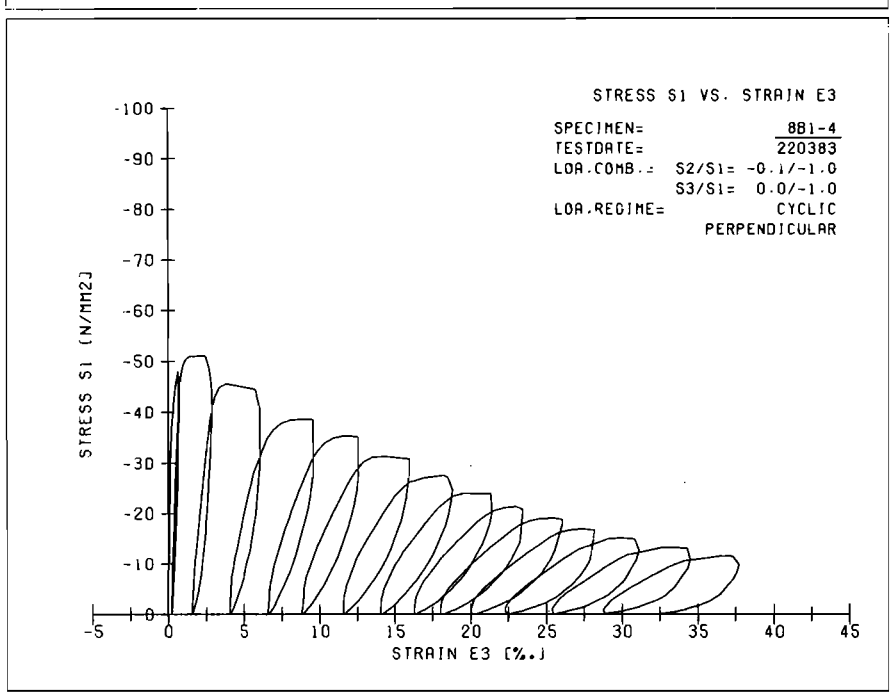

Fig. A5.17, a-b, biaxial stress-ratio test, cyclic loading, $\sigma_1 - \varepsilon_1$, $\sigma_1 - \varepsilon_2$ and $\sigma_1 - \varepsilon_3$ curves for specimen 8B1-4 ($\sigma_1/\sigma_2/\sigma_3$ = -1/-0.10/0).

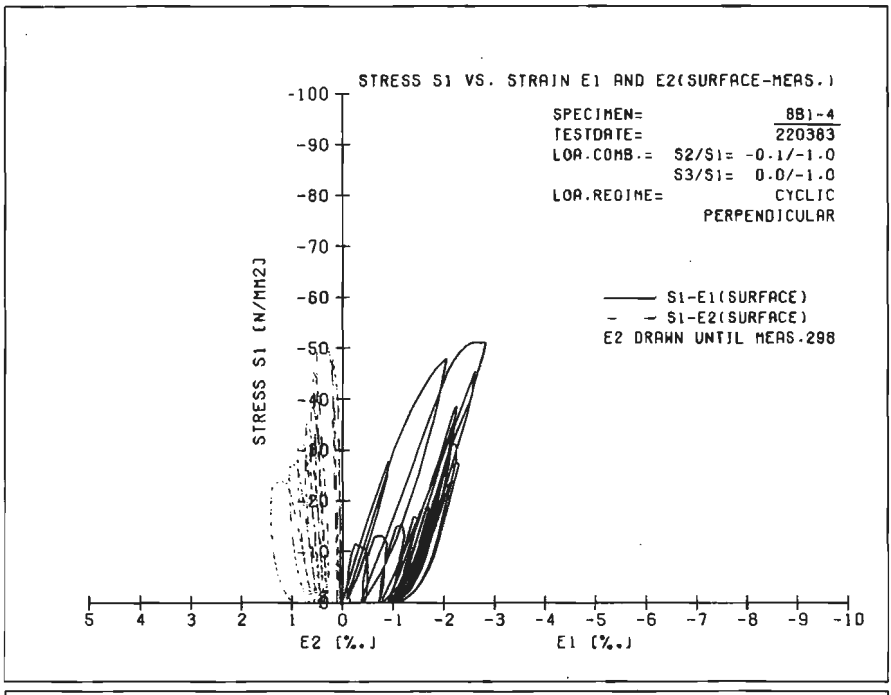

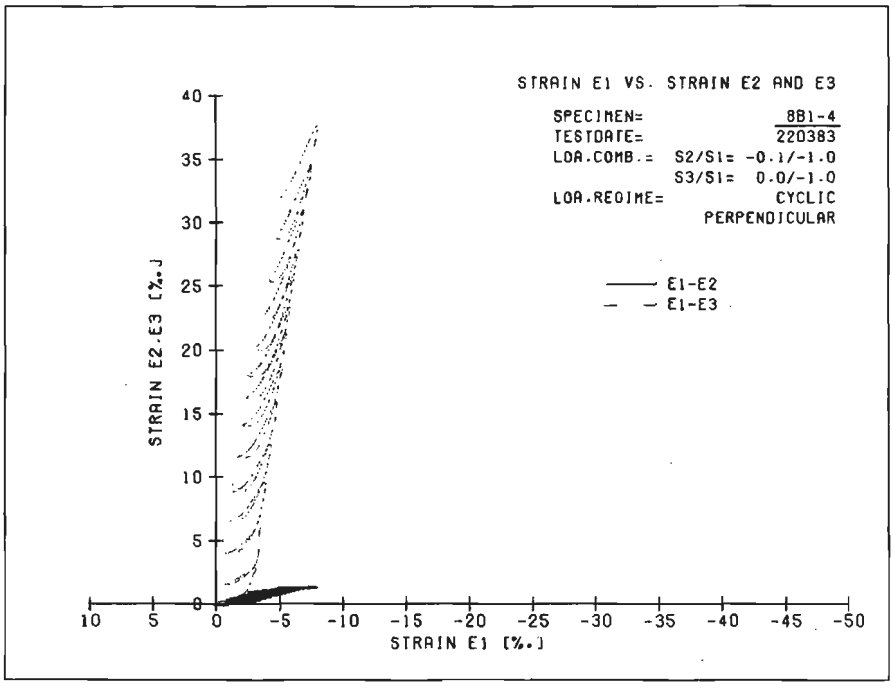

Fig. A5.17, c-d, specimen 8B1-4 ($\sigma_1/\sigma_2/\sigma_3$ = -1/-0.10/0), stress-strain curves σ_1 - ε_1(surf.) and σ_1 - ε_2 (surf.) and strain-paths, ε_1 -ε_2 and ε_1 - ε_3.

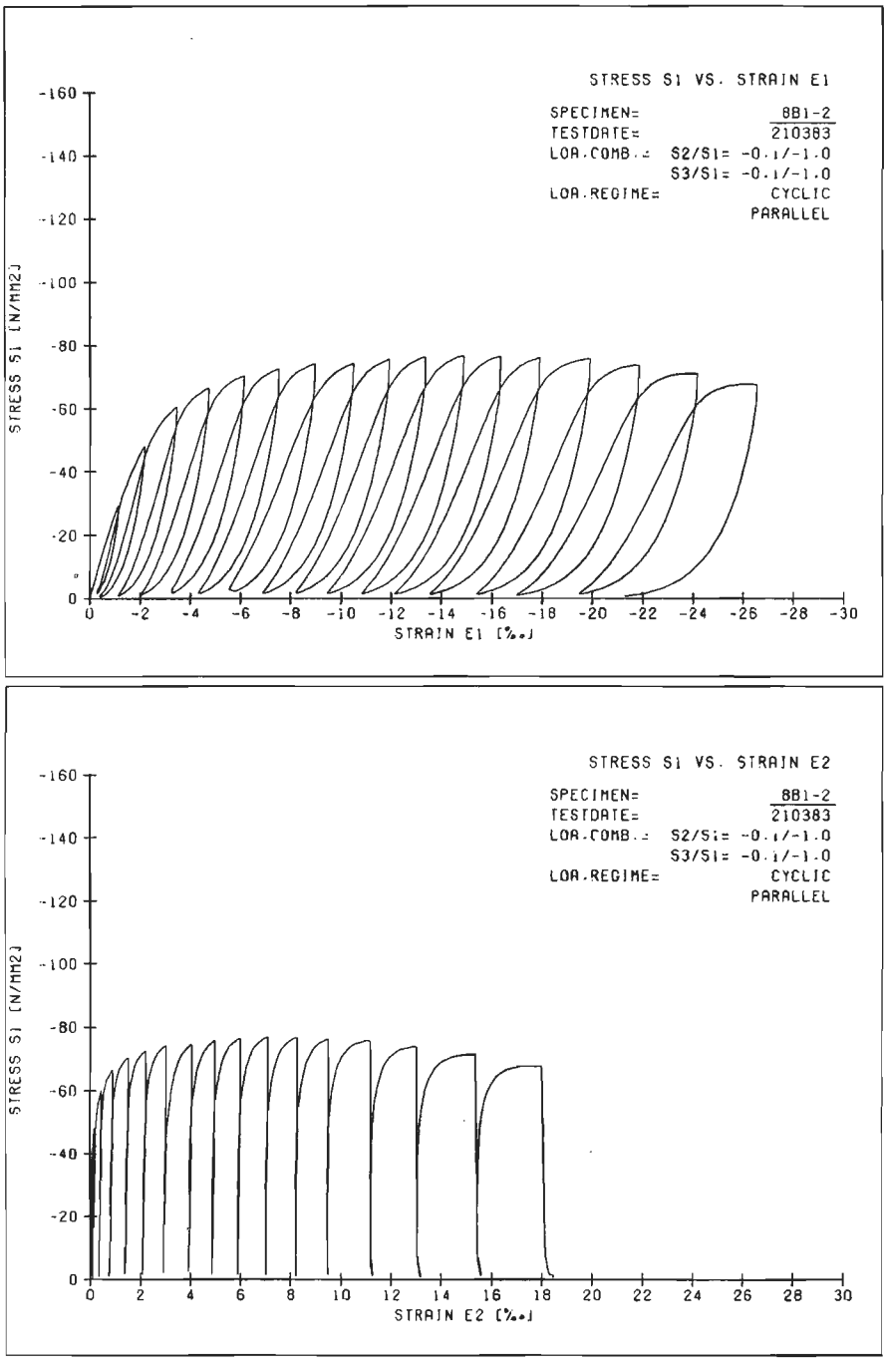

Fig. A5.18, a-b, triaxial stress-ratio test, cyclic loading, $\sigma_1 - \varepsilon_1$ and $\sigma_1 - \varepsilon_2$ curves for specimen 8B1-2 ($\sigma_1/\sigma_2/\sigma_3 = -1/-0.10/-0.10$).

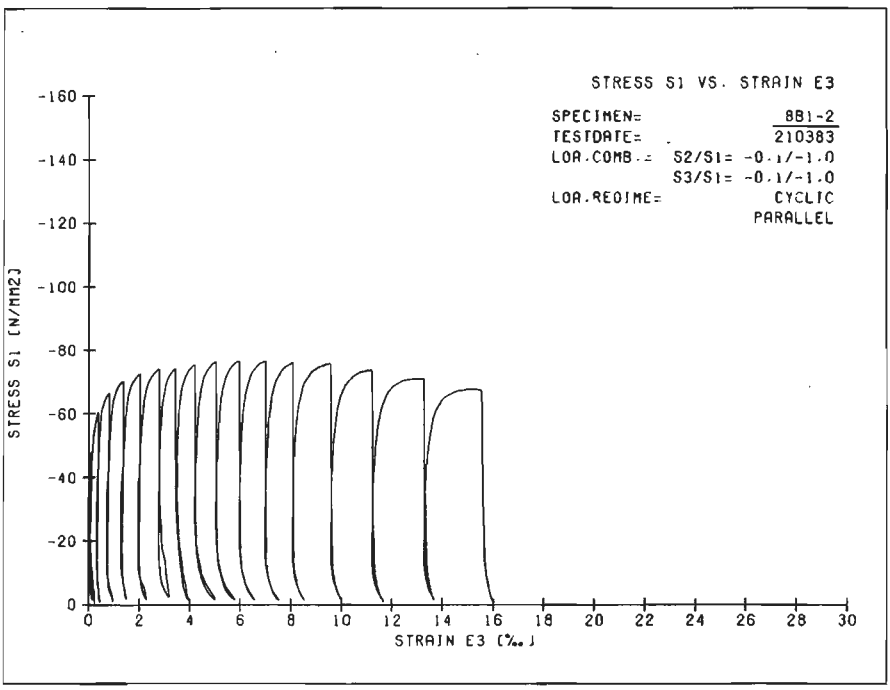

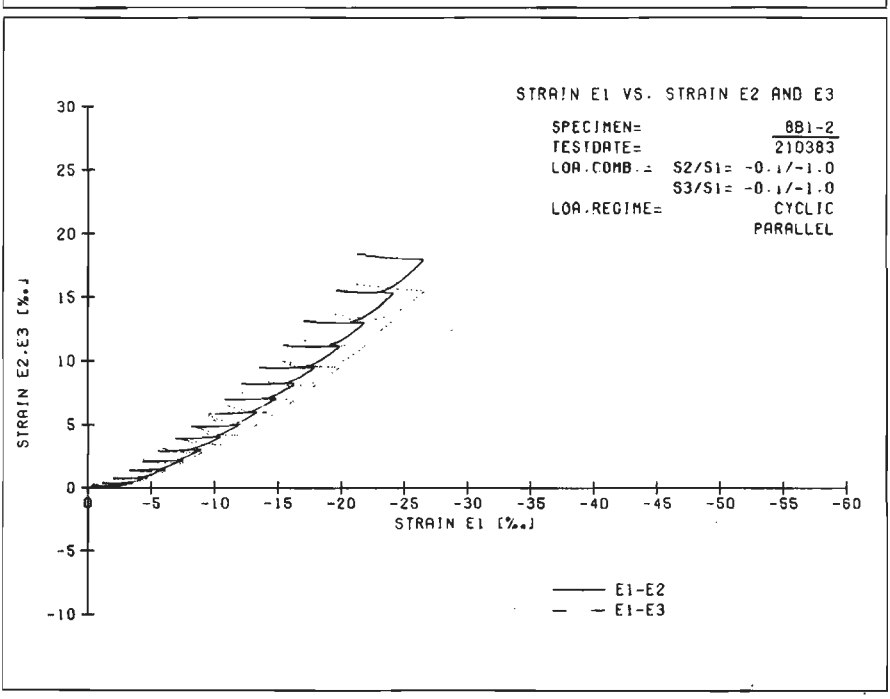

Fig. A5.18, c-d, specimen 8B1-2 ($\sigma_1/\sigma_2/\sigma_3$ = -1/-0.10/-0.10), $\sigma_1 - \varepsilon_3$ and strain-path curves, $\varepsilon_1 - \varepsilon_2$ and $\varepsilon_1 - \varepsilon_3$.

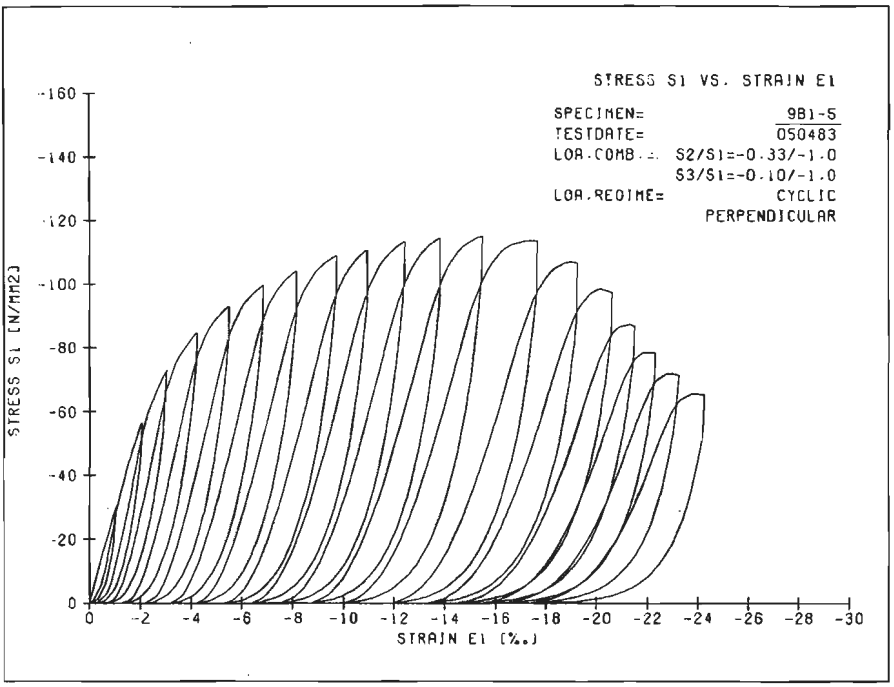

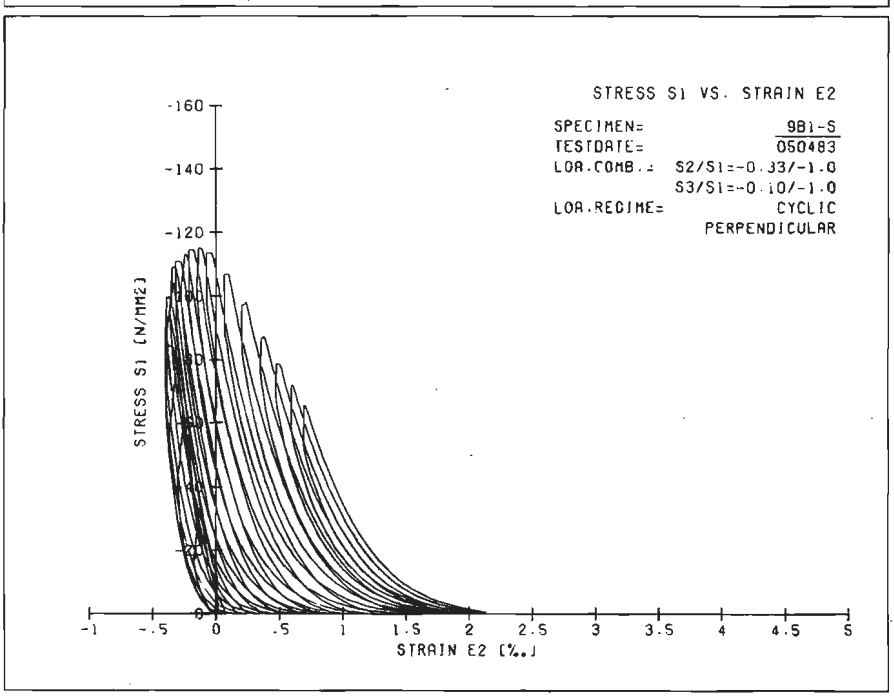

Fig. A5.19, a-b, triaxial stress-ratio test, cyclic loading, $\sigma_1 - \varepsilon_1$ and $\sigma_1 - \varepsilon_2$ curves for specimen 9B1-5 ($\sigma_1/\sigma_2/\sigma_3 = -1/-0.33/-0.10$).

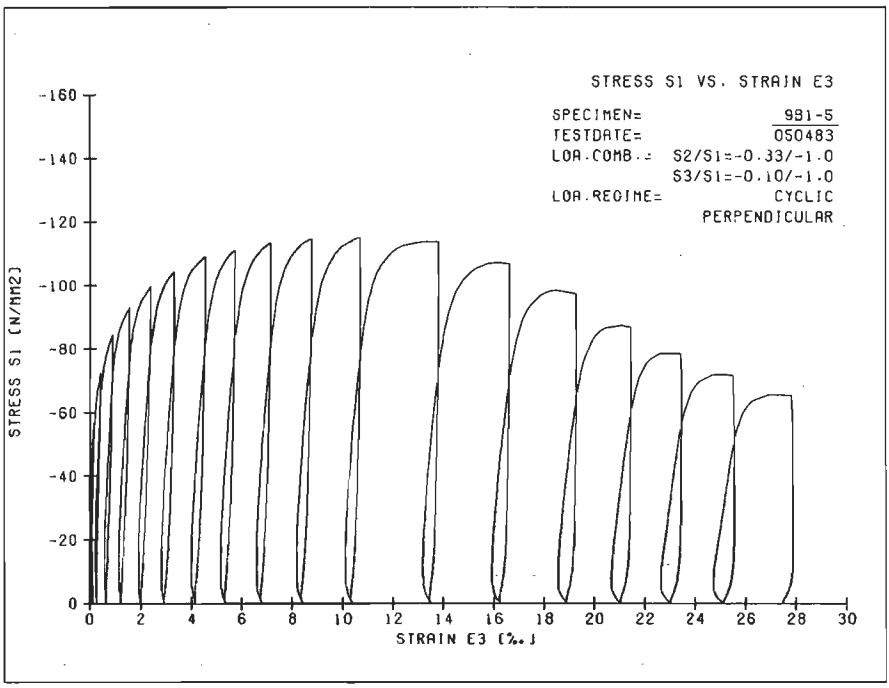

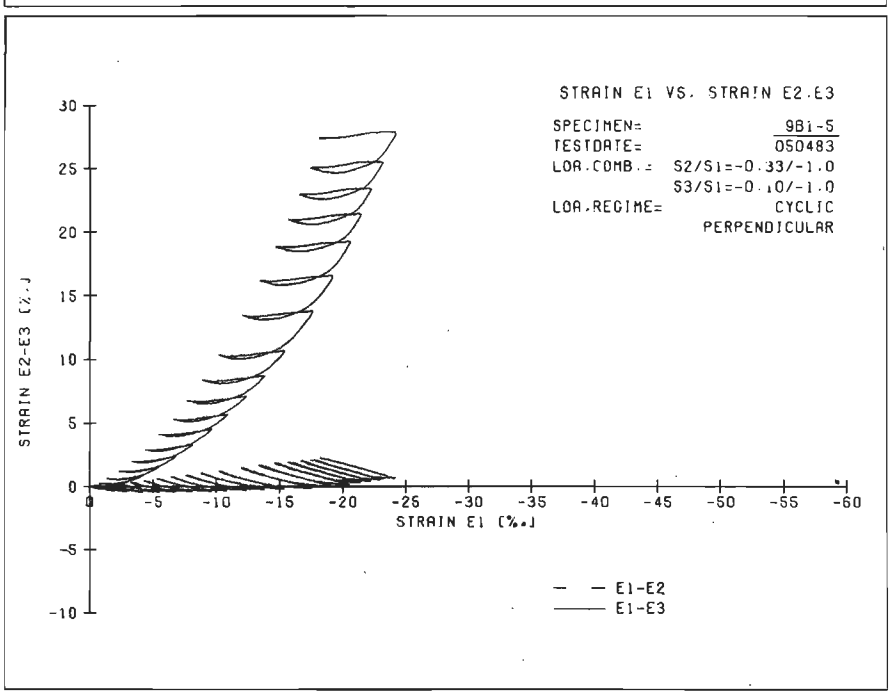

Fig. A5.19, c-d, specimen 9B1-5 ($\sigma_1/\sigma_2/\sigma_3$ = -1/-0.33/-0.10), $\sigma_1 - \varepsilon_3$ and strain-path curves, $\varepsilon_1 - \varepsilon_2$ and $\varepsilon_1 - \varepsilon_3$.

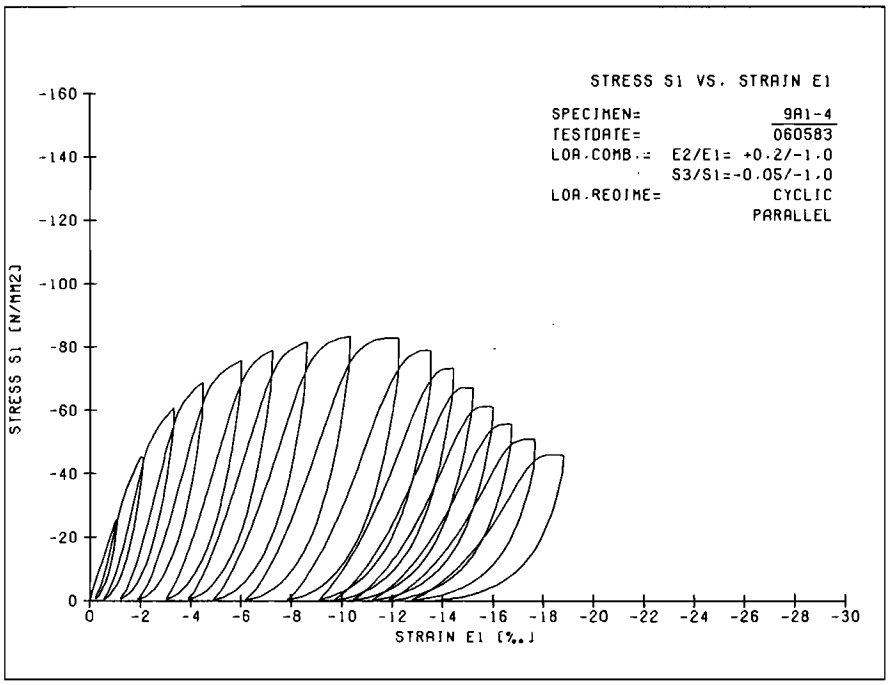

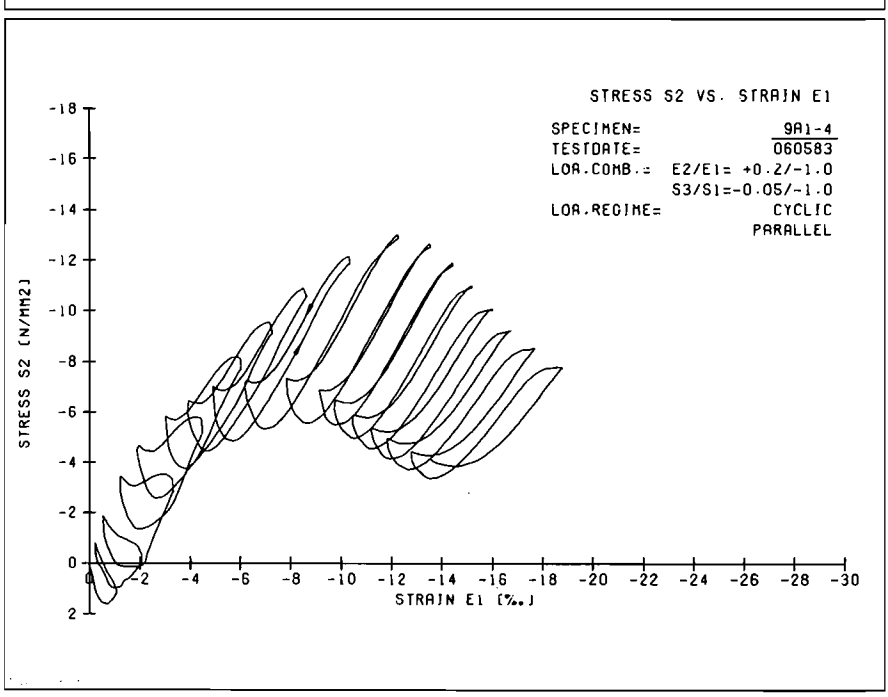

Fig. A5.20, a-b, triaxial displacement-ratio test, cyclic loading, $\sigma_1 - \varepsilon_1$ and $\sigma_2 - \varepsilon_1$ curves for specimen 9A1-4 (E2/E1 = +0.2/-1.0, $\sigma_3 = 0.05\,\sigma_1$)

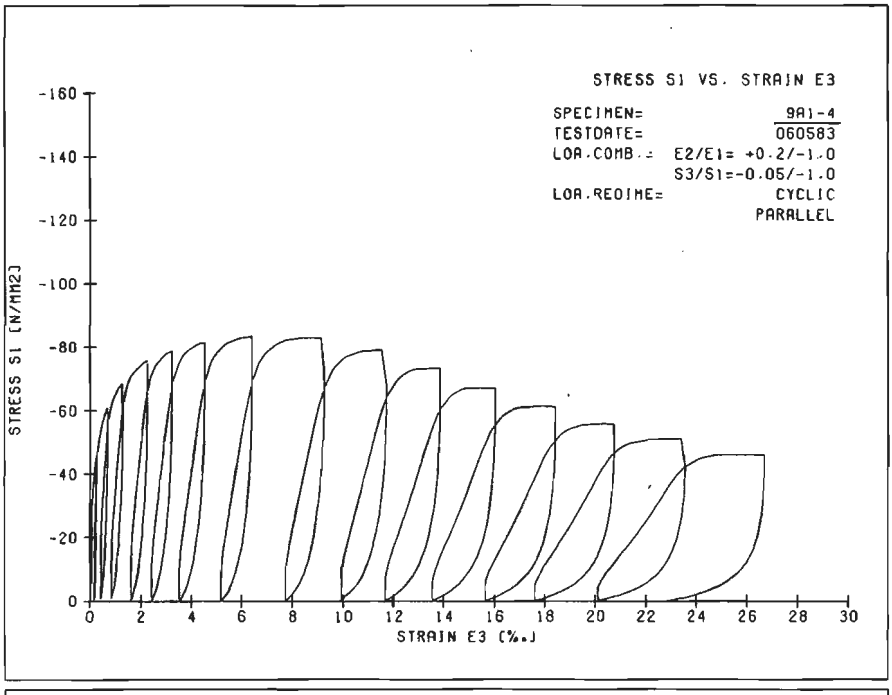

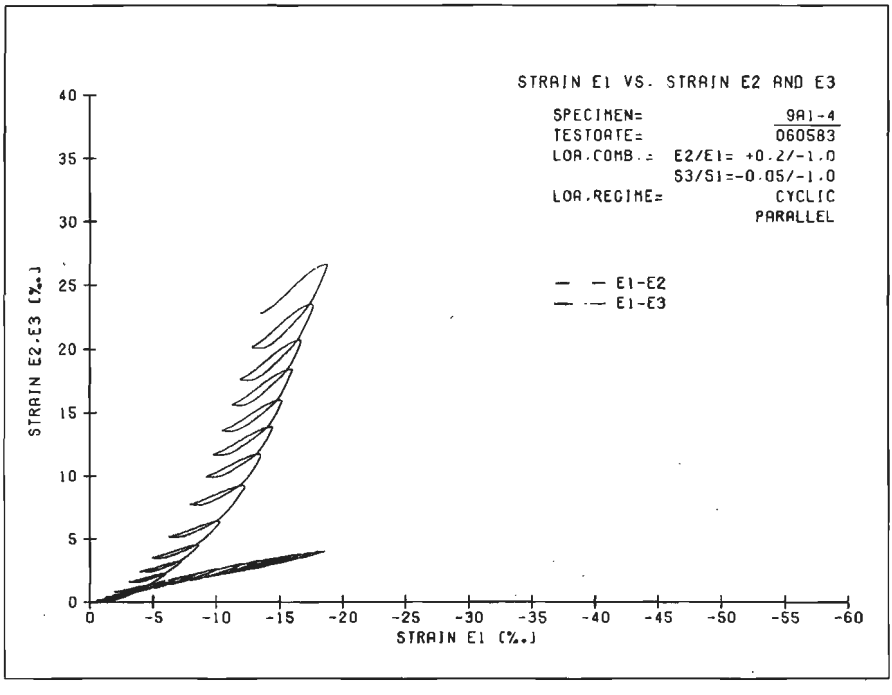

Fig. A5.20, c-d, specimen 9A1-4 (E2/E1 = +0.2/-1.0, $\sigma_3 = 0.05\ \sigma_1$), $\sigma_1 - \varepsilon_3$ curve and strain-path curves $\varepsilon_1 - \varepsilon_2$, $\varepsilon_1 - \varepsilon_3$

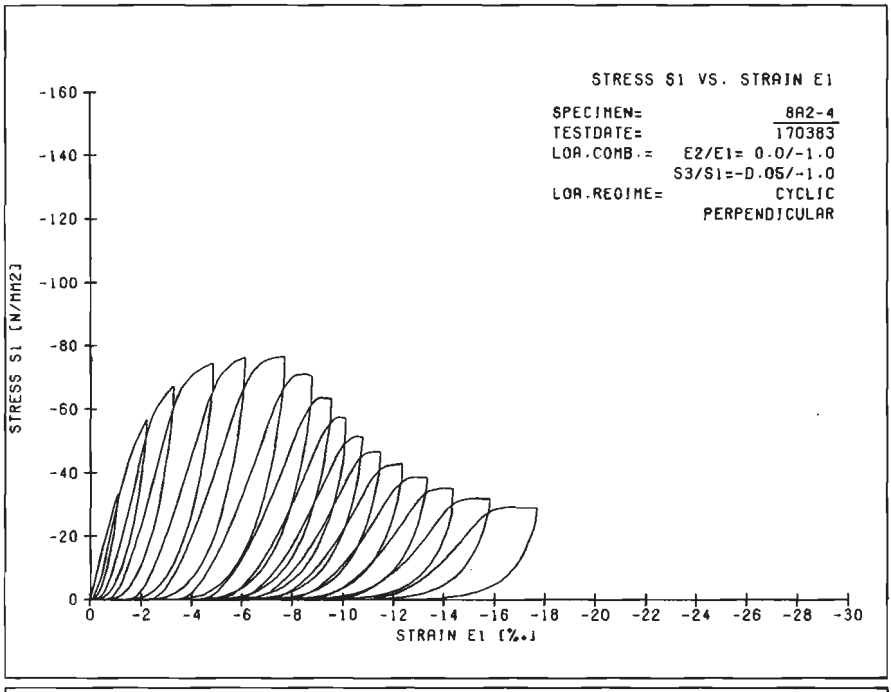

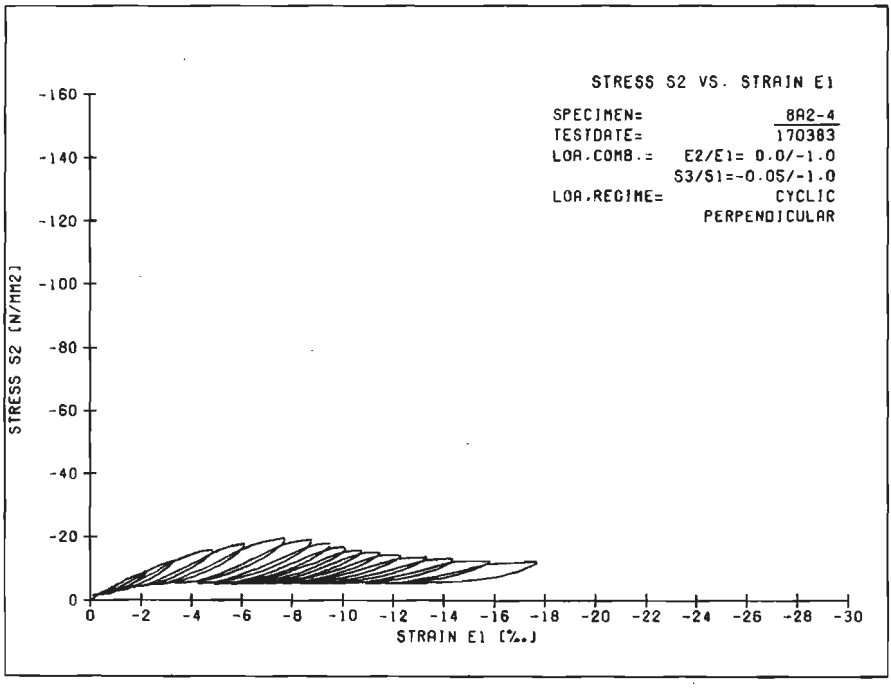

Fig. A5.21, a-b, triaxial displacement-ratio test, cyclic loading, $\sigma_1 - \varepsilon_1$ and $\sigma_2 - \varepsilon_1$ curves for specimen 8A2-4 (E2/E1 = 0.0/-1.0, $\sigma_3 = 0.05\sigma_1$).

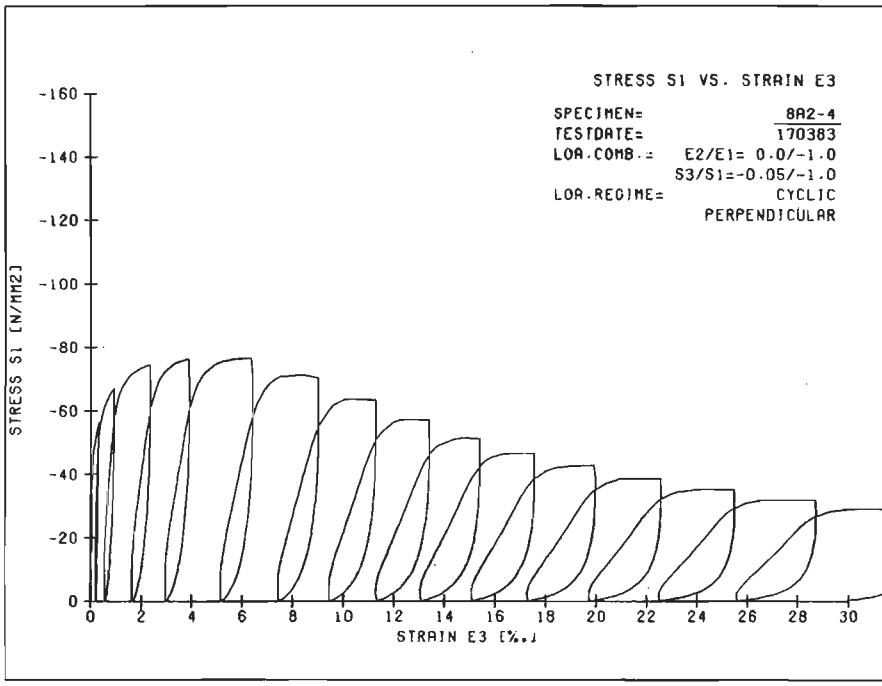

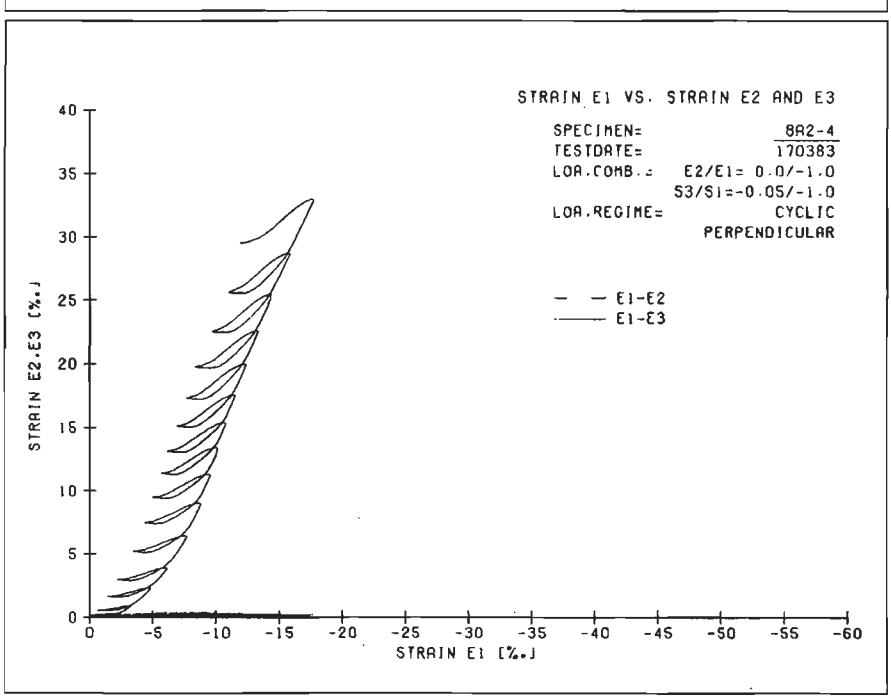

Fig. A5.21, c-d, specimen 8A2-4 (E2/E1 = 0.0/-1.0, $\sigma_3 = 0.05\,\sigma_1$), $\sigma_1 - \varepsilon_3$ curve and strain-path curves $\varepsilon_1 - \varepsilon_2$, $\varepsilon_1 - \varepsilon_3$

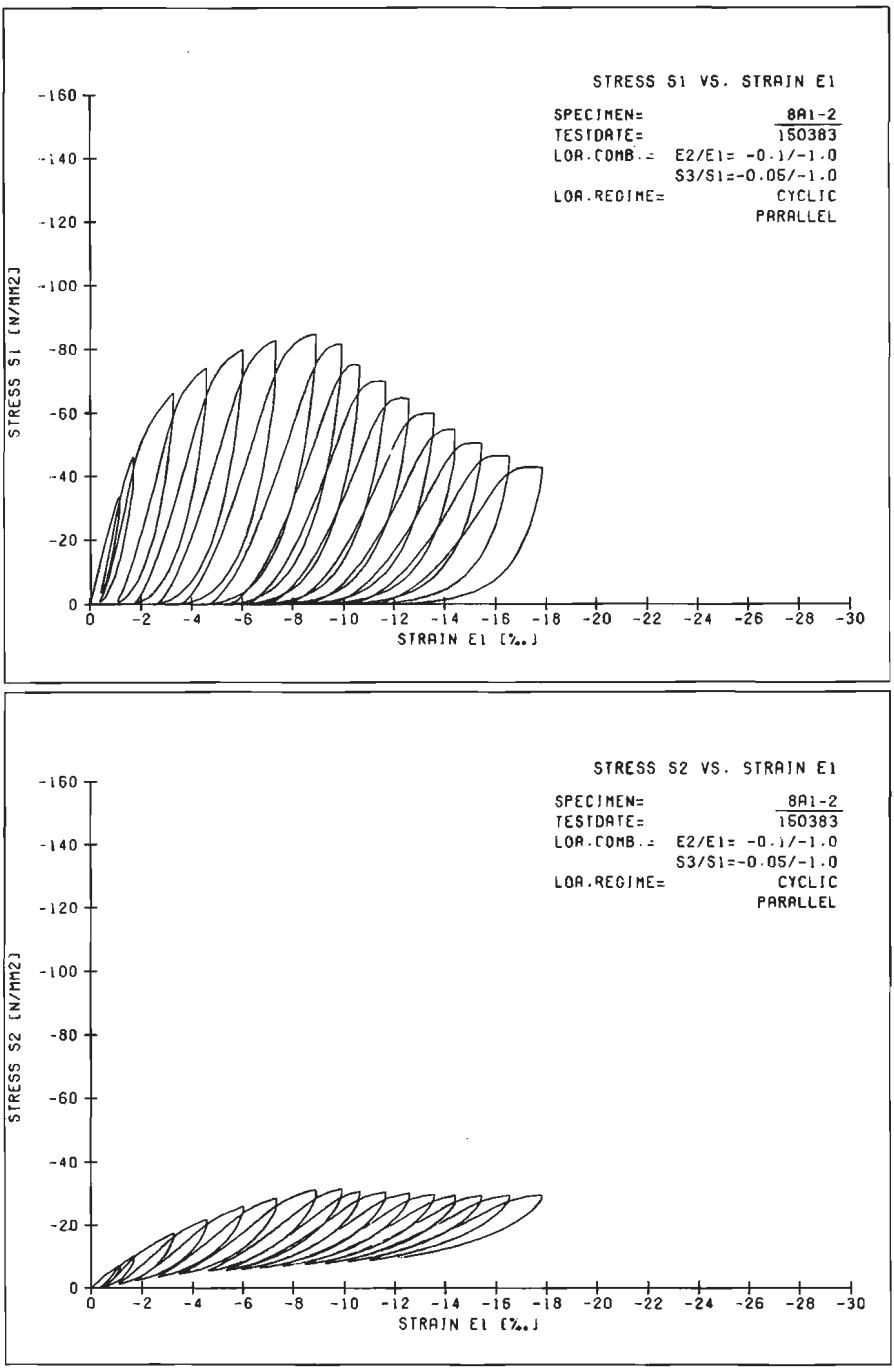

Fig. A5.22, a-b, triaxial displacement-ratio test, cyclic loading, $\sigma_1 - \varepsilon_1$ and $\sigma_2 - \varepsilon_1$ curves for specimen 8A1-2 (E2/E1 = -0.1/-1.0, $\sigma_3 = 0.05\ \sigma_1$)

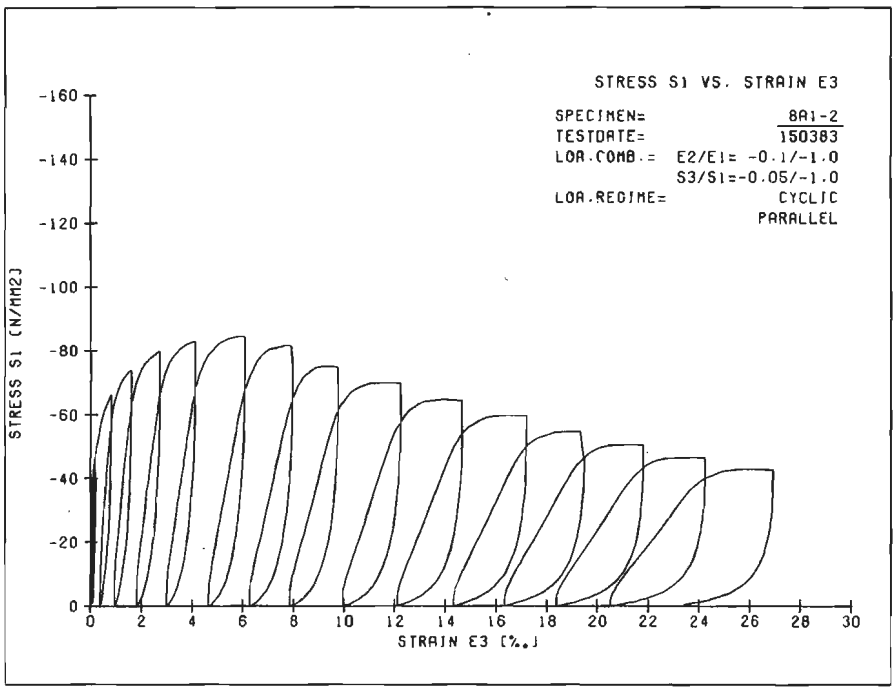

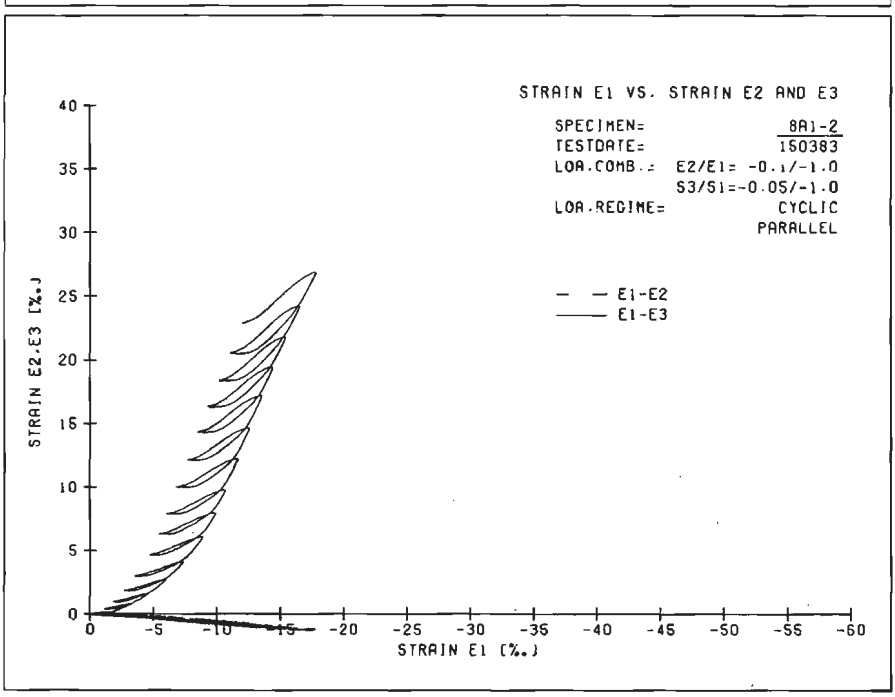

Fig. A5.22, c-d, specimen 8A1-2 (E2/E1 = -0.1/-1.0, $\sigma_3 = 0.05\ \sigma_1$), $\sigma_1 - \varepsilon_3$ curve and strain-path curves $\varepsilon_1 - \varepsilon_2$, $\varepsilon_1 - \varepsilon_3$

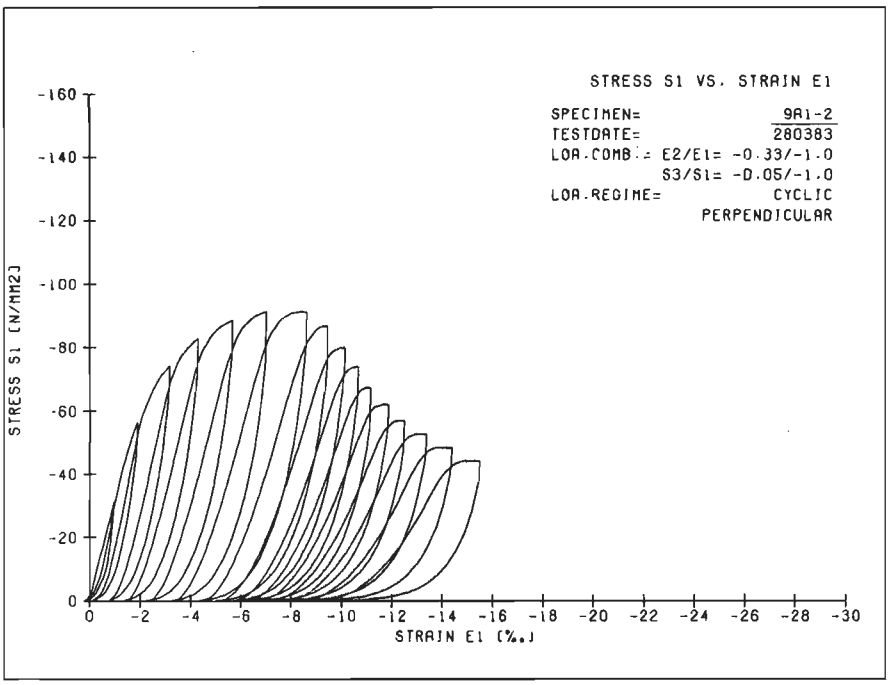

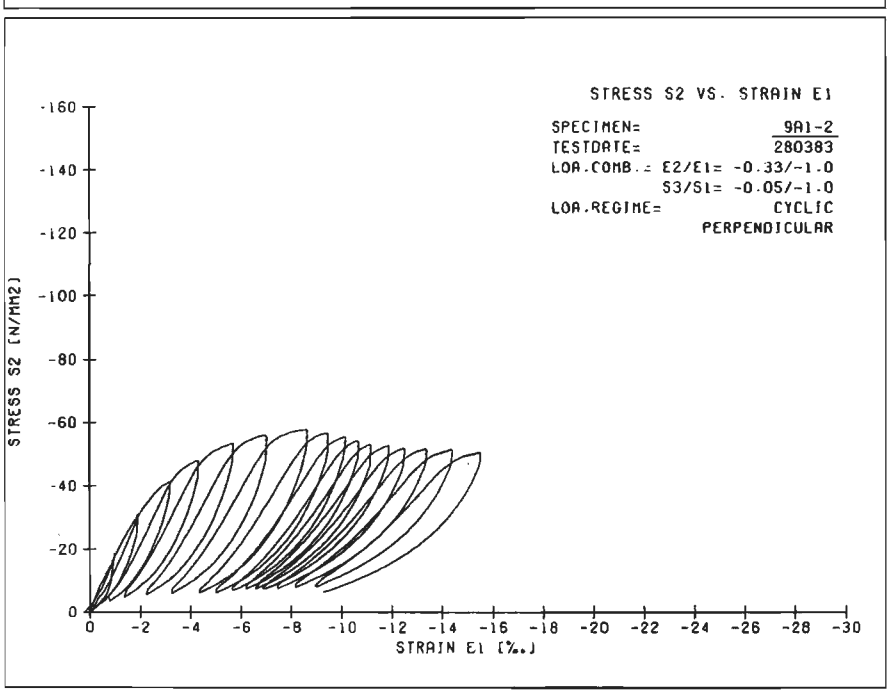

Fig. A5.23, a-b, triaxial displacement-ratio test, cyclic loading, σ_1 - ε_1 and σ_2 - ε_1 curves for specimen 9A1-2 (E2/E1 = -0.33/-1.0, $^1\sigma_3$ = 0.05 σ_1)

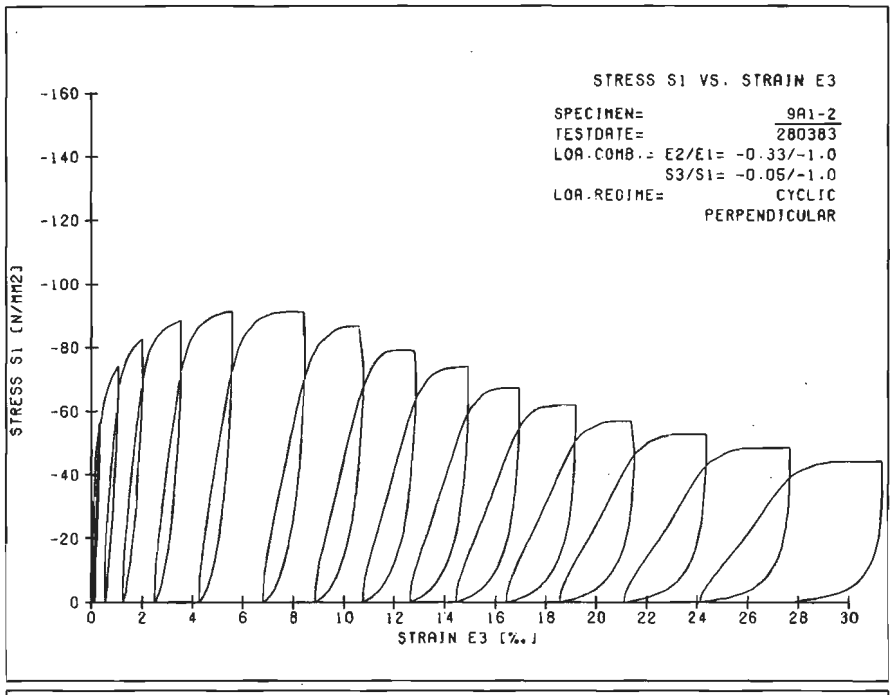

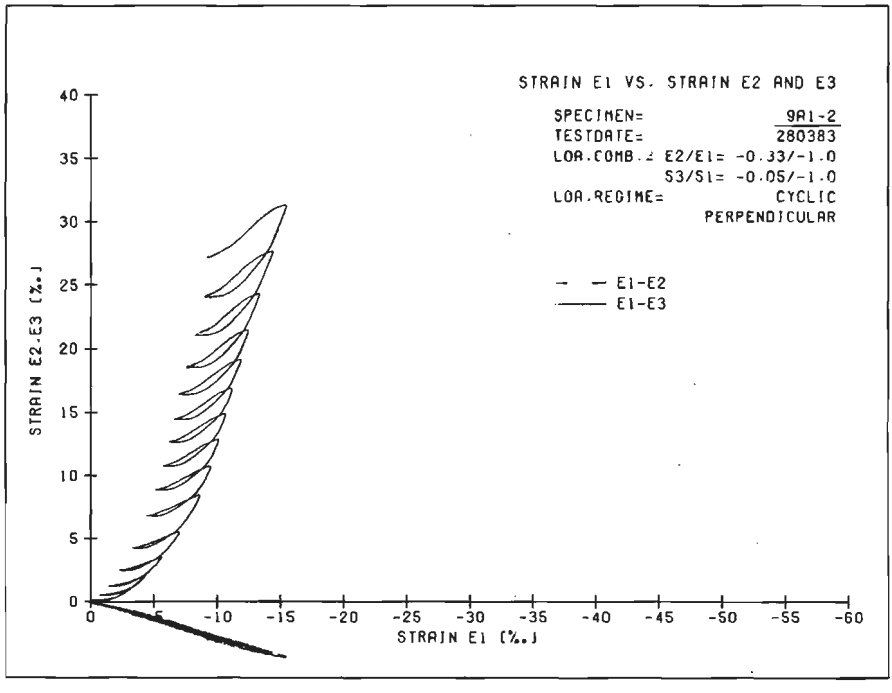

Fig. A5.23, c-d, specimen 9A1-2 (E2/E1 = -0.33/-1.0, $\sigma_3 = 0.05\ \sigma_1$), $\sigma_1 - \varepsilon_3$ curve and strain-path curves $\varepsilon_1 - \varepsilon_2$, $\varepsilon_1 - \varepsilon_3$

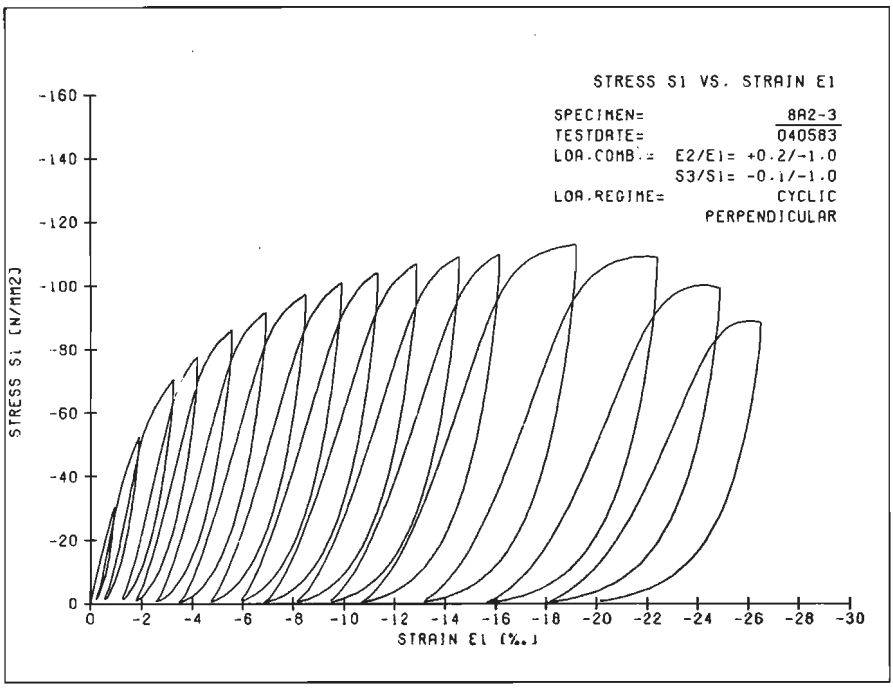

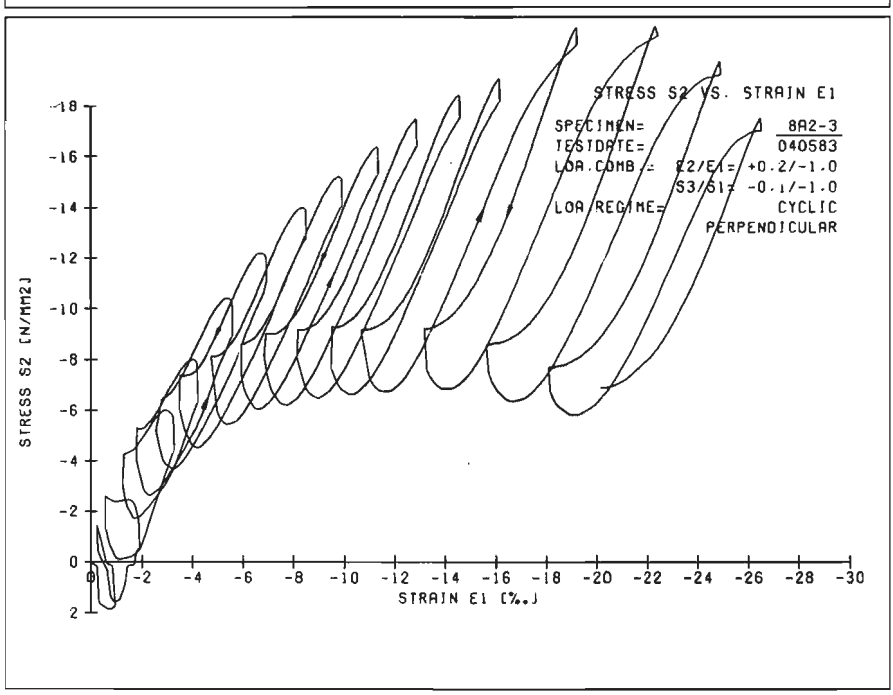

Fig. A5.24, a-b, triaxial displacement-ratio test, cyclic loading, σ_1 - ε_1 and σ_2 - ε_1 curves for specimen 8A2-3 (E2/E1 = +0.2/-1.0, σ_3 = 0.10 σ_1)

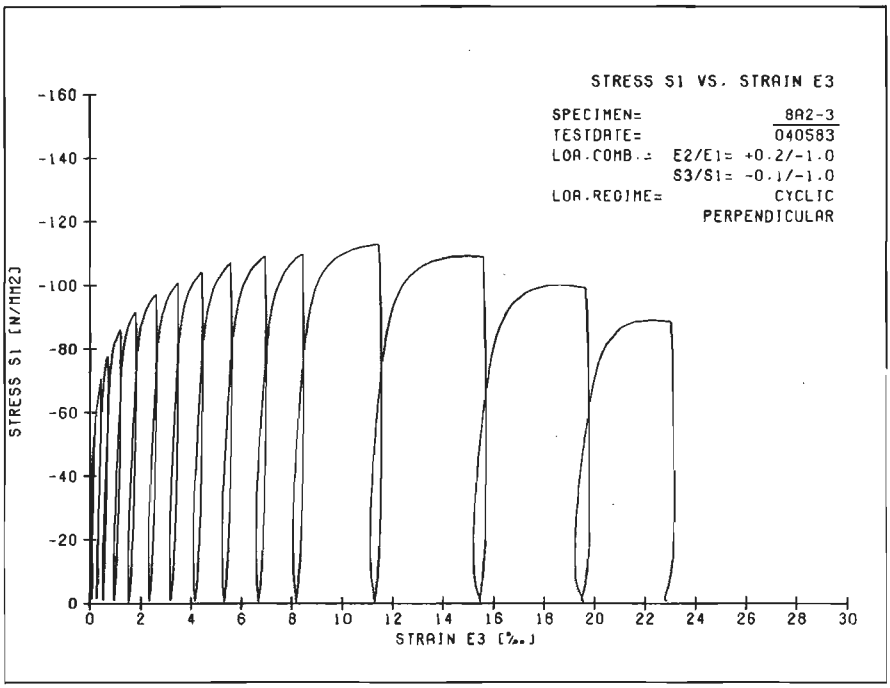

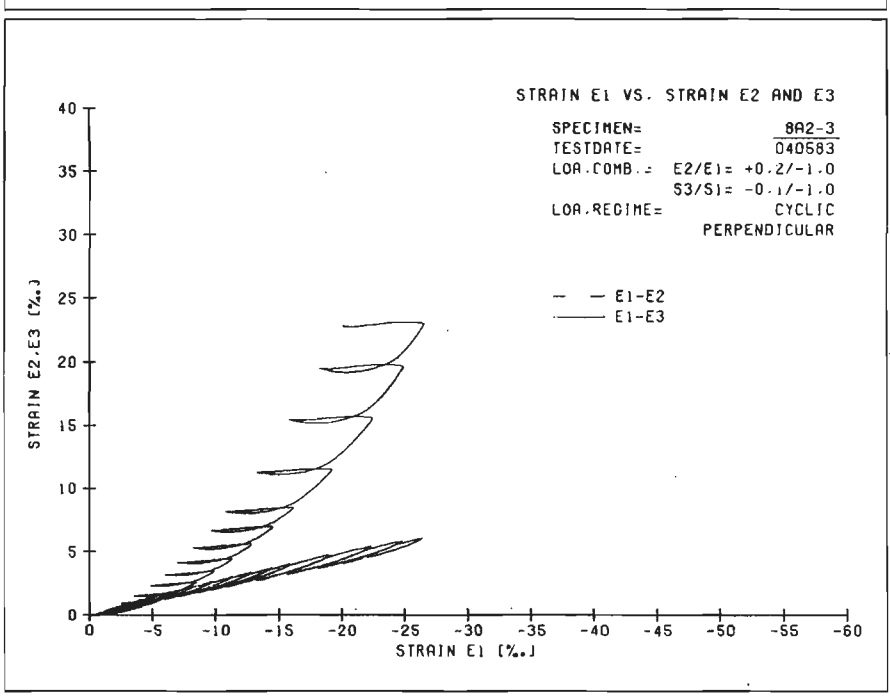

Fig. A5.24, c-d, specimen 8A2-3 (E2/E1 = +0.2/-1.0, $\sigma_3 = 0.10\ \sigma_1$), $\sigma_1 - \varepsilon_3$ curve and strain-path curves $\varepsilon_1 - \varepsilon_2$, $\varepsilon_1 - \varepsilon_3$

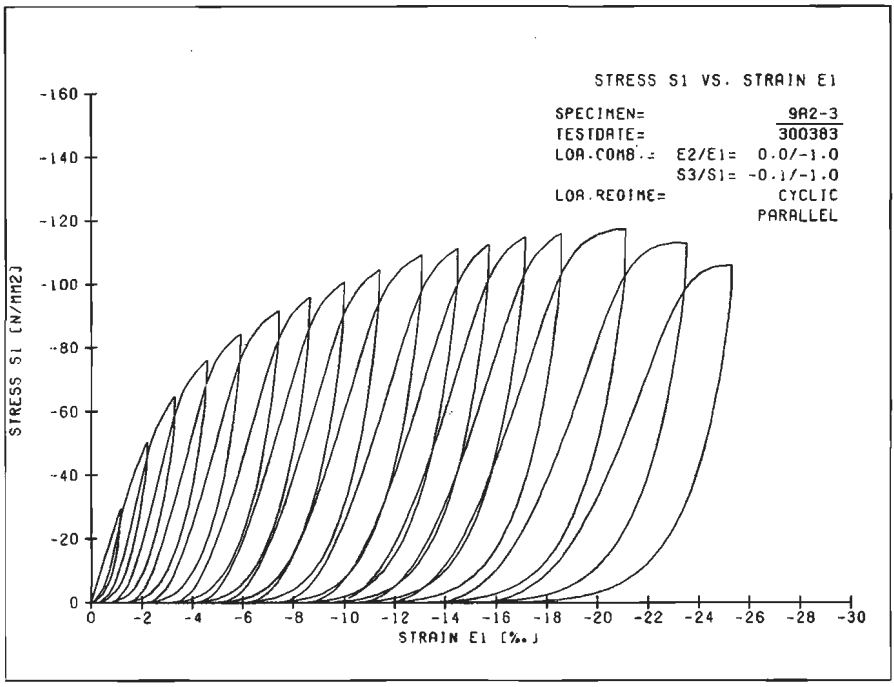

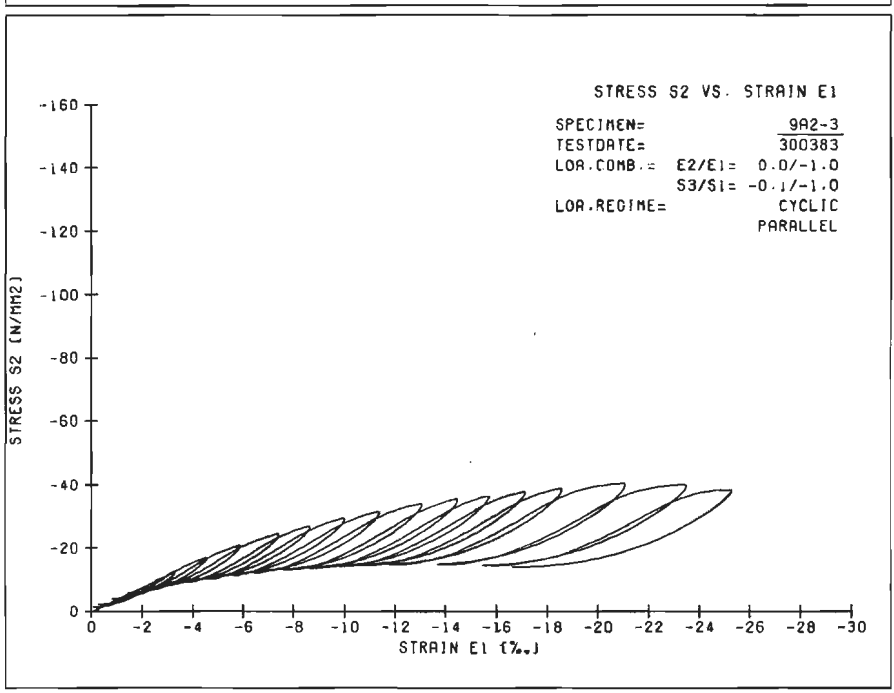

Fig. A5.25, a-b, triaxial displacement-ratio test, cyclic loading, σ_1 - ε_1 and σ_2 - ε_1 curves for specimen 9A2-3 (E2/E1 = 0.0/-1.0, $^1\sigma_3$ = 0.10 σ_1).

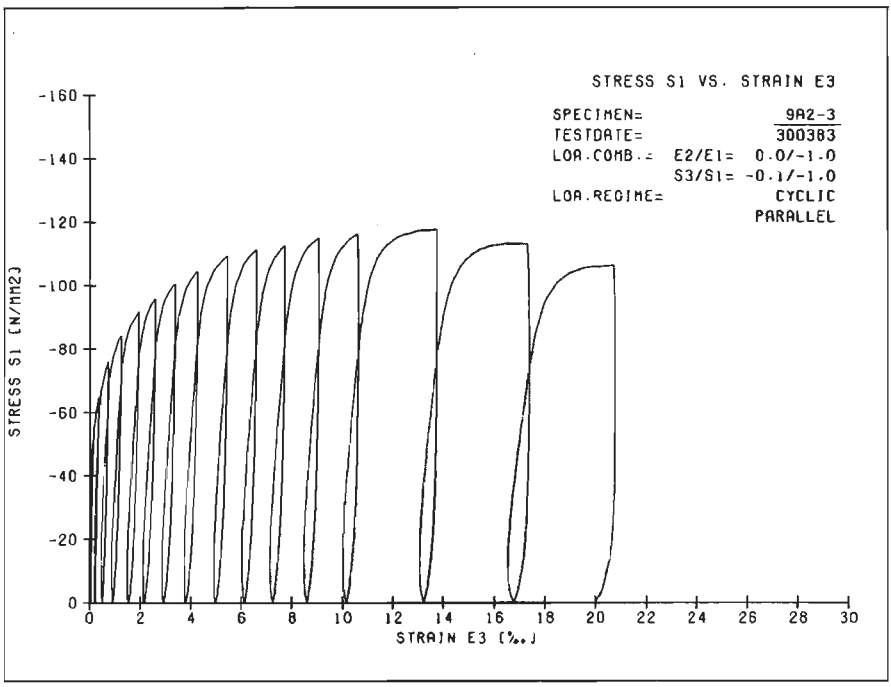

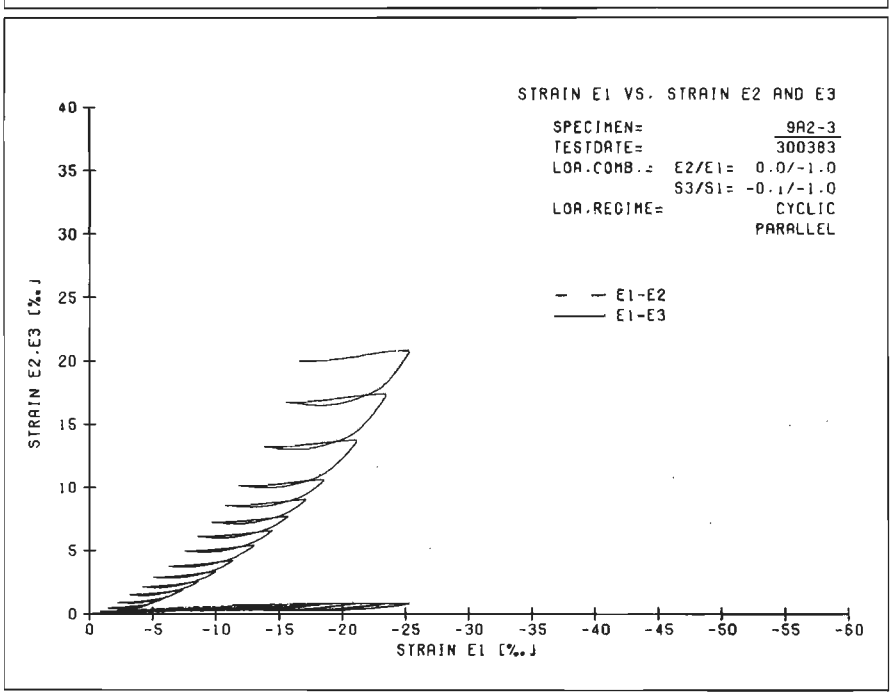

Fig. A5.25, c-d, specimen 9A2-3 (E2/E1 = 0.0/-1.0, $\sigma_3 = 0.10\ \sigma_1$), $\sigma_1 - \varepsilon_3$ curve and strain-path curves $\varepsilon_1 - \varepsilon_2$, $\varepsilon_1 - \varepsilon_3$

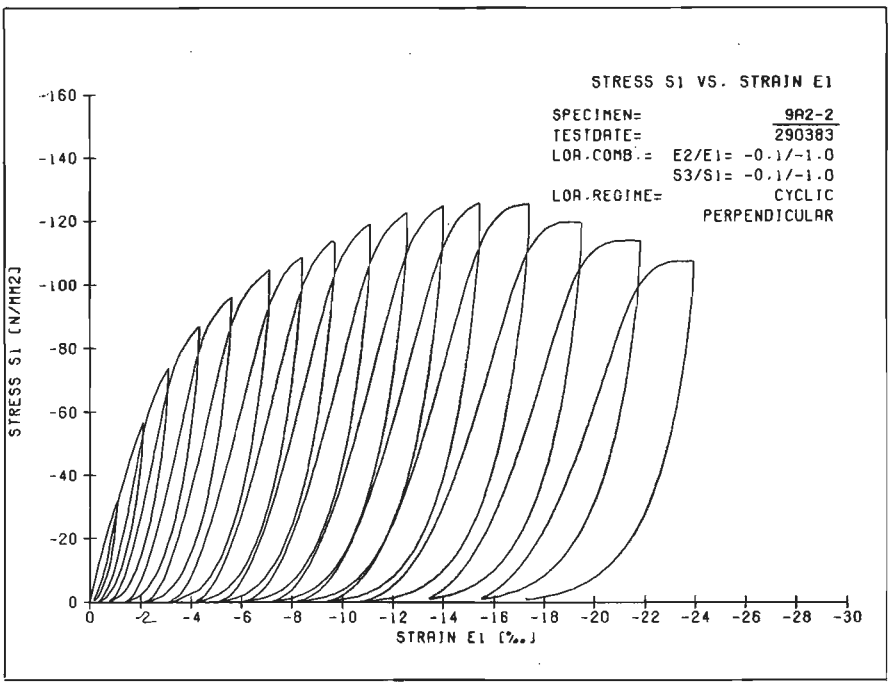

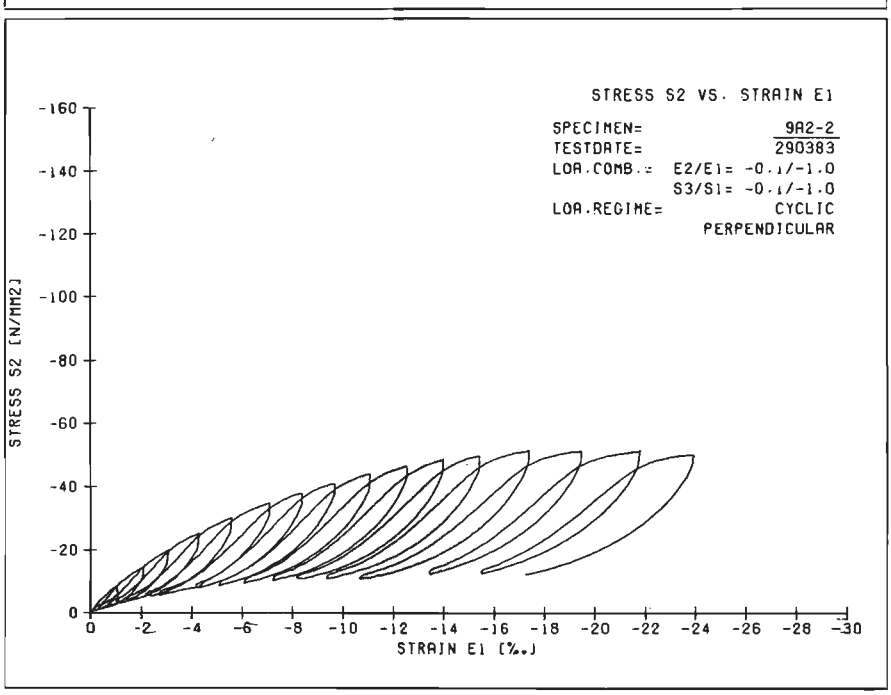

Fig. A5.26, a-b, triaxial displacement-ratio test, cyclic loading, $\sigma_1 - \varepsilon_1$ and $\sigma_2 - \varepsilon_1$ curves for specimen 9A2-2 (E2/E1 = -0.1/-1.0, $^1\sigma_3$ = 0.10 σ_1)

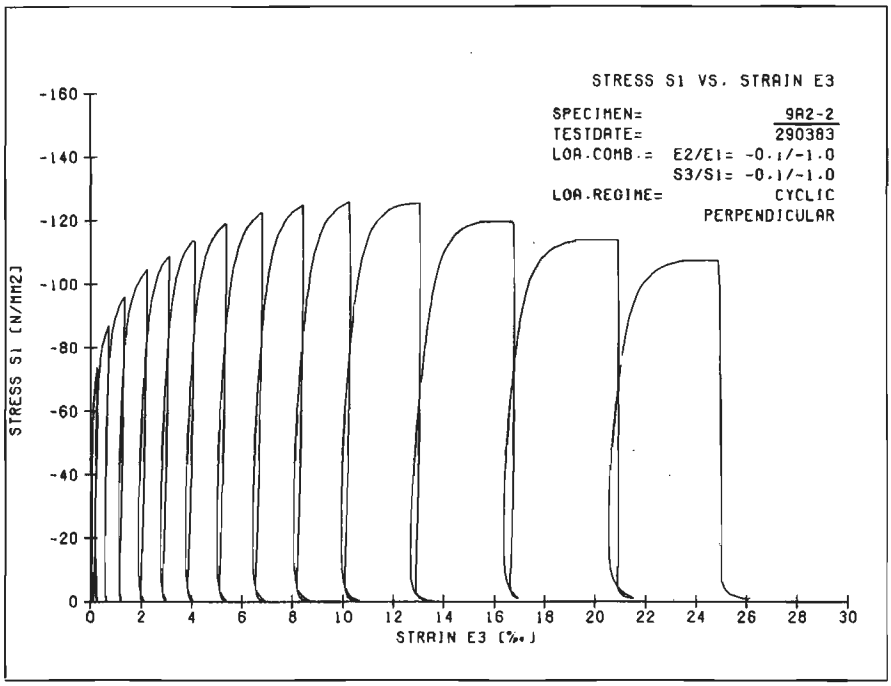

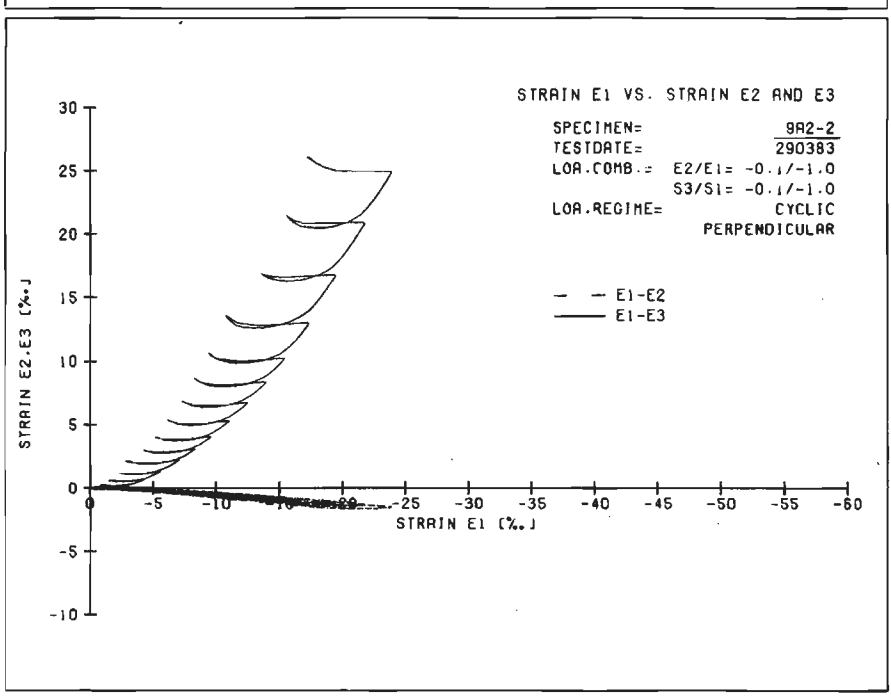

Fig. A5.26, c-d, specimen 9A2-2 (E2/E1 = -0.1/-1.0, $\sigma_3 = 0.10\ \sigma_1$), $\sigma_1 - \varepsilon_3$ curve and strain-path curves $\varepsilon_1 - \varepsilon_2$, $\varepsilon_1 - \varepsilon_3$

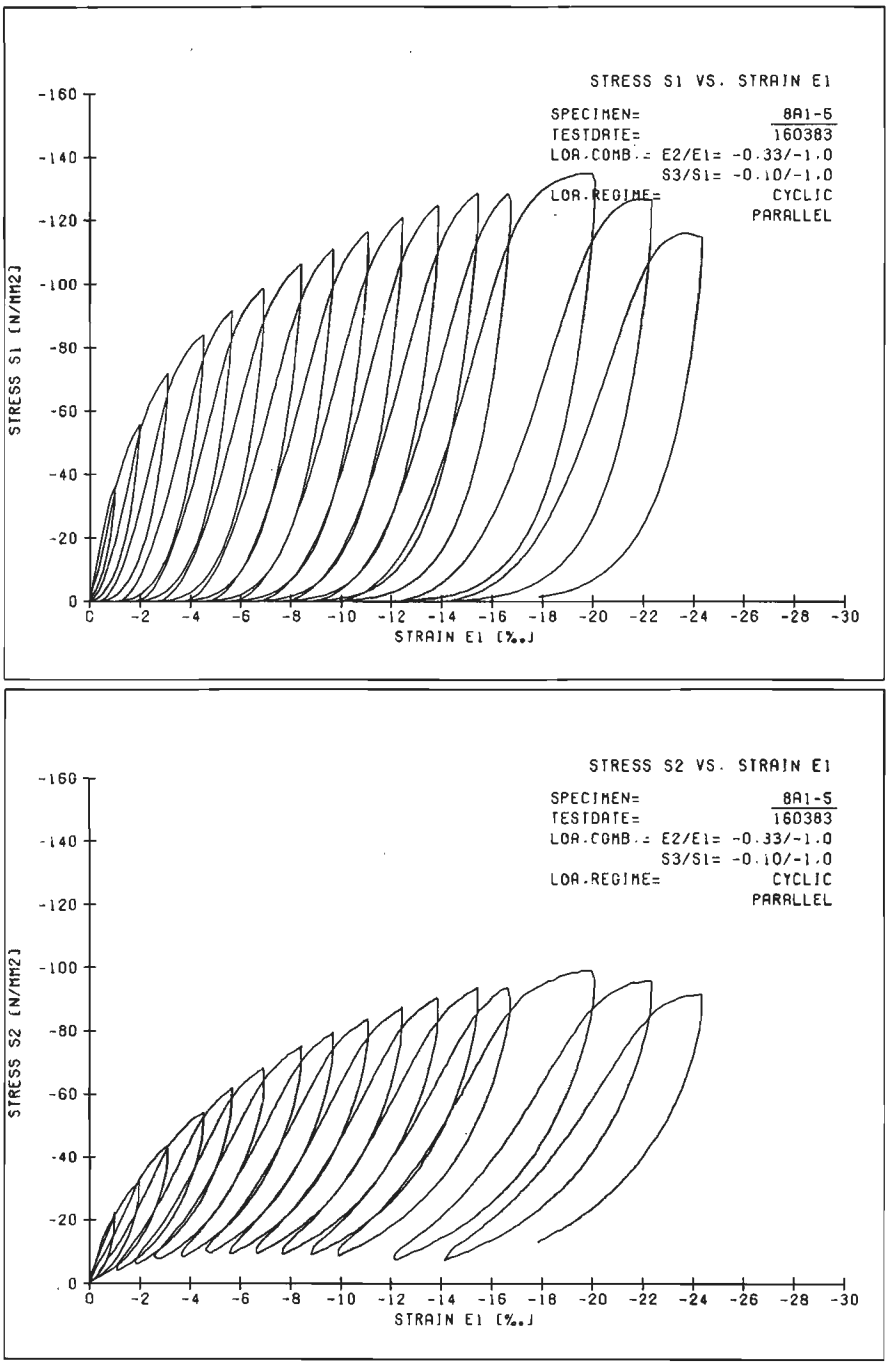

Fig. A5.27, a-b, triaxial displacement-ratio test, cyclic loading, σ_1 - ε_1 and σ_2 - ε_1 curves for specimen 8A1-5 (E2/E1 = -0.33/-1.0, $^1\sigma_3$ = 0.10 σ_1).

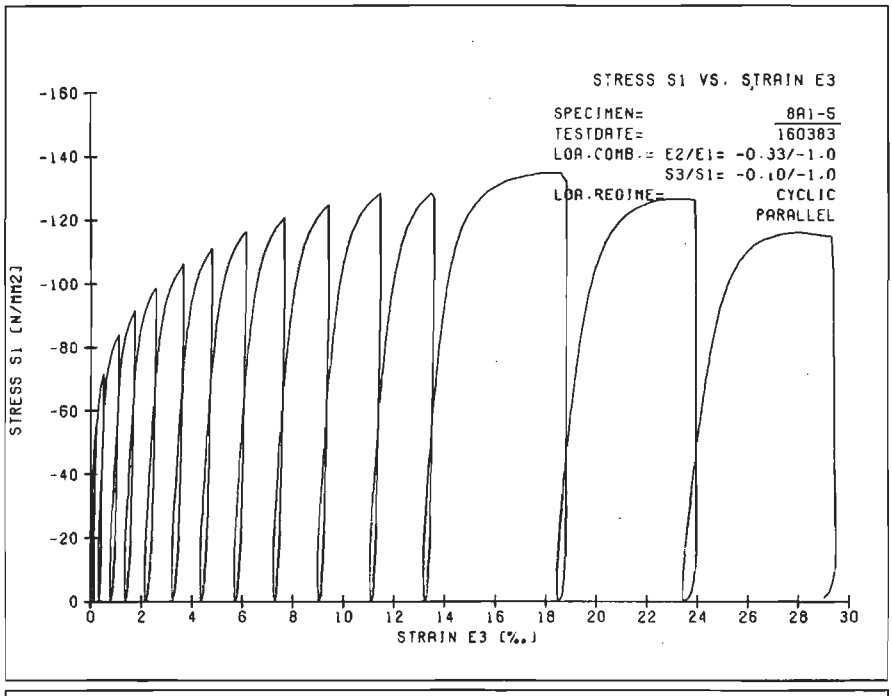

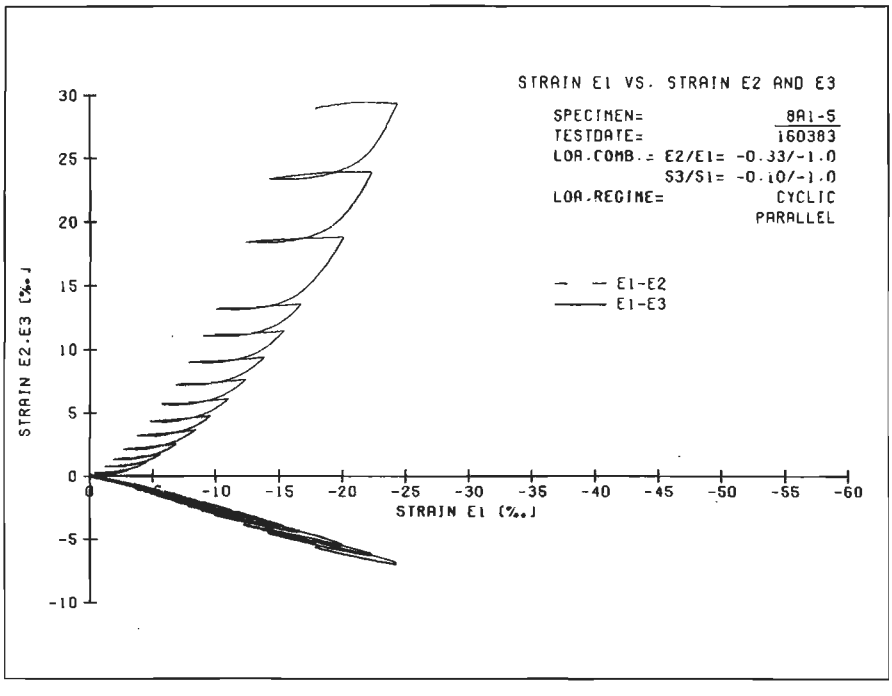

Fig. A5.27, c-d, specimen 8A1-5 (E2/E1 = -0.33/-1.0, σ_3 = 0.10 σ_1), σ_1 - ε_3 curve and strain-path curves ε_1 - ε_2, ε_1 - ε_3

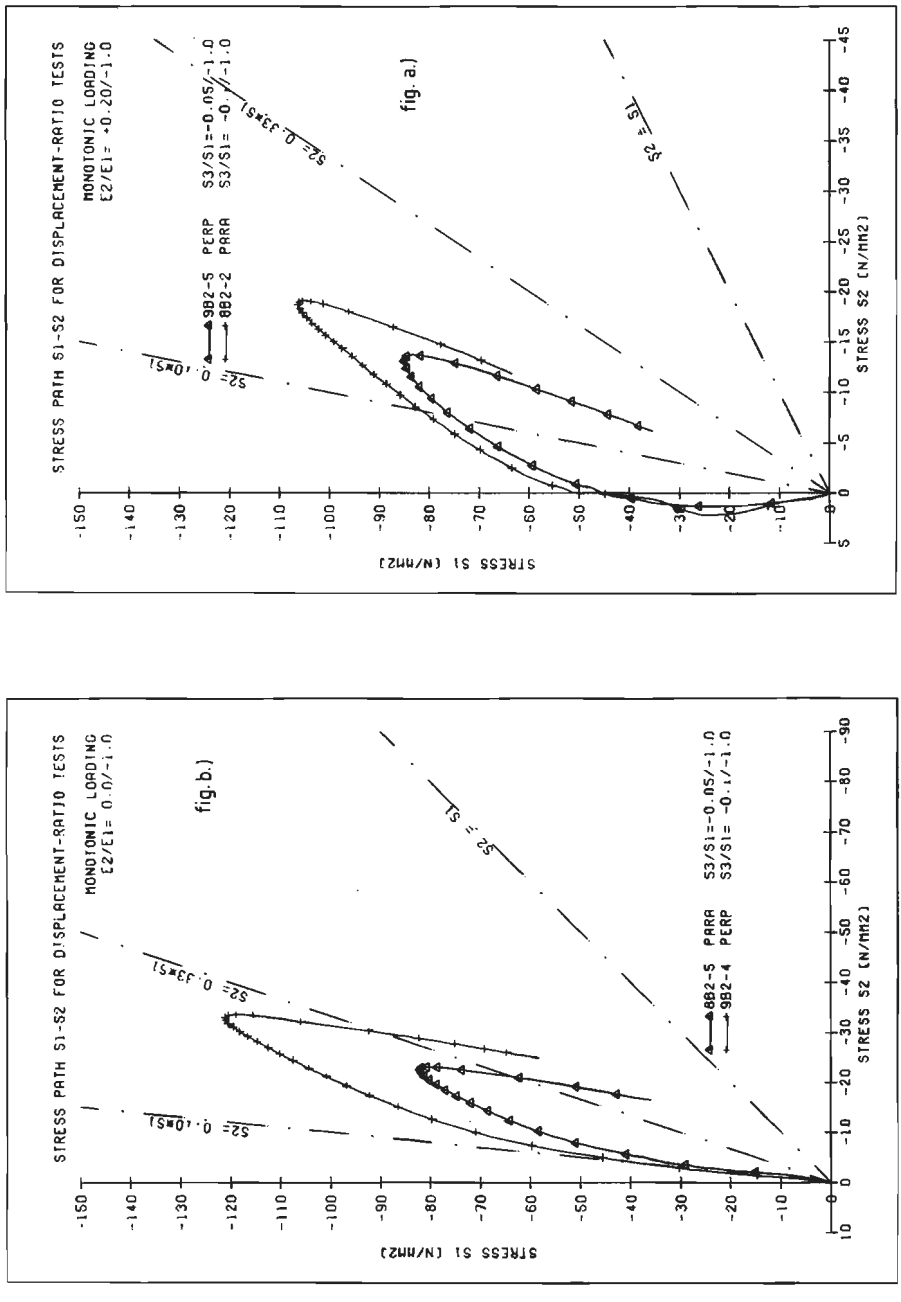

Fig. A5.28. a. Stress-path for constant displacement-ratio tests, E2/E1 = 0.2/-1.0, monotonic loading, specimens 9B2-5 ($\sigma_3 = 0.05\ \sigma_1$) and 8B2-2 ($\sigma_3 = 0.10\ \sigma_1$).
b. idem, E2/E1 = 0/-1.0, monotonic loading, specimens 8B2-5 ($\sigma_3 = 0.05\ \sigma_1$) and 9B2-4 ($\sigma_3 = 0.10\ \sigma_1$).

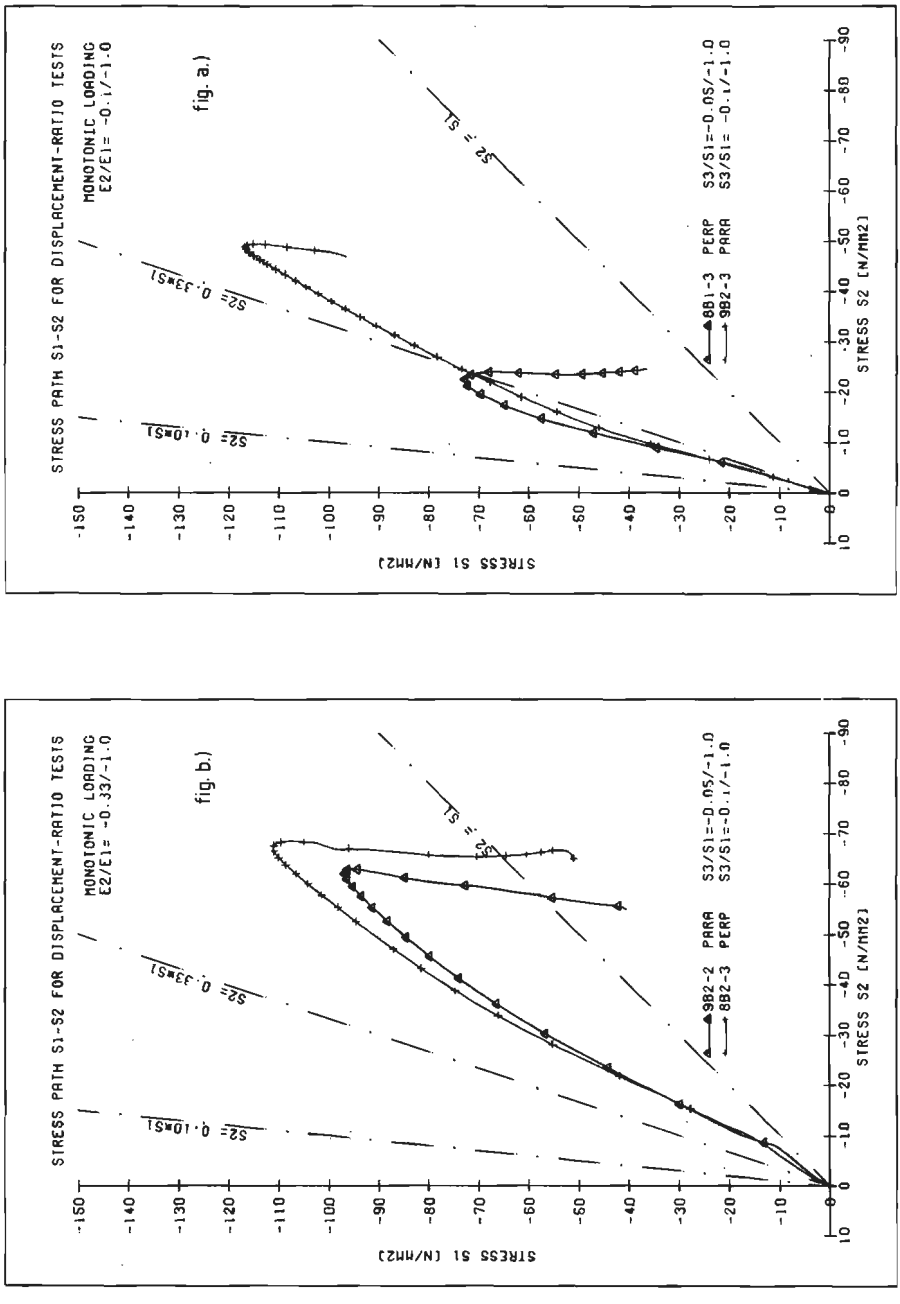

Fig. A5.29. a. Stress-path for constant displacement-ratio tests E2/E1 = -0.1/-1.0, monotonic loading, specimens 8B1-3 ($\sigma_3 = 0.05\ \sigma_1$) and 9B2-3 ($\sigma_3 = 0.10\ \sigma_1$).
b. idem, E2/E1 = -0.33/-1.0, monotonic loading, specimens 9B2-2 ($\sigma_3 = 0.05\ \sigma_1$) and 8B2-3 ($\sigma_3 = 0.10\ \sigma_1$).

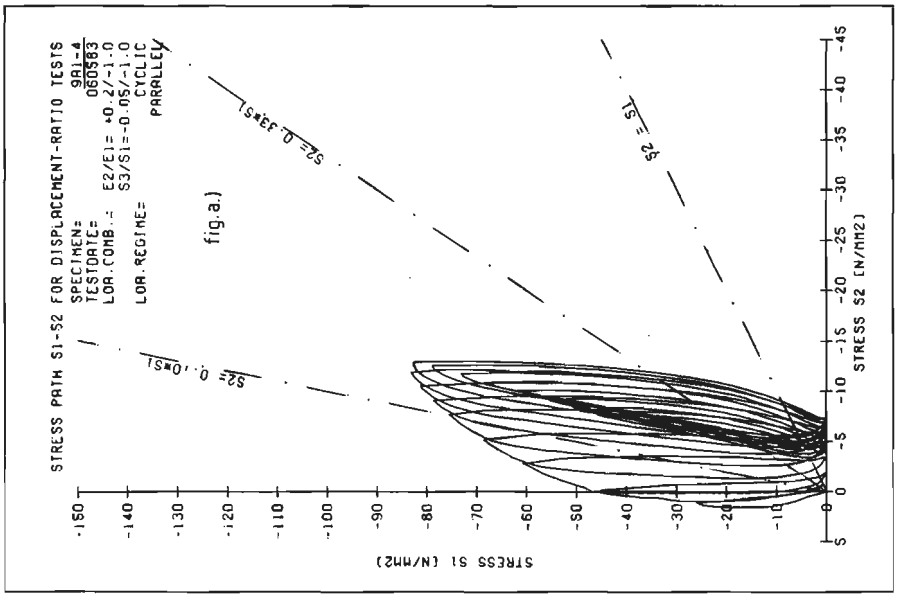

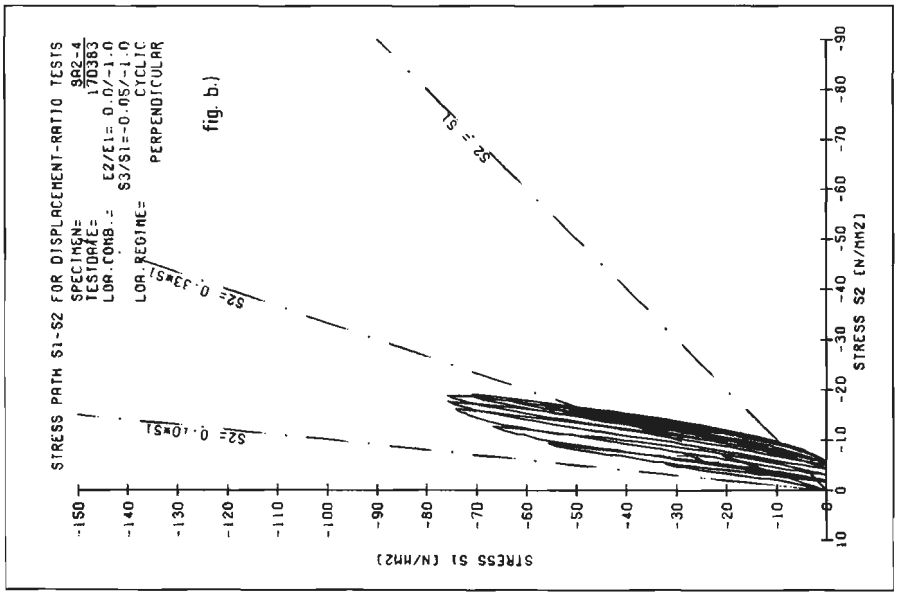

Fig. A5.30. a. Stress-path for constant displacement-ratio tests, E2/E1 = 0.2/-1.0, cyclic loading, specimens 9A1-4 ($\sigma_3 = 0.05\ \sigma_1$).
b. idem, E2/E1 = 0/-1.0, cyclic loading, specimen 8A2-4 ($\sigma_3 = 0.05\ \sigma_1$).

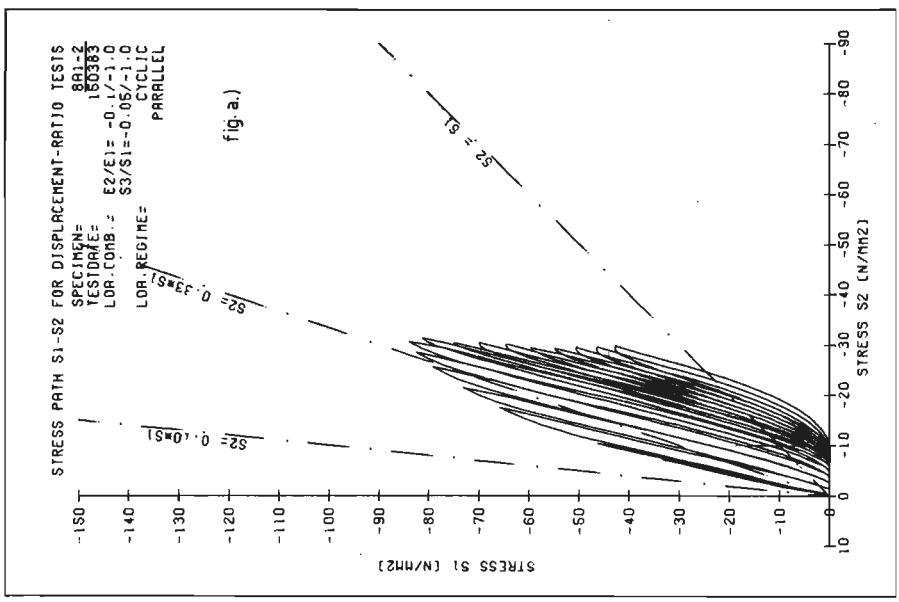

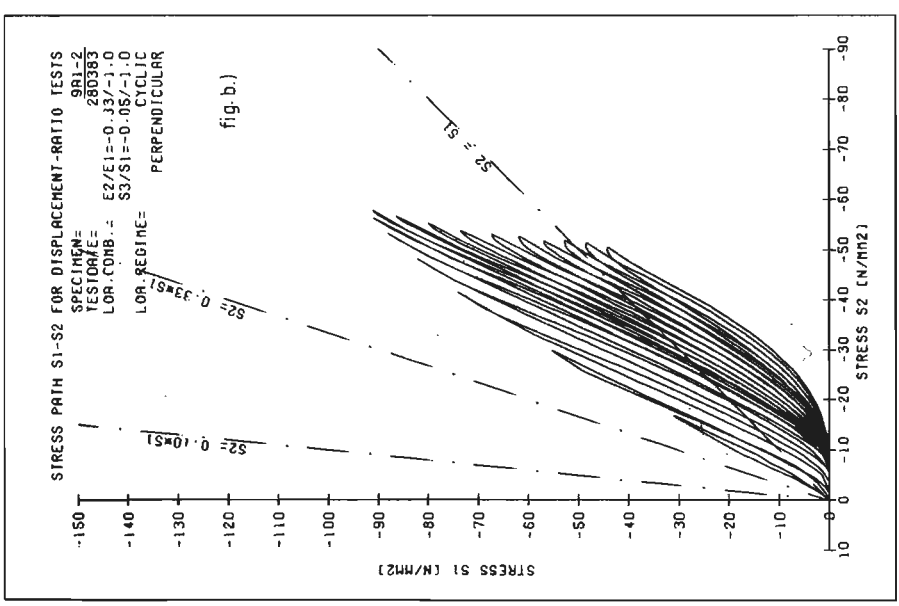

Fig. A5.31. a. Stress-path for constant displacement-ratio tests, E2/E1 = -0.1/-1.0, cyclic loading, specimen 8A1-2 ($\sigma_3 = 0.05\,\sigma_1$).
b. idem, E2/E1 = -0.33/-1.0, cyclic loading, specimen 9A1-2 ($\sigma_3 = 0.05\,\sigma_1$).

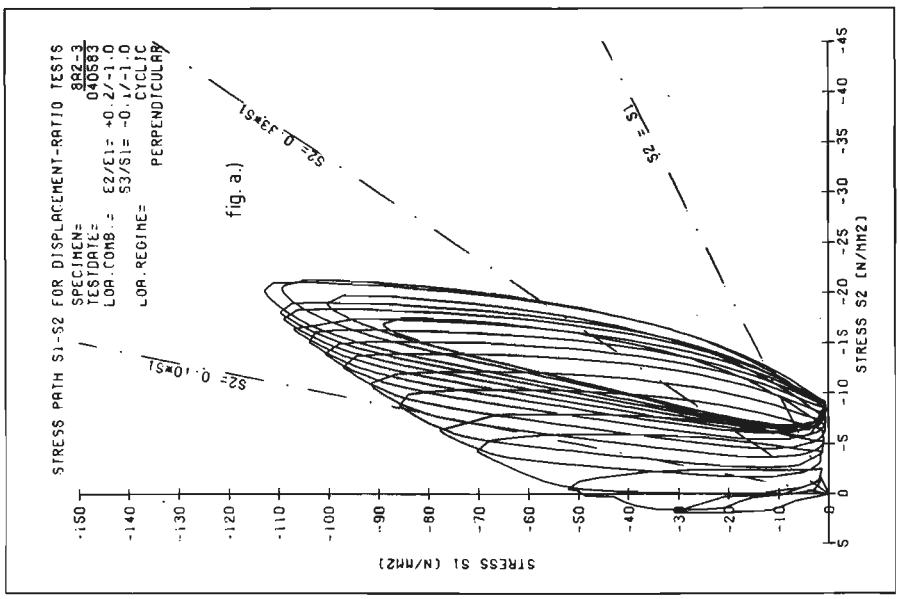

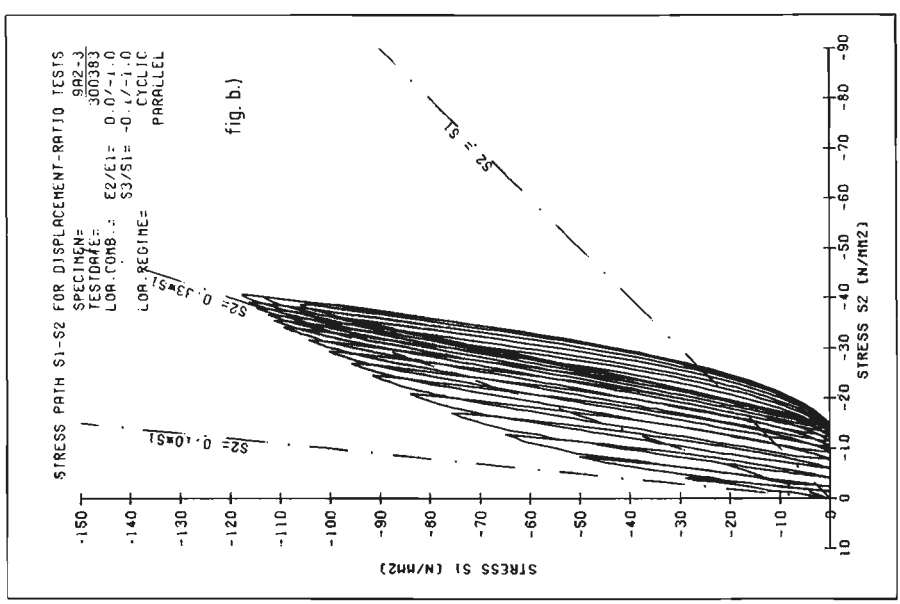

Fig. A5.32. a. Stress-path for constant displacement-ratio tests, E2/E1 = 0.2/-1.0, cyclic loading, specimen 8A2-3 ($\sigma_3 = 0.10\ \sigma_1$).
b. idem, E2/E1 = 0/-1.0, cyclic loading, specimen 9A2-3 ($\sigma_3 = 0.10\ \sigma_1$).

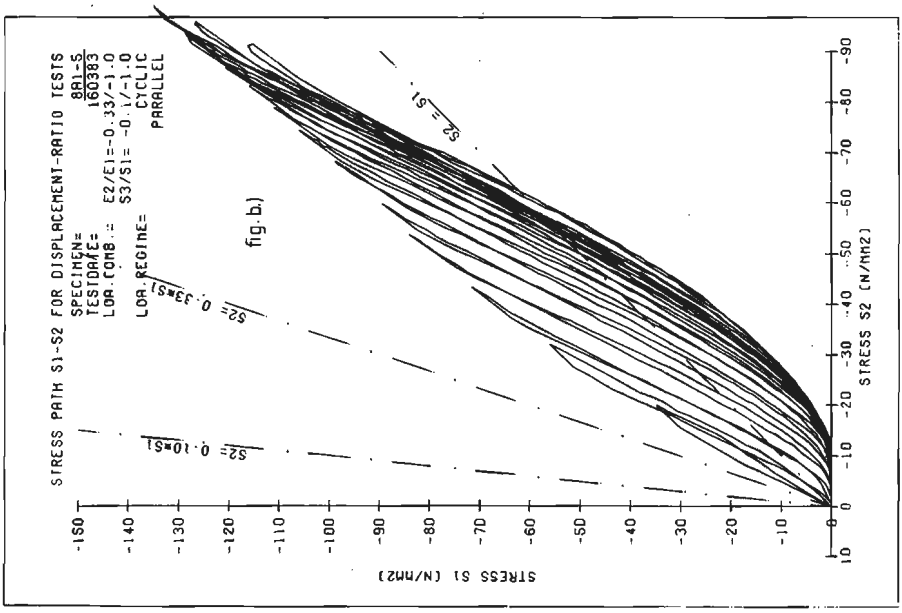

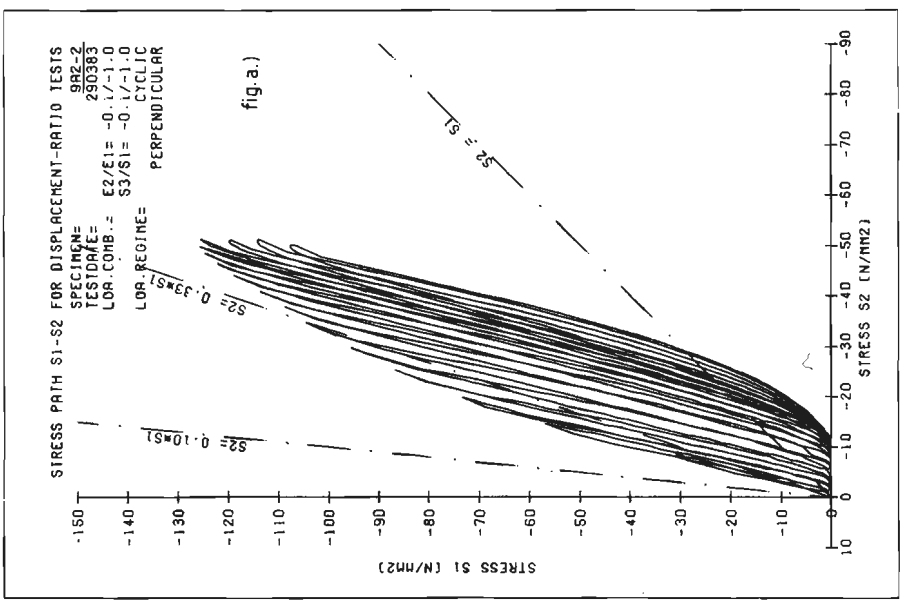

Fig. A5.33. a. Stress-path for constant displacement-ratio tests, E2/E1 = -0.1/-1.0, cyclic loading, specimen 9A2-2 ($\sigma_3 = 0.10\ \sigma_1$).
b. idem, E2/E1 = -0.33/-1.0, cyclic loading, specimen 8A1-5 ($\sigma_3 = 0.10\ \sigma_1$).

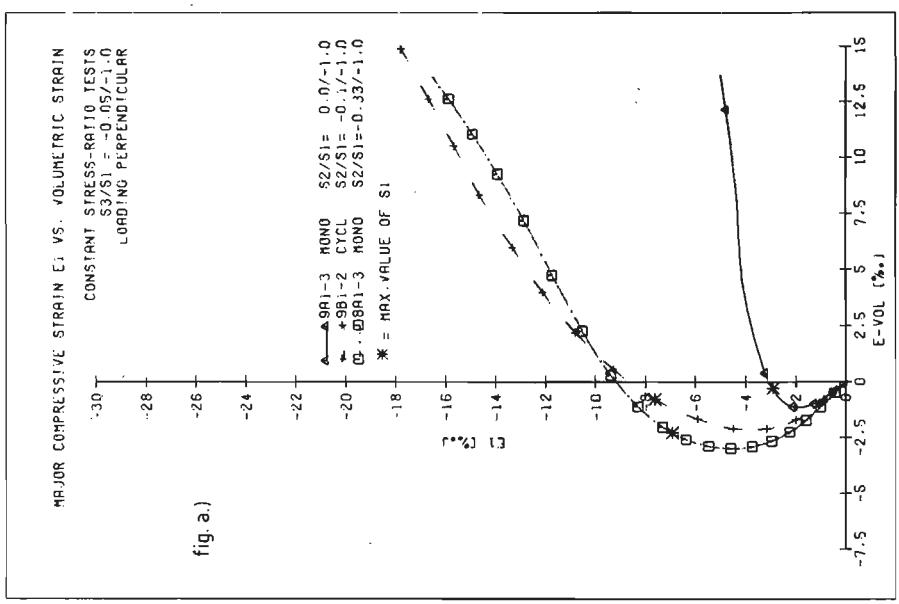

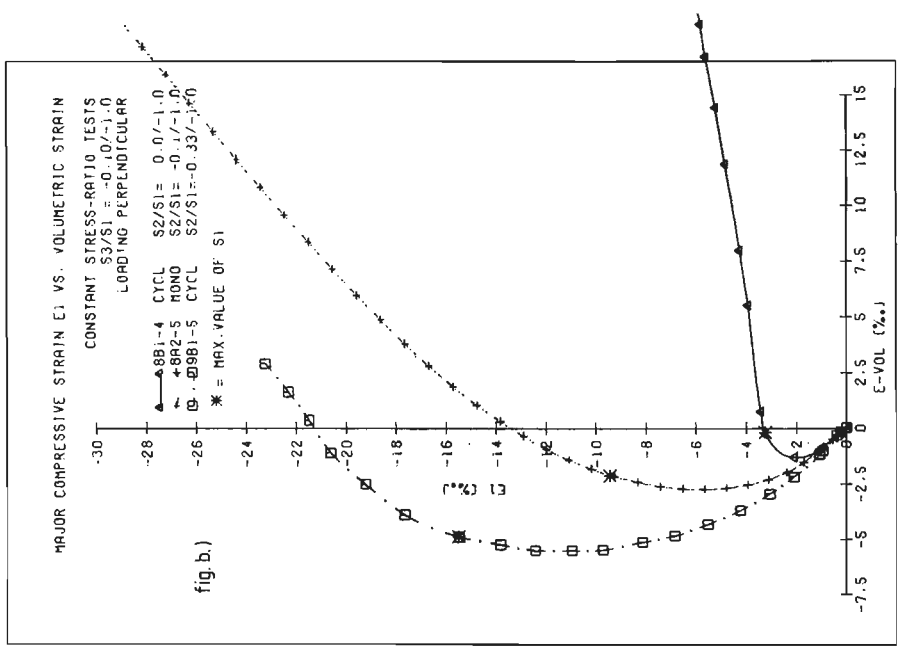

Fig. A5.34. a. Volumetric strain vs. axial strain ε_1, constant stress-ratio tests, $\sigma_3 = 0.05\ \sigma_1$, loading perpendicular.
b. Volumetric strain vs. axial strain ε_1, constant stress-ratio tests, $\sigma_3 = 0.10\ \sigma_1$, loading perpendicular.

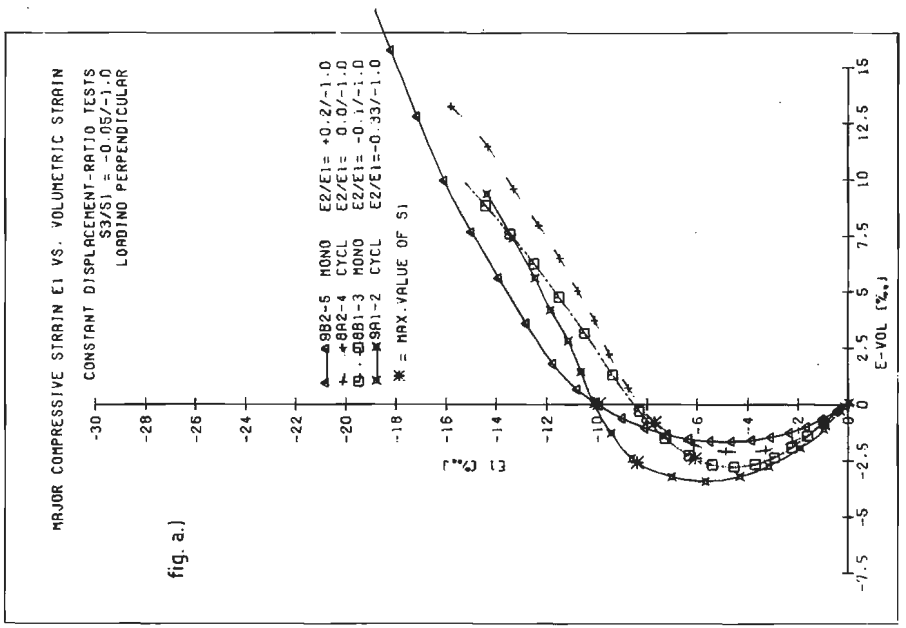

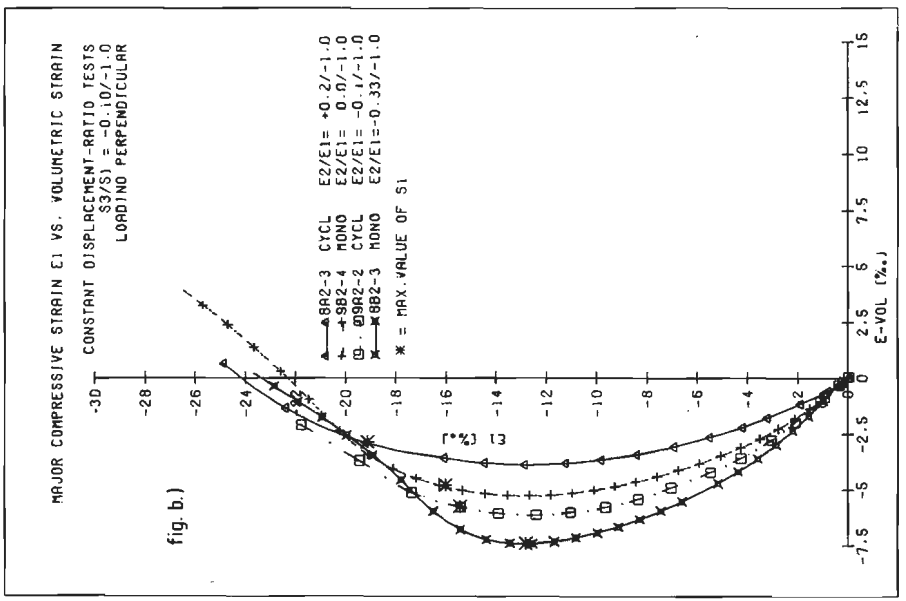

Fig. A5.35. a. Volumetric strain vs. axial strain ε_1, constant displacement-ratio tests, $\sigma_3 = 0.05\ \sigma_1$, loading perpendicular.
b. Volumetric strain vs. axial strain ε_1, constant displacement-ratio tests, $\sigma_3 = 0.10\ \sigma_1$, loading perpendicular.

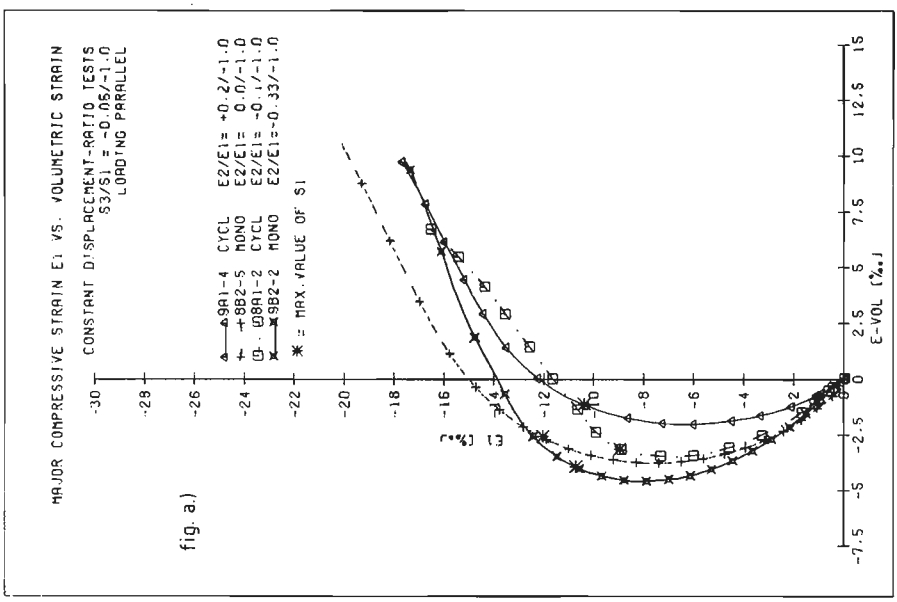

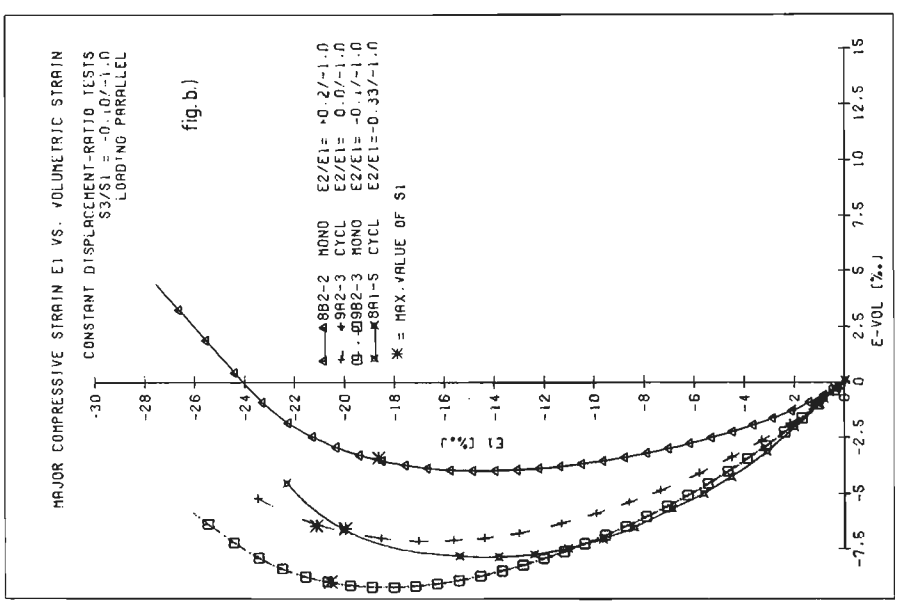

Fig. A5.36. a. Volumetric strain vs. axial strain ε_1, constant displacement-ratio tests, $\sigma_3 = 0.05\ \sigma_1$, loading parallel.
b. Volumetric strain vs. axial strain ε_1, constant displacement-ratio tests, $\sigma_3 = 0.10\ \sigma_1$, loading parallel.

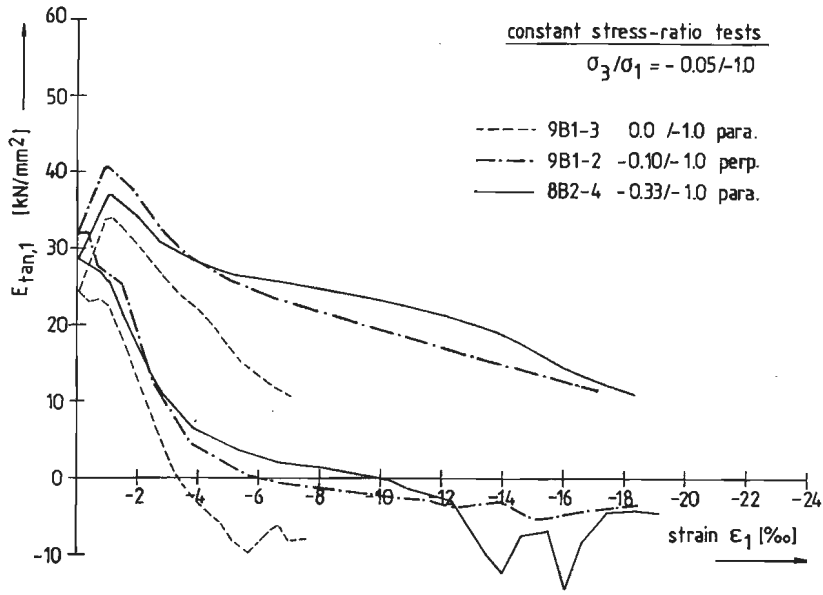

Fig. A5.37. Upper and lower tangential stiffness envelope curves for constant stress-ratio tests, $\sigma_3 = 0.05\ \sigma_1$, cyclic loading.

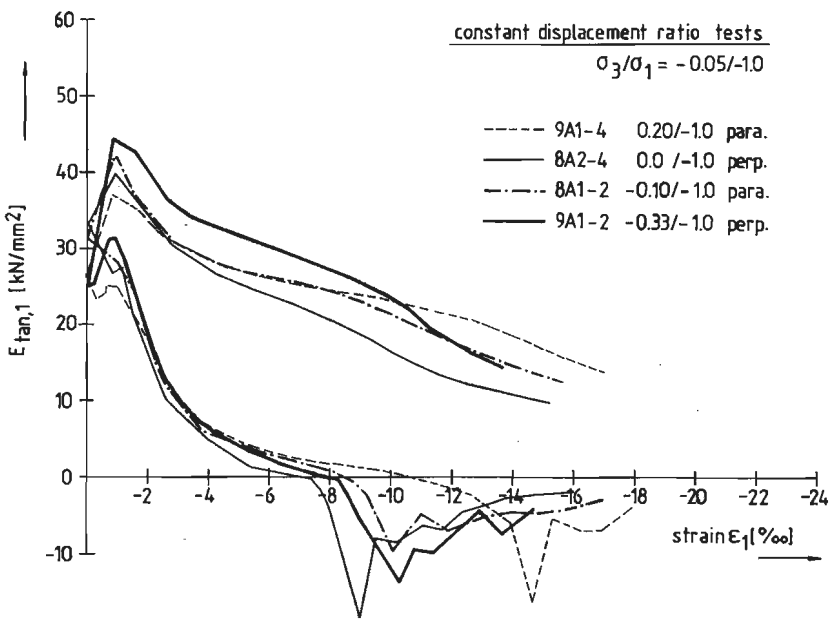

Fig. A5.38. Upper and lower tangential stiffness envelope curves for constant displacement-ratio tests, $\sigma_3 = 0.05\ \sigma_1$, cyclic loading.

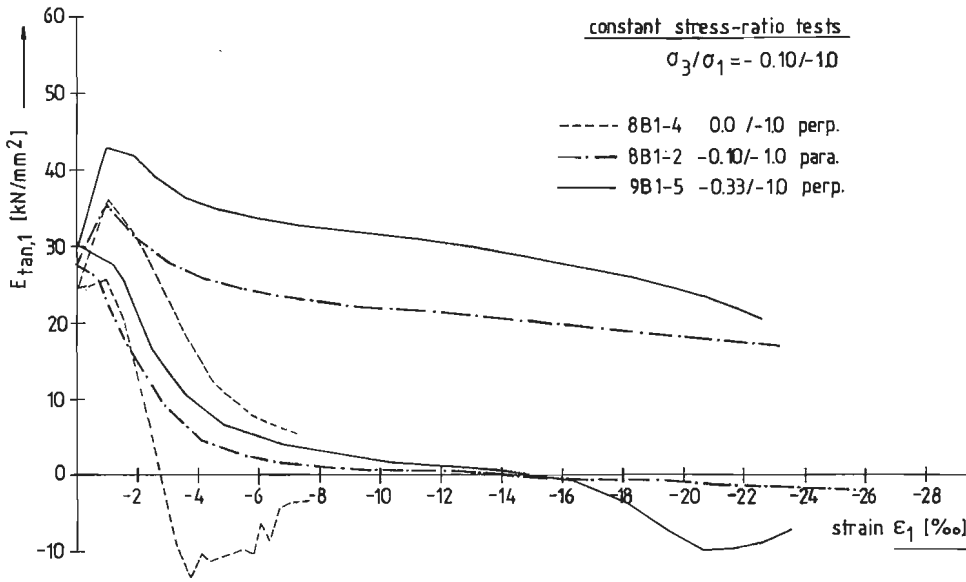

Fig. A5.39. Upper and lower tangential stiffness envelope curves for constant stress-ratio tests, $\sigma_3 = 0.10\ \sigma_1$, cyclic loading.

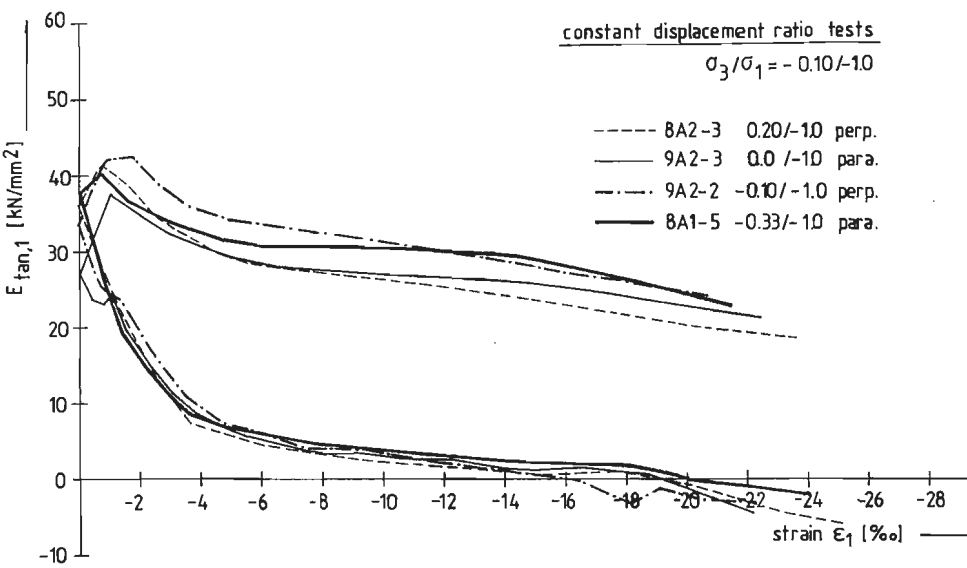

Fig. A5.40. Upper and lower tangential stiffness envelope curves for constant displacement-ratio tests, $\sigma_3 = 0.10\ \sigma_1$, cyclic loading.

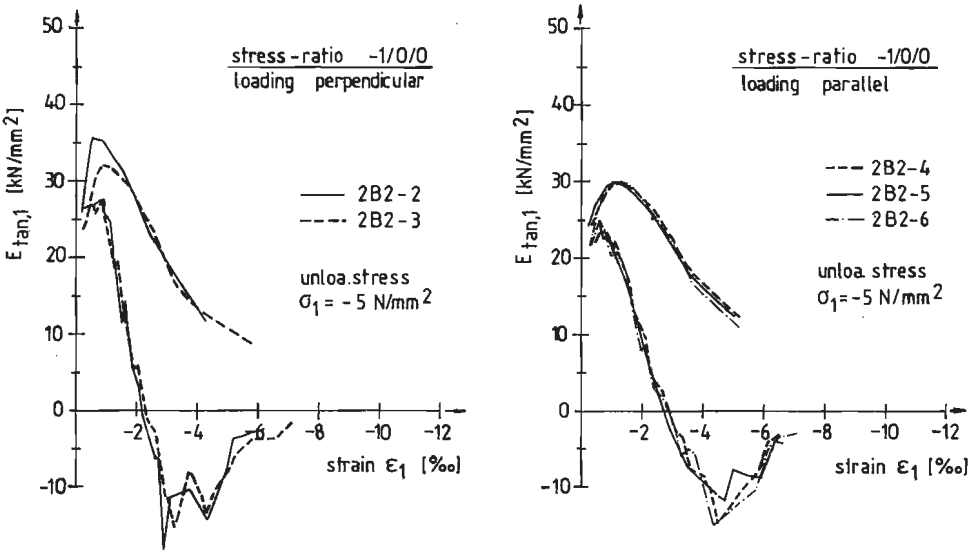

Fig. A5.41. a. Upper and lower stiffness for uniaxial compression (series 2B2), loading perpendicular.
b. idem, loading parallel.

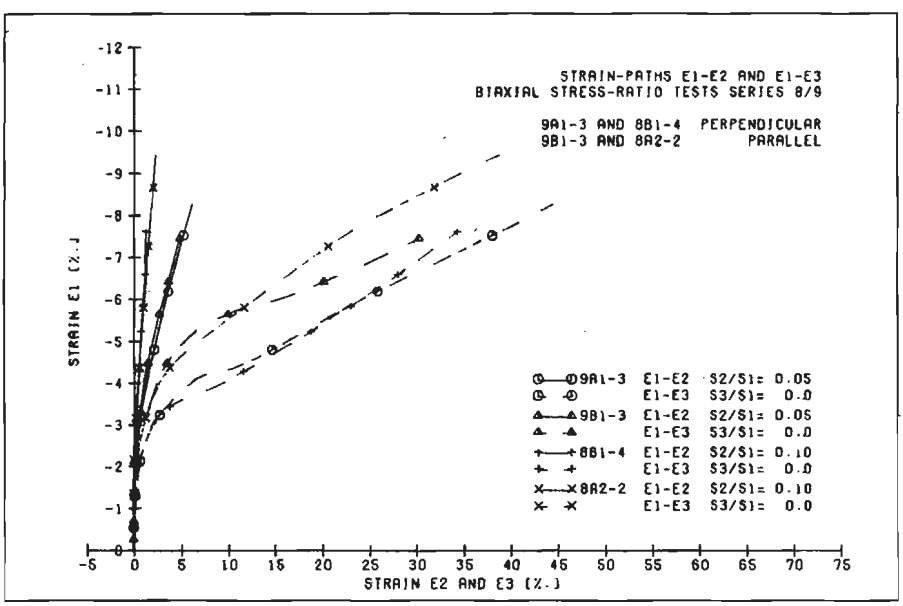

Fig. A5.42. Strain-paths for biaxial stress-ratio experiments ($\sigma_2 = 0.05\sigma_1$ and $\sigma_2 = 0.10\sigma_1$, $\sigma_3 = 0$).

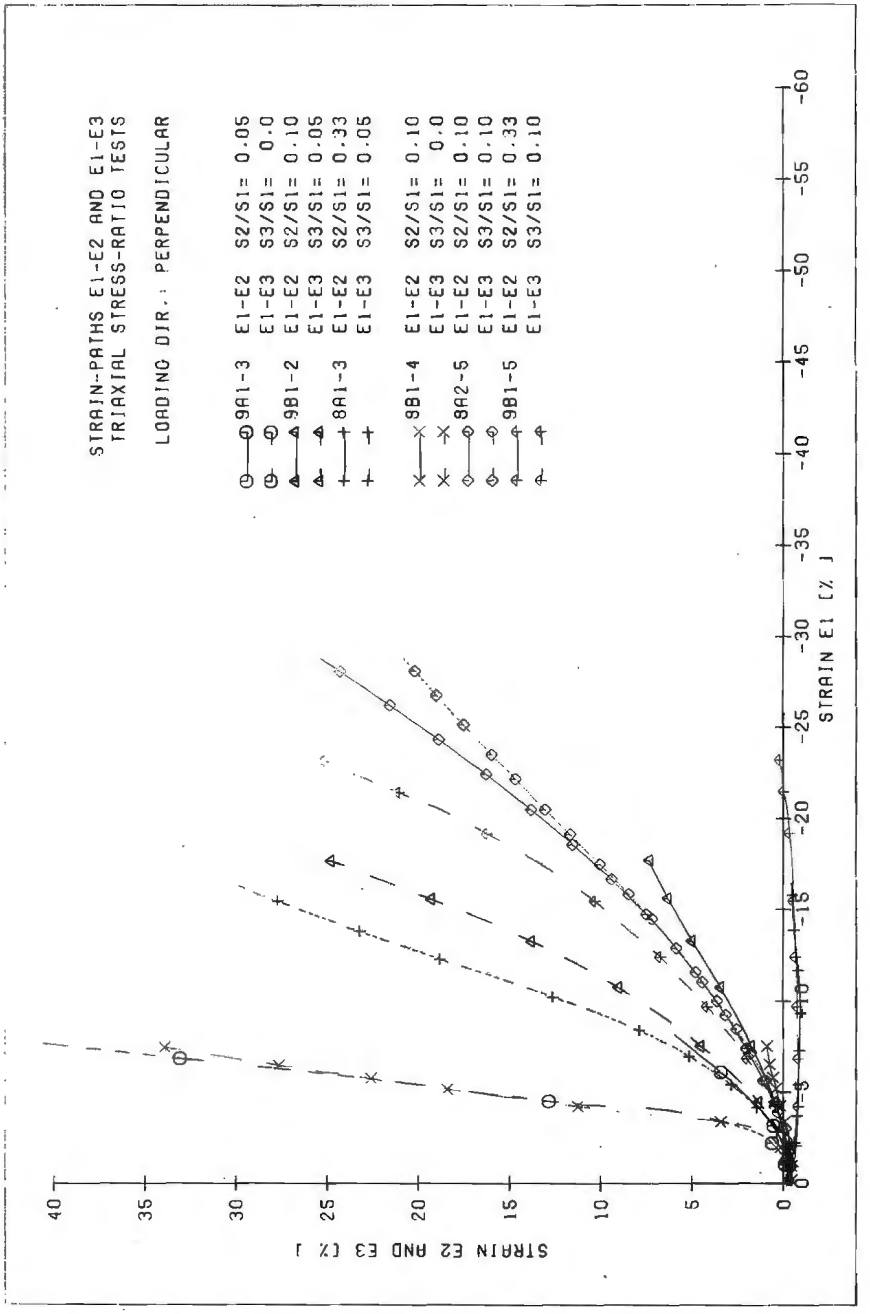

Fig. A5.43. Strain-paths ε_1 - ε_2 and ε_1 - ε_3 for triaxial stress-ratio tests, loading direction = perpendicular.

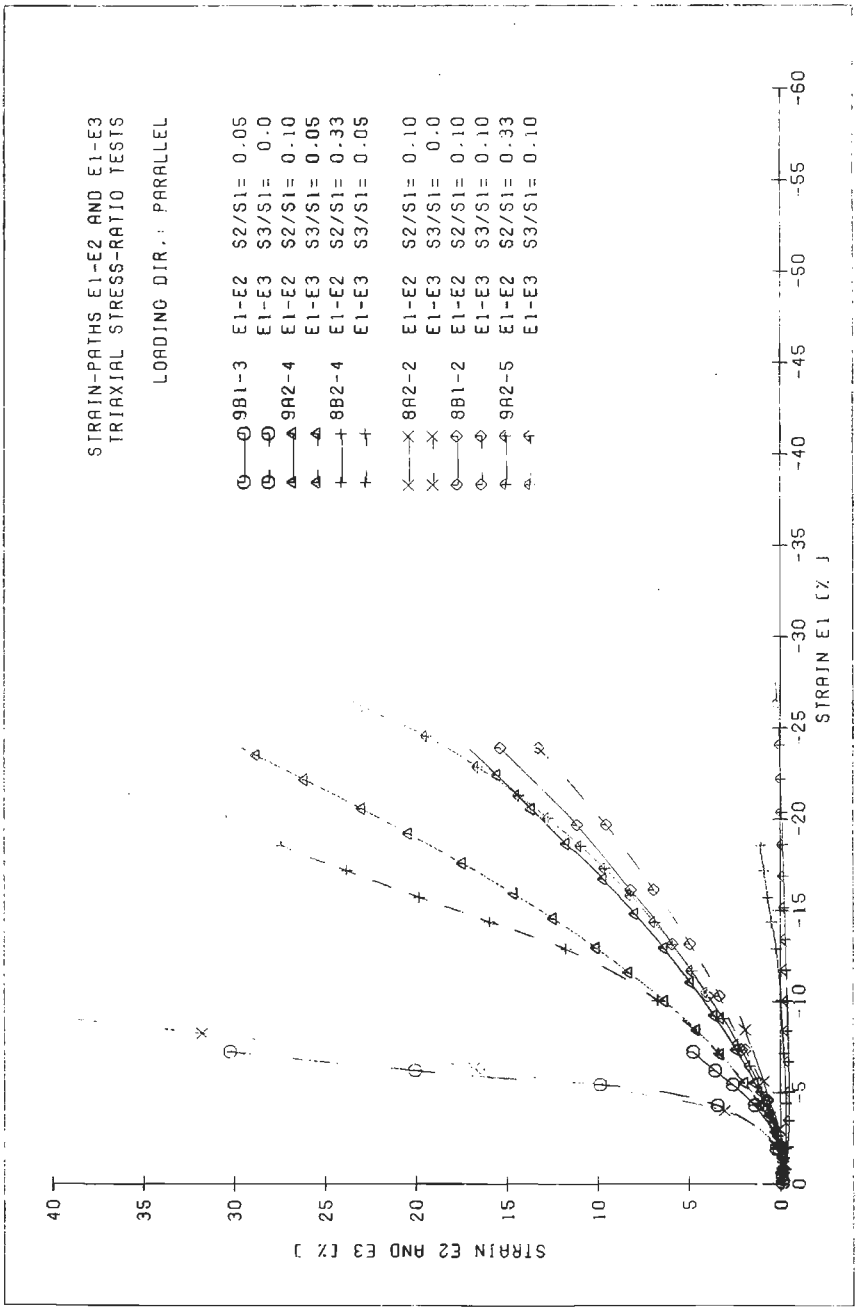

Fig. A5.44. Strain-paths ε_1 - ε_2 and ε_1 - ε_3 for triaxial stress-ratio tests, loading direction = parallel.

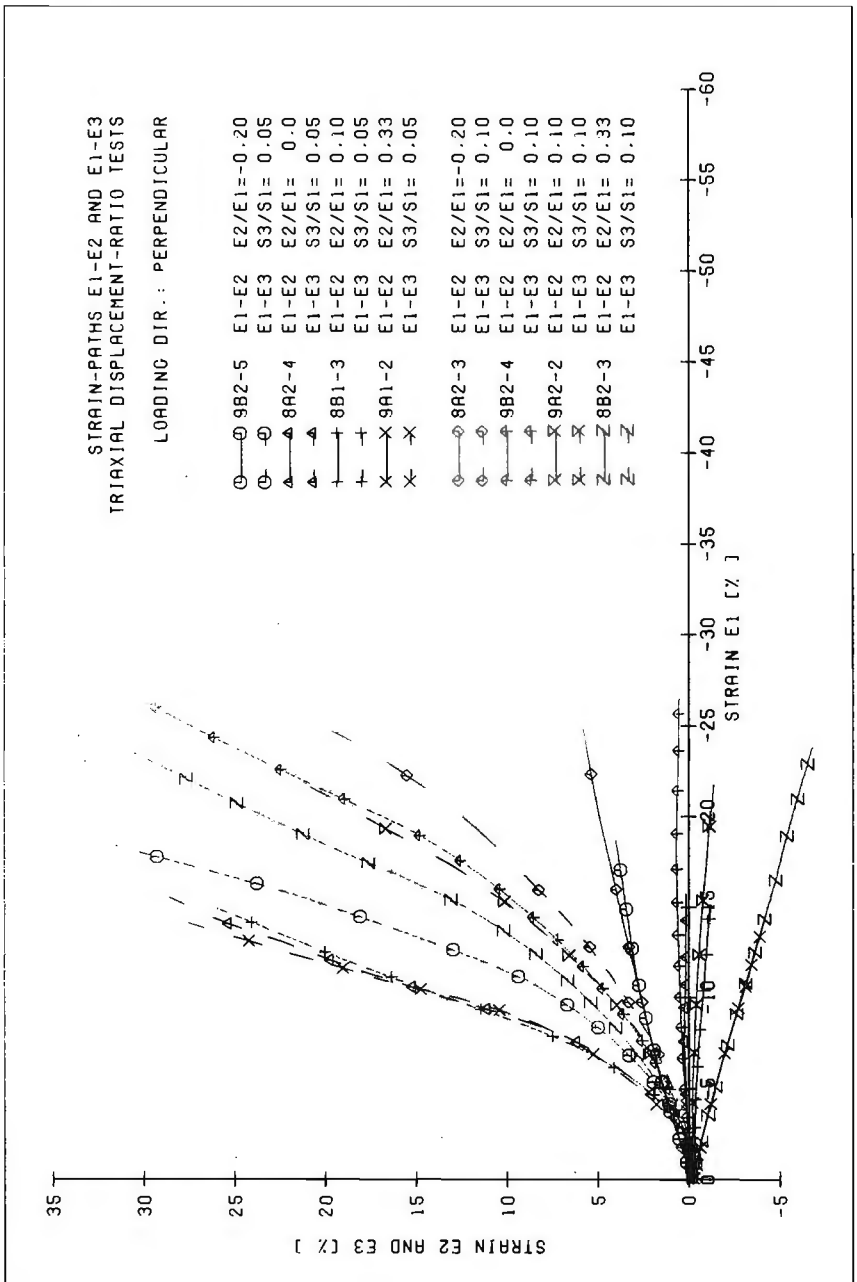

Fig. A5.45. Strain-paths ε_1 - ε_2 and ε_1 - ε_3 for triaxial displacement-ratio tests, loading direction = perpendicular.

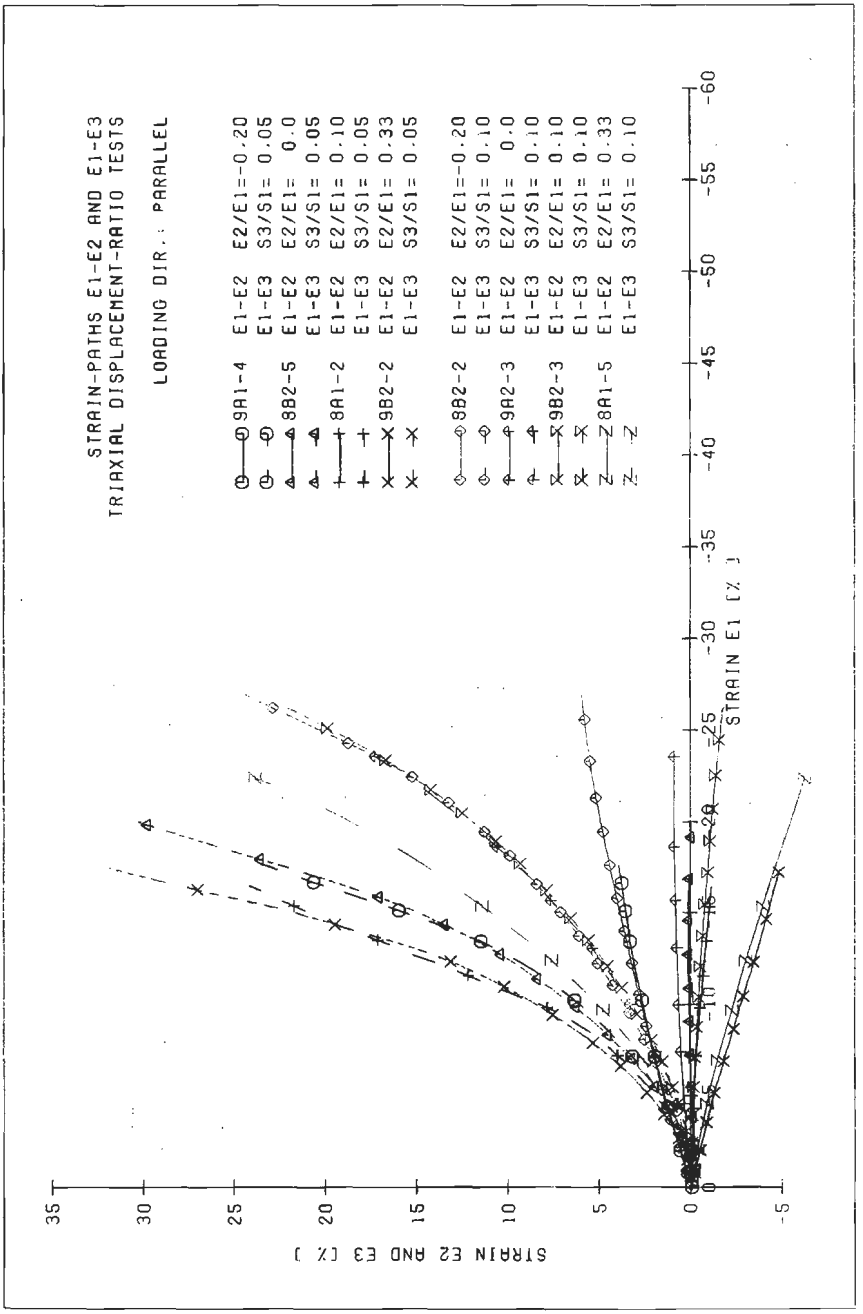

Fig. A5.46. Strain-paths ε_1 - ε_2 and ε_1 - ε_3 for triaxial displacement-ratio tests, loading direction = parallel.

APPENDIX A6

Boundary shear due to bending of brush-rods

The calculation of the brush-bearing platens was adapted from an extensive publication on the subject by Linse /95/. The Munich triaxial machine is also equiped with brushes as a load-transmitting medium. Differences with the Eindhoven equipment were discussed in chapter 3.
In this appendix not the full details of the brush-calculations are given, only some short comments on the 'frictional-behaviour' of the brushes are made.

The brush-rods can be schematized according to figure A6.1. The rods are assumed to be rigidly clamped at the machine end. A normal load P is acting at the free end. Due to a displacement f at the rod-end, the horizontal force H is determined by

$$H = \frac{\alpha^2 \cdot EI \cdot f}{(\tan \alpha l / \alpha - l)} \qquad \text{.....A6.1.,}$$

where $\alpha = \sqrt{|P|/EI}$. The variation of H with increasing applied normal force P is also shown in figure A6.1, for a constant horizontal displacement f = 1 mm.
The dimensions of the brush-rods were chosen as follows: length l = 85 mm, cross-sectional area A = 5 x 5 mm^2, distance between rods d = 0.2 mm. The complete brush-construction is shown in fig. 3.11.

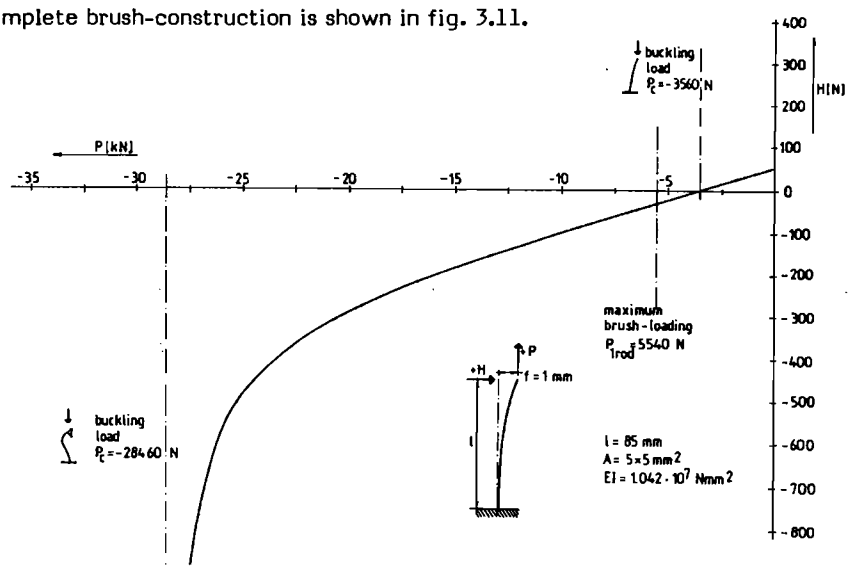

Fig. A.6.1. Horizontal force H acting at the brush-rod-tip as a function of the applied normal force P, due to a displacement f = 1 mm of the rod-end.

When the displacements of the brush-rod-tip are known, the shear-stress acting at the specimen-brush interface may be calculated from the horizontal force by equation A5.1. The horizontal force must be normalized with respect to the loading area of the brush-rod.

In fig. A.6.2 the estimated value of $\tau_x = \tau_y$ for a uniaxial compressed specimen (8A1-1) is shown. The lateral displacement of the brush-rods was assumed to be equal to the lateral displacement of the concrete cube, measured by means of the four strain-readers (see also section 4.2). The effects of the curved brush-surface, and the different behaviour of the outer layers of the concrete cube (see chapter 4.) are omitted in the calculation for simplicity.

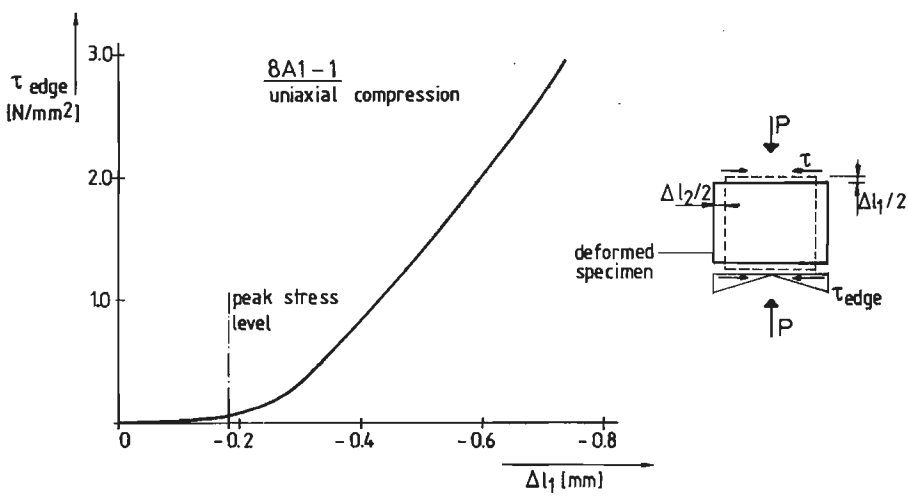

Fig. A.6.2. Estimate of the specimen-brush-boundary shear-stress for a uniaxial compressed specimen.

The value shown in fig. A.6.2 is the maximum shear-stress at the brush-edges, and the value will fall linear to zero at the specimen-centre. This is also indicated in the figure. The effects of boundary-shear are small, and probably not important up to the peak-stress-level. At the maximum specimen-loading, a peak-shear stress $\tau_x = \tau_y = 0.05\ N/mm^2$ is calculated.

Beyond peak, due to an increasing lateral displacement, and a decreasing normal force an increased value of τ is estimated. The $\tau - \Delta l_{axial}$ curve from fig. A6.2. shows a similar shape as a typical $\Delta l_{lateral} - \Delta l_{axial}$ curve for a uniaxial compressed specimen.

Similar calculations have been carried out for the triaxial loaded specimens. In table A6.3, the calculated shear-stresses, and their orientation for specimen 8B2-4 and 9A2-4 are given. The orientation of the cubes in the triaxial machine is clarified in figure A6.4.

8B2-4 $\sigma_1/\sigma_2/\sigma_3$ = -1/0.33/-0.05, C, para.
σ_2 is situated in the vertical loading axis, stress-strain-curve, fig. 5.11., fracture mode; pronounced shear-planes (fig.5.13.a.)

measured values

	σ_1	σ_2	σ_3	Δl_1	Δl_2	Δl_3
		(N/mm^2)			(mm)	
peak	-85.59	-26.27	-4,62	-1.027	0.014	0.689
desc.branch $0.6\sigma_{peak}$	-33.09	-11.28	-1.95	-1.943	0.133	2.923

9A2-4 $\sigma_1/\sigma_2/\sigma_3$ = -1/-0.10/-0.05, M, para.
σ_2 is situated in the vertical loading axis, stress-strain curves, fig. 5.11., fracture mode: multiple oriented shear planes, fig. 5.13.b.

measured values

	σ_1	σ_2	σ_3	Δl_1	Δl_2	Δl_3
		(N/mm^2)			(mm)	
peak	-67.06	-6.7	-3.91	-0.774	0.268	0.384
desc. branch $0.6\sigma_{peak}$	-39.91	-4.0	-2.53	-2.411	1.729	2.976

calculated shear-stresses
(maximum value at brush-edge)

	τ_{ij} (N/mm^2)			
	8B2-4		9A2-4	
	peak	desc.br.	peak	desc.br.
τ_{12}(1)			0.26	2.44
τ_{13}	0.24	2.21	0.19	2.10
τ_{21}	0.83	1.80	0.75	2.38
τ_{23}	0.56	2.72	0.37	2.93
τ_{31}	0.67	1.94	0.76	2.41
τ_{32}			0.53	3.45

(1) See fig. A6.4.

Table A6.3. Calculated boundary shear-stresses for specimens 8B2-4 and 9A2-4.

The shear-stresses are calculated at the maximum-loading level for both specimens, and also at the end of the descending branch, just before terminating the experiment. (respectively at 0.4. $\sigma_{1,peak}$ for 8B2-4, and 0.6. $\sigma_{1,peak}$ for 9A2-4).

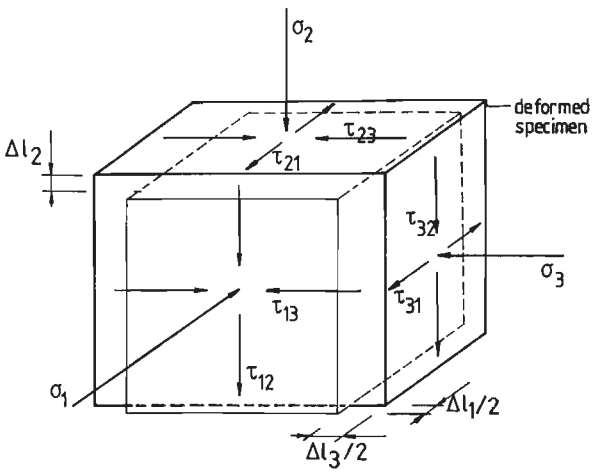

Δl_1 compressive deformation (symmetric)
Δl_2 tensile deformation (asymmetric)
Δl_3 " " (symmetric)

8B2-4 $\sigma_1/\sigma_2/\sigma_3$ = -1.0/-0.33/-0.05
9A2-4 $\sigma_1/\sigma_2/\sigma_3$ = -1.0/-0.10/-0.05

Fig. A6.4. Orientation and shear-stresses for specimens 8B2-4 and 9A2-4.

The effects are similar to the results obtained for the uniaxial loaded specimen. Only the shear-stresses at maximum load have increased considerably, when compared with the uniaxial test.
Another important aspect is apparent from the calculations. Due to the fact that the vertical displacement of the loading-frames with respect to each other is prevented, a deviation of the actual specimen load from the measured load will result. This is due to the non-symmetric shear-forces at the specimen boundary in the vertical direction, as shown in figure A6.4. The effect is mainly dependent on the level of the deformations in the vertical loading axis.

In general, the direction with the smaller deformation, was kept in the vertical loading axis. At peak-stress-level, (values tabulated in appendix A5), the deviations are generally negligible. In the descending branch however, as may be obvious from table A6.3, the deviations increase considerably. The complete loading conditions for the triaxial experiments are summarized in table A5.2, and should be used for modelling the post-peak behaviour.

The analysis and results shown in this section may be a little exaggerated, while the vertical axis is not completely fixed, and also the 'elastic deformation' of the frame should be taken into account!

APPENDIX A7 Results of rotation tests, series 7.

Specimen no.	loading-path (1)	loading-direction	σ_{1p}	σ_{2p} (N/mm^2)	σ_{3p}	ε_{1p}	ε_{2p} (o/oo)	ε_{3p}
7A1-2	planar	perp.	-74.29	-37.41	- 0.93	-3.46	-0.90	3.14
90°(2)			- 1.05	-36.17	-72.62	3.21	-1.10	-4.47
7A1-3	cylindrical	perp.	-53.46	- 1.02	- 1.14	-2.53	0.85	1.45
90°			- 1.02	- 1.02	-42.90	1.41	4.52	-3.84
7A1-4	cylindrical	para.	-55.67	- 1.00	- 1.41	-3.11	1.26	1.32
90°			- 3.37	- 1.01	-47.57	3.32	4.36	-5.29
7A1-6	planar	para.	-78.24	-39.16	- 0.92	-4.07	-0.81	3.09
90°			- 1.07	-34.05	-67.79	4.23	-0.95	-4.01
7A2-3	$\sigma_1/\sigma_2/\sigma_3$ = -1/0/0	para	-42.51					
7A2-4	$\dot{\varepsilon}_1 = 20.10^{-6}$/s, $\sigma_2 = \sigma_3$ = -1 N/mm^2, cyclic.	para.	-50.27	- 1.01	- 0.97	-3.10	1.54	1.93
7A-K1	cylindrical	$\varphi = 30°$	-46.58	- 0.94	- 1.01	-2.69	1.29	1.52
			- 0.85	- 0.95	-37.11	1.63	6.59	-3.80
7A-K2	$\dot{\varepsilon}_1 = 10.10^{-6}$/s $\sigma_2 = \sigma_3$ = -1 N/mm^2 monotonic	para.	-48.27	- 1.03	- 0.84	-2.94	1.56	1.18
7A-K3	$\sigma_1/\sigma_2/\sigma_3$ = -1/0/0	para	-45.16					
7B-K1	$\sigma_1/\sigma_2/\sigma_3$ = -1/0/0	para.	-44.47					
7B-K2	$\sigma_1/\sigma_2/\sigma_3$ = -1/0/0	para	-44.06 (loaded to 92% σ_{1p} in descending branch)					
7B-K22	cylindrical	$\varphi = 0°$	-43.55	- 0.96	- 0.81	-3.38	2.48	2.56
90°			- 1.01	- 0.96	-35.76	2.49	5.62	-3.55
7B-K3	$\sigma_1/\sigma_2/\sigma_3$ = -1/0/0	para.	-43.18 (loaded to 62% σ_{1p} in descending branch)					
7B-K32	cylindrical	$\varphi = 30°$	-31.87	- 0.99	- 0.86	-5.57	3.94	3.18
90°			- 0.93	- 0.98	-28.36	1.83	9.20	-4.88

(1) see also fig. 7.2.

(2) peak results after 90 deg. rotation $\sigma_1 \rightarrow \sigma_3$.

Table A7.1. Results of rotation tests, series 7.

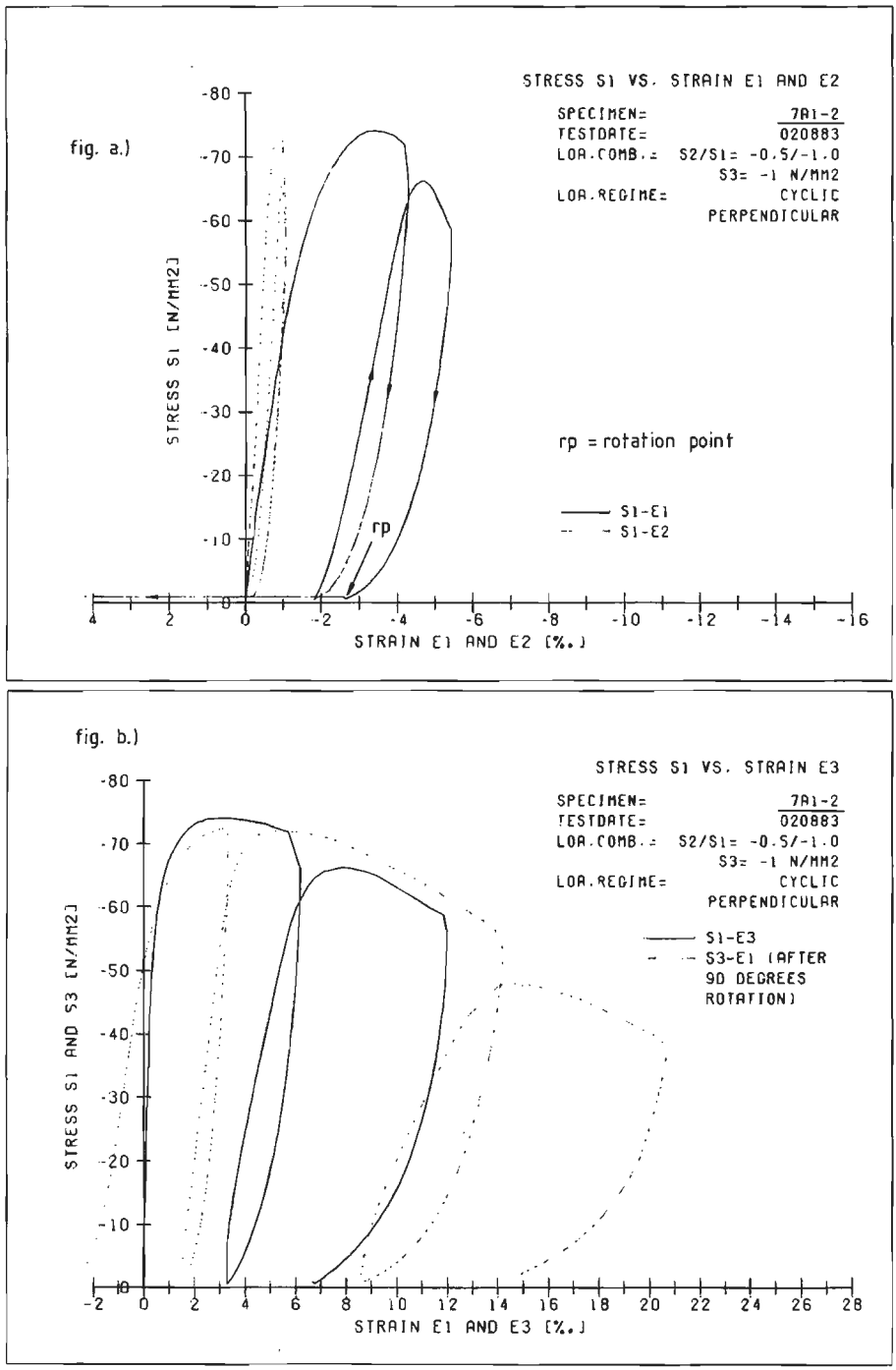

Fig.A7.2 a. Planar mode rotation test 7A1-2, loa. dir. perpendicular, $\sigma_1 - \varepsilon_1$ and $\sigma_1 - \varepsilon_2$ curves.

b. idem, $\sigma_1 - \varepsilon_3$ and $\sigma_3 - \varepsilon_1$ curves.

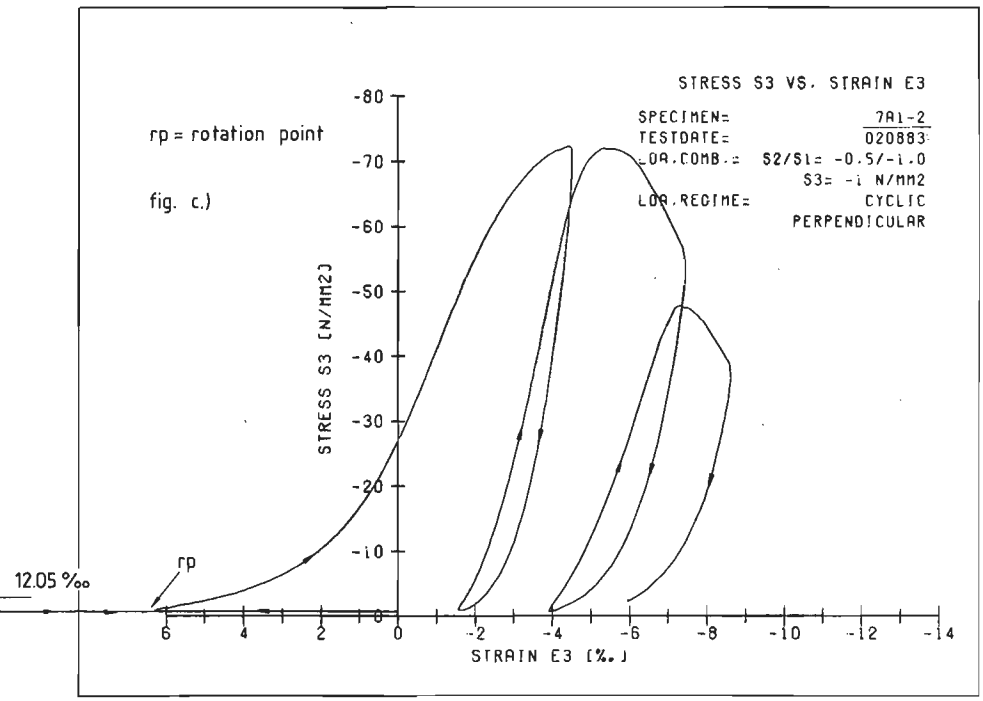

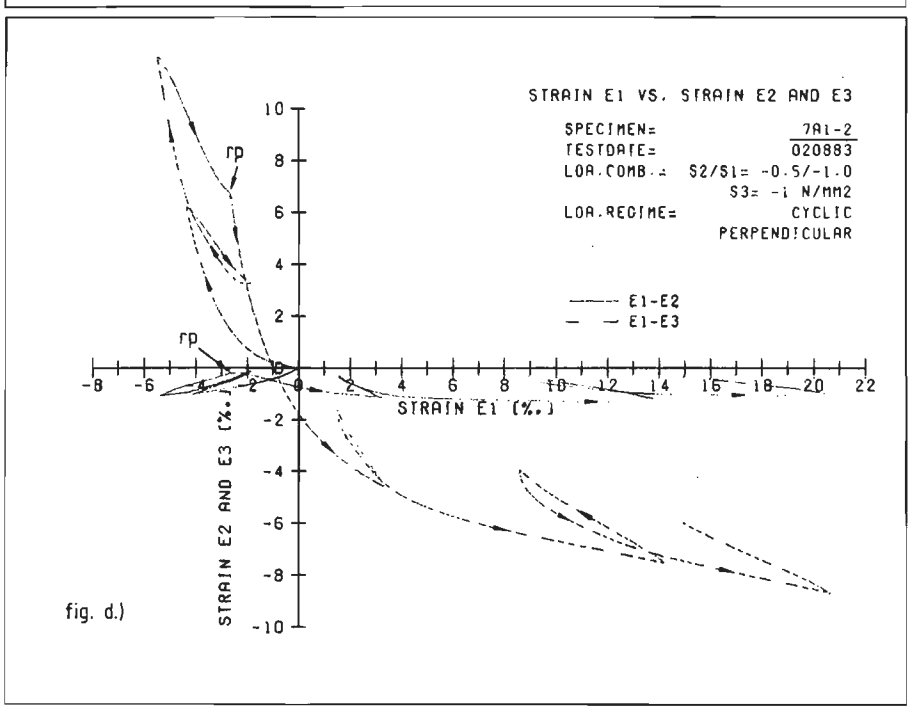

Fig.A7.2 c. Planar mode rotation test 7A1-2, loa. dir. perpendicular, $\sigma_3 - \varepsilon_3$ curve.

d. idem, strainpaths $\varepsilon_1 - \varepsilon_2$ and $\varepsilon_1 - \varepsilon_3$.

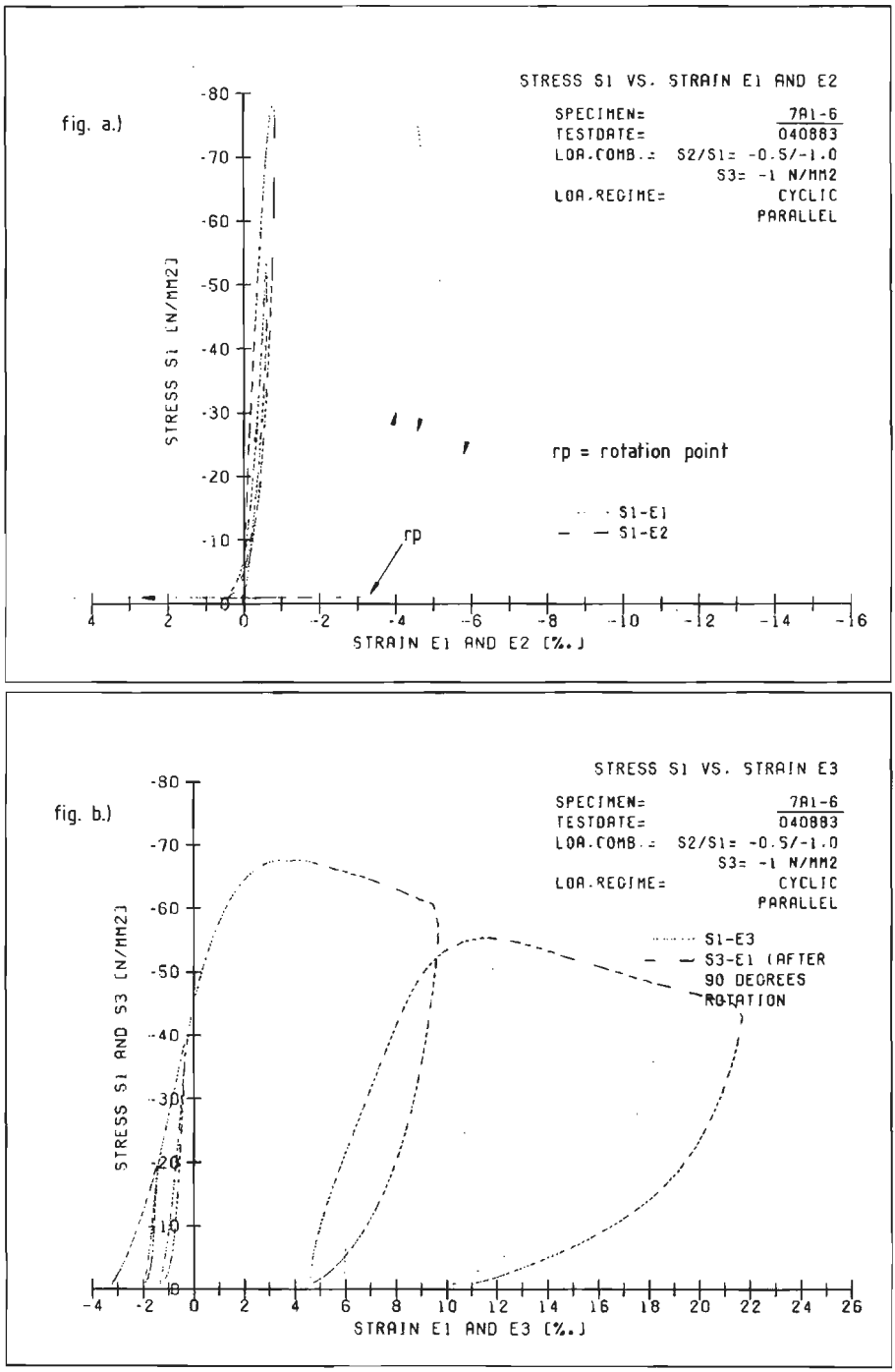

Fig.A7.3 a. Planar mode rotation test 7A1-6, loa.dir. parallel, $\sigma_1 - \varepsilon_1$ and $\sigma_1 - \varepsilon_2$ curves.

b. idem, $\sigma_1 - \varepsilon_3$ and $\sigma_3 - \varepsilon_1$ curves.

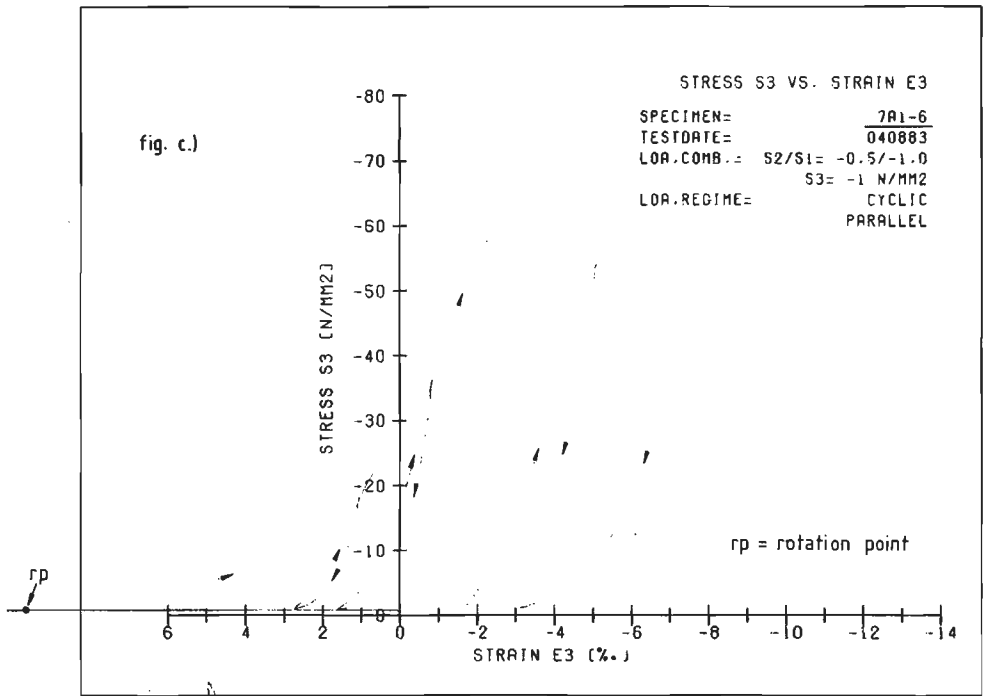

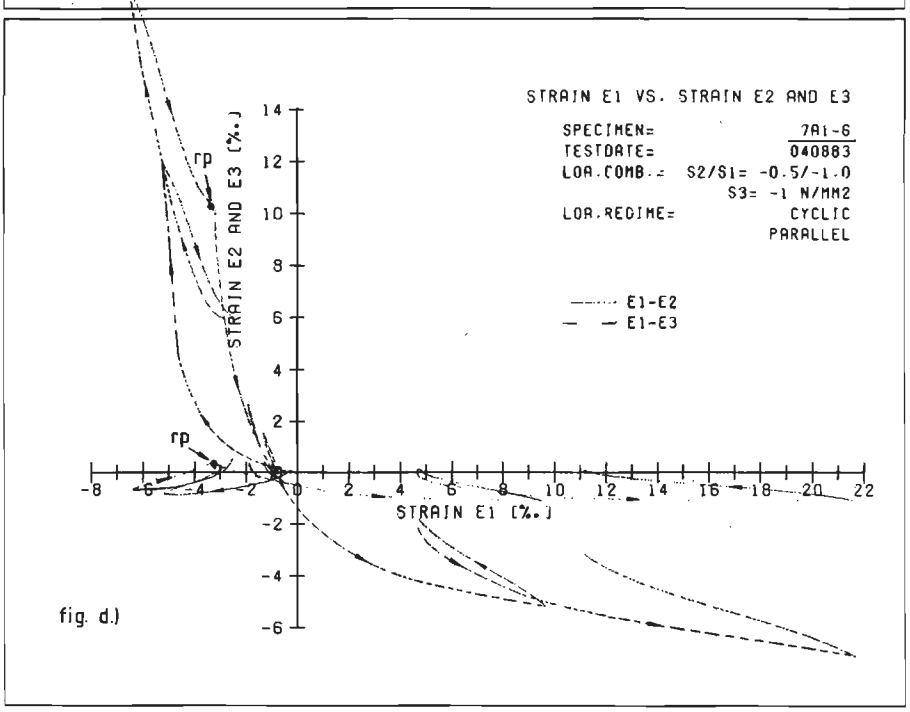

Fig.A7.3 c. Planar mode rotation test 7A1-6, loa.dir. parallel, $\sigma_3 - \varepsilon_3$ curve.
d. idem, strainpaths $\varepsilon_1 - \varepsilon_2$ and $\varepsilon_1 - \varepsilon_3$.

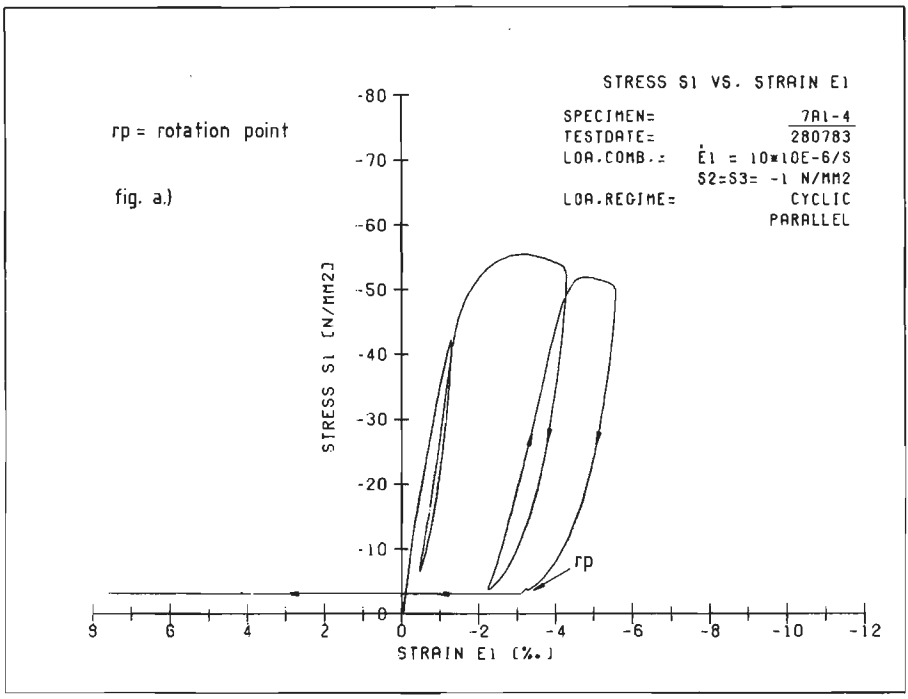

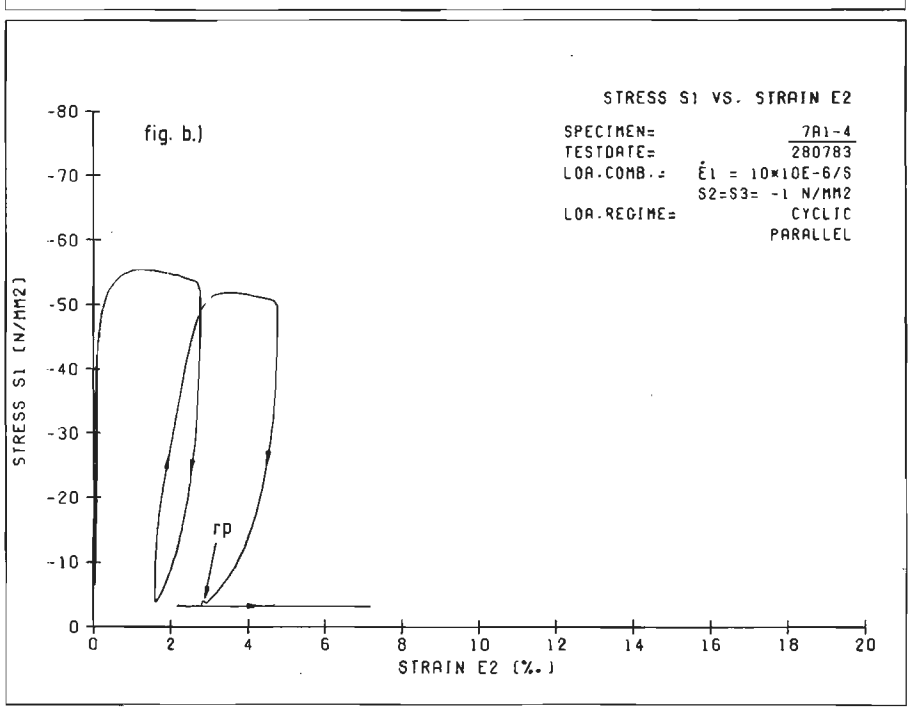

Fig.A7.4 a. Cylindrical mode rotation test 7A1-4, loa. dir. parallel, $\sigma_1 - \varepsilon_1$ curve.

b. idem, $\sigma_1 - \varepsilon_2$ curve.

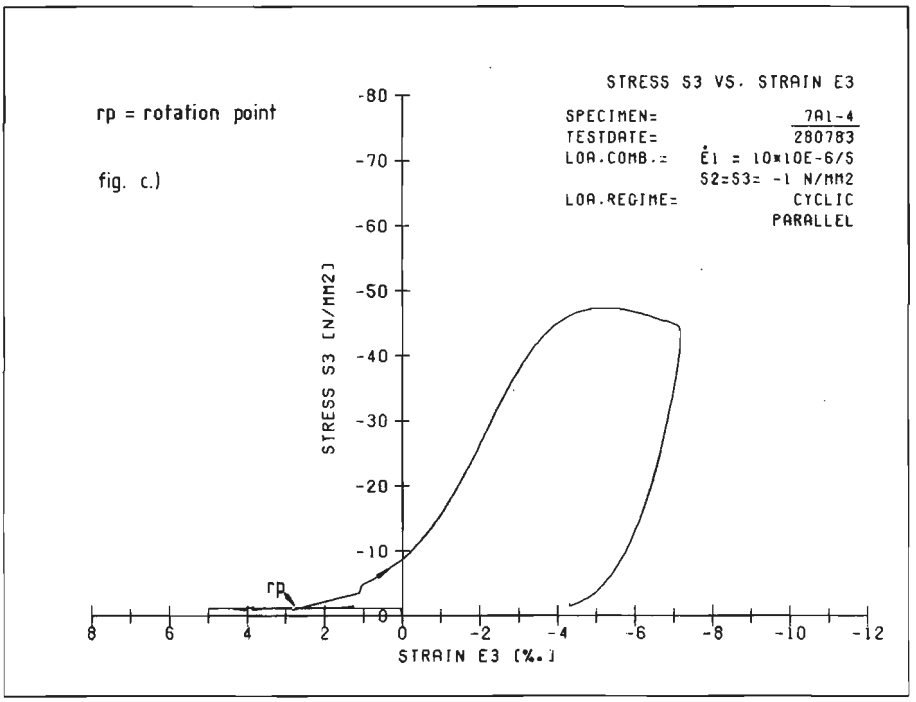

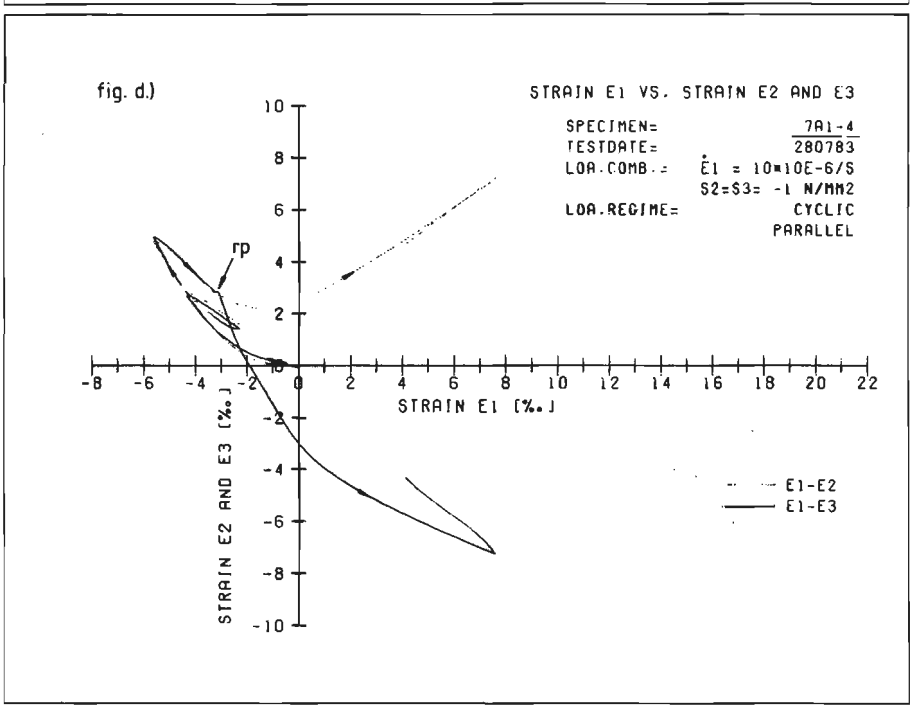

Fig.A7.4 c. Cylindrical mode rotation test 7A1-4, loa.dir. parallel, $\sigma_3 - \varepsilon_3$ curve.

d. idem, strainpaths $\varepsilon_1 - \varepsilon_2$ and $\varepsilon_1 - \varepsilon_3$.

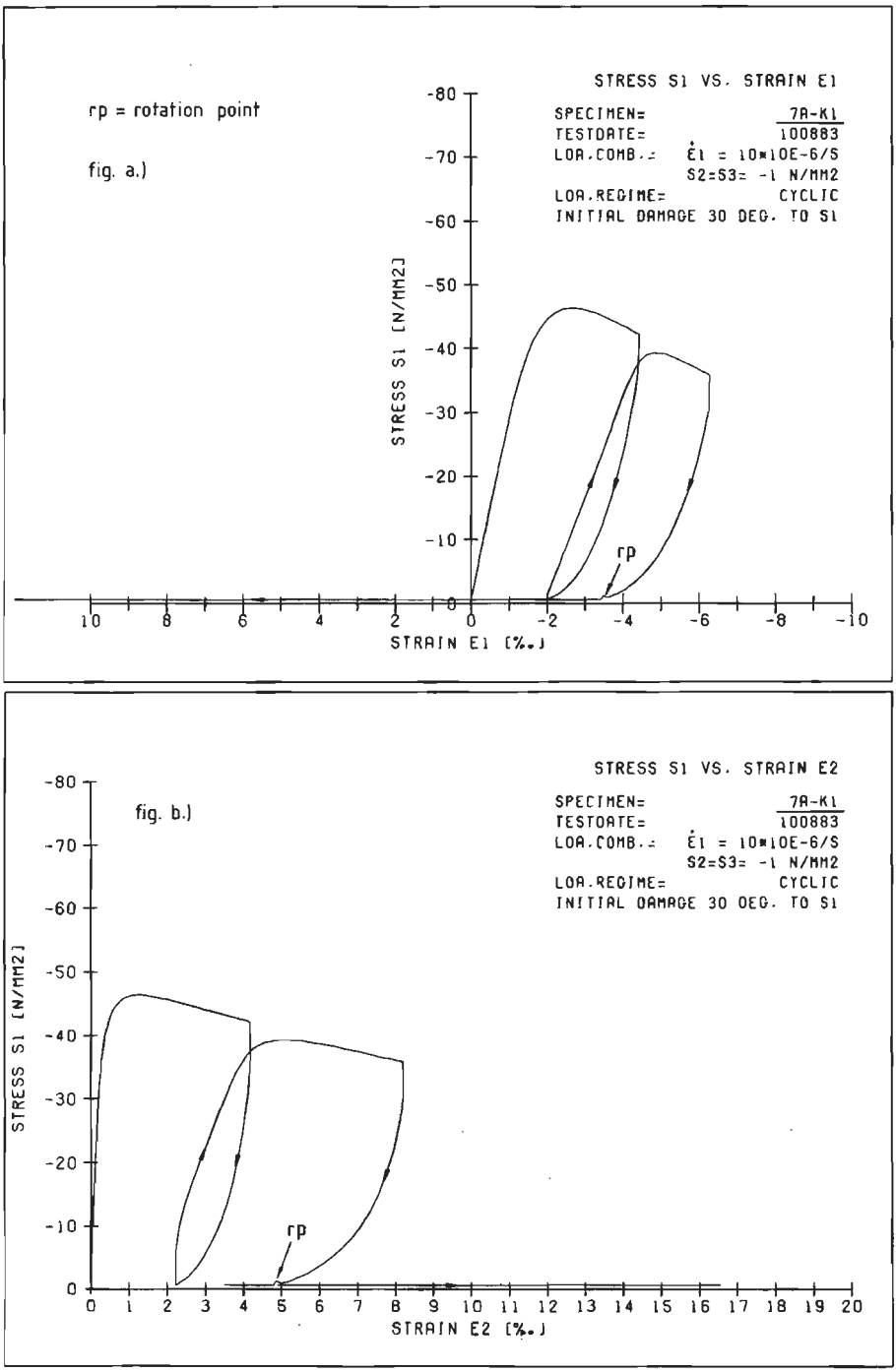

Fig.A7.5 a. Cylindrical mode rotation test 7A-K1, initial damage orientation $\varphi = 30^0$, $o_1 - \varepsilon_1$ curve.

b. idem, $o_1 - \varepsilon_2$ curve.

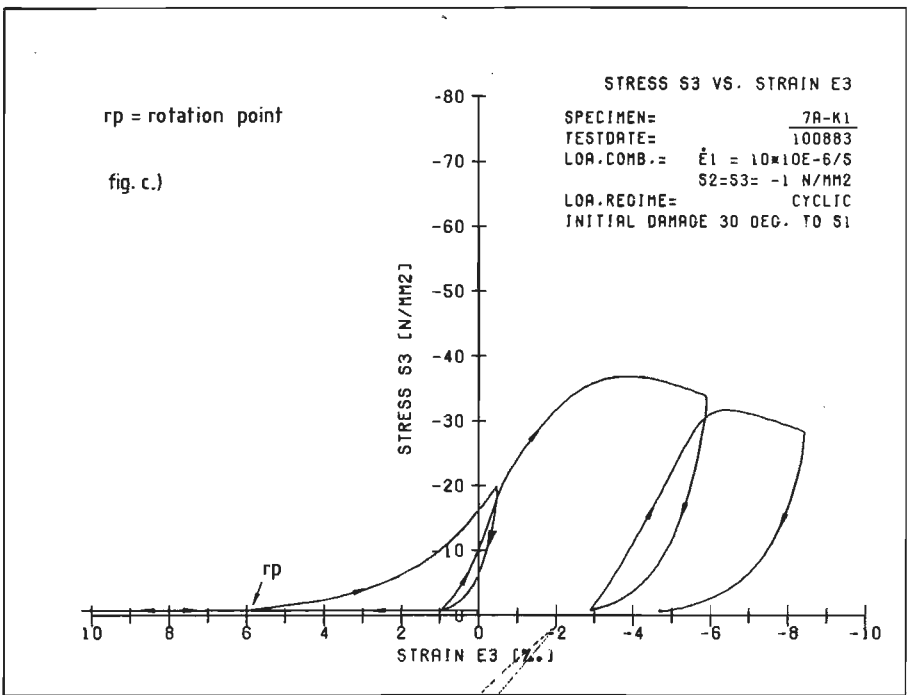

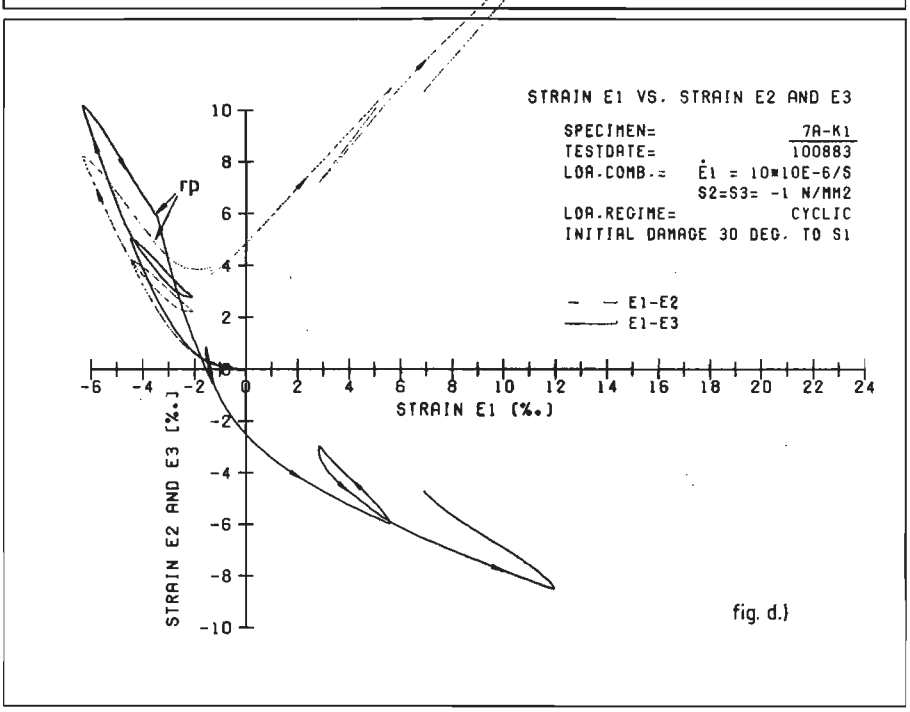

Fig.A7.5 c. Cylindrical mode rotation test 7A-K1, initial damage orientation $\varphi = 30^{o}$, $\sigma_3 - \varepsilon_3$ curve.

d. idem, strainpaths $\varepsilon_1 - \varepsilon_2$ and $\varepsilon_1 - \varepsilon_3$.

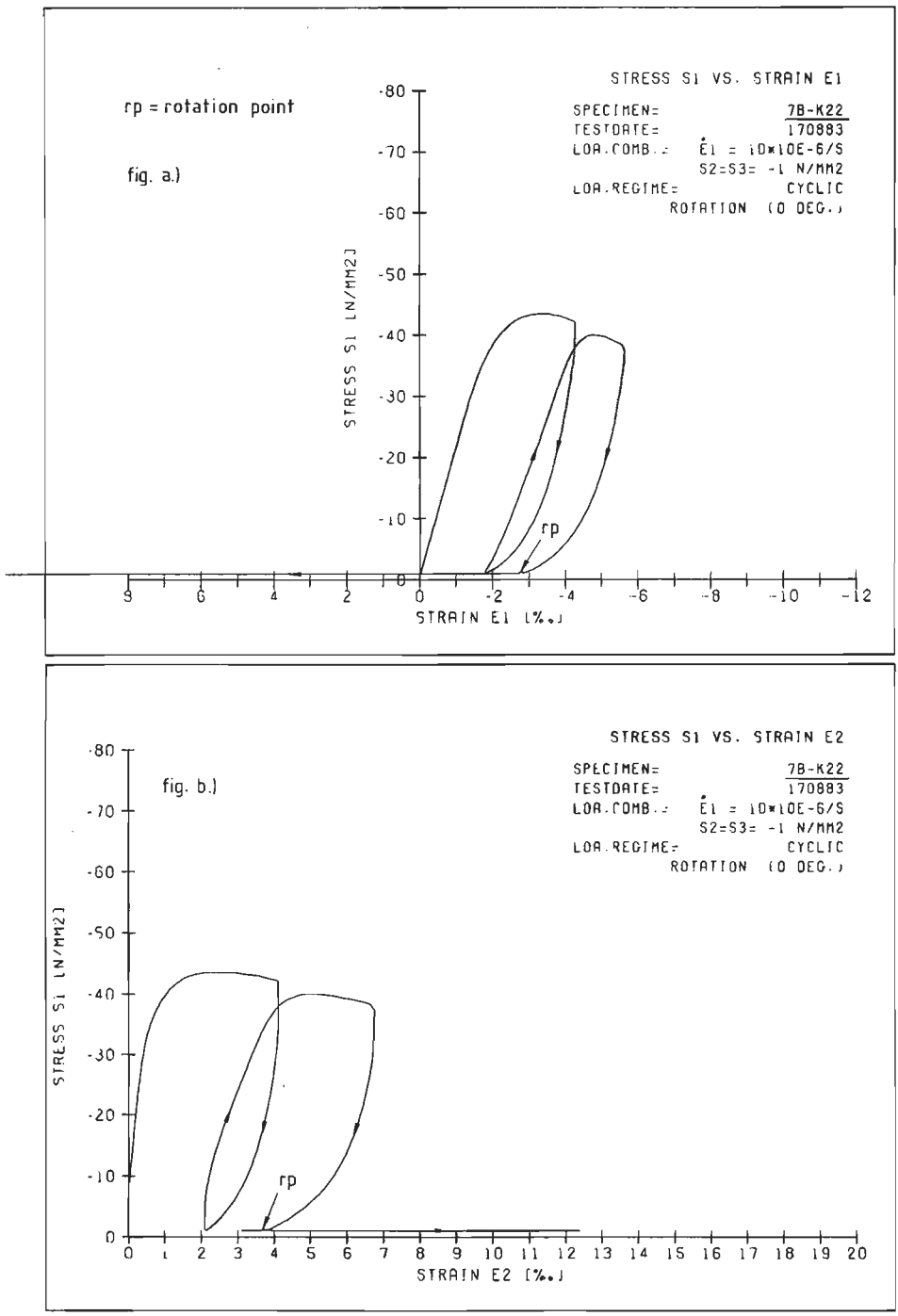

Fig.A7.6 a. Cylindrical mode rotation test, 7B-K22, pre-cracked, orientation $\varphi = 0^{o}$, $\sigma_1 - \varepsilon_1$ curve.

b. idem, $\sigma_1 - \varepsilon_2$ curve.

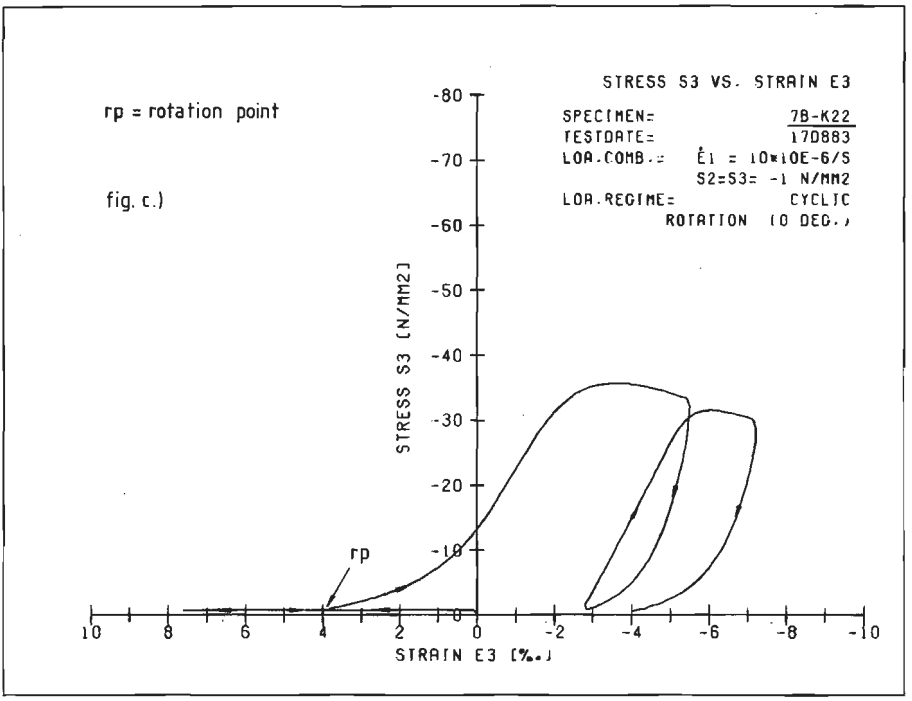

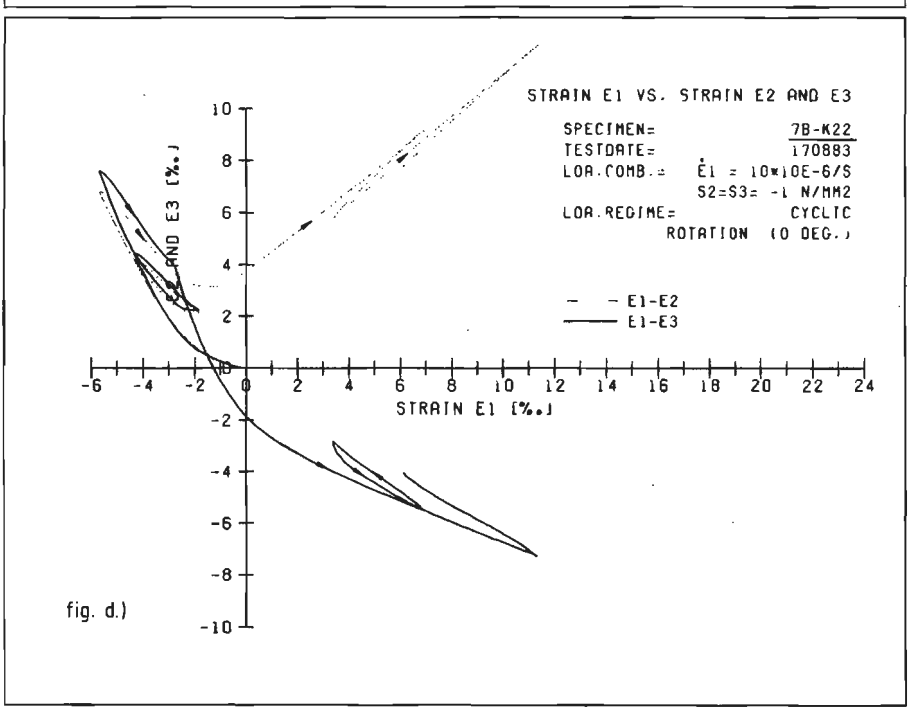

Fig.A7.6 c. Cylindrical mode rotation test, 7B - K22, pre-cracked, orientation $\varphi = 0^{o}$, $\sigma_3 - \varepsilon_3$ curve.

b. idem, strainpaths $\varepsilon_1 - \varepsilon_2$ and $\varepsilon_1 - \varepsilon_3$.

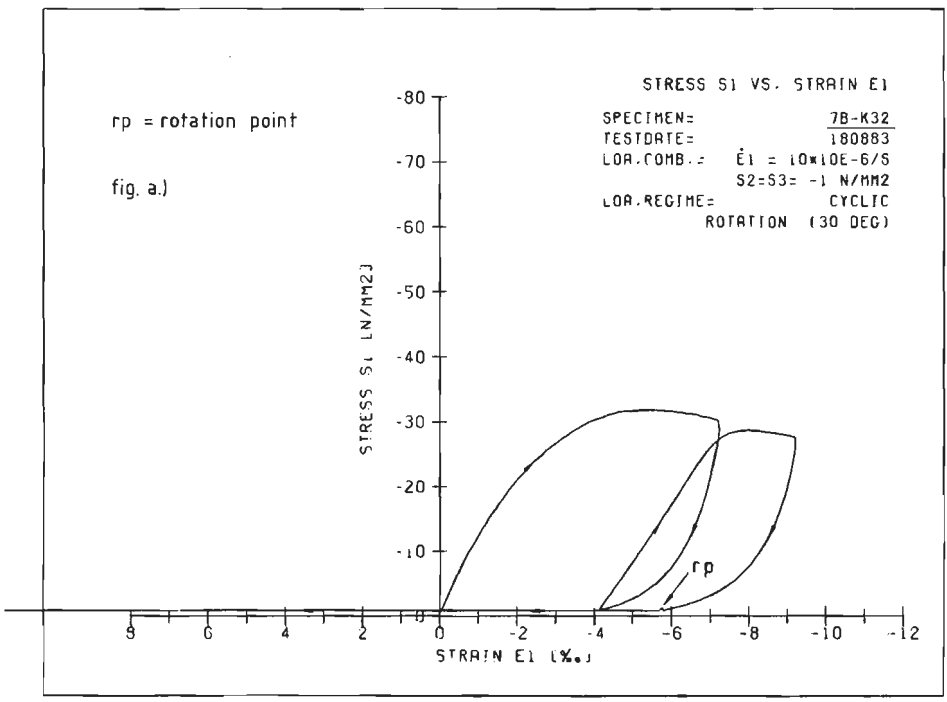

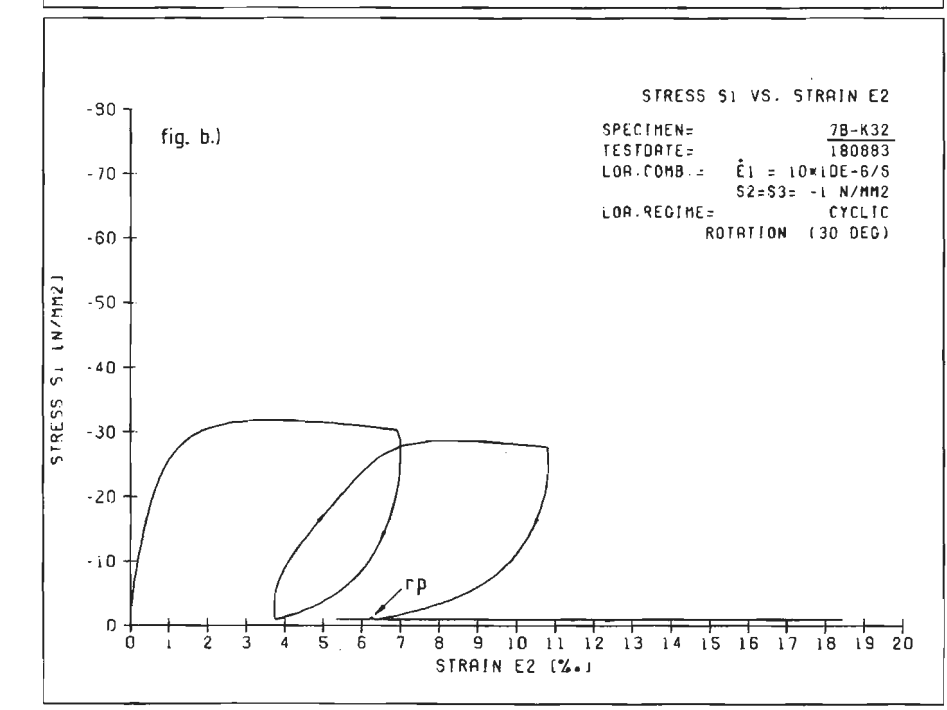

Fig.A7.7 a. Cylindrical mode rotation test 7B - K32, pre-cracked, orientation $\varphi = 30^{0}$, $\sigma_1 - \varepsilon_1$ curve.

b. idem, $\sigma_1 - \varepsilon_2$.

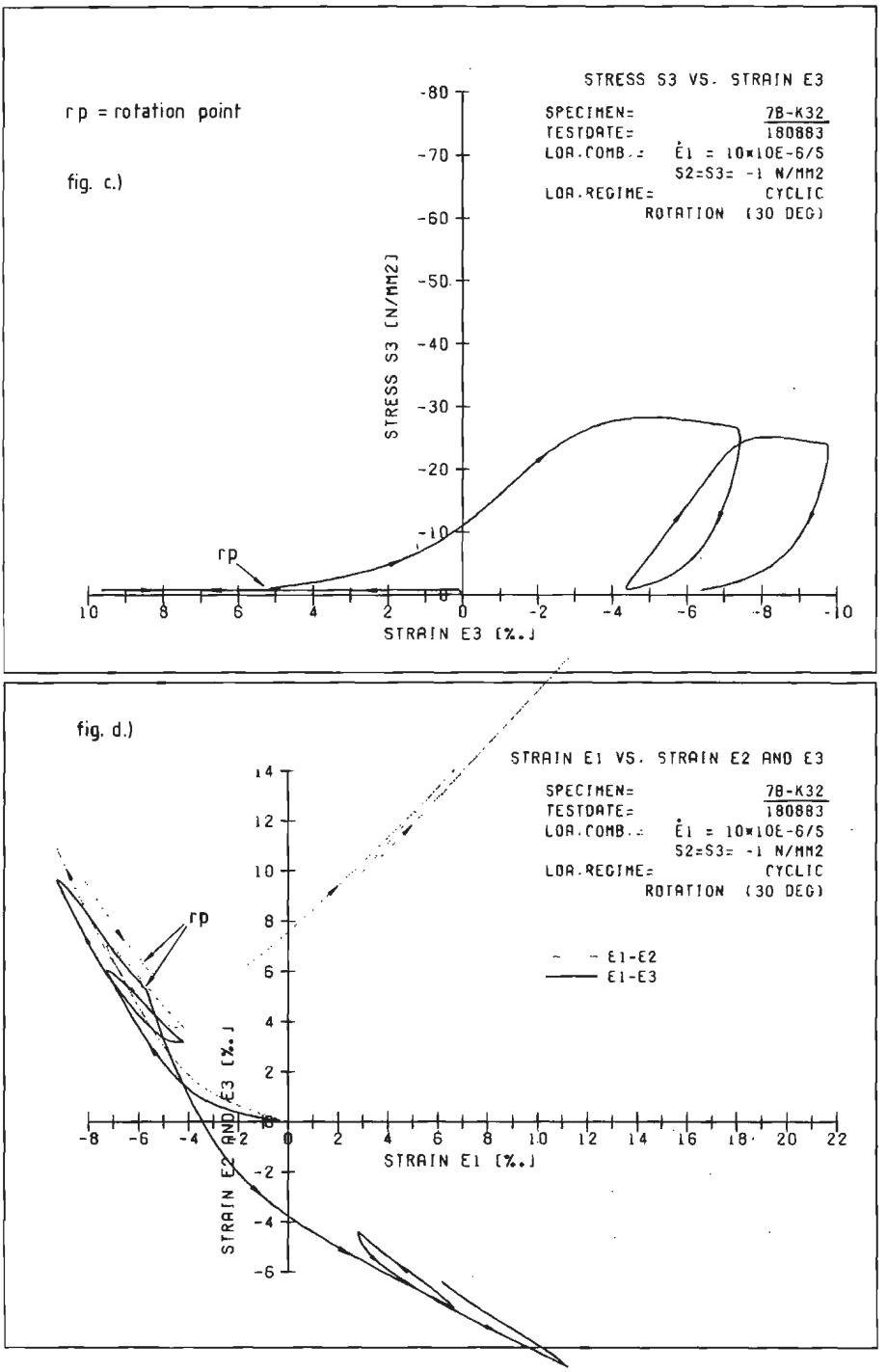

Fig.A7.7 c. Cylindrical mode rotation test, 7B - K32, pre-cracked, orientation $\varphi = 30^0$, $\sigma_3 - \varepsilon_3$ curve.

d. idem, strainpaths $\varepsilon_1 - \varepsilon_2$ and $\varepsilon_1 - \varepsilon_3$.

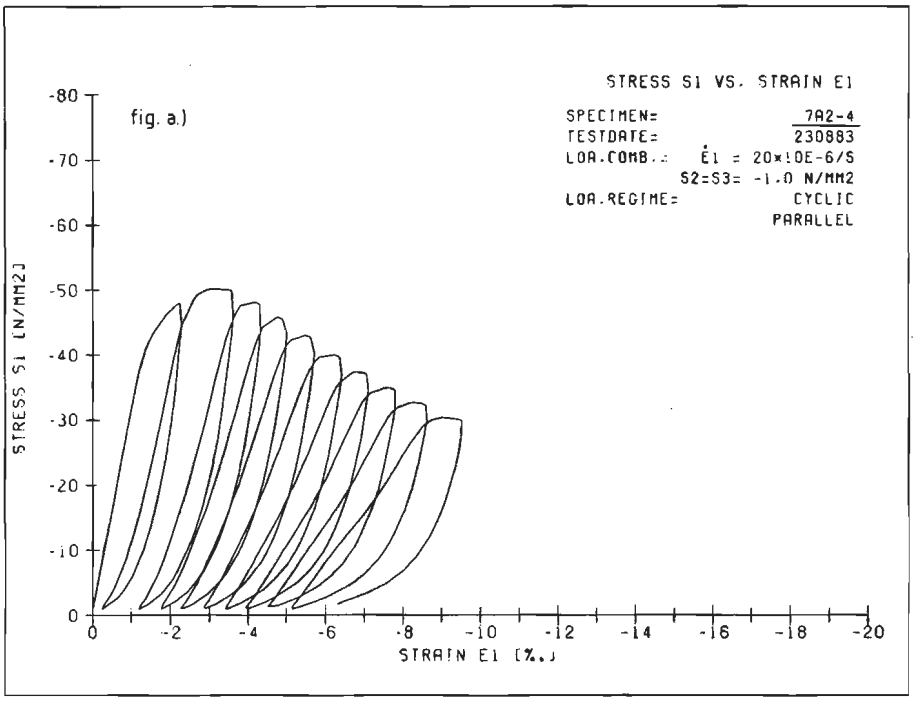

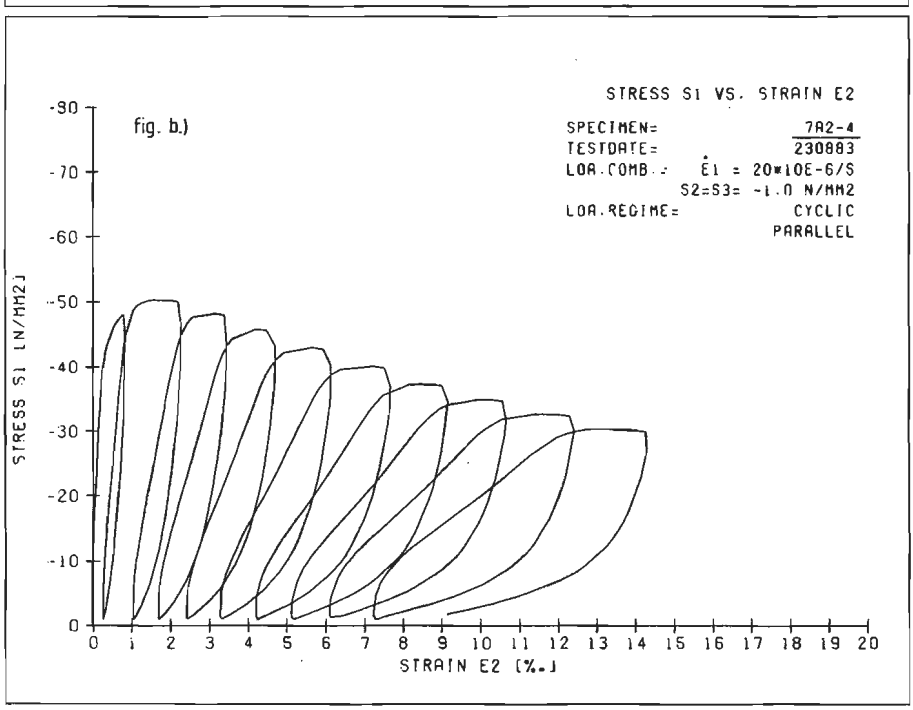

Fig.A7.8 a. Triaxial compression test 7A2-4, cyclic, parallel, $\sigma_1 - \varepsilon_1$ curve.
b. idem, $\sigma_1 - \varepsilon_2$ curve.

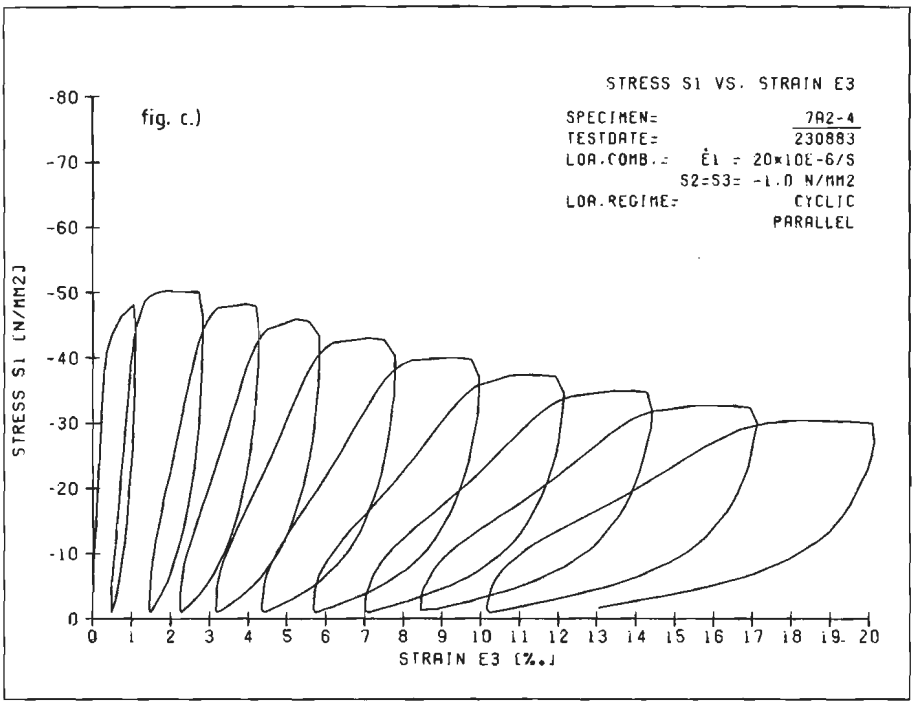

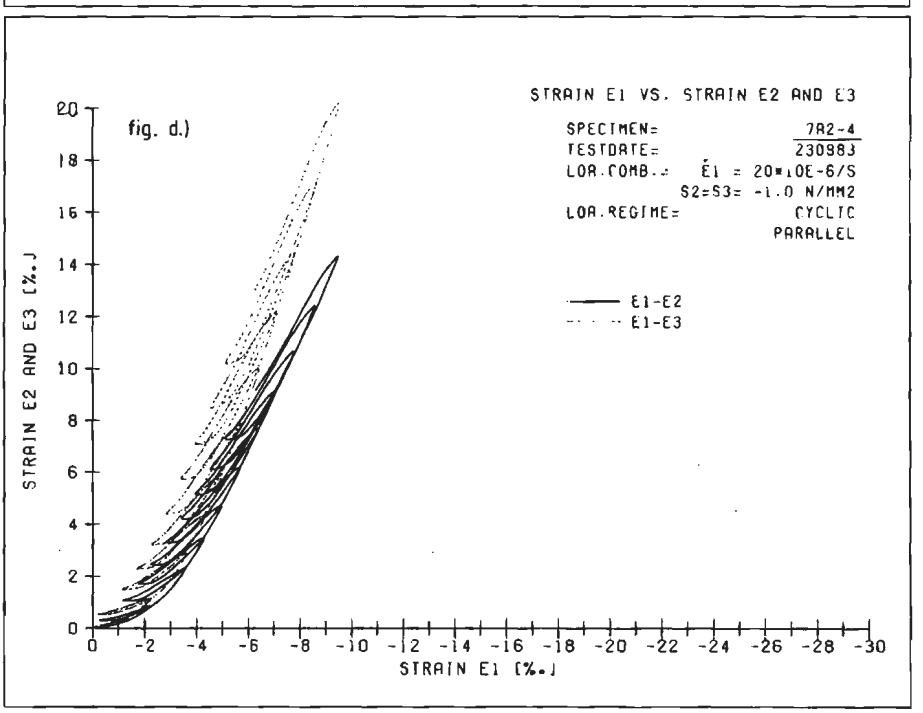

Fig.A7.8 c. Triaxial compression test 7A2-4, cyclic, parallel, $\sigma_1 - \varepsilon_3$ curve.
d. idem, strainpaths $\varepsilon_1 - \varepsilon_2$ and $\varepsilon_1 - \varepsilon_3$.

Stellingen behorende bij het proefschrift van
J.G.M. van Mier

1. Het bezwijken van beton, onderworpen aan een drie-assige drukspanningstoestand is een lokaal verschijnsel. De afmetingen van het proefstuk en de opgelegde belastingscombinatie bepalen de afmetingen van de reststukken.

2. Een drie-assige kubusproef wordt veelal bestempeld als zijnde 'true-triaxial'. Een spanningstoestand bestaande uit normaal- en schuifspanningen wordt daarbij vertaald in hoofdspanningen. Het ontstaan van georiënteerde beschadiging maakt echter dat een onbeperkte vertaling in hoofdspanningen niet is toegestaan.

3. Sterkte is geen vaste grootheid, maar is afhankelijk van structurele veranderingen in het materiaal. Een goed constitutief model beschrijft een 'sterkte' bezwijkomhullende, op basis van deze structurele veranderingen.

4. De stellingname van Kotsovos, dat de beste modellering van de dalende tak van het spannings-vervormings diagram voor beton die voor een ideaal bros materiaal zou zijn, is onjuist.

   Kotsovos, M.D., RILEM, Mat. & Struct.,
   vol. 16, no. 91, (1983).

   Dit proefschrift, hoofdstuk 4.

5. Bij het modelleren van de dalende tak van het spannings-vervormings diagram van beton, kunnen de randvoorwaarden van het experiment waaraan het model wordt getoetst, niet worden verwaarloosd.

6. Beton gedraagt zich onder drie-assige drukspanningstoestanden hetzelfde als sommige soorten rots.

7. De 'fundamentele bouwstenen' zoals deze in het nederlandse betonmechanica project worden onderscheiden, zijn ten onrechte als fundamenteel benoemd.

Betonmechanica, deel 1,
CUR-VB rapport 114, maart 1984.

8. Het tijdsaspect in een vierjarig experimenteel technisch promotie-onderzoek maakt adequate technische ondersteuning tot een eerste vereiste. Het is de vraag in hoeverre het onderzoek hiervan afhankelijk mag zijn.

9. Er bestaat een overeenkomst tussen de in dit proefschrift beschreven experimenten en bergbeklimmen: het uitzicht over de top is adembenemend en werkt zeer verruimend.

10. Een jaar ervaring in het buitenland is een noodzaak voor elke wetenschappelijk onderzoeker.

11. Een kabinet bestaande uit voornamelijk economen is een ernstige belemmering voor fundamenteel wetenschappelijk onderzoek.

12. In het licht van de huidige toestand op de binnenlandse arbeidsmarkt, is de eis dat een onderzoeker na een jaar verblijf aan een buitenlandse universiteit moet terugkeren in Nederland niet gerechtvaardigd.

13. Het verschil tussen een politicus en een onderzoeker is dat de eerste meent dat hij een zeker antwoord op een vraag geeft, terwijl de tweede er zeker van is dat dit niet mogelijk is.